Diffusion Tensor Imaging

A Practical Handbook

Wim Van Hecke
Louise Emsell
Stefan Sunaert
Editors

Springer

Diffusion Tensor Imaging

Wim Van Hecke
Louise Emsell • Stefan Sunaert
Editors

Diffusion Tensor Imaging

A Practical Handbook

Springer

Editors
Wim Van Hecke, PhD
icometrix
Leuven, Belgium

Department of Radiology
Antwerp University Hospital
Antwerp, Belgium

Stefan Sunaert, MD, PhD
Departments of Translational MRI and Radiology
KU Leuven and University Hospitals Leuven
Leuven, Belgium

Louise Emsell, PhD
Departments of Translational MRI and Radiology
KU Leuven and University Hospitals Leuven
Leuven, Belgium

Department of Old Age Psychiatry
Universitair Psychiatrisch Centrum (UPC) - KU Leuven
Leuven, Belgium

ISBN 978-1-4939-3117-0 ISBN 978-1-4939-3118-7 (eBook)
DOI 10.1007/978-1-4939-3118-7

Library of Congress Control Number: 2015954570

Springer New York Heidelberg Dordrecht London

Printed on acid-free paper

Springer Science+Business Media LLC New York is part of Springer Science+Business Media (www.springer.com)

Foreword

In the mid-1980s, some 30 years ago, investigators first developed the notion that magnetic resonance imaging (MRI) could be used to provide information about molecular diffusion in tissues. The concept of measuring diffusion was visionary, but the practical implementation turned out to present formidable challenges. It was a time when most MRI systems were operating at a field strength of 0.5 T and gradient hardware was not well developed; as a result, early diffusion images suffered from a very poor signal to noise ratio and were severely degraded by eddy currents and motion artifacts. The first trials were not very successful and the outcomes were rather disappointing. Moreover, the radiological community did not fully understand the potential of this technique, and many eminent scholars were doubtful that it would ever be possible to measure diffusion in the human body.

Slowly, but steadily, technical limitations were overcome. Vendors developed MRI scanners with higher field strength, improved magnet homogeneity, steeper gradients, decreased eddy currents, etc. By the middle to late 1990s, it became possible to produce good quality diffusion-weighted images (DWI) with "b-values" of up to 1000 s/mm^2. The "b-value" is a measure of the sensitivity to diffusion and depends on the intensity, duration, and time interval of the diffusion gradient pulses as well as on the gyromagnetic ratio. In DWI images, the intensity of each voxel reflects the magnitude (or rate) of water diffusion in that specific location. However, these images not only reflect "true" diffusion, but are also affected by "confounders" such as perfusion effects; this led to the introduction of the concept of the apparent diffusion coefficient (ADC). The higher the "b-value," the more the signal intensity reflects "true" tissue water diffusion changes. In DWI, the diffusion gradients are applied in three orthogonal directions (simultaneously); this allows an estimation of the "trace," which is an indicator of the average diffusivity. Trace-weighted diffusion images initially found their main area of application in neurological disorders, especially for the early detection of the cytotoxic edema associated with acute ischemic stroke. Since about 15 years ago, DWI has become a crucial part of routine clinical MRI examinations of the brain, and, increasingly, other organs.

Diffusion-weighted sequences provide information about the magnitude of free water diffusion in tissues. However, already in the early 1990s, it became clear that diffusion in white matter of the brain was anisotropic, depending on the orientation of nerve fibers. This observation led to the notion that diffusion-weighted techniques could be modified to provide additional information about the directionality and other properties of diffusion, at a microstructural level. In this way, diffusion tensor imaging (DTI) was born, where diffusion is probed in many more directions (typically >30) to describe the full diffusion tensor. When tissues have a complex (internal) structure, such as the bundles of myelinated axons in white matter, water diffusion occurs more rapidly along the longitudinal direction of these axonal fibers and more slowly when moving perpendicularly to the long axis. In order to obtain the directional information, which is essential for DTI, diffusion gradients need to be applied in at least 6 directions, and preferably more. From the acquired DTI data, metrics such as fractional anisotropy (FA) and mean diffusivity (MD) can be derived. Taking into account the main direction of the diffusion tensor, it becomes possible to extrapolate the connectivity of white matter tracts in the central nervous system. This technique is known as "tractography" and yields spectacular 3-dimensional images of the brain and spinal cord in which white matter tracts can be represented as colored spaghetti strands. In only a few years, DTI has emerged as the foremost technique for white matter disorders, revealing abnormalities in white matter fiber structure and providing maps of brain connectivity.

Unfortunately, for many newcomers (and even for more experienced professionals), the boundaries between the general field of DWI and the specific world of DTI are somewhat fuzzy. The complexities of DTI are difficult to fathom because of the advanced mathematics and physics involved in this technique. Moreover, it is always hard to see the forest for the trees; people have a natural tendency to focus on the many details and fail to see the overall view. This book aims at filling the knowledge gap between basic science and clinical applications of DTI. The editors have conceived this textbook as a practical manual, which covers the different steps of a DTI study, and provides advice and guidance toward optimization of the process. It is intended for radiologists, clinicians, technologists, and neuroscientists. Readers will learn tips and tricks and become familiar with the advantages and disadvantages of this complex diagnostic technique. The focus of the book is to help practitioners, in each clinical situation, to choose the parameters that are most likely to address the diagnostic issues and to guide clinical management. All chapters have been written by a team of experienced and well-known specialists in the field of DTI. The editors, Wim Van Hecke, Louise Emsell, and Stefan Sunaert, have done an excellent job to integrate the various contributions and to provide a comprehensive update of current knowledge and future developments of DTI.

We trust this book will inspire readers to learn all they can about the basic science and clinical applications of DTI, and that this knowledge will ultimately lead to the delivery of better health care to our patients.

Paul M. Parizel, MD, PhD
Professor of Radiology
University of Antwerp
Chair, Department of Radiology
Antwerp University Hospital
Antwerp, Belgium

Frederik Barkhof, MD, PhD
Professor of Neuroradiology
Director, Image Analysis Center (IAC)
Department of Radiology and Nuclear Medicine
VU University Medical Center
Amsterdam, The Netherlands

Preface

It is generally accepted that the best way to elicit an honest opinion is to ask a child. Having conducted this experiment with our own children, we hereby bring you a practical handbook about colorful hedgehogs (sometimes also confused with whole brain diffusion tensor imaging tractograms). Hedgehogs aside, diffusion tensor imaging (DTI) is certainly one of the most colorful medical imaging techniques available, one which creates such spectacular representations of the brain that at times it appears to effortlessly blur the boundaries of art and science. Some may argue that it does this rather too effortlessly. For indeed, the beauty of DTI is also its greatest handicap; its ability to create images that nearly always look good and appear plausible makes discerning between reliable and unreliable findings extraordinarily challenging. This all the more so when the ground truth to validate them is hard to find.

On the other hand, DTI is an incredibly powerful technique for visualizing and quantifying diffusion noninvasively in a matter of minutes. Its ability to provide insights into microstructural status through enhanced visualization and quantification has yielded thousands of scientific papers relating to its application in a broad range of basic science and clinical domains, and in neurology and psychiatry in particular.

We are therefore left with the situation in which we have an exceptionally powerful, ground-breaking imaging technique that when implemented correctly can be incredibly useful, but when implemented incorrectly can, at best, yield misleading findings, and at worst, be potentially harmful. It is our aim, through writing this book, to tip the balance in favor of the former, to help people acquire and analyze DTI data optimally to generate results that do not just look reliable, but are as reliable as possible.

Our motivation for writing *Diffusion Tensor Imaging*: *A Practical Handbook* was simple: to help nonexperts come to grips with the practical aspects of DTI, from understanding the basis of the technique through selection of the right protocols, troubleshooting data quality, and analyzing DTI data optimally. We also wanted to introduce our readers to advanced non-tensor-based diffusion MRI techniques, so we have included a special section on "Beyond DTI." Also, we wanted to showcase some clinical applications of DTI while being mindful of the special challenges associated with DTI in different disorders.

About the Contents

Notably, in this book, we have chosen to focus exclusively on DTI of the brain. This is because DTI is presently the most common clinical implementation of diffusion MRI, and the brain is currently the most studied organ using the technique and hence boasts the greatest wealth of associated knowledge, validation, and clinical application. In general, the principles and strategies described in this book are also broadly applicable to non-neurologic DTI applications. For detailed knowledge, however, the reader is encouraged to consult specialist literature on the topic.

In our professional practice, we are advocates of both DTI and other forms of diffusion MRI, such as High Angular Resolution Diffusion Imaging (HARDI), higher order modeling approaches, and multi-shell diffusion imaging, which we believe are and will be increasingly important techniques in the future. We are, however, mainly advocates of choosing the *right technique for a given application* and implementing it in the *best possible way given a certain set of circumstances*. And this is the position we have taken in writing this book.

Our mantra throughout was to keep our book as short and simple as possible, unburdened by extensive theory, but without losing important detail. In this context, there are other books and atlases available which provide a much more comprehensive theoretical coverage of DTI than this book. For example, Derek Jones' much acclaimed reference book, *Diffusion MRI*: *Theory, Methods and Applications* (Oxford University Press, 2009), remains the standard reference for the field, while other textbooks provide newcomers to DTI with comprehensive theoretical introductions, notably Susumu Mori and Donald Tournier's *Introduction to Diffusion Tensor Imaging and Higher Order Models*, Second Edition (Academic Press, 2014), and Heidi Johansen-Berg and Tim Behrens book entitled *Diffusion MRI*: *From Quantitative Measurement to in vivo Neuroanatomy*, Second Edition (Academic Press, 2014). For those looking for a comprehensive DTI atlas, Bram Stieltjes, Romuald M. Brunner, Klaus Fritzsche, and Frederik Laun's *Diffusion Tensor Imaging*: *Introduction and Atlas* (Springer, 2013) is an excellent choice. We are fortunate and grateful to Bram for providing an excerpt of this atlas for our book.

What sets our book apart from these other excellent reference texts is that we have aimed for our handbook to be as practical as possible. This means that you will find far fewer equations and theoretical content here than in other DTI books, and instead more decision schemes, practical examples, and lots of images illustrating the core material.

Acknowledgments and Thanks

A book is only as good as its content and therefore we aimed to share as much expert knowledge as possible. We are thus extremely fortunate and grateful that so many experts wanted to share their knowledge with us and with our wider readership. We unreservedly thank our team of coauthors for their

contributions to our book, for being patient and responsive with and to all the revision requests and email reminders despite their busy workloads and other commitments, for sharing their enthusiasm with us, and for delivering top quality chapters. In particular, we would like to highlight our inclusion of contributions from both leading experts in the field and from emerging talents. Our contributors have lived up to all expectations and provide excellent coverage of their topics. Thank you all!

On the topic of thanks and acknowledgment, we would also like to thank Springer for inviting us to write the book in the first place and for their support during the different phases of its development and publication. We extend particular gratitude to Janet Foltin, Patti Donofrio, and Michael Sova for their continued patience, enthusiasm, support, and editorial expertise throughout the publishing process.

Personal Notes

Undertaking such an endeavor is always challenging, takes far more time than planned, and involves the support of far more people than appear on the book cover or author list. We would therefore like to thank our friends and families for all their support and particularly our children, for not being remotely interested in colorful hedgehogs. We would also like to thank our employers and colleagues at icometrix, University Hospital Antwerp, KU Leuven, and University Hospital Leuven for supporting this work and in particular for providing us with the freedom and opportunity to spend so much time working on it, especially in the final phase leading up to the deadline.

Finally, we would like to thank you, the reader, for choosing to buy and read this book. We hope that you find it as enjoyable and educational as we have during its preparation, and that it inspires you to incorporate DTI and other advanced diffusion MRI-based techniques into your future work.

Leuven, Belgium

Wim Van Hecke, PhD
Louise Emsell, PhD
Stefan Sunaert, MD, PhD

Contents

Contributors

Federica Agosta, MD, PhD Neuroimaging Research Unit, San Raffaele Scientific Institute, Vita-Salute San Raffaele University, Milan, Italy

Division of Neuroscience, Department of Neurology, Institute of Experimental Neurology, San Raffaele Scientific Institute, Vita-Salute San Raffaele University, Milan, Italy

Daniel C. Alexander, PhD Microstructure Imaging Group, Centre for Medical Image Computing, University College London (UCL), London, UK

Roland Bammer, PhD Department of Radiology, Stanford University, Stanford, CA, USA

Matthan W.A. Caan, PhD Brain Imaging Center, Academic Medical Center Amsterdam, Amsterdam, The Netherlands

Kathleen M. Curran, PhD Complex and Adaptive Systems Laboratory, University College Dublin, Dublin, Ireland

School of Medicine and Medical Sciences, University College Dublin, Dublin, Ireland

Frank De Belder, MD Department of Radiology, Antwerp University Hospital, Antwerp, Belgium

Maya De Belder, MSc Department of Experimental Psychology, University of Ghent, Ghent, Belgium

Thijs Dhollander, PhD Medical Imaging Research Center (MIRC), KU Leuven, Leuven, Belgium

The Florey Institute of Neuroscience and Mental Health, Melbourne Brain Centre, Heidelberg, VIC, Australia

Louise Emsell, PhD Departments of Translational MRI and Radiology, KU Leuven and University Hospitals Leuven, Leuven, Belgium

Department of Old Age Psychiatry, Universitair Psychiatrisch Centrum (UPC) - KU Leuven, Leuven, Belgium

Shawna Farquharson, MSc Florey Institute of Neuroscience and Mental Health, University of Melbourne, Melbourne, VIC, Australia

Uran Ferizi, PhD Microstructure Imaging Group, Centre for Medical Image Computing, University College London (UCL), London, UK

Massimo Filippi, MD, PhD Neuroimaging Research Unit, San Raffaele Scientific Institute, Vita-Salute San Raffaele University, Milan, Italy

Division of Neuroscience, Department of Neurology, Institute of Experimental Neurology, San Raffaele Scientific Institute, Vita-Salute San Raffaele University, Milan, Italy

Martijn Froeling, PhD Image Sciences Institute, University Medical Center Utrecht, Utrecht, The Netherlands

Luc van den Hauwe, MD Department of Radiology, Antwerp University Hospital, Antwerp, Belgium

Josselin Houenou, MD, PhD INSERM U955, Equipe 15 "Psychiatrie Génétique", Fondation Fondamental, AP-HP, Hôpitaux Universitaires Mondor, Créteil, France

Alexander Leemans, PhD PROVIDI Lab, Image Sciences Institute, University Medical Center Utrecht, Utrecht, The Netherlands

Andrew I.R. Maas Department of Neurosurgery, Antwerp University Hospital, University of Antwerp, Antwerp, Belgium

Elias R. Melhem, MD, PhD Department of Diagnostic Radiology and Nuclear Medicine, University of Maryland Medical Center, Baltimore, MD, USA

Paolo G. Nucifora, MD, PhD Neuroradiology Section, Department of Radiology, University of Pennsylvania Medical Center, Philadelphia, PA, USA

Elisabetta Pagani, PhD Neuroimaging Research Unit, San Raffaele Scientific Institute, Vita-Salute San Raffaele University, Milan, Italy

Division of Neuroscience, Department of Neurology, Institute of Experimental Neurology, San Raffaele Scientific Institute, Vita-Salute San Raffaele University, Milan, Italy

Paul M. Parizel, MD, PhD Department of Radiology, Antwerp University Hospital, University of Antwerp, Antwerp, Belgium

Eric Peterson, PhD Department of Radiology, Stanford University, Stanford, CA, USA

Paolo Preziosa, MD Neuroimaging Research Unit, San Raffaele Scientific Institute, Vita-Salute San Raffaele University, Milan, Italy

Division of Neuroscience, Department of Neurology, Institute of Experimental Neurology, San Raffaele Scientific Institute, Vita-Salute San Raffaele University, Milan, Italy

Pim Pullens, PhD icometrix, Leuven Belgium

Department of Radiology, Antwerp University Hospital, University of Antwerp, Antwerp, Belgium

Simon Richardson, PhD Microstructure Imaging Group, Centre for Medical Image Computing, University College London (UCL), London, UK

Maria Assunta Rocca, MD, PhD Neuroimaging Research Unit, San Raffaele Scientific Institute, Vita-Salute San Raffaele University, Milan, Italy

Division of Neuroscience, Department of Neurology, Institute of Experimental Neurology, San Raffaele Scientific Institute, Vita-Salute San Raffaele University, Milan, Italy

Matthew Rowe, PhD Microstructure Imaging Group, Centre for Medical Image Computing, University College London (UCL), London, UK

Jan Sijbers, PhD iMinds-Vision Lab, Department of Physics, University of Antwerp, Antwerp, Belgium

Bernard Siow, PhD Microstructure Imaging Group, Centre for Medical Image Computing, University College London (UCL), London, UK

Matthias Spaepen, MD Department of Radiology, Antwerp University Hospital, Antwerp, Belgium

Edoardo Gioele Spinelli, MD Neuroimaging Research Unit, San Raffaele Scientific Institute, Vita-Salute San Raffaele University, Milan, Italy

Division of Neuroscience, Department of Neurology, Institute of Experimental Neurology, San Raffaele Scientific Institute, Vita-Salute San Raffaele University, Milan, Italy

Bram Stieltjes, MD, PhD Department of Radiology and Nuclear Medicine, University Hospital Basel, Basel, Switzerland

Sener Süleyman, MD Department of Neurosurgery, Antwerp University Hospital, Antwerp, Belgium

Stefan Sunaert, MD, PhD Departments of Translational MRI and Radiology, KU Leuven and University Hospitals Leuven, Leuven, Belgium

Chantal M.W. Tax, MSc PROVIDI Lab, Image Sciences Institute, University Medical Center Utrecht, Utrecht, The Netherlands

Jacques-Donald Tournier, PhD Florey Institute of Neuroscience and Mental Health, University of Melbourne, Melbourne, VIC, Australia

Division of Imaging Sciences and Biomedical Engineering, Department of Biomedical Engineering, King's College London, London, UK

Sophie Van Cauter, MD, PhD Translational MRI and Radiology, KU Leuven, Leuven, Belgium

University Hospital Leuven, Leuven, Belgium

Wim Van Hecke, PhD icometrix, Leuven, Belgium

Department of Radiology, Antwerp University Hospital, Antwerp, Belgium

Jelle Veraart, PhD iMinds-Vision Lab, Department of Physics, University of Antwerp, Antwerp, Belgium

Center for Biomedical Imaging, Department of Radiology, New York University School of Medicine, New York, USA

Sjoerd B. Vos, PhD PROVIDI Lab, Image Sciences Institute, University Medical Center, Utrecht, The Netherlands

Translational Imaging Group, Centre for Medical Image Computing, University College London (UCL), London, UK

Ronald L. Wolf, MD, PhD Neuroradiology Section, Department of Radiology, University of Pennsylvania Medical Center, Philadelphia, PA, USA

Part I

Introduction

How to Use this Book

1

Louise Emsell

Aim and Scope

As outlined in the Preface, the aim of this book is to provide the new or less experienced DTI user with a practical guide that provides an overview of the different steps in a DTI study and how to optimize each of these steps according to the aims of the DTI study. It stands apart from other contemporary works on the topic by focusing on the practical aspects of using DTI in the context of clinical research and future clinical practice.

Contents

The book is divided into six parts, which can be read in succession or consulted as stand-alone chapters. As a practical guide, it should be possible to dip in and out of different chapters to obtain helpful information quickly. This is facilitated by a summary of "learning points" at the beginning of each chapter, and decision schemes to assist in making informed choices at each stage of the DTI pipeline (see Sect. 3 in this chapter). At the end of the book, a comprehensive glossary provides a useful summary of many of the key terms related to the acquisition and analysis of DTI data.

"Part I: Introduction" introduces both the book (Chap. 1) and the DTI technique (Chap. 2). Specifically, Chap. 2 provides a conceptual framework for the rest of the book by introducing themes that will be developed throughout the remaining chapters, such as the basics of the technique, the DTI study pipeline and the role of DTI in clinical practice. The topics in this chapter are introduced in an accessible manner that assumes no prior knowledge of the DTI technique.

"Part II: Diffusion Tensor Imaging: From Theory to Practice" provides the necessary theoretical background to understand the core concepts of the technique and its practical implementation. The first three chapters (Chaps. 3–5) cover topics related to concepts of diffusion in MRI and how diffusion MRI measurements from the scanner translate into quantitative parameters. The part then concludes with two chapters covering the practical aspects of DTI acquisition (Chap. 6) and a guide to checking and correcting DTI data (Chap. 7).

"Part III: Diffusion Tensor Imaging Analysis" is concerned with obtaining useful information from DTI data. It begins with an introductory

L. Emsell, PhD (✉)
Translational MRI, Department of Imaging and Pathology, KU Leuven, and Radiology, University Hospitals Leuven, Herestraat 49, 3000 Leuven, Belgium

Universitair Psychiatrisch Centrum (UPC), KU Leuven, Leuven, Belgium
e-mail: louise.emsell@med.kuleuven.be

W. Van Hecke et al. (eds.), *Diffusion Tensor Imaging*, DOI 10.1007/978-1-4939-3118-7_1

chapter (Chap. 8) describing the different DTI analysis techniques in the context of the whole DTI study pipeline, practical considerations for optimizing DTI analysis, and an overview of software packages that are presently available for analyzing DTI data. The remaining chapters in this part provide more detailed information about how to perform region-of-interest (Chap. 9), voxel-based analysis (Chap. 10) and tractography-based analysis (Chap. 11), respectively.

In the spirit of practical utility, "Part IV: Normal Diffusion Tensor Imaging Anatomy" includes a reference atlas (Chap. 12. "DTI atlas"), which illustrates the appearance of different brain structures on colour fractional anisotropy maps in standard 2D radiological views. It also provides examples of 3D tractography reconstructions of the most commonly assessed white matter fibre tracts and detailed information about how the reconstructions were performed.

As in Part III, "Part V: Clinical Applications of Diffusion Tensor Imaging" opens with an introductory chapter (Chap. 13) that provides a detailed overview of the myriad challenges and considerations that should be taken into account when conducting DTI studies in clinical populations. The remaining chapters include example clinical applications of DTI, including neurosurgical planning, the assessment of brain tumours, demyelinating disease, dementing disorders, psychiatric disorders, and traumatic brain injury. Due to the nature of the book, which focuses primarily on the practical application of DTI rather than the applications per se, it has not been possible, nor would it have been appropriate to include chapters on the use of DTI in every clinical disorder. The selection included here is intended to simply provide the reader with an overview of how DTI can be applied to study a range of pathologies and how different diseases offer unique challenges, again emphasizing the need to tailor the DTI approach to the given application.

The final part of the book, "Part VI: Beyond Diffusion Tensor Imaging" introduces more advanced concepts and techniques based on multi-shell diffusion imaging (Chap. 21) and higher order models (Chap. 20). These techniques, which are primarily used in a research setting, aim to address some of the limitations of the simple diffusion tensor model and are likely to be increasingly useful in the future. In a certain sense, this part does not mark the end of the book, but the start of a new book in the diffusion MRI library.

It is important to understand that in order to present information in this book in an accessible manner, it has necessarily been oversimplified. The field of diffusion MRI is large and complex. The technique is based on physical principles and models that are not completely understood, and imperfect imaging techniques that, like the field itself, are continuously evolving. In this context, this book should be viewed as a complementary guide, akin to the "quick-start" guide provided with new computing or electrical equipment, that helps to get up and running, but which lacks the technical detail of the user manual. Throughout the book, the reader is therefore referred to important publications and educational texts, which provide more detail on the topics covered in the chapters. These "must-reads" are conveniently located in a separate section of each chapter. In addition to consulting these publications, the reader may also wish to refer to the papers cited within each chapter and to the reference works listed in the preface.

Decision schemes

One of the core themes of this book is encouraging readers to ask themselves questions throughout the course of a DTI study, from the initial decision to acquire DTI data, to interpreting the final results. It is only by answering such questions that DTI can be implemented optimally and to justify the reasons behind a given implementation. Although it is impossible to provide answers to all these questions, this book aims to provide guidance on which questions to ask and offers some generic solutions. This is the case in the majority of chapters; however, some chapters also include more formal decision schemes to guide this process, either as separate figures or as checklists.

When consulting such schemes it is important to bear in mind that they are simply intended as a guide and should not be viewed as formal prescriptive solutions. The complex nature of DTI means that it is simply not possible to provide a single answer to every question, as many solutions and implementation strategies exist each with their own strengths and weaknesses. Performing DTI optimally therefore involves finding the right balance for a given application.

It should become evident that with DTI, there is no "one size fits all." This book aims to teach DTI users the art of tailoring and hopefully how to go about creating the perfect fit for them.

Introduction to Diffusion Tensor Imaging

2

Louise Emsell, Wim Van Hecke, and Jacques-Donald Tournier

Learning Points

- Diffusion tensor imaging (DTI) is one of several diffusion MRI-based techniques that can be used to noninvasively, indirectly assess tissue macro- and microstructure.
- DTI can be used as a visualization tool to distinguish between large oriented macromolecular structures, such as white matter fiber bundles in the brain.
- Several scalar quantitative parameters can be derived from DTI, the most common of which are the (mean) apparent diffusion coefficient (ADC) and fractional anisotropy (FA).
- The primary application of DTI is in (pre) clinical research. It is also used in clinical practice for assessing the evolution of stroke and for neurosurgical planning.
- Acquiring and analyzing DTI data is not trivial and requires careful consideration of many choices throughout the acquisition and analysis pipeline.
- DTI is highly sensitive to changes in diffusion, but lacks specificity, which confounds the interpretation of underlying biological or pathological processes.
- DTI suffers from a number of limitations that confound the interpretation of quantitative measures and the accuracy of fiber tracking.

L. Emsell, PhD (✉)
Translational MRI, Department of Imaging and Pathology, KU Leuven and Radiology, University Hospitals Leuven, Herestraat 49, 3000 Leuven, Belgium

Universitair Psychiatrisch Centrum (UPC), KU Leuven, Leuven, Belgium
e-mail: louise.emsell@med.kuleuven.be

W.V. Hecke, PhD
icometrix, Leuven, Belgium

Department of Radiology, Antwerp University Hospital, Wilrijkstraat 10, Edegem, 2650 Antwerp, Belgium

J.-D. Tournier, PhD
Florey Institute of Neuroscience and Mental Health, University of Melbourne, Parkville, VIC, Australia

Biomedical Engineering, Division of Imaging Sciences and Biomedical Engineering, King's College London, London, UK

It is arguably one of the most beautiful imaging techniques presently available in the field of radiology, and has captured the imagination of neuroscientists and clinicians in equal measure. However, diffusion tensor imaging (DTI) should not be held aloft simply for its artistic merit. DTI has revolutionized the management of acute ischemia and the assessment of brain lesions. Its ability to visualize and segment white matter fiber bundles has opened up new perspectives for neurosurgeons. Its capacity to quantify diffusion within neural tissue has provided clinical research with a remarkable tool with which to investigate the living brain in health and disease; and beyond

W. Van Hecke et al. (eds.), *Diffusion Tensor Imaging,* DOI 10.1007/978-1-4939-3118-7_2

the brain, DTI continues to gain ground in the assessment of muscle and other organs such as the kidney and prostate. Yet despite such promise, since its inception two decades ago [1], the impact of DTI in general radiological practice has been surprisingly limited. Possible reasons for this include, amongst others, the relatively long time it takes to acquire and process the data compared to conventional clinical MRI methods; the vast number of different approaches to data acquisition and analysis; and the poor accuracy of the technique and its sensitivity to a number of factors (described in this book), which means that maps and measures cannot be reliably reproduced under different conditions, such as across MRI scanners or between individual patients. These important caveats have been a stumbling block to the widespread adoption of DTI in the clinic, where being able to obtain reliable information on disease status in as short a time frame as possible is paramount. Recognizing and understanding how such challenges could be overcome so that DTI can be used optimally in a clinical setting, either in research or potentially in clinical practice in the future, forms the basis of this book.

This opening chapter provides an introduction to the DTI technique. The following pages provide a brief overview of topics that will be covered in detail in the remainder of the book. In the first part of the chapter, the biophysical basis of DTI is introduced, as well as the quantitative measures that can be derived from it and some example applications. In the second part of the chapter, the typical DTI pipeline is introduced, from the initial hypothesis, through data acquisition, processing and analysis to interpretation. The final section of the chapter highlights the pros and cons of DTI in the context of different applications and considers the potential role of DTI and related diffusion MRI techniques in the future.

Introducing the DTI Technique

A Useful Contrast

Classical clinical MRI techniques provide a single scalar value for each image pixel (or, in 3D, each voxel), yielding an image made up of grey scale intensities that reflect the tissue property to which the imaging sequence is sensitized. So for example, in T1-weighted images, fluid will appear dark, whilst in T2-weighted images, fluid will appear bright. The seasoned radiologist will quickly be able to draw upon their knowledge of how different types of tissue appear on different scans to distinguish between normal tissue and that affected by pathology, and be able to describe approximately where such pathology is located in anatomical terms. However, such conventional scans are not intrinsically sensitive to the microstructural architecture of the tissue and do not explicitly capture or account for the influence of tissue orientation on the MRI measurements. This is the added value of DTI, which allows it to be used to identify ischemic changes before they are visible on non-diffusion-weighted scans and to map the orientation of (and thus differentiate between) white matter fiber bundles that cannot be distinguished using any other imaging technique (Fig. 2.1).

How Does DTI Work?

In an environment in which there are no obstacles in their path, such as in a glass of water, molecules jostling about due to thermal motion will disperse in a uniform manner, traveling an equal distance in all directions. This is termed *isotropic* diffusion. However, if the molecules encounter obstructions that are coherently oriented, they will no longer disperse equally in all directions, and diffusion will be *anisotropic*. When considered in the simplest terms, diffusion-weighted MRI measures the net displacement of water molecules in a voxel over a few milliseconds. By measuring the degree and direction of diffusion, it aims to infer the structure of the local environment of the diffusing molecules. Consider that during the short time frame of the diffusion measurement, the water molecules will travel a distance of several micrometers. If, during this time, the water molecules are not obstructed in any way, such as in cerebrospinal fluid, then the measured MRI signal will be approximately the same in all directions. However, if the molecules interact with a boundary, such as a cell membrane,

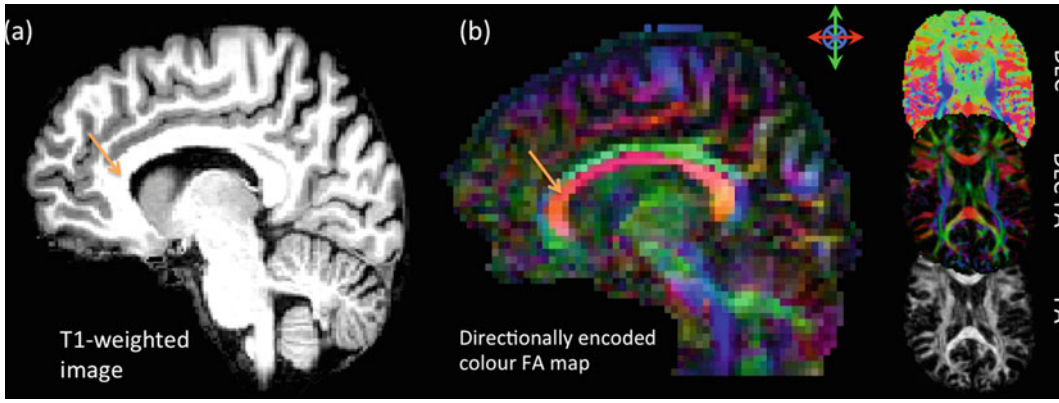

Fig. 2.1 Improved directional contrast with DTI: (**a**) On a T1-weighted image, white matter appears homogeneous. (**b**) DTI can be used to generate diffusion anisotropy (e.g., Fractional Anisotropy, FA) maps that can be color coded according to the principal direction of diffusion, termed "directionally encoded color," or DEC maps. The DEC-FA map is calculated by multiplying the FA map with the first eigenvector map. This is useful for distinguishing between different fiber bundles. For example, the cingulum bundle running anterior–posteriorly (*green*) is easily distinguished from the corpus callosum running ventromedially (*red*) on the color FA map (*orange arrow*), compared to the T1 image. Using the DEC convention, diffusion in an anterior–posterior direction is *green*, ventromedial is *red*, and superior–inferior is *blue*. [Images courtesy of T. Billiet and A. Leemans]

then their pathway will be obstructed, altering the measured MRI signal. Moreover, if these boundaries are coherently oriented, as for example within a white matter tract, then the measured signal will also be affected differently depending on the orientation of the diffusion gradients relative to the orientation of the tissue (Fig. 2.2).

In brain tissue, there are many obstructions to diffusion that molecules may encounter at the length scale of the MRI measurement, such as macromolecules, organelles, and cell membranes. These boundaries will give rise to both hindered and restricted diffusion, which is often attributed to water trapped within and between cells respectively. Therefore, by measuring changes in the MRI signal along different directions, it is possible to learn something about the underlying tissue architecture [2]. For example, in the case of white matter, the orientation of axons strongly influences the direction of diffusion [3], which forms the basis for diffusion tractography (described later in this chapter and in Chaps. 8, 11 and 12) (Fig. 2.3).

It is worth noting, however, that the DTI technique only provides a snapshot of diffusion within tissue over a given time frame and length scale, which is determined by the duration that the diffusion gradients are applied (typically around 40 ms in a clinical scanner) and the distance that separates the water molecules from a physical obstacle. In brain tissue, for example, diffusing molecules will travel several micrometers during a typical diffusion measurement. This means that the diffusion signal is most sensitive to changes in microstructure within this range of spatial scales [3].

It is also important to note that the typical spatial resolution of a DTI scan is 2–3 mm, meaning that diffusion across many heterogeneous microstructural environments, including different cell types, sizes, densities etc., contributes to the average signal in each image voxel.

In addition to the degree of potential molecular displacement, the snapshot of diffusion also depends on the traditional fundamental sources of contrast in the MRI signal, i.e., T1 and T2. In a typical DTI sequence, a long echo time is typically unavoidable, which means that some important microstructural elements with short T2 relaxation times do not contribute to the measured signal, notably myelin water. Concepts of diffusion in biological tissues and measuring it with MRI are introduced in the following chapter (Chap. 3).

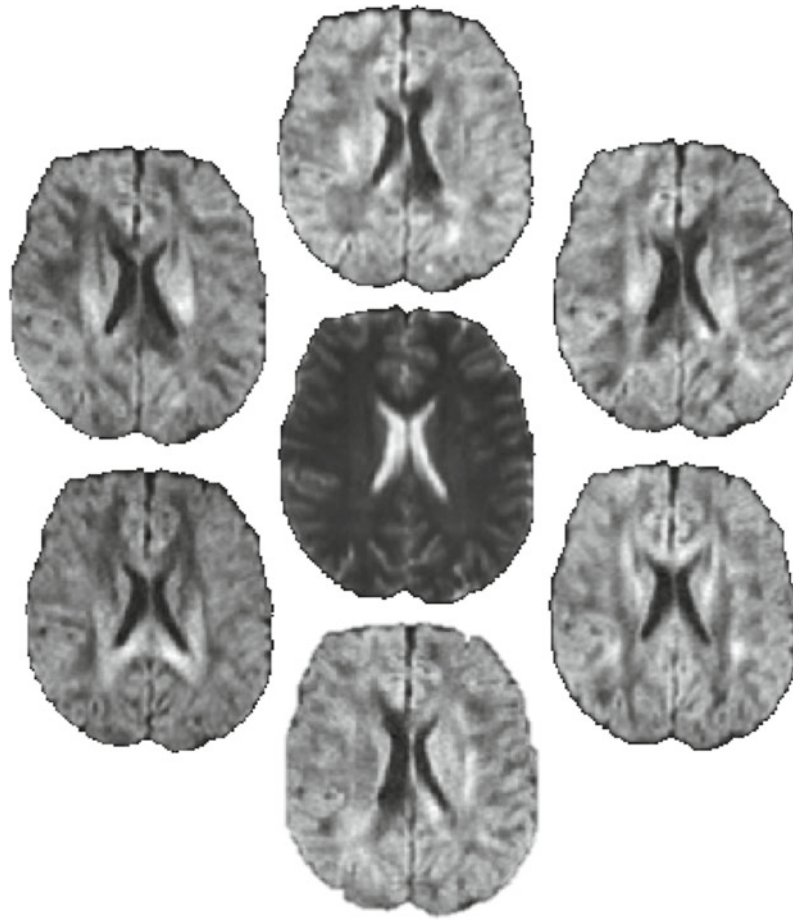

Fig. 2.2 Compared to the non-diffusion-weighted image (*center*), the contrast in the six diffusion-weighted images (outer images) changes as a function of the orientation of the tissue relative to the direction of the applied diffusion gradient

Diffusion tensor imaging extends these concepts further by modeling diffusion as a mathematical tensor, to describe the amount and direction of diffusion in each voxel by relating the measured signal to the applied diffusion-sensitizing gradient [1]. The tensor can be represented as an ellipsoid whose main axis represents the principal direction of diffusion, and which forms the basis of the most common quantitative DTI measures (Fig. 2.4) [4].

A Quantitative Technique

One of the great features of the DTI technique is its ability to capture information about complex microstructure and summarize it with a few simple quantitative metrics derived from the diffusion tensor. Unlike qualitative radiological assessments, such quantitative measures can be used to statistically compare patient groups with healthy subjects, or quantify changes over time, which may reflect normal developmental and neurodegenerative processes or stages of disease.

The most clinically useful DTI measures are presently the mean apparent diffusion coefficient (ADC) (alternatively, the "trace" or mean diffusivity (MD)), which describe the total amount of diffusion in a given voxel. The most commonly used metric in research studies is fractional anisotropy (FA), which characterizes the degree of anisotropy in each voxel. The FA is considered a summary metric describing the general status of the underlying tissue architecture. For example, a change in microstructural configuration, such as cell loss, changes in cell density, or increases in tissue water content, will result in a

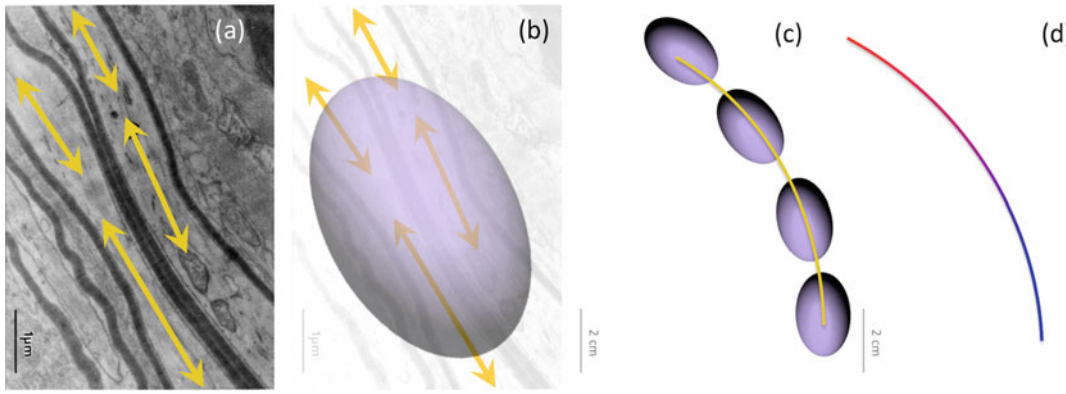

Fig. 2.3 Schematic representation illustrating how the diffusion tensor relates to axonal architecture. (**a**) Coherently organized structures such as axons give rise to anisotropic diffusion. (**b**) anisotropy can be characterized using the diffusion tensor, which can be represented geometrically as a three-dimensional ellipsoid. The longest axis of the ellipsoid represents the principal direction of diffusion and is assumed to reflect the underlying axonal orientation. (**c**) The contribution of many microscopic determinants of anisotropy is averaged and represented by a single tensor ellipsoid in each voxel. The principal direction of diffusion can then be followed in each voxel to reconstruct a path through the image. This is known as tractography or fiber tracking. (**d**) Many such tractography streamlines can be displayed together to form virtual reconstructions, which may provide a reasonable approximation of macroscopic anatomical white matter fiber bundles. Note the difference in scale between (**a**, **b**) and (**c**, **d**). [Adapted from Beaulieu C. The basis of anisotropic water diffusion in the nervous system—a technical review. NMR Biomed. 2002 Nov–Dec;15(7–8):435–55. With permission from John Wiley & Sons, Inc.]

change in FA. It is important to understand, however, that FA is only a very indirect measurement based on an oversimplified model of the behavior of diffusing water molecules averaged over the scale of the voxel. This model makes many assumptions that are not satisfied in real tissue. Moreover, the measurement of FA, and other DTI-derived parameters are strongly influenced by many different factors related both to the MRI technique itself, such as system-induced noise and artifacts, and physiological factors such as the effects of perfusion and partial volume. For these reasons, DTI parameters such as FA, MD, etc. should only ever be interpreted as a very indirect approximation of microstructural status [5, 6].

Applications

The main applications of DTI are in the assessment of tissue microstructure, predominantly in brain tissue (although the number of non-brain applications is increasing) and to segment white matter fiber bundles using tractography. In the clinic, this translates to the investigation of suspected acute ischemic stroke, to differentiate vasogenic versus cytotoxic oedema and to characterize intracranial lesions such as pyogenic abscess, infections, tumors, and trauma [7]. However, the predominant use of DTI is as a (pre)clinical research tool, where it has been applied to study, most typically, white matter microstructure in a broad range of neurological and psychiatric disorders [8].

The ability to estimate a principal direction of diffusion using the tensor has also yielded the tractography technique, which has been applied to study brain connectivity [9]. Essentially, tractography aims to virtually dissect white matter fiber bundles by propagating "streamlines" that follow the main direction of diffusion, which is assumed to reflect the underlying orientation of axons (Fig. 2.3). In one class of tractography applications, the dissected bundles are simply used as a visualization tool to locate the boundaries of fiber bundles which otherwise cannot be distinguished on conventional MRI images.

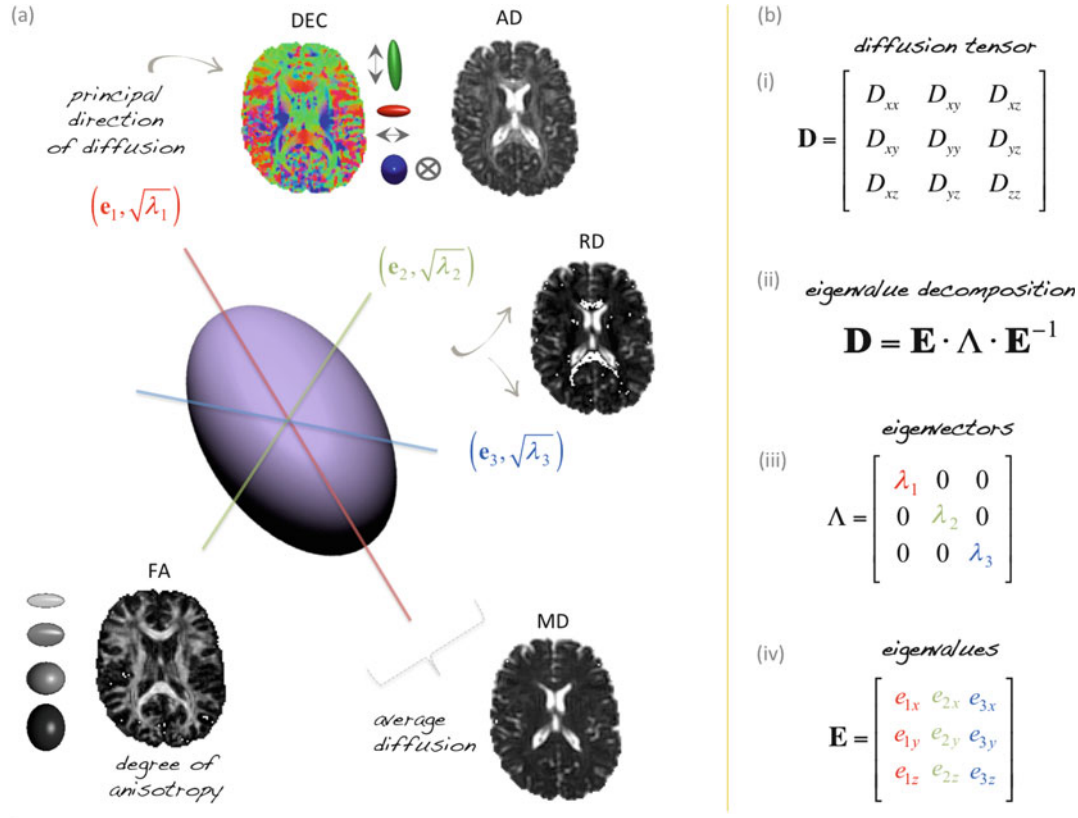

Fig. 2.4 The diffusion tensor. (**a**) geometric representation of the diffusion tensor and derivative DTI parameter maps. The diffusion tensor, (**b**(**i**)), can be mathematically decomposed (**b**(**ii**)), into eigenvectors (**b**(**iii**)) representing the direction of diffusion, and eigenvalues (**b**(**iv**)) representing the magnitude of diffusion. In the geometric representation, the eccentricity of the ellipsoid characterizes the degree of diffusion anisotropy. The longest axis is the first eigenvector and represents the direction of maximal diffusion, along which the axial diffusivity (AD) is calculated (sometimes referred to as $\lambda_{\|}$, longitudinal, or parallel diffusivity). The first eigenvector is also used to calculate the directionally encoded color (DEC) map. The second and third eigenvalues are used to calculate the radial diffusivity (RD) (sometimes referred to as $\lambda\perp$, transverse or perpendicular diffusivity). The mean diffusivity (MD) is a measure of the overall diffusivity in a particular voxel regardless of direction and is calculated as the average of the eigenvalues. The degree of anisotropy can be represented by the fractional anisotropy (FA), a scalar measure, without units, ranging between 0 (isotropic—darkest grey on a standard FA map) and 1 (anisotropic—lightest grey on a standard FA map). Further details about how to calculate and interpret FA and other DTI measures are provided in Chap. 5. [Images courtesy of A. Leemans]

This has been used in neurosurgical applications. In another application, the segmented bundles are used as regions of interest. One of the more controversial uses of tractography is to quantify relationships between DTI tractography derived measures and functional grey matter regions to infer something about the underlying brain connectivity. This latter application is confounded by the fact that DTI cannot characterize more than one dominant fiber direction in a voxel, and thus the reconstructed streamlines do not reflect the underlying anatomy. This major caveat of DTI is now widely accepted in the scientific field and has resulted in a concerted effort to develop new modeling techniques for assessing brain connectivity [10].

It is important to understand that although DTI is one of the most widely used implementations, it is just one of a number of techniques based on diffusion MRI (dMRI), *all* of which can

be used to characterize microstructure in vivo. It is therefore incorrect to equate or synonymize DTI with other dMRI-based methods, or consider it to be the only means to assess white matter "integrity" in vivo. The simplest form of dMRI is the basic diffusion-weighted scan, which is used widely in clinical practice to assess early ischemic injury; DTI is a relatively simple extension of this. Beyond DTI, there are a host of "higher-order" models, some of which can be applied to "DTI" data (i.e., acquired using the same protocol) and some that require different dMRI acquisition strategies, for example, acquiring data with several different *b*-values or many more gradient directions [10]. Such higher-order models are sometimes encompassed under the general umbrella term "high-angular resolution diffusion imaging" or HARDI. Although strictly speaking, the term HARDI refers to the data *acquisition* strategy and higher-order models refers to the data *reconstruction* method, the two terms generally apply to more advanced, non-DTI-based dMRI methods (see Chap. 20).

The DTI Pipeline

Designing and carrying out a DTI study in an optimal manner, either on an individual patient or in a research study, is not trivial. Extracting the rich, multivariate information captured in the diffusion signal requires careful attention at many different stages in the study pipeline (Fig. 2.5) [11]. This next section introduces some of these considerations, which form the framework of the remainder of this book.

The Goal of the DTI Investigation

Although often taken for granted, the motivation for undertaking a DTI study is most usually the expectation that there may be a measurable difference or change in microstructural properties in a given individual or group of individuals that can be correlated with a pathological or natural biological process such as neurodevelopment or aging. This motivation must exist to justify spending the extra time, cost, and potential inconvenience associated with extending an existing scan protocol by an extra 5–15 min.

The nature and extent of any hypothesized changes has an important impact on the choices that need to be made with regard to both the DTI data acquisition and analysis strategies. For example, if the goal of the DTI study is to identify acute ischemia, a simple <6 direction DWI acquisition of one or two minutes will suffice to calculate the ADC. However, if the goal is to visualize fiber tracts as part of a presurgical planning work-up, a much longer, more advanced sequence is required including many more gradient directions (>30), greater diffusion weighting (i.e., b-value), and more advanced (non-DTI) reconstruction techniques. It is therefore important to consider what the motivation and ultimate aim of the DTI investigation is prior to data collection.

In practice, particularly in a research context, a clear hypothesis may be lacking and DTI data is collected with a view to future exploratory analysis. In such situations, it is often helpful to at least anticipate what type of analysis might be conducted in the future by, for example, consulting current scientific literature, and to collect data of sufficient quality and with a sufficient number of gradient directions to be able to perform a range of different analyses. There are few things more frustrating than spending time collecting data only to discover later that it is unsuitable due to poor quality or an inadequate imaging sequence. The importance of optimizing the DTI acquisition protocol before collecting data, and checking data quality at the time of scanning or as soon as possible thereafter, cannot be stressed enough.

Data Acquisition

As anyone working with MRI data will understand, there are myriad parameter settings available that all interact to give rise to the final image. In conventional imaging, manipulating basic parameters will weight the sequence to a particular tissue property, such as T1, T2, diffusion, perfusion etc., alter the contrast and signal to noise

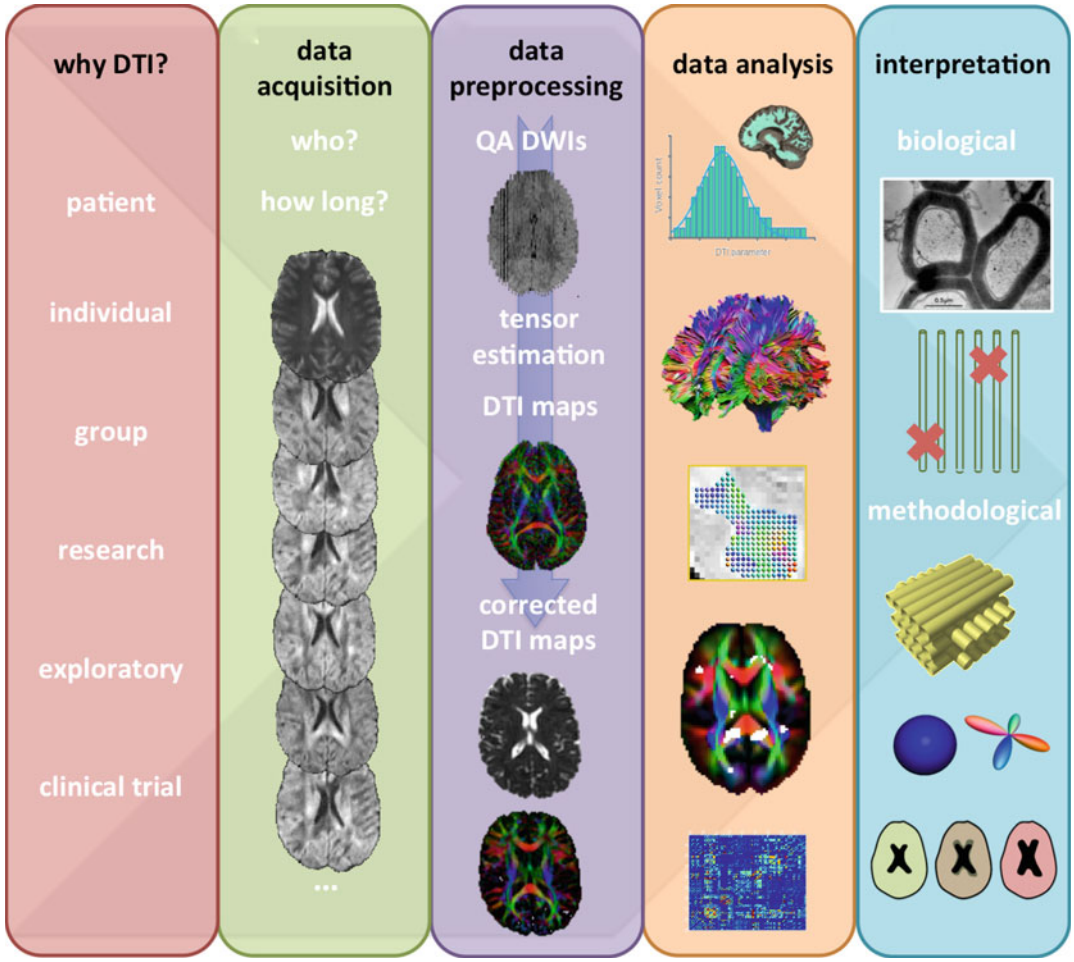

Fig. 2.5 Prototypal DTI study pipeline. Whole-brain tractogram and connectivity matrix. [Reprinted from Caeyenberghs K, Leemans A, Leunissen I, Gooijers J, Michiels K, Sunaert S, et al. Altered structural networks and executive deficits in traumatic brain injury patients. Brain Struct Funct. 2014 Jan;219(1):193–209. With permission from Springer Verlag]. Voxel-based analysis figure. [Adapted from Emsell L, Langan C, Van Hecke W, Barker GJ, Leemans A, Sunaert S, et al. White matter differences in euthymic bipolar I disorder: a combined magnetic resonance imaging and diffusion tensor imaging voxel-based study. Bipolar Disord. 2013 Jun;15(4): 365–376. With permission from John Wiley & Sons.] Axon micrograph. [Reprinted from Beaulieu C. The basis of anisotropic water diffusion in the nervous system—a technical review. NMR Biomed. 2002 Nov–Dec;15 (7–8):435–455. With permission from John Wiley & Sons, Inc.] Corrected DTI maps. [Courtesy of A. Leemans]

ratio (SNR), and the spatial resolution of the image. These same principles apply equally to DTI; however, the acquisition of both non-diffusion and multiple diffusion-weighted images adds an extra level of complexity. For example, one must decide along how many noncollinear gradient directions diffusion weighting will be applied. Mathematically, while only six are required for standard DTI [12] in practice acquiring more will improve the estimation of the diffusion tensor [13], and acquiring even more (e.g., >45) will allow more advanced reconstruction methods to be used that may be able to resolve complex fiber architecture [10]. However, acquiring more directions will extend the scan time and thus decrease tolerability and increase the likelihood of motion artifacts, which may degrade image quality. This is just one example

out of many more that are described in Chap. 6. The take-home message however is that it pays to spend some time becoming familiar with the parameter choices that are especially relevant in DTI, such as the degree of diffusion weighting (*b*-value), the number and orientation of the applied diffusion gradients, the echo time (TE), the need for adequate fat suppression and so on, and deciding what is the most optimal balance between scan time and image quality for your particular application [14].

Data Pre-processing

Having collected the raw DTI data (i.e., a series of diffusion-weighted image volumes, each comprising a number of 2D images with a particular diffusion weighting), it is necessary to perform a number of steps in order to both correct the data for typical artifacts associated with the EPI sequence used to acquire the data, and to generate DTI scalar maps (e.g., FA maps). For example, eddy currents induced by the rapid switching of the applied diffusion gradients often affect EPI sequences, which warp the DWIs along the direction of phase encoding. The relatively long scan time means that bulk motion effects are unavoidable in awake subjects. These geometric distortions are often corrected by realignment to a non- or less deformed image such as a non-diffusion-weighted image (sometimes known informally as the "b = 0") [10].

There are also different approaches for estimating the diffusion tensor from the raw DWI data, which will have an impact on the accuracy of any quantitative measures derived from it [15]. In fact, there are many such "under the hood" calculations and image processing steps that contribute to generating the final DTI parameters and derivative maps, and which are easily overlooked. While this may be due mainly to a lack of awareness, it does highlight the need to work with or consult specialists when collecting and analyzing DTI data. Image pre-processing for DTI analysis is addressed in more detail in Chaps 8-11 of this book, and Chaps. 4 (from raw DWI to tensor) and 7 (checking and correcting data) in particular.

Data Analysis

Having acquired and pre-processed the data, the next logical step is deciding how to extract useful information from it. Clearly, this will depend on the motivation for acquiring the data in the first place, e.g., is it for visualization or quantification, for clinical use in an individual patient, or in a group study as part of clinical research? Considering these types of questions prior to analyzing the data (or preferably, before acquiring it) will help in choosing which of the many available analysis strategies to use to gain the most useful and reliable insights. This topic is discussed and a decision tree to aid such a thought process is provided in Chap. 8 (Strategies and challenges in DTI analysis).

Briefly, DTI analysis strategies can be divided into three main classes: (1) techniques that can be used to assess the whole structure or organ (e.g., brain) as a single entity, (2) techniques that assess a specific region (e.g., a specific white matter fiber bundle or pathological lesion), and (3) techniques that assess individual voxels, and from this infer local alterations in DTI metrics. Examples include histogram analysis, manual or automated tracing of lesions, tractography-based segmentation of fiber bundles, voxel-based analysis (VBA), and graph-based analysis of "connectivity" (Fig. 2.6).

Each technique has its own strengths and limitations, and will be more or less suited to a given application than another. As the different techniques provide different information and are strongly influenced by their underlying assumptions and methodological implementation, it is often useful to perform more than one type of analysis to gain insight into any observed changes. The greatest insights however may be achieved by combining DTI with other imaging modalities, and with functional and clinical measurements.

Interpretation

Interpretation in the context of DTI imaging can be understood in terms of the qualitative visual interpretation of the DTI derived maps, or the

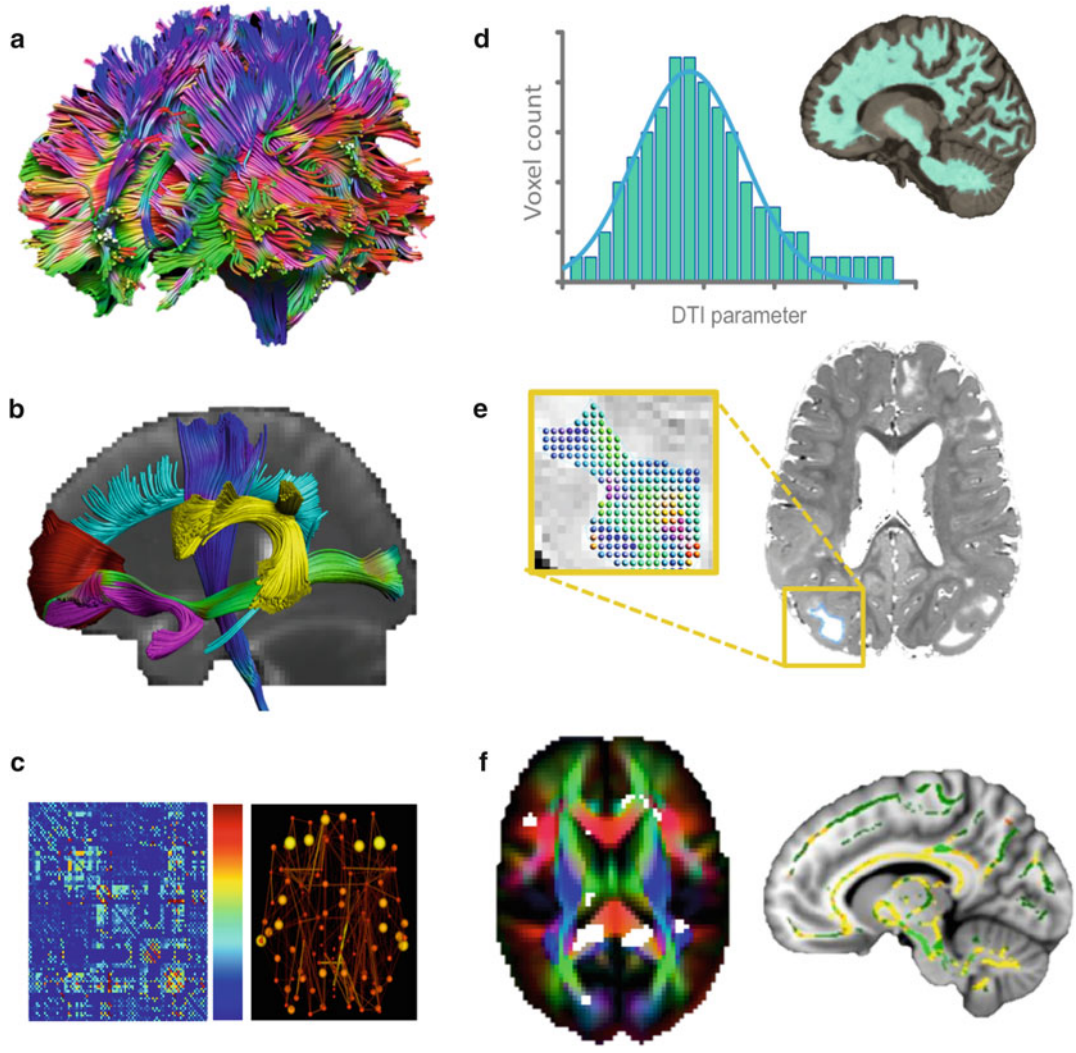

Fig. 2.6 DTI analysis methods: (**a**) Whole-brain tractography, (**b**), region-based tractography, (**c**) graph-based connectivity models, (**d**) histogram analysis, (**e**) region-of-interest analysis, and (**f**) voxel-based analysis. (**a** and **c**) [Reprinted from Caeyenberghs K, Leemans A, Leunissen I, Gooijers J, Michiels K, Sunaert S, et al. Altered structural networks and executive deficits in traumatic brain injury patients. Brain Struct Funct. 2014 Jan;219(1):193–209. With permission Springer Verlag]. (**f**) (*left*): [Reprinted from Emsell L, Langan C, Van Hecke W, Barker GJ, Leemans A, Sunaert S, et al. White matter differences in euthymic bipolar I disorder: a combined magnetic resonance imaging and diffusion tensor imaging voxel-based study. Bipolar Disord. 2013 15(4):365–76. With permission from John Wiley & Sons, Inc.] (**f**) (*right*): [Reprinted from Holleran L, Ahmed M, Anderson-Schmidt H, McFarland J, Emsell L, Leemans A, et al. Altered interhemispheric and temporal lobe white matter microstructural organization in severe chronic schizophrenia. Neuropsychopharmacology. 2014 Mar;39(4):944–54. With permission from Nature Publishing Group]

interpretation of changes in DTI parameters detected by quantitative statistical analysis. With respect to the former, visual interpretation involves both the assessment of the raw and processed data quality, and, in some cases, such as with lesion differentiation, the clinical interpretation of the DTI parameter maps. Data quality assessment is a vital and essential step in any DTI study and should not be neglected. The presence of artifacts in the raw DWI data results in the

misestimation of DTI parameters, and it is therefore important to be able to recognize them or their consequences in the derived parameter maps and tractograms [16]. Chapters 6 and 7 contain many pictorial examples of such artifacts, as well as information about how they can be avoided and corrected using different acquisition and image processing strategies.

The interpretation of statistically significant changes in quantitative parameters is particularly challenging. Although DTI is highly sensitive to changes in diffusion, it lacks specificity and the derived parameters are strongly influenced by many factors. As it is extraordinarily difficult to disentangle the relative contribution of these biological and methodological factors to a given DTI parameter value in a given voxel, it is simply not possible to ascribe changes in DTI parameters to changes in specific microstructural elements such as the degree of myelination, or axon density [5]. In this context, although DTI may be influenced by changes in microstructural integrity, it is by no means a direct measure of it. Nevertheless, given its sensitivity to changes in diffusion, DTI remains a useful tool for noninvasively identifying potential differences attributable to disease status, and when combined with other evidence can contribute valuable complementary information about pathological mechanisms, treatment effects, and neurobiology.

Chapter 5 (Quantitative DTI parameters) provides a detailed overview of this topic and guidelines for interpreting changes in quantitative parameters.

The DTI Balancing Act

Of all the possible take-home messages, one of the most useful to remember is that with DTI, there is no "*one-size fits all.*" Carrying out a DTI investigation optimally is not to say there is ever a perfect solution or implementation of the technique. As will become apparent throughout this book, the myriad choices that need to be made at multiple steps throughout the DTI pipeline will be influenced by the ultimate goal of the investigation, and will also determine the quality and nature of the final results. It pays to spend time becoming familiar with these considerations and choices, not only to optimize a given investigation but also to aid the understanding and assessment of other DTI-based studies and findings reported in clinical and scientific literature.

There are many pros and cons of DTI (see information box: "pros and cons of DTI") and the art of using the technique optimally (which also includes deciding whether it is appropriate for a given application at all) necessarily involves a careful cost-benefit analysis for a given application. For example, scientists conducting exploratory research studies on large numbers of subjects may be less concerned with limitations in estimated fiber bundle trajectories than a neurosurgeon planning an operation on a patient. In this context, it is clear that the limitations of DTI assume greater significance, and in some applications may outweigh the benefits, in a clinical setting (see Box 2.1).

The Future Role of DTI in Clinical Practice

In comparison to other radiological techniques, a dichotomy exists between the perceived utility of DTI in the clinic and in scientific research. Whilst DTI is sometimes considered to be an advanced, somewhat novel technique on the brink of entering mainstream clinical practice, a large body of the diffusion MRI scientific community is moving away from DTI-based imaging and developing new strategies to obtain information captured from the diffusion signal that aim to overcome some of the limitations of the technique. However, despite this transition away from DTI in the diffusion MRI field, and the fact that it is not widely used in clinical practice, DTI is used extensively in research, having been applied in thousands of (pre)clinical research studies to date.

It is worth considering why this dichotomy exists. In order to be clinically useful, a given technique or method of assessment should logically satisfy a number of criteria. For example, it should be performed as quickly and reliably as

Box 2.1: Pros and Cons margins are different

Strengths

+ Can be used for in vivo assessment of white matter
+ Simple way of summarizing complex data
+ Can visualize the location of major white matter bundles
+ Sensitive to changes in macro- and microstructure
+ Provides quantitative measures
+ Noninvasive
+ Useful complementary technique to conventional MRI
+ Can be acquired in a relatively short time (5–10 min)
+ Has clinical utility in the assessment of acute stroke
+ Has potential complementary clinical utility in neurosurgical planning
+ Group analysis has provided useful insights in neurology and psychiatry

Limitations

– Based on an oversimplified model
– Not specific to a particular microstructural feature (e.g., myelin content, axon density etc.)
– Unreliable in voxels with >1 dominant fiber direction: "crossing-fibers" (i.e., most of the brain white matter)
– Dependent on data quality
– Limited spatial resolution
– Dependent on data acquisition parameters
– Quantitative measures influenced by many non-biological factors
– Changes in quantitative measures are difficult to interpret
– Results are user and parameter dependent.
– Different scanners have different acquisition settings confounding reproducibility and standardization.
– Cannot differentiate the directionality of axons: afferent vs. efferent, anterograde vs. retrograde pathways, inhibitory vs. excitatory connections, direct vs. indirect routes

possible, and provide well-defined measures that are reproducible across different clinical centers and defined by standard, normative ranges. It should provide information that is complementary to other clinical measures by providing additional information that is not revealed by other techniques. It should have diagnostic or prognostic utility; for example, by being able to detect pathology, distinguish between different diseases or for staging disease processes. Preferably, it should also be inexpensive, accessible, and easy to implement on a large scale. When considering such criteria, it is clear why DTI has not yet been adopted in mainstream clinical practice. At the same time, one can also appreciate why after decades of failing to penetrate into clinical practice it has not yet been abandoned. The *potential* of DTI to provide unique clinical solutions and complementary biomarkers in some areas of medicine remains, and it is this potential that is presently fueling the substantial research efforts in this domain.

Since the inception of DTI, there have been significant technological and methodological advances in the field, as well as a greater awareness of the limitations of the technique. These advances in technology and understanding continue to contribute to improvements in data quality, to reducing scan time and to relating the diffusion signal to the microarchitectural properties that DTI aims to probe. Nowadays, it is perhaps more appropriate to think of DTI as just one out of a range of diffusion MRI-based techniques (see Chaps 20 and 21). Its future utility in *clinical practice* and that of its relatives will ultimately be determined by their ability to satisfy the aforementioned criteria and improve patient healthcare.

Acknowledgements The authors would like to thank Thibo Billiet and Alexander Leemans for providing images that were incorporated into the figures in this chapter.

References

1. Basser PJ, Mattiello J, LeBihan D. Estimation of the effective self-diffusion tensor from the NMR spin echo. J Magn Reson B. 1994;103(3):247–54.
2. Basser PJ, Jones DK. Diffusion-tensor MRI: theory, experimental design and data analysis—a technical review. NMR Biomed. 2002;15(7–8):456–67.

3. Beaulieu C. The basis of anisotropic water diffusion in the nervous system: a technical review. NMR Biomed. 2002;15(7–8):435–55.
4. Basser PJ, Pierpaoli C. Microstructural and physiological features of tissues elucidated by quantitative-diffusion-tensor MRI. J Magn Reson B. 1996;111(3):209–19.
5. Jones DK, Knösche TR, Turner R. White matter integrity, fiber count, and other fallacies: the do's and don'ts of diffusion MRI. Neuroimage. 2012;73:239–54.
6. Jones DK, Cercignani M. Twenty-five pitfalls in the analysis of diffusion MRI data. NMR Biomed. 2010;23(7):803–20.
7. Mukherjee P, Berman JI, Chung SW, Hess CP, Henry RG. Diffusion tensor MR imaging and fiber tractography: theoretic underpinnings. AJNR Am J Neuroradiol. 2008;29(4):632–41.
8. Mori S, Zhang J. Principles of diffusion tensor imaging and its applications to basic neuroscience research. Neuron. 2006;51(5):527–39.
9. Jbabdi S, Johansen-Berg H. Tractography: where do we go from here? Brain Connect. 2011;1(3):169–83.
10. Tournier JD, Mori S, Leemans A. Diffusion tensor imaging and beyond. Magn Reson Med. 2011;65(6):1532–56.
11. Soares JM, Marques P, Alves V, Sousa N. A hitchhiker's guide to diffusion tensor imaging. Front Neurosci. 2013;7:31.
12. Basser PJ, Pierpaoli C. A simplified method to measure the diffusion tensor from seven MR images. Magn Reson Med. 1998;39(6):928–34.
13. Jones DK. The effect of gradient sampling schemes on measures derived from diffusion tensor MRI: a Monte Carlo study. Magn Reson Med. 2004;51(4):807–15.
14. Mukherjee P, Chung SW, Berman JI, Hess CP, Henry RG. Diffusion tensor MR imaging and fiber tractography: technical considerations. AJNR Am J Neuroradiol. 2008;29(5):843–52.
15. Veraart J, Sijbers J, Sunaert S, Leemans A, Jeurissen B. Weighted linear least squares estimation of diffusion MRI parameters: strengths, limitations, and pitfalls. Neuroimage. 2013;81:335–46.
16. Le Bihan D, Poupon C, Amadon A, Lethimonnier F. Artifacts and pitfalls in diffusion MRI. J Magn Reson Imaging. 2006;24(3):478–88.

Part II

Diffusion Tensor Imaging: From Theory to Practice

Concepts of Diffusion in MRI

3

Matthew Rowe, Bernard Siow,
Daniel C. Alexander, Uran Ferizi,
and Simon Richardson

Learning Points

- Water molecules in biological tissue are in continuous motion. They collide with each other and with local molecules and structures such as cell membranes. Three separate types of diffusion are: free diffusion in free water and hindered and restricted diffusion in the presence of boundaries such as cell membranes.
- Tissue structure hinders and restricts diffusion of water; different tissue structures have different effects on the diffusion profile of the water.
- White matter has a highly coherent fibrous structure, which encourages anisotropic diffusion of water; this effect can be exploited to estimate the orientation of white matter fibers using DTI. Grey matter has a less coherent structure, water diffuses more isotropically in grey matter, and the overall effect on diffusion properties is much more complicated and harder to interpret.
- MRI scans can be made sensitive to the displacement of water molecules at millisecond time scales via the use of modulated magnetic gradients using the gradient coils present in standard MR scanners.
- The pulsed gradient spin echo (PGSE) sequence combined with EPI readout is the most commonly used sequence for diffusion MRI. It consists of an excitation pulse and a refocusing pulse, sandwiched between two equal magnetic gradients which affect the phase coherence of the spins and cause signal attenuation in the presence of diffusing molecules.

What Is Diffusion?

In 1826 a botanist named Robert Brown was studying the seemingly random pattern of motion that pollen grains exhibited when suspended in water through his microscope [1]. Initially puzzled, he attributed it to some biological phenomenon of the pollen, but when he later observed the same behavior with inanimate, inorganic substances, he rejected this hypothesis. It later became clear that the motion that he had observed was due to the buffeting of the pollen grains by water molecules surrounding them. This led to the revelation that liquids and gases were not static and lifeless as they might appear at first glance. The atoms and molecules from which

M. Rowe, PhD (✉) • B. Siow, PhD • D.C. Alexander, PhD
U. Ferizi, PhD • S. Richardson, PhD
Microstructure Imaging Group, Centre for Medical Image Computing, University College London (UCL), Gower Street, London WC1E 6BT, UK
e-mail: matthew.rowe.09@ucl.ac.uk

W. Van Hecke et al. (eds.), *Diffusion Tensor Imaging*, DOI 10.1007/978-1-4939-3118-7_3

they are constituent are in constant motion, undergoing persistent collisions and energy exchanges with other molecules and atoms. This led to an intuitive understanding of phenomena observed in everyday life, such as the spreading of an ink drop in a glass of seemingly motionless water or the propagation of a perfume scent through still air. The physical and mathematical theories of diffusion were developed and refined over the next two centuries by prominent scientists including Thomas Graham, Adolf Fick [2, 3], and eventually Albert Einstein [4, 5], who developed a rigorous mathematical framework, which is still in use today.

The principles of diffusion and its importance in biological tissue can be conceptualized simply, without a need to consider the mathematical basis of diffusion theory. Water molecules at room temperature, or at body temperature, are in constant motion due to their inherent thermal energy. In the absence of any obstacles, a water molecule would continue to move in the same direction forever in accordance with Newton's first law of motion. However, in the presence of many other water molecules, each and every molecule undergoes many collisions in a short space of time, each of which change the direction of the water molecule. The dynamics of this process are too complex to predict exactly, so from a practical perspective the direction of each molecule changes effectively at random. This process of translation and randomly changing direction is often referred to as a "random walk." In the following, we will refer only to the diffusion of water molecules, as this is of importance in diffusion tensor imaging (DTI). However, the basic principles discussed apply to all gases and liquids.

Consider the diagrams in Fig. 3.1. Let us imagine that the blue dots represent water molecules in an open body of water such as in a glass of water. In the first diagram, we see water molecules, all of which are in motion and randomly colliding with each other, performing a random walk. The paths taken by three randomly selected molecules are outlined by the red trails in Fig. 3.1a. If we could label a small cluster of the water molecules such as those highlighted in red in Fig. 3.1b and watch their progress over a short time, we would see the labeled molecules spread out evenly in each direction as in the latter diagrams 3.1c, d after times T and 2T respectively. In Fig. 3.1d it can also be seen that the labeled molecules are clustered around the point of origin of the labeled set.

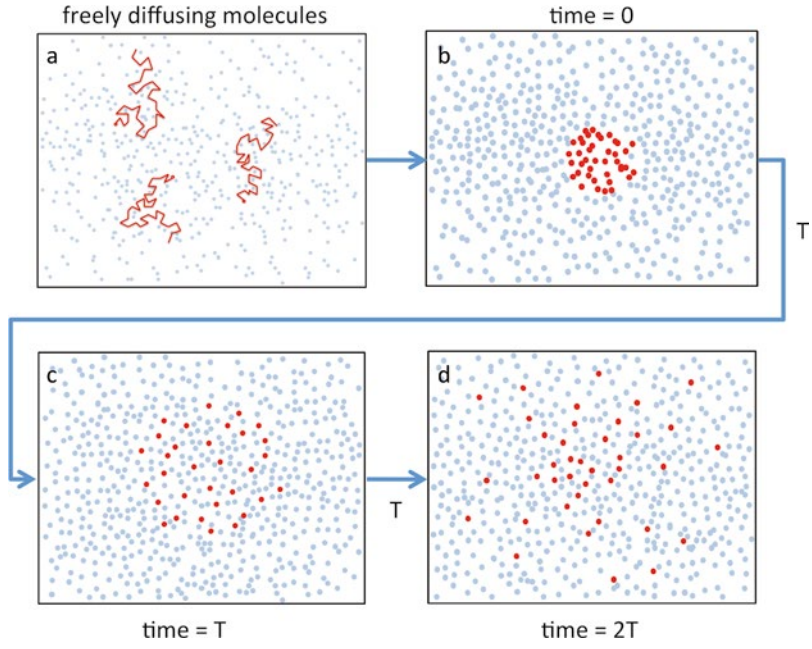

Fig. 3.1 Illustration of the free diffusion of water molecules in pure water over time interval 2T. The random walks of a selection of molecules are illustrated with *red lines*. The progression of a small group of molecules highlighted in *red* is shown in (*b–d*)

This kind of diffusion is normally referred to as "free diffusion" as the water molecules are free to move in any direction with only the other water molecules obstructing them. Free diffusion leads to a zero-mean Gaussian distribution of particle displacements. This means it is more likely for a molecule to travel a shorter distance, than a longer distance, and in fact the most likely distance to move is zero. It is important to note that a zero displacement does not imply that the molecule has not moved at all during a particular time period; it has simply back-tracked in its random walk and is in a similar position at the start and end of the time period we are observing.

If we were to view this process in three dimensions, we would observe that a labeled cluster of water molecules would spread out in a roughly spherical profile. In free diffusion the progress of molecules is unobstructed by obstacles and is therefore independent of direction. Diffusion that is independent of direction also has a special term: "isotropic diffusion." Things get more interesting when we consider the effect of the presence of boundaries on the propagation of water. If diffusing water molecules encounter boundaries, such as cell membranes in nervous tissue, the presence of such boundaries will cause a departure from the isotropic, free diffusion we observe in a glass of water. DTI gives us a powerful tool to examine this departure from free diffusion properties, which can give us insight into the geometric properties of the boundaries and allow us to infer details about tissue structure.

In water at room temperature, the average distance moved of a water molecule in one second is around 100 μm, or 1/10th of a millimeter. In 50 ms, which is a time of the order of magnitude relevant to DTI sequences, the average displacement of a water molecule is about 25 μm. This length scale is of a similar magnitude to that of many cellular structures of central nervous system tissue. Hence if we probe the motion of water molecules at such timescales with diffusion tensor imaging, we can probe the geometric structure of the tissue of the central nervous system at the cellular level from outside the body.

Hindered/Restricted/Free Diffusion

We have already covered the concept of "free diffusion," the diffusion of water molecules unimpeded by the presence of any boundaries. However, in the presence of boundaries, the diffusion properties of water are different. There are two more types of diffusion, which commonly occur in biological tissue: restricted diffusion and hindered diffusion.

Restricted Diffusion

Restricted diffusion occurs when water molecules are constrained by impermeable boundaries, which impedes the progress of water molecules beyond a certain maximum displacement in a particular direction. In the context of biological tissue, this kind of diffusion occurs for water molecules trapped inside a cell boundary, otherwise known as the "intracellular" region. The motion of water molecules within this region is restricted to within a certain range unless they can permeate the cell membrane. In this regime, the diffusion properties of water are largely governed by the geometric properties of the constraining membrane.

Hindered Diffusion

Hindered diffusion occurs when the progress of water molecules as they diffuse is impeded by obstacles, but not completely confined by a continuous boundary as in the case of restricted diffusion. Hence the mean displacement of a set of water molecules is reduced overall in any direction in which boundaries are encountered. The net result is that the average displacement of water molecules is reduced in directions, which impinge on boundaries. In biological tissue, this type of diffusion is exhibited by water present in the interstitial space between cells, otherwise known as the "extracellular" region.

In Fig. 3.2, we can see the difference between molecules exhibiting restricted diffusion and molecules exhibiting hindered diffusion. The red

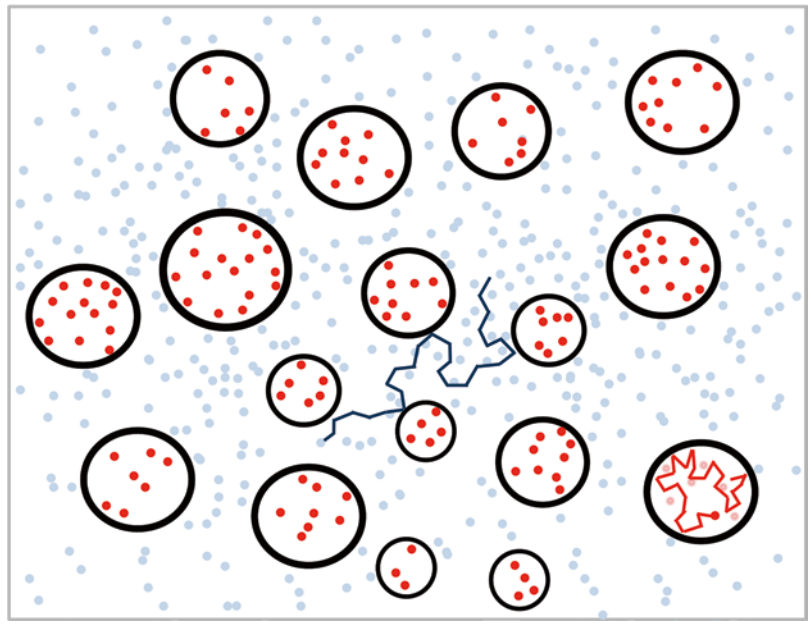

Fig. 3.2 Illustration of hindered and restricted water inside and around boundaries, such as cell membranes. The *red dots* represent molecules which are restricted by the presence of the boundaries while the *blue dots* represent molecules which are hindered by the presence of the boundaries

molecules inside the boundaries are restricted and cannot exceed a certain maximum displacement as they are restricted from doing so by the cell boundary. The motion of a single water molecule is exemplified by the red path. The blue molecules, however, can diffuse in any direction. Their progress is impeded, but not restricted, by the presence of the boundaries. A typical path of a "hindered" water molecule is exemplified by the dark blue path. Given enough time, these "hindered" molecules could reach any distance; however, their progress is impeded by the presence of the boundaries. Therefore we see a departure from free diffusion properties, which is dependant on the geometry of the boundaries.

Of particular interest in DTI is the effect of specifically shaped boundaries. It is easy to see from the previously mentioned examples and illustrations how water molecules would behave in and around a spherical boundary, but it is also interesting to consider how a diffusing water molecule would behave inside a cylindrical boundary as in Fig. 3.3. The cylindrical boundary presents an obstacle to diffusion in the direction perpendicular to its axis, while presenting no obstacle to diffusion along its axis. Therefore the diffusion properties of water in and around cylindrical boundaries become highly dependent on the orientation of the cylindrical boundaries. Water diffuses a lot more readily along the axis of a set of packed cylinders than perpendicular to it. This is a phenomenon that becomes highly important in DTI when studying neural tissue, as we will see when we examine the cellular structure of tissue in the next section. There is a special term for this kind of directionally dependent diffusion: "anisotropic diffusion." The terms "anisotropic" and "isotropic" are regularly used in DTI terminology, so it's worth taking note of what they mean.

Microstructural Tissue Properties at the Scale of Diffusion MR Measurements

In biological tissue, such as that of the central nervous system, the components of the cells that make up the tissue create boundaries to diffusion. The various properties of cellular structures such as the cell membrane, the viscosity of the material within the cell, and the presence of subcellular structures such as mitochondria, nuclei, and microfibrils have an effect on the diffusion

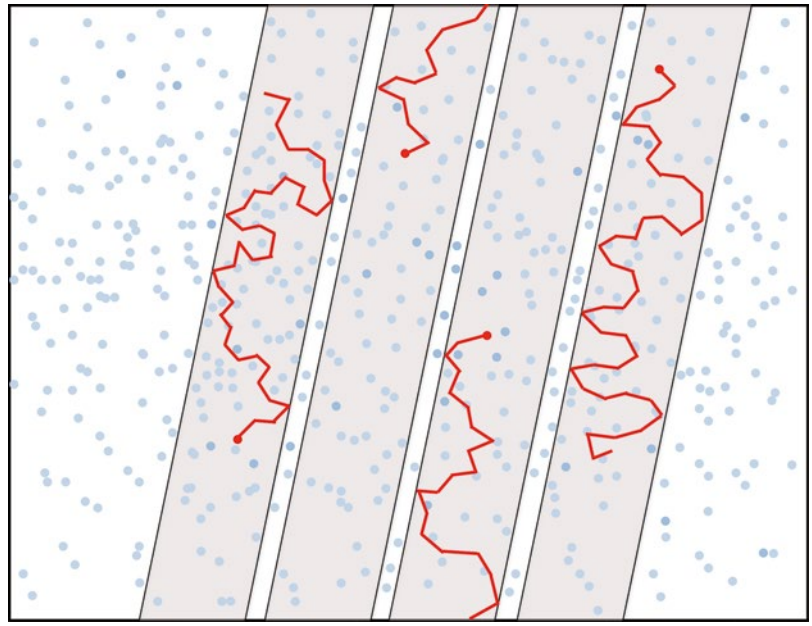

Fig. 3.3 Illustration of water molecules restricted inside a cylindrical boundary. The *red lines* represent the paths taken by a small selection of molecules trapped inside the cylinders

properties of water in and around the cell and this has an impact on the measurements we take in DTI. In the following, we will examine the cellular composition of central nervous system tissue.

The fundamental building blocks of the brain's processing network are neurons. Neurons are electrically excitable cells and are typically divided into two major parts, the soma or "body" of the neuron and the neuritic protrusions: dendrites and an axon [6].

The main cellular structures are illustrated in Fig. 3.4. The body of the neuron, the soma, varies in size and shape throughout the central nervous system, typical sizes range from 5 to 100 µm. The soma contains the cell nucleus and other cell structures such as Nissl bodies, mitochondria, and microfibrils.

The soma has numerous protrusions collectively termed "neurites." Neurites fall into two types: dendrites and axons. Dendrites are small, short, branched projections which taper towards the end. They facilitate short range exchange of electrical and chemical signals between neighboring neurons and axons. Most neurons typically also have a single axon. The axon is an elongated protrusion of the nucleus which facilitates long range connection with other neurons and there is only one axonal protrusion of each neuron. The longest axons in the bodies of mammals, such as the sciatic nerve in humans, can be many centimeters or even over a meter in length. They can vary in diameter between around 0.2 and 20 µm in the brain [7].

Many axons throughout the central nervous system are covered by a fatty layer known as the myelin sheath. The myelin sheath exhibits periodic gaps called Nodes of Ranvier, which are extremely important for the transmittance of electrical excitation along the axon. Charge builds up at each node and hops to the next one in rapid succession, facilitating fast, efficient communication of electrical excitation or "action potentials" along the axon. The myelin sheath serves to both facilitate the propagation of action potentials and insulate each axon from interference from action potentials traveling in other axons and electrically charged ions in the surroundings. The myelin sheath is composed of several layers, which are formed by the winding of the protrusion of an oligodendrocyte cell around the axon. Each oligodendrocyte can serve many axons. The myelin, made of a multilayered wrapping of a protrusion of an oligodendrocyte cell, is illustrated in Fig. 3.5.

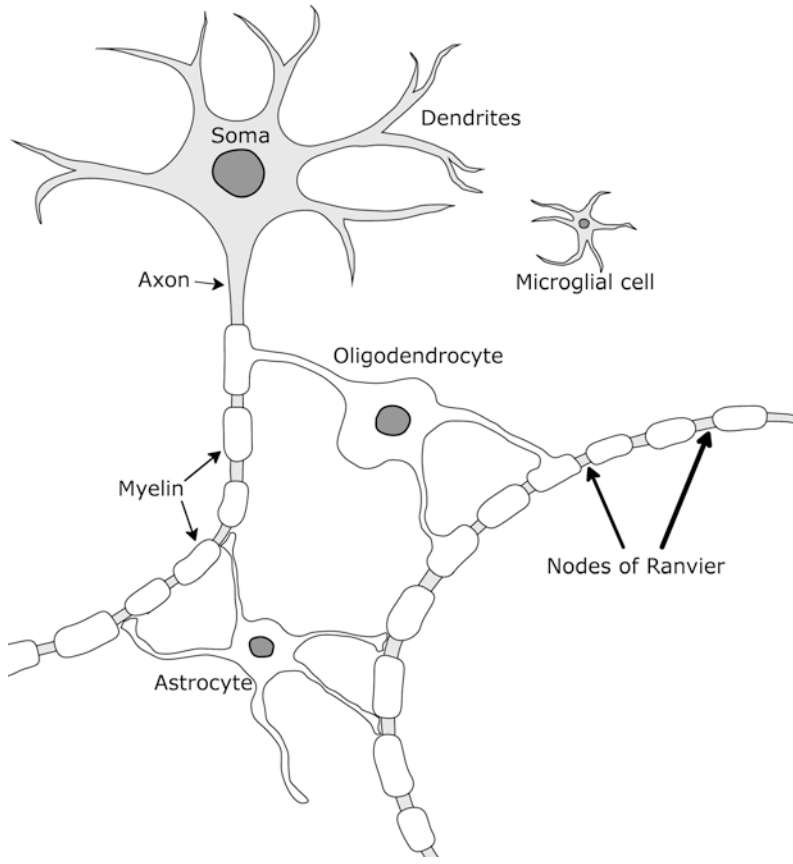

Fig. 3.4 Simple illustration of cellular components of neural tissue including the soma, axons, and glia

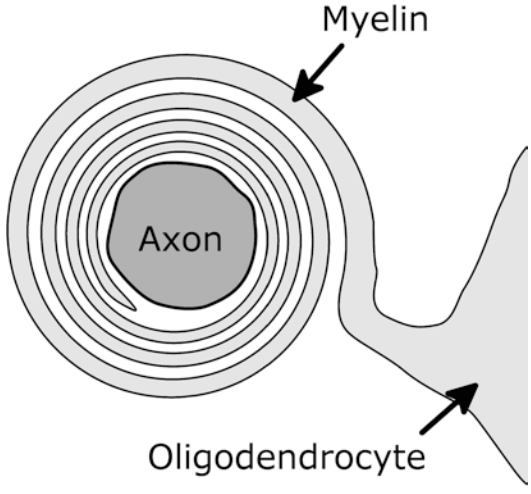

Fig. 3.5 Illustration of the multilayered myelin sheath formed from a protrusion of an oligodendrocyte

There are other types of cells that exist around neurons. The aforementioned oligodendrocyte cells are numerous and serve to provide the insulating myelin sheath to axons. Microglia are small cells which vary widely in size and shape and serve as the immune defence for the central nervous system. They act as macrophages do elsewhere in the body, i.e., identifying and clearing plaques, damaged neurons, and infectious agents. Astrocytes are star-shaped cells that serve a number of maintenance and metabolic functions. They are the most abundant cell type in the brain.

This brings us to an important distinction to make between the two major tissue types in the brain: grey matter and white matter. Figure 3.6 is a highly simplified illustration of the contrast between grey matter and white matter structure.

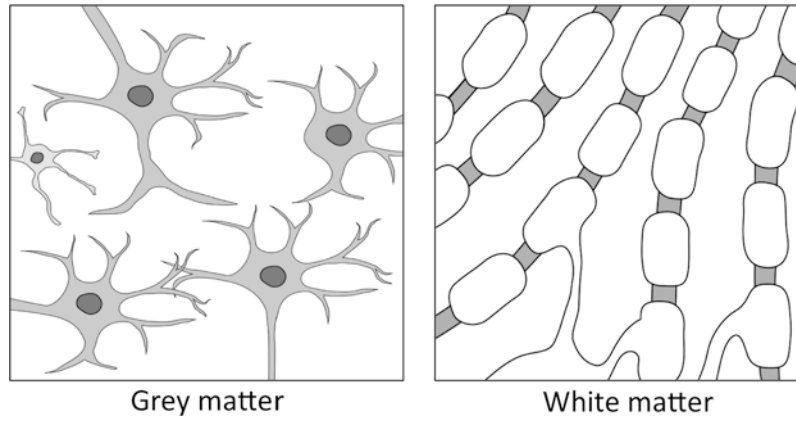

Fig. 3.6 Simple illustration of the contrast between *grey* matter and *white* matter

Grey matter is the tissue which can be observed on the surface of the brain; this region is often referred to as the "cerebral cortex." The cerebral cortex is the outermost layer of neural tissue and is usually 2–4 mm thick in humans. The cerebral cortex is divided up into different areas which are active in cognition, motor, and sensory responses. There are also some deep "subcortical" regions of grey matter, which are located in and around the brainstem and serve many basic purposes, such as cardiac and respiratory regulation, sleep and appetite regulation, and also as relays for connection between multiple cortex regions and the rest of the body. The grey matter mainly consists of the soma, the dendrites, and other cells such as microglia and astrocytes.

The organization of grey matter tissue is highly complex, with many neuron bodies and a complex web of dendrites and glial cells. The diffusion characteristics of water in grey matter are consequently highly complicated, due to complex structural trends in the tissue. As a result of this interpreting DTI measurements in grey matter is very challenging.

White matter is the tissue that lies underneath the cortex and serves to connect neurons in different parts of the brain to form the neural network. It is composed almost entirely of myelinated axons. The name "white matter" comes from the fact that myelin is a white substance; therefore white matter appears white when observed in dissection. The axons in white matter are organized into tight bundles of thousands or millions, which are coherent and tightly packed. Hence diffusion characteristics of water in white matter are often highly directionally dependent. The intracellular water tends to diffuse much more readily along the axis of the axons in a coherent bundle than in any other direction and the extracellular water is also heavily guided by the lattice structure formed by the axons. Intracellular water tends to exhibit restricted diffusion properties, while extracellular water tends to exhibit hindered diffusion properties, both of which were discussed in the previous section. Therefore probing the diffusion characteristics of water in white matter can yield information on the direction of bundles of axons as they traverse the brain. This is of critical importance to DTI as it provides us a very powerful tool to probe the connectivity of the brain.

There are many other structures and substances that affect the diffusion of water in and around cells in the central nervous system such as cytoplasm, neurofilaments, mitochondria, the extracellular matrix, and blood vessels. However the effect of these biological elements on DTI is often negligible or too complicated to be effectively modelled, and is hence beyond the scope of this book.

Figure 3.7 shows an electron micrograph of the optic nerve of a healthy rat sliced in a plane perpendicular to the axis of the nerve fibers. The optic nerve is a white matter structure comprised largely of myelinated axons. Many of the cellular structures discussed in this section can be

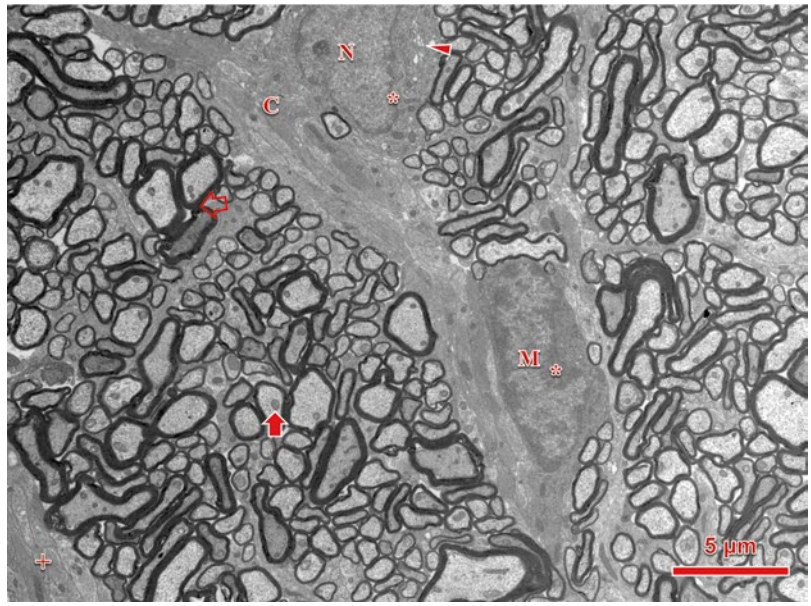

Fig. 3.7 Electron micrograph of the optic nerve of a healthy rat sliced in a plane perpendicular to the axis of the nerve fibers

observed in this picture. The filled red arrow indicates the interior of an axon and the open arrow points out the compact myelin layer surrounding axons. *N* indicates the nucleus of an oligodendrocyte; *C* indicates the cytoplasm of the same oligodendrocyte. *M* shows the nucleus of a microglial cell. + indicates part of an astrocyte, * shows hemochromatin, and the filled triangle shows the Gogli apparatus of the oligodendrocyte.

Sensitizing MR Measurements to Diffusion

Magnetic resonance imaging relies on the interaction of the applied magnetic fields with nuclei in the sample. "Spin" is a quantum mechanical property of a nucleus and over a large number of nuclei it gives rise to a net magnetization once placed in a magnetic field. The net magnetization of spins precesses with a frequency proportional to the local strength of the magnetic field. This is known as Larmor precession and it is by manipulating this relationship that we can acquire a magnetic resonance image and also apply diffusion weighting. For biological tissue, the majority of the signal arises from the hydrogen nuclei in water molecules.

Basic Concepts: How to Diffusion Weight the MRI Signal

The Pulsed Gradient Spin Echo Sequence

Currently, the Pulsed Gradient Spin Echo (PGSE) method is the most common way of sensitizing the MRI signal to molecular diffusion. PGSE sequences comprise a spin echo with magnetic field gradients before and after the refocusing pulse followed by an acquisition module (Fig. 3.8). The effects of diffusion on spin echo NMR experiments in a constant magnetic field gradient were first formulated by Hahn [8] and extended by Carr and Purcell [9]. Stejskal and Tanner [10] described the PGSE sequence in which the magnetic field gradients are "pulsed" instead of being constant over time. They also derived the signal equation for the sequence in freely diffusing liquids (Eq. 3.1). Such is the impact of their paper that the terms "Stejskal-Tanner sequence" and "Stejskal-Tanner equation" are still commonly used. The use of pulsed gradients for diffusion weighting allows more control over how the signal is weighted by diffusion. Furthermore, it allows the diffusion weighting

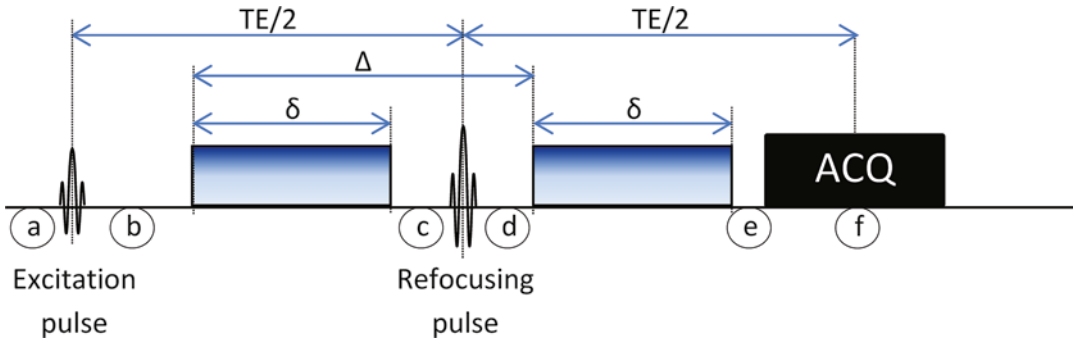

Fig. 3.8 Schematic of a PGSE pulse sequence

gradients to be separate from other pulsed gradients to be used for spatial localization, thus allowing for the quantification of diffusion in MRI experiments.

How the PGSE Signal Is Generated

Let us consider the evolution of net magnetization during the PGSE sequence, ignoring T_1 and T_2 relaxation, and assuming the pulsed gradients are short. We will need to know one key concept: the frequency of precession of the net magnetization is proportional to the field that the molecules experience (i.e., the Larmor equation, $f=\gamma B$, where f is the frequency in Hertz, γ is the gyromagnetic ratio in Hertz per Tesla, and B is the applied field in Tesla). Thus, when a magnetic field gradient is applied across a sample, the net magnetization will precess at different frequencies across that gradient (Fig. 3.9).

Figure 3.10 shows the evolution of magnetization during the PGSE sequence in the rotating frame. Also see Fig. 3.8 for corresponding points along the pulse sequence.

(a)>(b) The excitation pulse rotates net magnetization onto the transverse plane.

(b)>(c) The first pulsed gradient dephases the spin magnetization due to the variation of the frequency of precession along the gradient.

(c)>(d) The refocusing pulse rotates the magnetization about the y-axis.

(d)>(e) The second pulsed gradient rephases magnetization:

- **No diffusion**: Magnetization is completely rephased since the field experienced by the molecules has not changed.
- **Free diffusion**: (i) Molecules have changed position between the start of the first and second gradients (diffusion time) (ii) The field that they experience has changed. (iii) The frequency of precession has changed. (iv) The phase of the magnetization after the second gradient will not be the same as before the first gradient. (v) In free diffusion, the motion of molecules is incoherent and the magnetization will have a distribution of phases. (vi) The net magnetization is attenuated.

(e) The signal is acquired: In the presence of diffusion, the signal is attenuated.

b-Value: A Handy Way to Quantify Diffusion Weighting

The "*b*-value" [11] quantifies the applied diffusion weighting of a pulse sequence in a single number. This single number has become the standard metric of quantifying diffusion weighting in MRI sequences. A low *b*-value scan has more signal compared to a high *b*-value one (see Fig. 3.11), or, in other words, a high *b*-value scan exhibits more signal attenuation in the presence

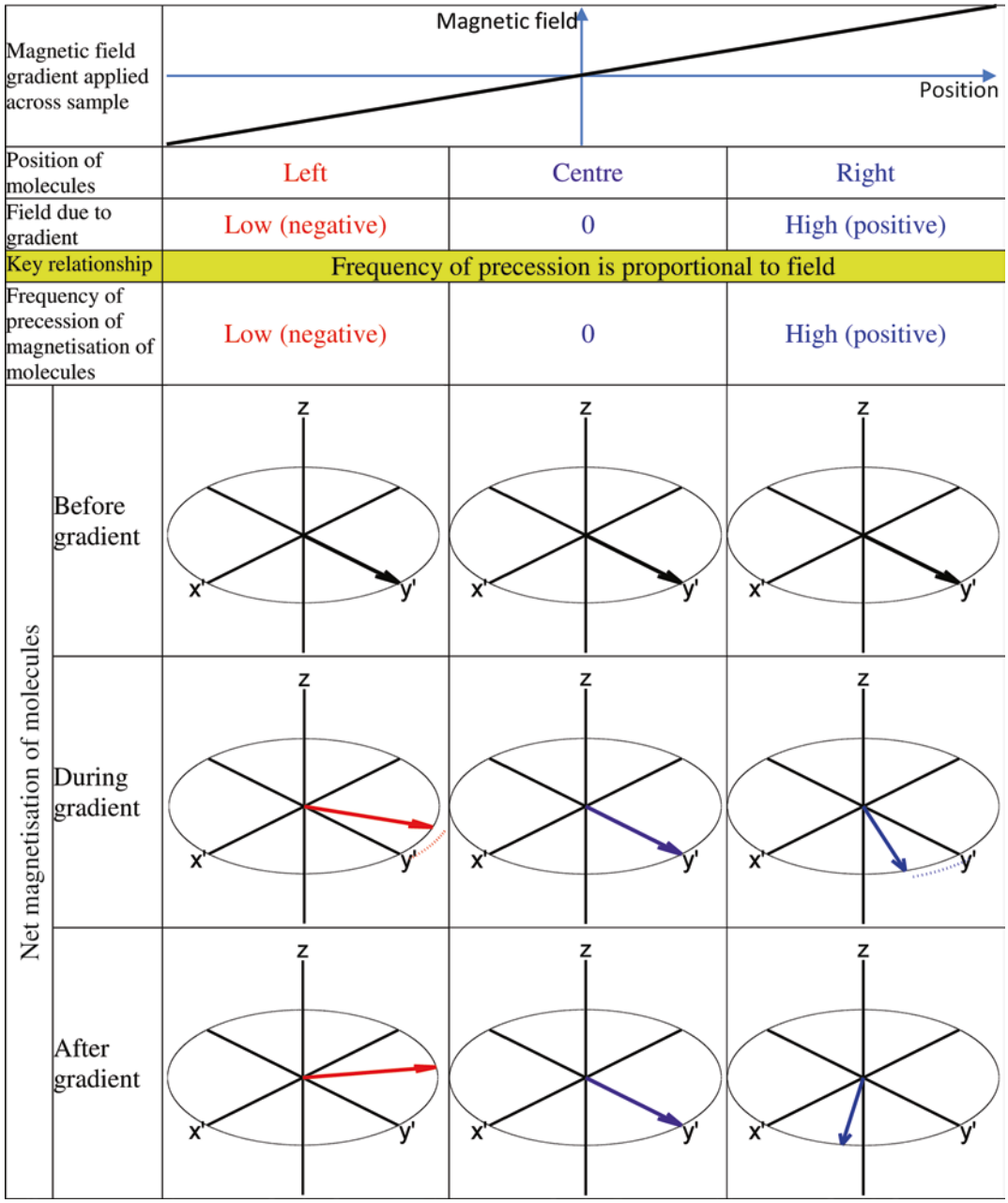

Fig. 3.9 Frequency and phase relationship of Larmor precession in the presence of a magnetic field gradient

of diffusion than a low *b*-value scan. So the *b*-value could be said to be a rough measure of how much the signal in an image will be affected by the diffusion of water in tissue. A *b*-value of zero will give no diffusion weighting at all in the image and diffusion weighted acquisitions normally include one or more zero *b*-value scans for normalization. These scans are often referred to as *b*-zero images.

Informally, the *b*-value is often given in units of s/mm^2. For example, "*b*-value of 1000" is an often heard phrase in the clinic—roughly, this

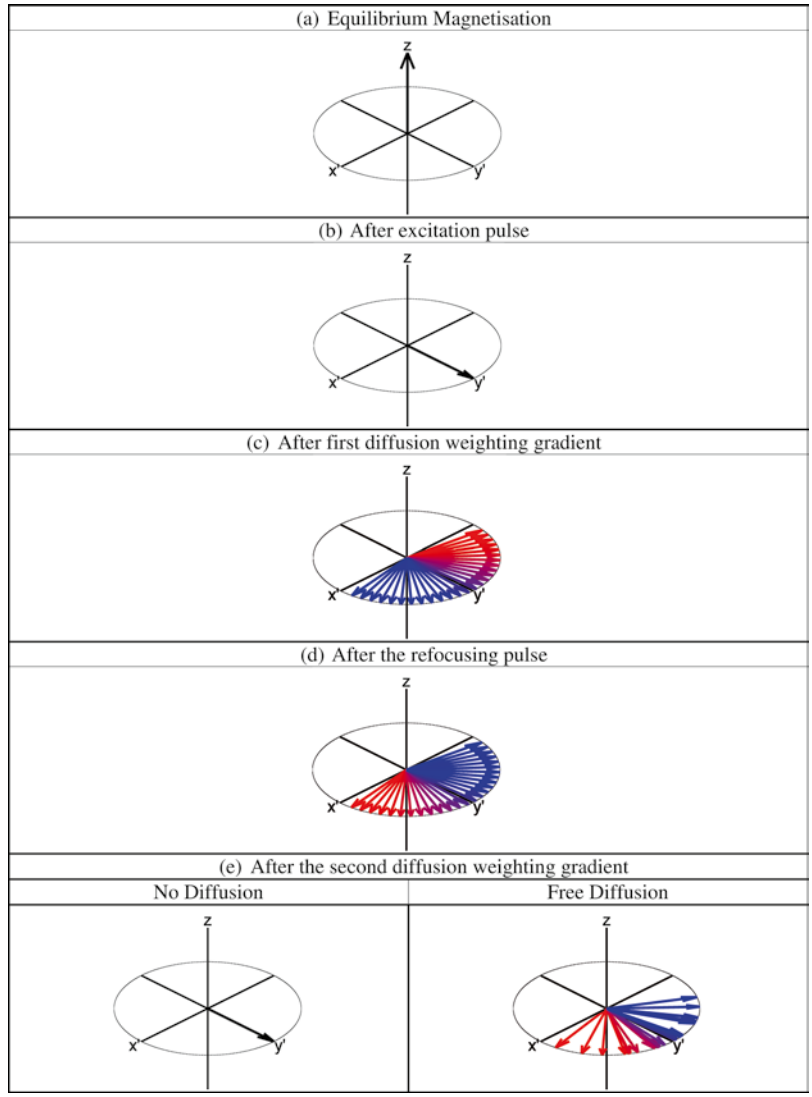

Fig. 3.10 The evolution of magnetization during the PGSE sequence

will normally give approximately 40–60 % signal attenuation in the brain, depending on the tissue type in which the water is embedded. Elsewhere in the body, *b*-values used in clinical investigations are often lower from 50 s/mm^2 and below to 500 s/mm^2 [12, 13]. Selection of *b*-value is influenced by the intended application and a balance between practical concerns and hardware limitations [14]. It is worth noting that at higher *b-values*, as there is more signal attenuation in the presence of diffusion, there is less overall signal; hence this lowers the signal to noise ratio (SNR). Therefore when choosing the *b*-value for diffusion weighted scans, it is important to consider the compromise between SNR and contrast. High *b*-value scans can offer extra information about tissue structure, especially structure at very small length scales. However, we must keep in mind that the SNR will be lower when planning an acquisition and processing image data. More advanced techniques often use considerably higher *b*-values of 2000 or above [15–17].

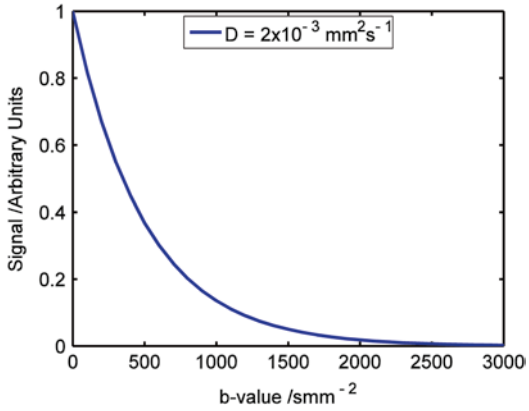

Fig. 3.11 Diffusion weighted MRI signal as a function of *b*-value

PGSE Signal

The signal of a PGSE scan of a freely diffusing sample is given by the Stejskal-Tanner equation:

$$\frac{S}{S_0} = e^{-(\gamma^2 G^2 \delta^2 (\Delta - \frac{\delta}{3}))D} \tag{3.1}$$

which can be written in terms of the *b*-value as such:

$$\frac{S}{S_0} = e^{-bD}$$
$$where$$
$$b = \gamma^2 G^2 \delta^2 (\Delta - \frac{\delta}{3}) \tag{3.2}$$

where δ is the gradient duration, Δ is the time between the start of each gradient, G is the gradient strength, γ is the gyromagnetic ratio, S is the signal, S_0 is the signal without diffusion weighting gradients, and D is the diffusion constant.

The PGSE signal decays exponentially as a function of the parameters of the applied gradients and the diffusion constant (see Fig. 3.11). In imaging experiments, additional pulse magnetic field gradients are applied for spatial localization. These gradients, and other applied magnetic field gradients, may contribute to diffusion weighting. These are often partially factored out by dividing signal from scans with diffusion weighting gradients by that of scan with no or low diffusion weighting gradients, the latter being used to minimize the effects from perfusion [18].

The *b*-value summarizes the three parameters G, δ, Δ used to control the amount of diffusion weighting in a PGSE sequence. It should be noted that the same *b*-value can produce very different contrast depending upon the combination of G, δ, Δ, the selection of which can be optimized for particular applications and tissue types [19].

Free, Hindered, and Restricted Diffusion

Thus far we have discussed the diffusion MRI signal in the case of free diffusion, i.e., molecules are free to diffuse as in a large pool of liquid (Fig. 3.1). Let us consider again a population of diffusing molecules, if at time $t=0$ they are all at the same point, then at $t>0$ their spatial distribution is Gaussian (or in shorthand a "Gaussian dispersion pattern" or just "Gaussian diffusion"). The average distance between the position of molecules at the start and end of the diffusion time (or more technically, the root mean square (RMS) displacement) is given by:

$$\text{RMS} = \sqrt{6Dt} \tag{3.3}$$

For biomedical applications there are only a few specific locations in which free diffusion occurs—for example in cerebrospinal fluid in large cavities in the ventricular system. In other tissues, diffusion is hindered and restricted by intra- and extra-cellular constituents and by the cellular membranes (Fig. 3.2). In these cases, the diffusion constant quantified using the Stejskal-Tanner equation is not the innate diffusion constant of the tissue water but rather an "apparent diffusion coefficient" (ADC)—equivalent to the self-diffusion constant of a more viscous, freely diffusing liquid.

In tissue water that is not confined within the microstructure of the tissue, for example in the extracellular space, the RMS displacement is approximated quite well by substituting D with ADC in Eq. (3.3). The relationship between ADC and RMS displacement is less straightforward in the case of molecules that are confined within the tissue microstructure (or more accurately, where water molecules have a low probability of leaving the bounding structure during the diffusion time

such as water inside myelinated axons). For short diffusion times, RMS diffusion is well approximated by ADC. At long diffusion times the molecules will have had enough time to traverse across the structure and "bounce off" the bounding wall. In this case, RMS displacement is not well approximated by Eq. (3.3). On the scale of an MRI voxel, tissue contains a mixture of hindered and restricted "compartments"; thus quantification of indices of microstructure based solely on Eq. (3.3) should be used in an informed manner.

References

1. Brown R. A brief account of microscopical observations made in the months of June, July and August, 1827, on the particles contained in the pollen of plants: and on the general existence of active molecules in inorganic bodies. Phil Mag. 1827;4:161–73.
2. Fick A. Concerns diffusion and concentration gradient. Ann Phys Lpz. 1855;170:59.
3. Fick A. Über diffusion. Ann Phys. 1855;94:59.
4. Einstein A. Über die von der molekularkinetischen Theorie der wärme gefordete Bewegung von in ruhenden Flüsigkeiten suspendierten Teilchen. Ann Physik. 1905;4:549–60.
5. Einstein A. Investigations on the theory of Brownian movement. New York, NY: Dover Publications, Inc; 1926.
6. Levitan IB, Kaczmarek LK. The neuron: cell and molecular biology. 3rd ed. New York, NY: Oxford University Press; 2002.
7. Waxman SG, editor. The axon: structure, function and pathophysiology. New York, NY: Oxford University Press; 1995.
8. Hahn EL. Spin echoes. Phys Rev. 1950;80(4):580–94. doi:10.1103/PhysRev.80.580.
9. Carr HY, Purcell EM. Effects of diffusion on free precession in nuclear magnetic resonance experiments. Phys Rev. 1954;94(3):630–8. doi:10.1103/PhysRev.94.630.
10. Stejskal EO, Tanner JE. Spin diffusion measurements: spin echoes in the presence of a time-dependent field gradient. J Chem Phys. 1965;42(1):288–92. doi:10.1063/1.1695690.
11. Le Bihan D, Breton E. Imagerie De Diffusion In Vivo Par Résonance Magnétique Nucléaire. Comptes Rendus De Académie Des Sciences De Paris. 1985;301:1109–12.
12. Koh DM, Collins DJ. Diffusion-weighted MRI in the body: applications and challenges in oncology. AJR Am J Roentgenol. 2007;188(6):1622–35.
13. Lansdown DA. Quantitative diffusion tensor MRI-based fibre tracking of human skeletal muscle. J Appl Physiol. 2007;103(2):673–81.
14. Le Bihan D, Poupon C, Amadon A, Lethimonnier F. Artefacts and pitfalls in diffusion MRI. J Magn Reson. 2006;24(3):478–88.
15. Jensen JH, Helpern JA, Ramani A, Lu H, Kaczynski K. Diffusional kurtosis imaging: the quantification of non-gaussian water diffusion by means of magnetic resonance imaging. Magn Reson Med. 2005;53(6):1432–40.
16. Tournier J, Calamante F, Connelly A. Determination of the appropriate b value and number of gradient directions for high-angular-resolution diffusion-weighted imaging. NMR Biomed. 2013;2013:1099–492.
17. Alexander DC, Hubbard PL, Hall MG, Moore EA, Ptito M, Parker GJ, et al. Orientationally invariant indices of axon diameter and density from diffusion MRI. Neuroimage. 2010;52(4):1374–89.
18. Le Bihan D, Breton E, Lallemand D, Aubin ML, Vignaud J, Laval-Jeantet M. Separation of diffusion and perfusion in intravoxel incoherent motion MR imaging. Radiology. 1988;168(2):497–505.
19. Alexander DC. A general framework for experiment design in diffusion MRI and its application in measuring direct tissue-microstructure features. Magn Reson Med. 2008;60:439–48.

Suggested Reading

Crank J. Mathematics of diffusion. Oxford: Clarendon; 1975.

Basser PJ, Mattiello J, Le Bihan D. Estimation of the effective self-diffusion tensor from the NMR spin echo. J Magn Reson B. 1994;103(3):247–54. doi:10.1006/jmrb.1994.1037.

Le Bihan D, Johansen-Berg H. Diffusion MRI at 25: exploring brain tissue structure and function. Neuroimage. 2012;61(2):324–41. doi:10.1016/j.neuroimage.2011.11.006.

From Diffusion to the Diffusion Tensor

4

Thijs Dhollander

Learning Points

- The diffusion coefficient; the apparent diffusion coefficient (ADC); their relation to the pair of acquired diffusion-weighted images (DWI) and nondiffusion-weighted images (B0); and a few general properties of the ADC in relation to the amount of diffusion weighting (the *b*-value).
- The concept of directionality of the diffusion sensitizing gradient; the concept of anisotropy in the acquired data; and inferring useful information on the orientation of axon bundles based on raw DWIs, normalized DWIs, ADC maps, and spherical polar plots of the latter two quantities.
- The apparent diffusion tensor; evaluating a tensor model; the link between the diffusion tensor and the acquired DWIs/B0; the meaning and interpretation of the tensor elements; and visualizing the tensors by spherical polar plots (ADC peanuts).
- Eigendecomposition of the tensor; the meaning and interpretation of eigenvalues and eigenvectors; and interpreting maps of eigenvalues and directionally encoded color (DEC) maps of eigenvectors.
- Basic visualization of tensors by glyphs; the meaning of the tensor ellipsoid; and maps of common measures such as mean diffusivity (MD), fractional anisotropy (FA), DEC FA, and a few other shape measures.
- The issue of tensor fitting; and specific tensor fitting methods: linear least squares (LLS), weighted linear least squares (WLLS), nonlinear least squares (NLS), and robust estimation of tensors by outlier rejection (RESTORE).

T. Dhollander, PhD (✉)
The Florey Institute of Neuroscience and Mental Health, Melbourne Brain Centre, 245 Burgundy Street, Heidelberg, VIC 3084, Australia

Medical Imaging Research Center (MIRC), KU Leuven, Leuven, Belgium
e-mail: thijs.dhollander@florey.edu.au

The (Self-)Diffusion Coefficient

Measuring (Self-)Diffusion in the MR Scanner

Sit down, relax, and grab yourself a glass of water. Now put it in a nearby MR scanner (or rather, imagine doing this). Acquire a (nondiffusion-weighted) T2-weighted image as well as one of those fancy new diffusion-weighted images. Now let's see if we can recover the diffusion coefficient of water from these two images. More accurately, we're talking about the *self diffusion coefficient* here: it quantifies the freedom of movement of any single molecule of water, in

W. Van Hecke et al. (eds.), *Diffusion Tensor Imaging*, DOI 10.1007/978-1-4939-3118-7_4

the glass of water. We'll simply refer to it as *D*. Also note that we need (at least) two images: the diffusion-weighted image would appear exactly the same as the T2-weighted image, if it were not *weighed down* by the appearance of diffusion; i.e., we're interested in the relative difference between both images. Since *D* should be the same in the entire glass of water, we simply choose one voxel. The intensity of the diffusion-weighted image in this voxel will be referred to as *S*, while the (non-diffusion-weighted) T2-weighted image's intensity equals S_0. As explained in Chap. 3, the process of diffusion should have caused *attenuation* in *S*, so *S* should always be smaller than S_0. The *decay* of *S* relative to S_0 is given by the so-called Stejskal-Tanner equation [1]:

$$S = S_0 \bullet e^{-b \bullet D} \tag{4.1}$$

The *b*-factor in this equation captures all the relevant *scanning parameters* and was introduced to take abstraction of them [2]. In general, it can be seen as the amount of *diffusion weighting* that is applied; i.e. how sensitive the acquisition is to diffusion. Its value is typically set and reported in s/mm^2. As a realistic value for our simple experiment at hand, we could have chosen e.g. 800 s/mm^2. We can rewrite this equation so it becomes

$$-\ln\left(\frac{S}{S_0}\right) = b \bullet D \tag{4.2}$$

The left side of the equation only contains measurements we obtained from the scanner (*S* and S_0), while the right side contains the scanning parameters in function of which we did so (all contained within the *b*-factor) and a constant (*D* for our glass of water at room temperature). From this we learn that a *logarithmic transform* (i.e., "$-\ln(\ldots)$") of our *normalized measurement* (i.e., "S/S_0") depends *linearly* on the applied diffusion weighting (i.e., *b*). As they are both simply related by a factor *D*, plotting $-\ln(S/S_0)$ in function of *b* yields a straight line through the origin, as shown in (Fig. 4.1). The slope of this line equals *D*:

$$D = \frac{-\ln\left(\frac{S}{S_0}\right)}{b} \tag{4.3}$$

The value of *D* is typically reported in mm^2/s. For our glass of water, $D = 2.2 \times 10^{-3}$ mm^2/s should be realistic at room temperature. If we were lying in the scanner ourselves and performed the above calculation for a voxel of cerebrospinal fluid (CSF) in the ventricles of our brain, a value of about 3.1×10^{-3} mm^2/s is to be expected. While CSF consists mostly (99 %) of water, the difference can be explained by our *body temperature*, which is of course higher than the normal room temperature. One point is enough to fully fix the slope of the line in (Fig. 4.1) and per consequence also determine *D*. If we would have performed the measurement using a different *b-value*, we would obtain another point on this exact same line. Using a *higher b*-value would result in *more decay*, and thus a *lower value for S* (this can be most easily appreciated by looking at Eq. 4.1). A *lower value for S* means a *higher value for* $-\ln(S/S_0)$. Consequently, we are simply considering a point further up the same line in (Fig. 4.1).

Conclusions

We are now able to calculate the *self-diffusion coefficient D* of free water (be it in a glass or as CSF in the ventricles), using measurements from

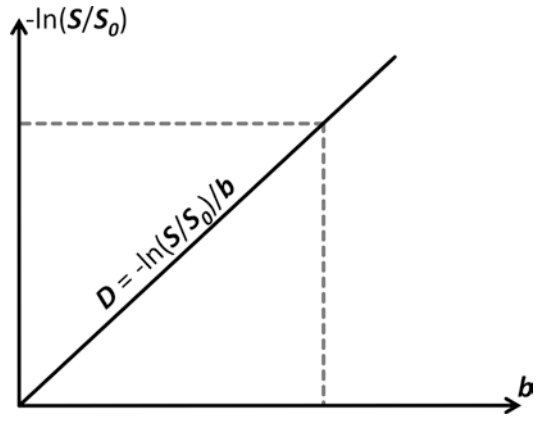

Fig. 4.1 In case of free diffusion (e.g., in a glass of water, or CSF in the ventricles of the brain), the plot of $-\ln(S/S_0)$ in function of *b*-value is a *straight line* through the origin. One point (*grey short dashed lines*) is enough to fully fix this line. It requires two images (*S* and S_0) as well as knowledge of the *b*-value used to acquire *S*. The slope of the resulting line equals the self-diffusion coefficient *D*

a MR scanner and the Stejskal-Tanner equation. The *minimum requirements* are a nondiffusion-weighted image (S_0), a diffusion-weighted image (S) and knowledge of the b-value that was used for performing the acquisition of the diffusion-weighted image.

The Apparent Diffusion Coefficient

Apparent Complications

Feeling confident about the newly gained ability to obtain D from the two images we acquired of our brain, we also attempt to perform the same calculation in a voxel of gray matter. Suddenly, however, we are confronted with a resulting value of about 0.9×10^{-3} mm^2/s. *Apparently*, the self-diffusion coefficient of water has changed, just because we measured it in the gray matter. Maybe something went wrong with the scan? We perform the acquisition again for a couple of different b-values. Carefully dotting out the obtained values of $-\ln(S/S_0)$ in function of b and connecting everything loosely by hand, we obtain a curve such as the one depicted in (Fig. 4.2). *Apparently*, the self-diffusion coefficient of water now even changes in function of our chosen acquisition parameters. Using Eq. (4.3) to calculate D equates to connecting a certain measured point on this curve with the origin by a *straight line* (as shown in Fig. 4.2) and assuming its slope still equals D. Since the obtained values are clearly lower than expected and they also seem to vary in function of b, such a value is referred to as an *apparent diffusion coefficient* (*ADC*) [3]. It's calculated from the measurements in exactly the same way as D:

$$\mathrm{ADC} = \frac{-\ln(\frac{S}{S_0})}{b} \tag{4.4}$$

To understand the behavior of the obtained ADC in regions containing tissue (e.g., gray matter), we need to look into how the acquisition of a diffusion-weighted image works. An existing (e.g., T2-weighted) sequence is modified by adding a

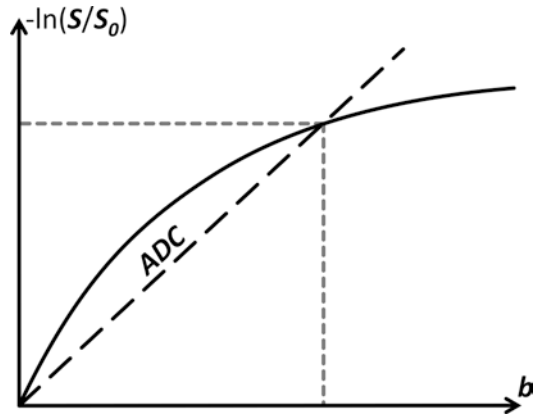

Fig. 4.2 In case of hindered/restricted diffusion (in tissue, e.g. the grey matter of the brain), the plot of $-\ln(S/S_0)$ in function of b-value is a *curve* through the origin. Based on one point (*grey short dashed lines*), we can calculate an apparent diffusion coefficient (ADC). Just like D, it equals the slope of the line that connects this point to the origin (*black long dashed line*)

couple of diffusion-sensitizing gradients. By taking abstraction of any complicated MR physics, we could say the MR scanner actually performs a simple experiment in each voxel: it takes a snapshot of all the water molecules, waits a bit, and then takes another snapshot. During the short waiting time, however, the molecules have the opportunity to *diffuse* a bit. Per consequence, a relative *displacement* of each molecule can take place in between both snapshots. The expected signal of the original (e.g., T2-weighted) sequence is *attenuated* in function of the amount of *displacement* of all water molecules in the voxel (as well as the amount of applied diffusion weighting). From the measurements of such an experiment (relative to a nondiffusion-weighted image), the Stejskal-Tanner equation is able to reliably calculate D… if and only if nothing disturbs the experiment. However, in tissue, such as gray matter, there are *cell membranes* all over the place. Because the water molecules happen to bump into the cells—i.e., they are *hindered*—they have a harder time to diffuse further away during the experiment. Water inside the cells may even be *restricted* to a confined space. And thus, our calculation of D will *apparently* yield a lower outcome, which is why we call it the ADC instead. The time the experiment allows the molecules to

diffuse is one of the parameters that makes up the *b*-value. It's easy to imagine that a larger diffusion time will allow more molecules to hit some of these cell membranes. Hence, the effect of the *hindered/restricted* diffusion on our measurement will increase with *b*-value; yet another reason to refer to the outcome of our calculations using the term "ADC". This is also illustrated in (Fig. 4.3): using a *larger b*-value renders the measurement of *S less sensitive to* (*truly*) *free diffusion*, in favor of hindered/restricted diffusion. As such, *S* will be *less attenuated* and the value of $-\ln(S/S_0)$ will be *smaller* than expected, yielding a *downward curvature* when plotting $-\ln(S/S_0)$ in function of *b*. This finally leads to an important property of the ADC in tissue, as indicated in (Fig. 4.3): using a *higher b*-value results in a *lower ADC*.

Apparent Advantages

At this point, you might start to wonder what the point is of trying to find out *D* in voxels containing tissue, only to end up having to deal with a deceiving ADC instead. However, you have to look at it from the bright side: we now effectively have access to a *probe* that tells us something about these *cells* that hinder/restrict diffusion. That's right: even though our voxel size might be quite crude ($2\times2\times2$ mm^3 or larger is not unusual), the measured values are sensitive to differences in structure at a *micrometer* scale! We are not interested in the ADC for the purpose of quantifying diffusion itself, but rather to *investigate properties of the tissue* that apparently caused the diffusion process to behave in the way that we measure.

Before moving on, let's investigate one more property of the ADC that teaches us something else about its capacity in distinguishing different tissues. Consider the setting in (Fig. 4.4): it presents again $-\ln(S/S_0)$ in function of *b*, but this time for measurements at two different locations (e.g., in the brain). Looking at the plots and applying what we just learned, we can safely say that the voxel at position p_g contains more hindering/restricting tissue than the voxel at position p_f. The former voxel's plot shows greater curvature,

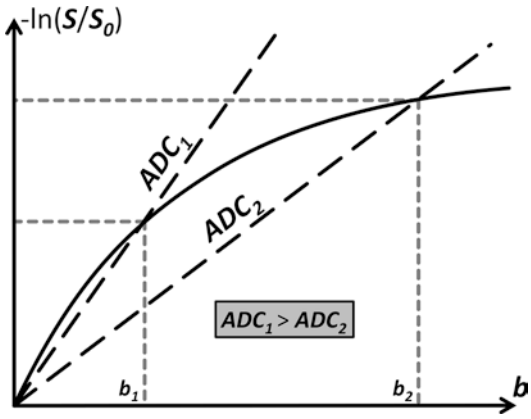

Fig. 4.3 The ADC is dependent on the *b*-value used to acquire *S*. Due to the downwards curvature of the plot of $-\ln(S/S_0)$ in function of *b*-value, a larger *b*-value results in a lower ADC. An explanation lies, e.g., in the fact that increasing the diffusion time allows more molecules to bump into cell membranes. This will on average decrease their final displacement, resulting in a reduced amount of attenuation of *S* and finally leading to a lower value for $-\ln(S/S_0)$ than expected in a free (non-hindered/restricted) environment

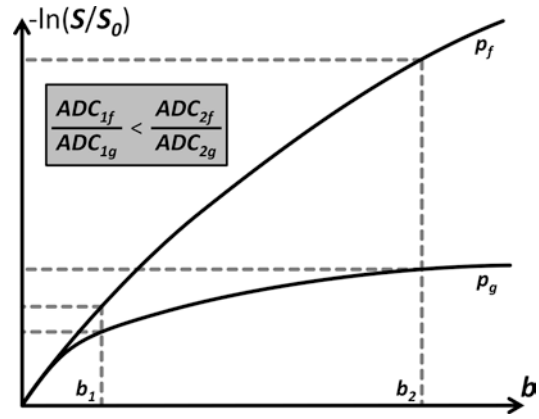

Fig. 4.4 The contrast of the ADC, e.g., between two different tissues at voxel positions p_f and p_g, is dependent on the *b*-value used to acquire *S*. Due to different tissue properties, both plots of $-\ln(S/S_0)$ in function of *b*-value show a different curvature. The tissue at p_f imposes less hindrance/restriction on the diffusion as compared to the tissue at p_g and thus the accompanying curve is closer to a *straight line*. Hence, ADC_f is larger than ADC_g for a given *b*-value. Increasing the *b*-value also results in an increase of the relative difference between both ADC values, i.e., an increase of contrast

while the latter better approximates the straight line we would expect in case of free diffusion. Due to this difference in curvature of both plots, the *relative difference* in magnitude of $-\ln(S/S_0)$, and thus also ADC, *increases for larger b-values*. In other words, using a *larger b*-value results in a *better contrast* when calculating an ADC map. This fact of course begs the question why we should still limit ourselves to a certain *b*-value. That is, why not use an absurdly high *b*-value for maximal contrast? The two most important factors that generally contribute to the *b*-value are the strength of the applied diffusion-sensitizing gradients and the time that we allow the water to diffuse during the experiment. The former is limited by what we can achieve with available hardware. The latter is fully under our control. Allowing a too long diffusion time, however, might result in other more macroscopic motion to be captured and thus confounding our measurements. Even if this would not be the case, we also have to recall that *S* only *decays* further in function of *b*-value (remember Eq. 4.1 again?). The *noise level* of our measurements, on the other hand, *does not decrease*; that is, using a *higher b*-value yields a *lower signal-to-noise ratio* (*SNR*)!

Conclusions

We have learned why the MR measurements in combination with the Stejskal-Tanner equation are not suited to calculate the true self-diffusion coefficient of water in voxels containing tissue, e.g., where diffusion is *hindered* or even *restricted*. The obtained *apparent diffusion coefficient* (*ADC*), on the other hand, can provide interesting information about the microstructure of the tissue under investigation. The *minimum requirements* for obtaining it are again a nondiffusion-weighted image (S_0), a diffusion-weighted image (*S*) and knowledge of the *b*-value that was used for performing the acquisition of the diffusion-weighted image. The ADC is, however, dependent on the *b*-value: a *higher b*-value results in a *lower ADC*. It also *improves the contrast* (e.g., of the ADC map), but at the cost of a *reduced SNR*. Due to these dependencies, interpreting/reporting the ADC only makes sense when the *b*-value is also specified. Finally, comparing ADC values or maps originating from acquisitions with different *b*-values does *not* make a lot of sense.

Gradient Directions and Anisotropy

Anisotropic Complications

Up to now, we've been silently ignoring yet another important fact that will complicate everything even more. It concerns that diffusion-sensitizing gradient: it's about time we started taking into account that it's applied along a certain *direction*. Nothing to worry about, if it were not for the fact that our measurements are only sensitive to diffusion along this direction. Actually, that is not fully correct; it's better to say that they are *only sensitive to diffusion with a component along this direction*. Before we start talking further about directions, let's settle on some reference frame. We define three (perpendicular) axes through the brain as follows: *x* runs from *left to right*, *y* from *back to front*, and *z* from *bottom to top*. So suppose we would apply the diffusion gradient along the direction of *x*, what are the implications then? It basically means that the measurements are *fully sensitive* to diffusion *along x*, but *gradually less sensitive* to diffusion along directions that *increasingly deviate* from *x*, up to the point where they are *completely insensitive* to diffusion along directions *perpendicular* to *x* (i.e., directions in the *yz*-plane).

But why should we worry about directionality of diffusion anyway? In our earliest experiments with a glass of water or CSF in the ventricles, we shouldn't: diffusion takes place *equally in all directions*. In tissue randomly containing cells—imagine a bunch of spherical cells packed together—diffusion is hindered and restricted, yet probably more or less *equally in all directions*. So again, there's nothing to worry about: as we are in both cases studying *isotropic* measurements, it is sufficient to only measure along a single direction. Our findings (e.g. calculating the

ADC) should have been the same for measurements along any other direction. But let's consider the more interesting case of the white matter in the brain: it consists of long coherent bundles of axons, almost resembling a bunch of cylindrical tubes packed closely together (see Chap. 3). One can imagine that water molecules in between and inside these tubes have *an easier time diffusing along them rather than perpendicular to them*. We thus say that diffusion in the white matter is *anisotropic*.

But how relevant is this? Is this anisotropy large enough to be measured; i.e. can we see it in our diffusion-weighted images? To answer this question, we'll introduce some real data. In (Fig. 4.5), we start by presenting a classic T1-weighted and T2-weighted image for reference. Next is the nondiffusion-weighted image: it's again a T2-weighted image, but it already shows the *lower spatial resolution* at which DWI datasets are typically acquired. In this case, the voxel size equals $2.2 \times 2 \times 2$ mm^3. Because the image is not diffusion-weighted, but it is acquired as part of a DWI dataset, we also sometimes (informally) refer to it as the "B0" (it equals a diffusion-weighted image with a b-value of 0). For convenience, we already applied a whole brain mask to it. On the second row of (Fig. 4.5), three diffusion-weighted images (DWIs) are shown (also masked). They were all acquired

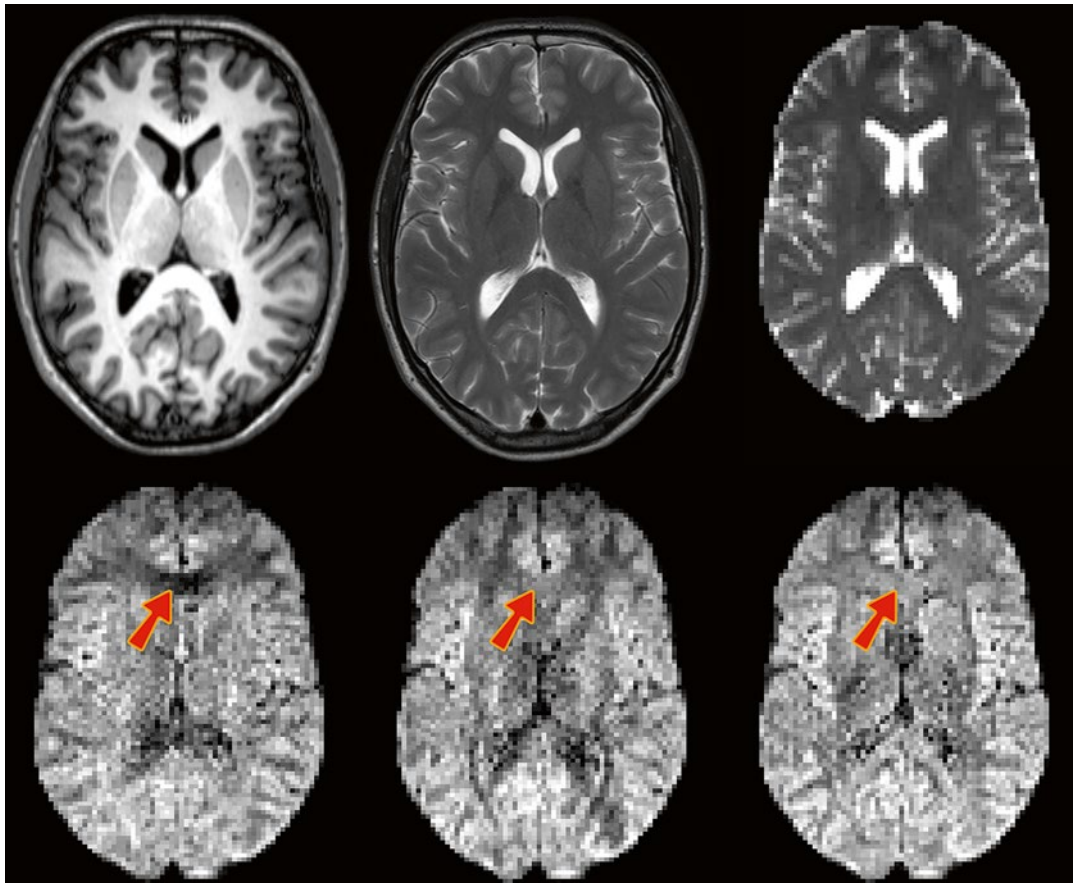

Fig. 4.5 *Top row*: T1-weighted image, T2-weighted image, B0 image ("diffusion-weighted image" with a b-value of 0, i.e., non diffusion-weighted). *Bottom row*: diffusion-weighted images (DWIs) acquired by applying gradients along the direction of x, y and z. The *arrows* indicate a region in the genu of the corpus callosum (GCC), where the anisotropy can be easily seen and understood

using exactly the *same amount* of diffusion weighting: $b = 800$ s/mm^2. The diffusion-sensitizing gradients are, however, applied *along different directions*: respectively along the direction of x, y and z. Differences in contrast can clearly be seen, which consequently confirms that we will have to account for *anisotropy* in our measurements.

Anisotropic Advantages

Just as when we introduced the ADC, we'll also try to use this fact to our advantage: we now have access to a probe that might even provide us with information on the *anisotropy of the microstructure* that hinders and restricts the process of diffusion. Applying what we have learned from this chapter up to this point, let's see if we can already figure out something useful from these three diffusion-weighted images. Consider the indicated region in the genu of the corpus callosum (GCC): it has *a low DWI-intensity along x*, but a (relatively) *higher DWI-intensity along y and z*. Because we know that more diffusion causes increased decay of S (the DWI-intensity), we can conclude from these images that there is *more free diffusion along x*, while there is *more hindrance and restriction along y and z*. Translating this to "reality", we might infer that *a bundle of tubelike axons runs along the left-right axis* in this region, connecting both hemispheres of the brain. Note that we are applying *inductive* reasoning here: we know that such a left-right oriented structure would result in such a pattern of diffusion and thus also such DWI measurements along these three directions, yet we reason that the latter measurements were effectively caused by the former structure. Considering we only measured along three directions, that's a pretty strong conclusion. Of course, inherently we might have also applied possible anatomical knowledge and the fact that a structure along this direction makes sense considering the spatial/anatomical neighborhood of the region (i.e., the region is in between both hemispheres).

Getting a Grip on the Information Overload

In practice, however, we will typically perform the acquisition using more than three different gradient directions. In the previous example, we were just lucky that the structure under investigation accidently happened to run along one of the three mutually perpendicular directions that we sampled. If it would instead be running at any other oblique angle, these three measurements would clearly be *inadequate* to determine its direction. In our experiment at hand, however, we actually acquired DWIs for a total of *45 different gradient directions*! The specifics of such an acquisition are presented in the *gradient table*, that contains *one row for each acquired image*, representing its gradient direction and b-value. The gradient table for our current experiment is provided in (Fig. 4.6). As it was already quite tedious to infer information by mentally combining three images, considering 45 DWIs all at once is nearly impossible. To begin with, we will no longer visualize the original DWIs, as they are still only representing a (partially) decayed T2-weighted signal. Because of this, these DWIs suffer so-called *T2 shine-through*: a higher intensity might not (only) result due to hindered/restricted diffusion; it might also be caused by an originally high T2 intensity (e.g., in areas containing CSF). Therefore, it is more evident to consider DWIs after *normalization by the B0* (i.e., the normalized measurements "S/S_0"). Such normalized versions of our original DWIs for the three x, y, and z gradient directions are shown in (Fig. 4.7). Next up is the actual challenge of visualizing the information of all 45 normalized DWIs in a conveniently organized way. Rather than showing 45 separate images, we could try to combine all information of each single voxel and visualize it within that particular voxel. Since the different values of S/S_0 are a *function of the gradient direction*, a *spherical polar plot* is the perfect candidate for the job. In such a plot, the radius of a sphere is locally manipulated to equal the function value at that three-dimensional angle. We also smoothly interpolated the values

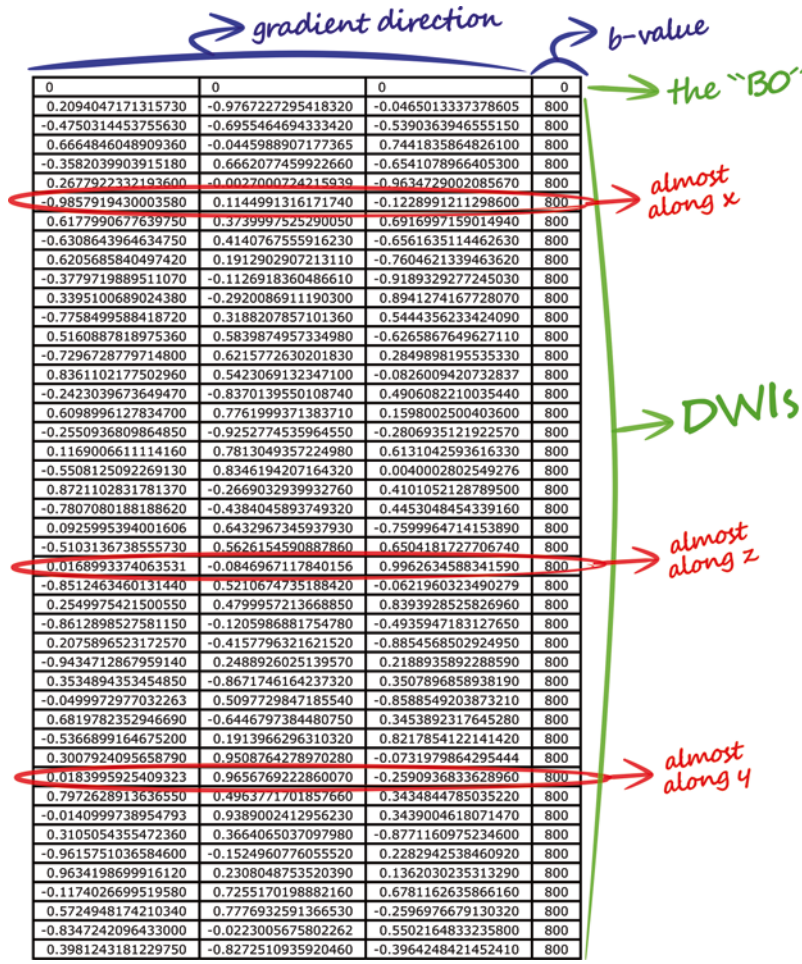

0	0	0	0
0.2094047171315730	-0.9767227295418320	-0.0465013337378605	800
-0.4750314453755630	-0.6955464694333420	-0.5390363946555150	800
0.6664846048909360	-0.0445988907177365	0.7441835864826100	800
-0.3582039903915180	0.6662072459922660	-0.6541078966405300	800
0.2677922332193600	-0.0027000724215939	-0.9634729002085670	800
-0.9857919430003580	0.1144991316171740	-0.1228991211298600	800
0.6177990677639750	0.3739997525290050	0.6916997159014940	800
-0.6308643964634750	0.4140767555916230	-0.6561635114462630	800
0.6205685840497420	0.1912902907213110	-0.7604621339463620	800
-0.3779719889511070	-0.1126918360486610	-0.9189329277245030	800
0.3395100689024380	-0.2920086911190300	0.8941274167728070	800
-0.7758499588418720	0.3188207857101360	0.5444356233424090	800
0.5160887818975360	0.5839874957334980	-0.6265867649627110	800
-0.7296728779714800	0.6215772630201830	0.2849898195535330	800
0.8361102177502960	0.5423069132347100	-0.0826009420732837	800
-0.2423039673649470	-0.8370139550108740	0.4906082210035440	800
0.6098996127834700	0.7761999371383710	0.1598002500403600	800
-0.2550936809864850	-0.9252774535964550	-0.2806935121922570	800
0.1169006611114160	0.7813049357224980	0.6131042593616330	800
-0.5508125092269130	0.8346194207164320	0.0040002802549276	800
0.8721102831781370	-0.2669032939932760	0.4101052128789500	800
-0.7807080188188620	-0.4384045893749320	0.4453048454339160	800
0.0925995394001606	0.6432967345937930	-0.7599964714153890	800
-0.5103136738555730	0.5626154590887860	0.6504181727706740	800
0.0168993374063531	-0.0846967117840156	0.9962634588341590	800
-0.8512463460131440	0.5210674735188420	-0.0621960323490279	800
0.2549975421500550	0.4799572713668850	0.8393928525826960	800
-0.8612898527581150	-0.1205986881754780	-0.4935947183127650	800
0.2075896523172570	-0.4157796321621520	-0.8854568502924950	800
-0.9434712867959140	0.2488926025139570	0.2188935892288590	800
0.3534894353454850	-0.8671746164237320	0.3507896858938190	800
-0.0499972977032263	0.5097729847185540	-0.8588549203873210	800
0.6819782352946690	-0.6446797384480750	0.3453892317645280	800
-0.5366899164675200	0.1913966296310320	0.8217854122141420	800
0.3007924095658790	0.9508764278970280	-0.0731979864295444	800
0.0183995925409323	0.9656769222860070	-0.2590936833628960	800
0.7972628913636550	0.4963771701857660	0.3434844785035220	800
-0.0140999738954793	0.9389002412956230	0.3439004618071470	800
0.3105054355472360	0.3664065037097980	-0.8771160975234600	800
-0.9615751036584600	-0.1524960776055520	0.2282942538460920	800
0.9634198699916120	0.2308048753520390	0.1362030235313290	800
-0.1174026699519580	0.7255170198882160	0.6781162635866160	800
0.5724948174210340	0.7776932591366530	-0.2596976679130320	800
-0.8347242096433000	-0.0223005675802262	0.5502164833235800	800
0.3981243181229750	-0.8272510935920460	-0.3964248421452410	800

Fig. 4.6 The gradient table contains one row for each acquired image. The x, y and z components of the gradient direction are provided in the first three columns, while the b-value is given in the last one. A b-value of 0 indicates a B0 image; the gradient direction is irrelevant in such a case. The *red encircled rows* refer to the DWIs presented in Fig. 4.5

between the 45 directions in order to achieve the final visualization in (Fig. 4.7). Note that, due to the multitude of information on display, we have to zoom in up to a reasonable level to show everything with the required amount of detail. We choose to further focus on the region of the GCC that was the subject of our earlier thought experiment. Furthermore, a little extra *color* was added to the plot: each point on the surface of the spherical polar plots is colored according to its *direction*: *red* is assigned to x, *green* to y and *blue* to z. In (the middle of) the GCC, we spot larger values for green (y) and blue (z), and smaller values for red (x). By linking *larger values* to *hindrance/restriction*, we can thus confirm our hypothesis of an axonal bundle connecting left and right.

Associating larger values with less diffusion still feels a bit awkward, to say the least. So why don't we simply employ the ADC values? Easy enough: just calculate the 45 ADC maps from the normalized DWIs using Eq. (4.4). We present these maps—again for the three x, y, and z gradient directions—in (Fig. 4.8). This time, *larger values* equal *more free diffusion*. We can just as well create a spherical polar plot of the 45 ADC values in each voxel, which is again provided for the GCC region in (Fig. 4.8). *Larger values* are now conveniently oriented along the direction of the *greatest amount of free diffusion*, and colored accordingly. Finally, remember that property of the contrast increasing with b-value? Of course, it also applies for measurements (and ADC values) acquired using different gradient directions: using

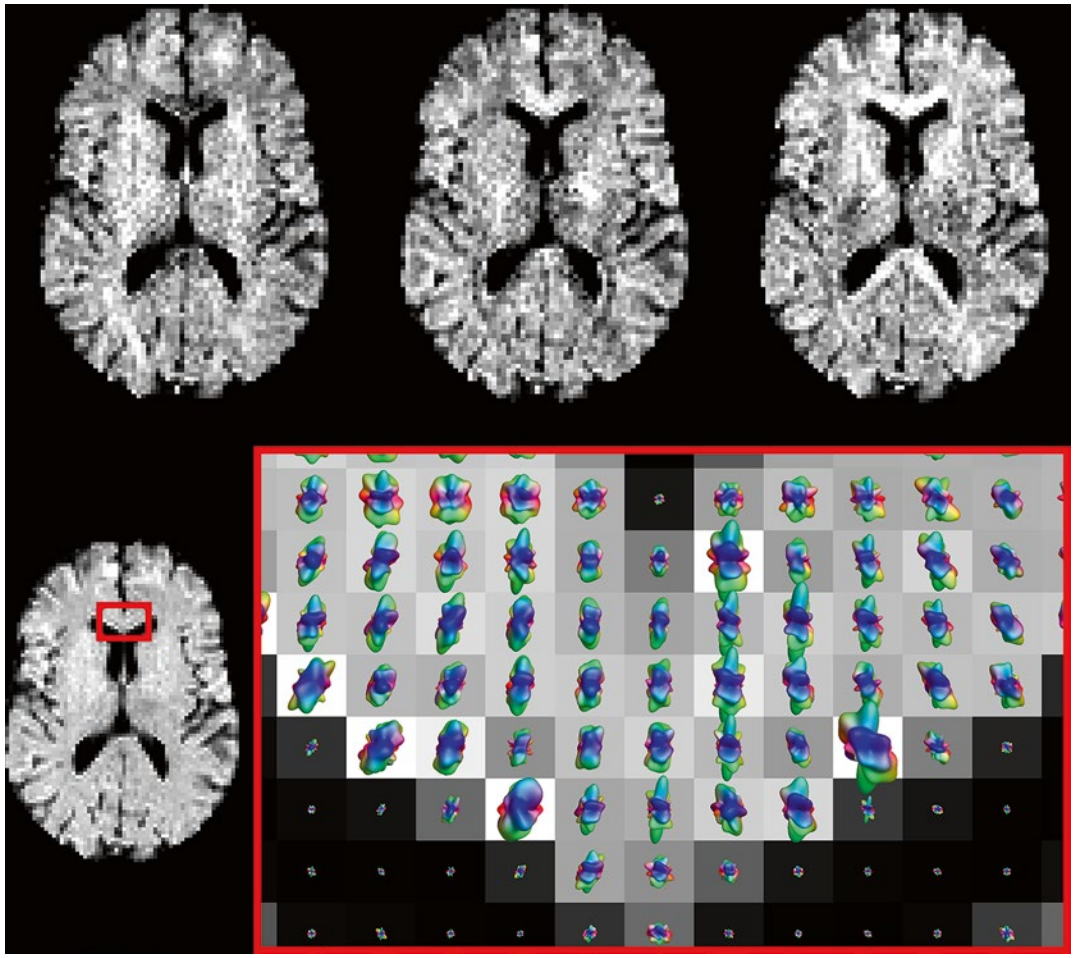

Fig. 4.7 *Top row*: DWIs for the x, y, and z gradient directions, after normalization by the B0 (i.e., the normalized measurements "S/S_0"). *Bottom row*: Spherical polar plots of the normalized DWI values in a region of the GCC, overlaid on a map of the average normalized DWI value

a *higher b*-value will *increase the contrast* in these spherical polar plots. However, as we reasoned before, the SNR will also drop.

Conclusions

We started taking into account the fact that the diffusion-sensitizing gradient is applied along a certain *direction*. The resulting DWI measurement is only sensitive to *diffusion with a component along this direction*. From DWIs acquired using different gradient directions, we could conclude that *anisotropic diffusion* takes place in the *white matter* up to a measurable extent. Again using this to our advantage, we now have a probe for the *anisotropy of microstructure* in each voxel. There are different ways to visualize data resulting from acquisitions using many different gradient directions, yet the most convenient option was *a spherical polar plot of the ADC values* in each voxel: such a visualization shows *larger values* along the direction exhibiting the *greatest amount of free diffusion*. Optional *color coding* is typically done according to a directional scheme: *red for x* (*left-right*), *green for y* (*back-front*), *and blue for z* (*bottom-top*). The *requirements* for investigating the anisotropic nature of diffusion are a B0

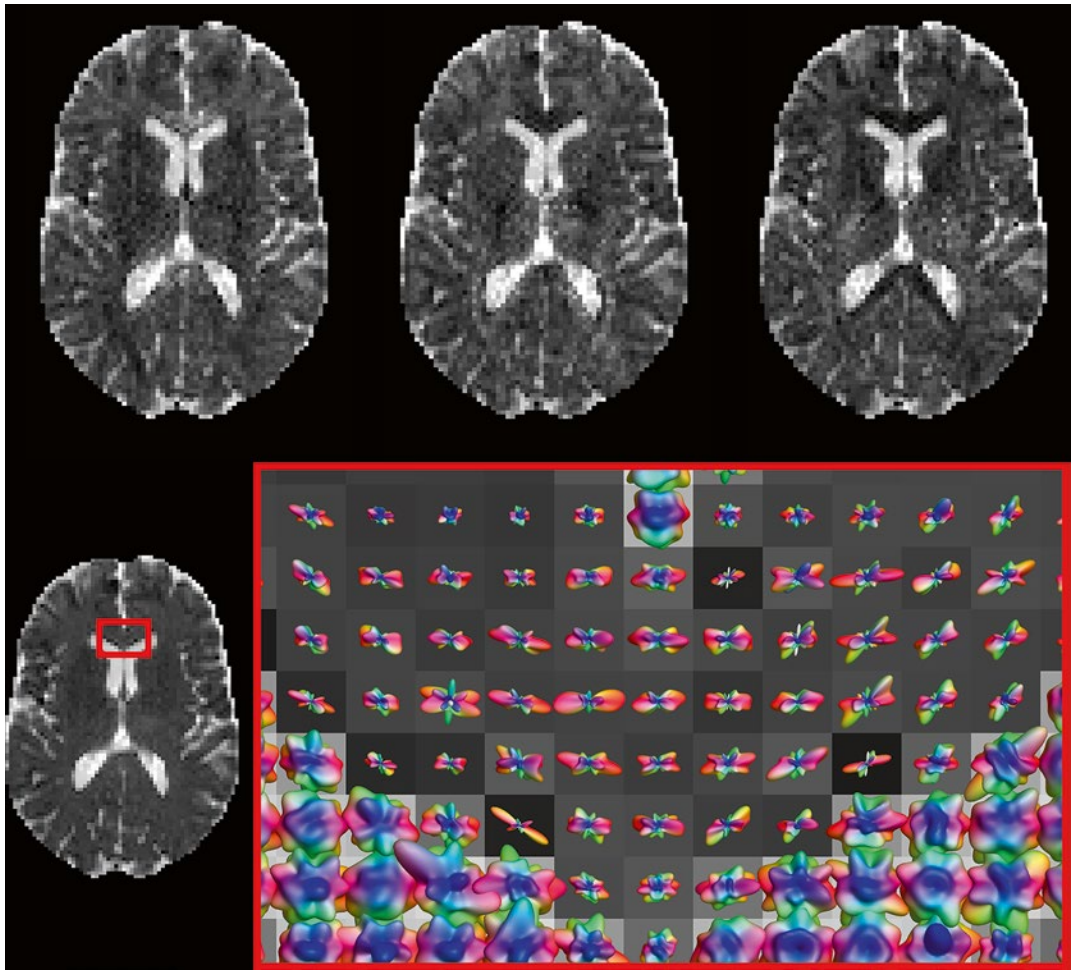

Fig. 4.8 *Top row*: ADC maps for the *x*, *y*, and *z* gradient directions. *Bottom row*: Spherical polar plots of the ADC values in a region of the GCC, overlaid on a map of the average ADC value

(nondiffusion-weighted image), a number of DWIs and knowledge of the *b*-value *and* ***gradient directions*** that were used for performing the acquisition of the DWIs. ***This latter point is very, very important***! Did we just stress that enough? Because it is (very, very important): without the accompanying *b*-value *and* ***gradient directions***, the full set of carefully acquired DWIs is nigh *useless*; we wouldn't be able to associate the (normalized) measurements nor the ADC values with any directions. This vital piece of information should thus be stored with the data; it is often summarized in a gradient table, as shown in (Fig. 4.6). On the number of gradient directions: more measurements are of course always better, yet require more scanning time. And finally, a *higher b*-value yields *better contrast*—also in the spherical polar plots of, e.g., the ADC values—but will *reduce SNR*.

The (Apparent) Diffusion Tensor

Motivation and Implications of Modeling

Looking back at the spherical polar plots of the ADC values in (Fig. 4.8), we notice that they appear quite noisy. That's not surprising, since they simply present a logarithmic transformation

of the original (normalized) data: nothing is modeled, all the measurement noise is still showing (albeit logarithmically transformed … remember this, as it will happen to bug us later on). And thus models were invented. Without going into the how and why of some historical choices that have been made in model development, we'll just introduce the (legendary) *diffusion tensor model* [4] that is central to the theory and practice of DTI. In this context, to be exact, we should refer to it as the *apparent* diffusion tensor. This name refers to the fact that we will employ a tensor to represent/model *the values of the ADC* in function of (gradient) direction, in each voxel. This means that, once we have somehow determined the correct parameters of this model in each voxel, we can evaluate it for as many directions as we like in order to visualize it again as a spherical polar plot of (*modeled*) *ADC values*. As the diffusion tensor model has *only six parameters* (compare this to the 45 ADC values we just obtained from our dataset in each voxel!), it will greatly simplify the features of our directional profile of the ADC.

Understanding DTI, in Theory: The Maths!

Mathematics … it's not as hard as it sounds, so let's just get to it then! From this point on, we will represent a (gradient) direction by a three-element column *vector* **g**, and the apparent diffusion tensor **D** by a 3×3 *symmetric matrix*:

$$\mathbf{g} = \begin{bmatrix} g_x \\ g_y \\ g_z \end{bmatrix} \quad \mathbf{D} = \begin{bmatrix} D_{xx} & D_{xy} & D_{xz} \\ D_{xy} & D_{yy} & D_{yz} \\ D_{xz} & D_{yz} & D_{zz} \end{bmatrix} \tag{4.5}$$

For the mathematics (and software that employs it) to work out well, **g** should be a *unit vector*. As stated before, the tensor **D** has *only six free parameters* (the tensor elements D_{xx}, D_{yy}, D_{zz}, D_{xy}, D_{xz}, D_{yz}) because its matrix is *symmetric*: the elements above and below the main diagonal are the same. We'll get into the meaning of these separate tensor elements later. Given such a tensor **D**, we can "*evaluate*" it for a given direction **g** by using the following expression:

$$\begin{aligned} \mathbf{g}^{\mathrm{T}}\mathbf{D}\mathbf{g} = {} & g_x^2 D_{xx} + g_y^2 D_{yy} + g_z^2 D_{zz} \\ & + 2g_x g_y D_{xy} + 2g_x g_z D_{xz} + 2g_y g_z D_{yz} \end{aligned} \tag{4.6}$$

where $\mathbf{g}^{\mathrm{T}}$ is the transpose of **g**. The right side of the equation simply shows what you would obtain if you did the symbolic math by hand using the vector and tensor element symbols from Eq. (4.5). The outcome of this expression—if we were to fill in some specific numbers representing the vector and tensor elements—is thus a single scalar number: *the value of our tensor model, along a given direction*. As we will now employ such a tensor to symbolize the ADC values, we can simply plug it into the good old Stejskal-Tanner Eq. (4.1) to obtain the following expression:

$$S = S_0 \bullet e^{-b \bullet \mathbf{g}^{\mathrm{T}}\mathbf{D}\mathbf{g}} \tag{4.7}$$

Don't take this one lightly: **this is the *essence* of DTI**. It provides the direct relationship between the chosen experimental parameters (b and **g**), the measurements (S and S_0), and the parameters of the diffusion tensor model (**D**). It now effectively includes the gradient direction **g** that we took abstraction of before, while the vehicle to describe the ADC is no longer a single number, but a *tensor* that can describe values that vary in function of (gradient) direction. Just like we did before with the Stejskal-Tanner equation, we can rewrite Eq. (4.7) to single out the parts that equate to the ADC:

$$\mathbf{g}^{\mathrm{T}}\mathbf{D}\mathbf{g} = \frac{-\ln\left(\frac{S}{S_0}\right)}{b} \tag{4.8}$$

The right-hand side equals the expression of the ADC that we introduced before (i.e. Eq. 4.4), while the left-hand side simply says that we would like to see this ADC value arising from our model **D** when evaluated for the gradient direction **g** that this particular ADC value relates to. Completely writing out the left-hand side

expression using Eq. (4.6) finally yields the following result:

$$\begin{aligned} & g_x^2 D_{xx} + g_y^2 D_{yy} + g_z^2 D_{zz} \\ & +2g_x g_y D_{xy} + 2g_x g_z D_{xz} + 2g_y g_z D_{yz} \\ & = -\ln(S / S_0) / b \end{aligned} \tag{4.9}$$

If we now perform a DWI experiment as before (acquiring S and S_0, carefully noting down b and **g**), we can fill in everything but the *six unknown parameters* of the diffusion tensor model. As solving a single equation for six unknowns is quite an impossible task, we'll clearly need more of these equations, and by consequence more acquisitions. Mathematically, we know that at least six equations will be necessary to be able to determine the full apparent diffusion tensor. In practice, we'll be needing *at least* six DWIs for *different* gradient directions as well as a single B0 to normalize our measurements to. As stated before, it is essential that every DWI is tied to its respective gradient direction. Acquiring *more* DWIs (for different gradient directions) will lead to more than six equations. In such a setting, no exact solution for the six unknown tensor elements generally exists, because the full system of equations is *overdetermined*. This actually is a good thing! Even though we can find a single exact solution in case of six DWI measurements, this solution will also exactly represent all the *noise* in the data. If we perform the acquisition using a *larger* amount of different gradient directions, a solution will have to be found that *fits* the data as good as possible. We then hope that the part that *doesn't fit* the model (i.e., the *residuals*) is the *noise*, which we (optimally) don't want to model anyway. We'll focus on the issue of tensor fitting later. For the time being, let's take it for granted.

Understanding the Tensor Elements, in Practice

So, effectively applying such a tensor fitting method to our 45 gradient direction dataset at hand, we end up with six numbers in each voxel, i.e., the components which describe an apparent diffusion tensor. Now what can we actually do with it? For starters, let's take a look at some maps of these six tensor elements. There are two distinct categories amongst them: the *diagonal* elements (D_{xx}, D_{yy}, D_{zz}) and the *off-diagonal* elements (D_{xy}, D_{xz}, D_{yz}). The former are presented on the first row of (Fig. 4.9), while the latter are shown on the second row. The interpretation of the *diagonal* elements is straightforward: they represent ADC values along the respective directions of x, y, and z. Because we've shown maps of the original (unfitted) ADC values along these directions in (Fig. 4.8), we can compare them directly to the maps of D_{xx}, D_{yy}, and D_{zz} in (Fig. 4.9). Indeed, they look more or less alike. The more careful observer may note that the latter look less noisy. This is not surprising: they represent fitted values, i.e., all 45 measurements contributed to them. From what we already know, we can even figure out mathematically why e.g. D_{yy} corresponds to the value of the tensor model (i.e. the ADC) along y: just fill in $[0\ 1\ 0]^T$ (i.e., the direction of y) as direction **g** in Eq. (4.6) and evaluate using the right-hand side expression; the outcome trivially equals D_{yy}. We can thus conclude that the *diagonal* elements are in practice meaningful and quite easy to understand. The *off-diagonal* elements (second row of Fig. 4.9), on the other hand, offer a less intuitive source of information. They represent the covariance between each pair of axes (i.e., xy, xz, and yz). That's because the full diffusion tensor is actually a covariance matrix. Apart from being a great conversation starter at an engineering party, those last two sentences won't get you anywhere in daily practice: the *off-diagonal* elements just don't really have a *direct practical use* or meaning. The only reason we do discuss them here, is to emphasize what they *don't mean*: they do *not* represent the values of the ADC along some diagonal direction (so don't mistake them for that!). This should also be clear from the fact that they equally cover a range of positive as well as *negative* values (while ADC values should *not* be negative). One final property worth mentioning though: if all off-diagonal elements are zero, the tensor is perfectly *aligned* to the x-, y-, and z-axes. What that means will become more clear if we visualize the tensor in 3D.

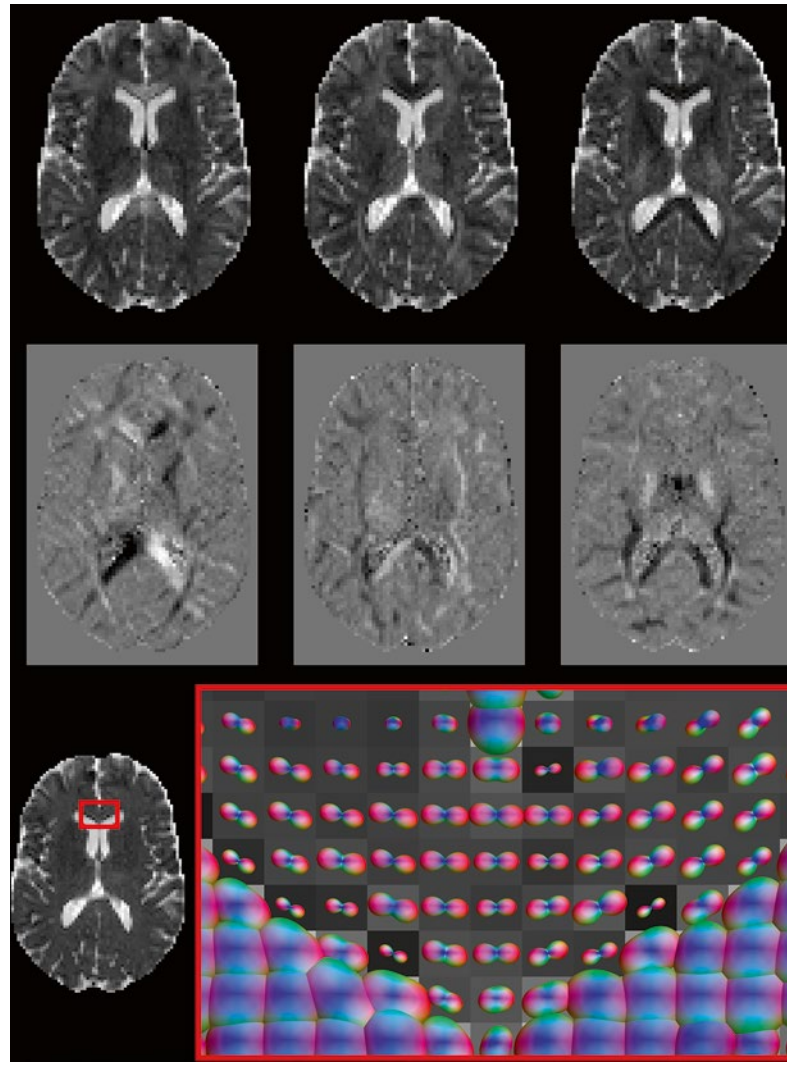

Fig. 4.9 *Top row*: Maps of the diagonal diffusion tensor elements (D_{xx}, D_{yy}, D_{zz}). *Middle row*: Maps of the off-diagonal diffusion tensor elements (D_{xy}, D_{xz}, D_{yz}). The *background grey* level equals zero; darker/brighter levels represent negative/positive values. *Bottom row*: Spherical polar plots of the ADC values provided by the diffusion tensor model in a region of the GCC, overlaid on a map of the average ADC value. Note the characteristic peanut shapes that appear in the GCC

Understanding the Tensor, in Practice: Peanuts!

Talking about visualization, let's take a look at a spherical polar plot of the ADC values actually represented by the fitted diffusion tensors. These are shown for our trustworthy GCC region on the bottom row of (Fig. 4.9), and can again be directly compared to the original (unfitted) values in (Fig. 4.8). From this comparison, it is obvious that the noisy appearance has been greatly reduced: while the original plots showed a unique and different pattern in each voxel (due to the varying noise), the directional profiles that represent the tensor fitted values are much more *consistent* within regions. In regions where a single bundle of axons is present, e.g. the GCC, these plots typically take on the shape of *peanuts*. The advantage of modeling is that some features of interest, such as the *main direction* of the tensor, are recovered more prominently. From the region shown in (Fig. 4.9), it is now also more evident that the nearby CSF in the ventricles exhibits an isotropic pattern of diffusion. And finally, for those who'd like to go just that extra mile in interpretation: consider again one of those curious maps of the *off-diagonal* elements, D_{xy}, and note that it indeed shows a value of *zero* for the voxels right in the middle of the GCC, where the main directions of the tensors are nicely *aligned* to the x-axis.

Conclusions

We have introduced the (apparent) *diffusion tensor* model [4], which is used in DTI to represent the *ADC values* of our measurements along different (gradient) directions. The diffusion tensor **D** is represented by a 3×3 *symmetric matrix*, containing *six unique tensor elements*, and can be evaluated along any direction **g** by the expression $\mathbf{g}^T\mathbf{D}\mathbf{g}$. Casting this expression in the role of the ADC value in the Stejskal-Tanner equation yields the one and only equation at **the *core* of DTI**: it directly relates the experimental parameters, the measurements and the parameters of the diffusion tensor model to each other. This equation can again be rewritten to show clearly that the *diffusion tensor* model is meant to fit the *ADC values*. As there are now *six unknowns* in this equation, the *minimum requirements* for obtaining the diffusion tensor are a B0 (non diffusion-weighted image), at least six DWIs and knowledge of the *b*-value *and* ***gradient directions*** that were used for performing the acquisition of the DWIs. We simply cannot stress enough that knowledge of the *b*-value *and* ***gradient directions***, i.e., the full gradient table as shown in (Fig. 4.6), is absolutely *essential* to fill in the equations and obtain the diffusion tensors! Fitting the tensor model to data with a larger (than six) number of DWIs *reduces the noisy appearance of the ADC values* when visualized as a spherical polar plot. In regions of white matter containing a single consistent bundle of axons, the plot has a characteristic *peanut* shape that clearly shows features such as the *main direction* of the tensor. The *diagonal* elements of the diffusion tensor represent *ADC values along the x-, y-, and z-axes*, while the *off-diagonal* elements represent the covariance between pairs of those axes. Maps of the former thus provide a *meaningful* interpretation, while maps of the latter are neither intuitive nor useful in daily practice. Just *don't mistake the off-diagonal elements* for ADC values along some oblique angle. A final overview of the most important steps taken up to this point is shown for a single voxel in the middle of the GCC in (Fig. 4.10): from raw DWI measurements, to calculated ADC values, and finally the fitted tensor!

Eigenvalues and Eigenvectors

The Tensor Elements: Not Very Practical

Looking back at the ADC peanuts that represent the diffusion tensor values in (Fig. 4.9) and (Fig. 4.10), we notice that the tensor model indeed did a good job in capturing the most important *features* of the angular ADC profile: we can clearly observe its main direction, the maximal ADC value (along this main direction), etc. and how these features relate to each other over larger regions (e.g., qualitatively observe the curving global path of the axon bundle in the GCC). Although these very practical features are in each voxel captured and described by those six unique tensor elements, it's not immediately clear *how*. We do have the diagonal tensor elements (D_{xx}, D_{yy}, D_{zz}) that come with a clear interpretation (i.e., the ADC values along *x*, *y*,

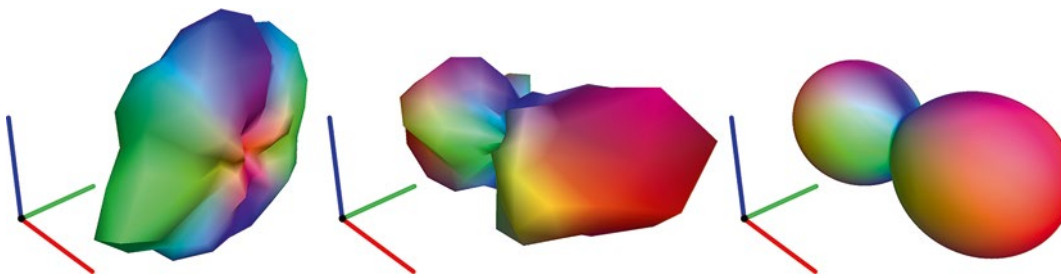

Fig. 4.10 From DWI data to the tensor, for a single voxel in the middle of the GCC. Spherical polar plots of the DWI values (*left*), the ADC values (*middle*) and the ADC values evaluated from the fitted tensor (*right*)

and z). From the ADC peanuts in (Fig. 4.9), we can tell for instance that the value of D_{xx} will coincide with the maximal ADC value of the peanuts right in the middle of the GCC, because those peanuts are nicely *aligned* along x. However, as we move away from that middle region, the orientation of the peanuts changes, causing D_{xx} to gradually take on lower values. The information on the maximal ADC value of the peanuts is now "spread out" somewhere between D_{xx} and D_{yy}. And to make matters even worse, the information on how this "spread" is balanced between those components, is in turn encoded somehow by D_{xy}, one of those elusive off-diagonal tensor elements. That's also why we didn't run into all that trouble right in the middle region: D_{xy} equals zero in that part of the GCC.

Reasoned Wishful Thinking of Alternatives

So, what is at the core of all this confusion and why do we need to be so tedious about trying to infer useful information from the tensor components? The answer is simple: our definition of axes (i.e., x, y, and z) is in fact quite artificial and—more importantly—*very rigid*. To formulate it in another, maybe more clear, way: the axon bundles simply couldn't care less about how we happened to define our *globally fixed axes*; they just happily twist and curve through the full 3D space. On those rare occasions where the tensor perfectly *aligns* to our predefined axes, we get lucky: the off-diagonal elements become zero and the three diagonal components describe the *shape and size* of the tensor in a more direct, intuitive manner. But how do we solve our problem in all those other voxels then? As we just stated, the axon bundles are not going to adjust themselves to our axes; and thus the only solution will be to *adjust our axes* to them in each voxel instead. So, what we are looking for is a new description of the diffusion tensor that provides *a set of axes aligned to the tensor* as well as *three* "*new diagonal tensor elements*" to describe the tensor within this new local set of axes (the "new off-diagonal tensor elements" become zero). The benefits are twofold. These "new diagonal tensor elements" should provide us with everything we need to know about the *shape and size* of the tensor, *independently of its orientation*. On top of that, the customized set of axes by itself also describes the full 3D *orientation* of the tensor. To conclude, such a representation thus effectively *splits up* information about the orientation and the shape/size of the tensor, while the classical six tensor elements *mix it all up*.

Maths to the Rescue: The Eigendecomposition

Now that we know what we want, the question remains how to obtain it. In this case, we are lucky: the mathemagician can help us out with something called *eigendecomposition*. Applied to the diffusion tensor, it basically boils down to rewriting the 3×3 symmetric tensor in the following format:

$$\mathbf{D} = \begin{matrix} \vdots & \vdots & \vdots \\ \epsilon_1 & \epsilon_2 & \epsilon_3 \\ \vdots & \vdots & \vdots \end{matrix} \cdot \begin{bmatrix} \lambda_1 & 0 & 0 \\ 0 & \lambda_2 & 0 \\ 0 & 0 & \lambda_3 \end{bmatrix} \cdot \begin{matrix} \cdots & \epsilon_1 & \cdots \\ \cdots & \epsilon_2 & \cdots \\ \cdots & \epsilon_3 & \cdots \end{matrix} \tag{4.10}$$

where $\lambda_1 \geq \lambda_2 \geq \lambda_3$, and $\boldsymbol{\epsilon_1}$, $\boldsymbol{\epsilon_2}$, and $\boldsymbol{\epsilon_3}$ are three-element unit vectors that are mutually perpendicular to each other. The right-hand side intuitively reads: start with a tensor (with diagonal elements λ_1, λ_2, and λ_3) aligned to the axes (x, y, and z), and then *reorient* it to a new set of axes ($\boldsymbol{\epsilon_1}$, $\boldsymbol{\epsilon_2}$, and $\boldsymbol{\epsilon_3}$). The process of eigendecomposition aims to *reverse* this set of actions: it starts with the diffusion tensor $\mathbf{D}$, and subsequently tries to figure out which axis aligned tensor could have been reoriented to which new set of axes in order to obtain $\mathbf{D}$. The result is referred to as the *eigenvalues* (λ_1, λ_2, and λ_3) and *eigenvectors* ($\boldsymbol{\epsilon_1}$, $\boldsymbol{\epsilon_2}$, and $\boldsymbol{\epsilon_3}$) of $\mathbf{D}$. They come in so-called *eigenpairs* (e.g., λ_2 is paired to $\boldsymbol{\epsilon_2}$): an eigenvalue (e.g., λ_2) represents the ADC value of the tensor along the direction of the corresponding eigenvector (e.g., $\boldsymbol{\epsilon_2}$). The eigenvector $\boldsymbol{\epsilon_1}$ that is associated

with the largest eigenvalue λ_1 is also referred to as the *principal eigenvector*. It plays quite an important role in DTI: due to its orientation along the peak direction of the ADC peanut, it's indicative of *the local direction of the axon bundle*. While the *largest* eigenvalue λ_1 equals the *maximal* value of the ADC peanut, the *smallest* eigenvalue λ_3 represents its *minimal* value.

Understanding the Eigenvalues, in Practice

Maps of the eigenvalues (λ_1, λ_2, and λ_3) are presented in the top row of (Fig. 4.11). A strict ordering ($\lambda_1 \geq \lambda_2 \geq \lambda_3$) is always enforced. As stated before, the combination of all three eigenvalues fully encodes the exact total *shape and size* of the tensors (and by consequence, the ADC peanuts) by providing the ADC value along three perpendicular axes aligned to the tensors (the eigenvectors). In some regions (e.g., the GCC, or the white matter in general) a larger mutual difference between the eigenvalues can be seen as compared to other regions (e.g., the CSF). This clearly relates to the differing amounts of anisotropy that we could also see in the ADC peanuts. Because all information on the shape and size of the tensors is stored in the eigenvalues, they will also be the basis for other tensor *measures* that are *independent* of the tensor's *orientation*; but we'll get to that later.

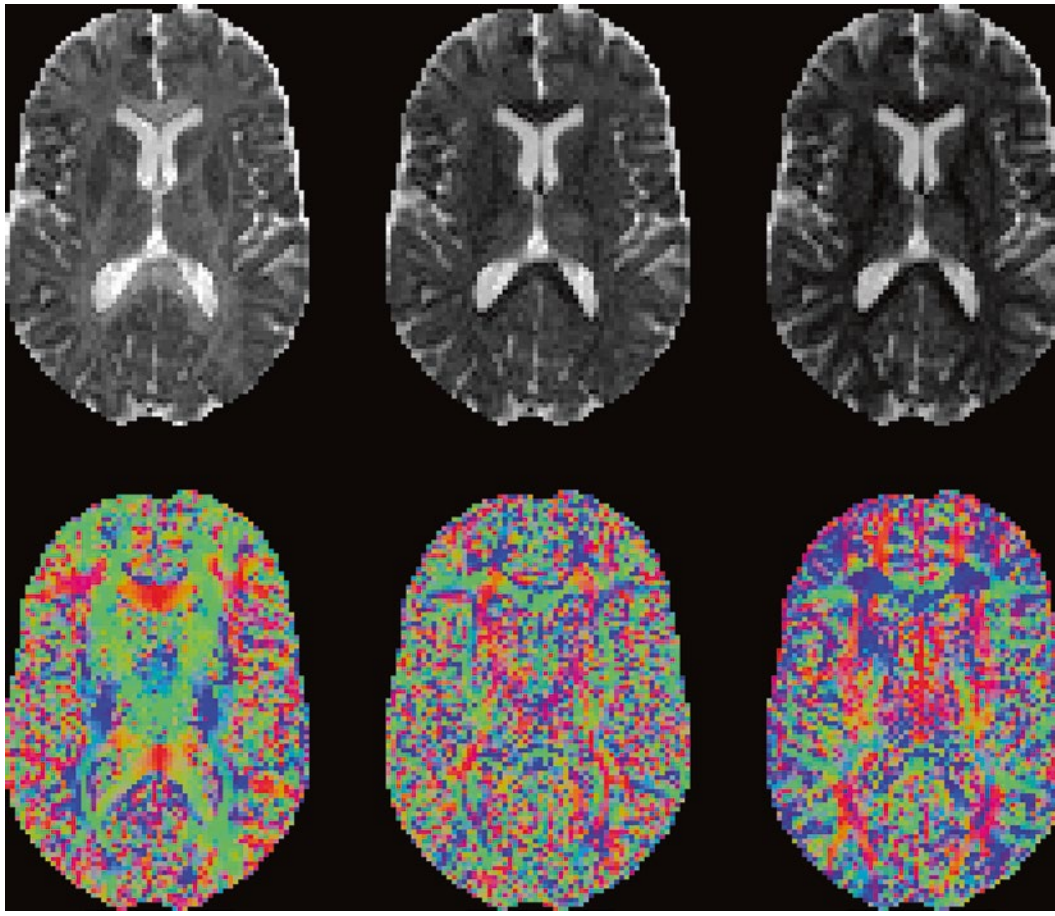

Fig. 4.11 *Top row*: Maps of the eigenvalues (λ_1, λ_2, λ_3). *Bottom row*: Directionally encoded color (DEC) maps of the eigenvectors ($\boldsymbol{\epsilon_1}$, $\boldsymbol{\epsilon_2}$, $\boldsymbol{\epsilon_3}$)

Understanding the Eigenvectors, in Practice

Directionally encoded color (*DEC*) *maps* [5] of the eigenvectors ($\boldsymbol{\epsilon_1}$, $\boldsymbol{\epsilon_2}$, and $\boldsymbol{\epsilon_3}$) are provided in the bottom row of (Fig. 4.11). Since each eigenvector has unit length, no magnitude information is represented in these maps; only *orientation* is encoded. This is achieved by assigning the three elements of an eigenvector to *the red*, *green and blue channels* of a color image. As the eigenvector itself is specified relative to the original (x, y and z) axes, the meaning of the colors is similar to the scheme we used before for displaying spherical polar plots: *red* is linked to x, *green* to y, and *blue* to z. As mentioned before, one of the most important outcomes of DTI is the orientation of the *principal eigenvector* $\boldsymbol{\epsilon_1}$. Within regions of the white matter (e.g., the GCC), the DEC map of $\boldsymbol{\epsilon_1}$ shows a consistent and smoothly evolving pattern that can intuitively be related to the *local orientation of the axon bundles*. In regions such as the CSF, the orientation of $\boldsymbol{\epsilon_1}$ proves to be more or less *random*, resulting in a *noisy* appearance of its DEC map in those particular regions. Associated with the isotropic pattern of diffusion in these regions, we should ideally observe a *spherical* ADC plot (instead of a peanut), satisfying $\lambda_1 = \lambda_2 = \lambda_3$. However, due to random noise in the data, there might be a slight *deviation* from this pattern. The orientation of the principal (and any other) eigenvector is entirely determined by the *random* noise in such a case. Whenever two (or all three) of the eigenvalues of a given tensor are (nearly) equal, we say that the corresponding eigenvectors become *ill defined*.

Conclusions

We introduced the *eigendecomposition* of the diffusion tensor in its *eigenvalues* and *eigenvectors*. The six diffusion tensor components *mix up* information on the shape, size and orientation of the tensor and it becomes hard to untangle the information we're typically interested in by purely intuitive reasoning on these components. Our new representation, however, nicely *separates* information on the *size*/*shape* of the tensor from information on its *orientation*. This is achieved by recovering a set of *axes* (the eigenvectors) that is locally aligned to the tensor as well as three *ADC values* (the eigenvalues) of the tensor along these new axes. The solution thus comes as a set of *eigenpairs*: a certain eigenvalue encodes the ADC along a specific eigenvector. Whereas the eigenvalues encode the size/shape *independently* of the orientation, the eigenvectors describe the orientation *independently* of the size/shape. A final schematic (2D) example, illustrating these properties and providing an overview of the relation between the most important tensor-related numbers we've come across up to this point, is shown in (Fig. 4.12). The eigenvector associated to the *largest* eigenvalue is also referred to as the *principal eigenvector*. Mapping eigenvectors is typically done by use of *directionally encoded color* (*DEC*) *maps*. One of the key practices in DTI consists of mapping the *principal eigenvector*, since it is indicative of the *local orientation of the axon bundles*. In regions of white matter such as the GCC, this map shows a *consistent* pattern. In regions of (nearly) isotropic diffusion such as the CSF, however, the principal eigenvector becomes *ill defined*, leading to a *noisy* appearance of the associated DEC map. Since there are no axon bundles hindering/restricting the diffusion in such a region, the principal eigenvector therein is pretty *meaningless* anyway.

Visualizations, Measures, and Maps

Aiming for Usability: Tensor Glyphs

While all maps and visualizations (using, e.g., spherical polar plots) presented up to this point have provided us with great insight into the underlying information that eventually leads to the diffusion tensors and describes their main features, we are yet to encounter the visualizations and maps that we're most likely to run into when processing DTI data *in practice*. Let's first have a look at the most common 3D visualization of the diffusion tensor, which is not the ADC peanut we've already become acquainted with

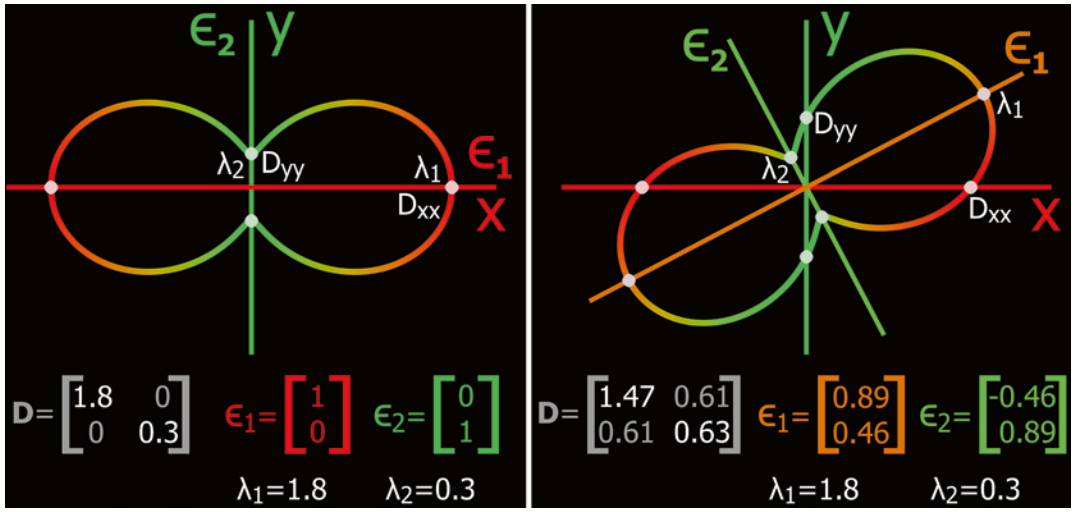

Fig. 4.12 Example of 2D tensors and the convenience of eigenvalue decomposition. *Left*: Perfectly axis aligned tensor. The diagonal tensor elements directly define the tensor shape. The eigenvectors coincide with the global axes and the eigenvalues are equal to the diagonal tensor elements. *Right*: General (not axis aligned) tensor. The diagonal tensor elements encode the value of the ADC peanut along the global axes, yet do not fully define the tensor shape. The eigenvectors provide a new set of axes along which the eigenvalues directly provide the information on the shape

(even though it most directly shows all the values that the tensor represents). Instead, we will only visualize the *most prominent features* that define its size/shape and orientation, as provided by its eigenvalues and eigenvectors: meet the *tensor glyphs*! Two variations are shown in (Fig. 4.13) for our familiar GCC region: *cuboids* and *ellipsoids*. In general, a mostly primitive 3D shape is chosen (e.g., a rectangular cuboid or a scalene ellipsoid) and its three main dimensions are *scaled by the eigenvalues* (or a transformation thereof) and *aligned along the eigenvectors*. Optionally, the glyph is *colored* according to the DEC map of the *principal eigenvector* (i.e. using the map of $\boldsymbol{\epsilon}_1$ in (Fig. 4.11)). Comparing our previous ADC peanuts in (Fig. 4.9) with the newly obtained glyphs in (Fig. 4.13), we can clearly tell the latter score higher on the *usability* scale: they show a more contrasting description of the features that really matter (and still fully define the tensor and thus its ADC peanut). The most commonly visualized glyph shape is the ellipsoid [6], but since a cuboid requires far fewer polygons to be drawn onscreen, it lends itself for faster interaction with larger tensor fields. Interaction with a field of glyphs is useful for a better characterization of their full *3D shapes*: e.g. in (Fig. 4.13), we freely rotated the slice of glyphs to a certain angle. Especially when the axon bundles are not running "in plane", the ability to freely rotate the tensor field is a helpful addition. A reason to prefer ellipsoids (instead of e.g. cuboids) might be that they do not overexaggerate some features of the tensor in cases where those features are not very meaningful or appropriate anyway. A good example is the isotropic diffusion in the CSF, as seen in (Fig. 4.13): the cuboids become cubes, but still clearly indicate the orientation of the eigenvectors, even though they are *ill defined* in this region. The ellipsoids, however, take on the shape of spheres, and thus any visual cues of the eigenvectors inherently *fade away* (apart from the coloration, which is of course also not very informative in this region). Another reason why *ellipsoids* are a meaningful choice is that they actually come with a true *meaning* when scaled using the *square roots of the eigenvalues* [6]: under the model of diffusion that DTI assumes, if we would investigate a single water molecule that starts at the center of the ellipsoid and is allowed to diffuse randomly during a fixed time interval, then there is an equal chance for it to

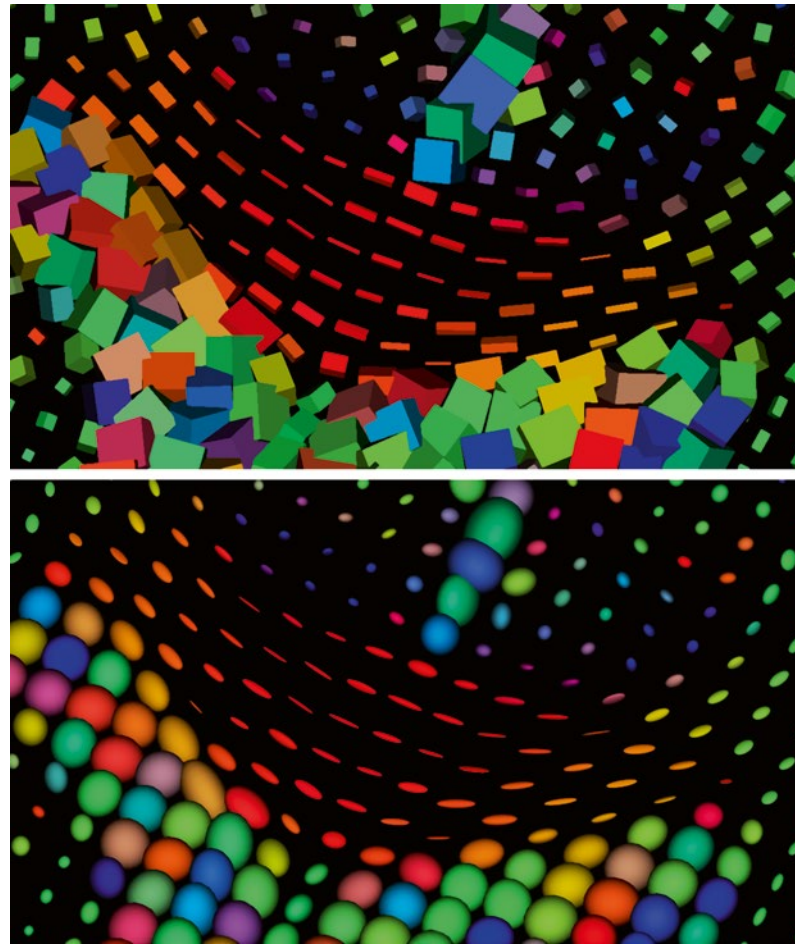

Fig. 4.13 Tensor glyphs (*top*: cuboids; *bottom*: ellipsoids) in a region of the GCC. The glyphs are colored according to the DEC map of the principal eigenvector $\boldsymbol{\epsilon}_1$

displace to any specific point on the surface of this ellipsoid. It might take a few reads of that sentence before one may grasp its meaning, and we won't even go into why it is true; the fact just is that there exists a pretty good reason to prefer these ellipsoids over any other specific glyph! *In practice*, however, *any glyph will do* for exploring the data (even though some software may offer many different options), as long as it's easy on the eyes and the processing power of the machine one is working on.

Mapping Size: Mean Diffusivity (MD) and Friends

Now let's consider some of the more common diffusion tensor measures. All the measures we're about to present are so-called *rotationally invariant* measures: they tell us something about the size or shape of the tensors, *independently* of their orientation. Therefore, they are typically defined in function of the *eigenvalues* of the tensors. Let's start with a straightforward one: the *mean diffusivity* (*MD*) [7]. It is defined as follows:

$$\mathrm{MD} = \frac{\lambda_1 + \lambda_2 + \lambda_3}{3} = \frac{D_{xx} + D_{yy} + D_{zz}}{3} \qquad (4.11)$$

As simply being the *average of the eigenvalues*, it describes the overall *size* of the tensor and as such represents a rotationally invariant ADC measure. A map of it is provided in (Fig. 4.14). The same contrast is sometimes also referred to as the *trace* [7], which equals the *sum* of the eigenvalues. Other related variants exist, such as the pair of *axial diffusivity* (equating to the first eigenvalue) and *radial diffusivity* (equating to the average of the second and third eigenvalues). As

seen in Eq. (4.11), the MD can (surprisingly) also be obtained by averaging the *diagonal tensor elements*: even though these individual elements are dependent on the orientation of the tensor, their average is not. An important warning at this point: this does *not* mean that we can simply acquire three DWIs using perpendicular gradient directions, and subsequently average the three ADCs in order to obtain the *same rotationally invariant MD* [7]! It only applies for three perpendicular ADC values as evaluated from a *tensor model*, so *six gradient directions* are still the bare mathematical minimum in order to account for the anisotropy in the measurements!

Mapping Fractional Anisotropy (FA) and Orientation

Next up is the *fractional anisotropy* (*FA*) [7], probably the most unique selling point of DTI. It is calculated by the following hefty formula:

$$\mathrm{FA} = \sqrt{\frac{3}{2}} \cdot \frac{\sqrt{(\lambda_1 - \bar{\lambda})^2 + (\lambda_2 - \bar{\lambda})^2 + (\lambda_3 - \bar{\lambda})^2}}{\sqrt{\lambda_1^2 + \lambda_2^2 + \lambda_3^2}} \quad (4.12)$$

where $\bar{\lambda}$ is the average of the three eigenvalues. In words, this amounts to the *standard deviation* of the eigenvalues *divided by* their *root mean square*. Or, more simply: a measure for how much the eigenvalues *differ*, but *normalized*, so it becomes *independent* of their absolute magnitude. As such, it describes an aspect of the *shape* of the tensor, *independently* of its size (and of course, orientation). Because of the way the formula is carefully normalized, the FA takes on values in an interval *between zero and one*, the former representing perfect *isotropy* (i.e., all eigenvalues are equal) and the latter corresponding to perfect *anisotropy* (e.g., the extreme case where only λ_1 would have a nonzero value). An FA map is provided in (Fig. 4.14). From this, we learn that the white matter clearly has higher anisotropy than any other (healthy) tissue in the brain. As we already know, in regions of low anisotropy, the principal eigenvector's orientation becomes *ill defined*. Hence, the FA map is the perfect candidate to weight the DEC map of the principal eigenvector from (Fig. 4.11): doing so will *hide* the colors in regions where they are *ill defined* (i.e., where they are noisy, confusing, and meaningless). The result is known as the *DEC FA map* [5], and is also presented in (Fig. 4.14). This map isn't the most iconic DTI map for no reason: it's a very handy one and becoming acquainted with the color encoding is key to quickly interpreting a lot of the valuable and unique information in the dataset at once. Mentally processing DEC should become second nature; *red for x* (*left-right*), *green for y* (*back-front*), *and blue for z* (*bottom-top*). Take a look again at the original (grayscale) FA map. Notice how easily we could be tempted to believe that every bundle-like feature of this map represents an in-plane axonal bundle. Now shift your attention back to the DEC FA map, and realize that *blue* stands for an orientation *perpendicular* to the visualized slice. There you have it; that's some *indispensable DEC information* for you!

Exploring Shape Space and Reaching Beyond…

Finally, let's briefly touch upon a triplet of slightly more exotic measures: a *linear* measure (c_l), a *planar* measure (c_p), and a *spherical* measure (c_s) [8]. This is what their formulas look like:

$$c_l = \frac{\lambda_1 - \lambda_2}{\lambda_1 + \lambda_2 + \lambda_3} \qquad c_p = \frac{2 \cdot (\lambda_2 - \lambda_3)}{\lambda_1 + \lambda_2 + \lambda_3}$$
$$c_s = \frac{3 \cdot \lambda_3}{\lambda_1 + \lambda_2 + \lambda_3} \quad (4.13)$$

All of them are again automatically restricted to an interval of values *between zero and one*. The *sum* of these three measures exactly equals *one*. The full triplet of measures provides the coordinates of our tensor in some "*shape space*": a higher c_l means a more linear, *prolate*, cigar-shaped tensor ellipsoid; a higher c_p means a more planar, *oblate*, pancake-shaped tensor ellipsoid; a higher c_s means a more spherical, *isotropic*, ball-shaped tensor ellipsoid. Just like the FA, these

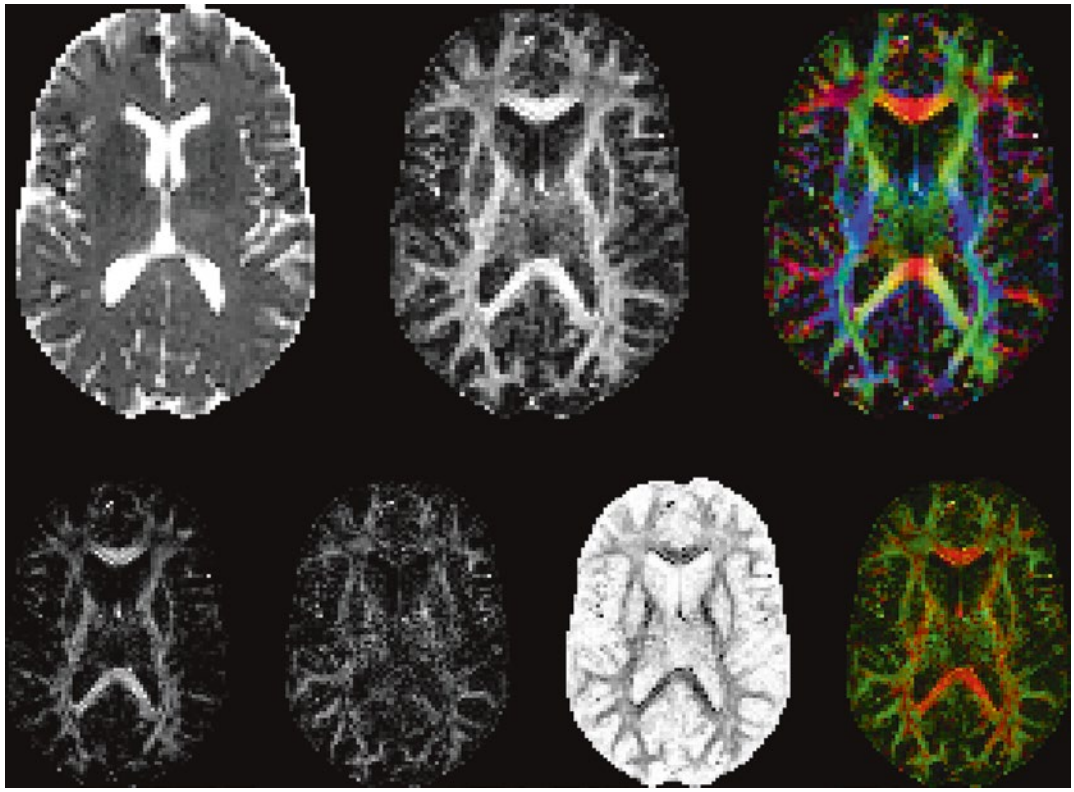

Fig. 4.14 *Top row*: Maps of the mean diffusivity (MD), fractional anisotropy (FA), DEC FA. *Bottom row*: Maps of a linear measure (c_l), planar measure (c_p), spherical measure (c_s), combination of c_l and c_p using *red* and *green* color channels

measures each describe an aspect of the *shape* of the tensor, *independently* of its size (and of course, orientation). One could even use them to come up with new *anisotropy* measures, such as $1-c_s=c_l+c_p$ [8]. Maps of the shape measures are provided in (Fig. 4.14). We also present a map where we employ the red and green color channels to encode c_l and c_p. This final map's absolute intensity thus equals the custom anisotropy measure we just mentioned, while the color somehow shows what "*kind* of anisotropy" is present: *linear or planar*. Interestingly, we notice (in the presented slice) that mostly the central part of the corpus callosum (including the GCC region we have been considering in all our examples) shows highly linear behavior, while *many other regions* of white matter contain a decent portion of *planar diffusion*. Reasoning about the axon bundles as a bunch of cylindrical tubes, as we did before, cannot simply cause such a pattern if all axons in the voxel are coherently running along the same direction: they must be curving or dispersing (within certain planes), or maybe more than one population of axons is present in such voxels. Whatever the underlying situation might be in those voxels, the planarity hints at certain *limitations* of the DTI model ….

Conclusions

We introduced some of the most *mainstream* visualizations and maps that one is bound to run across in daily DTI practice. These include the visualization of the tensors by *glyphs* (most notably the *diffusion tensor ellipsoid*) and maps of the *mean diffusivity* (*MD*), *fractional anisotropy* (*FA*), *DEC FA* as well as a slightly more exotic

triplet of *linear*, *planar and spherical measures* (c_l, c_p, c_s). Other measures exist, but these are typically variations of—or at least heavily inspired by—the ones we presented: axial diffusivity, radial diffusivity, the trace, several variants of anisotropy measures, etc. The most *standard* measures of them all, however, are the typical couple of *MD* and *FA*: the former representing the average *size* of the tensor (independent of shape and orientation) and the latter encoding its *anisotropy*, an aspect of the *shape* of the tensor (independent of size and orientation). Information on the *orientation* can also be included by *combining* the FA map and a DEC map of the principal eigenvector in order to obtain *the DEC FA map*. This map is not only iconic for DTI, but it's also a very handy tool to quickly gain insight into any DTI dataset.

Tensor Fitting Methods

Facing the Issue

Up to now, we've been taking an essential step in the whole process for granted: the actual *tensor estimation*. As a matter of fact, this is the *least trivial* step along the pipeline; everything else we've discussed up to this point simply consists of applying some *well-defined* and quite straightforward formulas in the right order. Even the eigendecomposition—or at least what we desire it to yield for an outcome—is exactly defined (i.e., Eq. 4.10; no more, no less), and we can rely on computer science to provide us with an algorithm that does the job. In those cases where the outcome proved to be ill defined (e.g., isotropic diffusion), the ill defined parts of the outcome (i.e., the eigenvectors) were not informative anyway. But the *tensor estimation* … that's an entirely different beast! Different, because this time even the definition of "*what we want*" is not all that clear. Or is it? We simply want the tensor to *fit* the data (or the ADC values …?) *as good as possible*, right? But what is "*as good as possible*"? It's *vague*, that's what it is; and hence, a plethora of definitions and associated fitting methods exist. While it easily provides enough material to write a decent book on the subject alone, consider the following as your average quick and dirty hitchhiker's guide to making the right choice. In the foreign restaurant of tensor fitting, it should enable you to more or less translate the menu, pick something that you're not allergic to, all the while giving you the confidence that your choice will leave you satisfied up to a certain level, but also allow you to leave the restaurant in time, so you can still catch your bus. How they actually arrange stuff in the kitchen though, is the least of our concerns. Have a seat; the daily menu consists of: *linear least squares* (*LLS*), *weighted linear least squares* (*WLLS*), and *nonlinear least squares* (*NLS*). On top of that, there's also today's special: *robust estimation of tensors by outlier rejection* (*RESTORE*). Now let's have a look at our advice!

LLS: Quick and Dirty

Linear least squares (*LLS*) is the most basic choice. It will solve your system of equations—of which each single one takes on the form of Eq. (4.9)—by *minimizing the sum of squared residuals* of those equations. In the case where we have more than six equations (as opposed to only six unknowns), it is typically impossible to perfectly satisfy all equations. The error or difference that still exists between the left- and right-hand sides of one such equation is referred to as its *residual*. In practice, minimizing the sum of the squared residuals of all the equations amounts to "*spreading out*" those unavoidable residuals as much as possible *over all of them*. This is equivalent to stating that each equation has an "*equal say*" in the process of the fit. A great advantage of LLS is that it can be implemented as a *single-step process*. That's right: it just takes a single specific operation on the whole system of equations to automatically obtain the solution that optimally minimizes that sum of squared residuals. Depending on your hardware and the size and number of DWIs in the dataset, you can have your tensors rolling out in mere *seconds*! In fact, the tensors we generated in this chapter—and thus all the resulting visualizations and maps

we've been looking at—are the result of a single quick application of LLS. For that specific purpose, LLS is certainly well suited: *qualitatively* speaking, our tensors and the subsequently calculated maps of tensor measures look *perfectly fine*. So, why don't we just stick with LLS for all intents and purposes then? The *problem* is subtle and quite well hidden: it actually concerns the fact that we allowed each equation to have *an equal say* in the fit. This assumes that each value that we are trying to fit, was provided to us with an error (i.e., the measurement noise) of a "similar magnitude". In more professional words and adapted to how we specifically formulated Eq. (4.9): LLS assumes that the noise *on the ADC values* (i.e., the right-hand side of each equation, which we are trying to fit with the left-hand side) results from a distribution that has the *exact same variance* for all our different ADC values. While this is the case for our DWI values (that originate directly from the scanner, where the noise is "officially" added to the measurements), it does *not* apply to the ADC values: the distribution of the noise on the original data is logarithmically transformed along with those data to obtain the ADC values! You might remember that we mentioned this before, additionally stating that it would happen to "bug us later on". So now, here it is: officially bugging us. The problem at hand is that each "measured" (i.e., calculated) ADC comes with noise of a *different* variance: i.e., we can trust some ADCs more (or less) than others. It seems sensible to *weigh* the amount of say of each equation in the fit with this information. That's where *weighted linear least squares* (*WLLS*) kicks in.

WLLS: Still Quick, Less Dirty

Weighted linear least squares (*WLLS*) assigns to each equation (still of the form of Eq. 4.9) a *weight* according to how much the original noise variation is affected by the logarithmic transform of the data. These weights directly *depend on the magnitudes of the original data* (i.e., the intensity of the different DWIs). In practice, once these weights are known, only a limited modification has to be made to LLS to take them into account and obtain a WLLS fit, which now truly provides us with the optimal correct fit! It still only takes a single (slightly bigger) operation on the whole system of equations to get this solution: it might take a few extra seconds, but it still just remains a matter of mere *seconds* to have your tensors again rolling out; yet much more *accurately*. If we would have generated all the maps in this chapter based on a WLLS fit of the tensors, you wouldn't have noticed the difference: it doesn't suddenly change the *visually* informative contrast of those maps. For *quantitative* purposes (such as group studies) though, it certainly matters, *a lot*: WLLS already *removes* a great deal of inherent *biases* on final measures (such as MD and FA) that are typically caused by careless use of LLS. So, why don't we just stick with WLLS for all intents and purposes then? Again, a sneaky problem manifests itself: to determine the weights, we need the magnitudes of the original data … *without the noise*. Of course, once we have obtained a fitted tensor, we could reason that we got rid of the noise (because, optimally, only the noise is left in the residuals). We could then evaluate that tensor for all gradient directions and calculate from the ADCs back to the DWIs, i.e. the *noiseless* magnitudes that we needed to determine the weights. So, if we could obtain a fitted tensor, then we would also have our weights; but in order to obtain a fitted tensor, we need those weights in the first place. Yes, that's a *chicken-and-egg problem* we're facing here. No perfect solution exists (and thus, unfortunately, also *WLLS can never be perfect*). A first approach could be to just use the magnitudes of the original noisy data to determine the weights. This may, however, result in a *worse* outcome as compared to using plain old LLS! A second trick is to start by performing *a LLS fit*, and get DWI magnitudes from this fit (where the noise should then already be accounted for up to a great extent) *in order to determine the weights for a subsequent WLLS fit*. One could then even repeat this process in the hope of getting gradually better fits and subsequent weights for the next fit (but this typically does not add much: most of the "magic" is in using that first LLS just for a robust set of

weights). In practice, *it's all still fast*: a LLS followed by a WLLS. The *danger* lies in the fact that some software packages might perform WLLS using the first approach, yielding worse results as compared to LLS. On the other hand, a responsible implementation of WLLS using the second approach should *definitely lead to better results*, without any significant increase in computation time as compared to LLS: it's typically still done in mere *seconds*! However, we can never truly know the correct weights due to the chicken-and-egg format of the problem: so the approach doesn't fix everything. The core of the *original* problem was that the noise got *logarithmically* transformed in the ADC values, and that we formulated Eq. (4.9) based on an ADC value in the left and right hand side of the equation. Knowing now that we actually want to compare the values of the original signals, can't we modify that equation so it compares stuff *that isn't logarithmically transformed*? Easy enough: just remove the logarithm by taking the *exponential* of both sides! Now we are facing the correct form of the equation, but sadly, it also lost its linearity in the unknowns: the linear sum of these unknowns on the left hand side now appears under that *exponential function*. Long story short: it's a nonlinear equation. That's where *nonlinear least squares* (*NLS*) kicks in.

NLS: A Long and Brave Quest in the Mountains

Nonlinear least squares (*NLS*) will try to solve an overdetermined system of *nonlinear* equations, again aiming to *minimize the sum of squared residuals* of those equations. Going into details about this one is nigh impossible: many methods exist. They all share a common thing, though: they take a much, much *longer time* to reach a solution as compared to LLS and WLLS. They are basically facing the fiendishly difficult problem of finding the lowest point in the lowest valley of a mountainous landscape in a six-dimensional world. Actually, LLS and WLLS also did, but due to the specific simple shape of the landscape when the equations are linear, they could come up with a nifty trick of finding that lowest point in *a single step*. NLS, on the other hand, is just dropped somewhere on the landscape and has to start a *walk* in the unprepared hitchhikers fashion: without a map (because the landscape is too big and complex) and just relying on its eyes and feeling to *gradually* move to lower regions. In theory, truly solving the NLS problem will yield the optimal result. However, the problem is not easy to solve. Due to the *limited range of sight* in the mountains, an NLS algorithm might get stuck in a *suboptimal* valley (not knowing there exists another lower valley somewhere). Some algorithms are more *robust* against this than others, but it's nearly impossible to come up with an algorithm that *never* makes these mistakes. In general, many NLS algorithms exist that will in most cases further *outperform WLLS*. In some specifically challenging voxels though, such an algorithm *might fail to converge* or get stuck in the previously mentioned *suboptimal* valleys. If and when the algorithm might detect this, it could for instance perform a WLLS fit instead (still better than nothing or something really wrong, right?). Because NLS algorithms are forced to take a walk in the mountains anyway, they may also come with extra bells and whistles allowing them to generate a solution that specifically satisfies some *constraints*. Due to noise in the data, LLS and even WLLS can sometimes come up with tensors that have one or more *negative eigenvalues*. Of course, this doesn't make sense: negative eigenvalues, and thus negative ADCs, have *no physically sensible meaning*. An NLS algorithm can be guided to not encounter such unwanted cases in the first place: barriers can be put up on the landscape in order to simply deny the NLS hitchhiker access to these forbidden areas. This all typically does come at an extra computational cost, and thus your valuable *time*. Depending on your hardware, the size of the dataset and the kind of NLS algorithm (and the bells and whistles it might come with), some of these strategies may take anywhere from a few *minutes* to several *hours* to finish calculating your tensors. Using a *brain mask* (so no unnecessary calculations are performed for voxels outside of the brain) is typically strongly advised to

reduce running time. And guess what? Even if the hitchhiker would be so extremely experienced that he would always find the lowest point in the landscape, his optimal NLS solution could still be unsatisfying. That's because the data aren't only messed up by noise, but possibly also by *outliers*! Motion, distortions, cardiac pulsation, signal dropout, ghosting … *artifacts* are abundant in MRI. Some can be avoided during acquisition, others can be partially dealt with by preprocessing, but in the end some *still leave their mark* on the data when we offer it to our favorite tensor fitting method. They cause *outliers*: data points that have lost all of their informative value by taking on truly silly values that *don't fit the picture*, at all. That's where *robust estimation of tensors by outlier rejection* (*RESTORE*) kicks in.

RESTORE and Beyond: Expecting the Unexpected

Robust estimation of tensors by outlier rejection (*RESTORE*) [9], as its name suggests, will handle outliers by *rejecting* them. To reject them, they first have to be *detected* though. To do this, it will start with a NLS fit. It will subsequently assign each measurement a *weight*, depending on how well it fits the picture. Another NLS is performed, where each equation is weighted according to how well its measurement fit the picture before. This process is *repeated until convergence*. The final weights should now be a reliable measure for how well each measurement does (not) fit in, i.e., for its "*outlier-ness*". Those measurements that meet a certain threshold are officially regarded as *outliers*, and simply kicked out of the game. The *final fit* is then performed by employing only the surviving "*non-outlier*" data. While this is an ingenious and very *robust* strategy, it does have a few implications. A first one is the fact that it might have to perform *several* subsequent NLS fits: that will surely have an impact on the total computation *time*. It could on average take more than three times as long as compared to a single NLS fit [9]. A second one is the fact that, after kicking out a possibly decent amount of outliers, *enough* measurements should of course still be left to reliably obtain the final fit. Those measurements are even needed to actually reliably classify the other ones as outliers in the first place. Hence, data *redundancy* is an important requirement. Even very recently, further improvements have still been made to relax that redundancy requirement up to a certain extent [10]. Given that the DTI model is about 20 years old now, this certainly proves that the fitting problem still remains *far from trivial*.

Conclusions

We took a bite out some of the most common tensor fitting methods: *linear least squares* (*LLS*), *weighted linear least squares* (*WLLS*), *nonlinear least squares* (*NLS*), and *robust estimation of tensors by outlier rejection* (*RESTORE*). It is typically said that this specific ordering is one of *increasing complexity*, implying *increasingly better results* at the cost of an even steeper *increase of computation time* (especially for the nonlinear methods). This is generally true; provided that each variant is implemented as good as possible (we rely on the responsibility of the software developers here). If your dataset has enough data *redundancy* (let's say, DWIs for more than 30–40 unique gradient directions [10]), we could easily always advise you to use *RESTORE*. However, depending on the specific implementation of RESTORE, the hardware, the size or even number of datasets you have to process, etc. it might take quite a while (possibly up to *several hours*) before you have access to your tensors for further processing. All the bells and whistles in these advanced nonlinear algorithms may not be necessary, if you're just concerned about having a quick *qualitative* look at the data. For *quantitative* purposes though, we certainly advice to go "*beyond LLS*." A very big gain is already achieved by WLLS (if implemented responsibly), at a minimal extra computational cost. Certainly be on the lookout for the method your favorite piece of DTI software is packing, or even what different choices it might be offering; as you now speak and understand some basic tensor fitting language!

Final Conclusions

In this chapter, we provided an overview that took us all the way from the raw DWI data to the diffusion tensor and even further to some of the more common visualizations and measures. This fact by itself makes for the most important conclusion: while the more "classical" imaging modalities (e.g., T1, T2) are obtained straight from the scanner, the maps that are typically employed in the practice of DTI (e.g., MD, FA, DEC FA) result from a *postprocessing* pipeline: i.e. *these maps are calculated*, *not directly acquired*. Most of this pipeline is clearly defined; but for the actual *tensor fitting*, there are *quite a few options*. The more advanced methods may also take a reasonable time to be computed. Some *scanner software* offers the option to directly show and export MD, FA, DEC FA, and even other maps; however, *don't let that fool you*: this software still has to go through all the steps we've come across in this chapter. Also, if the software almost instantly provides you with e.g. a DEC FA map, you should now be aware that it may probably not have performed much more than a simple LLS fit (which might of course be sufficient, if you're just qualitatively inspecting the data). The scanner software also has to rely on the same DWI dataset for this, and thus is *not any more or less reliable* in general than any other piece of software if it comes to providing you with accurate maps: if you do use its features, certainly also try to find out what (tensor fitting) algorithms it employs under the hood! If you want to take advantage of the plethora of different available (*freeware*) *software packages* that implement several advanced tensor fitting methods (and further postprocessing steps, such as fiber tractography), you'll need to *export* the raw DWI data from your scanner. We've also stressed at several occasions that these images are quite worthless if they don't come with the *accompanying gradient directions and b*-value*s*. More and more manufacturers are starting to take this into account and tuck that information safely away in, e.g., the DICOM headers, the headers of their own proprietary formats, or even in separate files (containing a *gradient table* in one way or another). However they do it, just try to somehow make sure that it is effectively packed with your data. Your next concern then is to get it *imported* correctly into your DTI software package. Unless that package supports a whole list of different (more and less) standards, you might be up for yet another daunting task. We're lucky up to some extent, however, as the "*diffusion community*" and the specific supporting communities revolving around some software packages are often very active and responsive: your specific question could be answered quickly after a simple e-mail to a support mailing list. Once you get your workflow up and running, the use of DTI in your daily practice should provide you with *new and exciting insights*!

References

1. Stejskal EO, Tanner JE. Spin diffusion measurements: spin echoes in the presence of a time-dependent field gradient. J Chem Phys. 1965;42:288–92.
2. Le Bihan D, Breton E. Imagerie de diffusion in vivo par résonance magnétique nucléaire. C R Acad Sci Paris. 1985;301(Série II):1109–12.
3. Le Bihan D, Breton E, Lallemand D, Grenier P, Cabanis E, Laval-Jeantet M. MR imaging of intravoxel incoherent motions: application to diffusion and perfusion in neurologic disorders. Radiology. 1986;161:401–7.
4. Basser PJ, Mattiello J, Le Bihan D. Estimation of the effective self-diffusion tensor from the NMR spin echo. J Magn Reson Ser B. 1994;103:247–54.
5. Pajevic S, Pierpaoli C. Color schemes to represent the orientation of anisotropic tissues from diffusion tensor data: application to white matter fiber tract mapping in the human brain. Magn Reson Med. 1999;42:526–40.
6. Basser PJ, Mattiello J, Le Bihan D. MR diffusion tensor spectroscopy and imaging. Biophys J. 1994;66:259–67.
7. Basser PJ. Inferring microstructural features and the physiological state of tissues from diffusion-weighted images. NMR Biomed. 1995;8:333–44.
8. Westin CF, Peled S, Gudbjartsson H, Kikinis R, Jolesz FA. Geometrical diffusion measures for MRI from tensor basis analysis. Proc Intl Soc Mag Reson Med. 1997;5:1742.
9. Chang LC, Jones DK, Pierpaoli C. RESTORE: robust estimation of tensors by outlier rejection. Magn Reson Med. 2005;53:1088–95.
10. Chang LC, Walker L, Pierpaoli C. Informed RESTORE: a method for robust estimation of diffusion tensor from low redundancy datasets in the presence of physiological noise artifacts. Magn Reson Med. 2012;68:1654–63.

Suggested Reading

Basser PJ, Özarslan E. Anisotropic diffusion: from the apparent diffusion coefficient to the apparent diffusion tensor. In: Jones DK, editor. Diffusion MRI: theory, methods, and applications. New York, NY: Oxford University Press; 2010.

Kingsley PB. Introduction to diffusion tensor imaging mathematics: Part I. Tensors, rotations, and eigenvectors. Concept Magn Reson A. 2006;28: 101–22.

Kingsley PB. Introduction to diffusion tensor imaging mathematics: Part II. Anisotropy, diffusion-weighting factors, and gradient encoding schemes. Concept Magn Reson A. 2006;28:123–54.

Kingsley PB. Introduction to diffusion tensor imaging mathematics: Part III. Tensor calculation, noise, simulations, and optimization. Concept Magn Reson A. 2006;28:155–79.

Jones DK, Basser PJ. "Squashing peanuts and smashing pumpkins": how noise distorts diffusion-weighted MR data. Magn Reson Med. 2004;52:979–93.

Quantitative DTI Measures

5

Kathleen M. Curran, Louise Emsell,
and Alexander Leemans

Learning Points

- Visual assessment of diffusion MR images can be supported by nonspecific quantitative measures that can be derived from DTI data, including fractional anisotropy and mean diffusivity.
- Variation in image acquisition parameters in both individual cases and group studies affects both qualitative and quantitative analysis.
- Fractional anisotropy can be modulated by numerous biological and methodological factors and should not be blindly interpreted as a quantitative marker of white matter integrity.
- Interpreting changes of the axial and radial diffusivities on the basis of the underlying tissue structure should not be performed unless accompanied by a thorough investigation of their mathematical and geometrical properties.
- Normal brain development and ageing, and the timing and severity of injury/pathology should be considered when interpreting DTI metrics.

Why Is Quantification Important in Medical Imaging?

Radiological diagnosis is based almost entirely on subjective visual evaluation and quantitative image analysis is rarely employed. While routine clinical diagnosis can be determined qualitatively, image quantification is essential for understanding the basic disease mechanisms which underlie neurological or psychiatric disorders of the human brain, and for the development of biomarkers of brain disease which can be used to evaluate pathology status and treatment efficacy.

Advanced and automated tools play an essential role in extracting such information about specific brain regions or structures within the patient population (e.g., hippocampal atrophy). These tools provide objective criteria, quantification, and a high level of precision (reproducibility), which can inform statistically driven conclusions. Without quantification, group differences cannot be statistically analyzed, and image-based findings cannot be correlated with clinical outcomes.

K.M. Curran, PhD (✉)
Complex & Adaptive Systems Laboratory,
School of Medicine & Medical Sciences,
University College Dublin, Dublin, Ireland
e-mail: kathleen.curran@ucd.ie

L. Emsell, PhD
Translational MRI, Department of Imaging
and Pathology, KU Leuven and Radiology,
University Hospitals Leuven, Leuven, Belgium

Universitair Psychiatrisch Centrum (UPC), KU
Leuven, Leuven, Belgium

A. Leemans, PhD
PROVIDI Lab, Image Sciences Institute, University
Medical Center Utrecht, Utrecht, The Netherlands

W. Van Hecke et al. (eds.), *Diffusion Tensor Imaging*, DOI 10.1007/978-1-4939-3118-7_5

Whilst clinicians are well trained in reading scalar images, i.e., the grayscale images characteristic of computed tomography and conventional MRI sequences, they are less familiar with deriving quantitative information from complex imaging data such as captured using dMRI. As the preceding chapters of the book demonstrate, dMRI data provides additional information that requires nontrivial processing before the data can be analyzed and interpreted. Not only does it offer insight into tissue microstructure, but also the orientational information captured in the diffusion-weighted MR signal can be used to generate impressive and useful qualitative results on the shape of fibre bundles and the connection patterns of brain regions. However, whilst the orientation information contains important information on brain connectivity, it is important to remember that it is insufficient for its complete characterisation and there are many challenges in disentangling the true meaning of quantitatively derived metrics (see Chap. 11 for further details about using DTI to study brain connectivity).

The reduction of the measured diffusion information to a diffusion tensor and then to a scalar value means that when changes or differences are found in one of the scalar metrics, it is difficult to draw conclusions about the exact cause at a microstructural level. While this can be considered a drawback of dMRI, the systematic information reduction can also be advantageous. For example, the human brain is a complex system, the complete characterization of which is currently not possible. If we want to characterise its anatomical status, and compare it with different populations, we need to find a way to summarise the complexity in a more simple form. dMRI offers such a solution as it provides a quantitative means of systematically reducing the anatomical information into manageable scalar indices.

Which Quantitative Measures Can Be Calculated from a DTI Dataset?

Earlier chapters in this section (e.g., 4) describe how the dMRI signal can be used to calculate the diffusion tensor, the basic building block from which several quantitative measures describing the amount of diffusion and its orientational preference can be derived [4]. While direct visualisation of the diffusion tensor components is not readily interpretable, the ellipsoid model is perhaps the most widely used visual representation [4]. An ellipsoid is a three-dimensional representation of the diffusion distance in the *X*, *Y*, and *Z* planes by molecules in a given diffusion time. In the ellipsoidal representation (Fig. 5.1), the orientation of the axes is provided by the three eigenvectors **e1**, **e2**, and **e3** while the radius of the ellipsoid along its axes is proportional to $\sqrt{\lambda_1}$, $\sqrt{\lambda_2}$, and $\sqrt{\lambda_3}$ (see Box 5.1).

Box 5.1 What Is the Difference Between Eigenvalues and Eigenvectors?

Eigenvalues: The ADC values of the tensor along the directions of the eigenvectors. They describe the **shape and size of a tensor**, independently of its orientation.

Eigenvectors: A new set of customized axes for a tensor, aligned along its specific orientation. They describe the **orientation of a tensor**, independently of its size and shape.

Eigenvalues are rotationally ***invariant***, whilst eigenvectors are rotationally ***variant***.

Having obtained the diffusion tensor for each voxel and having computed the eigenvectors and the corresponding eigenvalues, several metrics can be derived (Fig. 5.2), including standard metrics such as fractional anisotropy (FA), a measure of the diffusion anisotropy, and trace or mean diffusivity [6] which reflect the average amount of water diffusion in a voxel.

It is important to note that some measures depend on the orientation of the tissue relative to the applied gradient (rotationally variant), whilst others do not (rotationally invariant) as this has implications for interpretation and for image

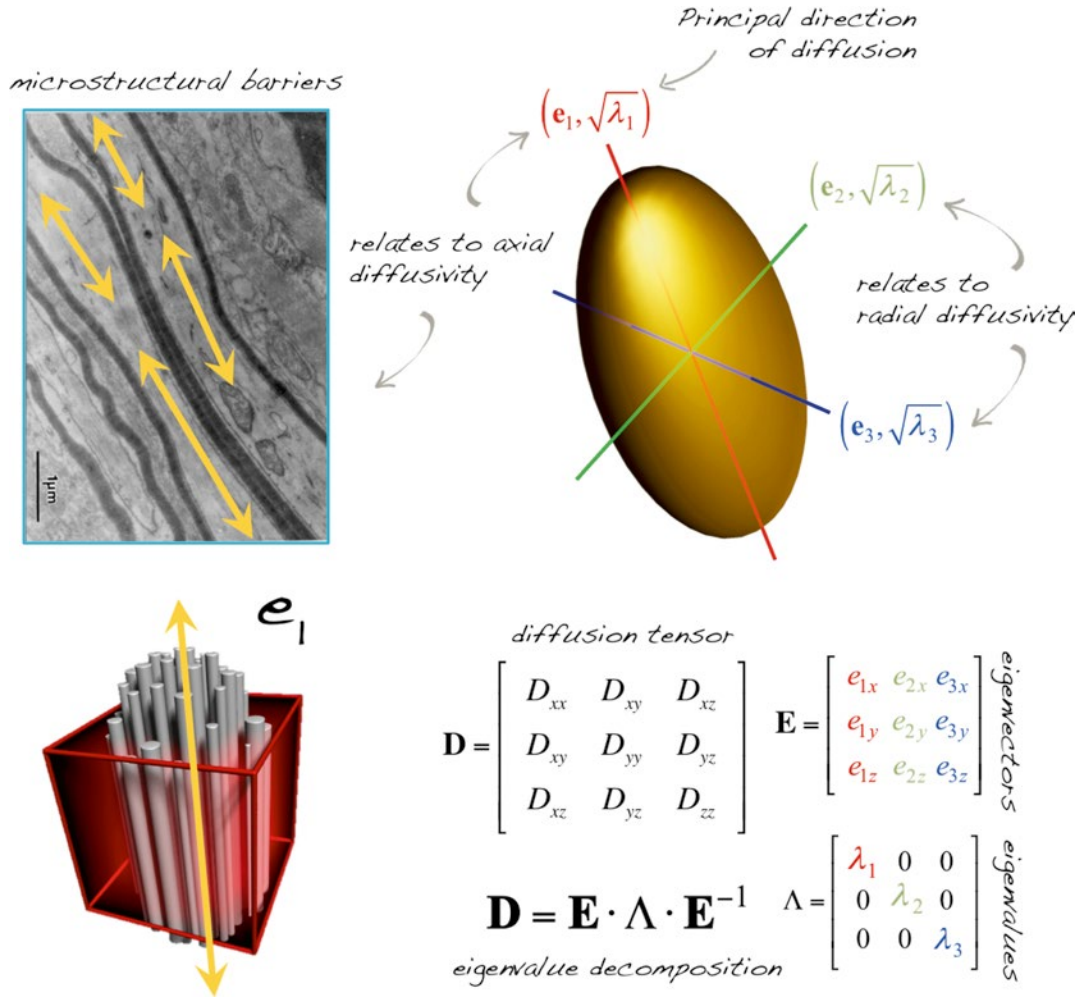

Fig. 5.1 Schematic illustration of the relationship between the mathematical diffusion tensor and its ellipsoid representation. Decomposition of the tensor into eigenvectors and eigenvalues provides information on the orientation and amount of diffusion, respectively. Various mathematical formulas as a function of the eigenvalues and vectors form the basis of quantitative DTI parameters. *Top left* image: Adapted from Beaulieu C. The basis of anisotropic water diffusion in the nervous system – a technical review. NMR Biomed. 2002 Nov-Dec;15(7–8):435–55. With permission from John Wiley & Sons, Inc.

registration (see Chap. 10). For example, eigenvector orientations are rotationally variant but FA and trace are rotationally invariant. Apparent diffusion coefficient (ADC) values, on the other hand, are rotationally variant. Recall from Chap. 4 that ADC quantifies the magnitude of diffusion along a given gradient direction and depends on the strength of the diffusion weighting, i.e., *b*-value. In the case of anisotropic tissue, for example, ADC is highest (diffusion is fastest) along the length of the pathway and lower in other directions [7].

Diffusivity Measures

Trace

The trace (Tr) of the diffusion tensor (***D***) reflects the overall water content. Trace, Tr (***D***), is a commonly used clinical measure, which gives an indication of the overall diffusivity in a given voxel and is computed as the sum of the three eigenvalues λ_1, λ_2, and λ_3 or the sum of the diagonal elements of ***D*** (D_{xx}, D_{yy}, D_{zz}). Trace is completely rotationally independent, and therefore unlike with ADC, changes in Tr(***D***) can be attributed

solely to changes in tissue structure. Trace has become an important metric in the assessment and diagnosis of stroke [1, 8]:

$$\mathrm{Tr}(D) = \lambda_1 + \lambda_2 + \lambda_3 = D_{xx} + D_{yy} + D_{zz}$$

Mean Diffusivity (MD)

Mean diffusivity characterizes the overall mean squared displacement of molecules (average ellipsoid size) and is simply a scaled version of the trace Tr(***D***) [9, 10]:

$$D = \frac{Tr(D)}{3} = \frac{\lambda_1 + \lambda_2 + \lambda_3}{3} = \frac{D_{xx} + D_{yy} + D_{zz}}{3}$$

MD, sometimes denoted mathematically as D, is a measure of the overall diffusivity in a particular voxel regardless of direction. Just like Tr(***D***), MD is low within white matter but high, for example, in the ventricles, where the movement of water molecules is unrestricted. This measure of overall diffusion rate can be used to delineate the area affected by stroke, as demonstrated by van Gelderen [8].

Axial Diffusivity (AD)

Axial (or longitudinal or parallel) diffusivity, $\lambda_{\parallel}$ is simply the diffusivity along the principal axis of the diffusion ellipsoid and is given by λ_1 (see Box 5.2).

Box 5.2: What Is the Difference Between ADC, Trace, and MD?

ADC: amount of diffusion in a single direction

Trace: sum of the eigenvalues, or "mean ADC"

MD: Trace/3

The ADC depends on diffusion anisotropy and is rotationally variant, whereas trace and MD are measures of the average amount of diffusion in a voxel irrespective of the gradient direction or underlying microstructure.

Radial Diffusivity (RD)

Radial (or transverse or perpendicular) diffusivity, $\lambda_{\perp}$, is a measure used to express the diffusivity perpendicular to the principal direction of diffusion:

$$\lambda_{\perp} = \frac{\lambda_2 + \lambda_3}{2}$$

Westin Measures

In addition to the basic ellipsoidal representation, Westin et al. [11] proposed a set of geometrical diffusion measures to quantify the diffusion ellipsoid's shape in terms of its linear (c_l), planar (c_p) and spherical (c_s) anisotropy components:

$$c_l = \frac{\lambda_1 - \lambda_2}{\lambda_1}$$

$$c_p = \frac{\lambda_2 - \lambda_3}{\lambda_1}$$

$$c_s = \frac{\lambda_3}{\lambda_1}$$

$$c_l + c_p + c_s = 1$$

The linear component describes how prolate or cigar shaped the ellipsoid is, the planar component describes how oblate or disc shaped it is, and the spherical component describes how sphere or ball-like the ellipsoid is. See Fig. 5.3 for an illustrative example.

The linear and planar diffusion tensor geometry indices have been used as criteria to distinguish single-fibre voxels from crossing-fibre voxels [12]. To some extent, voxels where the planar diffusion coefficient (c_p) is largest, i.e., larger than linear (c_l) and spherical coefficients (c_s) can be classified as crossing-fibre configuration voxels; all voxels where linear diffusion is largest can be classified as single-fibre configuration voxels. A high c_s may not only arise from multiple-fibre populations but also from partial volume effects with CSF [12].

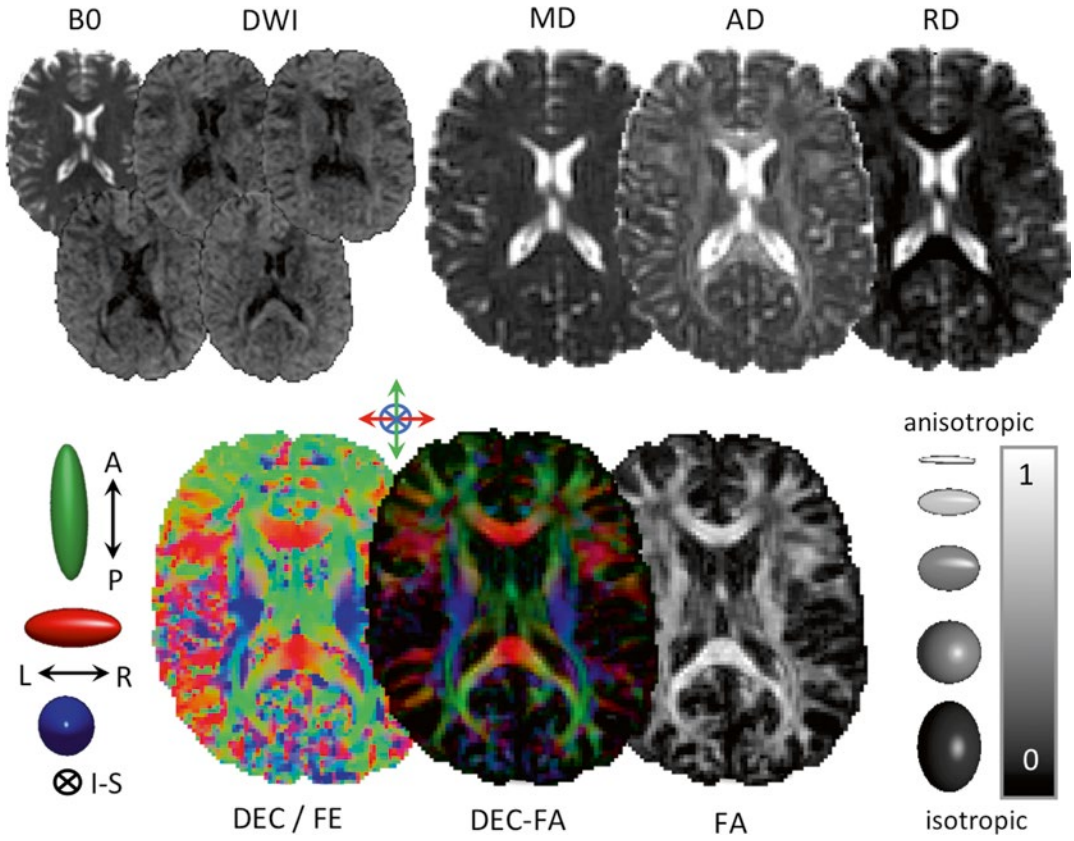

Fig. 5.2 Example parameter maps derived from diffusion imaging. Note the changing contrast in the diffusion-weighted images (DWIs), reflecting tissue orientation changes relative to the applied diffusion gradients. The color FA map, *bottom center*, is generated by multiplying the direction-encoded color map, generated from the principal eigenvector of the diffusion tensor, with the FA map. The colour FA map therefore contains information about fibre orientation (color) and the degree of anisotropy (intensity). Abbreviations: B0, non-diffusion-weighted image, DWI, diffusion-weighted image, MD, mean diffusivity, AD, axial diffusivity, RD, radial diffusivity, A-P, anterior-posterior, L-R, left-right, I-S, inferior-superior, DEC, direction-encoding color, FE, first eigenvector, FA, fractional anisotropy

Anisotropy Measures

The degree of **anisotropy** describes how molecular displacements vary as a function of orientation (ellipsoid eccentricity) and is related to the presence and coherence of oriented structures [9].

Fractional Anisotropy (FA)

FA is a metric used to quantify the ratio between the magnitude of the anisotropic component of $\boldsymbol{D}$ and the entire magnitude of $\boldsymbol{D}$, the diffusion tensor. FA values lie in the range [0, 1] and can be calculated in each voxel using the following expression based on the eigenvalues of the diffusion tensor:

$$\mathrm{FA} = \sqrt{\frac{3}{2}}\sqrt{\frac{(\lambda_1-\lambda)^2+(\lambda_2-\lambda)^2+(\lambda_3-\lambda)^2}{\sqrt{\lambda_1^2+\lambda_2^2+\lambda_3^2}}}$$

This rotationally invariant, dimensionless measure, expresses the anisotropy of the tensor ranging from 0, when the tensor is completely isotropic to 1 when diffusion is bound to a single axis.

In addition to the FA, many other measures of anisotropy have been proposed, including, but

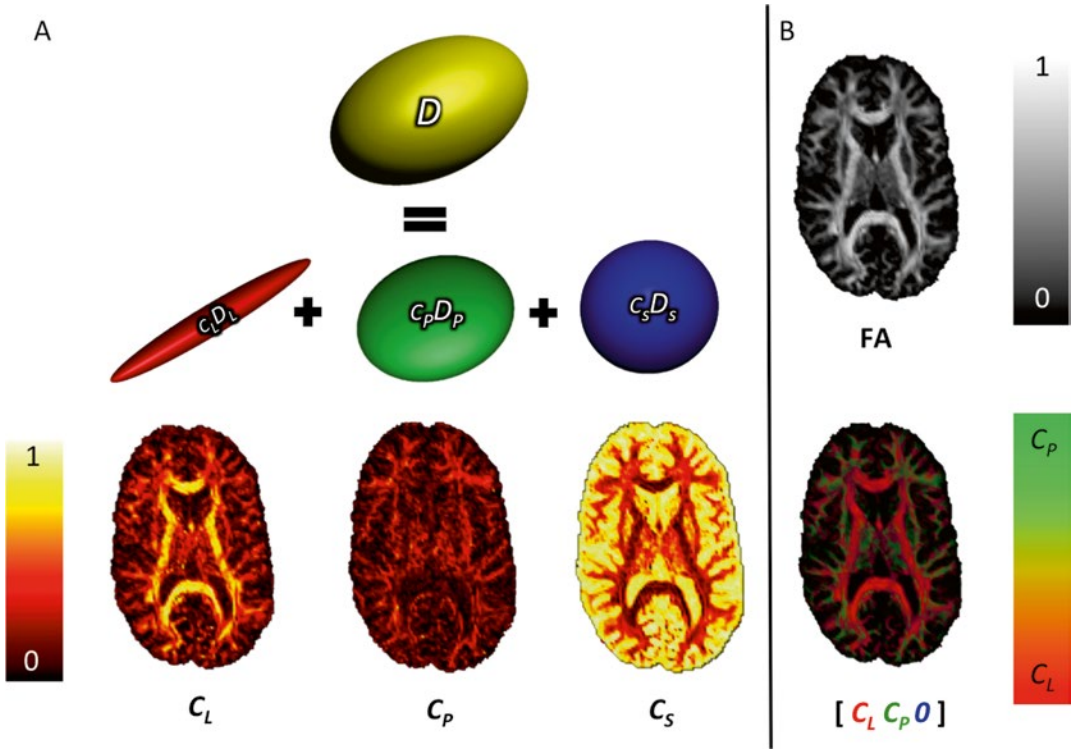

Fig. 5.3 Westin measures: Panel (**a**) illustrates the geometric decomposition of the diffusion tensor, ***D***, (*yellow*), into triangular barycentric space, characterised by cigar (*red*), disc (*green*), and ball-shaped (*blue*) ellipsoids. Axial maps of the corresponding Westin measure, c_l, c_p, and c_s can be found beneath each ellipsoid. Panel (**b**) illustrates how useful additional information can be obtained by combining the measures in a single map. By omitting the spherical component, it is possible to more easily distinguish between linear and planar diffusion (*bottom image*). Compare to the fractional anisotropy map (*top*)

not limited to, the relative anisotropy [6], dispersion of the principal diffusion direction [13] or mode of anisotropy [14].

Further discussion of how FA relates to tissue microstructure and other technical features of dMRI data are discussed in a later section of this chapter.

Quantitative Parameters Derived from Multi-Shell dMRI

Anisotropy present at a microscopic level (for instance, in the presence of oriented structures, such as dendrites in the brain cortex) may not exist at a voxel level due to the averaging effect over the many different directions present in the voxel. This presents a problem for single-shell data (i.e., data acquired with one non-zero *b*-value, e.g., $b = 1000$ mm/s^2), reconstructed with the diffusion tensor, which cannot model more than one orientation per voxel (see Chap. 20). However, new multi-shell approaches can be used to generate alternative metrics, which provide additional information about the underlying tissue microstructure. These multi-shell approaches are described in detail in Section VI of this book "Beyond DTI"; however, a brief summary of representative examples is provided below.

Diffusion Kurtosis Imaging

Diffusion kurtosis imaging (DKI) is a recent MR technique that employs diffusion-sensitising gradients similar to that used in DTI, but acquires

three or more diffusion weighting *b*-values instead of two [15]. While this technique is generally not used in a clinical environment due to time constraints (typical scan times are in the order of 20 min), DKI has been applied to study microstructural changes in a number of preclinical and clinical research populations [16–18]. Whilst DTI is concerned with modeling hindered Gaussian diffusion (see Chap. 3), DKI captures information about redistricted diffusion, which can be approximated to water bound by cell membranes and which is inaccessible to DTI. This means that DKI may provide more sensitive and specific markers for tissue injury than DTI data alone [19, 20]. Since the acquisition protocol used to obtain a DKI dataset includes all the information necessary to derive a standard DTI dataset, it can be used to calculate both types of indices. DKI measures include the kurtosis anisotropy (KA), mean, axial and radial kurtosis (MK, AK, RK, respectively). These measures quantify the degree of non-Gaussianity and can be regarded as indices of tissue compartmentalization or complexity [15]. For example, a high mean kurtosis may reflect an increase in tissue complexity. This is in contrast to high mean diffusivity, which would reflect an increase in freely diffusing water. Further information about DKI can be found in Chap. 21.

Tissue (Compartment) Model-Based Approaches

Whilst DTI and DKI do not assume a specific biophysical tissue model, other MRI based frameworks aim to incorporate additional features into their models that reflect some properties of tissue microstructure such as the behavior of water in intracellular and extracellular compartments [21]. For example, approaches such as CHARMED [22], AxCaliber [23], and ActiveAx [24] enable the extraction of a multitude of microstructural parameters (axon diameter distribution, mean axonal diameter, and axonal density) [25]. To date however, these approaches have been applied primarily in a research context owing to the complexity of analyzing such data and because of clinically prohibitive scan times. Neurite orientation dispersion and density imaging (NODDI) has recently been proposed as a more clinically feasible alternative and can be used to estimate the density and angular variation of neurites (dendrites and axons) in-vivo [26]. NODDI is based on a three-compartment tissue model and data is acquired using at least two shells differing from one another only in choice of *b*-values and optimized for clinical (research) feasibility (scan time <30 min).

It should be remembered however that all the techniques based on tissue models are still limited by the simplicity of the model and provide only indirect measures that may relate to tissue features, but do not actually directly quantify, for example, neurite density, in the same way as a histological examination.

Section Summary

- The diffusion tensor provides a means to quantify the amount and orientational preference of diffusion at a voxel level.
- A number of rotationally invariant scalar parameters can be derived from the diffusion tensor, including the FA, MD, AD, and RD.
- The mean ADC, trace($\boldsymbol{D}$), and MD are all measures of the average diffusion in a voxel. They relate to the absence of barriers to water diffusion.
- FA is the most widely used DTI measure and describes the degree of diffusion anisotropy in a voxel. It is related to the presence of barriers to diffusion, such as axonal membranes.

The Influence of Image Acquisition on DTI Parameters

Deriving scalar values from dMRI data and eventually comparing them between groups of subjects and/or correlating them with other parameters begins with the raw data acquisition, followed by a pipeline of image processing steps.

Each one of these steps is susceptible to sources of bias, which may not only limit the accuracy and precision of DTI parameter estimation, but can lead to substantial errors. A more detailed coverage of this topic is performed in the following chapters of this section (Chaps. 6 and 7); however, a brief summary of selected influential factors is presented below.

Effect of Field Strength

Clinical MR systems typically used for routine DTI scanning of humans are 1.5 or 3 T, although a small number of specialist research centers offer the possibility of scanning (predominantly healthy) subjects at 7 T. As DTI parameters should not be dependent on the static magnetic field strength, the reproducibility of measures at different field strengths is largely dependent on signal-to-noise ratio and the effect of artifacts [27]. It is commonly accepted that scanning at higher field strengths increases signal-to-noise (SNR); therefore one would expect higher fields to equate with higher quality. Although this is the case for conventional imaging, the competing decreases in T2 time and increased b0 inhomogeneity associated with increasing field strength, coupled with increased distortions due to eddy currents, magnetic susceptibility, and chemical shift artifacts, off-set the gain in image quality in DTI. Nevertheless, it has been shown that the uncertainty of fitted DTI parameters decreases with increasing field strength, which may impact positively on fibre-tracking results [27]. Figure 5.4 illustrates the effect of field strength in a single subject.

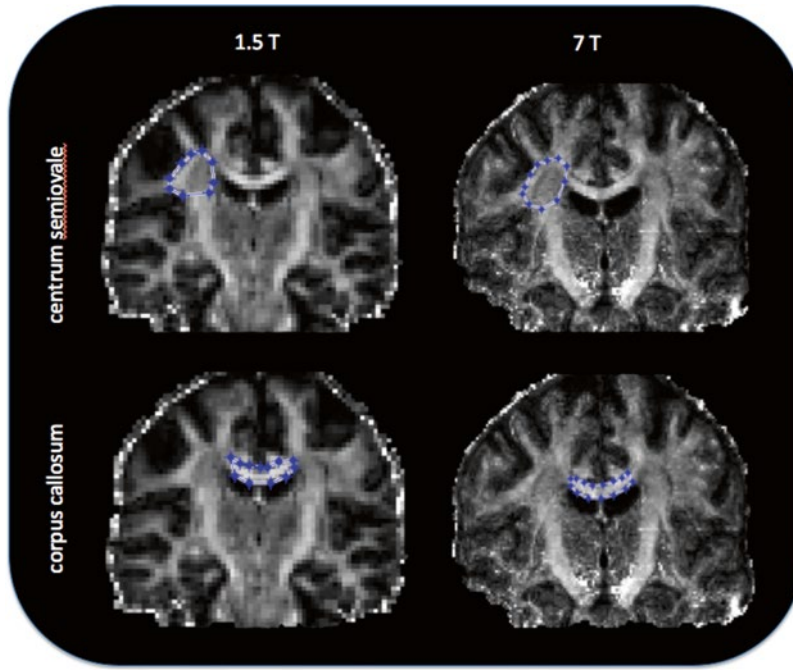

Fig. 5.4 Comparison of FA measured in two ROIs in the same subject at 1.5 and 7 T. Coronal DTI data of the human brain in the same subject acquired at 1.5 and 7 T. FA was calculated in the centrum semiovale at 1.5 T: FA mean = 0.48 (SD = 0.11) and 7 T: FA mean = 0.47 (SD = 0.08); and in the genu of the corpus callosum at 1.5 T: FA mean = 0.67 (SD = 0.18) and at 7 T: FA mean = 0.66 (SD = 0.14). Note the difference in image quality at different field strengths, which in this subject has a relatively minor effect on the FA when averaged across each ROI. SD = standard deviation [Legend data provided courtesy of FMRIB Centre, University of Oxford]

Effect of Number of DWIs

Reconstruction of the diffusion tensor requires a minimum of seven MR images [28], one without any diffusion sensitizing gradients applied and at least six diffusion-weighted images with gradients applied in non-collinear directions. Mathematically, only six non-collinear diffusion-weighted directions are necessary to reconstruct the diffusion tensor; however, in practice more images should be acquired to improve the accuracy of tensor estimation [29].

When using the tensor model, the more directions that are acquired the better the angular resolution that can be achieved; however, research has shown that the "cost" (in this case scan time) versus benefit curve starts to flatten out at around 30–32 unique directions. Jones et al. [29] found that robust determination of mean diffusivity, FA and tensor orientation requires a dMRI sampling scheme in which at least 30 unique and evenly distributed sampling orientations are employed. However, for anisotropy measurement only, the measurements will be robust when at least 20 unique sampling orientations are used. When comparing indices derived from DT-MRI, if the number of sampling orientations is low (<30) and not uniformly distributed over the surface of a sphere, then the variance in derived indices can be strongly dependent on structural orientation [30]. For example, the lowest variance in a parameter such as FA is found when the fibre is aligned with one of the sampling orientations, and is largest when the fibre is at the greatest angle to the sampling vectors. These variations will effectively increase the standard deviation of measurements obtained from a region of interest (ROI) encompassing voxels containing tissue with different fibre orientations. Such increased variance will reduce the statistical power for quantitative analyses of mean diffusivity in different ROIs and will, in general, spuriously increase the heterogeneity of the apparent trace within ROIs (Fig. 5.5).

Combined with the number of diffusion weighting directions used, there is a requirement to acquire multiple non-diffusion-weighted images if large numbers of DWIs are acquired using different gradient orientations. The optimal ratio of diffusion weighted to non-diffusion-weighted images was calculated to be roughly 9:1 [31]. Typically one $b=0$ image is acquired for every 8–9 diffusion-weighted images. HARDI methods typically use a higher number of gradient directions (>45) depending on the reconstruction method used, and similar to DTI, increasing the number of directions improves the angular precision achievable [32].

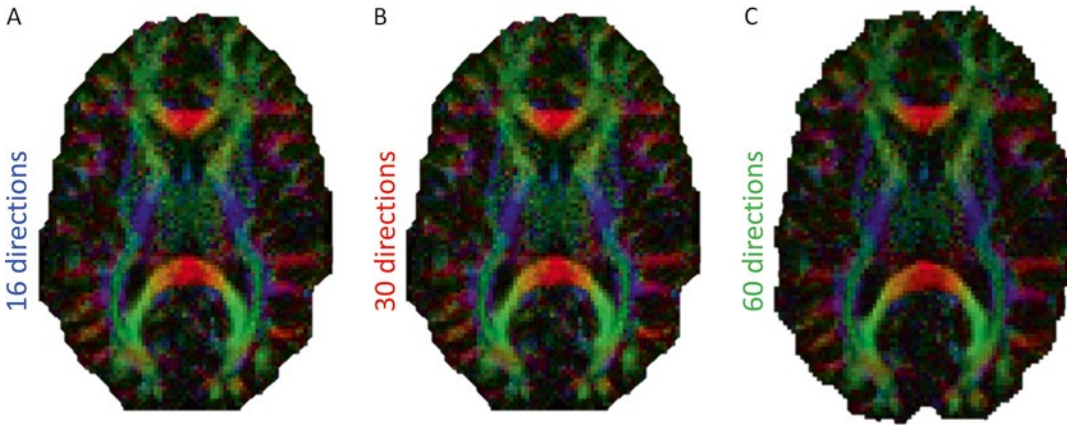

Fig. 5.5 Illustrates synthetic color FA maps for (**a**) 16 (*blue*), (**b**) 30 (*red*), and (**c**) 60 (*green*) directions. Increasing the number of gradient directions increases SNR and therefore the accuracy of estimated the DTI measurements

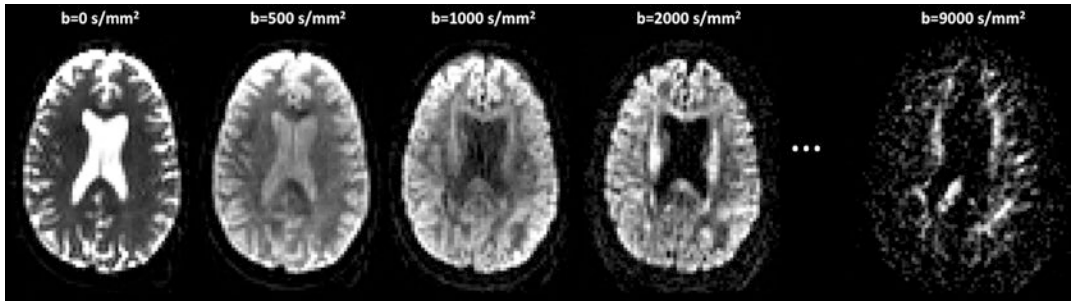

Fig. 5.6 Illustration of change in contrast and SNR with increasing *b*-value [33]

Effect of *b*-Value

The number and strength of *b*-values influence the derived measures of diffusion and anisotropy [30] (Fig. 5.6). Attention to the choice of diffusion sensitisation parameters is important when making decisions regarding clinical feasibility (acquisition time) and obtaining normative measures.

Within an ROI, the mean and variance of the trace will be dependent on the *b*-value [30]. The trace of the tensor is dependent on the amount of diffusion weighting used to characterise it [30]. As the diffusion weighting is increased there is an increasing dissociation between grey and white matter, with the trace in white matter being lower than in grey matter. This not only introduces more heterogeneity within ROIs, but also means that comparison with normative databases or data from other centres and, by extension, multicenter studies is problematic unless the same degree of diffusion weighting is employed (which is seldom the case).

The diffusion characteristics of a voxel containing a single-fibre population can be characterized by a tensor whose associated ellipsoid is prolate. In voxels containing multiple fibre populations (e.g., crossing-fibre regions), the diffusion characteristics observed at low *b*-values can still be described by a single tensor but the diffusion ellipsoid may be less prolate or may become spherical or even oblate. In such cases, the tensor model does not adequately reflect the underlying tissue microstructure. Unfortunately, this is the case in an estimated 60–90 % of brain voxels [34], which again emphasizes the need for caution when interpreting DTI measures. Several groups have proposed methods for elucidating complex tissue microstructure by examining the non-Gaussian diffusion behavior that only becomes apparent at higher *b*-values (see [32] for a review).

Effect of Image Quality

Noise

The effect of noise on anisotropy measurements derived from DT MRI was first described by Pierpaoli and Basser [35]. Noise in the diffusion-weighted signals will mean that, even in a perfectly isotropic medium such as a glass of water, it is not possible to obtain three identical eigenvalues. Low signal-to-noise ratios correspond to high eigenvalue discrepancies. Thus, there is a noise-induced bias in measurements of anisotropy. The variance in anisotropy increases as the added noise increases. However, the mean value remains approximately constant in the white matter, but increases rapidly in the grey matter [30]. Therefore unless the acquisitions are matched so that the SNR in the non-diffusion-weighted images is the same and, equally importantly, so that the same number of $b=0$ images and diffusion-weighted images are acquired, then comparing anisotropy values across different subjects, time points, and centers is particularly problematic (see Box 5.3).

Box 5.3: Comparing DTI Measures in Different Studies

It is not trivial to directly compare DTI measures (e.g., FA) derived from data acquired on different scanners with different acquisition parameters (e.g., *b*-value).

Example: For a given patient, the FA in the corpus callosum is found to be 0.8. In another study, the FA in the corpus callosum in a healthy individual is reported to be 0.9. Intuitively, one may conclude that the patient has a lower FA than normal. This is incorrect because the FA was calculated based on data with different acquisition parameters, and possibly also using different tensor estimation and analysis techniques. The correct way to assess if a patient has a different FA value in the corpus callosum compared to a healthy individual would be to do a case–control group study with patients and healthy control subjects scanned with identical scan protocols and processed/analyzed in an identical manner.

The SNR depends linearly on the voxel volume. Clinical protocols typically limit voxel sizes to a minimum of about 2 mm^3 at 3 Tesla (T) or 2.5 mm^3 at 1.5 T. Reducing the edge length from 2 to 1.5 mm would reduce the SNR by more than half [36]. This reduction in SNR can only be compensated for by repeating and averaging the measurements, if averaging is performed in the complex domain and appropriate models of noise are invoked [36]. The SNR should never be below about 3:1 in any of the DW images in order to avoid the problems associated with the rectified noise floor [30]. Results reported in [37] and [38] suggest 10:1 as a safe minimum (Box 5.3).

It has also been found that that even within the three popular regression methods (linear least squares, LLS, weighted-linear least squares, WLLS, nonlinear least squares, NLLS) that do not explicitly account for the noise-floor, there are differential responses [37, 39]. This means that results will be different when using different estimation methods, and therefore, it is important when comparing measures of diffusion anisotropy to establish not only what acquisition was used, but also what tensor estimation routine was used (see previous Chap. 4 for further discussion on the topic of tensor estimation strategies).

SNR of the diffusion-weighted images is also influenced by the diffusion weighting factor or *b*-value used. Low *b*-values provide higher SNR but at a cost of reduced angular resolution. Correspondingly, high *b*-values are better for HARDI acquisitions but SNR is significantly reduced.

Artifacts

Although general guidelines exist for optimizing a DTI acquisition protocol in terms of SNR, *b*-value, voxel size, diffusion gradient directions, and cardiac gating [40], large variations in data quality remain as a result of differences in scanner hardware, pulse sequences and available scan times. Tournier et al. [32] and Jones et al. [36] present excellent reviews on pre-processing dMRI data and the recommended quality assessment that should be performed. There are a number of artifacts that can be identified in DTI data, including geometric distortions, ghosting, and signal dropouts. Detailed information regarding the prevention, recognition, and correction of such artifacts is provided in Chaps. 6 and 7 of this book.

Such artifacts can affect the accuracy of the tensor estimation, and by extension, the derived DTI parameters. For example, FA values greater than one can result from negative eigenvalues in the diffusion tensor, which typically occur at the interface between the CSF and the surrounding white matter, as artificially low-intensity rims [36]. Correcting for CSF-contamination partial volume effects in the structures of interest on a voxel-by-voxel basis prior to drawing inferences about underlying changes in white matter structures is therefore recommended [41].

Not only the artifacts themselves, but also the strategies employed to correct them may also

introduce errors. For example, when correcting for motion and eddy-current induced geometric distortions by performing affine registration of the diffusion-weighted images to one of the non-diffusion weighted images, it is important to also reorient the encoding vectors with the same rotation matrix [42]. Neglecting to perform this important step may have minimal impact on scalar indices such as FA but it can introduce biases of the order of a couple of degrees to estimates of the principal eigenvector, or peaks in the fibre orientation distribution (fODF) or diffusion orientation distribution (dODF).

It is also important to correct for any residual eddy currents along the phase-encode direction by modulating the signal intensity back to its correct value by scaling the intensity in proportion to the change in the volume of the voxel. Neglecting to do this can introduce biases in quantitative metrics and estimates of orientation [30].

Section Summary

- DTI metrics are influenced by a number of factors related to data acquisition, including the magnetic field and gradient strength, the *b*-value, the number of gradient directions, and image quality.
- Pre- and post-processing strategies used to estimate the tensor and correct for artifacts will affect the calculation of DTI measures.

Interpreting Quantitative Diffusion Measures

> … in most in vivo DTI cases, all that is proven is that there is a change in the diffusion parameters of water in a specific neural region, the interpretation of which is merely a plausible hypothesis. (C. Beaulieu, [43]).

Diffusion-weighted MRI measurements reflect the amount of hindrance and restriction experienced by water molecules moving with a component of displacement along the axis of the applied gradient, averaged over a voxel. Exactly how restriction and hindrance influence the signal is an open and complicated question and relies on a number of modelling assumptions, which may or may not be correct [36]. The general mobility of water molecules depends on barriers and obstacles imposed by microstructure, e.g., cell membranes, myelin sheaths, and microtubules. Such barriers slow down the diffusing particles ("hindered diffusion") or even impose an upper limit on their overall mean-square displacement ("restricted diffusion"). The distinction between restriction and hindrance is important when interpreting diffusion MR data. While the tensor parameters are influenced by both restricted and hindered diffusion, the tensor model assumes Gaussianity and therefore translates restricted into hindered diffusion.

It is important to understand that when there is any component of displacement along the applied gradient axis that this will lead to signal attenuation. In other words, if the gradient is applied along a given axis, water molecules do not have to be moving parallel to this axis to cause signal loss. It is only when the displacement is perfectly perpendicular to the encoding axis that there will be no contribution to signal loss since it is only at this orientation that there is no component of displacement along the encoding axis.

Relating DTI Parameters to Neurobiology

Fractional Anisotropy

Several DTI indices can be derived from the eigenvalues to quantify the properties of white matter noninvasively, but the most widely used is FA, which is an index of the amount of anisotropy. FA describes the directional coherence of water diffusion in tissue and is generally interpreted as a quantitative biomarker of white matter "integrity." This is because pathological studies tend to show a reduction of FA associated with neurodegenerative processes [44–48] and developmental studies tend to show an increase of FA through infancy, childhood, and adolescence [49–53], whilst IQ or improved performance in particular cognitive domains often

Box 5.4: The Effect of Timing on DTI Metrics: Stroke

The acute assessment and monitoring of stroke evolution remain the most useful and widely adopted clinical applications of DTI. Within several minutes of stroke onset there is a substantial decrease in mean ADC/MD in ischaemic brain tissue (by 30–50 %). The basic mechanism underlying this decrease remains unclear [1], but may be due to reduction in extra- and intracellular water mobility, a shift of water from the extracellular to intracellular space, an increase in the intracellular diffusion restriction due to changes in membrane permeability, an increased tortuosity in the extracellular space due to cell swelling [2] and the consequences of cytotoxic oedema. The initial drop in MD pseudo-normalizes around a week later, as a result of blood–brain barrier breakdown, damage to cell membranes, and vasogenic oedema, and gradually continues to rise over the following months. In contrast, anisotropy briefly increases in the hyper-acute phase (<7 h) before decreasing to below pre-lesion levels within 2 or 3 days [3].

correlates with increased FA [54–56]. However, equating FA with an index of white matter "integrity" is an oversimplified interpretation because FA cannot disentangle the individual microscopic contributions (partly due to the relatively large voxel size) [12, 30, 36].

FA is influenced by large, oriented macromolecules, organelles and membranes. The degree of myelination, axon packing, the relative membrane permeability to water, the internal axonal structure, and the tissue water content all contribute to tissue anistropy [57]. The degree of anisotropy is often most strongly correlated with axon count and density [43], whilst the degree of myelination correlates with FA, but does not determine tissue anisotropy, which has also been demonstrated in non-myelinated fibres. Furthermore, as axon count and myelin are strongly correlated, it is impossible to differentiate between them when interpreting FA changes. For this reason, FA should not be equated with an index of myelination or myelin damage.

Large regional differences have been observed in WM FA measurements. These differences follow a typical pattern of high FA in the core of fibre bundles and low FA in the periphery [58], although there are exceptions. For example, in regions of where fibre bundles cross, FA is low. Regional anisotropy may arise from differential rates in developmental and degenerative trajectories for different fibre pathways [51]. For example the superior longitudinal fasciculus matures at a relatively later stage of development than other white matter fibre bundles, and an anterior-posterior gradient of FA decline in later adulthood has been observed [59, 60]. This regional heterogeneity introduces its own challenges with regard to both study design and the interpretation of results, as discussed later in this chapter and in Chaps. 8 and 13.

Mean Diffusivity

Recall that MD is a measure of the overall diffusivity in a particular voxel regardless of direction. It is highest in areas where water diffuses most freely, such as in the ventricles, and is lowest in areas of high tissue complexity and hence, more barriers to diffusion, such as in grey matter. MD or "mean" ADC is an important measurement when assessing the evolution of stroke as ischemia-induced changes in tissue water content can be visualized on DWI and ADC maps before they appear on T2-weighted images (see Box 5.4). In the adult brain, white matter water content is lower than that of the grey matter (65 % versus 85 %); however, the MD values for the two regions are virtually identical [61, 62]. This indicates that white matter is less restrictive to water diffusion than grey matter and may be related to the fact that water diffusion parallel to axons is relatively unrestricted, compared to diffusion perpendicular to axons or in grey matter.

Brain water content decreases with maturation. In the immature brain, the MD of white matter is almost twice that of the fully myelinated brain due to the large extracellular spaces present in unmyelinated white matter [63]. During brain maturation, structures such as cell and axonal membranes become more densely packed, and water molecule mobility becomes increasingly restricted. As white matter develops, changes in water diffusion perpendicular to white matter fibres may indicate changes due to premyelination (change in axonal width) and myelination [23]. Differences in water content could also affect the contrast between white and grey matter in the paediatric brain [64, 65]. Therefore, as with FA, it is important to consider the age of the study population when interpreting changes in MD.

Axial and Radial Diffusivities

Recall that **axial diffusivity**, $\lambda_{\parallel}$ is simply the diffusivity along the principal axis of the diffusion ellipsoid (λ_1), whilst **radial diffusivity**, $\lambda_{\perp}$ is an average of diffusion along its two minor axes, which expresses the amount of diffusivity perpendicular to the principal direction of diffusion, or, in single-fibre populations, perpendicular to the direction of fibre orientation. Some studies have related AD and RD to specific microstructural features. For example, axial diffusivity has been associated with axonal damage, and fragmentation in particular, whilst radial diffusivity has been associated with axonal density, myelin integrity, axonal diameter, and fibre coherence [3, 66].

However, it is important to emphasize that the diffusion direction associated with the axial diffusivity is not always preserved in pathological tissue and is not always aligned with the underlying expected tissue architecture [67]. Therefore, interpreting changes in axial and radial diffusivities in terms of underlying biophysical properties, such as myelin and axonal density is discouraged, unless accompanied by a thorough investigation of their mathematical and geometrical properties [68]. In this context, it also inappropriate to statistically compare the eigenvalues of the diffusion tensor without checking the alignment of the corresponding eigenvectors with the underlying tissue structures, especially when comparing patients with healthy controls [68]. The comparison of eigenvalues between different subjects or comparisons of the contralateral side of a tract affected by pathology in the same subject may be meaningless because they could represent completely different physical information.

Fibre Count

Although not strictly a DTI parameter, the "fibre count" (number of streamlines that pass through or between given regions of interest) can be derived from DTI-based tractography analysis (see Chap. 11). It is sometimes (incorrectly) used as a direct measure of connectivity or fibre density [36]. For this reason, the use of the term "fibre count" has been discouraged and it is proposed that reporting the number of streamlines is a safer and unambiguous way of reporting results [36]. Similarly, the number of streamlines passing through a voxel will be modulated by features of the pathway (curvature, length, width, myelination) and local variations in SNR and therefore interpreting this measure as fibre density is problematic. In this context, it may also be inappropriate to compare the streamline count between white matter structures that have different shapes [36].

DTI Parameters as Complementary Measures

Measures derived from the diffusion tensor, such as FA, essentially combine the contributions from the different sub-compartments of white matter into a single metric. Improving the biological specificity of diffusion MRI demands improvements in both acquisition and modeling schemes. Advanced MR methods may provide putative cellular markers, such as "axon/neurite density," mean axon diameter, axon diameter distributions, and neurite dispersion (e.g., CHARMED [22],

AxCaliber [23], ActiveAx [24], and NODDI [26]). As quantification of myelin via diffusion is extremely problematic, other MR contrast mechanisms may provide complementary information, for example, quantitative magnetization transfer imaging [69, 70] and multicomponent relaxometry (e.g., [71, 72]). Indeed, recent work has demonstrated the utility of this approach in the assessment of the microstructural basis of T2 hyperintensities in neurofibromatosis (NF1) [18].

Section Summary

- DTI measures can be correlated with microstructural features such as axon count and density, myelination, and membrane permeability.
- It is inappropriate to attempt to interpret DTI measures in terms of specific microstructural features or as a measure of white matter integrity
- Fiber count cannot be equated with fibre or axon density. Reporting the number of streamlines is more appropriate.
- Complementary information from other imaging modalities, advanced dMRI techniques, and histology can support the biological interpretation of DTI metrics.

Challenges of Interpretation

One of the great accomplishments of DTI is reducing complex information into a handful of simple, sensitive, useful measures. However, this oversimplification comes at a price, and that price is the lack of specificity of DTI metrics and their dependence on many methodological and biological factors. By extension, this means that changes in DTI metrics cannot be ascribed to a single factor (or biological/pathophysiological feature), and this makes the interpretation of changes in DTI metrics extremely challenging. For example, the demographics of subjects and controls, the timing and severity of injury or pathology, technical factors related to image acquisition and analysis, and the nature and location of abnormalities, are all important factors when relating DTI metrics to clinical outcome measures. This next section summarizes some of these issues.

Model Limitations

As described earlier in this chapter, and revisited throughout this book, DTI measures are derived from an oversimplified mathematical representation of the average diffusion in a given voxel given a number of assumptions, most of which cannot be satisfied in the "real-world" situation. Although it is beyond the scope of this introductory text to go into detail on this topic, it is useful to consider some of the limitations of the tensor model (further discussion can be found in Chap. 20).

For example, the tensor model assumes that diffusion follows a Gaussian distribution, when in fact, typical dMRI sequences primarily capture signal from intracellular water, which is restricted and hence follows a non-Gaussian distribution. It also assumes a single fibre direction in each voxel, but we know that this condition is rarely satisfied in (complex mammalian) neural tissue. Other, perhaps less intuitive assumptions are that the temperature of the diffusing molecules remains constant and they remain in the same environment, e.g. there is no exchange between intra and extracellular compartments. In reality, variations in temperature will occur as a function of the thermal conductivity of the examined tissue and the proximity of blood vessels, and water molecules may move between compartments during the application of the diffusion-sensitizing gradients.

Another important limitation concerns the ellipsoid representation of the diffusion tensor. Recall that the degree of eccentricity of the ellipsoid reflects the degree of anisotropy, i.e., a long, thin ellipsoid reflects highly anisotropic diffusion (i.e., high FA), and a more spherical ellipsoid reflects more isotropic tissue and (i.e., low FA). However, FA reflects the relative contributions of the axial and radial diffusivities, such that different combinations of axial or radial diffusivity can

give rise to the same FA. In this context, by only examining FA, it is not possible to identify the origin of the observed values. For instance, the prolate ellipsoid with $\lambda_1=3$, $\lambda_2=1$, $\lambda_3=1$ and oblate ellipsoid: $\lambda_1=7$, $\lambda_2=7$, $\lambda_3=1$ (arbitrary units) have the same FA value of $2/\sqrt{11}$, but have different AD and RD values [73].

Biological Confounds

Demographics

Abnormalities in DTI pararmeters are typically defined on the basis of comparison with a healthy control group because universal thresholds for abnormality have not yet been established. In this context, a number of studies have examined DTI changes in healthy controls across the lifespan. As described earlier, FA typically increases and MD decreases through childhood and adolescence [74] until the fourth decade when white matter volume begins to decrease [51, 75]. However, the lack of standardized DTI acquisition and analysis protocols, means that standard, normative data describing thresholds of normality across the general population are presently unavailable. This situation is likely to change in the future as large-scale, harmonized multicenter studies and data-sharing gain ground.

In addition to age-related effects, other factors may confound DTI findings, including brain volume, gender, ethnicity, level of education, handedness, medical comorbidity, alcohol and smoking use, and medication status, to name but a few (see Chap. 13 for further information).

Timing

In addition to age, sex and anthropometrics, injury mechanism and the chronicity of injury can greatly influence DTI metrics and it is therefore important that these issues are considered when designing studies and interpreting results. Primary injury and secondary injury play different roles in the evolution of pathology as a function of time post-injury. Microstructural pathology, as detected with DTI, may change over time and it is therefore important to systematically assess the timing of DTI after injury, particularly in the acute and sub-acute periods (between 2 weeks and 1 year) [76] (see Box 5.4).

Complex Tissue Architecture and Crossing Fibres

One of the most important confounds in DTI analysis is the inability of the tensor model to correctly characterise diffusion in regions of complex fibre architecture (i.e., when an image voxel contains fibre populations with more than one dominant orientation, such as in bending or interdigitating fibre configurations at the voxel level) [32] (Chap. 20). The impact of crossing fibres on the main DTI metrics is summarized below.

Impact of Crossing Fibres on FA

The FA, in particular, is strongly affected in areas of complex fibre architecture [35]. FA values are lower in such areas because there is no single dominant diffusion direction and the diffusion profiles of the different fibre configurations average out. Consider how the shape of the diffusion ellipsoid would change in a voxel with more than one fibre bundle. This effect is clearly visible on a standard mid-coronal FA in the semiovale region, at the intersection of multiple fibre pathways (Fig. 5.7).

In neurodegenerative conditions, the deterioration of one fibre bundle could result in an adjacent or functionally related fibre bundle becoming more dominant, resulting in a paradoxical increase in FA. In some neuropathological studies, for example, investigating Wallerian degeneration and mild cognitive impairment, higher FA values have been observed in patients than in healthy controls [77, 78].

Impact of Crossing Fibres on the Trace

The *b*-value and the number, orientation, and trace of individual fibre populations within a voxel affect the trace [48]. In a voxel with two fibre populations, the trace in that voxel is not

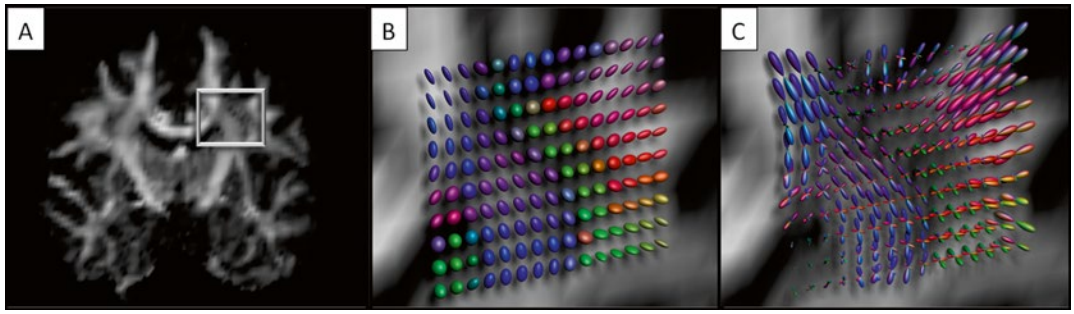

Fig. 5.7 The dark, low-anisotropy region (*silver box*) that is typically visible in the centrum semiovale on coronal FA maps (**a**) reflects the inability of the tensor to characterize more than one dominant fibre direction in a given voxel. Compare the more spherical tensor ellipsoid glyphs in this region (**b**), with those obtained from higher order models (in this case, constrained spherical deconvolution) (**c**)

only dependent on the trace values of the underlying fibre populations but also depends on the angle of intersection between these two fibre populations. As the angle between the two populations increases, the trace in a crossing fibre region gradually decreases with respect to trace in a region with only a single population, reaching its minimum when the populations are orthogonal. The trace therefore depends on the configuration of the crossing, i.e., the angle of intersection between populations and the volume fraction of each of the fibre populations in a voxel [12].

Impact of Crossing Fibres on Mean Diffusivity

There are a number of factors that may influence the estimate of MD, for example the choice of tensor estimation routine or the set of gradient sampling vectors [79]. Vos et al. [12] demonstrate that the MD is lower in complex white matter configurations, compared with tissue where there is a single dominant fibre (SF) orientation within the voxel. They also show that the magnitude of this reduction depends on various factors, including the relative contributions of different fibre bundles, microstructural properties, and acquisition settings such as the *b*-value.

The dependence of the MD on the tissue geometry has implications for statistical testing. In regions that are comprised of voxels with purely SF-configurations, the MD will be relatively uniform. Likewise, for areas of tissue where there is uniformity in the complexity of the tissue, the MD may be lower but it will be uniformly lower. However, in regions that contain a mixture of SF and crossing fibre configurations that take different geometrical forms, there will be a larger variation in MD. Consequently, there will be a higher variance in such regions, and therefore less statistical power to detect differences in MD.

Impact of Crossing Fibre Configurations on AD and RD

Wheeler-Kingshott and Cercignani [68] have demonstrated the challenges of interpreting changes in axial diffusivity (AD) and radial diffusivity (RD) in crossing fibre regions. Their experiments revealed that AD increased when the RD of one of the underlying fibre populations was increased. Similarly, RD decreased when there was a reduction in AD in one of the underlying populations. They propose a framework to address some of these issues [80]. Vos et al. [12] have also shown an associated reduction in one or more of the tensor's eigenvalues with lower MD values in regions of complex fibre architecture. With two fibre populations in a voxel, the diffusivity becomes more planar, leading to an underestimation of λ_1 and an overestimation of λ_2.

Technical Issues

Partial Volume Effects

Spatial resolution is an important consideration when assessing anisotropy and the aggregate range of diffusivities across the tissues composing the voxel, as it will determine to a large extent, the influence of partial volume effects (PVEs) (Fig. 5.8).

PVE is defined as the intra-voxel heterogeneity of different tissue organizations. For example, within one voxel, a variety of tissue types (grey matter, white matter, CSF, vascular tissue) may be present, each with a different type and degree of cellular architecture and fluid content. When averaged out over the voxel as part of the tensor reconstruction, the contribution of all these different tissue structures will give rise to a single dominant diffusion direction. The relative contribution of each tissue type will determine the dominant diffusion direction, so for example, a voxel located in the core of a white matter bundle will be less influenced by PVE than for example, a voxel at the edge of a bundle, or near the ventricles. Vos et al. demonstrated that FA and MD are modulated by fibre bundle thickness, orientation and curvature as a result of PVE [36] and recommend accounting for these features in DTI analysis.

Impact of CSF Contamination on Diffusion Metrics

Given that diffusion in CSF is isotropic and has a mean diffusivity that is approximately four times larger than water in tissue, it is clear that partial volume contamination any voxel by CSF will influence DTI parameter measurements [82]. This is particularly problematic at the interfaces of tissue with CSF-filled spaces [83] and is an important confound in studies of development and ageing, and in pathological volume change [82].

CSF-suppression techniques such as FLAIR have been used to ameliorate CSF contamination at the point of acquisition [84] but this can prolong acquisition time. Jones et al. [36] recommend the use of a multicomponent modeling solution [85, 86].

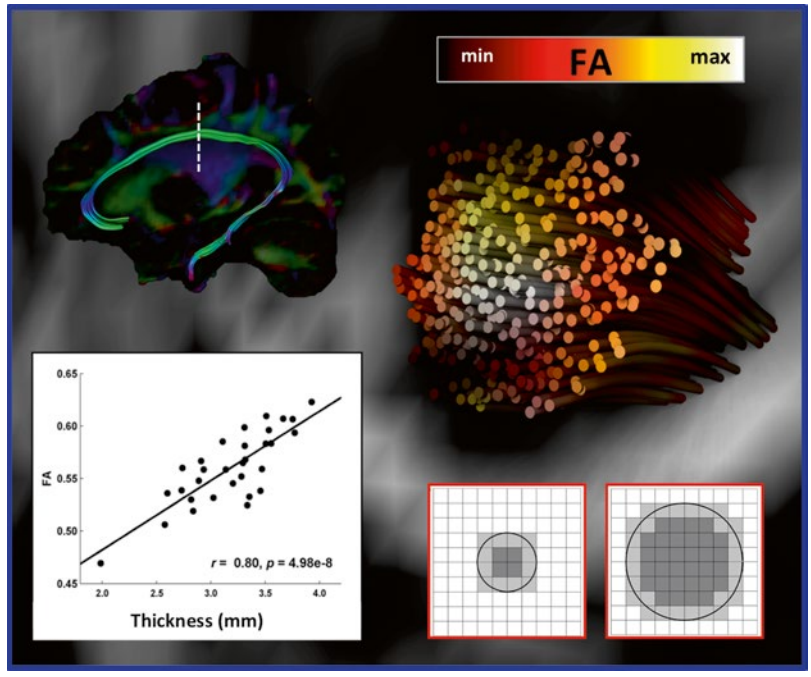

Fig. 5.8 The thickness of a fibre bundle modulates the DTI metrics along its length, with smaller, thinner bundles being more susceptible to PVE than larger, thicker bundles. In this example, FA is highest in the middle of a cross-sectional ROI of the cingulum compared to at the bundle periphery. The scatter plot (*left bottom*) is based on data from Szczepankiewicz et al. 2013 [81]

In a recent study, Metzler-Baddeley et al. [41] highlight the importance of correcting for CSF-contamination partial volume effects in structures of interest on a voxel-by-voxel basis prior to drawing inferences about underlying changes in white matter structures. They found that diffusivity metrics (mean diffusivity, axial and radial diffusivity) were more prone to partial volume CSF contamination errors than fractional anisotropy. After free water elimination (FWE) based voxel-by-voxel partial volume corrections [85], the significant positive correlations between age and diffusivity metrics, in particular with axial diffusivity, disappeared whereas the correlation with anisotropy remained. Free water elimination may be a more useful strategy than correcting for whole brain volume, which had little effect in removing these spurious correlations [41].

The Role of the Analysis Technique

DTI can be used to study brain structure at a voxel, regional or whole-brain level (See Section III). Regional analyses include those in which an a priori region of interest is chosen for study, and tractography-based analysis, in which an a priori fibre bundle (or bundles) of interest is selected for investigation. In both approaches, typically, average diffusion values such as FA are extracted from voxels within the ROIs or tracts for subsequent analysis. Whole-brain analyses include voxel-based analysis (VBA) (Chap. 10) and histogram analyses of all the voxels in the brain image or in a white matter mask.

Because the different analysis approaches utilize different assumptions and image processing strategies, it is possible that different results can be obtained from each type of analysis. For example, in a recent investigation of bipolar disorder endophenotypes, Chaddock et al. [87] and Emsell et al. [88] report differences in the extent of regional FA changes and association with genetic risk in the same dataset. This does not necessarily mean the results from one type of analysis are correct and the other incorrect. In fact using multiple analytic strategies is important for cross-validation of results. The most commonly implicated regions are generally similar across approaches, whilst subtle, more local effects or spurious findings tend to occur less frequently.

Section Summary

- Disentangling the relative contributions of biophysical, pathological and methodological factors to DTI measures is challenging and confounds their interpretation.
- The tensor model is an over-simplification, which provides useful summary measures in single-fibre regions such as the corpus callosum and fornix, but has limited applicability in regions of complex microstructure or "crossing-fibres."
- Investigators should consider biological confounds such as subject demographics, the timing and severity of pathology and the location of DTI changes when interpreting results
- Cross-validation of results using different analysis techniques can yield useful information about the reliability and location of DTI metric changes.

Chapter Summary

Qualitative assessment of diffusion MR images can be supported by quantitative measures derived from DTI data. However, such metrics are influenced by many biological and methodological factors, and should therefore be interpreted with due caution. Fractional anisotropy is a summary measure derived from DTI, which describes the directional coherence (anisotropy) of water diffusion within tissue, while mean axial and radial diffusivity may more specifically describe the direction and magnitude of tissue water diffusion.

Equating FA with an index of white matter integrity is an oversimplified interpretation because FA cannot disentangle individual microscopic contributions at the voxel level. Similarly, the interpretation of measures that are sensitive to the sorting of the eigenvectors or to the effect of

noise and partial volume, such as the axial and radial diffusivities, should be discouraged unless accompanied by a thorough investigation of their geometrical properties.

It is important to emphasise that comparing data that have been acquired using different acquisition parameters may be meaningless. This is particularly important in ROIs that contain complex tissue geometry, which will result in greater variation in diffusion measures leading to higher variance in ROIs across subjects and therefore less statistical power to detect differences in diffusion measures.

The accuracy and reliability of DTI based results can be improved by undertaking quality assurance, appropriate pre- and post-processing to correct for artifacts, and by incorporating PVE-related covariates into statistical analysis.

Acknowledgements The authors would like to thank Dr. Niall Colgan, University College London for producing and analysing the synthetic data using the Camino: Open-source diffusion-MRI reconstruction and processing tool [89] and Dr. Karla Miller and FMRIB Centre, University of Oxford for supplying the 1.5 and 7 T data.

References

1. Sotak CH. The role of diffusion tensor imaging in the evaluation of ischemic brain injury - a review. NMR Biomed. 2002;15(7-8):561–9 [Review].
2. Norris DG, Niendorf T, Leibfritz D. Health and infarcted brain tissues studied at short diffusion times: the origins of apparent restriction and the reduction in apparent diffusion coefficient. NMR Biomed. 1994;7(7):304–10.
3. Concha L. A macroscopic view of microstructure: using diffusion-weighted images to infer damage, repair, and plasticity of white matter. Neuroscience. 2014;276:14–28.
4. Basser PJ, Mattiello J, LeBihan D. Estimation of the effective self-diffusion tensor from the NMR spin echo. J Magn Reson B. 1994;103(3):247–54.
5. Beaulieu C, Allen PS. Determinants of anisotropic water diffusion in nerves. Magn Reson Med. 1994;31(4):394–400 [Research Support, Non-U.S. Gov't].
6. Basser PJ, Pierpaoli C. Microstructural and physiological features of tissues elucidated by quantitative-diffusion-tensor MRI. J Magn Reson B. 1996; 111(3):209–19.
7. Moseley ME, Cohen Y, Kucharczyk J, Mintorovitch J, Asgari HS, Wendland MF, et al. Diffusion-weighted MR imaging of anisotropic water diffusion in cat central nervous system. Radiology. 1990;176(2):439–45 [Research Support, Non-U.S. Gov't Research Support, U.S. Gov't, Non-P.H.S. Research Support, U.S. Gov't, P.H.S.].
8. van Gelderen P, de Vleeschouwer MHM, DesPres D, Pekar J, van Zijl P, Moonen CTW. Water diffusion and acute stroke. Magn Reson Med. 1994;31(2):154–63.
9. Basser PJ. New histological and physiological stains derived from diffusion-tensor MR images. Ann N Y Acad Sci. 1997;820:123–38.
10. Le Bihan D. Diffusion, perfusion and functional magnetic resonance imaging. J Mal Vasc. 1995;20(3): 203–14.
11. Westin CF, Maier SE, Mamata H, Nabavi A, Jolesz FA, Kikinis R. Processing and visualization for diffusion tensor MRI. Med Image Anal. 2002;6(2):93–108.
12. Vos SB, Jones DK, Jeurissen B, Viergever MA, Leemans A. The influence of complex white matter architecture on the mean diffusivity in diffusion tensor MRI of the human brain. Neuroimage. 2012;59(3): 2208–16.
13. Douaud G, Behrens TE, Poupon C, Cointepas Y, Jbabdi S, Gaura V, et al. In vivo evidence for the selective subcortical degeneration in Huntington's disease. Neuroimage. 2009;46(4):958–66.
14. Ennis DB, Kindlmann G. Orthogonal tensor invariants and the analysis of diffusion tensor magnetic resonance images. Magn Reson Med. 2006;55(1):136–46.
15. Jensen JH, Helpern JA. MRI quantification of non-Gaussian water diffusion by kurtosis analysis. NMR Biomed. 2010;23(7):698–710 [Research Support, N.I.H., Extramural Research Support, Non-U.S. Gov't Review].
16. Van Cauter S, De Keyzer F, Sima DM, Croitor Sava A, D'Arco F, Veraart J, et al. Integrating diffusion kurtosis imaging, dynamic susceptibility-weighted contrast-enhanced MRI, and short echo time chemical shift imaging for grading gliomas. Neuro Oncol. 2014;16:1010.
17. Gooijers J, Leemans A, Van Cauter S, Sunaert S, Swinnen SP, Caeyenberghs K. White matter organization in relation to upper limb motor control in healthy subjects: exploring the added value of diffusion kurtosis imaging. Brain Struct Funct. 2014;219:1627.
18. Billiet T, Maedler B, D'Arco F, Peeters R, Plasschaert E, Leemans A, et al. Characterizing the microstructure of "unidentified bright objects" in neurofibromatosis type 1: a combined in vivo multi-exponential T2 relaxation and multi-shell diffusion MRI analysis. Neuroimage Clin. 2014;4:649–58.
19. Van Cauter S, Veraart J, Sijbers J, Peeters RR, Himmelreich U, De Keyzer F, et al. Gliomas: diffusion kurtosis MR imaging in grading. Radiology. 2012;263(2):492–501.
20. Veraart J, Poot DH, Van Hecke W, Blockx I, Van der Linden A, Verhoye M, et al. More accurate estimation of diffusion tensor parameters using diffusion Kurtosis imaging. Magn Reson Med. 2011;65(1): 138–45 [Research Support, Non-U.S. Gov't].

21. Panagiotaki E, Schneider T, Siow B, Hall MG, Lythgoe MF, Alexander DC. Compartment models of the diffusion MR signal in brain white matter: a taxonomy and comparison. Neuroimage. 2012;59(3):2241–54 [Comparative Study Research Support, Non-U.S. Gov't].
22. Assaf Y, Basser PJ. Composite hindered and restricted model of diffusion (CHARMED) MR imaging of the human brain. Neuroimage. 2005;27(1):48–58.
23. Assaf Y, Blumenfeld-Katzir T, Yovel Y, Basser PJ. AxCaliber: a method for measuring axon diameter distribution from diffusion MRI. Magn Reson Med. 2008;59(6):1347–54.
24. Alexander DC, Hubbard PL, Hall MG, Moore EA, Ptito M, Parker GJM, et al. Orientationally invariant indices of axon diameter and density from diffusion MRI. Neuroimage. 2010;52(4):1374–89.
25. Assaf Y, Alexander DC, Jones DK, Bizzi A, Behrens TEJ, Clark CA, et al. The CONNECT project: combining macro-and micro-structure. Neuroimage. 2013;80:273.
26. Zhang H, Schneider T, Wheeler-Kingshott CA, Alexander DC. NODDI: practical in vivo neurite orientation dispersion and density imaging of the human brain. Neuroimage. 2012;61(4):1000–16 [Research Support, Non-U.S. Gov't].
27. Polders DL, Leemans A, Hendrikse J, Donahue MJ, Luijten PR, Hoogduin JM. Signal to noise ratio and uncertainty in diffusion tensor imaging at 1.5, 3.0, and 7.0 Tesla. J Magn Reson Imaging. 2011;33(6):1456–63.
28. Basser PJ, Pierpaoli C. A simplified method to measure the diffusion tensor from seven MR images. Magn Reson Med. 1998;39(6):928–34.
29. Jones DK. The effect of gradient sampling schemes on measures derived from diffusion tensor MRI: a Monte Carlo study. Magn Reson Med. 2004;51(4):807–15.
30. Jones DK, Cercignani M. Twenty-five pitfalls in the analysis of diffusion MRI data. NMR Biomed. 2010;23(7):803–20.
31. Jones DK, Williams SC, Gasston D, Horsfield MA, Simmons A, Howard R. Isotropic resolution diffusion tensor imaging with whole brain acquisition in a clinically acceptable time. Hum Brain Mapp. 2002;15(4):216–30.
32. Tournier JD, Mori S, Leemans A. Diffusion tensor imaging and beyond. Magn Reson Med. 2011;65(6):1532–56.
33. Froeling M, Tax CMW, Vos SB, Luijten PR, Leemans A, editors. MASSIVE: multiple acquisitions for standardization of structural imaging validation and evaluation. International Society for Magnetic Resonance Imaging in Medicine Annual Scientific Meeting & Exhibition; 2014; Milan, Italy.
34. Jeurissen B, Leemans A, Tournier JD, Jones DK, Sijbers J. Investigating the prevalence of complex fiber configurations in white matter tissue with diffusion magnetic resonance imaging. Hum Brain Mapp. 2013;34(11):2747–66.
35. Pierpaoli C, Basser PJ. Toward a quantitative assessment of diffusion anisotropy. Magn Reson Med. 1996;36(6):893–906.
36. Jones DK, Knösche TR, Turner R. White matter integrity, fiber count, and other fallacies: the do's and don'ts of diffusion MRI. Neuroimage. 2013;73:239–54.
37. Jones DK, Basser PJ. "Squashing peanuts and smashing pumpkins": how noise distorts diffusion-weighted MR data. Magn Reson Med. 2004;52(5):979–93.
38. Descoteaux M, Deriche R, Le Bihan D, Mangin JF, Poupon C. Diffusion propagator imaging: using Laplace's equation and multiple shell acquisitions to reconstruct the diffusion propagator. Inf Process Med Imaging. 2009;21:1–13.
39. Veraart J, Sijbers J, Sunaert S, Leemans A, Jeurissen B. Weighted linear least squares estimation of diffusion MRI parameters: strengths, limitations, and pitfalls. Neuroimage. 2013;81:335–46 [Research Support, Non-U.S. Gov't].
40. Jones DK, Leemans A. Diffusion tensor imaging. Methods Mol Biol. 2011;711:127–44.
41. Metzler-Baddeley C, O'Sullivan MJ, Bells S, Pasternak O, Jones DK. How and how not to correct for CSF-contamination in diffusion MRI. Neuroimage. 2012;59(2):1394–403.
42. Leemans A, Jones DK. The B-matrix must be rotated when correcting for subject motion in DTI data. Magn Reson Med. 2009;61(6):1336–49.
43. Beaulieu C. What makes diffusion anisotropic in the nervous system? In: Jones DK, editor. Diffusion MRI: theory, methods and applications. New York, NY: Oxford University Press; 2011. p. 92–109.
44. Assaf Y, Pasternak O. Diffusion tensor imaging (DTI)-based white matter mapping in brain research: a review. J Mol Neurosci. 2008;34(1):51–61.
45. Budde MD, Kim JH, Liang HF, Schmidt RE, Russell JH, Cross AH, et al. Toward accurate diagnosis of white matter pathology using diffusion tensor imaging. Magn Reson Med. 2007;57(4):688–95.
46. Filley CM. White matter and behavioral neurology. Ann N Y Acad Sci. 2005;1064:162–83.
47. Horsfield MA, Jones DK. Applications of diffusion-weighted and diffusion tensor MRI to white matter diseases – a review. NMR Biomed. 2002;15(7-8):570–7.
48. Werring DJ, Clark CA, Barker GJ, Thompson AJ, Miller DH. Diffusion tensor imaging of lesions and normal-appearing white matter in multiple sclerosis. Neurology. 1999;52(8):1626–32.
49. Cascio CJ, Gerig G, Piven J. Diffusion tensor imaging: application to the study of the developing brain. J Am Acad Child Adolesc Psychiatry. 2007;46(2):213–23.
50. Hüppi PS, Maier SE, Peled S, Zientara GP, Barnes PD, Jolesz FA, et al. Microstructural development of human newborn cerebral white matter assessed in vivo by diffusion tensor magnetic resonance imaging. Pediatr Res. 1998;44(4):584–90.

51. Lebel C, Walker L, Leemans A, Phillips L, Beaulieu C. Microstructural maturation of the human brain from childhood to adulthood. Neuroimage. 2008;40(3):1044–55.
52. Partridge SC, Mukherjee P, Henry RG, Miller SP, Berman JI, Jin H, et al. Diffusion tensor imaging: serial quantitation of white matter tract maturity in premature newborns. Neuroimage. 2004;22(3): 1302–14.
53. Wozniak JR, Lim KO. Advances in white matter imaging: a review of in vivo magnetic resonance methodologies and their applicability to the study of development and aging. Neurosci Biobehav Rev. 2006;30(6):762–74.
54. Mabbott DJ, Noseworthy M, Bouffet E, Laughlin S, Rockel C. White matter growth as a mechanism of cognitive development in children. Neuroimage. 2006;33(3):936–46.
55. Nagy Z, Westerberg H, Klingberg T. Maturation of white matter is associated with the development of cognitive functions during childhood. J Cogn Neurosci. 2004;16(7):1227–33.
56. Schmithorst VJ, Wilke M, Dardzinski BJ, Holland SK. Cognitive functions correlate with white matter architecture in a normal pediatric population: a diffusion tensor MRI study. Hum Brain Mapp. 2005;26(2):139–47.
57. Hüppi PS, Dubois J. Diffusion tensor imaging of brain development. Semin Fetal Neonatal Med. 2006;11(6):489–97.
58. Zhai G, Lin W, Wilber KP, Gerig G, Gilmore JH. Comparisons of Regional White Matter Diffusion in Healthy Neonates and Adults Performed with a 3.0-T Head-only MR Imaging Unit. Radiology. 2003;229(3):673–81.
59. Sullivan EV, Pfefferbaum A. DTI in aging and age-related neurodegenerative disorders. In: Jones DK, editor. Diffusion MRI: theory, methods and applications. New York, NY: Oxford University Press; 2011.
60. Huang H, Zhang J, Wakana S, Zhang W, Ren T, Richards LJ, et al. White and gray matter development in human fetal, newborn and pediatric brains. Neuroimage. 2006;33(1):27–38 [Research Support, N.I.H., Extramural].
61. Maas LC, Mukherjee P, Carballido-Gamio J, Veeraraghavan S, Miller SP, Partridge SC, et al. Early laminar organization of the human cerebrum demonstrated with diffusion tensor imaging in extremely premature infants. Neuroimage. 2004;22(3):1134–40.
62. Ulug AM, Beauchamp Jr N, Bryan RN, van Zijl PC. Absolute quantitation of diffusion constants in human stroke. Stroke. 1997;28(3):483–90.
63. Engelbrecht V, Scherer A, Rassek M, Witsack HJ, Mödder U. Diffusion-weighted MR imaging in the brain in children: findings in the normal brain and in the brain with white matter diseases. Radiology. 2002;222(2):410–8.
64. Oishi K, Mori S, Donohue PK, Ernst T, Anderson L, Buchthal S, et al. Multi-contrast human neonatal brain atlas: application to normal neonate development analysis. Neuroimage. 2011;56(1):8–20.
65. Xu D, Mukherjee P, Barkovich AJ. Pediatric brain injury: can DTI scalars predict functional outcome? Pediatr Radiol. 2013;43(1):55–9.
66. Song SK, Sun SW, Ramsbottom MJ, Chang C, Russell J, Cross AH. Dysmyelination revealed through MRI as increased radial (but unchanged axial) diffusion of water. Neuroimage. 2002;17(3):1429–36 [Research Support, Non-U.S. Gov't Research Support, U.S. Gov't, P.H.S.].
67. Field AS, Alexander AL, Wu Y-C, Hasan KM, Witwer B, Badie B. Diffusion tensor eigenvector directional color imaging patterns in the evaluation of cerebral white matter tracts altered by tumor. J Magn Reson Imaging. 2004;20(4):555–62.
68. Wheeler-Kingshott CAM, Cercignani M. About "axial" and "radial" diffusivities. Magn Reson Med. 2009;61(5):1255–60.
69. Cercignani M, Alexander DC. Optimal acquisition schemes for in vivo quantitative magnetization transfer MRI. Magn Reson Med. 2006;56(4):803–10.
70. Sled JG, Pike GB. Quantitative imaging of magnetization transfer exchange and relaxation properties in vivo using MRI. Magn Reson Med. 2001;46(5): 923–31.
71. Kolind SH, Deoni SC. Rapid three-dimensional multicomponent relaxation imaging of the cervical spinal cord. Magn Reson Med. 2011;65(2):551–6 [Research Support, Non-U.S. Gov't].
72. MacKay A, Laule C, Vavasour I, Bjarnason T, Kolind S, Madler B. Insights into brain microstructure from the T2 distribution. Magn Reson Imaging. 2006;24(4):515–25.
73. Leemans A. Visualisation of diffusion MRI data. In: Jones DK, editor. Diffusion MRI: theory, methods and applications. New York, NY: Oxford University Press; 2011. p. 354–79.
74. Dubois J, Dehaene-Lambertz G, Perrin M, Mangin J-F, Cointepas Y, Duchesnay E, et al. Asynchrony of the early maturation of white matter bundles in healthy infants: quantitative landmarks revealed noninvasively by diffusion tensor imaging. Hum Brain Mapp. 2008;29(1):14–27.
75. Giedd JN, Blumenthal J, Jeffries NO, Castellanos FX, Liu H, Zijdenbos A, et al. Brain development during childhood and adolescence: a longitudinal MRI study. Nat Neurosci. 1999;2(10):861–3.
76. Hulkower MB, Poliak DB, Rosenbaum SB, Zimmerman ME, Lipton ML. A decade of DTI in traumatic brain injury: 10 years and 100 articles later. AJNR Am J Neuroradiol. 2013;34:2064.
77. Douaud G, Jbabdi S, Behrens TE, Menke RA, Gass A, Monsch AU, et al. DTI measures in crossing-fibre areas: increased diffusion anisotropy reveals early white matter alteration in MCI and mild Alzheimer's disease. Neuroimage. 2011;55(3):880–90.
78. Pierpaoli C, Barnett A, Pajevic S, Chen R, Penix L, Virta A, et al. Water diffusion changes in Wallerian

degeneration and their dependence on white matter architecture. Neuroimage. 2001;13(6):1174–85.
79. Leemans A, Sijbers J, Verhoye M, Van der Linden A, Van Dyck D. Mathematical framework for simulating diffusion tensor MR neural fiber bundles. Magn Reson Med. 2005;53(4):944–53.
80. Wheeler-Kingshott CA, Ciccarelli O, Schneider T, Alexander DC, Cercignani M. A new approach to structural integrity assessment based on axial and radial diffusivities. Funct Neurol. 2012;27(2):85–90 [Research Support, Non-U.S. Gov't].
81. Szczepankiewicz F, Latt J, Wirestam R, Leemans A, Sundgren P, van Westen D, et al. Variability in diffusion kurtosis imaging: impact on study design, statistical power and interpretation. Neuroimage. 2013;76:145–54 [Research Support, Non-U.S. Gov't].
82. Vos SB, Jones DK, Viergever MA, Leemans A. Partial volume effect as a hidden covariate in DTI analyses. Neuroimage. 2011;55(4):1566–76.
83. Concha L, Gross DW, Beaulieu C. Diffusion tensor tractography of the limbic system. AJNR Am J Neuroradiol. 2005;26(9):2267–74.
84. Chou MC, Lin YR, Huang TY, Wang CY, Chung HW, Juan CJ, et al. FLAIR diffusion-tensor MR tractography: comparison of fiber tracking with conventional imaging. AJNR Am J Neuroradiol. 2005;26(3):591–7.
85. Pasternak O, Sochen N, Gur Y, Intrator N, Assaf Y. Free water elimination and mapping from diffusion MRI. Magn Reson Med. 2009;62(3):717–30.
86. Pierpaoli C, Jones D, editors. Removing CSF contamination in brain DT-MRIs by using a two-compartment tensor model. Proceedings of the International Society for Magnetic Resonance in Medicine. 12th Scientific meeting ISMRM04; 2004. p. 1215
87. Chaddock CA, Barker GJ, Marshall N, Schulze K, Hall MH, Fern A, et al. White matter microstructural impairments and genetic liability to familial bipolar I disorder. Br J Psychiatry. 2009;194(6):527–34.
88. Emsell L, Chaddock C, Forde N, Van Hecke W, Barker GJ, Leemans A, et al. White matter microstructural abnormalities in families multiply affected with bipolar I disorder: a diffusion tensor tractography study. Psychol Med. 2013;27:1–12.
89. Cook PA, Bai Y, Nedjati-Gilani S, Seunarine KK, Hall MG, Parker GJ, et al., editors. Camino: open-source diffusion-MRI reconstruction and processing 2006. Proceedings of the International Society for Magnetic Resonance in Medicine. 14th Scientific Meeting, Seattle, WA, May 2006; p. 2759

Suggested Reading

90. Jones DK, Cercignani M. Twenty-five pitfalls in the analysis of diffusion MRI data. NMR Biomed. 2010;23(7):803–20.
91. Jones DK, Knösche TR, Turner R. White matter integrity, fibre count, and other fallacies: the do's and don'ts of diffusion MRI. Neuroimage. 2013;73:239–54.
92. Tournier JD, Mori S, Leemans A. Diffusion tensor imaging and beyond. Magn Reson Med. 2011;65(6):1532–56.
93. Wheeler-Kingshott CAM, Cercignani M. About "axial" and "radial" diffusivities. Magn Reson Med. 2009;61(5):1255–60.
94. Concha L. A macroscopic view of microstructure: using diffusion-weighted images to infer damage, repair, and plasticity of white matter. Neuroscience. 2014;276:14–28.

Survivor's Guide to DTI Acquisition

6

Eric Peterson and Roland Bammer

Learning Points

- Common acquisition methods used for DTI
- Basic imaging considerations in DTI
- Standard parameters for DTI acquisitions
- Common EPI artifacts and their cause
- Appearance of common EPI artifacts
- How to reduce or avoid most DTI artifacts
- How to diagnose and correct for DTI artifacts

Introduction

In this chapter, we will discuss acquisition methods for DTI. This discussion will focus on *Echo Planar Imaging* (EPI) and touch on *Fast Spin-Echo* (FSE) acquisition methods. We will address situations where these methods are particularly well suited, as well as common problems seen when using these methods in DTI. Please note that many of the image quality aspects are independent of whether DTI or DWI is performed. Hence for this chapter, unless specifically mentioned, the terms DWI and DTI can be used interchangeably.

E. Peterson, PhD (✉) • R. Bammer, PhD
Department of Radiology, Stanford University,
300 Pasteur Drive, Stanford, CA 94305-5105, USA
e-mail: etpeters@stanford.edu

Throughout this chapter, we strive to help the reader to best understand DTI acquisitions and DTI parameters so that one can select and adjust the acquisition that fits best. However, in order to produce the highest quality results for any kind of diffusion imaging study, it is important to plan and test the acquisition beforehand because there are often complicated image changes from a single parameter modification. This planning ensures that the scan goes smoothly, and that costly and potentially impossible reacquisitions are not required.

This chapter is presented in seven major parts: Stejskal-Tanner diffusion encoding, an image acquisition background, echo planar imaging, fast spin-echo imaging, motion sensitivity of diffusion imaging, image reconstruction, and pediatric imaging considerations.

We hope that the information presented here about possible DTI acquisition methods and their associated pitfalls will help you establish reliable acquisitions and diagnose acquisition problems. Our aim is that this will enable you to choose the acquisition method with the greatest chances of success and get the best performance out of your MRI scanner.

Stejskal-Tanner Diffusion Encoding

Diffusion theory was discussed in detail in a previous chapter (Chap. 3). For this chapter, it is important to keep in mind how water molecules

W. Van Hecke et al. (eds.), *Diffusion Tensor Imaging*, DOI 10.1007/978-1-4939-3118-7_6

behave in different tissues. Regions of the brain—such as gray matter—are only slightly structured at the cellular level, and therefore have relatively similar diffusion in all directions. However, white matter, which is predominantly axons and other tissues that are structured at the cellular level, often have significantly anisotropic diffusion. That is, the diffusion coefficient that one can observe will differ dependent along which direction it is measured.

This cellular structure can be uniquely probed with MRI using the pulsed gradient acquisition introduced by *Stejskal and Tanner* [1] (Fig. 6.1). Here, a long-TE spin-echo sequence is modified by straddling the 180° refocusing RF pulse with a pair of strong gradients of equal polarity. To review from the diffusion chapter, these gradients, often termed diffusion-encoding gradients or motion-probing gradients, reduce the signal from randomly moving (diffusing) water while leaving the signal amplitude from stationary or coherently flowing water unchanged. It is important to remember that the diffusion information extracted from this sequence is often termed the *Apparent Diffusion Coefficient* (ADC) as it is an approximation of the diffusion coefficient that is made up from the contribution of individually diffusing spins (a spin is the individual signal unit in MRI; many spins make up a voxel) within the voxel under investigation and certain sequence parameters (i.e., "shutter speed" of the diffusion measurement). These assumptions allow for an easy evaluation of the ADC, which closely reflects the actual diffusion in the tissues.

Also note that one can measure the ADC only along the direction of the applied diffusion-encoding gradient. This can be in any direction in the magnet by using a combination of the gradients in the *x*-, *y*-, and *z*-axes. The conventional notation for diffusion direction is the so-called unit vector (i.e., magnitude of the vector equals "1"), in which the tip of the vector points along the direction one wants to measure diffusion. It is important to note that the diffusion section of the pulse sequence (i.e., the diffusion amplitudes on the *x*, *y*, and *z* gradients) is independent from the rest of the pulse sequence, and in fact, a non-diffusion-weighted ($b=0$) scan is a part of every diffusion protocol and is simply the diffusion sequence with the diffusion gradient amplitudes set to zero.

For our purposes, the diffusion tensor acquisition can be considered an extension of the Stejskal-Tanner DWI acquisition. The only difference between DWI and DTI is that a DTI acquisition requires a minimum of six or more DWIs, along with at least one image (and often more) without diffusion encoding (i.e., where the diffusion-encoding gradients are turned off, often called a T2w or $b=0$ scan) [2, 3]. The acquisition of the set of diffusion images is followed by diffusion post-processing, which is used to calculate the directionality and diffusion coefficient, both of which were covered in more detail in the preceding chapter (Chap. 4). For the purposes of this chapter, note that the six or more diffusion directions required to measure the tensor need to be spread out as much as possible in the 3D sphere of diffusion (D_x, D_y, D_z). The sphere of diffusion refers to the diffusion direction (direction from the center of the sphere) and the strength of the diffusion-encoding gradients (the distance from the center of the sphere) and directions that are spread evenly around the sphere are mathematically best for the diffusion post-processing and therefore produce the best diffusion tensor results. The minimum of six diffusion directions is required because there are six unknown elements of the diffusion tensor (D_{xx}, D_{yy}, D_{zz}, D_{xy}, D_{xz}, and D_{yz}).

The groups of diffusion directions (and sometimes multiple diffusion sensitivities, called *b*-values) are often called "schemes" or "sets." These sets are often chosen individually for specific applications. One example of these is schemes, often termed *High Angular Resolution Diffusion Imaging* (HARDI) acquisitions, with generally more than 60 diffusion-encoding directions [4]. A HARDI gradient scheme allows for better differentiation of complex white matter structures and is often used in white matter tract tracing applications. The high spherical

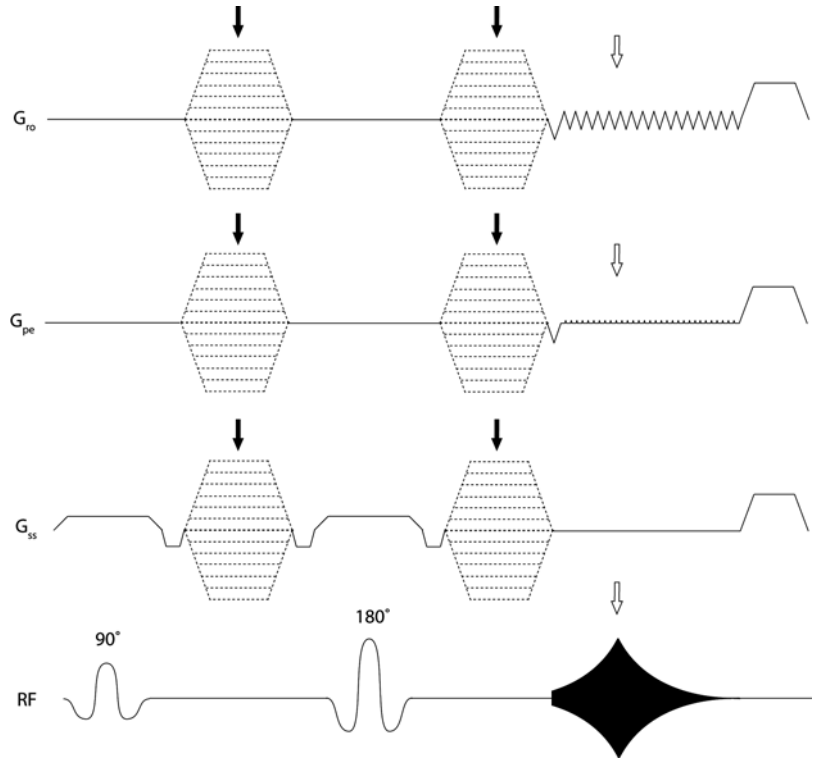

Fig. 6.1 This figure shows the readout, phase encode, slice select, and radiofrequency (G_{ro}, G_{pe}, G_{ss}, and RF respectively) of a typical Stejskal-Tanner diffusion pulse sequence with an EPI readout. The Stejskal-Tanner core (the diffusion gradients labeled with *arrows*) is the bipolar gradients, which are separated by a 180° RF pulse. These gradients are dotted to show that they change to vary the amount (amplitude or *b*-value) and direction of the diffusion sensitivity. The *hollow arrows* indicate the EPI readout, which in this case is a partial Fourier readout. An EPI readout very efficiently covers *k*-space and the *black* RF envelope indicates that the spin echo is designed to occur in the center of *k*-space (*hollow arrow*) in the readout

resolution allows for observation of directional diffusion differences in highly complex white matter structures such as crossing or fiber bundles with other complex patterns (see Chap. 21 for more details about HARDI techniques). However, regardless of the direction scheme chosen (HARDI or otherwise), the rest of the acquisition (RF pulses, readout method, etc.) is often entirely interchangeable and can be modified to best suit the anatomy and physiology being imaged.

To review, there are two elements essential to Stejskal-Tanner DTI:

- Paired diffusion gradients, typically spaced around a 180° RF pulse.
- A set of six or more diffusion gradients well spaced around the D_x, D_y, and D_z axes.

Acquisition Background

In order to better describe DTI acquisitions, it is important to understand some of the elements of MRI data acquisition. In this section, we will discuss *k*-space—the form of the image as it is acquired on the scanner—and complex numbers, both of which are important to keep in mind when discussing the distortions and artifacts typical in DTI acquisitions.

K-Space

The inherent "image" that is acquired by any MRI scanner is not the image that is shown on the scanner. When mapping the acquired MR signal

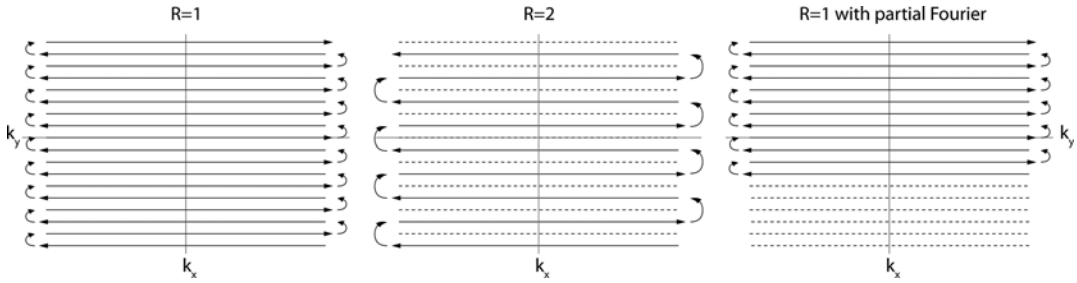

Fig. 6.2 This figure shows the readout in *k*-space of three bidirectional EPI acquisitions. The different readout direction on odd (*arrows* going *left*) and even (*arrows* going *right*) *lines* is the source of EPI "ghosting." Parallel imaging with a reduction factor of 2 is shown, and for this reduction factor every *second line* is skipped. Partial Fourier imaging is shown in the third panel. In this case, *k*-space lines are skipped at the beginning of the readout rather than every other. The acquisition diagram for EPI is shown in Fig. 6.1

into *k*-space, it actually becomes the spatial frequency spectrum of the MR image so that a simple Fourier transform (after some processing not discussed here) will yield the MR image and vice versa. In this chapter, we will call the axes in *k*-space k_x and k_y for the *x*- and *y*-axes respectively. The typical acquisition is a Cartesian—also called a rectilinear or raster—sampling of *k*-space, which is shown in Fig. 6.2. For typical MR imaging, all the points in *k*-space are acquired, and then a 2D or 3D Fourier transform is applied to create the 2D or 3D image itself. More details about the transition from *k*-space to image space—generally called the reconstruction—will be discussed in detail in a later chapter.

Another tricky detail with EPI is that the gradient polarity changes for every other line in *k*-space, which leads to the well-known "zig-zag" pattern of the EPI readout (Fig. 6.2). While the k_y-axis increases linearly for the entire readout, the *k*-space axis reverses for every other line. Thus, the time axis for every other gradient echo needs to be reversed to match the MR data sample with its location in *k*-space. If the timing of the odd and even gradient echo lines is off, ghosting artifacts can occur, a phenomenon that will be discussed later.

To review, *k*-space from an EPI acquisition has three important characteristics:

- *K*-space is the "image" acquired directly from the MRI scanner.
- A Fourier transform can be used to convert *k*-space to an image.
- The traversal of *k*-space may change significantly depending on scan parameters, such as parallel imaging and partial Fourier acquisitions.

Complex Numbers

Each point in *k*-space, and each point in the image itself is a complex number—even though it is not often shown in the final results. A complex number is a number that consists of both real and imaginary parts—often called magnitude and angle or magnitude and phase in MRI. The phase of the *k*-space points is important during the image generation, and unwanted phase is the source of most of the image artifacts in EPI.

While the signal magnitude is straightforward for most users to understand because it is simply the strength of the MR signal in each voxel, the concept of having an image where each voxel is a complex number is not as easily understood. An intuitive way to think about it is that if in general the spins in a voxel precess (rotate) slightly faster or slower than normal, by the time the sequence reads out, the angle that is seen is slightly larger or smaller than normal. An analogy to this is a clock that is slightly faster or slower than a perfect clock. If fast, slow, and perfect clocks are set and started at noon, and checked an hour later,

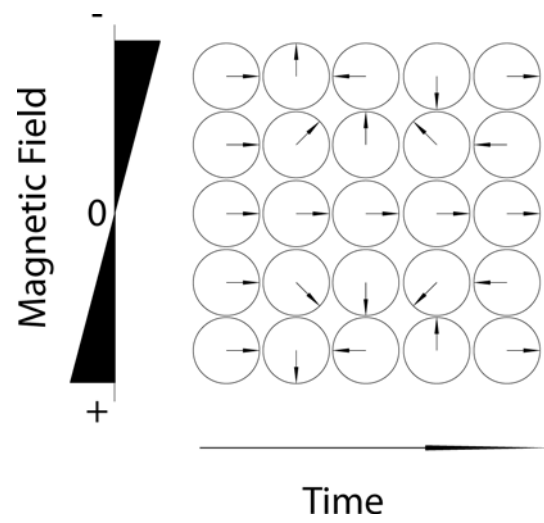

Fig. 6.3 This figure shows the phase or angle in regions of an image with different magnetic fields over time. This phase is often removed from the final images; however this change in phase over time is the source of shim and B_0 artifacts. In some cases, the phase can also affect the combination of data, which can result in cancellation of signal

the minute hand of the perfect clock will be pointing up at 12 again. However, the minute hand of the slow clock may only be pointing at 50, and the fast clock may be pointing at 5. In this example, the angle (phase) at the time the clock is checked (TE or echo time in MRI) is the angle of the minute hand relative to 12. The phase accrual can be slowed down or sped up deliberately by applying a magnetic field gradient or unintentionally by eddy currents, B_0 inhomogeneities, susceptibility differences, and RF.

The schematic in Fig. 6.3 shows how phase angles change over time with respect to a magnetic field. In fact, phase accrual is the basis for diffusion imaging—the use of the phase coupled with the random walk (diffusion) of spins across very small distances is the indicator that diffusion occurred. The phase is also used in the image acquisition to help form *k*-space. Many of the artifacts discussed in this chapter are the result of incorrect phase in *k*-space or image space due to a wide range of factors including motion, diffusion, B_0 inhomogeneities, readout gradient inconsistencies, and others.

To review, complex numbers are important in EPI-MRI for two reasons:

- All MRI data are complex.
- In diffusion processing, the phase is typically discarded at the end of the processing, but it is important to understand because it is the source of many image artifacts in EPI.

The Echo Planar Imaging Acquisition

Echo Planar Imaging

Echo Planar Imaging (EPI) is the clinical and research standard acquisition for DTI. The standard EPI acquisition is usually a single-shot spin-echo acquisition which consists of a 90° excitation, 180° refocusing pulse (Fig. 6.1), and a bidirectional Cartesian readout which linearly traverses *k*-space (Fig. 6.2) in one go. The EPI trajectory uses a small "blip gradient" to inch its way up the k_y-axis, which is orthogonal to the readout. The diffusion-encoding pulses, which are not an inherent part of an EPI readout, are placed on either side of the 180° pulse for Stejskal-Tanner imaging.

The number one reason why the EPI readout is the most popular option for DTI is that any DWI method is notoriously sensitive to motion. This motion sensitivity becomes immediately apparent if one thinks about the minute molecular motion we are trying to capture with this sequence. Any bulk motion while these strong motion-probing gradients are on would pick up substantial phase. Due to the unpredictable nature of bulk motion, these phase changes would most likely differ for each diffusion preparation—readout pair and compete with regular gradient encoding and lead to considerable artifacts.

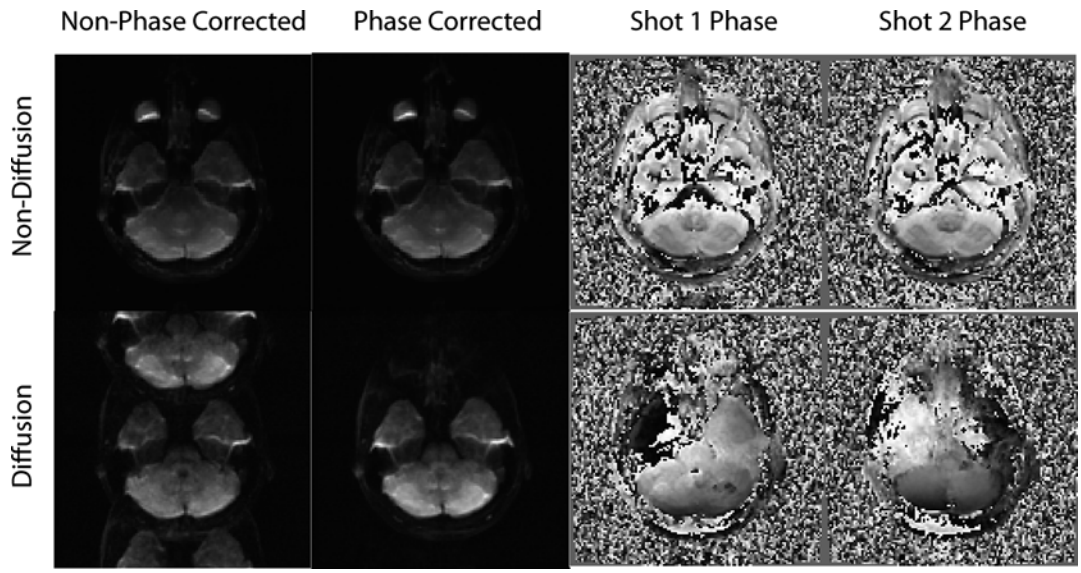

Fig. 6.4 This figure shows an example of a non-corrected and corrected shot combination in non-diffusion and diffusion imaging. Note how the non-diffusion imaging shots have nearly identical phase patterns, and therefore can be combined cleanly—without any noticeable artifacts—even without phase correction. However, because of the sensitivity of diffusion imaging to motion, the diffusion images have phase differences, and it is therefore often impossible to combine the shots without inducing artifacts before phase correction is applied. This case was a two-shot acquisition, so the artifact from poor phase combination largely manifests itself as FOV/2 ghosts, which will be discussed later

With single-shot EPI the phase errors do not disappear but they are the same for the entire *k*-space data set and do not bother us. DWI motion sensitivity becomes a problem again when we want to average multiple measurements together. If the number of signal averages is larger than one, the typical method to perform averaging is to directly average the acquired MR signals as they come in. This standard form of MR signal averaging does not work for diffusion images as the individual measurements may interfere destructively (Fig. 6.4). A simple remedy is to reconstruct each acquisition separately and average the magnitude images afterwards. However, averaging in magnitude mode is a challenge in itself. As the noise in MR magnitude data is no longer Gaussian distributed (for the nerds amongst you: it is a Rice-Nakagami distribution), the image becomes hazy in regions with *low signal-to-noise ratio* (SNR) as the signal effectively "bounces" off the nonzero mean noise floor. The interested reader is referred to the literature for methods used to resolve this problem [5, 6].

With the increasing demand for ever thinner slices, the TR of DTI sequences increases along with the large number of diffusion-encoding directions or intensities for HARDI, Q-ball or q-space imaging. This creates another challenge for diffusion imaging, which is the lengthening of the overall scan time. Single-shot EPI is currently the fastest and most time-efficient diffusion imaging technique, as it is capable of acquiring a whole 2D image in a single excitation and therefore a full DTI dataset in a very short amount of time (Fig. 6.5). Only recently, a further speed-up has emerged through simultaneous multi-band acquisition, but at the time of this writing, this technique is not yet commercially available and is currently only used in research settings [7].

In summary, acquiring the entirety of *k*-space in a single excitation confers two major advantages in DTI. The first is simply the scan efficiency—the speed—of the acquisition. For each slice in DTI, a minimum of seven images—and often many more—must be acquired to fully calculate the diffusion tensor parameters. This is a

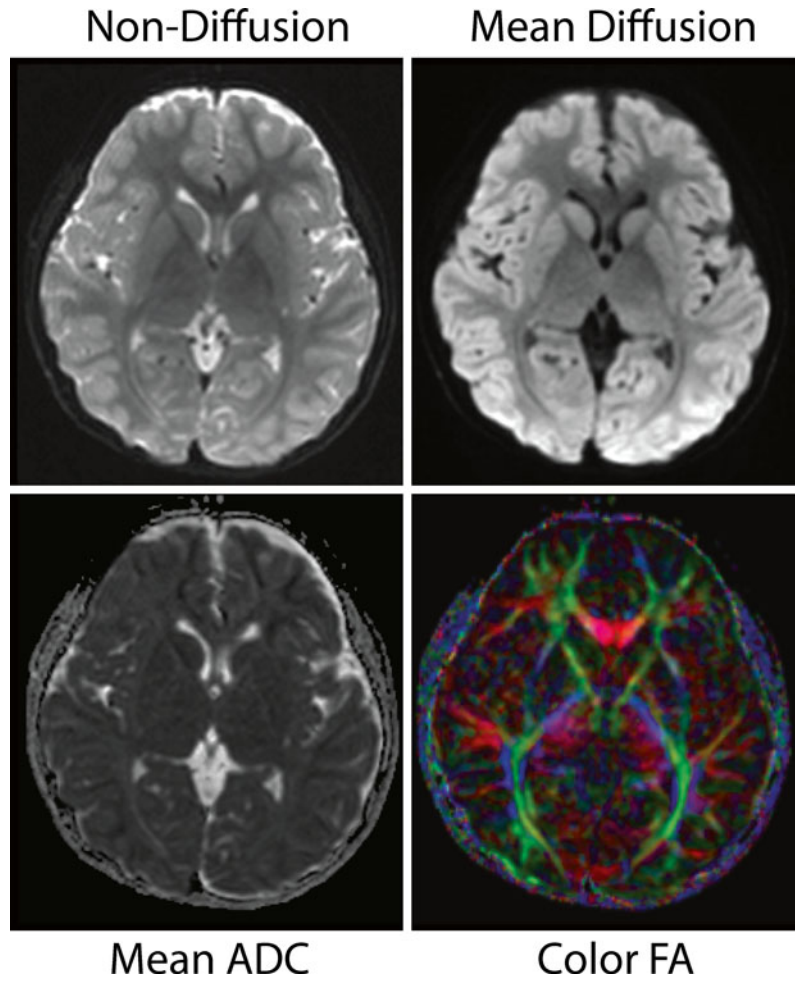

Fig. 6.5 This figure shows DTI results from a medial slice in a "typical" EPI acquisition. It shows the non-diffusion-weighted ($b=0$), mean diffusion ($b=1000$), mean apparent diffusion coefficient (ADC), and the color FA map. The mean diffusion is simply the average signal intensity from all of the diffusion images acquired. The mean ADC is calculated using the average of the ADC in all three directions (for those of you interested, it is the average of eigenvalues 1–3), and higher values reflect more diffusion in those regions. The color FA indicates the major unidirectional regions of diffusion color coded based on the direction (*red* is left-right, *blue* is superior-inferior, and *green* is anterior-posterior)

significant increase in scan time from a single anatomical scan; and by acquiring each image in a single—albeit longer—TR, it allows DTI to remain achievable within a clinical setting. The second advantage of EPI for DTI is the whole image coverage means that it does not require a complicated reconstruction involving data combination in order to prevent phase cancellation between acquisitions. Despite these strengths, and the standard use of EPI in DTI, single-shot EPI is not without its disadvantages, which will be discussed in the following sections.

To review, EPI is used for DWI and DTI for two major reasons:

- It is fast because a single image can be acquired for each excitation.
- The full image does not require complicated acquisition and reconstruction tricks to avoid image phase cancellation.

Scan Parameters and Their Effects

In DTI, several scan parameters are changed from standard anatomical imaging in order to work best with the constraints of DTI. A list of the basic parameters, typical values, and comments about them is in Table 6.1. This table is intended as a general guide rather than rules for DTI acquisitions and we hope this will aid your understanding of the parameters and the EPI acquisition.

Generally, a DTI acquisition is slower and has more images than anatomical imaging because of

Table 6.1 Typical DTI parameters

Parameter	Value	Comment
Flip angle	90°	90° for the excitation and 180° for the spin echo(es) to achieve maximum signal
TR	>3 s	At least $2 \times T_1$ of tissue to allow full signal recovery—keep large number of slices within 1 TR by simply increasing TR
TE	60–110 ms	As short as possible—depends on maximum gradient strength available for a given *b*-value as well as whether or not partial Fourier imaging is used
Partial Fourier	Yes	20 overscan lines for 128 × 128
		7/8 partial Fourier
		70 % partial Fourier
		Go higher on this factor to avoid "worm hole" artifacts. When in doubt use full echo but this increases TE significantly
Matrix size	128 × 128	96–192 are typical, mostly isotropic in plane
rFOV	100 %	Cannot do rFOV because PE is along A/P
Scan %	100 %	Keep an isotropic in-plane resolution
FOV	24 × 24 cm	Large enough to prevent aliasing
Phase-encode direction	A/P	To keep distortions L/R symmetric on axial scans
Frequency-encode direction	L/R	
Parallel imaging factor	2–3	Highly dependent on the RF coil
		Some coils afford 4—if reduction factor is too high the parallel imaging noise enhancement impairs image quality
# of $b=0$ images	1–3	About 1 per 6 diffusion images
# of diffusion directions	Approx. 21	6+ required, more than 100 possible
Slice thickness	3 mm	1–6 mm
Slice gap	0 mm	To avoid gaps and better fiber tracking—use interleaved slice acquisition to minimize SNR penalty from slice cross-talk
b-value	1000 s/mm^2	500–5000+
		For HARDI acquisitions 2500
		For q-space even higher, e.g., 5–8000
Bandwidth	Maximum for bandwidth	Almost always the maximum (minimum for water-fat shift) possible for the system
Bandwidth per pixel		
Water-fat shift	Minimum for water-fat shift	
Imaging axis	Axial/Oblique	Axial or oblique close to axial
Lipid/fat suppression	Yes	SPIR/SPSP/SPAIR/CHESS

Note that this is only intended as a guideline for the most important parameters for standard single-shot EPI sequences. For all acquisitions there are more parameters to consider, and some sequences may typically have parameters well outside of these ranges

the time needed to acquire diffusion-weighted images in at least six directions plus at least a single non-diffusion-weighted (T2w or $b=0$) image. It is important to remember that this is the minimum number of images to compute the diffusion tensor. Diffusion acquisitions like HARDI [4] or Q-Ball [8] require many more diffusion directions, sometimes calling for more than 100 diffusion-weighted images per slice. Multiple diffusion magnitudes (*b*-values) can also be acquired in a single scan [9], as in Q-space imaging. Using more diffusion directions and more *b*-values can improve the fidelity of the tensor estimation, especially in cases where there are multiple structures

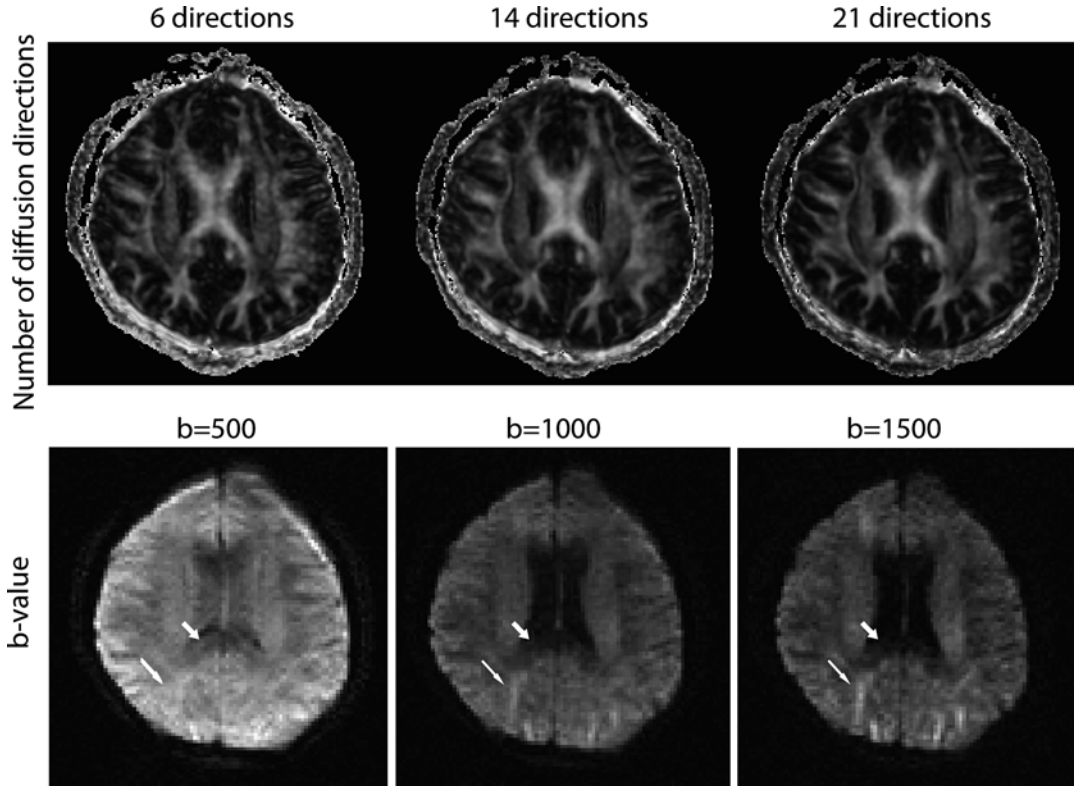

Fig. 6.6 This figure shows images with different numbers of diffusion directions used (*top row*) as well as different *b*-values used (*bottom row*). The *top row* shows the fractional anisotropy maps (*brighter* indicates more directionality in the tissue) all with a *b*-value of 1000, calculated using 6, 14, and 21 directions from *left* to *right*. Note that even though nothing else is changed between the acquisitions, the clarity of the images improves as more diffusion directions are added, which is primarily due to the averaging effects of more images. The *bottom row* shows (in a separate slice) a single diffusion direction (applied left-right) with *b*-values of 500, 1000, and 1500 s/mm. Note that the signal is higher in the $b = 500$ s/mm scan, but it is difficult to differentiate between structures. Also note that depending on the direction of the fiber tract, higher *b*-values tend to emphasize (*thin arrow*) or de-emphasize (*thick arrow*) the structures

within a voxel, such as two tensor tracts crossing or splitting. These methods use more advanced processing methods beyond the standard eigenvalue DTI processing; however a discussion of these methods is beyond the scope of this chapter.

A side effect of acquiring many diffusion directions and *b*-values is that the many acquisitions act as a form of averaging, which increases the *signal-to-noise-ratio* (SNR) of the diffusion tensor images (Fig. 6.6). This is advantageous because another consideration is that the reduction of the MR signal due to diffusion weighting causes the SNR to be generally lower in the diffusion-weighted images when compared to an anatomical image with similar scan parameters. In clinical practice, acquiring more diffusion directions rather than repeating diffusion directions is the preferred method of performing averaging. This is done because it is a robust way to both increase the SNR and ensure more than enough diffusion directions were acquired.

Furthermore, as the *b*-value increases, the SNR in the individual diffusion images decreases (Fig. 6.6). This becomes a trade-off between the contrast between the diffusion-weighted images and their SNR; the former potentially showing more detail and the latter providing less-noisy images. A simple solution to counteract the lower SNR is to increase the voxel size compared to that used with anatomical imaging.

Another consideration of increased *b*-values is increased eddy current distortions, which are covered in detail later in this chapter. In short, higher *b*-values—stronger diffusion gradients—can cause distortions in the image. These may not be obvious by looking at the images, but they may cause artifacts around the edge of the brain in the processed maps.

The first general MRI scan parameter to discuss is the *echo time* (TE). With the inclusion of the diffusion-encoding gradients, the minimum TE is increased by the duration of the gradients. While the minimum TE—or very close to the minimum—is often used, the minimum TE is often far longer than what is possible without the diffusion gradients, as in the non-diffusion-weighted image. The one caveat for the TE is that it should be the same for all diffusion directions and weightings, including the non-diffusion-weighted image, in order to prevent any T_2 decay (or differences thereof) from influencing the calculation of the diffusion coefficient. A standard TE for DTI is around 80 ms, although it can vary greatly depending on the scanner's gradient hardware as well as the requested scan and diffusion parameters.

The increased TE is also a source of decreased SNR relative to anatomical MRI. In conjunction with the diffusion-encoding gradients, which also decrease the signal, DTI acquisitions have a lower SNR than anatomical images. It is in part because of the low signal that often more than 15 diffusion-encoding directions and multiple T_2-weighted images are used in standard clinical DTI.

Note that unlike in anatomical imaging where a long TE generates T_2-weighted contrast in the image, the ADC images only have diffusion contrast. While the individual images in the series have T_2-weighted contrast from the TE, this contrast is removed in the DTI processing because all of the diffusion images have the same TE. This results in images which are unaffected by image contrast beyond that intentionally created by the diffusion gradients.

Because of the increased TE, the minimum *repetition time* (TR) is also increased. An important point to remember for DTI is that the TR should be at least three times the tissue T_1-relaxation time in order to allow near full relaxation of the spins. In the brain, this means that the minimum TR is considered to be at least 3 s, and preferably more than 5 s. Often, however, with multi-slice scans, the time it takes to acquire all of the slices—and make it fit into one TR—is more than the 3, or even 5-s minimum. While a TR that is too low reduces the SNR and can induce T_1-weighting into the diffusion images, anything beyond approximately 5 s does not improve or degrade the images in any way.

Another important scan parameter is the resolution of the scan. EPI-DTI is typically acquired at a relatively low resolution compared to anatomical imaging protocols that take approximately the same amount of time. The low resolution is primarily because of the reduced signal in the diffusion-weighted images caused by the diffusion-encoding gradients, as well as the time required to encode the seven or more diffusion-encoding directions, which are required for a sufficient SNR for the tensor calculation.

Typically, the resolution is as high as possible while still allowing a high enough SNR as is required by the application. The balance between resolution, SNR, and the number of diffusion-encoding directions in general is an open research question, and even for specific applications it is not easy to determine without specific testing. It often depends on the anatomy under exploration, as well as the SNR and resolution that the post-processing methods require. Because of these complicated trade-offs, it is important to check previous protocols and work to verify what is required of the technique and to confirm that it is possible with your scanner before scanning patients.

To review, there are three major parameters that are treated differently for DTI than most other MRI scans:

- The TE is set as short as possible to get the highest SNR possible because the contrast is created with the diffusion gradients, not the TE and TR.
- The TR is set to be as short as possible for speed, but it must stay longer than three times

the expected T_1 of the tissue—typically more than 3 s.
- The resolution is set as high as possible while still allowing for good SNR. There is no equation for this; it is all determined by testing.

Consequences of the EPI Trajectory

This section will discuss the EPI trajectory and common artifacts, which are often seen in conjunction with DTI-EPI. The EPI trajectory is unique because it samples multiple Cartesian lines in *k*-space in a single readout. This is very efficient in terms of scan time and has the nice property for diffusion-weighted imaging that the whole image can be acquired in a single excitation, which helps prevent problems from diffusion-encoding induced phase errors which will be discussed later.

However, acquiring data in a single, long readout enhances several types of artifacts, which can pose problems when reading or analyzing the images. These consist of:

- Chemical shift artifacts in which fat/lipid signal is also shifted significantly relative to the rest of the image and can cause masking of the true image in places of overlap.
- Distortions due to off-resonance in the object from main magnetic field distortions such as B_0 inhomogeneities or a bad shim.
- Ghosting, which is due to inconsistent phase encoding in odd and even lines in *k*-space.

The main consequence of a Cartesian EPI readout with the phase-encode lines acquired linearly from one edge of *k*-space to the other is that the EPI readout is very fast in the readout direction (k_x), but very slow in the phase-encode direction (k_y) (Fig. 6.2). The consequence of this readout is that artifacts, which in other scan types manifest in the readout direction, present very strongly in the phase-encode direction in EPI. For example, the fat-water shift can be tens of pixels in the phase-encode direction in EPI images, whereas in normal gradient or spin-echo imaging, the shift is typically less than two pixels in the readout direction. Do note that different vendors report either bandwidth in kHz (GE), bandwidth in Hz per pixel (Siemens), or water-fat shift (Philips).

This water-fat shift is caused by the different resonant frequency of fat compared to water. As mentioned above, the slow read progression in k_y causes the chemical shift artifact as in standard gradient or spin-echo imaging. However, chemical shift is not limited to chemical species; the same principle applies to any region where off-resonance is present. In EPI images this causes the signal from the off-resonance regions to be shifted, which—due to the gradual off-resonance change—looks like stretching or signal pileup in the image rather than a distinct shift (Fig. 6.7). This can be caused by off-resonance effects such as a poor shim, or more commonly by air-tissue interfaces such as those adjacent to the sinuses or other cavities in the head, which cause irregular magnetic fields in the neighboring brain tissue.

The B_0 (main magnetic field) and chemical shift artifacts are caused by off-resonance differences or natural chemical frequency in different regions of the image. These artifacts can be reduced with careful shimming and fast scans, and fat saturation pulses respectively. In fact, because the resonance frequency of fat is not the same as water, fat is typically shifted a significant amount when compared to the rest of the image, often into the brain itself (Fig. 6.8). Lipids have a very low diffusion coefficient and therefore voxels that have fat overlaid appear hypointense (dark) on ADC maps. Similarly, residual lipid ghost often confounds diffusion anisotropy maps. Because of this, a fat saturation pulse, or some other method of suppressing the fat signal, is required. Alternatively, one can use "water-only" excitation pulses (i.e., spectral-spatial RF pulses) that do not excite fat protons within a slice.

Another artifact called "ghosting" is inherent to EPI in which the *k*-space readout is performed in both directions, which is what is shown in Fig. 6.2. This is the most common type of EPI used in the clinic. Ghosting is caused by differences between odd and even (readouts progressing to the right and left respectively) *k*-space lines. These differences manifest as image "ghosts" at a

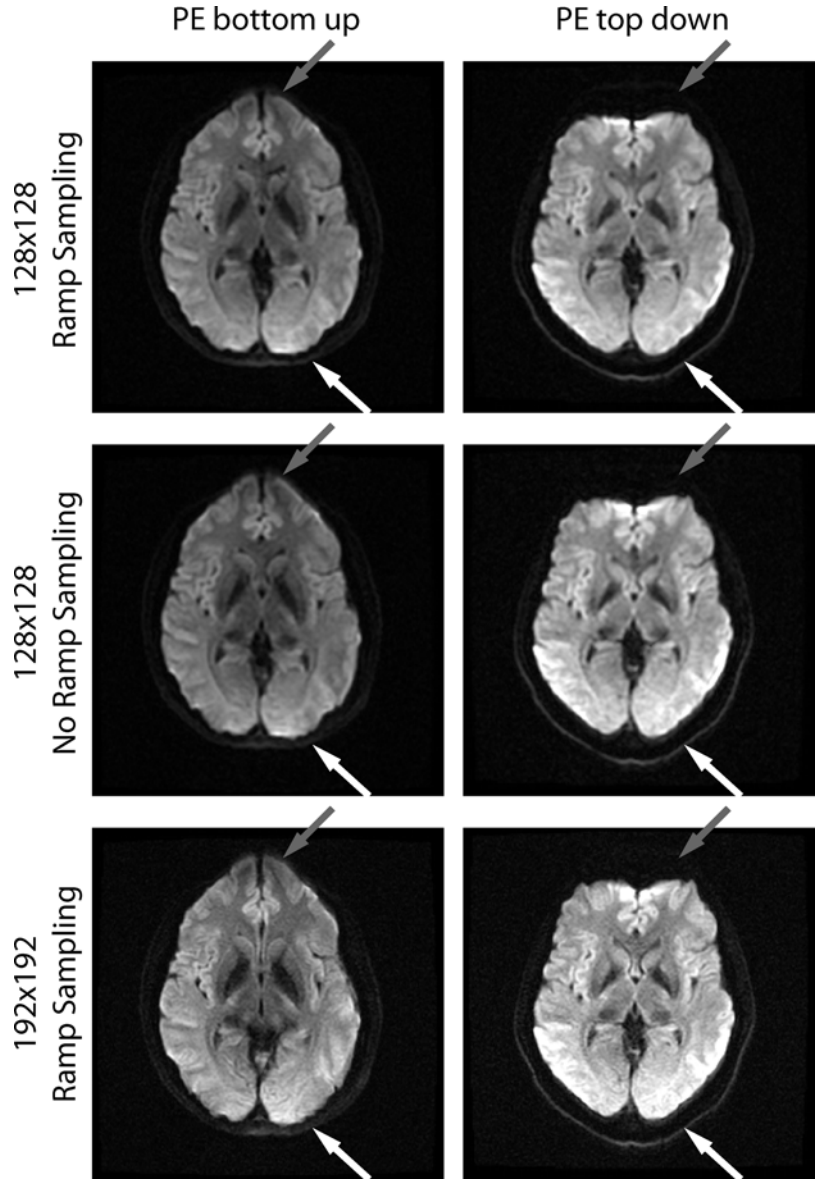

Fig. 6.7 These EPI images show off-resonance induced artifacts due to an inhomogeneous magnetic field. When comparing the phase encode (PE) up vs. down, it is clear that the image is either stretched or compressed in regions with off-resonance, such as the regions indicated by the *gray* and *white arrows*. Even though this artifact affects the whole image, the *gray* and *white arrows* show regions where the differences between the up and down PE artifact are easy to see. The speed at which the image is acquired decreases from the fastest, (a matrix of) 128 × 128, to 128 × 128 without ramp sampling, to the slowest, 192 × 192. Because of this reduction in the sampling speed, the artifacts increase, which is easy to see when comparing regions near the *gray* or *white arrows* for the three different sampling speeds. Note that decreasing the resolution is not the only way to increase the sampling speed and therefore decrease the off-resonance artifacts; however it is a way to modulate the distortion

fraction of the field of view. For single-shot EPI, with altering odd and even echoes, the ghost is shifted by half the FOV. Ghost artifacts like this (called FOV/2 ghosts) are often fixed in the reconstruction, though this is not always the case and ghosting may be more prevalent if the imaging plane is oblique. Similar to residual fat overlaying on the tissue of interest, the diffusion tensor information can be confounded by the aliased FOV/2-ghost. Quantitative measurements as well as scalar images (e.g., $b = 0$) will be most corrupted when there is a substantial signal intensity difference between the original and the aliased voxel (e.g., brain tissue vs. eyeball).

There are two different causes of ghosting: the phase difference and shift between the even and odd echoes in *k*-space. Both of these result in ghosting, but their appearance is different and they are caused by the intercept and slope of the phase terms, respectively [6]. Figure 6.9 shows

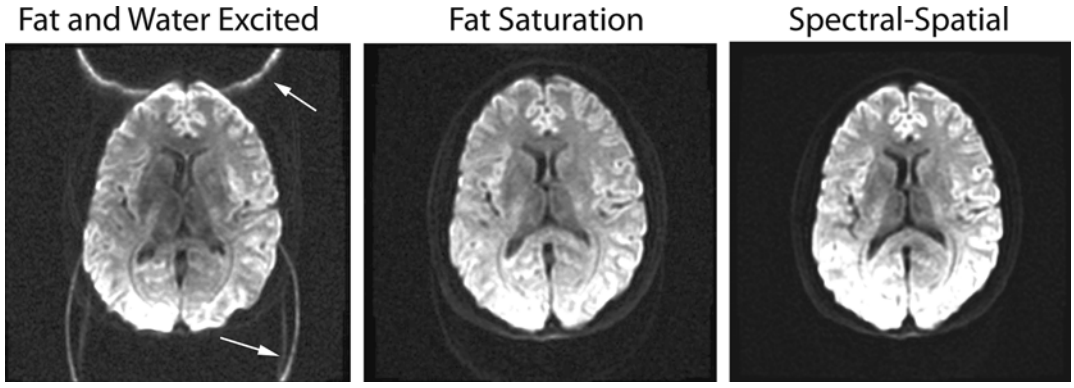

Fig. 6.8 Lipid suppression is very important in EPI and DTI imaging in order to remove the unwanted fat signal from the diffusion calculations. The first image, in which both fat and water are excited with a normal RF pulse, shows how the fat signal is shifted and can disrupt regions in the image. The next two images show how both fat saturation and spectral-spatial pulses work well to suppress the unwanted fat signal

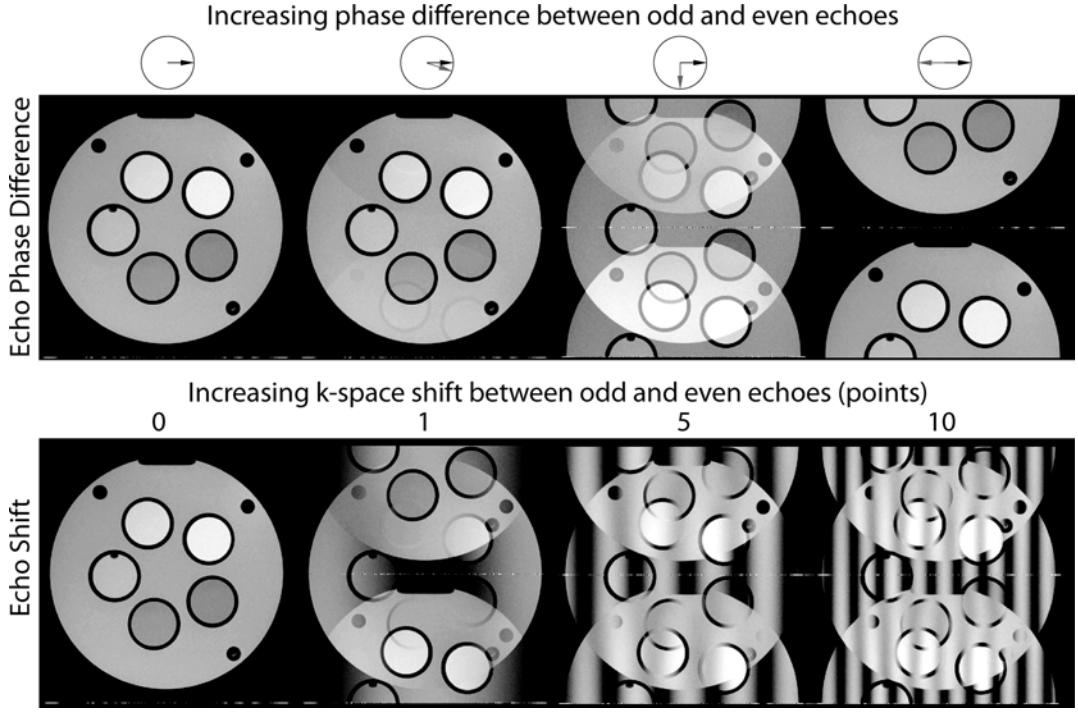

Fig. 6.9 This figure shows how differences between odd and even echoes cause EPI ghosting. The first row shows how the phase difference between the echoes causes varying intensity ghosts in the image. Note how (from *left* to *right*) the 0° (no ghosting) and 18° vary only slightly, but at 90° the ghost and original have equal intensities, and at 180° only the aliased image remains visible. The *arrows* in the *circles above the first row* show the phase of the even echo and odd echo in *black* and *gray* respectively. The *second row* shows how shifts between the odd and even echoes cause bands of aliased and un-aliased regions in the image. Note that (from *left* to *right*) the number of ghosted bands is equivalent to an increased echo shift in *k*-space. For all these images the phase-encode direction is up-down

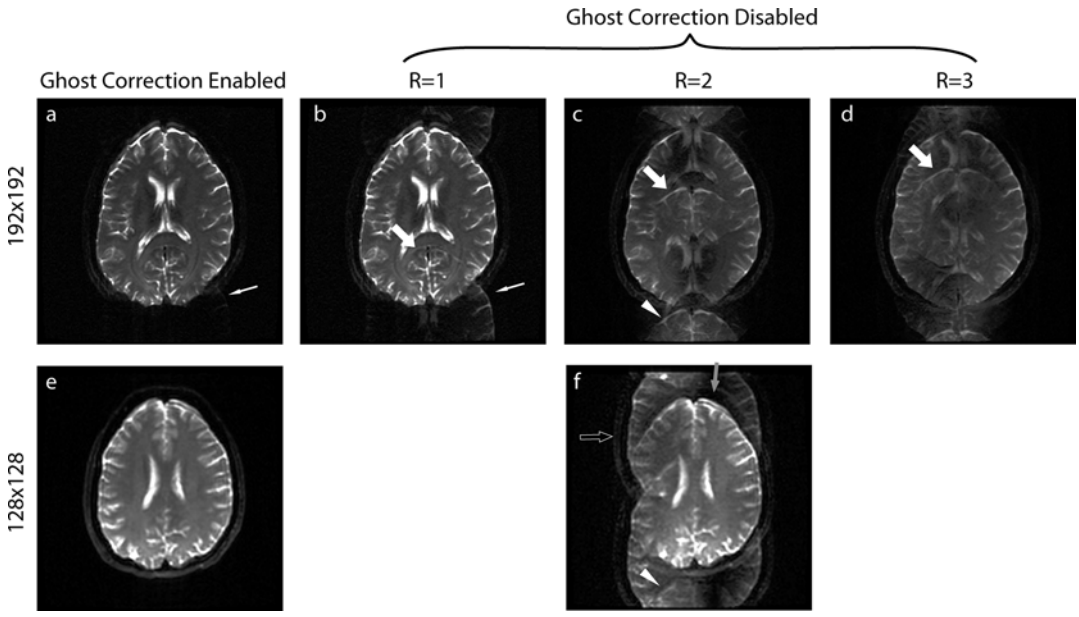

Fig. 6.10 These images show EPI ghosting with different parallel imaging factors. Note that with the exception of (**a, e**) these images were generated by turning off the "ghost correction" portion of the reconstruction, ghosting can also arise when the ghost correction is used, but is simply unsuccessful. This is the case in the 192 × 192 resolution ghost corrected image (**a**, *white arrow*) where some slight aliasing is still present, which is similar to that in (**b**). The "ghosts" are shifted by a fraction related to the parallel imaging used and are caused by inconsistent even and odd readout lines (see Fig. 6.2). Traditional EPI ghosts (also called *N*/2 or Nyquist ghosts) are shifted halfway around the image like in (**b**), i.e., FOV/2. However, when parallel imaging is used, the ghost shift changes relative to the parallel imaging factor: FOV/(2*R*) where *R* is the parallel imaging acceleration. The *thick arrows* show the top of a "ghosted" brain in the $R = 1$, 2, and 3 images **(b–d)**, which shows how it shifts with the changes in the parallel imaging factor. The two images for a parallel imaging acceleration of 2 show how different ghosting can look between similar images. The *gray arrow* in (**f**) shows a vertical band where no correction is needed to produce a good image; however in the same image, the *hollow arrow* shows a band where the image is entirely ghosted and the true image **(e)** is not represented

different types of ghosting, and disabling ghost correction as seen in Fig. 6.10 shows combinations of both echo phase and echo shift ghosts.

Another variant of magnetic field distortions is due to eddy currents (see section "Examples and Mitigation of DTI-EPI Artifacts") induced in the conducting elements of the magnet by switching the strong diffusion-encoding gradients and which cause spatiotemporal variations of the effective field "seen" by the protons.

To review, there are three common types of artifacts which can manifest—typically, but not always—in the phase-encode direction:

- Chemical (fat/water) shift (Fig. 6.8).
- Magnetic field (susceptibility and shim) distortions (Fig. 6.7).
- Ghosting, which is caused by differences between back-and-forth readout lines (Figs. 6.9 and 6.10).

Hardware Limitations

There are many hardware limitations in MRI that are considerations for DTI; some of which are imposed by engineering challenges, and some by the human body itself. There are two major limitations when it comes to the performance of the magnetic field gradients and one for the use of the radiofrequency (RF) system.

For the gradient systems, which are especially stressed during DTI acquisitions due to the extremely strong diffusion gradients, the two

Table 6.2 Scan parameter and gradient limitations

Parameter	Gradient "Difficulty"
↑ Matrix size	↑
↑ FOV	↓
↑ *B*-value	↑
↑ Slice thickness	↓

Here we loosely define difficulty as those applications that require higher gradient performance, which includes both gradient strength and slew rate

major limitations are the maximum gradient strength and the rate at which the gradient changes strength (slew rate). Table 6.2 lists several scan parameters that can affect the gradient system and influence the maximum gradient strength and slew rate in some way.

In diffusion imaging, the maximum gradient strength is often reached during the diffusion sensitizing gradients. If the gradient strength can be increased, the duration of the diffusion pulses can be decreased for the same desired *b*-value. To review the diffusion equation from the diffusion chapter, the *b*-value for a diffusion-weighted (single) spin-echo sequence is defined by $(\gamma G_{\text{Diff}}\delta)^2(\Delta - \delta/3)$ where γ is the gyromagnetic ratio, G_{Diff} is the strength of the diffusion gradients, Δ is the time from the beginning of the first diffusion gradient to the beginning of the second diffusion gradient, and δ is the duration of the diffusion gradient. A rule of thumb is that the *b*-value increases quadratically with the diffusion gradient strength, G_{Diff}, and with the third power of diffusion time, δ. A shorter diffusion gradient duration equates to a shorter TE and thus higher SNR as well as shorter TR and thus a faster scan. The gradient coils (i.e., their diameter, inductance, and resistance) and amplifiers (i.e., peak power and sustained power) often limit the maximum gradient strength in the system, and beyond changing scanners or using a gradient insert, there is unfortunately no way to change how fast the gradients can be switched or their maximum gradient strength.

The slew rate is the speed at which the gradients can change strength. A high slew rate is very advantageous for an EPI readout, which requires very fast positive and negative switching of the gradients to achieve an efficient back-and-forth trajectory (Figs. 6.1 and 6.2); the faster the gradients switch, the faster the acquisition becomes and the smaller the geometric distortions become. The limitations on the slew rate are twofold. The first, like the maximum gradient strength, is caused by hardware limitations, as it is difficult to increase and decrease the power in the gradient coils very quickly. The second is *peripheral nerve stimulation* (PNS), which is nerve stimulation caused by rapidly changing magnetic fields around the scan subject. It actually occurs in body parts that are located near the edges of the gradient coil, i.e., far away from isocenter, where the temporal change in the effective field produced by the gradient is highest. PNS is typically felt as a muscle twitch, and is normally only an annoyance, but can be painful and should be avoided if possible. The easiest way to avoid PNS is simply to decrease the intensity of the gradient switching. This can be achieved by decreasing the resolution or the readout bandwidth. In fact, even changing the orientation of the scan is often used to help alleviate PNS.

The limitation on the *radiofrequency* (RF) system is called the *Specific Absorption Rate* (SAR), which is in effect the heating of the subject by the RF excitations. RF excitations are done through the RF coil and are a vital part of any MRI pulse sequence. SAR limitations can vary based on the regulations at the institution as well as the body part being imaged. This heating is not enough for the patient to notice or is noticed with delay as the heating occurs inside the body and not from the outside where the people would be able to sense it with the thermoreceptors in the skin, which is why it is very important not to exceed the tissue heating limit. Luckily, it is a US Food and Drug Administration (FDA) requirement that all clinical scanners in the United States track the SAR of the pulse sequences and stop the scan if it exceeds the allowed limits. Similar limits are generally used worldwide, and different countries and regions have their own laws and regulations regarding limits.

Because the SAR is caused by the RF pulses, and higher flip angles cause more tissue heating, any pulse sequence with many 90° and especially 180° pulses is prone to having a high tissue heating. Unfortunately, once the maximum tissue heating is reached, the only option is to wait until

the tissue cools. Because waiting during an MRI is highly undesirable, it is important to avoid the SAR threshold when prescribing the sequence. Sequences that may reach the SAR limits are FSE—where there are many 180° pulses—as well as some spin-echo EPI sequences with fast repetition times. It is important to notice that SAR also goes up quadratically with field strength. So SAR management is very important at 3 T and even more so at experimental high-field systems, such as 7 T scanners.

Another component to the SAR limit is the weight of the subject and even the body part being scanned. Different body parts have different SAR limits as determined by the FDA, and these limits are set per body weight (W/kg). Even though DTI is typically performed on the head, the weight of the subject determines the SAR limit for head scans. Variations in patient weight typically do not cause problems, but if the sequence is set very close to the SAR limit, a very small patient may cause the sequence to pause or abort. This is easily understood when considering that an arbitrary RF pulse deposits a certain amount of energy—in this case heat measured in Watts—in the body. A SAR limit is the amount of energy per amount of tissue (W/kg) over time; therefore heavier patients can be scanned with more energetic pulses than lighter-weight patients.

To review, there are three limitations caused by MRI hardware, which may cause limitations for EPI-DTI.

- Slew rate—the speed at which the gradients can change strength, which is important during the readout.
- Maximum gradient strength, which is reached during the diffusion-encoding gradients.
- SAR—the maximum tissue heating from RF.

Examples and Mitigation of DTI-EPI Artifacts

Even though there are a few fundamental types of EPI artifacts, there are many causes of EPI artifacts. It is important to be able to recognize the major types and be familiar with the causes of each in order to reduce or remove the artifacts.

The first artifact to discuss is "ghosting" as explored above (Figs. 6.9 and 6.10). The typical EPI readout is the back-and-forth type that is shown in Fig. 6.2. The consequence of inconsistent data in the odd and even readout lines is shown in Figs. 6.9 and 6.10. Even though the odd and even readouts are spaced differently with different parallel imaging accelerations, the result is always similar. In each case, there are shifted "ghosts" that are seen in the phase-encode direction. This artifact can be complicated, especially when high parallel imaging values are used; however it is often corrected in the reconstruction [10]. If the ghosts are not easily corrected, scans in the axial plane may have less inherent ghosting than oblique, sagittal, or coronal scans. This has to do with the fact that the physical gradient coils are all slightly different, especially the z-gradient coil, and therefore demonstrate different timing errors that in turn cause the data inconsistencies that cause "ghosts." When prescribing oblique scans, a combination of the physical gradients (with different temporal responses) is used to generate the logical gradient and corrections are no longer simple. Alternatively, if ghosts are still present, a flyback EPI trajectory can be used. This trajectory samples all readouts in the same direction, but is slower than the back-and-forth trajectory and may not be available on all systems.

Ghosting may also be caused by motion in some cases. In these cases, it can be very difficult to differentiate between the acquisition ghosts discussed above and the motion ghosts. However, if other slices and EPI scans are ghost-free, then it is likely that it is a motion ghost. Also, if there is additional distortion like signal smearing or blurring, that is a good indication that the ghosting is due to motion.

Another major source of EPI artifacts are off-resonance distortions that are regional imperfections in the shim that cause distortions in the phase-encode direction. The influences of off-resonance distortions can be seen in Fig. 6.7 where opposite phase-encode directions are compared. Typical sources for off-resonances are: B_0 inhomogeneities (i.e., deviation in the static field provided by the magnet), susceptibility errors (i.e., when spins are magnetized differently due

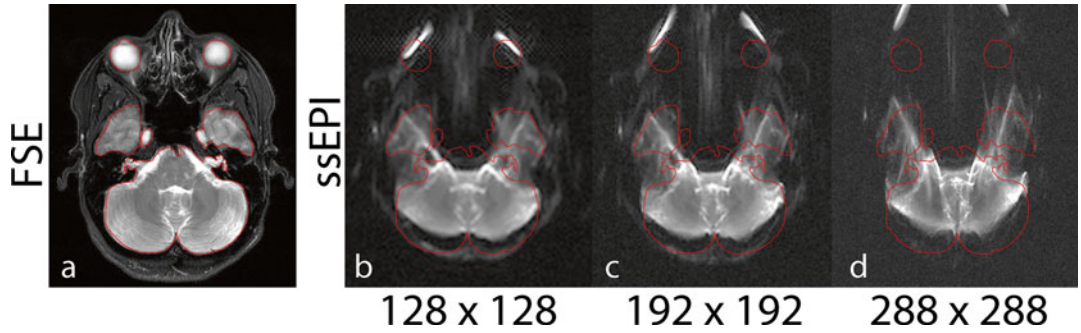

Fig. 6.11 This comparison shows the difference between an FSE (**a**) and single-shot EPI at three different resolutions (**b**–**d**). Note how the off-resonance distortions are much greater in the EPI images when compared to the FSE image (*red outline*). The increasing distortions in the EPI images are caused by the progressively slower speed in which *k*-space is traversed in the phase-encode direction: from 128 to 288. The distortions are caused by the combination of off-resonance distortions and the EPI readout

to the differential field they produce at interfaces of matter with different susceptibility, e.g., air and tissue), eddy currents (residual magnetic fields from the diffusion gradients), and lipids (which are not actually off-resonance, but precess at a different frequency, which then looks similar to off-resonance). These distortions can be from the aforementioned sources, but they are inherently related to the slow sampling speed of EPI in the phase-encode direction. Figure 6.7 highlights these differences by showing the same slice, sampled in different directions and at different speeds, and Fig. 6.11 shows the distortion of different sampling speeds when compared to a fast spin-echo (FSE) scan. These are the typical distortions in EPI, and these artifacts are often accepted in order to acquire DTI data in clinically acceptable times; however these may cause issues when trying to quantify the diffusion in the brain [11].

For the same reason that susceptibility gradients, main field inhomogeneities, and eddy currents all cause geometric distortions, the fat signal is shifted by a significant amount relative to the brain water signal. Because of this, some kind of fat suppression should be used for any EPI acquisition. This is shown in Fig. 6.8, which illustrates how the fat signal is shifted and overlaps the brain. However, when a fat saturation or water selective excitation is used, the fat signal is removed. There are various methods that can be used, and each vendor has their preferred method, which often has the best performance on their respective systems. These methods can differ not only in the effectiveness of the lipid suppression but also in how much time is spent to acquire each slice. Here, spectral-spatial pulses are obviously much more effective than inversion (SPIR, SPAIR, STIR) or saturation/binomial (CHESS, ProSet). Fat suppression is not only important because of the unpleasant visual appearance of fat rings. Since lipids have very low diffusion coefficients, any residual lipid artifact will affect the ADC in the voxel that contain the fat ghost.

An EPI image artifact type that is uniquely associated with DTI and diffusion imaging is eddy current artifacts. These are due to the strong diffusion gradients that are used to visualize the structures in the brain. These extremely strong gradients can cause residual magnetic field gradients on any combination of the gradient axes during the imaging section of the pulse sequence [12]. Note that eddy current artifacts also belong to the family of off-resonance artifacts. These residual currents cause transient changes in the magnetic field that lead to scaling, translation, or shearing in the image depending on the axis in which the eddy current occurs. An example of this can be seen in Fig. 6.12, which shows the differences between images with eddy currents in three different directions. These distortions generally increase with increasing diffusion gradient strength and therefore are not significant under typical (non-diffusion) imaging conditions. A dual spin-echo acquisition, which will be

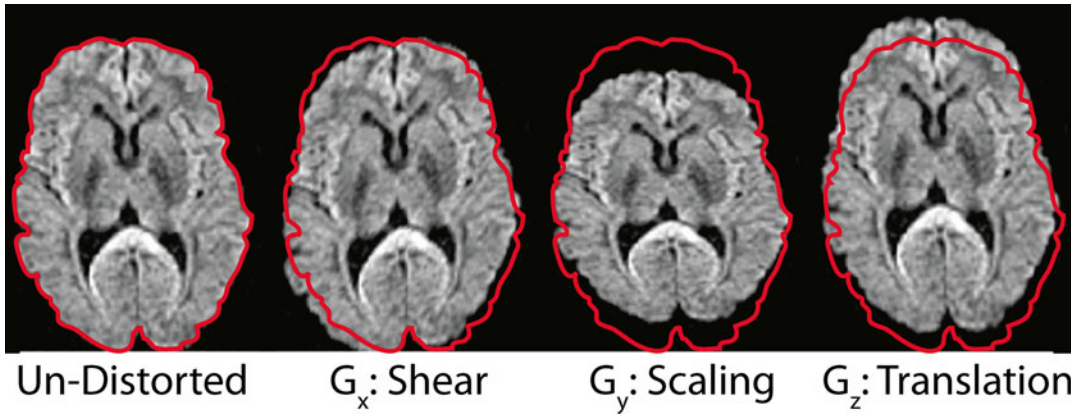

Fig. 6.12 The switching of strong diffusion-encoding gradients leads to eddy currents and associated field perturbations, which in turn can cause different distortions based on the direction of the diffusion-encoding gradients. This is commonly called "eddy current" distortion, and is a concern in diffusion-weighted EPI. These images show the distortion caused by gradients along the *x*-, *y*-, and *z*-axes, which are shear, scaling, and translation, respectively. As you can see from the *outline*, there are many smaller differences in the outlines between the images as well. Eddy current effects can be reduced by using a dual spin-echo imaging sequence, reducing the strength or slew rate of the diffusion gradients, or by simply increasing the speed at which *k*-space is traversed along the phase-encode direction (e.g., via parallel imaging, interleaved EPI, or ramp sampling)

discussed later, can be used to mitigate these distortions at the cost of slightly reduced SNR.

Other distortion effects, in the same family as off-resonance distortions, are caused if the shim is set incorrectly. The difference between local susceptibility artifacts and distortions caused by incorrect shim values are that shim-related artifacts generally affect the whole image and are preventable with careful shimming, whereas susceptibility-related artifacts are local and typically manifest around air-tissue interfaces.

In fact, the distortions from poor shim values look like eddy current distortions where the images are stretched, compressed, and sheared; the cause is off-resonance spins due to bad shim settings. Even though the shims on modern MR systems are typically very good, in some cases the available shim gradients may be insufficient to properly account for the major inhomogeneities in the imaging volume. Most clinical scanners only have linear, or at most first-order nonlinear shims, so any field changes that are not corrected by those are uncorrectable and the remaining field changes result in the distortions seen in Fig. 6.13. Typical clinical scanners have robust auto-shim procedures, but in some cases the shim may be determined incorrectly, and in these cases it is possible to re-run the auto-shim or manually shim the volume.

A further aspect to the shim and fat-induced artifacts is that when the off-resonance distortions are severe, fat suppression can cause the suppression of nonfat signal because the off-resonance distortions cause the frequency of the brain to shift to frequencies near fat. It is also clear that in these regions the image is greatly distorted due to the off-resonance distortions. This is shown in Fig. 6.14, which demonstrates unsaturated and saturated fat in the case of severe off-resonance distortions.

To review, there are three major types of artifacts that are caused by off-resonance effects in EPI images:

- Shim and local magnetic field off-resonance (Figs. 6.11 and 6.13).
- Eddy current distortions caused by the diffusion gradients (Fig. 6.12).
- Fat suppression errors (Fig. 6.14).

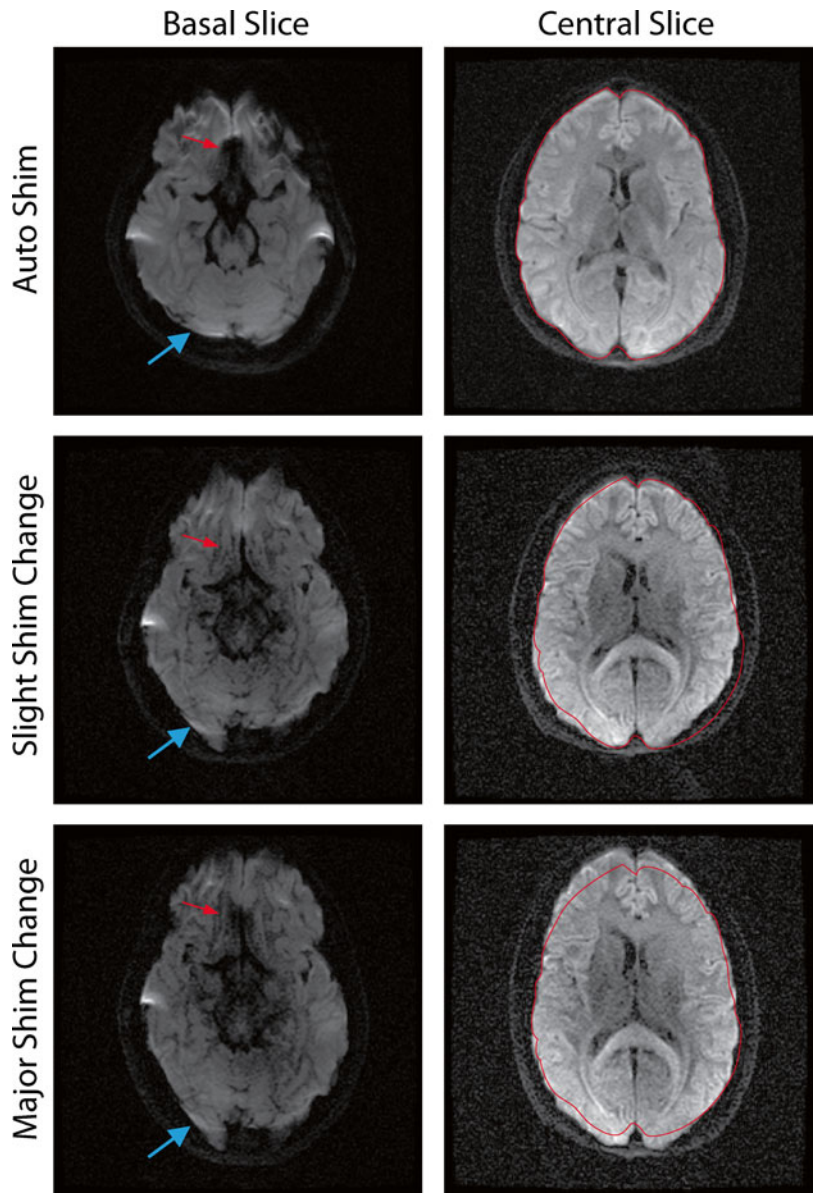

Fig. 6.13 This figure shows how the shim quality can distort and change the image. In the *left* column, the small *red* and *large blue arrows* indicate regions that change significantly inside the brain due to the shim changes, with changing distortion as the shim progresses from *top* to *bottom*. In the *right* column, the *red* boundary shows how the brain shape is changed by the shim. Also note how the SNR of the images decreases as the shim worsens. To fix this, the shim values may be manually changed, and there may also be higher order shims, which can help smooth the magnetic field over larger regions. In this example, only the linear shims were changed. If higher order shims were used, the distortions would become increasingly complex

Considerations When Prescribing EPI

There are a number of factors to pay attention to when prescribing an EPI scan. Many of them are similar in non-EPI imaging, but often their effects are amplified or altered in some way in EPI. The previous section described these artifacts and this section discusses how to best avoid these issues when prescribing scans.

Checklist 1 is a generic outline for troubleshooting DTI. We intend it to help troubleshoot the potential major problems in a clinical setting. It is written generically and may not apply well to all applications. We encourage you to use this as a basis for an "artifact checklist" that applies to your scans that you can use to quickly and efficiently diagnose and fix common DTI errors.

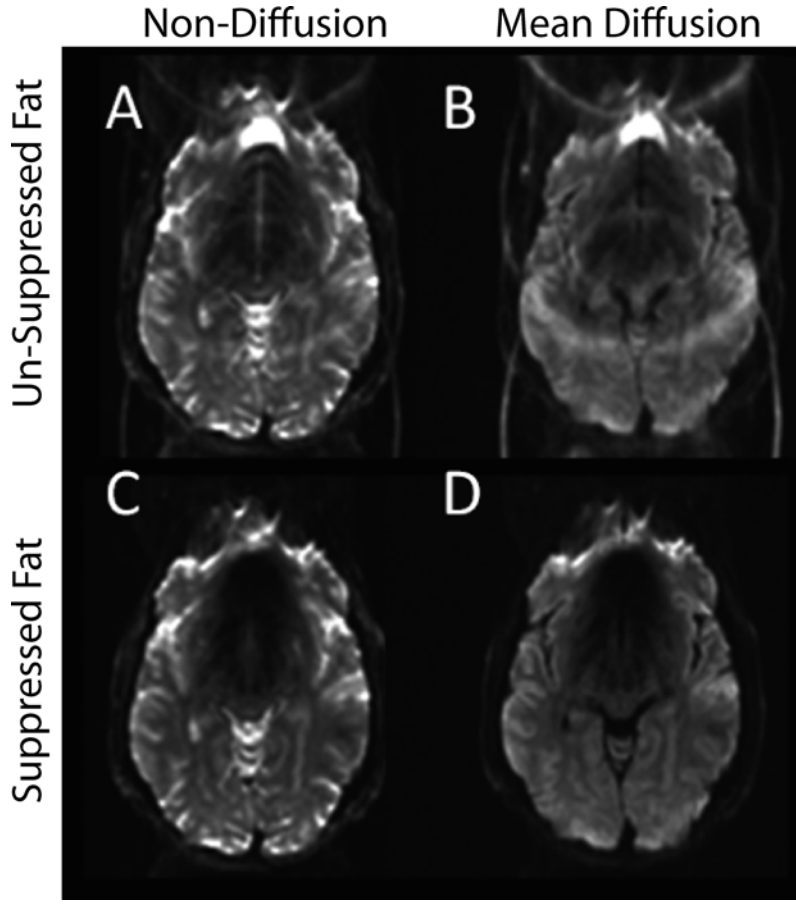

Fig. 6.14 This image shows a brain with large off-resonance inhomogeneities with unsuppressed (**a**, **b**) and suppressed fat (**c**, **d**) images. In this case, because of the off-resonance inhomogeneities, the fat suppression removes signal from the center of the brain because its resonance frequency was too far away from the base water frequency

If the scan is artifacted:

1. Does it look like motion? Is there ghosting, signal variation, or blurring?
   (a) Did the person move? Ask them, or a simple test for large motion is to re-run the localizer to check for major motion. Ask them to hold still and re-run the scan. Alternatively, use better head restraints or turn on motion correction, if available.
2. Is the image geometrically distorted (squeezed, stretched)?
   (a) The shim may be bad, or eddy currents may be distorting the diffusion images.
   (b) If the localizer looks okay, but if both the diffusion images and the non-diffusion images look distorted, it could be a bad shim.
   - Try looking at the line width of the spectrum from a manual prescan to evaluate the shim.
   - A manual or a local automatic shim may help.
   - Use parallel imaging or multi-shot regime.
   (c) If the non-diffusion images are not distorted, but the diffusion images are distorted—typically differently from image to image—it may be caused by eddy currents.
   - Try a dual spin-echo acquisition, or a post-processing eddy current correction. You could also reduce the *b*-value as eddy currents increase disproportionally as you increase the *b*-value.
   - A lower *b*-value will reduce the distortions, but it is often not possible to

change the *b*-value for typical DTI protocols. Alternatively, try to increase TE and lower the diffusion gradient strength.
- Use parallel imaging or multi-shot regimes.
- Some scanners allow the combination of two gradient coils to increase maximum gradient strength at the cost of lower gradient slew rate and hence slower *k*-space progression. If you desire to have less geometric distortion, try to avoid these enhanced modes and go for the higher slew rate. The lack of gradient strengths can increase TE but can be mitigated by extra averages.

3. Is the image distorted in local regions or asymmetrically?
   (a) Is/are these distortion(s) near the sinuses e.g., the nose/ears?
   - These are common off-resonance distortions near the air/tissue interfaces.

   Increasing the bandwidth, increasing the parallel imaging factor, or reducing the readout length will reduce the distortions.

   Multi-shot EPI also often has reduced distortions from off-resonance, so even though this will lengthen the scan time, it may be possible to use it to minimize the distortions.

   (b) If the distortions is/are exceptionally large and potentially located in a place that does not often suffer from large off-resonance distortions, it could be from metal in or near the brain.
   - Metal can cause extremely large distortions and a fast spin-echo sequence may be required if the methods listed above for air/tissue interfaces do not work.

   (c) If the distortions in a brain scan are asymmetric and oriented in the left/right direction, you probably have chosen L/R as phase-encode direction (and A/P as readout direction). These are the orientations for normal brain imaging but for EPI to keep distortions symmetric you want to choose phase-encode direction to be along A/P and readout along L/R.
4. Are there "worm"-like artifacts or fluctuating signal near the ventricles or even the whole brain?
   (a) The partial Fourier fraction could be too low.
   - Try a larger partial Fourier setting in your scan or avoid it entirely.
5. Is there ghosting?
   (a) Try changing the orientation to be axial, if possible. Also, if possible, a unidirectional (flyback) EPI readout would remove the ghosting at the expense of increased off-resonance artifacts, i.e., distortions etc., because of the slower *k*-space traversal.
6. Do the individual images look good, but the tensor does not?
   (a) It could be caused by motion, eddy currents, or low SNR.
   - Try to determine if motion occurred by looking at the images and asking the subject.
   - Try a double spin-echo scan or increase the bandwidth along the phase-encode direction (by parallel imaging, ramp sampling, or smaller matrix) to reduce the time it takes to read one line of k-space and thus reduce eddy current artifacts.
   - It could be the SNR is too low or there are too few diffusion or non-diffusion-weighted images.
7. Is there a distinct ring, or part of a ring, in the images that may overlap the brain in places?
   (a) It is likely that the fat suppression method is turned off or failed. Verify that some type of fat suppression is on. If it is on and failed, this is often due to poor shimming.
   (b) If possible, use a spectral-spatial pulse, but test all the available methods as some may work better than others on your system.
   (c) If you are using a thin slice, try to increase your slice thickness until you can use spectral-spatial water-only excitation pulses. Spectral-spatial excitation pulses

are not available for extremely thin slices, so if residual fat is visible it may be necessary to sacrifice slice thickness for improved fat suppression.

(d) If possible, change the polarity of slice select gradient for your excitation pulse and the refocusing pulse to improve fat suppression. Only spins that are on-resonance will see both the 90° and 180° pulses and show up in the image.

(e) Band-like artifacts could also be residual aliasing from a poorly calibrated SENSE or ASSET scan. Particularly at high field, there can be a large mismatch between undistorted coil sensitivity calibration scans and the distorted (stretched or compressed) EPI scans. Try to use calibration scans that have similar levels of distortions as the EPI scan.

If the scan has a low SNR:

1. Check the receiver coil
   (a) You could have picked the body coil rather than the head coil.
   (b) Some of your coil elements might be defective. Try to reconstruct them individually.
2. Check the parallel imaging value
   (a) It could be too high if regions at the center of the image look noisier than the periphery or if this noisy region repeats itself as a fraction of the FOV.
3. Check the resolution and slice thickness
   (a) The FOV/matrix gives the resolution, and if this is smaller than 4 mm^3 the resolution may be too high for DTI.
   (b) Try not to be too aggressive and attempt imaging slices that are too thin. SNR is directly proportional to slice thickness. Too aggressive reduction can have significant SNR loss as a result.
4. If the image is also distorted
   (a) It is very likely the shim is bad; try automatically or manually re-shimming.
5. If the images look good but the diffusion tensors are noisy
   (a) Check the *b*-values, about 1000 s/mm^2 are normal for clinical imaging.
   (b) For HARDI acquisitions *b*-values above 2000 s/mm^2 are recommended. To get reasonable SNR back down on your voxel size, i.e., use a larger FOV, smaller matrix size, and thicker slices.

Checklist 1: How to diagnose common DTI artifacts and SNR issues. Use this as a basis for troubleshooting DTI artifacts and lack of SNR. Each system and application has their own sources of artifacts, so this is only a template containing common artifacts. This is intended as an example checklist, and you are encouraged to use this as a basis for your own checklist that better suits your acquisition.

The speed of the readout—the bandwidth—can be changed in order to speed up or slow down the acquisition. An increased bandwidth results in a faster scan and reduces off-resonance artifacts, but it may alter—positively or negatively—eddy current artifacts and ghosting. The bandwidth has a dual effect on SNR: with a higher bandwidth noise is increased, but the TE is shorter. For EPI, generally the best results are when the bandwidth is close to the maximum so that the distortions are kept minimal and the TE is short.

As previously discussed, in EPI the phase-encode direction is the direction in which most of the artifacts manifest. Therefore, it is important to consider how the artifact may affect the image, and which phase-encode direction would be best to mitigate the expected artifacts. Typically, for brain DTI the slices are prescribed axially or obliquely (although close to axial), and the PE direction is anterior-posterior or another direction that causes symmetric artifacts in both hemispheres of the brain (Fig. 6.15).

Even though the artifacts predominantly appear in the in-plane direction, reformatting the scans can effectively mask the distortions. Figure 6.16 shows how multi-slice axially acquired images can be displayed in other axes. The distortions are still present in this case, but this is a good way to view axial and sagittal

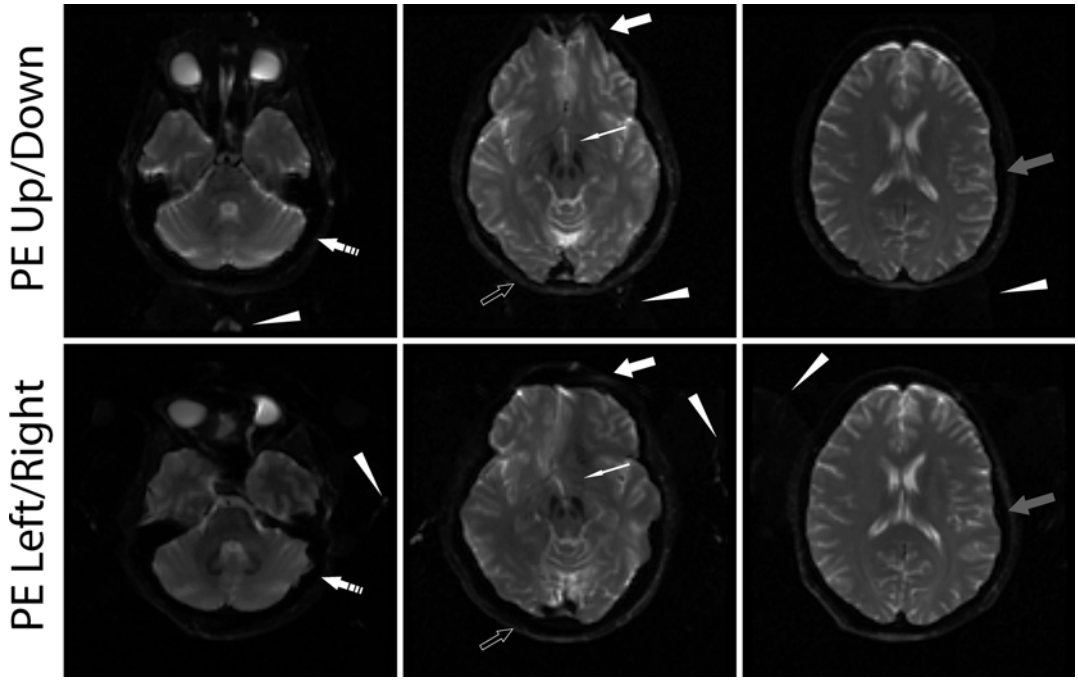

Fig. 6.15 This figure shows how the phase-encode direction affects off-resonance artifacts in the brain. The *thick*, *gray*, *hollow*, and *thin* arrows show how the distortions change significantly when changing the phase-encode direction in various slices. Even though the distortions are often in the periphery of the brain, this is not always the case. The *thin arrows* indicate clear distortions in the middle of the brain, which are especially important because these distortions can make it difficult for radiologists to read the scans. Because of the asymmetry caused by the left/right phase-encode direction, the phase-encode direction is normally chosen to be up/down, which causes the distortions to be symmetric in the brain. This creates more visually pleasant distortions, where the structures near the *dashed*, *thick*, and *thin* arrows are more symmetric when the phase-encode direction is up/down rather than left/right. The *wedge* indicates the residual ghosting and shows how slight ghosting is present in the phase-encode direction in all cases. Important Note: For technologists it is common practice for brain scans to choose left/right as the phase-encode direction. However, for EPI the phase-encode direction should almost always be anterior/posterior or frequency-encode left/right. Choosing the wrong phase-encode direction is the most frequent technologist error one encounters with EPI scanning

images rather than acquiring EPI data in these axes. While it is possible, the artifacts and distortions are generally less significant in the axial plane rather than the coronal, sagittal, or oblique planes.

In some cases the gradient performance, particularly in the *z*-axis, may be significantly different from the other axes. This can induce stronger than normal ghosting, and because of this oblique—or even non-axial—imaging may be discouraged on some systems. However, this is highly system dependent, and as the gradients are improving in more modern scanners, this is increasingly less problematic.

Magnetic field inhomogeneities greatly affect EPI acquisitions, and in the brain the sinuses cause significant distortions. Additionally, if there is any metal (e.g., surgical clips) close to the imaging area there can be significant distortions and signal dropout close to the object as well as distortions away from the object (Fig. 6.17). Unfortunately, it is difficult to avoid these artifacts entirely, but increasing the sampling speed, multi-shot methods (e.g., interleave EPI, readout-segmented EPI), or parallel imaging can help reduce them.

However, increasing the speed is not always possible because of *peripheral nerve stimulation*

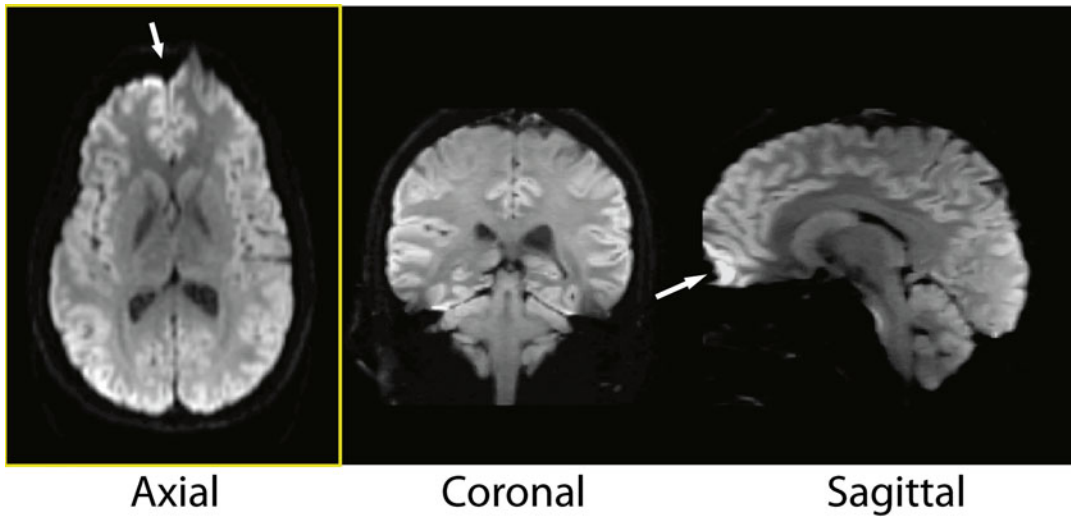

Fig. 6.16 When scanning in an axial orientation, it is possible to view multi-slice images in the coronal and sagittal axes. In this case, the distortions remain primarily in the anterior/posterior direction, so the reformatted images are relatively clear of distortions. The *arrow* shows a distortion in the axial plane, and in the sagittal reformat, the *arrow* shows the same artifact. The trick is that when one performs multi-planar reformation with the slice direction chosen in the phase-encode direction of the acquisition, the reformation algorithm usually uses a slice thickness of several millimeters and thus reduces the visual effect of the distortions by moving the most obvious distortions into the reformatted slice direction

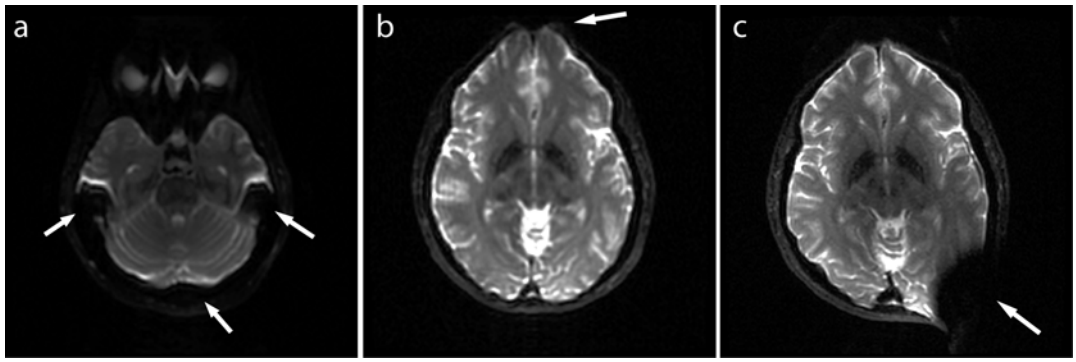

Fig. 6.17 This figure shows common sources of distortion in EPI, such as distortions near the base of the brain (**a**), sinus (**b**), and metal (**c**). The effects of each are similar, but the intensity of the artifacts is very different. Note how the metal artifact (**c**) is much more potent than the sinuses (**b**) and even larger than the similar artifacts in the base of the brain (**c**) such as the ear canals. Because of the large image distortion in (**c**), it is clearly important to know if the subject has any metal implants in or near their head. Even metal implants that are MR safe—such as dental fillings or implants—can cause distortions in large regions of the brain

(PNS) limitations. PNS is caused by fast gradient switching, which is essential for EPI, especially as the scan speed is increased. Even though the scanner has a limited slew rate, it is easy to cause PNS in some subjects with EPI-DTI. Simply slowing down the sampling rate or increasing the FOV can help reduce the effects of gradient switching; however those have the side effects of increased distortion and lower resolution respectively. It is important to remember that PNS is patient-specific, so scans which cause no PNS in some people can be uncomfortable for others.

At times it may be necessary to abort a scan and re-scan with slightly different parameters in order to avoid PNS.

No matter the speed, it is always necessary to use fat/lipid suppression with EPI. This is because of the extremely large fat-water shift (Fig. 6.8), which is an important characteristic of EPI. While it may seem like there is not much fat in the head, there is enough subcutaneous fat present that some may shift into the brain during an EPI acquisition, causing difficulties in radiological reads as well as distortions in the quantification of the diffusion tensor. Notice that spectral-spatial-based fat suppression also uses a fast slewing, EPI-type waveform—played simultaneous to the RF pulses—for the slice selection gradient. When very thin sections are used, the gradient strength might be maxed out and PNS thresholds might be reached. This is particularly problematic for coronal EPI, such as is used for hippocampus DTI, as the slice is parallel to the largest cross-sectional area of the body.

To remove fat from EPI scans, there are many kinds of lipid suppression methods available, such as lipid spoiling (CHESS), lipid presaturation with an inversion pulse (SPIR, SPAIR), inversion of the lipid signal and imaging at a time with no lipid signal (signal null) (STIR), binomial RF pulses, and selective excitation of the water signal without exciting the lipids at all (SPSP). Each of these has its own advantages and disadvantages and each vendor has their preferred method, so it is best to evaluate each system and application individually. Generally with a good shim, any method may be used; however STIR is typically avoided with EPI as it inherently decreases the SNR and is additionally sensitive to the presence of contrast agents.

Besides the lipid suppression method, other preparations are used to reduce the artifacts associated with DTI. A method called *Dual Spin-Echo* (DSE) diffusion preparation can be used to reduce the effects of the eddy currents (Fig. 6.18) [13, 14]. Here, rather than performing a typical Stejskal-Tanner diffusion preparation with the gradients spaced around a single 180° pulse, a series of four diffusion gradients are used. Having four shorter—rather than two longer—diffusion gradient lobes helps to cancel out eddy currents in the EPI readout. This DSE diffusion preparation greatly reduces eddy current effects, but since a second 180° refocusing pulse is needed, the longer echo time reduces the SNR of the acquisition. Therefore, if significant eddy current artifacts are anticipated, a DSE acquisition may be considered, but with the cost of reduced SNR due to a longer echo time. The DSE acquisition is becoming increasingly popular, but as the trend is to move to ever-smaller voxel sizes and is therefore becoming increasingly SNR starved, the DSE approach may be abandoned and sophisticated eddy current correction methods used.

Another method for diffusion preparation is the *Stimulated Echo* (STE) diffusion preparation. It consists of three non-180° RF pulses. STE imaging inherently has half the signal of Stejskal-Tanner imaging simply due to the spin physics of the three excitations (Fig. 6.19). STE, however, can have a shorter TE than a Stejskal-Tanner diffusion preparation scheme. This makes the STE preparation more effective for tissues with a short T_2 (e.g., liver, muscles), as well as some applications in high-field systems (higher than 3 T) where the T_2 times are reduced by the field strength. However, because its uses are limited, STE is not a common acquisition method, and it is not typically supported on current clinical scanners.

To review, there are four major considerations when prescribing DTI-EPI:

- The phase-encode direction should always be anterior/posterior rather than the more typical left/right for non-EPI scans (Fig. 6.15).
- Magnetic field inhomogeneities (Fig. 6.17) can cause significant artifacts for any EPI-based imaging.
- Lipid/fat suppression is necessary because of the large chemical shift of lipids with EPI.
- Eddy currents become significant with clinical DTI-EPI diffusion gradients and may require DSE or post-processing compensation (Fig. 6.18).

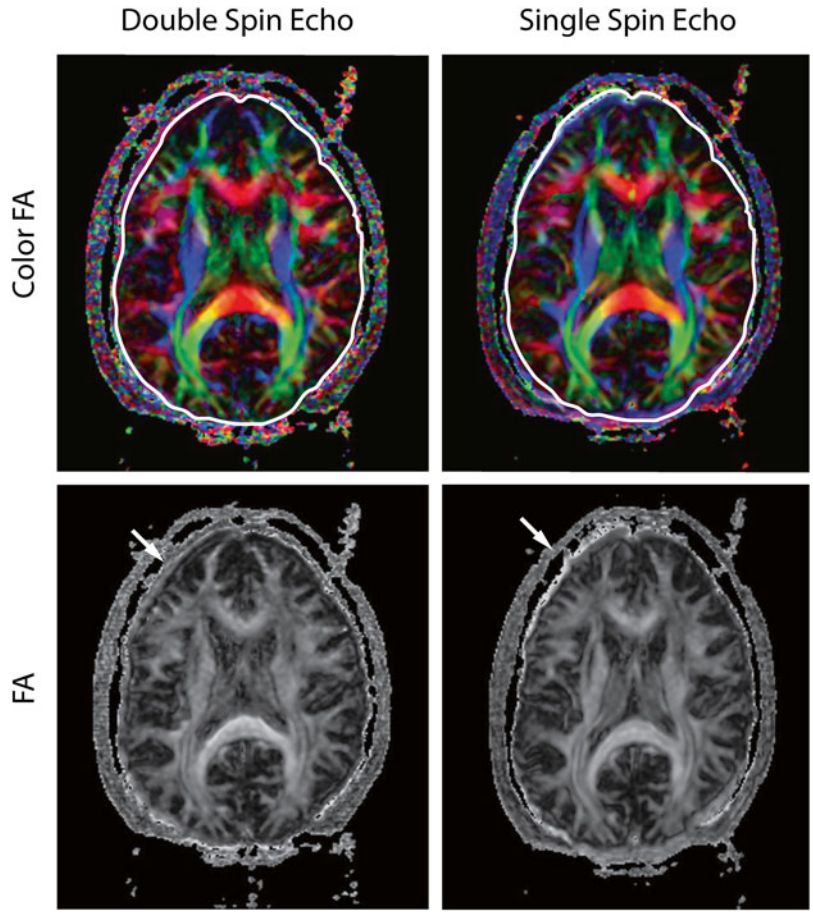

Fig. 6.18 The Double Spin-Echo (DSE) image has less shearing and stretching than the single spin-echo (Stejskal-Tanner) image. This is caused by eddy currents, which can also be seen in Fig. 6.12. The distortions are not typically very large, but in certain cases, such as strong diffusion gradients (high *b*-values) and single spin echo, if not addressed, can disrupt the results. The major distortion can be seen where the *arrow* is pointing to the FA images where a band of artificially high FA is visible in the single spin-echo image. This can also be seen in the color FA image in the same region. Bands of high diffusion anisotropy at the cortex are usually the hallmark for eddy current mis-registration. The advantage of the single spin-echo imaging method is a higher SNR, which is due to a much shorter echo time than with a double spin echo

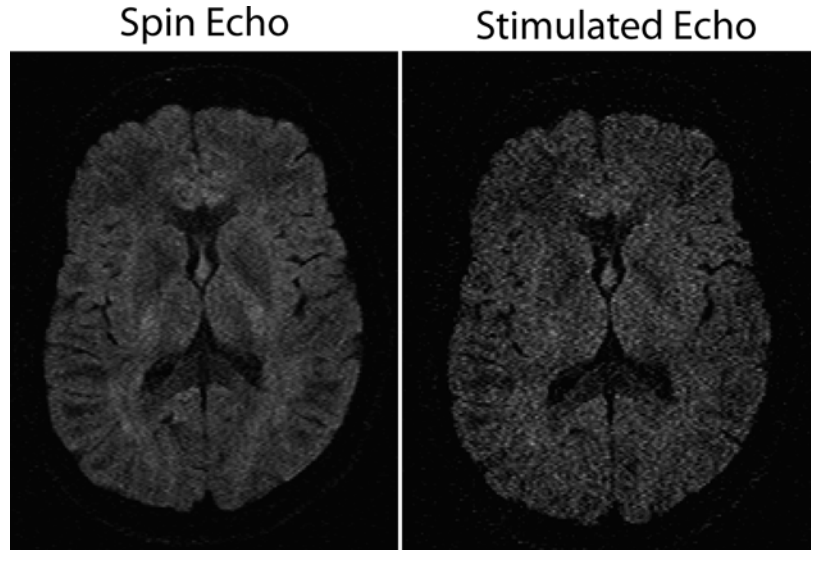

Fig. 6.19 This figure shows a comparison of a spin-echo and stimulated echo diffusion acquisition with similar imaging parameters. The lower SNR of the STE image is obvious

Pros and Cons of Multi-shot EPI

Separating *k*-space into several groups (called segments or interleaves), each of which is acquired with separate excitations, can reduce many of the distortions previously discussed. This results in acquisitions that have less distortion from T_2*-decay and higher SNR due to a shorter TE time. Depending on how *k*-space is separated, multi-shot acquisitions can also reduce off-resonance artifacts. Also, using a multi-shot acquisition can allow higher resolution images than would otherwise be possible. However, splitting *k*-space into multiple segments means taking longer to acquire the whole image, so scan time increases approximately by the number of segments.

Another, more difficult, problem arises from issues of motion and motion-induced phase differences between the readouts. If there are any motion or phase differences between the data, a simple combination of the data will result in an artifacted image (Fig. 6.4). This is because the extra phase accrued due to motion between individual interleaves is inconsistent between the shots, and this inconsistency results in false signal cancellations and additions. Because of this, when using multi-shot acquisitions, it is necessary to run a phase and motion navigator to correct for any phase changes as well as motion, both of which may have occurred between the shots. For many years this has been poorly understood or no effective phase-correction methods were in place. Only recently have multi-shot techniques emerged that can reliably handle this problem.

A method of acquiring multi-shot data with reduced distortions from off-resonant spins and T_2 decay, as well as higher SNR, is called Readout-Segmented EPI (RS-EPI) (Fig. 6.20) [15]. It splits *k*-space into segments along the readout direction rather than the phase-encode dimension as is traditionally performed in multi-shot imaging, e.g., interleaved EPI. As with all multi-shot imaging methods, there is a navigator acquired before or after the data acquisition in order to correct for phase and motion differences between the segments [16–18].

Other methods that are robust to motion and distortions, such as Short Axis PROPELLER (SAP) [19], can be used as well; however, they generally have similar advantages and disadvantages as RS-EPI [6].

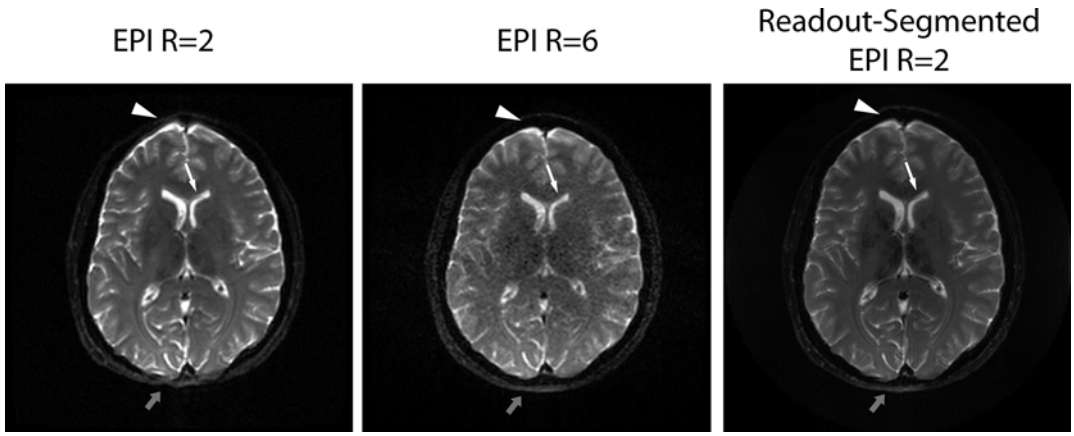

Fig. 6.20 There are several kinds of EPI, and this figure shows some differences between different EPI readout trajectories. These are single shot with low (2) and high (6) parallel imaging factors, and multi-shot Readout-Segmented EPI (RS-EPI) with a low parallel imaging factor of 2. Note how the artifacts are reduced significantly in RS-EPI and $R=6$ EPI due to the faster progression through *k*-space. However, the distortions are similar between $R=6$ EPI and $R=2$ RS-EPI because the splitting of *k*-space in RS-EPI speeds up the phase encode progression through *k*-space. The SNR of the RS-EPI case is also similar to the $R=2$ EPI because they both have the same parallel imaging acceleration and similar echo and repetition times

To review, multi-shot EPI has one major advantage and two disadvantages:

- The advantage is that the distortions are reduced with multi-shot EPI (Fig. 6.20).
- A disadvantage is that the SNR is reduced because of the parallel imaging (Fig. 6.20).
- A second disadvantage is that the processing becomes more difficult due to phase differences between shots.

The Fast Spin-Echo Acquisition

A *Fast Spin-Echo* (FSE) imaging sequence consists of a single 90° excitation RF pulse followed by a train of 180° refocusing RF pulses, often called a *Carr-Purcell-Meiboom-Gill* (CPMG) pulse train (Fig. 6.21). It is also possible to use refocusing pulses less than 180°, which allows for longer echo trains to be used but introduces additional signal modulations and cancellations beyond the scope of this chapter. An interested reader may refer to [20]. A single line of *k*-space is acquired between each 180° pulse, which results in a pulse/readout train that is typically between 32 and 128 echoes long. The reason for using 180° pulses to refocus the signal between each line is that this creates the much longer-lived T_2-weighting rather than the shorter-lived T_2*-weighting observed with EPI. In fact, FSE readouts can also use much lower flip angles than 180°, which helps to sustain the echo train beyond the duration of normal T_2 times due to contributions from STE and higher order spin echoes. Regardless of the type, FSE is a very robust imaging method (Fig. 6.11), which is typically free from significant distortions and artifacts because each readout is centered on an RF-refocused spin echo.

Despite its advantages, because of technical difficulties with exciting exactly 180° pulses, a certain amount of the signal is lost beyond the expected T_2 decay. This results in a decay in the echo train that is faster than T_2 decay alone,

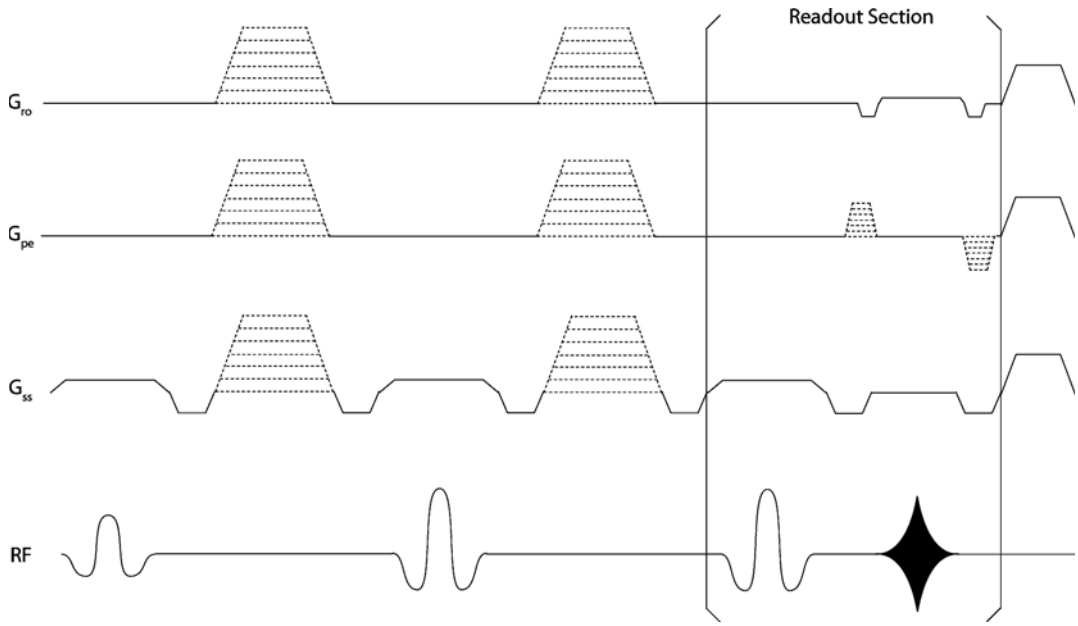

Fig. 6.21 This figure shows a fast spin-echo sequence diagram. The readout section is repeated until the desired number of phase-encode lines is completed for each FSE train. Note the similarities to an EPI readout, which is seen in Fig. 6.1. However, despite the similarities, the EPI readout is much faster and has a much lower SAR than the FSE readout due to the lack of refocusing pulses for each readout line

which limits the image resolution. Another issue with using a train of 180° pulses is that the tissue heating (SAR) from all the RF pulses is quite high, often requiring an increased TR in order to allow for tissue cooling, thus increasing scan time.

These restrictions often limit the number of 180° pulses to less than what is required for a single-shot acquisition. This necessitates a multi-shot acquisition, which has the same shot combination issues as multi-shot EPI acquisitions as well as phase differences between the readout lines if non-180° refocusing RF pulses are used. A common solution to the shot combination difficulties is a PROPELLER acquisition (also called BLADE on Siemens systems), which is an acquisition with rotated segments [21]. These segments can be ordered and acquired in many different ways, all of which are designed to reduce the distortion and to improve robustness to motion. An improvement called SPLICE can be used in PROPELLER to counteract some of the phase inconsistencies between readout lines when non-180° pulses are used; however this reduces the SNR and increases the scan time [22].

Generally, as with segmented *k*-space acquisitions using EPI, multi-shot FSE acquisitions—PROPELLER or standard Cartesian—result in significantly longer scan times and residual image phase inconsistencies which result in distortions and signal loss. Because of these characteristics, FSE acquisitions are not commonly used with DTI and are often only used in regions where EPI is too distorted to effectively acquire the image. In the brain this is often in the brainstem, near the orbits and sinuses, or in regions close to metallic implants.

To review, the FSE acquisition can be used in similar situations as EPI, but there are two key differences between the techniques to keep in mind:

- FSE is more robust to off-resonance distortions.
- EPI is faster and is therefore more commonly used for DTI.

Motion Sensitivity of Diffusion-Weighted Imaging

Motion is the most common source of artifacts in DTI MRI. It is also one of the few artifacts that cannot be reliably avoided with proper setup and testing. Because of this, and the relative sensitivity of DTI to motion, motion corruption is the most common reason to re-run a scan. Motion also is often hard to diagnose, as different motions cause different artifacts. There are too many different types of motion artifacts to cover in this chapter, but it should be the first possibility evaluated when an image is artifacted.

Because of this variability, this section will attempt to outline types of motion and generic correction methods in a general fashion. This will allow you to understand the sources of motion artifacts, and use that knowledge to avoid or choose acquisitions that are robust to motion whenever possible.

The simplest types of motion in DTI are turns and shifts of the head. These are commonly called "rigid" motion. These motions can be intentional, such as a reaction to the scanner or discomfort from lying motionless in the scanner. They can also be unintentional, such as slight motion from breathing, falling asleep, or an involuntary reaction to the noise of the scan.

As with all MRI, motion causes problems in DTI. Because single-shot EPI or FSE acquires a single image in very little time from a single excitation, motion does not often occur during the image generation. It primarily occurs between images, which must then be re-aligned before the processing is performed.

However, if multi-shot EPI or FSE—where data from several excitations are combined to form an image—is used, or if the motion occurs during the image generation during single-shot EPI/FSE, signal changes and image distortions can occur. In this case, rigid motion of the head during imaging will cause blurring of the brain at best, and signal dropout at worst. An example of slight rigid motion can be seen in Fig. 6.22, which shows un-corrected and corrected images with rigid—in this case a turning of the head—motion.

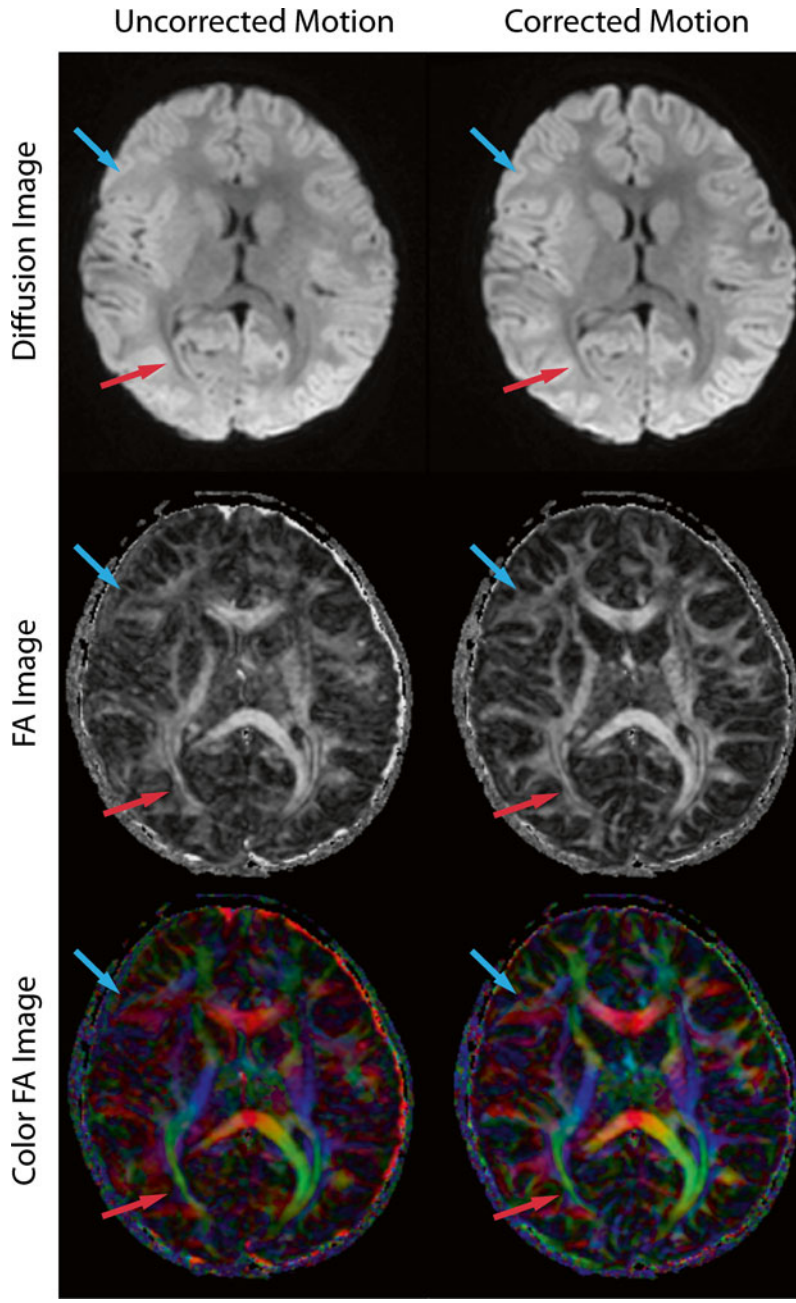

Fig. 6.22 Rigid motion—even minor motion as in this case—can induce blurring in the diffusion tensor calculation. When prospective motion correction is used, these artifacts can be reduced or removed entirely. This allows low contrast (*blue arrow*) and smaller (*red arrow*) regions to be resolved with motion correction. The FA shows how directionally intense the diffusion is while the color FA incorporates the direction of the diffusion as well (*red* is left-right, *blue* is superior-inferior, and *green* is anterior-posterior). Also note that the diffusion image without diffusion correction is relatively crisp, but both the FA and color FA without motion correction look noisy and generally poorly resolved in contrast with the motion correction images. This is typical of motion between the images, and therefore the diffusion images do not properly align for the tensor calculation

Unfortunately, the motion sensitivity of DTI does not stop with rigid motion and single-shot EPI. There are many distortions and artifacts caused by motion in DTI, and in order to understand the more complicated multi-shot scans and other effects of rigid and nonrigid motion, it is important to briefly review MRI data acquisition.

For all MRI, many imaging parameters, such as the field of view (FOV), resolution, and readout type, are controlled at the physical level by the magnetic field gradients in the scanner. The magnetic field gradients that control the imaging are the same ones that are used for diffusion. Thus the magnetic field gradients used for imaging are similar to those used for diffusion, just

with different strengths and shapes. This similarity can cause mixed effects—the diffusion gradients can cause imaging-like effects, and the imaging gradients can cause diffusion-like effects.

In order to understand these effects, however, it is important to remember that the acquired *k*-space and the images themselves are inherently complex valued. This means that each pixel in the image—in both *k*-space and image space—contains a magnitude and phase.

The changes in phase due to motion are called motion-induced phase errors and are common in diffusion imaging. This is because the diffusion-encoding gradients are designed to be very sensitive to molecular motion, which means that any small motion—a heartbeat, a small shift of the head, or even blood flow-induced distortions—can cause a large change in image phase and potentially the magnitude as well. This motion can be rigid, such as a translation or rotation, or nonrigid, such as cerebral spinal fluid or blood pulsing.

The motion-induced phase error (from either rigid or nonrigid motion) can cause interferences and signal cancellation in the image (Figs. 6.4 and 6.23). Importantly, this phase is generated by the diffusion gradients, so each shot (excitation) can have a different phase error. These differences can make it difficult to combine data across shots, and often multi-shot scans require an extra step in the acquisition, called a "navigator" (echo/image) in order to combine the shots without signal cancellation and generation artifacts (Fig. 6.4).

While rigid motion artifacts can be greatly reduced with navigators as well as more advanced motion correction methods, such as prospective motion correction, nonrigid motion artifacts can be more difficult to remove due to the complicated motion that can occur. Generally, the majority of nonrigid phase errors in the brain are caused by pulsation of both blood and cerebral spinal fluid. Luckily, this means that most of the nonrigid phase errors manifest primarily in the basal regions of the brain near the hippocampus, cerebellum, thalamus, and hypothalamus. Therefore, if the scan is focused on more apical regions in the head, the effects of nonrigid phase errors can often be ignored. However, if the region of interest is basal, it is often advantageous to use cardiac gating—and potentially respiratory gating as well—in order to reduce the effects of nonrigid motion in those regions. It is important to note that while this primarily applies to multi-shot techniques, gating can help improve single-shot techniques as well improve the consistency between images.

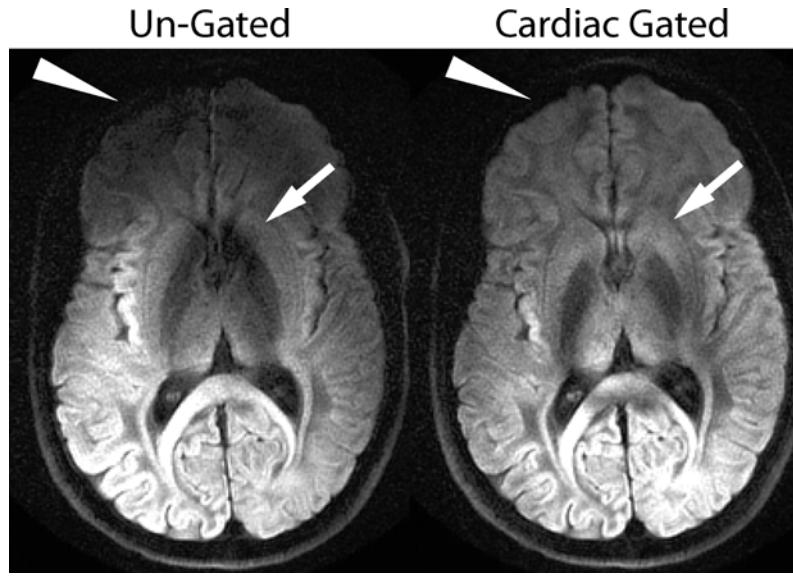

Fig. 6.23 Images of the brain without and with cardiac gating show the signal cancellation that occurs due to the pulsatile motion of brain regions caused by blood or as a consequence of CSF spaces. The gating effectively increases the signal in the affected regions as well as helps to produce consistent signal across all diffusion directions. Note that the pulsatile motion can almost completely remove the signal in specific regions (*arrow*) or generally dim the signal from large regions (*wedge*)

As mentioned above, another source of artifacts due to motion in DTI is that if the images themselves are artifact free, but not well aligned, this can produce significant error in the diffusion calculation. This misalignment can often be remedied through aligning the images before diffusion processing, a process called registration. While this process works well, and is often used in the standard DTI processing chain, it is best to try to avoid motion in the first place if at all possible.

To review, motion is most frequently caused by two sources, both of which can cause major or minor artifacts:

- Motion of the head during scanning, either intentional or unintentional.
- Motion of blood or cerebral spinal fluid in the head due to respiration, the heart, or cerebral spinal fluid pulsations.

The Reconstruction

The reconstruction takes the acquired data and produces images from that data. The acquisition and reconstruction need to work together to produce the final images. In this section we will briefly discuss the reconstruction techniques that have a direct link to how the acquisition is performed.

Parallel Imaging

Parallel imaging was a significant development in MRI because it allows the acquisition of less data than is normally required for the image. Parallel imaging is possible through the use of multi-channel receive coils and pulse sequences which are designed to best take advantage of the speed-up characteristics of parallel imaging.

The parallel imaging reconstruction can be done in many different ways, but the two major groups of methods operate in either *k*-space (GRAPPA) [23] or image space (SENSE) [24]. Parallel imaging is often relatively fast and robust, but it requires a good RF coil shape with an acquisition method that works with—not against—the RF coil. In addition to this, all parallel imaging methods require some kind of coil calibration in conjunction with the standard images.

The classic parallel imaging acquisition is Cartesian acquisitions performed by skipping phase-encode lines in *k*-space. The skipped lines effectively reduce the FOV of the image, which results in a "wrapped" or "aliased" image. The *acceleration factor* (*R*) starts at one (which is a fully sampled image) and the *R* number indicates that every *R*th line is sampled. While it is theoretically limited by the number of receive coils, it is typically less than four for standard brain DTI acquisitions for SNR and artifact reasons. The coil geometry—the placement of the subcoils around the object—also matters. The coil elements (subcoils) may be more or less suited for parallel imaging in different directions, depending on the construction of the coil as a whole.

While the specifics of any parallel imaging method can be very complicated, the advantages are significant. The acquisition speed is increased by the acceleration factor, as is the speed at which *k*-space is traversed in an EPI acquisition. This not only speeds up the acquisition itself, resulting in shorter TE and TR times, but for EPI it also reduces off-resonance distortions by the acceleration factor as well.

However, these benefits do not come without a price: the SNR of a parallel imaging acquisition is lower than the same acquisition when fully sampled (Figs. 6.24 and 6.25). Also, the SNR is no longer homogeneous across the image; it is coil and region dependent, which often results in a lower SNR at the center of the coil, which unfortunately is also often the center of the object. The inherent lower SNR can be offset to some extent by a shorter TE time, but generally the SNR of a parallel imaging acquisition is lower than that of the same acquisition performed without parallel imaging.

Another previously mentioned limitation of parallel imaging is that a coil calibration of some kind is necessary in order to perform the parallel imaging reconstruction. The coil calibration

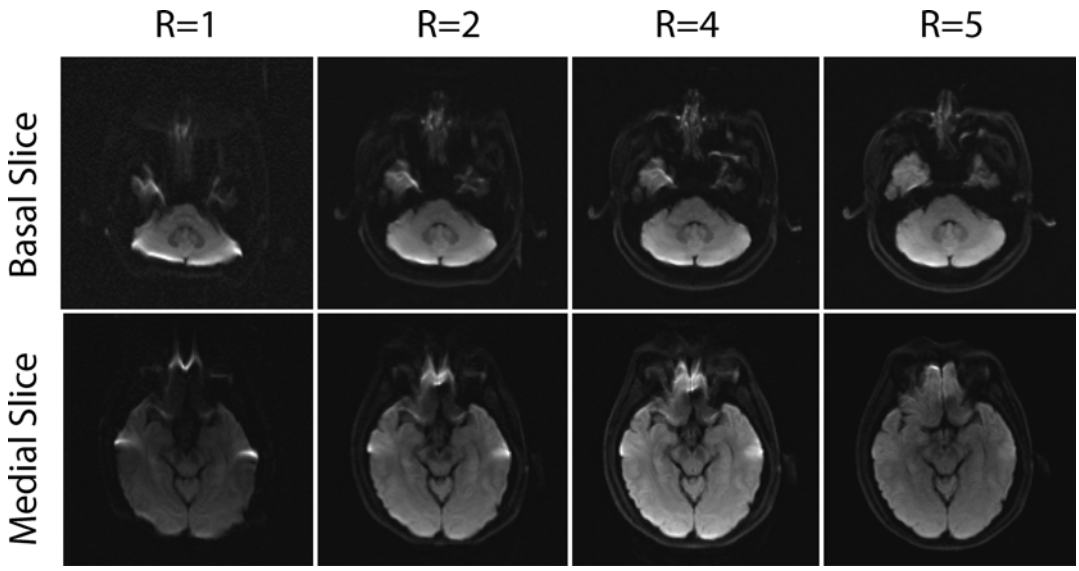

Fig. 6.24 This figure shows progressive parallel imaging values from no parallel imaging ($R=1$), to values of $R=2$, 4, and 5. Note how the most distorted image is $R=1$—the one without parallel imaging—which is due to the reduced scan speed, and the noisiest is the one with a parallel imaging value of 5. When comparing the geometric distortions of the images with different parallel imaging values, it is clear how much distortion is present, even in the $R=2$ images. However, the trade-off is the reduced SNR of the higher parallel imaging factors. It is clear that parallel imaging factors of $R=4$ and above have increased noise values when compared to lower parallel imaging values. This demonstrates the balance between distortion and SNR that parallel imaging can provide

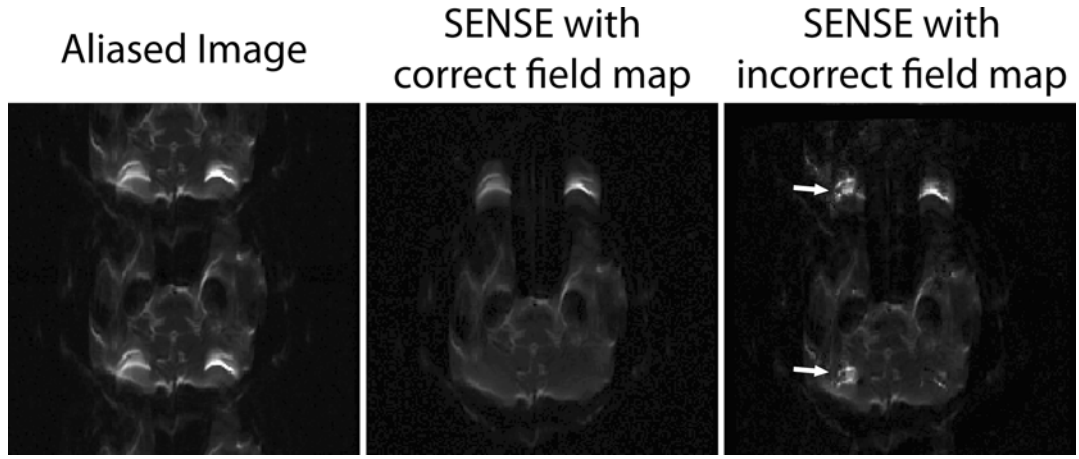

Fig. 6.25 The demonstration in Fig. 6.24 used GRAPPA (a *k*-space based) parallel imaging, but a different set of parallel imaging errors can occur with SENSE (an image space based) parallel imaging. SENSE is based on a coil calibration scan, and this scan can easily become corrupted through motion or distortion differences between the calibration and the EPI scan. When the calibration is correct, the SENSE reconstruction performs very well when un-aliasing the image. However, when the calibration is incorrect—as in the right-most image—the un-aliasing does not perform as well. As the *arrows* indicate, this results in images that are incorrectly un-aliased. In this case, the major artifact is the eye causing a bright spot in the brain, which could potentially be confused with abnormal pathology by a radiologist unaware of the possibility for this error

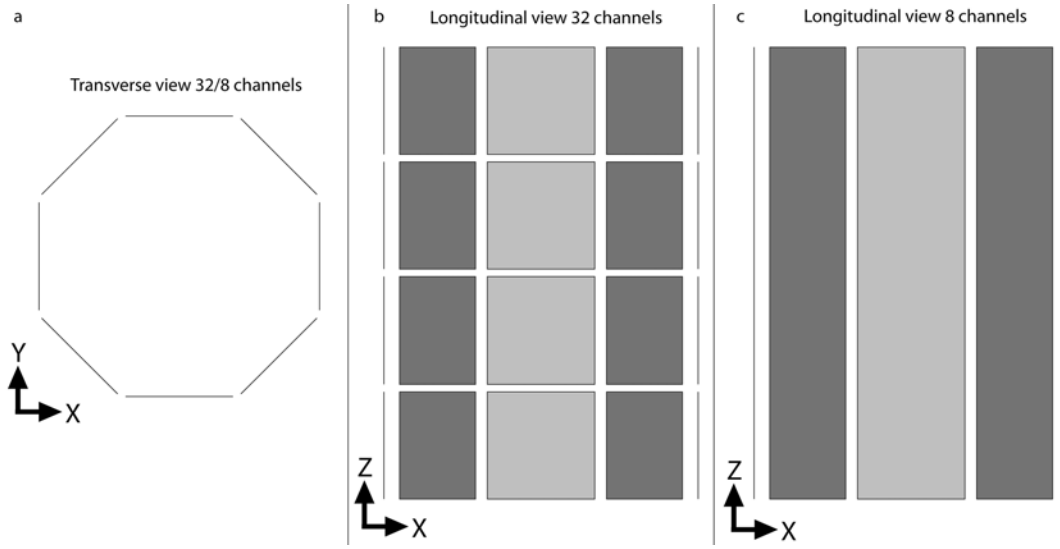

Fig. 6.26 This schematic shows common head coil configurations. It shows a transverse view of a typical 8- or 32-element head coil (**a**), a longitudinal view of a 32-element coil (**b**), and a longitudinal view of an 8-element coil (**c**). Note that this is just an example of a common element setup, and they may vary significantly from coil to coil

method varies between parallel imaging techniques, but in essence all of the calibration methods are ways to interpret the sensitivity of the RF coils, which are then used to form the final image. If the calibration is incorrect, serious artifacts can be produced, which can either mask or appear to be actual medically important information in the images (Fig. 6.25). As a rule of thumb, the *k*-space velocity of the calibration scan should ideally be identical to the *k*-space velocity of the SENSE scan to be distortion matched.

Often, parallel imaging coils for head imaging contain multiples of eight channels (Fig. 6.26). These are typically arranged symmetrically in rings around the head, with each set of eight channels in a different position respective to the apex of the coil. Therefore, a typical 8-channel head coil has a single ring of coils, and a 32-channel head coil has four rings spaced equally along its length. Because of this, a 32-channel head coil should be able to support accelerations in any direction, whereas an 8-channel coil can only reliably support parallel imaging in the *x*- and *y*-axes. With parallel imaging, it is therefore important to consider the coil geometry when deciding on the imaging plane and acceleration factor, in conjunction with the previously discussed imaging parameters. Typically, clinical scanners will have some awareness of the parallel imaging capabilities and the allowed acceleration, but this is often intended to prevent scans from being run which will fail completely.

To review, parallel imaging is frequently used in MRI for three major reasons:

- Parallel imaging reduces the distortion from off-resonance with a negligible SNR penalty if used conservatively.
- Multi-channel coils are commonly available in the clinic.
- Parallel imaging reconstructions are robust and readily available.

Partial Fourier Imaging

Partial Fourier acquisition is another method used to reduce the TE and TR. In this case, *k*-space lines are also skipped; however the lines

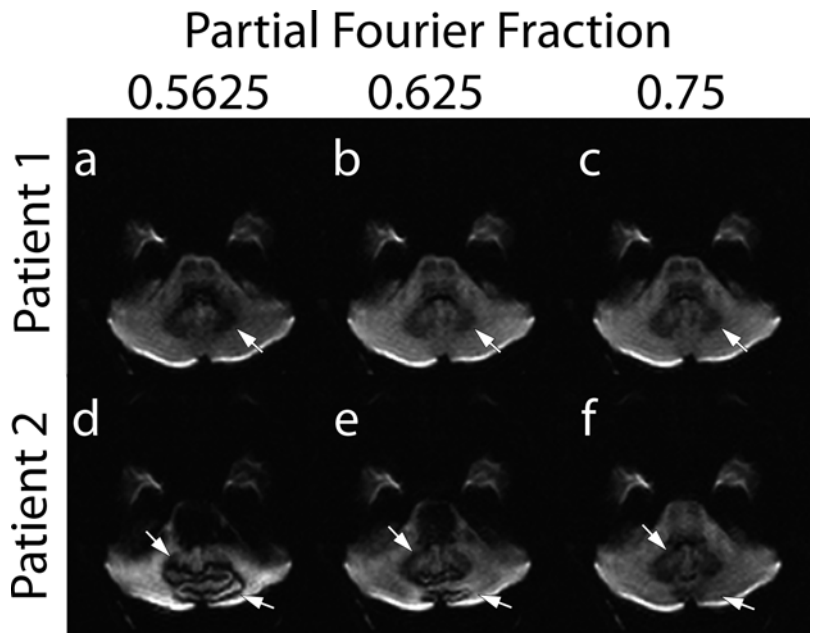

Fig. 6.27 This figure shows images with progressively more partial Fourier sampling, with values from 0.5625 (**a**, **d**), 0.625 (**b**, **e**) to 0.75 (**c**, **f**). Patient 1 shows a case where a very low partial Fourier fraction causes very little artifact (compare **a**–**c**). However, patient 2 is a case where a much higher partial Fourier fraction is required in order to allow a good reconstruction (compare **d**–**f**). The susceptibility of the patients to the partial Fourier fraction is impossible to predict, so a sufficiently high fraction is necessary to avoid significant artifacts in all cases

omitted are a contiguous block of high-frequency readouts that are often skipped before the echo, thereby shortening the TE. The partial Fourier reconstruction then relies not on multiple RF coils but on an assumption about the image—that the phase angle across the image changes slowly. In essence, if the phase angle change across the image is assumed to be slow, the whole *k*-space is not required to correctly reconstruct the image. Because this is generally a valid assumption, a partial Fourier approach is often used to decrease the scan and TE times.

However, as with any imaging technique where *k*-space is sampled less than it should be, sampling too few lines in *k*-space will result in a distorted image (Fig. 6.27). It is difficult to determine how much is too much, as it often depends on the scan and the phase angle change in the object [25]. As with parallel imaging, it is always better to err on the side of caution rather than have an artifacted scan.

To review, partial Fourier imaging is often used clinically for two reasons:

- It is a straightforward way to shorten the TE and TR of scans without inducing significant artifacts if used conservatively (Fig. 6.27).
- The reconstruction is robust and widely implemented.

Eddy Current Correction

Eddy currents, as previously discussed, can cause geometric distortions in diffusion-weighted images (Figs. 6.12 and 6.18). While the Double Spin-Echo (DSE) pulse sequence approach to eddy current distortion reduction is one possible solution, it is also possible to correct eddy current distortions in post-processing [11, 26]. The post-processing consists of an alignment of the group of images in the diffusion series to ensure they

are all well aligned with one another before the diffusion tensor processing step takes place. This alignment is typically performed as part of the DTI post-processing pipeline in conjunction with motion correction (and sometimes even distortion correction) because without correcting for even mild motion and eddy currents, the tensor computation can become significantly degraded.

To review, eddy currents can be corrected in the acquisition and reconstruction:

- In the acquisition a DSE scan can significantly reduce the eddy current distortions.
- In the reconstruction, registration can be performed to reduce the eddy current distortions.

Pediatric Considerations

The previous sections of this chapter have been written generally for any kind of DTI—pediatric or otherwise. However, as pediatric imaging is performed much less often than adult imaging, protocols are often adapted from adult studies for use in pediatric exams. This conversion is typically minor; however there are few changes that should be considered when modifying a standard DTI protocol for pediatric imaging.

An important consideration in the acquisition for pediatric imaging is that children often are less likely to follow instructions and are more likely to move while in the scanner. Because of this, acquisitions that are robust to motion, such as PROPELLER or single-shot EPI, are more commonly used. Other types of prospective and retrospective motion corrections are beneficial and can be used; however these are beyond the scope of this section. A simple method to help reduce motion is to simply add more pads around the patient's head to help discourage head movement during the scan session.

Another pediatric DTI imaging consideration is the size of the head. Often protocols designed for adults will have FOVs that are substantially larger than what is required for children. In this case, it is important to remember that a smaller FOV requires stronger gradients than a larger FOV, so reducing the FOV to better tailor it to the smaller head asks more of the imaging gradients. It simply may not be possible to achieve the desired scan parameters (e.g., TE and TR) with a smaller FOV, but this is very system dependent.

Additionally, the SAR limit for children—who are significantly lighter than adults—is significantly lower. This can cause problems for FSE or spin-echo sequences, and can be a hidden surprise when transitioning from adult to pediatric imaging. The SAR is difficult to change without significantly changing the type of imaging, so it may be necessary to change the imaging type or slow down the acquisition (increase the TR) in order to perform the desired type of imaging.

Finally, as children's brains are still growing, there is less developed structure to provide diffusion contrast, so the diffusion values need to be reduced. As values around 1000 s/mm^2 are typically used in adults, values less than that, typically around 700 s/mm^2, are used in pediatric DTI studies [27].

As we have suggested earlier, it is vitally important to test the adapted sequence and protocol before using it on a child. This will ensure that it proceeds smoothly and quickly—which is crucial to ensure high quality results with the least amount of motion in pediatric studies.

To review, there are four major changes to be made for pediatric DTI:

- Because children are more unlikely to follow instructions and hold still, any motion correction or motion restriction is greatly encouraged.
- The head is smaller, so the FOV should be reduced to better fit the smaller anatomy.
- The SAR limit is lower because children are smaller than adults, so it is important to test the SAR of the sequence before scanning a child.
- Because the brain is still developing, the diffusion of water is typically higher in children, so a lower *b*-value should be used when compared to adults.

Conclusion

We hope that this chapter has given you a basic understanding of the acquisition for diffusion tensor imaging. Above all, we advise you to test parameters for yourself to see how best to tune them for your application. In order to help you with this process, we have provided basic descriptions and images of the most important parameters and acquisition methods. Our hope is that these descriptions and examples will help you run the best DTI acquisitions for your applications.

Acknowledgements The authors would like to acknowledge Samantha Holdsworth for the helpful discussions and assistance in collecting some of the images used in this chapter, Didem Aksoy for assistance in acquiring some of the images used herein, and Eric Aboussouan for help in creating some of the figures.

References

1. Stejskal EO, Tanner JE. Spin diffusion measurements: spin echoes in the presence of a time-dependent field gradient. J Chem Phys. 1965;42(1):288. doi:10.1063/1.1695690.
2. Basser PJ, Mattiello J, LeBihan D. MR diffusion tensor spectroscopy and imaging. Biophys J. 1994;66(1):259–67. doi:10.1016/S0006-3495(94)80775-1.
3. Pierpaoli C, Basser PJ. Toward a quantitative assessment of diffusion anisotropy. Magn Reson Med. 1996;36(6):893–906. Retrieved from http://www.ncbi.nlm.nih.gov/pubmed/8946355.
4. Tuch DS, Reese TG, Wiegell MR, Makris N, Belliveau JW, Wedeen VJ. High angular resolution diffusion imaging reveals intravoxel white matter fiber heterogeneity. Magn Reson Med. 2002;48(4):577–82. doi:10.1002/mrm.10268.
5. Bammer R, Holdsworth SJ, Aksoy M, Skare ST. Phase errors in diffusion-weighted imaging. In: Jones DK, editor. Diffusion MRI: theory, methods, and applications. New York, NY: Oxford University Press; 2011. p. 218–49.
6. Skare ST, Bammer R. EPI-based pulse sequences for diffusion tensor MRI. In: Jones DK, editor. Diffusion MRI: theory, methods, and applications. New York, NY: Oxford University Press; 2011. p. 182–202.
7. Setsompop K, Gagoski BA, Polimeni JR, Witzel T, Wedeen VJ, Wald LL. Blipped-controlled aliasing in parallel imaging for simultaneous multislice echo planar imaging with reduced g-factor penalty. Magn Reson Med. 2012;67(5):1210–24. doi:10.1002/mrm.23097.
8. Tuch DS. Q-ball imaging. Magn Reson Med. 2004;52(6):1358–72. doi:10.1002/mrm.20279.
9. Assaf Y, Cohen Y. Structural information in neuronal tissue as revealed by q-space diffusion NMR spectroscopy of metabolites in bovine optic nerve. NMR Biomed. 1999;12(6):335–44. Retrieved from http://www.ncbi.nlm.nih.gov/pubmed/10516615.
10. Skare ST, Clayton DB, Newbould RD, Moseley ME, Bammer R. A fast and robust minimum entropy based non-interactive Nyquist ghost correction algorithm. In 14th Annual Meeting of ISMRM, Seattle, WA, 2006.
11. Andersson JLR, Skare S. A model-based method for retrospective correction of geometric distortions in diffusion-weighted EPI. Neuroimage. 2002;16(1):177–99. doi:10.1006/nimg.2001.1039.
12. Van Vaals J, Bergman AH. Optimization of eddy-current compensation. J Magn Reson. 1990;70(August 1989):52–70.
13. Reese TG, Heid O, Weisskoff RM, Wedeen VJ. Reduction of eddy-current-induced distortion in diffusion MRI using a twice-refocused spin echo. Magn Reson Med. 2003;49(1):177–82. doi:10.1002/mrm.10308.
14. Wider G, Doetsch V, Wuerthrich K. Wider_1994_eddy_current_correction.pdf. J Magn Reson. 1994;108:255–8.
15. Holdsworth SJ, Skare S, Newbould RD, Guzmann R, Blevins NH, Bammer R. Readout-segmented EPI for rapid high resolution diffusion imaging at 3 T. Eur J Radiol. 2008;65(1):36–46. doi:10.1016/j.ejrad.2007.09.016.
16. Bammer R, Stollberger R, Augustin M, Simbrunner J, Offenbacher H, Kooijman H, et al. Diffusion-weighted imaging with navigated interleaved echo-planar imaging and a conventional gradient system. Radiology. 1999;211(3):799–806. Retrieved from http://www.ncbi.nlm.nih.gov/pubmed/10352609.
17. Butts K, Crespigny AD, Pauly JM, Moseley M. Diffusion-weighted interleaved echo-planar imaging with a pair of orthogonal navigator echoes. Magn Reson Med. 1996;35(5):763–70.
18. Butts K, Pauly J, Crespigny AD, Moseley M. Isotropic diffusion-weighted and spiral-navigated interleaved EPI for routine imaging of acute stroke. Magn Reson Med. 1997;38(5):741–9.
19. Skare S, Newbould RD, Clayton DB, Bammer R. Propeller EPI in the other direction. Magn Reson Med. 2006;55(6):1298–307. doi:10.1002/mrm.20890.
20. Busse RF, Brau ACS, Vu A, Michelich CR, Bayram E, Kijowski R, et al. Effects of refocusing flip angle modulation and view ordering in 3D fast spin echo. Magn Reson Med. 2008;60(3):640–9. doi:10.1002/mrm.21680.
21. Pipe JG. Motion correction with PROPELLER MRI: application to head motion and free-breathing

cardiac imaging. Magn Reson Med. 1999;42(5): 963–9. Retrieved from http://dx.doi.org/10.1002/(SICI)1522-2594(199911)42:5<963::AID-MRM17>3.0.CO;2-L.

22. Deng J, Omary RA, Larson AC. Multishot diffusion-weighted SPLICE PROPELLER MRI of the abdomen. Magn Reson Med. 2008;59(5):947–53. doi:10.1002/mrm.21525.
23. Griswold MA, Jakob PM, Heidemann RM, Nittka M, Jellus V, Wang J, et al. Generalized autocalibrating partially parallel acquisitions (GRAPPA). Magn Reson Med. 2002;47(6):1202–10. doi:10.1002/mrm.10171.
24. Pruessmann KP, Weiger M, Scheidegger MB, Boesiger P. SENSE: sensitivity encoding for fast MRI. Magn Reson Med. 1999;42(5):952–62. Retrieved from http://www.ncbi.nlm.nih.gov/entrez/query.fcgi?cmd=Retrieve&db=PubMed&dopt=Citation&list_uids=10542355.
25. Jaermann T, Pruessmann KP, Valavanis A, Kollias S, Boesiger P. Influence of SENSE on image properties in high-resolution single-shot echo-planar DTI. Magn Reson Med. 2006;55(2):335–42. doi:10.1002/mrm.20769.
26. Horsfield MA. Mapping eddy current induced fields for the correction of diffusion-weighted echo planar images. Magn Reson Imaging. 1999;17(9): 1335–45.
27. Sundgren PC, Dong Q, Gómez-Hassan D, Mukherji SK, Maly P, Welsh R. Diffusion tensor imaging of the brain: review of clinical applications. Neuroradiology. 2004;46(5):339–50. doi:10.1007/s00234-003-1114-x.

Checking and Correcting DTI Data

7

Chantal M.W. Tax, Sjoerd B. Vos,
and Alexander Leemans

Learning Points

- Data quality assurance is important in DTI.
- Artifacts can severely affect subsequent qualitative and quantitative analyses.
- Bad data quality can be detected during acquisition or image processing.
- Correction of artifacts can be done during the acquisition and image processing stage.
- Quality assurance can be used to improve data quality on the scanner.

Introduction

Diffusion MRI data is, like any other MRI technique, prone to artifacts. Most diffusion MRI analyses are based on a voxel-wise computation of quantities from a series of diffusion-weighted images (DWIs) acquired with different orientation and magnitude of diffusion sensitization, and the results may be severely affected by artifacts. It is therefore of great importance to avoid or correct for these artifacts before subsequent analyses [1].

There are various ways to classify artifacts in diffusion MRI data. They may be present in the DWIs themselves (e.g., Gibbs ringing, susceptibility artifacts), or become apparent when combining all DWIs (e.g., subject motion). Some artifacts are related to MRI acquisition in general (e.g., Gibbs ringing and EPI distortions) or are specific to diffusion weighting. Spin-echo echo-planar imaging (SE EPI) is often the method of choice for diffusion acquisition since it is a relatively fast technique, but the resulting images are locally distorted due to differences in tissue susceptibility. The rapid switching of gradients required when acquiring diffusion MRI data leads to eddy current distortions. The origin of some artifacts is system related (e.g., eddy current distortions, signal dropouts, vibration artifacts), whereas others are subject related (subject motion, susceptibility artifacts).

In this chapter, we will review the most clinically relevant artifacts from different angles. It is not the purpose to extensively discuss each artifact, but to focus on the practical issues instead. The origin, recognition, and correction methods for each artifact are briefly outlined in the first section, where we specifically focus on the different processing stages (Fig. 7.1). We will distinguish

C.M.W. Tax, MSc (✉) • A. Leemans, PhD
PROVIDI Lab, Image Sciences Institute, University Medical Center Utrecht, Room E.02.5.54, 3508 GA Utrecht, The Netherlands
e-mail: chantal@isi.uu.nl

S.B. Vos, PhD
PROVIDI Lab, Image Sciences Institute, University Medical Center Utrecht, Room E.02.5.54, 3508 GA Utrecht, The Netherlands

Translational Imaging Group, Centre for Medical Image Computing, University College London (UCL), London, UK

W. Van Hecke et al. (eds.), *Diffusion Tensor Imaging*, DOI 10.1007/978-1-4939-3118-7_7

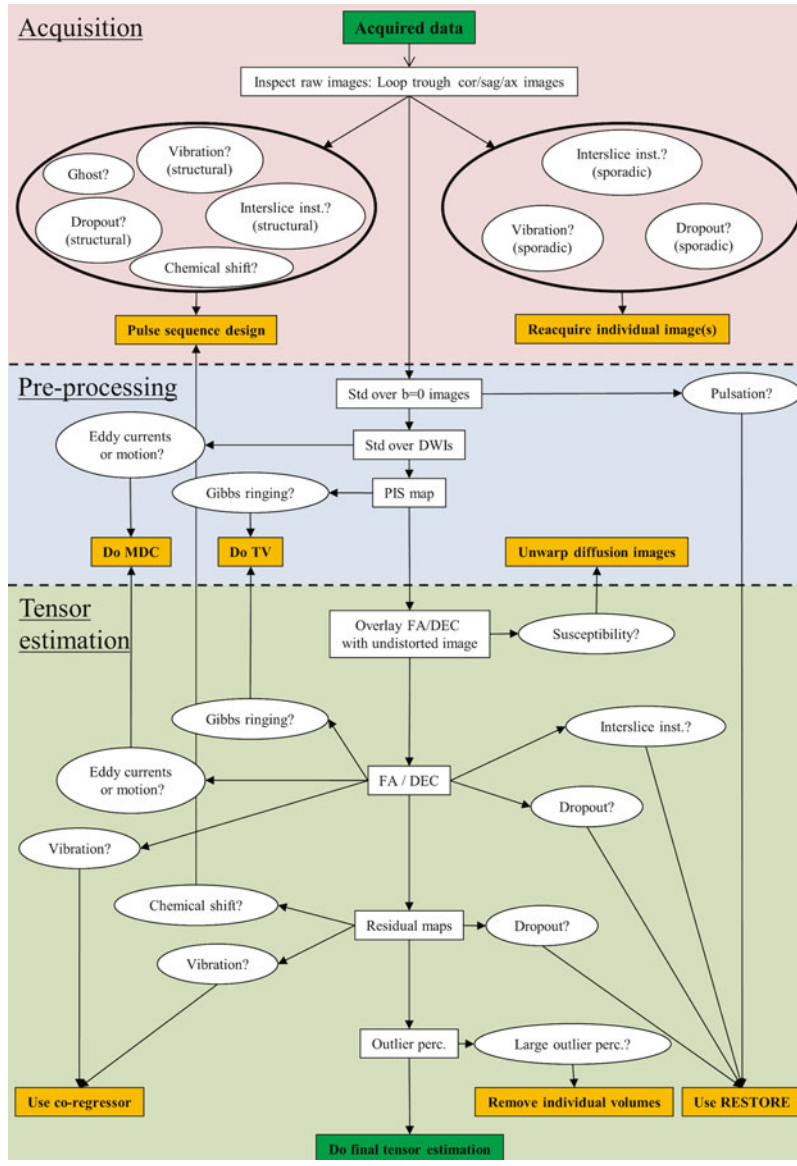

Fig. 7.1 Decision tree scheme for checking and correcting of diffusion data. *Std standard deviation*, *interslice inst.* interslice instabilities, *PIS* physically implausible signal, *MDC* motion-distortion correction, *TV* total variation, *FA*/*DEC* direction-encoded FA map, *perc.* percentage

the acquisition stage, in which we consider recognition and correction on raw data only, from the image processing stage, which includes any form of processing of the data (e.g., fitting a tensor or calculating standard deviations of the measurements). The central question throughout this chapter is: *How can I recognize and, potentially, correct for artifacts, either during scanning or when I have already acquired the data*? We present a decision tree scheme, which can be used as a stepwise manual for optimal data acquisition and processing (including pre-processing and tensor estimation), answering the question to *which acquisition and processing methods to consider in a stepwise manner for optimal data quality for subsequent analysis*? Obviously, prevention is better than cure, which is why we will discuss methods to assure data quality in the second section. Quality assurance (QA) focuses on *how to make sure that the scanner is able to acquire high quality data, before actual patient data acquisition*. We provide some examples when to accept or reject data. Finally, it is important to understand *how artifacts influence quantitative and directional diffusion MRI mea-*

sures. To this end, the last section focuses on the possible effect of artifacts on voxel-wise computed quantitative measures such as mean diffusivity (MD) and fractional anisotropy (FA) and on tractography results. The guidelines for checking and correcting data presented in this chapter are not specific to DTI only, but often extend to other diffusion acquisition techniques such as high angular resolution diffusion imaging (HARDI).

Recognition and Correction of Artifacts

Eddy Current-Induced Distortions

Origin

Conductive elements of the MRI scanner (e.g., the gradient coils) permit the flow of electric charges. When a conductor is located in a changing magnetic field, this will induce currents in the conductor. Because their flow patterns resemble swirling eddies in a river, they are called eddy currents. Besides gradients for spatial localization of the MR signal, additional magnetic gradients are used to make MR sensitive to diffusion. The diffusion-sensitizing gradients have to be switched on and off very rapidly, and induce eddy currents [2] in conductors present. The eddy currents, in turn, induce additional magnetic gradient fields which will change the actual diffusion gradient, as can be seen in Fig. 7.2b, where the actual diffusion gradient is different from the desired one in Fig. 7.2a. The effect on the DWIs is twofold: overlap of the changed diffusion gradient with spatial encoding gradients will lead to geometric distortions and thus misalignment of individual DWIs; and the deviation of the diffusion gradient from what we expect will lead to errors in diffusion estimates.

Recognition and Correction in Acquisition Stage

When eddy current-induced fields overlap with the spatial encoding period of the image acquisition, this will lead to geometric distortions. These distortions are visible in the raw DWIs in the phase-encoding direction (PE, most commonly anterior–posterior or y-direction) and depend on the direction of the eddy current gradient. An eddy current gradient in left–right (x) direction will result in a shear in the axial (xy) plane, assuming that the PE direction is anterior–posterior (y). Likewise, an eddy current gradient in y-direction causes scaling in y-direction (Fig. 7.3a shows compression in y-direction), whereas eddy current gradients in inferior–superior (z) direction translates each slice in y-direction dependent on the slice position [3].

Generation of eddy currents is inevitable in diffusion MRI; however, there are methods to minimize them. Replacing the single-refocused spin-echo diffusion preparation (Fig. 7.2a) by a twice-refocused spin-echo (TRSE) preparation (Fig. 7.2c) reduces the eddy currents resulting in less severe geometric distortions [4]. This is also

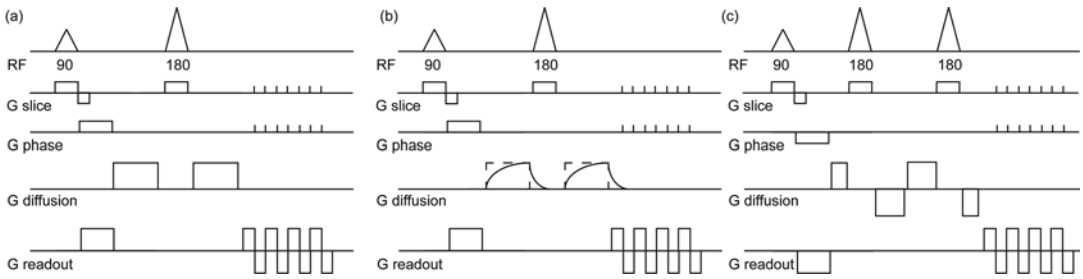

Fig. 7.2 Diffusion MR sequences. (**a**) For the standard, once-refocused, diffusion preparation, after the excitation (90° RF pulse) there are two gradients that sensitize the signal to diffusion, with a refocusing pulse (180° radio-frequency (RF) pulse) at half the echo time (TE/2) to form an echo during the readout. (**b**) The diffusion gradient is not as desired and overlaps with the spatial encoding gradients. (**c**) TRSE: The twice-refocused diffusion preparation (*bottom line*) has two refocusing pulses splitting four gradient blocks to form an echo during the readout

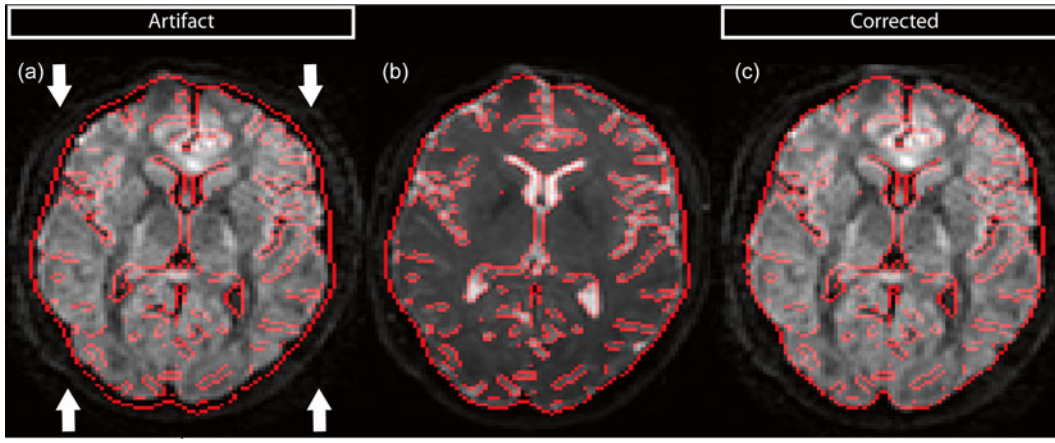

Fig. 7.3 Example of DW image with scaling induced by eddy currents in the phase-encoded anterior–posterior (AP, indicated by the *arrows*) direction (**a**), compared to the undistorted B_0 image (**b**). The lines overlaid in red indicate brain edges and boundaries of the undistorted B_0 image. (**c**) Raw data in which the effect of eddy currents is minimized

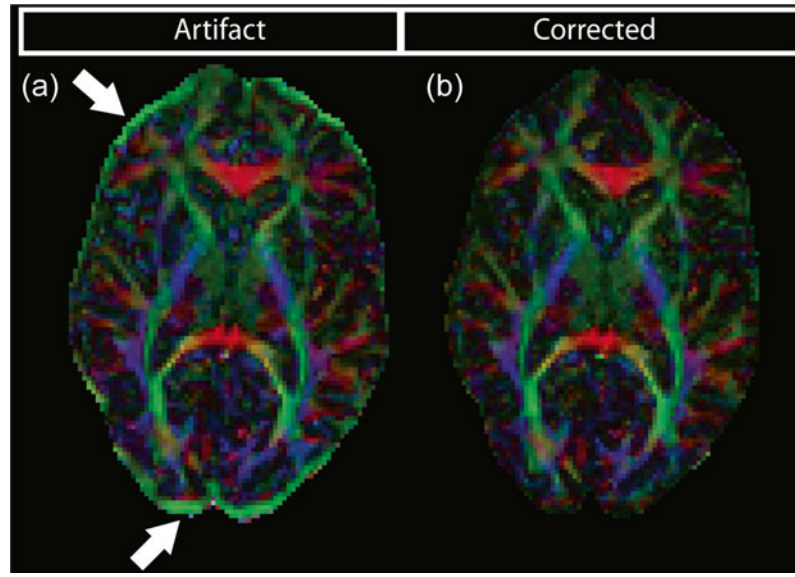

Fig. 7.4 (**a**) DEC map showing an orientational bias in the high anisotropy rim at the periphery of the brain. (**b**) The same map calculated after distortion correction

called dual spin-echo (DSE) diffusion imaging. The TRSE/DSE diffusion sequence is available in most, if not all, recent MRI scanners, making this an easy to use option. Figure 7.3c shows a raw image with minimal eddy current distortions. The downside of a TRSE sequence is a small increase in echo time (TE), caused mainly by the additional 180 pulse. As a result, the signal-to-noise ratio (SNR) decreases and the repetition time (TR) may increase, which would result in a longer acquisition time.

Recognition and Correction in Image Processing Stage

Different geometric distortions of every individual DWI will result in misalignment of the images, which will, in general, affect diffusion-derived measures that are estimated on a voxel-by-voxel basis. Eddy current-induced misalignment artifacts become visible as bands of increased FA at the periphery of the brain (Fig. 7.4a) but, although less pronounced, are also present throughout the brain. The direction-

encoded color (DEC) maps [5] furthermore show a dominant orientation in these bright rims, which is typical for eddy current-induced geometric distortions when they are only visible in the phase-encoding (PE) orientation of the image.

Correction for eddy current-induced distortions is commonly done in the diffusion MRI image processing pipeline. Various image registration based methods have been developed for correction [2, 6, 7]. Typically, mutual information is used to register all DWIs to the non-DW ($b=0$) image, which has no eddy current-induced distortions. For this purpose no additional scans are needed. Figure 7.4b displays the DEC map after correction.

Besides image distortions, eddy currents can also influence diffusion measurements in another way. Figure 7.2b already showed that the actually applied diffusion gradient differs from the desired one. The diffusion weighting of an image is thus not exactly what we expect, which will result in errors in the estimates of the diffusion parameters. This is often hard to recognize and impractical to correct for.

Subject Motion

Origin

The acquisition of a typical clinical DTI dataset takes around 5–10 min, for research purposes this can even be longer. Although subjects are instructed to lie still during a scan, head or body motion is difficult to avoid. Motion can be subdivided into translations (in *x*-, *y*-, and *z*-direction) and rotations (yaw, pitch, and roll). Many DWIs have to be acquired to estimate diffusion properties accurately, and misalignment due to motion will lead to errors in these estimates.

Recognition and Correction in Acquisition Stage

Instead of a time-consuming detailed slice-by-slice inspection of the raw DW MRI data, subject motion can also be investigated by looping through the DW images at a frame rate of approximately ten frames per second, or quickly toggling between the first and last acquired DW MRI image.

During acquisition, all care should be taken to immobilize the subject. This is commonly done by placing cushions, or pads, between the subject's head and the inside of the head coil. This makes it easier for the subject to keep his or her head still.

Even for the most willing and cooperative subjects, head motion is likely to occur to some extent. Slight movement of the brain may result in a mismatch between subsequent slices, which means these slices cannot be combined correctly. Several new pulse sequences have been proposed that can correct for *in-plane* motion, e.g., PROPELLER or SNAILS [8]. However, these cannot correct for *through-plane* motion. Prospective volume registration can account for through-plane motion. Here, the field-of-view (FOV) is repositioned after each 3D image volume, so after each TR. This method can correct the motion for any subsequent volume accurately, but the volume in which motion occurred is corrupt and must be re-acquired, elongating the scan time. To truly account for any motion, however, the motion must be detected with a higher temporal resolution. Zaitsev et al. [9] proposed such a real-time prospective motion correction setup: when head motion is detected, the imaging field-of-view is adjusted accordingly for the next excitation. Their system used a mouthpiece with markers outside the mouth that could be imaged by optical cameras outside of the magnet bore. In this way, rigid body motion of the head can be detected and corrected for a wide range of rotations and translations. Recent advances in this field were focused on ease-of-use as well as correction accuracy, with methods that use a small object attached to the subject's forehead that is imaged by a camera within the bore, capable of correcting translations and rotations as small as 10 μm and 0.01° [10, 11]. For an extensive overview, one is referred to [12]. Currently, these methods are transforming from a purely developmental setup to products shared between neuroscientific research groups.

Recognition and Correction in Image Processing Stage

Subject motion will, just like eddy current geometric distortions, result in misregistration of DW volumes. This misregistration can in some cases also be recognized by rims of high anisotropy

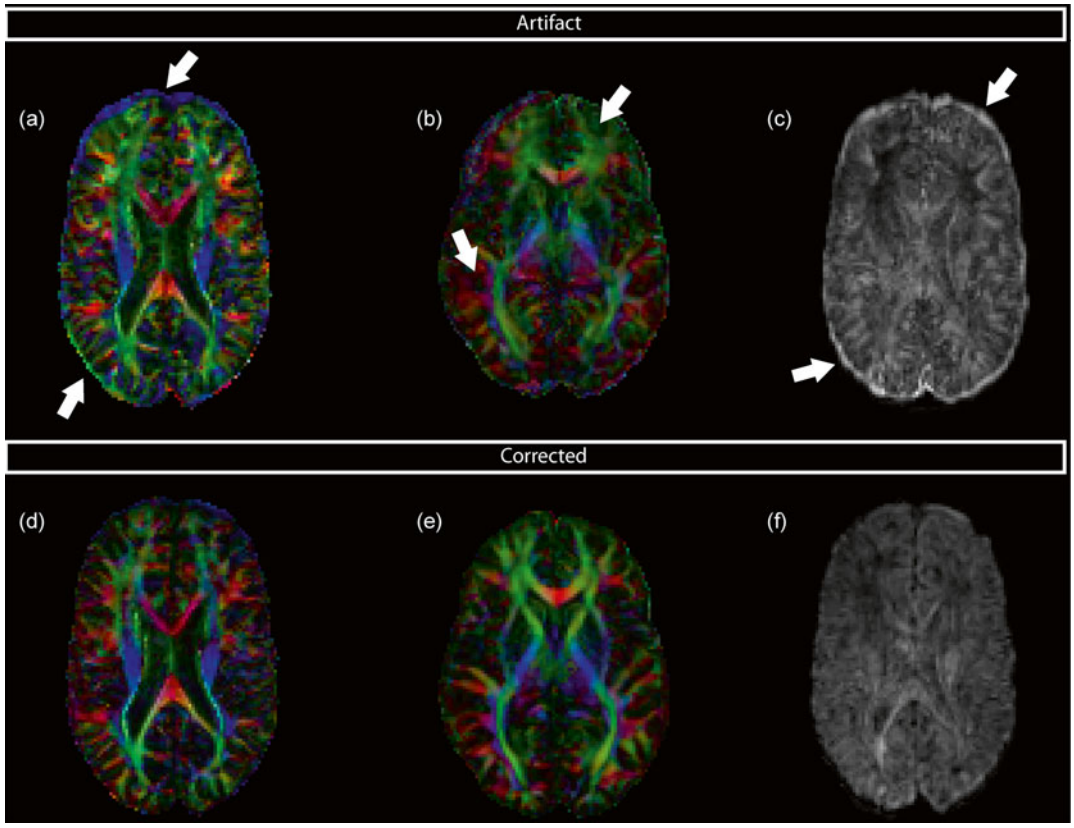

Fig. 7.5 Subject motion can be recognized on FA/DEC maps by a bright rim (**a**) or an overall change of FA (**b**). (**c**) When plotting the standard deviation across all DWIs, bright rims at brain edges indicate misalignment. (**d–f**) show the same maps, corrected for subject motion

with orientational bias at the periphery of the brain, but this will, in contrast to misregistration produced by eddy currents, appear on all sides of the brain (Fig. 7.5a). In other cases, overall changes in FA or MD can be observed (Fig. 7.5b). In addition to DEC maps, misregistration artifacts (resulting from either eddy currents or subject motion) can also be recognized by inspecting images of the standard deviation across the DWIs, in which the size and brightness of the rims at brain edges and tissue interfaces reflect the degree of misalignment (Fig. 7.5c). Recognition and correction of subject motion on these maps is not always straightforward and depends largely on the kind of motion (abrupt or gentle, small or large).

Image registration is commonly employed in diffusion MRI to correct for subject motion, and uses six parameters in total for translation and rotation. The corrected maps are visualized in Fig. 7.5d–f. The total transformation of eddy current distortion correction and subject motion are ideally applied at once on the original images [2]. A complication when dealing with registration of DWIs is that they contain directional information: diffusion gradients are applied in a specified direction. When the subject is rotated, one should rotate the *b*-matrix associated with each DWI. Neglecting to rotate the *b*-matrix can lead to incorrect diffusion metrics and erroneous tractography [13].

Interslice Instabilities

Origin

A specific type of motion artifact is interslice instability. This is discussed separately, since it only arises when motion occurs during an acquisition in which slices are scanned interleaved, i.e., even and odd-numbered slices of an EPI volume are collected sequentially (so first slices 1, 3, 5… and subsequently slices 2, 4, 6…).

Recognition and Correction in Acquisition Stage

Although it seems straightforward, checking the raw data in orthogonal views other than the slice direction is often omitted. Interslice instabilities such as intensity differences between slices resulting from interleaved acquisition can be recognized on these orthogonal views, see Fig. 7.6a. Artifacts arising from the interleaved acquisition are visible in the corpus callosum and at the brain edges, and result in signal dropouts. The best way to prevent these artifacts if they are motion related is to properly immobilize the subject or to use prospective motion correction as discussed above.

Recognition in Image Processing Stage

Interslice instabilities can become visible on FA DEC maps. The influence of motion in combination with interleaved acquisition is illustrated in Fig. 7.6b, where the artifact becomes apparent in different brain regions, such as the corpus callosum.

Table Vibrations

Origin

Table vibrations are the result of low-frequency mechanical resonances of the system due to application of the diffusion gradients [14, 15]. Spatial phase ramps in the phase image occur when neighboring voxels move over a different distance. These phase ramps correspond with shifts in k-space that result in signal loss. The amount of signal loss for a standard *b*-value of 1000 s/mm^2 can be 5–17 %, and increases with the *b*-value. Moreover, the twice-refocused spin-echo sequence suffers more from these vibrations due to the even more rapid switching of the gradients [15]. So, although the TRSE sequence ameliorates the eddy current-induced distortions, one must ensure that it does not come at the cost of increased table vibration.

Recognition and Correction in Acquisition Stage

Table vibrations can result in localized signal loss, which is not a result of diffusion. The movement resulting from vibration is primarily directed in left–right direction, and the artifact is therefore visible in DWIs with a large component of the diffusion gradient in the left–right direction.

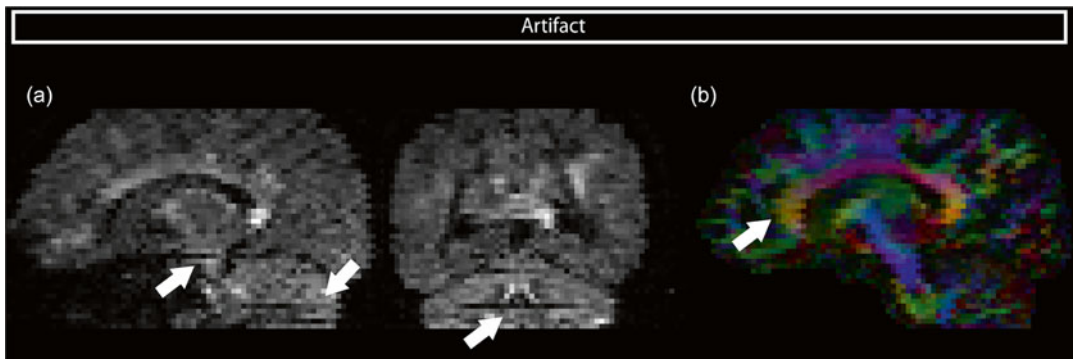

Fig. 7.6 (**a**) Interslice instabilities might not be visible on the axially interleaved acquisition plane, but becomes visible on the orthogonal planes in a DWI volume. (**b**) DEC map with interleave artifact

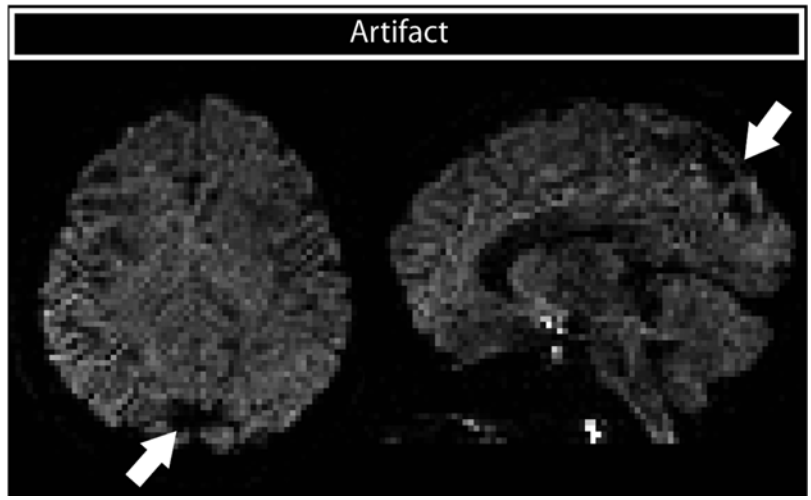

Fig. 7.7 Signal dropouts in DWIs with a large component of the diffusion gradient in *left–right* orientation resulting from table vibrations

Figure 7.7 illustrates this signal loss in a left–right sensitized image. When the region of signal loss overlaps with pathology, important diagnostic information can get lost.

Most diffusion protocols do not acquire the whole k-space, but use partial coverage instead to shorten TE which reduces scan time and increases SNR. In case of partial k-space acquisitions, vibrations could move the center of k-space out of the scanned k-space, resulting in severe loss of information for proper reconstruction of the DWI. Several acquisition options exist to reduce vibrations. Most conveniently, a mechanical decoupling of the patient table and gradient coils would reduce the vibrations themselves. This is, however, not a user acquisition choice as such, since this is determined by the vendor when designing the scanner. Second, full k-space coverage avoids this issue, generally at the expense of increases in TE [14]. At the expense of longer scan times, one could opt for a longer TR which would allow for the decay of vibrations between subsequent excitations.

Recognition and Correction in Image Processing Stage

Quantitative measurements such as FA and MD can be influenced by local signal dropouts in DWIs. In DEC maps, areas of the artifact can have artificially high FA in left–right orientation as can be seen in Fig. 7.8a. To improve the reliability of diffusion measures such as FA, a tensor fitting approach should be used that can account for the influence of this signal dropout. One possibility is to include the influence of the artifact as co-regressor in the tensor estimation [14]. The result of data correction can be appreciated in Fig. 7.8b. When one is not very familiar with these color-coded DEC maps or when pathology is involved, it might be hard to recognize areas of artificially high FA. In such cases, residual maps, which represent the difference between the actual measurement and the prediction after fitting the tensor model to the data, can illustrate the artifact more specifically. Signal dropouts in one or a few DWIs generally cause the tensor fit to be less accurate in those regions, which causes locally higher residuals (Fig. 7.8c). After correction, the residual map does not show the vibration artifacts anymore (Fig. 7.8d).

Pulsation

Origin

Even when the subject lies still, motion of brain tissue occurs due to the inflow of arterial blood following cardiac systole. These displacements are in the order of 1 mm and cannot be considered as simple rigid body motion as different brain regions have different displacement profiles. The largest motion can be observed in inferior

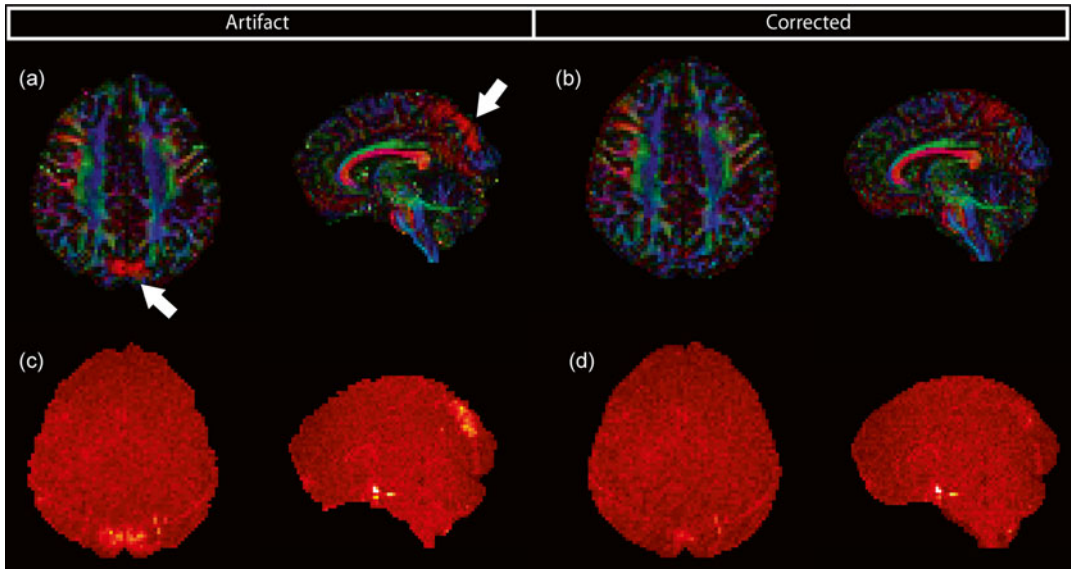

Fig. 7.8 (**a**) Areas of artificially high FA in *left–right* direction resulting from vibration artifacts. (**b**) Same FA map after correction for the vibration artifact by accounting for signal dropouts in tensor estimation. Mean residual map of the tensor fit (**c** and **d**) gives an indication of data quality and is sensitive to artifacts (**c**)

regions of the brain that move mostly along the inferior–superior direction [16]. Pulsation can be recognized for example around the lateral ventricles and brainstem. Two complications arise in further DTI analysis due to these pulsations. When DWIs are acquired in different stages of the cardiac cycle, they will have different local deformations, which results in local misregistration of structures between successive images. Furthermore, incoherent intra-voxel motion leads to additional signal attenuation [17–19].

Recognition and Correction in Acquisition Stage

The raw images can be used to detect local deformations, which are most pronounced in the region of the brain stem. Due to the differential contrast and eddy current-induced distortions between DWIs, it is hard to determine whether any observed deformations are caused by pulsation. When multiple non-DWIs are acquired, looping through the raw images at a high frame rate (e.g., 10 fps) may already illustrate the effect of cardiac pulsation.

As there is a direct mathematical relation between the image and the k-space, any artifact in the image is also present in k-space. Pulsation can result in dispersion or corruption in k-space leading to signal dropouts in the image. Holdsworth et al. [20] proposed the use of k-space entropy as a measure for k-space dispersion, where images with higher entropy than a given threshold value are defined as corrupted. Once a threshold is set, any corrupted slices can then be re-acquired later in the scan without the need for user input. Although this provides an automated method, the implementation requires online processing of the acquired data, and therefore nontrivial alterations to the scanner software.

To prevent the pulsation artifact from occurring in the acquired data, it is possible to acquire images only during several phases of the cardiac cycle, called cardiac gating. By ensuring that each slice is scanned during diastole, where there is little pulsatile motion, it is possible to acquire images that are unaffected by pulsation [21]. Although effective, gating comes at the cost of increased scan time, since there are periods in the cardiac cycle where no images can be acquired. In general, pulsation affects regions at and below the level over the corpus callosum [22]. With this knowledge, Nunes et al. [23] devised an

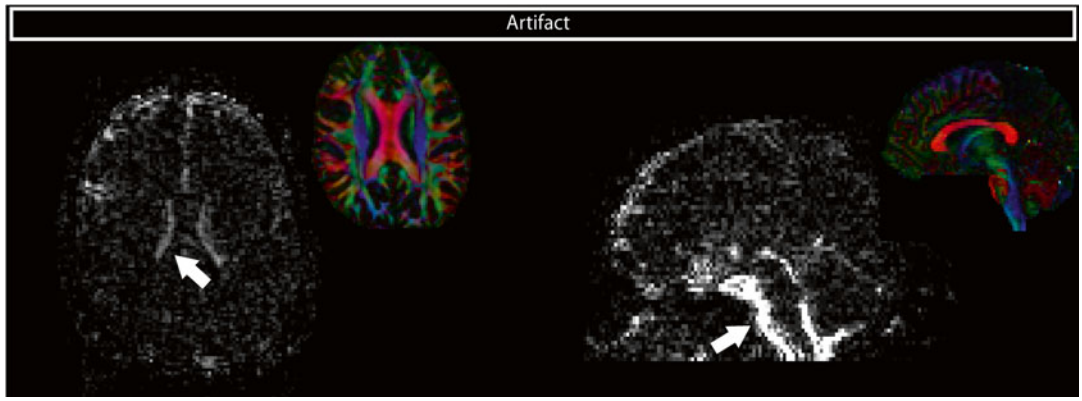

Fig. 7.9 Standard deviation across all non-DW (B_0) images shows high signal variability around the ventricles and the brainstem due to pulsation. FA DEC maps of the same slices are shown for anatomical reference

optimized acquisition setup where these inferior areas are scanned in the diastolic phase and supracallosal slices during the systolic phase. Using this setup they demonstrated a decrease in scan time of 30 % compared to the traditional cardiac-gated scan, while obtaining the same artifact-free images. Most MR vendors provide a cardiac gating option in their DWI sequences, making this a very convenient solution to pulsation artifacts, albeit at the expense of increased scan time.

Recognition and Correction in Image Processing Stage

Plotting the standard deviation across the non-DWIs for each voxel can show a high variability near moving regions, such as the medial parts of the brainstem and the lateral ventricles, due to pulsatile artifacts (Fig. 7.9).

On top of local misalignment artifacts, intravoxel dephasing leads to additional signal attenuation, which will be interpreted as increased diffusion. This will bias the diffusion tensor estimate and will influence anisotropy measures and tractography results [17].

Tensor estimation in the presence of cardiac-induced artifacts can be improved by more advanced tensor estimation methods that recognize corrupted data as outliers. Robust estimation approaches such as Robust Estimation of Tensors by Outlier Rejection (RESTORE, see also Chap. 6 and [24]) and Robust Extraction of Kurtosis INDices with Linear Estimation (REKINDLE) [25] can be very effective in obtaining diffusion tensor parameters that are not affected by cardiac-induced artifacts.

Susceptibility-Induced Distortions

Origin

Magnetic susceptibility refers to the degree of magnetization of an object in response to an applied magnetic field. Tissue is diamagnetic, which means that it creates a magnetic field in opposition to the externally applied magnetic field. The magnetic field in the tissue will therefore be slightly lower than the scanner magnetic field. Different tissues have different magnetic susceptibilities, which makes the magnetic field (B_0) dependent on the shape and composition of the body part that is imaged. Susceptibility differences are particularly large in regions where air-filled sinuses are close to bone or tissue, such as in the temporal and frontal lobe. EPI images are prone to these susceptibility differences in particular, since a whole volume is acquired within a single excitation. In clinical practice, k-space is filled as displayed in Fig. 7.10a. The locally altered magnetic field will cause a local displacement of the object in the PE direction [26, 27]. More specifically, the geometric distortions scale linearly with the FOV in the PE direction, and with the time between two consecutive points in the PE direction.

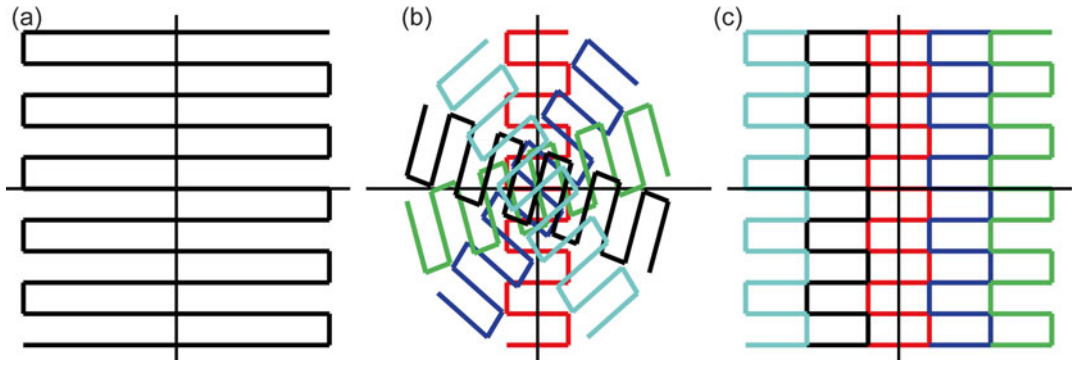

Fig. 7.10 (**a**) k-space trajectory of single-shot EPI, where the entire k-space is read after a single excitation. (**b**) Short-axis propeller EPI, where rotating "blades" in k-space are read out after each excitation. (**c**) Readout-segmented EPI reads out "blinds" of k-space in each excitation

Recognition and Correction in Acquisition Stage

The distortions may cause regions of signal "pile up," where the signal of several voxels is compressed into one voxel (Fig. 7.11b), or signal "smearing," where the signal from one voxel is stretched over several voxels (Fig. 7.11a).

To compensate for B_0 inhomogeneities, an additional magnetic field can be created by running currents through small coils [28]. This is called shimming, and the coils used are called shim coils. In MRI brain imaging, there is always some form of shimming. Mostly, linear shimming is used, also called first-order shimming, where additional magnetic fields along x, y, and z are applied to make the B_0 field more homogeneous. Higher-order shimming is also possible, where second- or third-order fields are applied to account for highly nonlocalized magnetic inhomogeneities [29]. These higher-order shimming methods require additional coils and software, but are widely available in dedicated brain imaging centers.

In the presence of an object that causes an inhomogeneous B_0 field, shimming is the accepted method to correct these inhomogeneities. However, the acquisition of the DWIs can be adjusted such that the effects of inhomogeneities are minimized. One way to do this is by parallel imaging methods, e.g., SMASH, SENSE, or GRAPPA, which were designed to speed-up MR image acquisition by acquiring only parts of k-space, and then reconstructing the whole image [30–32]. The use of multiple receiver coils that detect the MR signal then provides the additional spatial information to reconstruct the complete image from an incompletely sampled, or undersampled, k-space. It is most efficient to undersample in the PE direction because this provides the largest speed-up. An additional benefit is that in EPI, this also reduces the image distortions caused by local field inhomogeneities, with higher parallel imaging factors giving lower distortions.

Another way to reduce image distortions is to change the way k-space data is acquired. Several pulse sequences have been designed that do this, including short-axis PROPELLER EPI (SAP-EPI, [27]) and readout segmented EPI (RS-EPI, [20]). SAP-EPI acquires multiple rotating and overlapping "blades" in k-space that together create a full k-space (Fig 7.10b). Instead, RS-EPI acquires several parallel adjacent "blinds" in k-space that combine to a full k-space (Fig 7.10c). However, these techniques require multiple blades or blinds to be scanned to construct a full k-space. Since the individual blades or blinds are acquired after separate excitations, this results in longer scan times. Recently, diffusion-weighted vertical gradient and spin-echo EPI was proposed, which basically acquires all the RS-EPI blinds after a single excitation, significantly increasing the imaging speed compared to RS-EPI [33]. Although these techniques provide

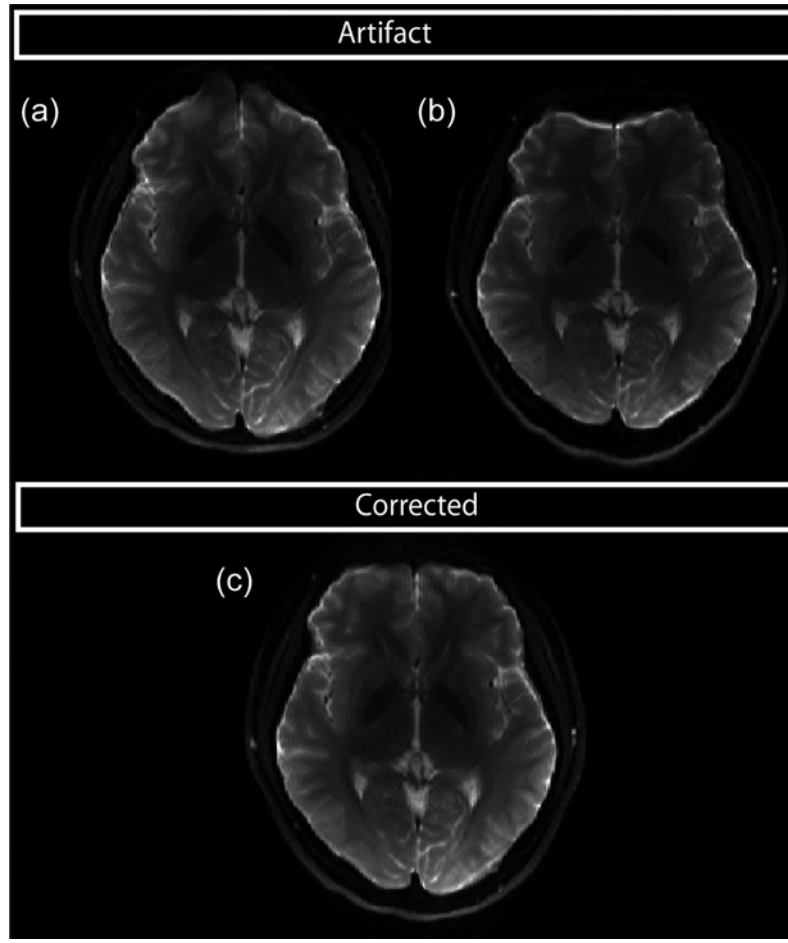

Fig. 7.11 (**a**) Susceptibility-induced distortions when using negative EPI blips, displacements toward the front. (**b**) Positive EPI blips result in displacements posteriorly. (**c**) Corrected data. [Courtesy of Dr. Roland Bammer, Stanford University]

a higher image quality and have been shown to provide improved diagnostic confidence [34], they are not widely available and thus not widely used in diffusion MRI.

Recognition and Correction in Image Processing Stage

Deformations of the DWIs can be recognized when fusing them with an anatomical image which is less geometrically distorted. Figure 7.12a shows the overlay of the DEC map with a T1 image after rigid registration, showing a clear mismatch between the two images.

There are several "unwarping" methods that can be used to deal with these distortions in image processing stage. Most of these methods, however, require additional image acquisitions and as such are not purely post-processing strategies. One option is distortion correction with the use of a field map. An example field map is shown in Fig. 7.13, which illustrates the deviation of B_0 from the Larmor frequency. Spatial variations in B_0 cause the distortions, and knowing these variations enables us to calculate the shift per voxel and compensate for the shift [35]. A drawback of this method is that it cannot correct for signal "pile up," because the intensity of that particular location is then a mix of intensities from different voxels, and this is impossible to resolve [36].

An alternative method is to acquire two datasets with opposite PE direction (and thus oppositely directed distortions), so that one could reconstruct the undistorted image from these two data sets [37]. This is called the reverse polarity gradient method because of the opposite polarity

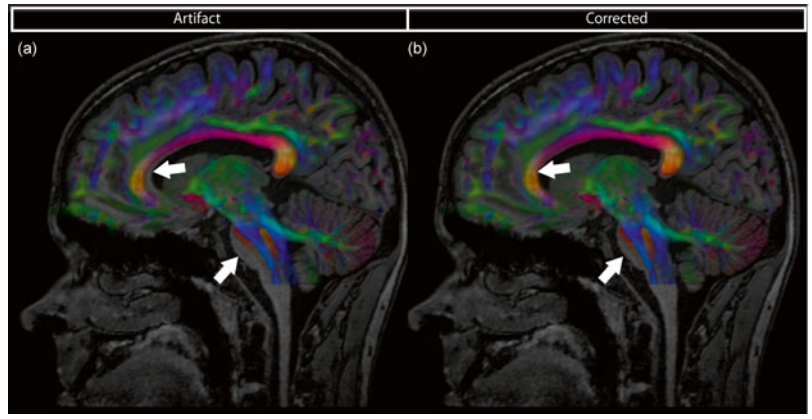

Fig. 7.12 Color FA map derived from DW-MRI data overlaid on anatomical undistorted image. Due to EPI deformations in the DWI, there is a misregistration that is most obvious near the brain stem and corpus callosum (**a**). (**b**) Result after correction by non-rigid image registration

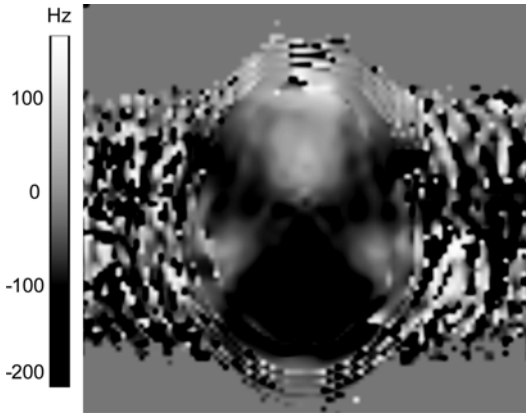

Fig. 7.13 Field map with the gray values representing B_0 variations in Hz

of the PE gradient in this method. The benefit here is that regions with signal "pile up" in one image have signal "smearing" in the other image, and vice versa. Recall Fig. 7.11a, b. This overcomes the main drawback of the field map method. A downside to this method is that more images should be acquired, increasing the scan time.

Finally, an undistorted image (e.g., T1, T2) can be used to unwarp residual EPI distortions present in DWI data by non-rigid image registration [38], see Fig. 7.12b.

Conceptually, the last two correction methods could be combined, where the registration to an undistorted image fine-tunes the images corrected with the field map of reverse polarity method.

Nyquist Ghosting

Origin

The origin of Nyquist ghosting is hardware related. In the scanner, there is a time delay of microseconds between the application of the readout gradient and the actual acquisition. This leads to a shift of the data in k-space, which corresponds to a phase ramp in image space: the "ghost" [39]. The ghost arises due to a mismatch between readout from positive and negative readout directions.

Recognition and Correction in Acquisition Stage

Ghosting can immediately be recognized in the raw images as a copy of the object, shifted by half of the FOV (see Fig. 7.14).

Multiple correction methods have been proposed and generally fall into methods that require additional acquisitions (e.g., a reference scan) or those that do not. To correct for the shift in k-space, the reference scan is composed of multiple readouts through the center of k-space which can be used to determine the difference between positive and negative readouts. This difference—acquired without diffusion weighting—can then be used to correct all acquired non-DWI and DWIs in the rest of the session [40]. Although this is a very quick method, the downside is that it is not suitable for longer DWI scans, which are more and more

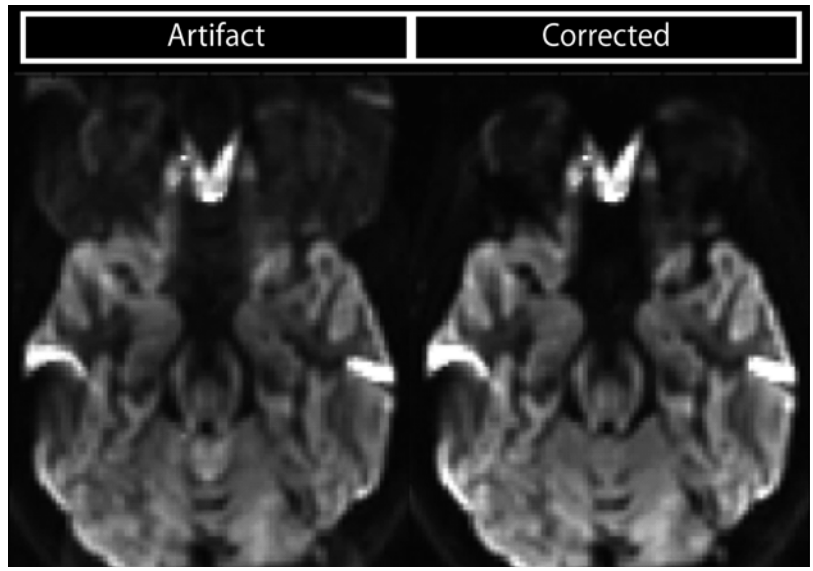

Fig. 7.14 Nyquist ghosting can be recognized as a copy of the image that is shifted over half the FOV

common to accommodate HARDI (see also Chap. 13). Subtle changes in the MR system during the scan may render the reference acquired at the beginning inadequate for ghost correction at the end of the scan. To resolve this, reference scans can be acquired intermittently during scanning to update the correction parameters. If multiple non-DWIs are acquired and these are spread out over the session, these references can be scanned during the "dead time" because of the missing diffusion-weighting gradients. Mostly, the scanner has one fixed method to do ghost correction, which leaves the user with no alternatives. However, if these "standard" methods prove insufficient to fully correct for ghosting, one should realize there are alternative methods that could prove to be beneficial.

Recognition and Correction in Image Processing Stage

Alternatively, one can use the acquired images themselves to do ghost correction. By generating separate images from the odd and even echoes, phase maps of those two images can be generated. Under the assumption that phase changes have a low spatial frequency, the two phase maps can be used to calculate a phase correction and reconstruct one final un-ghosted image [39, 41].

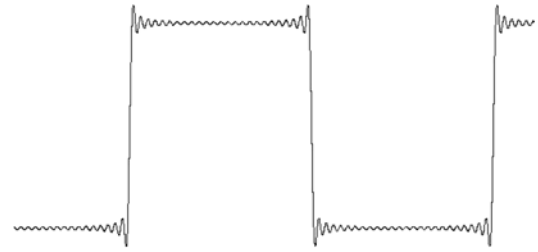

Fig. 7.15 Ringing artifact around large steps in intensity

Gibbs Ringing

Origin

Gibbs ringing is a common artifact in MRI but is often overlooked in diffusion MRI applications [3]. To describe steep intensity transitions in an image (e.g., cerebrospinal fluid, CSF, next to white matter), one needs high frequencies. When acquiring k-space, however, the acquisition window is not infinitely large but rectangular. High frequencies beyond the acquisition window are assumed to be zero. This leads to the well-known ringing artifact in the image [42], see Fig. 7.15.

Recognition and Correction in Acquisition Stage

Gibbs ringing artifacts are the most prominent in the non-DW image because the intensity differences are

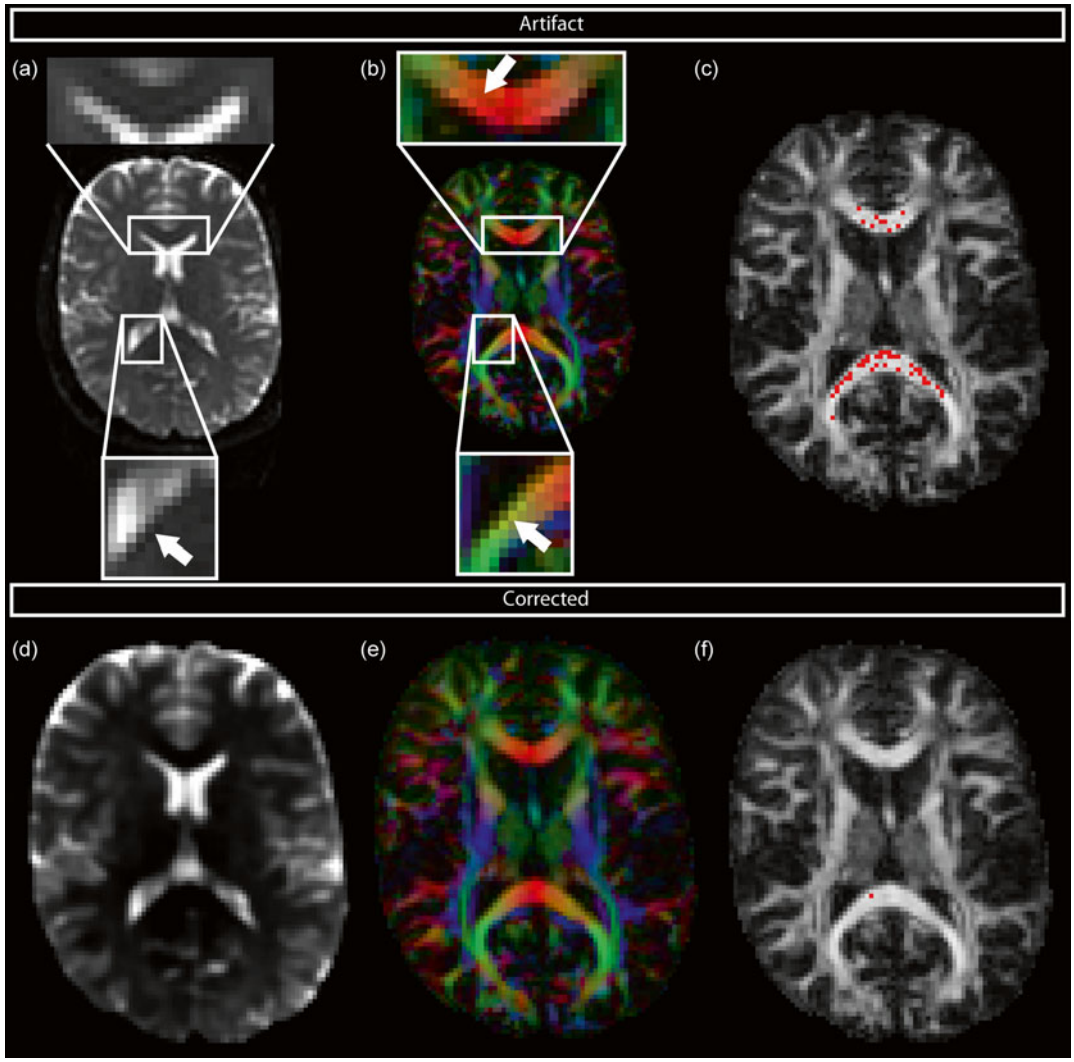

Fig. 7.16 Gibbs ringing artifact. (**a**) B_0 image shows the artifact at the location of high intensity gradients. (**b**) DEC map with Gibbs ringing artifact. (**c**) PIS map, indicating regions where the $b=0$ image has smaller intensity than the DWIs. (**d**–**f**) show the corrected images

largest in this image, as shown in Fig. 7.16a at the interface of CSF and brain tissue.

Sampling a larger interval in k-space (with proportionally more points in k-space) for a fixed field-of-view will reduce the pixel width, and therefore the spatial distance over which the ringing propagates. Running two scans with different k-space intervals can give insight in the Gibbs ringing artifact, but this is not often an option due to prolonged acquisition time.

Recognition and Correction in Image Processing Stage

The Gibbs ringing artifact can also be recognized on DEC maps as intensity variations, see Fig. 7.16b. Since diffusion will lead to signal decay, the non-DW image should always have a larger intensity than DWIs for each voxel. Due to Gibbs ringing artifacts, amongst others, this is not always the case. Visualizing the occurrence of these physically implausible signals (PIS)

overlaid on an FA map indicates at which locations these artificial signals occur, as shown in Fig. 7.16c [3].

Gibbs ringing artifacts have influence on diffusion estimates, and it is therefore desirable to correct for these artifacts. There are several approaches that deal with Gibbs ringing artifacts, e.g. [43–47]. The total variation (TV) approach, for example, calculates a corrected image by including a term that preserves edge information in the image and meanwhile minimizes the contribution of large adjacent intensity differences [46].

Chemical Shift Artifact

Origin

When placed in a magnetic field, protons in fat have a different resonance frequency than those in water. During acquisition of the MR images, the frequency and phase of the signal are used for spatial encoding of the signal. The difference in frequency of fat and water can therefore be interpreted as a difference in position. In EPI images, fat containing structures are therefore shifted from their true positions in the phase-encoding direction.

Recognition and Correction in Acquisition Stage

On a 3T clinical system, the fat/water chemical shift can approach 5 cm [48]. When imaging the brain, the largest fat component can be found between the skull bone and skin. The hyperintense band of the fat signal can be visible on raw DWIs, as shown in Fig. 7.17a.

To ensure there is no fat signal to disrupt the image, several "fat suppression" methods have been proposed that can be generally classified into three different methods: specifically exciting the water protons; saturation of the fat magnetization; moving the fat signal away from the imaged object. The first method was initially proposed by [49] as a spectral-spatial (SPSP) selective excitation, where interplay between switching slice-selection gradients and RF pulse excites only the water protons. This is the most effective method in terms of fat suppression, but suffers from two main drawbacks: (1) Due to hardware constraints on clinical systems (mostly the gradient slew rate), slice thicknesses is limited to around 2.4 mm or thicker; (2) The SPSP pulse can be relatively long in order to get a good fat suppression, thus increasing scan time. The second method uses an RF pre-pulse, to null the fat magnetization before the actual water excitation.

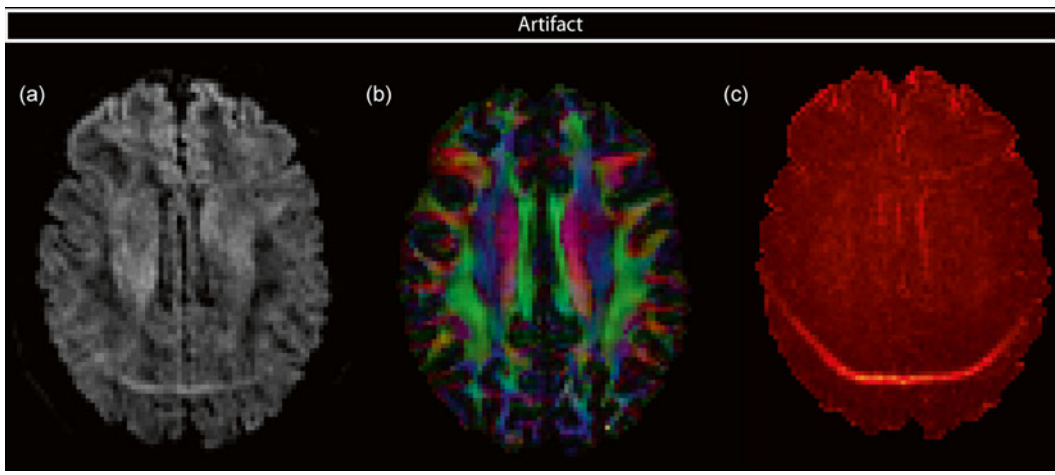

Fig. 7.17 Fat band is sometimes visible as bright intensity band on raw images (**a**), whereas it is often missed on DEC maps (**b**). Residual map clearly shows the chemical shift artifact (**c**)

Two pre-pulses exist: (1) An inversion pulse (e.g., SPIR, [50]), where the fat magnetization is inverted and the actual excitation is done at the time that fat has zero magnetization. The time between inversion and excitation is called the inversion time, and tuning this is critical for good suppression. (2) The fat is excited and then "spoiled" before excitation (CHESS, [51]), resulting in no magnetization of fat. Unfortunately, at current clinical field strengths of 1.5T or 3T, this approach commonly provides incomplete fat suppression (as illustrated in Fig. 7.17a and a slight increase in scan time). The third method uses slice-selection gradient reversal (SSGR) [52, 53]. Due to relative differences in frequency, the slice of fat that is excited is shifted along the slice direction compared to the excited water. When opposite gradient polarities are used during the excitation and refocusing RF pulse, the fat slice will in turn be shifted in opposite directions in the excitation and refocusing part. As a result, the volume of fat tissue that experiences both the excitation and refocusing pulse is very small, which means there is little signal from fat. This is shown schematically in Fig 7.18.

In a recent overview, Sarlls et al. [54] compared different fat suppression methods for twice-refocused DW imaging: CHESS, SSGR, SPSP, and a combined CHESS-SSGR approach. The SPSP and CHESS-SSGR methods performed similarly in terms of effective fat suppression and SNR, but the CHESS-SSGR combination resulted in a slightly shorter scan time.

Depending on the vendor, one or several of these fat suppression options are available. Even within one option, there are specific parameters that can be tuned to try and optimize fat suppression. In SPIR, for instance, the inversion time can be set for each scan. Alternatively, the difference between the water and fat resonance frequency can be set in SPIR, CHESS, and SPSP. Optimal values of these parameters are dependent on several scanner-specific settings, including the main field strength, gradient strength, and gradient slew rate, but are certainly worth investigating to provide proper suppression.

Recognition in Image Processing Stage

Insufficient fat suppression can become visible on DEC maps, but this is not always obvious (Fig. 7.17b). The easiest method to detect these artifacts is by making a residual map of the diffusion tensor residuals, where the chemical shift artifact can be recognized as a bright band of higher residuals (Fig. 7.17c). It is difficult to correct for this artifact at this stage, and one should be careful with interpretation of the data in these corrupted regions. The locally biased tensor estimation can become apparent globally in tractography analyses.

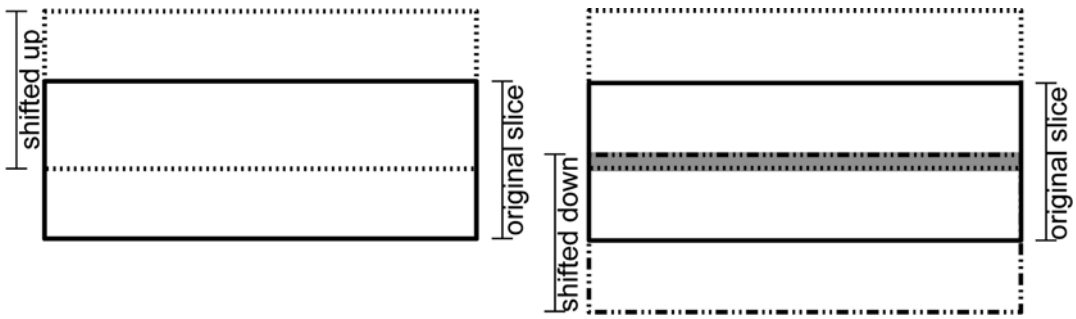

Fig. 7.18 Schematic representation of the slice-selection gradient reversal (SSGR) method. The *solid black line* indicates the spatial location of the slice of water that is excited. The fat slice that is excited is displaced with respect to the water slice along the slice direction (*shifted up*, *dashed line*). The refocusing pulse is then combined with a gradient that has an opposite polarity to that used in the excitation pulse. The fat volume that experiences this pulse is shifted downwards (*dashed-dotted line*). The overlapping area in the middle of the slice (*gray*) is the only part of the fat signal from this slice that will give an echo

Signal and Slice Dropouts

Origin

Signal dropouts can have many origins, such as gross subject motion, cardiac pulsation, strong local susceptibility difference (e.g., dental braces), and hardware problems, among others. Since the first three causes have been described at length previously, we focus here on the hardware-related problems. One example is a loose connection in the scanner, which can cause part of k-space to not be stored. Depending on the part of k-space missing, and the extent, this artifact can have various representations in the image. Alternatively, receiver calibration can be incorrect. Prior to scanning, the scanner performs a quick test scan to see what the maximum signal will be to calibrate the system. If this is set too low, points in k-space may have their intensities "clipped," resulting in artificial contrast differences in the image.

Recognition and Correction in Acquisition Stage

Given that hardware-related problems can present themselves as a broad range of image artifacts, the artifacts can be difficult to detect and their origins hard to pinpoint. On raw data, detection can best be done by looking for structural hypointense areas, such as slice dropouts, shown in Fig. 7.19. One should be aware, however, that not all dropouts are as obvious as this example, and the best way of detection is in the post-processing stage.

Recognition and Correction in Image Processing Stage

Signal dropouts are sometimes subtle and not always obvious to recognize on raw images or FA maps (Fig. 7.7). Residual maps of the tensor estimation are sensitive to dropouts, see Fig. 7.20. When fitting a tensor, the RESTORE

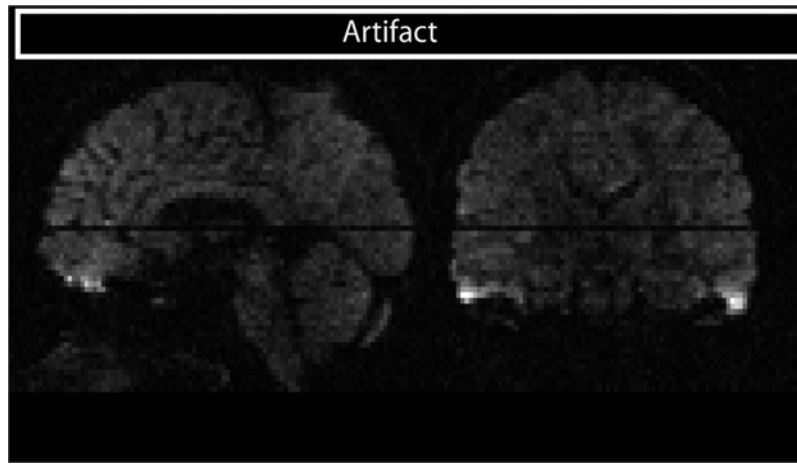

Fig. 7.19 Total slice dropout in the sagittal (*left*) and coronal (*right*) view

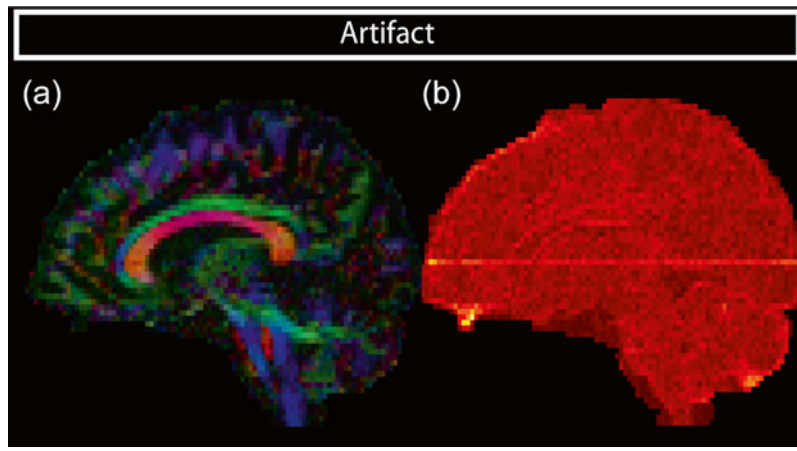

Fig. 7.20 (**a**) Slice dropouts are hard to spot on FA maps, but do influence diffusion measures locally. (**b**) On the tensor residual map, the slice dropout can well be recognized

and REKINDLE approaches can deal with these outliers by ignoring them during tensor estimation [24].

Quality Assurance

Several of the artifacts discussed in this chapter can be corrected for, either at the acquisition or the processing stage. As such, they do not limit the analyses of DTI data, but rather force the user to consciously consider the acquisition and processing steps prior to the analyses. Since the introduction of DWI and DTI, much research has been devoted to solve or reduce image artifacts. Eddy current-induced and susceptibility-induced image distortions, for instance, can now be addressed both by tuning the acquisition and the image processing side, with clear pros and cons to both options. In terms of the image processing steps described here, most software packages available to date provide users with adequate options to do these correction steps. Although there are various ways to correct for artifacts, it is of major importance to check quality requirements before acquiring data on clinical or research subjects, by using quality assurance (QA) tests.

QA and Phantoms

QA is concerned with the implementation of activities to fulfill quality requirements, such as comparison to a gold standard. Standard QA tests consist of gradient calibration (including linearity, uniformity, and agreement in amplitude), field mapping to minimize B_0 inhomogeneities, and eddy current compensation [55]. This is most commonly done by imaging phantoms with different gradient directions and *b*-values. Phantoms are suitable for validation of acquisition parameters, as well as diffusion measures and fiber tractography results [56–59]. It is important to quantify precision, accuracy, and reproducibility in diffusion MRI analysis. Vegetables (like asparagus [60]) or animal nerve structures (like rat spinal cord, garfish, or lobster nerves [61, 62]) are sometimes used. However, in such organic matter it is more difficult to manipulate the natural geometry of the tissue in order to reflect more complex microstructural configurations (i.e., to construct interdigitated crossing fibers), and the diffusion properties of such organic material may change over time. Hardware phantoms can be made of isotropic media (e.g., liquids of known diffusivity) or anisotropic media (e.g., capillaries or artificial fibers). The properties of these phantoms are tuned to resemble human white matter. Liquids of known diffusivity (e.g., Dodecane) can be used to calibrate absolute gradient power. Glass capillaries or PTFE (Teflon) capillaries [63] are rigid, while for example hydrophobic fiber materials (with high FA, [64]) can be adapted to the desired geometry to create artificial fiber phantoms.

Quality Control

One important aspect of quality assurance and control is that the user should always remain critical when employing automated correction methods. One example could be the use of robust estimation procedures on data with artifacts. When a DW image is partly corrupted, RESTORE or REKINDLE might classify those corrupted voxels as outliers, and disregard them in tensor estimation. However, if a large portion of the image is corrupted, the image might not be correctly registered, which could mean that the "good" voxels that are included in tensor estimation are also unreliable because they provide diffusion information about different spatial locations. An example of this is shown in Fig. 7.21 for a DW image (Fig. 7.21a) simulated to have an interleaved artifact (Fig. 7.21b). The coregistration of such an image to the other images will not be accurate. Residual maps (Fig. 7.21c) will not show this. However, the number of outliers detected is a very good indicator of a subtle image artifact (Fig. 7.21d). As shown here, the interleaved artifact only causes 7 % of all brain voxels to be judged by RESTORE as outliers, even though at least half of all WM voxels are misaligned and therefore provide erroneous information. This is because misregistration of voxels within the WM might not provide a strong

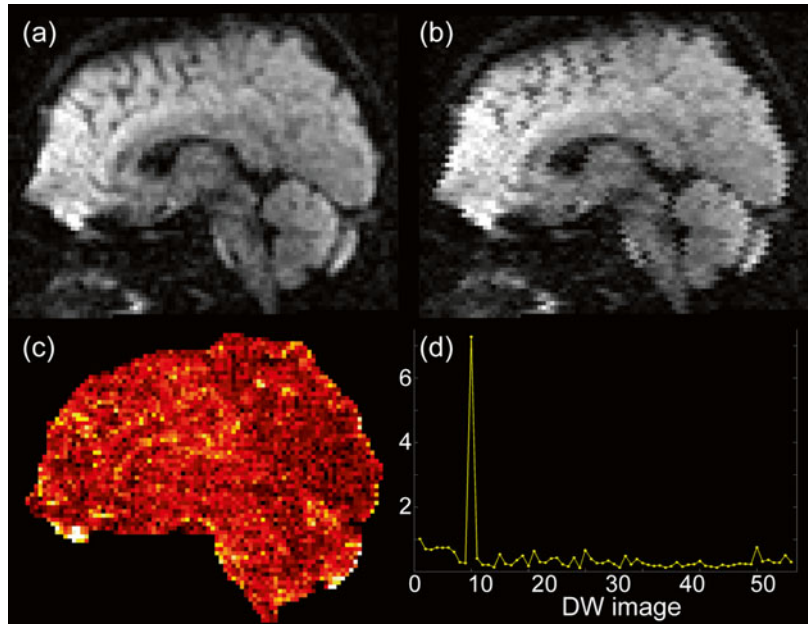

Fig. 7.21 Importance of manual data quality assurance. One DW image (the tenth) shown uncorrupted (**a**) and with interleaved artifact (**b**). The tensor residual map at this slice (**c**) does not show the presence of any artifact. However, outlier percentages per DW image (**d**) strongly indicate an artifact. Interesting, only 7 % of all brain voxels are classified as outliers, whereas roughly half of the image is misaligned

enough contrast difference to be classified as artifact. In such cases, one could argue to remove the entire DW volume from further analyses to ensure they are not negatively affected.

Implications for Further Analysis

Effects of Bad Quality Data on Quantification

MD and FA are, amongst others, important quantitative measures that can be used in subsequent ROI analyses, voxel based analyses (VBA), and tractography analyses (See Chaps. 6, 7). Comparison of these values between different groups can reveal associations with clinical parameters, which has been the focus of a large amount of studies. Artifacts can influence the diffusion measures, as shown in Fig. 7.22, where FA values (top two rows) and MD values (bottom row) are locally altered. Furthermore, artifacts can complicate proper analyses in particular areas. It is well known that structures in the orbitofrontal cortex, for example, are prone to susceptibility artifacts, which makes these white matter areas less accessible to study. This might attribute to the fact that larger white matter tracts with densely packed neuronal fibers tend to be studied more than less prominent pathways. For example, the corpus callosum is a pathway that can readily be identified, which makes this pathway better suited for investigation in quantitative studies [65]. We have seen that most artifacts cause difficulties in the registration of individual DWIs, which will eventually affect any subsequent analysis. One should be aware that the corpus callosum, for example, can also be corrupted by artifacts, such as susceptibility distortions (Fig. 7.10), Gibbs ringing (Fig. 7.13), and interleave artifacts (Fig. 7.15).

Effects of Bad Quality Data on Tractography Results

With tractography, the architectural configuration of white matter fiber bundles can be investigated in vivo (See Chap. 11). For DTI tractography, the local first eigenvector is typically used for tract propagation (Chap. 6). Besides noise and partial volume effects, data artifacts and lack of proper

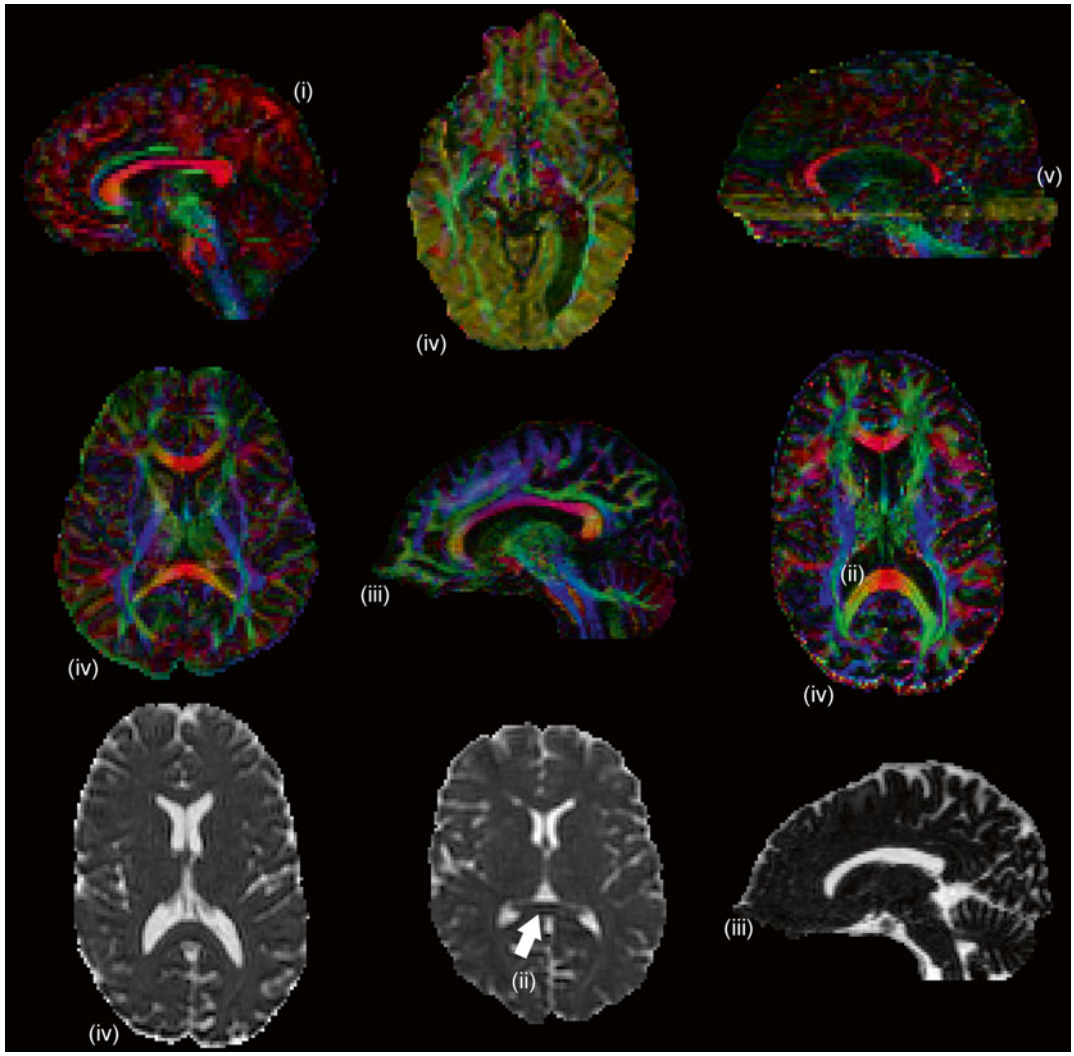

Fig. 7.22 Effects of bad quality data on quantitative measures (FA *top two rows*, MD *bottom row*), showing (**i**) vibration artifact, (**ii**) Gibbs ringing, (**iii**) Susceptibility distortions anterior, (**iv**) Motion and eddy current distortions, (**v**) interleave artifacts

correction can severely confound local fiber configurations and therefore fiber tractography results. Figure 7.23 shows examples of the influence of bad quality data on tractography results using a deterministic algorithm, for different artifacts. The results clearly show the deviation in the reconstructed pathways when proper correction methods are not taken into account. Pathways can have a different geometry and may even terminate in other brain areas [66]. To date, tractography is mostly used for analyses in which quantitative measures along tracts are compared between patients and controls, to study which areas in the brain are connected, and for neurosurgical planning. It is of major importance to assure data quality before acquisition and correct for artifacts during acquisition and image processing to ensure the reliability of all subsequent analyses.

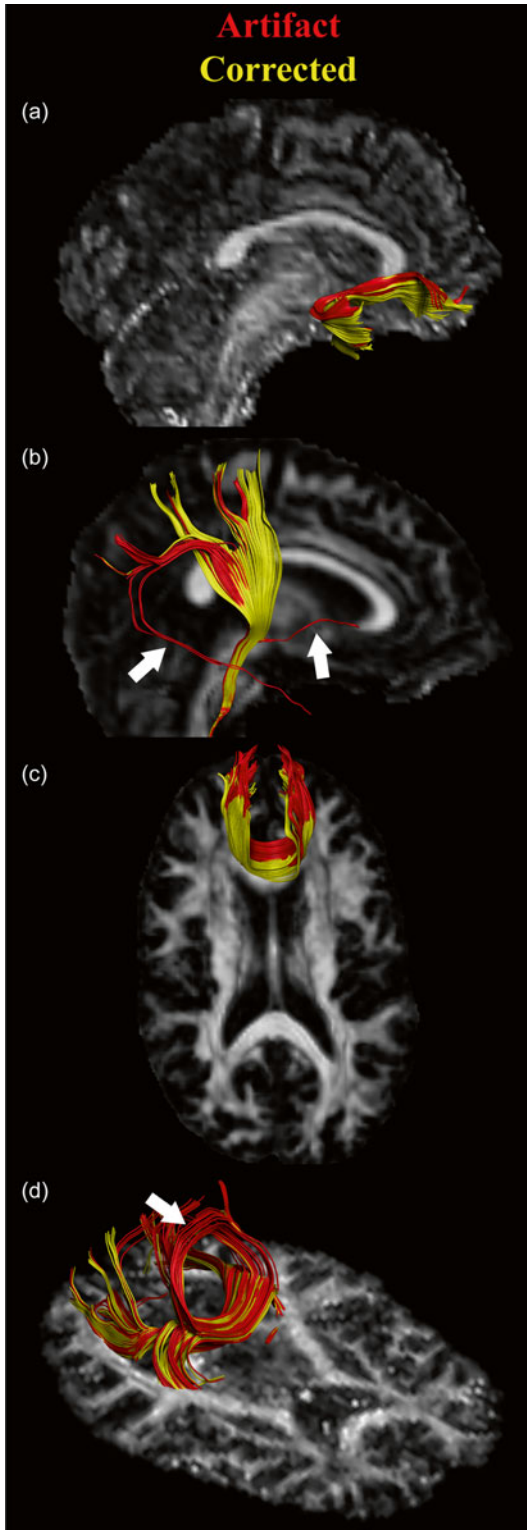

Fig. 7.23 Effects of bad quality data on tractography results. (**a**) Tractography of the uncinate fasciculus before (*red*) and after (*yellow*) motion and eddy current distortion.

References

1. Heemskerk AM, Leemans A, Plaisier A, Pieterman K, Lequin MH, Dudink J. Acquisition guidelines and quality assessment tools for analyzing neonatal diffusion tensor MRI data. AJNR Am J Neuroradiol. 2013;34(8):1496–505.
2. Rohde GK, Barnett AS, Basser PJ, Marenco S, Pierpaoli C. Comprehensive approach for correction of motion and distortion in diffusion-weighted MRI. Magn Reson Med. 2004;51(1):103–14.
3. Tournier JD, Mori S, Leemans A. Diffusion tensor imaging and beyond. Magn Reson Med. 2011;65(6):1532–56.
4. Reese TG, Heid O, Weisskoff RM, Wedeen VJ. Reduction of eddy-current-induced distortion in diffusion MRI using a twice-refocused spin echo. Magn Reson Med. 2003;49(1):177–82.
5. Pajevic S, Pierpaoli C. Color schemes to represent the orientation of anisotropic tissues from diffusion tensor data: application to white matter fiber tract mapping in the human brain. Magn Reson Med. 1999;42(3):526–40.
6. Haselgrove JC, Moore JR. Correction for distortion of echo-planar images used to calculate the apparent diffusion coefficient. Magn Reson Med. 1996;36(6):960–4.
7. Andersson JL, Skare S. A model-based method for retrospective correction of geometric distortions in diffusion-weighted EPI. Neuroimage. 2002;16(1):177–99.
8. Pipe JG. Motion correction with PROPELLER MRI: application to head motion and free-breathing cardiac imaging. Magn Reson Med. 1999;42(5):963–9.
9. Zaitsev M, Dold C, Sakas G, Hennig J, Speck O. Magnetic resonance imaging of freely moving objects: prospective real-time motion correction using an external optical motion tracking system. Neuroimage. 2006;31(3):1038–50.
10. Aksoy M, Forman C, Straka M, Skare S, Holdsworth S, Hornegger J, et al. Real-time optical motion correction for diffusion tensor imaging. Magn Reson Med. 2011;66(2):366–78.
11. Maclaren J, Armstrong BS, Barrows RT, Danishad KA, Ernst T, Foster CL, et al. Measurement and correction of microscopic head motion during magnetic resonance imaging of the brain. PLoS One. 2012;7(11):e48088.

Fig. 7.23 (continued) (**b**) Corticospinal tract in a set where we simulated an interleave artifact (*red*) and in the "ground truth" set (*yellow*). The artifact results in clearly artificial tracts. (**c**) Frontal projections of the corpus callosum in a dataset with susceptibility distortions (*red*) and the corrected dataset (*yellow*). (**d**) Occipital projections of the corpus callosum. Artifactual parietal fibers connect the two hemispheres due to a vibration artifact (*red*), whereas this is not the case when the artifact is corrected (*yellow*)

12. Maclaren J, Herbst M, Speck O, Zaitsev M. Prospective motion correction in brain imaging: a review. Magn Reson Med. 2013;69(3):621–36.
13. Leemans A, Jones DK. The B-matrix must be rotated when correcting for subject motion in DTI data. Magn Reson Med. 2009;61(6):1336–49.
14. Gallichan D, Scholz J, Bartsch A, Behrens TE, Robson MD, Miller KL. Addressing a systematic vibration artifact in diffusion-weighted MRI. Hum Brain Mapp. 2010;31(2):193–202.
15. Hiltunen J, Hari R, Jousmaki V, Muller K, Sepponen R, Joensuu R. Quantification of mechanical vibration during diffusion tensor imaging at 3 T. Neuroimage. 2006;32(1):93–103.
16. Greitz D, Wirestam R, Franck A, Nordell B, Thomsen C, Stahlberg F. Pulsatile brain movement and associated hydrodynamics studied by magnetic resonance phase imaging. The Monro-Kellie doctrine revisited. Neuroradiology. 1992;34(5):370–80.
17. Jones DK, Pierpaoli C. Contribution of cardiac pulsation to variability of tractography results. 2005. p. 222.
18. Pierpaoli C, Marenco S, Rohde G, Jones DK, Barnett AS. Analyzing the contribution of cardiac pulsation to the variability of quantities derived from the diffusion tensor. 2003. p. 70.
19. Le Bihan D, Turner R. Intravoxel incoherent motion imaging using spin echoes. Magn Reson Med. 2005;19(2):221–7.
20. Holdsworth SJ, Skare S, Newbould RD, Guzmann R, Blevins NH, Bammer R. Readout-segmented EPI for rapid high resolution diffusion imaging at 3 T. Eur J Radiol. 2008;65(1):36–46.
21. Skare S, Andersson JL. On the effects of gating in diffusion imaging of the brain using single shot EPI. Magn Reson Imaging. 2001;19(8):1125–8.
22. Wirestam R, Greitz D, Thomsen C, Brockstedt S, Olsson MB, Stahlberg F. Theoretical and experimental evaluation of phase-dispersion effects caused by brain motion in diffusion and perfusion MR imaging. J Magn Reson Imaging. 1996;6(2):348–55.
23. Nunes RG, Jezzard P, Clare S. Investigations on the efficiency of cardiac-gated methods for the acquisition of diffusion-weighted images. J Magn Reson. 2005;177(1):102–10.
24. Chang LC, Jones DK, Pierpaoli C. RESTORE: robust estimation of tensors by outlier rejection. Magn Reson Med. 2005;53(5):1088–95.
25. Tax CMW, Otte WM, Viergever MA, Dijkhuizen RM, Leemans A. REKINDLE: robust extraction of kurtosis INDices with linear estimation. Magn Reson Med. 2015;73(2):794–808.
26. Farzaneh F, Riederer SJ, Pelc NJ. Analysis of T2 limitations and off-resonance effects on spatial resolution and artifacts in echo-planar imaging. Magn Reson Med. 1990;14(1):123–39.
27. Skare S, Newbould RD, Clayton DB, Bammer R. Propeller EPI in the other direction. Magn Reson Med. 2006;55(6):1298–307.
28. Romeo F, Hoult DI. Magnet field profiling: analysis and correcting coil design. Magn Reson Med. 1984; 1(1):44–65.
29. Gruetter R. Automatic, localized in vivo adjustment of all first- and second-order shim coils. Magn Reson Med. 1993;29(6):804–11.
30. Sodickson DK, Manning WJ. Simultaneous acquisition of spatial harmonics (SMASH): fast imaging with radiofrequency coil arrays. Magn Reson Med. 1997;38(4):591–603.
31. Pruessmann KP, Weiger M, Scheidegger MB, Boesiger P. SENSE: sensitivity encoding for fast MRI. Magn Reson Med. 1999;42(5):952–62.
32. Griswold MA, Jakob PM, Heidemann RM, Nittka M, Jellus V, Wang J, et al. Generalized autocalibrating partially parallel acquisitions (GRAPPA). Magn Reson Med. 2002;47(6):1202–10.
33. Engstrom M, Bammer R, Skare S. Diffusion weighted vertical gradient and spin echo. Magn Reson Med. 2012;68(6):1755–63.
34. Holdsworth SJ, Yeom K, Skare S, Gentles AJ, Barnes PD, Bammer R. Clinical application of readout-segmented- echo-planar imaging for diffusion-weighted imaging in pediatric brain. AJNR Am J Neuroradiol. 2011;32(7):1274–9.
35. Jezzard P, Balaban RS. Correction for geometric distortion in echo planar images from B0 field variations. Magn Reson Med. 1995;34(1):65–73.
36. Jones DK, Cercignani M. Twenty-five pitfalls in the analysis of diffusion MRI data. NMR Biomed. 2010; 23(7):803–20.
37. Chang H, Fitzpatrick JM. A technique for accurate magnetic resonance imaging in the presence of field inhomogeneities. IEEE Trans Med Imaging. 1992; 11(3):319–29.
38. Irfanoglu MO, Walker L, Sarlls J, Marenco S, Pierpaoli C. Effects of image distortions originating from susceptibility variations and concomitant fields on diffusion MRI tractography results. Neuroimage. 2012; 61(1):275–88.
39. Buonocore MH, Gao L. Ghost artifact reduction for echo planar imaging using image phase correction. Magn Reson Med. 1997;38(1):89–100.
40. Hu X, Le TH. Artifact reduction in EPI with phase-encoded reference scan. Magn Reson Med. 1996; 36(1):166–71.
41. Zhang Y, Wehrli FW. Reference-scan-free method for automated correction of Nyquist ghost artifacts in echoplanar brain images. Magn Reson Med. 2004; 51(3):621–4.
42. Haacke EM, Brown RW, Thompson MR, Venkatesan R. Magnetic resonance imaging: physical principles and sequence design. 82nd ed. New York, NY: Wiley-Liss; 1999.
43. Sarra SA. Digital total variation filtering as post-processing for Chebyshev pseudospectral methods for conservation laws. Numer Algorithm. 2006;41(1): 17–33.

44. Archibald R, Gelb A. A method to reduce the Gibbs ringing artifact in MRI scans while keeping tissue boundary integrity. IEEE Trans Med Imaging. 2002; 21(4):305–19.
45. Bakir T, Reeves SJ. A filter design method for minimizing ringing in a region of interest in MR spectroscopic images. IEEE Trans Med Imaging. 2000;19(6): 585–600.
46. Perrone D, Aelterman J, Pižurica A, Jeurissen B, Philips W, Leemans A. The effect of Gibbs ringing artifacts on measures derived from diffusion MRI. Neuroimage. 2015;120:441–55. http://www.ncbi.nlm.nih.gov/pubmed/26142273.
47. Veraart J, Fieremans E, Jelescu IO, Knoll F, Novikov DS. Gibbs ringing in diffusion MRI. Magn Reson Med. 2015. Forthcoming. http://www.ncbi.nlm.nih.gov/pubmed/26257388
48. Le Bihan D, Poupon C, Amadon A, Lethimonnier F. Artifacts and pitfalls in diffusion MRI. J Magn Reson Imaging. 2006;24(3):478–88.
49. Meyer CH, Pauly JM, Macovski A, Nishimura DG. Simultaneous spatial and spectral selective excitation. Magn Reson Med. 1990;15(2):287–304.
50. Kaldoudi E, Williams SC, Barker GJ, Tofts PS. A chemical shift selective inversion recovery sequence for fat-suppressed MRI: theory and experimental validation. Magn Reson Imaging. 1993;11(3):341–55.
51. Haase A, Frahm J, Hanicke W, Matthaei D. 1H NMR chemical shift selective (CHESS) imaging. Phys Med Biol. 1985;30(4):341–4.
52. Gomori JM, Holland GA, Grossman RI, Gefter WB, Lenkinski RE. Fat suppression by section-select gradient reversal on spin-echo MR imaging. Work in progress. Radiology. 1988;168(2):493–5.
53. Nagy Z, Weiskopf N. Efficient fat suppression by slice-selection gradient reversal in twice-refocused diffusion encoding. Magn Reson Med. 2008;60(5):1256–60.
54. Sarlls JE, Pierpaoli C, Talagala SL, Luh WM. Robust fat suppression at 3T in high-resolution diffusion-weighted single-shot echo-planar imaging of human brain. Magn Reson Med. 2011;66(6):1658–65.
55. De Santis S, Evans CJ, Jones DK. RAPID: a routine assurance pipeline for imaging of diffusion. Magn Reson Med. 2012;70(2):490–6.
56. Walker L, Curry M, Nayak A, Lange N, Pierpaoli C. A framework for the analysis of phantom data in multicenter diffusion tensor imaging studies. Hum Brain Mapp. 2012;34(10):2439–54.
57. Teipel SJ, Reuter S, Stieltjes B, Acosta-Cabronero J, Ernemann U, Fellgiebel A, et al. Multicenter stability of diffusion tensor imaging measures: a European clinical and physical phantom study. Psychiatry Res. 2011;194(3):363–71.
58. Pullens P, Roebroeck A, Goebel R. Ground truth hardware phantoms for validation of diffusion-weighted MRI applications. J Magn Reson Imaging. 2010;32(2): 482–8.
59. Fillard P, Descoteaux M, Goh A, Gouttard S, Jeurissen B, Malcolm J, et al. Quantitative evaluation of 10 tractography algorithms on a realistic diffusion MR phantom. Neuroimage. 2011;56(1):220–34.
60. Boujraf S, Luypaert R, Eisendrath H, Osteaux M. Echo planar magnetic resonance imaging of anisotropic diffusion in asparagus stems. MAGMA. 2001;13(2): 82–90.
61. Campbell JS, Siddiqi K, Rymar VV, Sadikot AF, Pike GB. Flow-based fiber tracking with diffusion tensor and q-ball data: validation and comparison to principal diffusion direction techniques. Neuroimage. 2005; 27(4):725–36.
62. Beaulieu C. The basis of anisotropic water diffusion in the nervous system: a technical review. NMR Biomed. 2002;15(7–8):435–55.
63. Lin CP, Wedeen VJ, Chen JH, Yao C, Tseng WY. Validation of diffusion spectrum magnetic resonance imaging with manganese-enhanced rat optic tracts and ex vivo phantoms. Neuroimage. 2003;19(3): 482–95.
64. Lorenz R, Bellemann ME, Hennig J, Il'yasov KA. Anisotropic phantoms for quantitative diffusion tensor imaging and fiber-tracking validation. Appl Magn Reson. 2008;33(4):419–29.
65. White T, Nelson M, Lim KO. Diffusion tensor imaging in psychiatric disorders. Top Magn Reson Imaging. 2008;19(2):97–109.
66. Andersson JL, Richter M, Richter W, Skare S, Nunes RG, Robson MD, et al. Effects of susceptibility distortions on tractography. Kyoto: ISMRM; 2004.

Suggested Reading

67. Andersson JLR, Skare S. Image distortion and its correction in diffusion MRI. In: Jones DK, editor. Diffusion MRI: theory, methods, and applications. New York, NY: Oxford University Press; 2010.
68. Pierpaoli C. Artifacts in diffusion MRI. In: Jones DK, editor. Diffusion MRI: theory, methods, and applications. New York, NY: Oxford University Press; 2010.

Part III

Diffusion Tensor Imaging Analysis

Strategies and Challenges in DTI Analysis

8

Wim Van Hecke and Louise Emsell

Learning Points

- DTI analysis forms only one part of a DTI study and is mutually dependent on other stages in the DTI pipeline, such as data acquisition.
- There are many different approaches for analyzing DTI and the most optimal method depends on the goal(s) of the DTI investigation.
- DTI analysis methods can be categorized into three main classes: whole-brain, regional, and voxel-based approaches.
- There are pros and cons in all DTI analysis approaches, and there is no single best or worst analysis method, but a range of techniques that are more or less suited to any given application.
- Many software packages and tools are available to process and analyse DTI data, which vary considerably in functionality.
- The broad range of analysis approaches and heterogeneous functionality in software packages contributes to a lack of standardization that complicates the analysis of DTI data and the interpretation of results.

Introduction to DTI Analysis

Since its introduction, DTI has been used to study microstructural tissue changes in a wide range of neurologic and psychiatric disorders, as well as in normal development and ageing [1]. Many approaches have been proposed to extract DTI measures from the data and compare them across subjects. As each of these methods have some advantages and limitations, the most optimal analysis approach will depend on the clinical and research questions that need answering. Furthermore, the limitations of the selected method should be considered during the interpretation of the results. This chapter provides a brief overview of the different options that are available for the analysis of DTI data. In the following chapters, more detailed information is provided about three main analysis techniques, i.e., region of interest analysis (Chap. 9), voxel-based analysis (Chap. 10), and tractography and connectivity analysis (Chap. 11).

W. V. Hecke, PhD (✉)
icometrix, Tervuursesteenweg 244,
3001 Leuven, Belgium

Department of Radiology, Antwerp University Hospital,
Wilrijkstraat 10, Edegem, 2650 Antwerp, Belgium
e-mail: wim.vanhecke@icometrix.com

L. Emsell, PhD
Departments of Translational MRI and Radiology,
KU Leuven and University Hospitals Leuven,
Leuven, Belgium

Department of Old Age Psychiatry,
Universitair Psychiatrisch Centrum (UPC) - KU
Leuven, Leuven, Belgium

W. Van Hecke et al. (eds.), *Diffusion Tensor Imaging*, DOI 10.1007/978-1-4939-3118-7_8

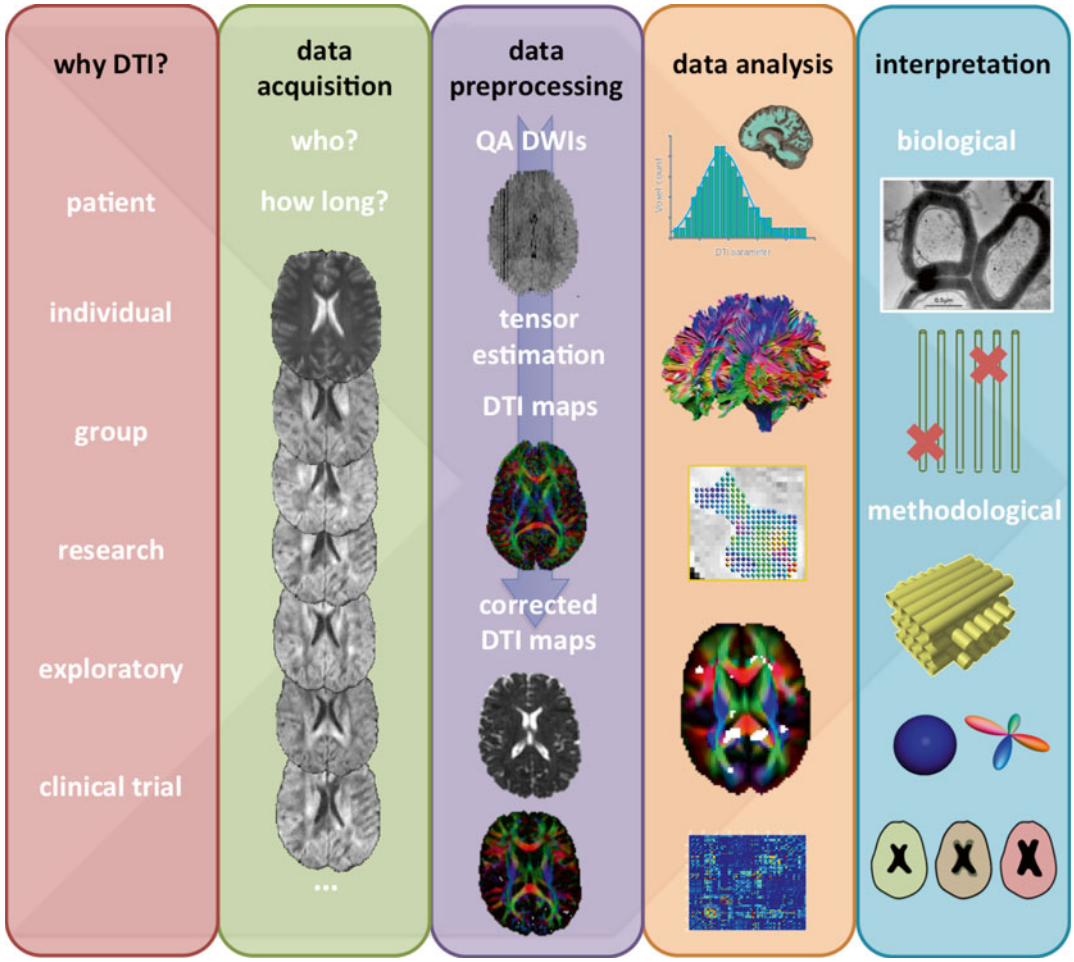

Fig. 8.1 Prototypal DTI study pipeline. Whole-brain tractogram and connectivity matrix. [Reprinted from Caeyenberghs K, Leemans A, Leunissen I, Gooijers J, Michiels K, Sunaert S, et al. Altered structural networks and executive deficits in traumatic brain injury patients. Brain Struct Funct. 2014 Jan;219(1):193–209. With permission from Springer Verlag]. Voxel-based analysis figure. [Adapted from Emsell L, Langan C, Van Hecke W,Barker GJ, Leemans A, Sunaert S, et al. White matter differences in euthymic bipolar I disorder: a combined magnetic resonance imaging and diffusion tensor imaging voxel-based study. Bipolar Disord. 2013 Jun;15(4):365–376. With permission from John Wiley & Sons.]Axon micrograph. [Reprinted from Beaulieu C. The basis of anisotropic water diffusion in the nervous system—a technical review. NMR Biomed. 2002 Nov–Dec;15 (7–8):435–455. With permission from John Wiley & Sons, Inc.] Corrected DTI maps. [Courtesy of A. Leemans]

Analyzing DTI data is only one part of the whole DTI processing pipeline. Figure 8.1 summarizes a prototypal DTI pipeline, from the goal of the DTI study, through to data acquisition, data analysis, and interpretation of the results. As highlighted in Chap. 2 and discussed in more detail in the chapters of Section 2, many choices have to be made at each step of this pipeline. Note that these different steps are not independent of each other; for example, the most optimal analysis technique will depend on the quality of the data and how it is acquired.

Why Do We Need to Analyze DTI Data?

Diffusion-weighted imaging (DWI) is widely used in clinical practice as it provides unique, rapidly accessible information that can be used in the assessment of ischaemic stroke, to differentiate vasogenic versus cytotoxic oedema and to characterize intracranial lesions such as pyogenic abscess, infections, tumors, and trauma [2]. However, whilst the processing of DWI data is relatively easy, the analysis of DTI data is significantly more complex. For example, the need for more diffusion-weighted images makes the acquisition longer and more challenging. In addition, motion correction becomes more important, and the tensor estimation is more complex compared to ADC calculations. There are also more techniques available for analyzing DTI data compared to DWI. In clinical practice, DWI information, typically the DWI and ADC maps, is interpreted visually by a radiologist. It has been demonstrated that DTI can be useful in evaluating changes in the normal appearing white matter. However, qualitative assessment of DTI information, such as FA maps, may be more difficult there.

To illustrate the challenge of qualitatively assessing scalar DTI maps, consider the axial color-encoded FA maps in Fig. 8.2. This random assortment of images comprises seven pairs of axial slices generated from patients with pathology that has been associated with changes in white matter microstructure, and two healthy subjects. There are two patients with tinnitus, two with cerebral palsy, two with multiple sclerosis,

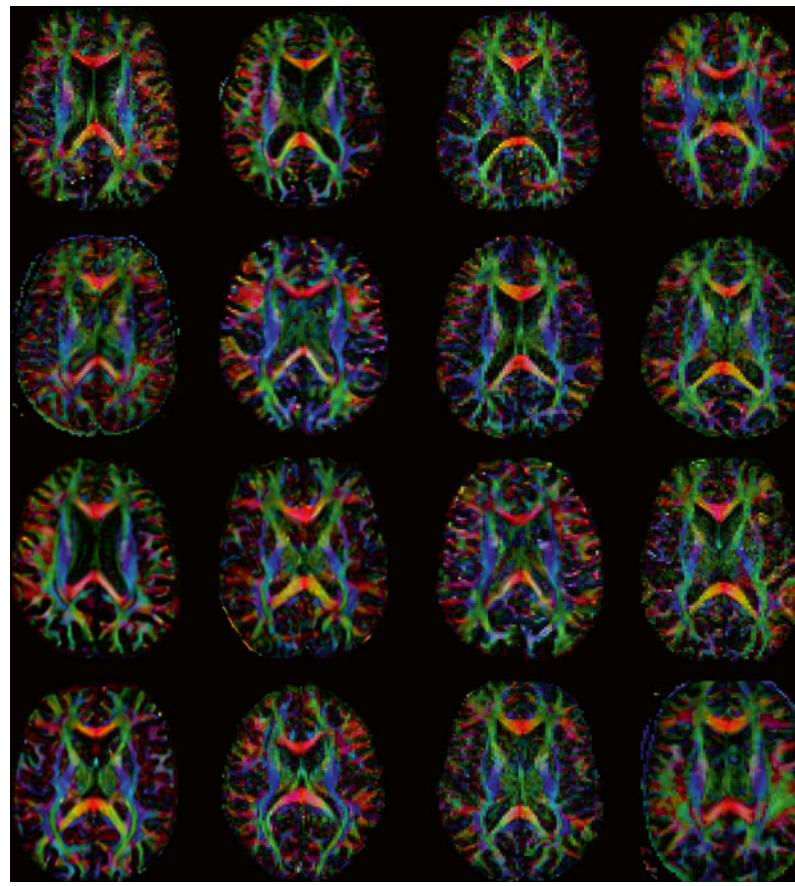

Fig. 8.2 A matching puzzle with DTI. Match the axial colour-encoded FA maps with the correct pathology. In addition to two healthy subjects, there are two images of patients with tinnitus, cerebral palsy, multiple sclerosis, schizophrenia, Alzheimer's disease, spinocerebellar ataxia, and amyotrophic lateral sclerosis

two with schizophrenia, two with Alzheimer's disease, two with spinocerebellar ataxia and two with amyotrophic lateral sclerosis. Is it possible to match the FA maps with the correct pathology and identify the healthy controls?

For all subjects, a similar axial slice was selected. Data from the subjects with the same pathology were acquired using the same protocol in the same study, whereas data from subjects with different pathologies were acquired in different studies (and therefore mostly with different acquisition protocols). Hence, it may be possible to match some subjects based on image quality or based on prior knowledge about the presence of neurodegeneration and ventriculomegaly in some of these disorders. However, when these factors are excluded from the visual assessment of the data, it becomes very difficult to match the pathology to the DTI data. This demonstrates firstly, that changes in FA that occur due to pathology are not always readily visualised on colour FA maps, and secondly, that such FA changes are not specific to one particular disorder. Although visual assessment of colour FA maps can be useful, in general, there is a need for reliable quantitative analysis methods that allow meaningful conclusions to be drawn from the DTI data.

DTI Analysis Techniques

Many different DTI analysis techniques and approaches have been applied to study a range of pathologies and include region of interest analysis, tractography, histogram analysis, atlas-based segmentation, quantification of graph-based connectivity networks, and voxel-based analysis to name but a few. Each of these techniques has its own strengths and limitations and there is no single technique that can be regarded as superior to all the others. The most optimal analysis approach depends on many factors, including:

- The purpose of the analysis (e.g., to delineate a known fibre bundle, to explore the data)
- Whether it is for a single subject or group comparison
- If there is a hypothesis about the location and extent of change or difference in DTI measures
- The data acquisition protocol (e.g., # of directions, b-value, voxel size)
- The data quality
- …

For simplicity, the different techniques that are available to analyze DTI data sets can be classified into three categories:

- Whole-brain analyses
- Region-specific analyses
- Voxel-based analyses

This subdivision of analysis techniques is based on the scale that is used to evaluate the DTI measures in the brain. As shown in Fig. 8.3, DTI analysis can be performed at the level of the whole brain (Fig. 8.3a), at a regional level (Fig. 8.3b), or at the smallest scale, i.e., the voxel (Fig. 8.3c).

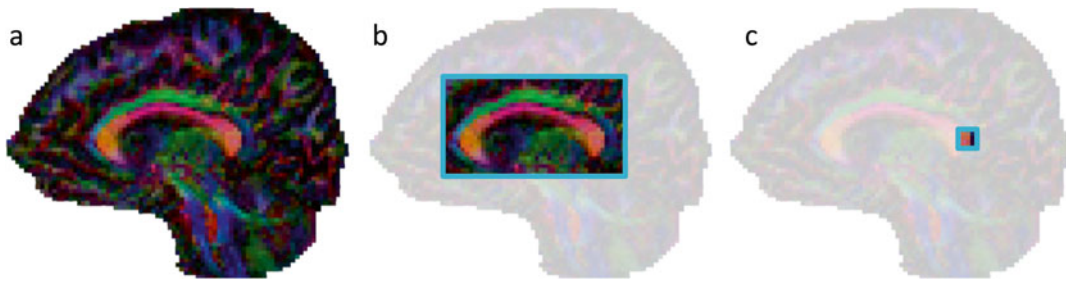

Fig. 8.3 Subdividing DTI analysis methods into three parts: whole-brain analysis approaches (**a**), region-specific analysis methods (**b**), and voxel-based analysis methods (**c**)

In most voxel-based analysis approaches, DTI measures are evaluated at the voxel level, but at the same time in every voxel of the brain. As such, this method can also be regarded as a whole-brain analysis technique. This next section provides a brief overview of each of these major classes of DTI analysis methods.

Whole-Brain Analysis Techniques

The general concept of whole brain DTI analysis techniques is to obtain quantitative DTI measures from all the voxels that include brain white matter, and can thus be subdivided into two parts (see Fig. 8.4):

- An approach to define which voxels are part of the brain white matter
- An approach to extract relevant DTI information from these voxels

The selection of the voxels to be included in the analysis can be done using brain segmentations from anatomical MRI data sets (located in the same image space as the DTI data) or by performing whole-brain tractography. In whole-brain tractography, all brain voxels are used as seed regions to start the tractography process. Using specific parameter constraints such as an FA and curvature threshold, the tracts will mainly traverse white matter voxels, as the FA is lower in grey matter and cerebrospinal fluid.

Once the voxels are selected, the DTI information can be extracted. If anatomical MR based segmentations are used, it is important to ensure that the anatomical image and the DTI data set are located in the same space. It is therefore necessary to register both images to each other (image registration is introduced in Chap. 10). Usually, the anatomical image is transformed to the non diffusion-weighted image using a rigid-body or affine transformation. As all the diffusion-weighted images should already be in the same space as the non-diffusion-weighted image (done during the motion correction, see Chap. 7), the calculated tensors and diffusion metrics will also be aligned with the anatomical MRI. Extracting the diffusion information after whole-brain tractography doesn't involve image registration with an anatomical MR image. DTI measures from voxels that contain a streamline from the whole-brain tractography result will be selected.

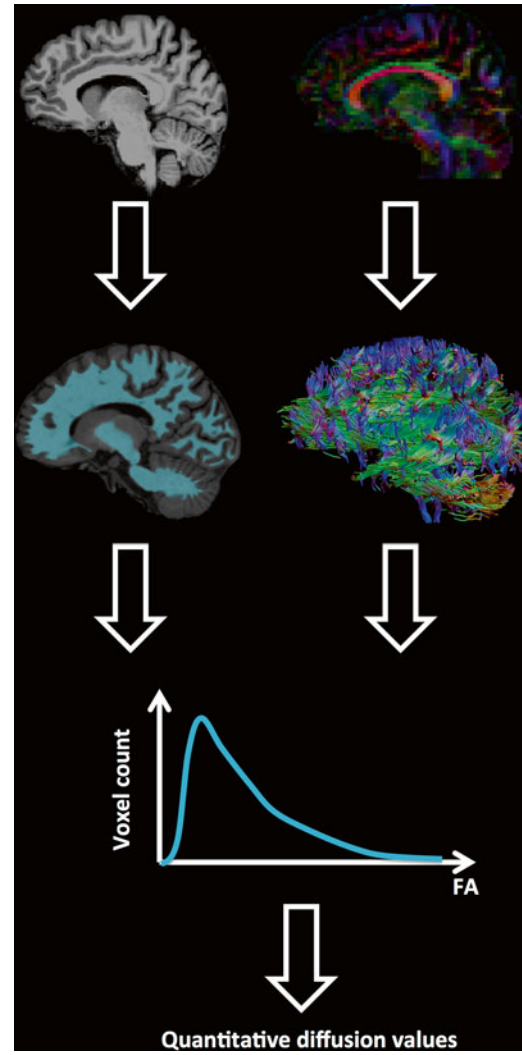

Fig. 8.4 An example of whole-brain analysis of DTI measures. Brain or white matter voxels are defined by a mask created from either an anatomical MRI segmentation or by performing whole brain tractography. A histogram of the diffusion values in these voxels is obtained and relevant information can be extracted and compared

Histogram Analysis

Once the DTI measures have been extracted from the selected voxels of interest, they can be summarized using a histogram (see Fig. 8.4). This histogram is a frequency distribution that displays the number of voxels with a specific value of the diffusion measure (e.g., FA). From this histogram, the following parameters can be extracted:

- Mean or median of the diffusion measure values
- The peak height of the histogram: voxel count of the value that is present the most
- The peak location of the histogram: the diffusion measure value that is present the most in the data set

Usually, studies will only obtain the mean or median value of the diffusion measure. The resulting values can then be statistically compared across groups of subjects or correlated with other variables, such as clinical, neuropsychological or other test scores.

Whole-brain analysis of DTI data has the following strengths and limitations:

Strengths

- Does not require prior knowledge of where hypothesized differences could be found
- Less reliant on user intervention than other approaches
- Results obtained quickly, without labor-intensive interventions
- Fewer statistical tests (i.e., multiple comparisons), compared to other techniques as only one set of diffusion measures is obtained for the whole brain

Limitations

- Regional information is lost as DTI measures are averaged over the whole-brain white matter
- Results are sensitive to partial volume effects due to atrophy
- Results can depend on segmentation/registration accuracy or whole-brain tractography parameters

Region-Specific Analysis Techniques

In region specific analysis techniques, diffusion measures are obtained in one or more predefined areas of the brain. DTI measures, such as the FA and MD are thus statistically evaluated in an anatomical region or white matter tract reconstruction. There are two main approaches:

- Region of interest analysis
- Tractography analysis

Region of Interest Analysis

In *region of interest* (*ROI*) *analysis*, diffusion measures are obtained from a specific brain region, which is defined by manual delineation or by automated segmentation or parcellation. As automated segmentations are less observer dependent and thus more reproducible, they have some clear advantages over manual delineations. However, automated segmentations are not always appropriate, for example due to ill-defined boundaries in regions of pathology.

Manual delineation of ROIs is typically performed by freehand drawing of the region or by placing basic shapes such as circles or squares on 2D slices. Due to the manual interaction that is needed, the results are observer dependent. In addition, manually delineating specific regions in a group of subjects is time consuming. This is especially the case when white matter fibre bundles need to be delineated, as they run through several slices, and thus many 2D ROIs need to be drawn in order to delineate as much of the bundle as possible. Ideally, ROIs should be drawn on maps that are independent of the diffusion measures of interest. For example if FA maps are used to delineate regions, and the FA is a measure of interest, a bias can be introduced in the results because ROIs are typically drawn around regions with a higher FA. However, FA might be lower in areas of pathology, which could then be excluded from the analysis, thereby artificially decreasing differences with the control group. In contrast, regions delineated on an anatomical MR (T1/T2) image are drawn independently of the diffusion measures that will be analyzed. However, this approach also has some potential

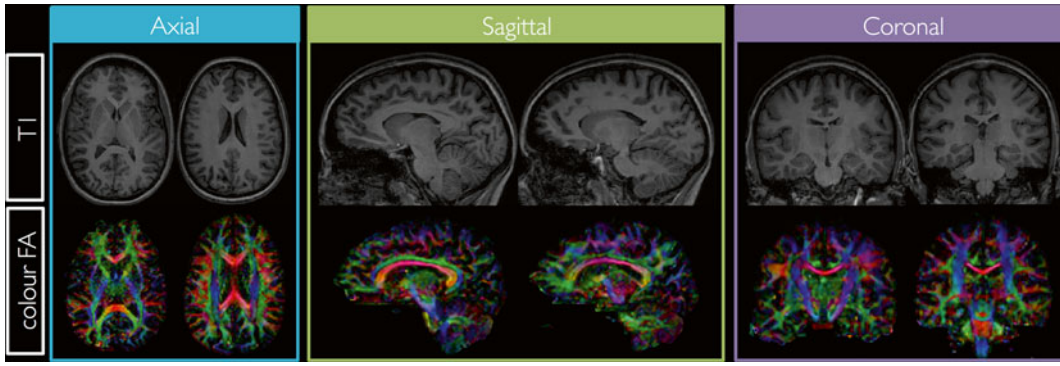

Fig. 8.5 Axial, sagittal, and coronal slices of a T1 weighted image and the color-encoded FA maps of a healthy subject

limitations, as the anatomical MRI data set needs to be registered accurately to the DTI data set, which is not always straightforward due to different distortions in both images [3]. An alternative approach is to delineate the regions on the non-diffusion-weighted image, which should be in the same space as the quantitative diffusion maps after motion correction. However, the delineation of white matter bundles on either the anatomical scans or non-diffusion-weighted images is confounded by the lack of orientational contrast (which is provided by the color FA map). This is illustrated in Fig. 8.5, which shows axial, sagittal, and coronal slices of a T1-weighted image and corresponding color-coded FA slices of a healthy subject

In the presence of lesions, ROI analysis (actually all DTI analyses) can become challenging. This is demonstrated in Fig. 8.6, which illustrates axial non-diffusion-weighted and color-encoded FA slices from five patients with cerebral palsy. The lesions in the left hemisphere clearly affect the visualization of the corticospinal tract (CST). Reliably comparing diffusion values from the left CST with the contralateral CST in this population or of a healthy population would be difficult. For example, delineating the ROI based on the color-encoded FA maps can be biased by the lower FA values in the lesion. However, drawing the ROI on the non-diffusion-weighted image, which is independent from the diffusion measures, is also challenging.

Instead of delineating regions and structures manually, automatic segmentation methods can be used. Such automated methods are especially useful when structures or lesions can be accurately segmented on the anatomical MRI. As an example, T2 lesions could be segmented in a patient with multiple sclerosis. After registering the T1/T2 MR image to the DTI data set and applying the deformation field to the segmented lesion masks, DTI measures can be derived from these lesions. Bear in mind that these results will strongly depend on the segmentation and registration accuracy, especially when some of the lesions are small. In addition, the resolution of the DTI image is typically lower than the resolution of the anatomical MRI that is used for the segmentation, leading to partial volume effects. Finally, note that it is not easy to obtain automatic segmentations of white matter tracts based on anatomical MR images.

Region-specific analysis of DTI data by using the ROI approach has the following advantages and limitations:

Strengths

- In comparison to whole-brain analyses, more regionally specific information is obtained
- Manual delineation is closer to the original data than other techniques which require more complex modeling and image processing
- ROI analysis is less dependent on parameter settings than tractography or voxel-based analysis

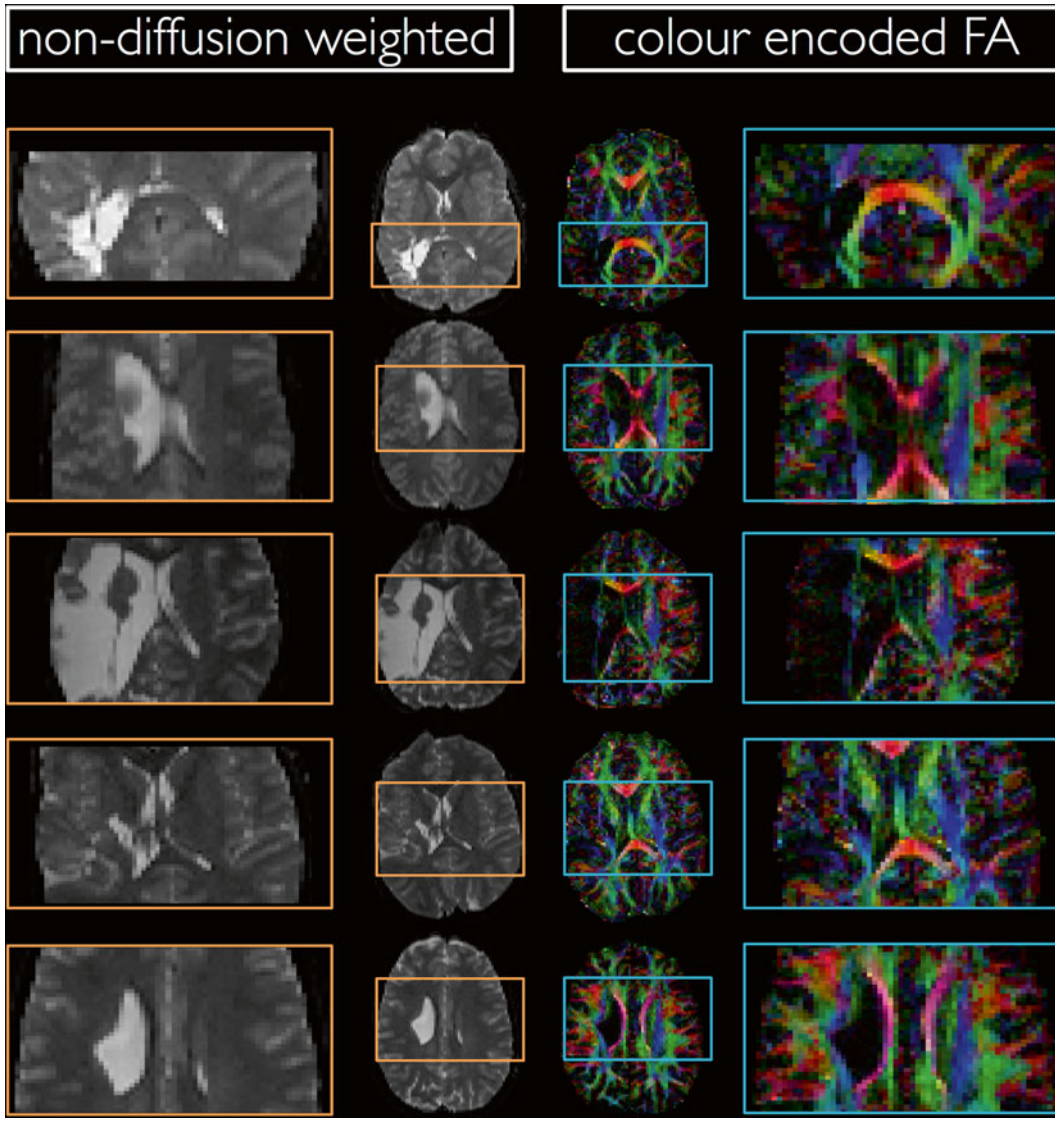

Fig. 8.6 Axial non-diffusion-weighted and color-encoded FA slices in five patients with cerebral palsy. The presence of lesions make ROI delineation challenging

Limitations

- Requires a prior hypothesis about where differences could be found, as that is where the ROI will be placed.
- Intra- and inter-observer reproducibility of results should be assessed, as manual delineation is subjective.
- Requires clear guidelines that describe how the ROI should be defined (e.g., size, anatomical location, boundaries).
- The selection of many ROIs increases the number of statistical tests that are performed and therefore correction for multiple comparisons is required.

- Results can be biased if ROIs are drawn on the parameter map of the measure of interest, e.g., drawing an ROI on a color FA map when investigating FA.
- Results can depend on segmentation/registration accuracy when ROIs are delineated on anatomical MR images.
- Delineating regions manually is very time consuming and laborious.
- Excludes (potentially valuable) information from regions that are not selected/studied.
- Drawing an ROI or segmenting a structure can be challenging in the presence of pathology.

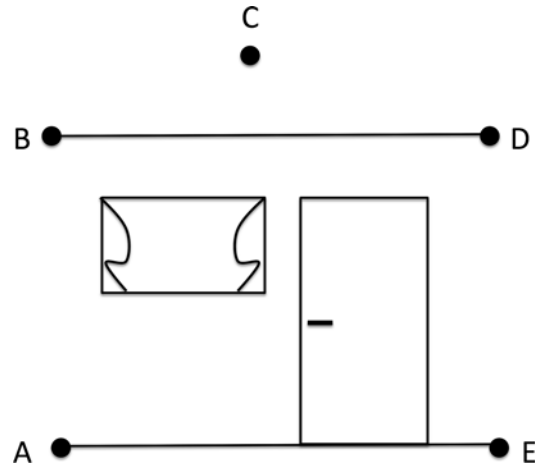

Fig. 8.7 Connecting the dots: by following the alphabet and drawing a line between subsequent letters, the global picture (i.e., a house) becomes clear

Tractography Analysis

The delineation of white matter tracts using only 2D manually drawn ROIs or anatomical MR images is not optimal for the reasons outlined previously. However, by using the inherent directional diffusion information in the DTI data set, virtual representations of white matter fibre bundles can be reconstructed, using *tractography* (or "fibre tracking"). Tractography refers to the mathematical reconstruction of white matter fibre bundle representations by integrating the local diffusion tensor information from every voxel. In its simplest form, tractography can be compared with a puzzle "connecting the dots." As shown in Fig. 8.7, by following the letters alphabetically, and drawing lines between subsequent letters, one can complete the drawing and the global picture.

How diffusion tractography relates to "connecting the dots," is shown in Fig. 8.8. Instead of the alphabet and the natural sequence of letters, the orientational diffusion information can be followed and connected to create a more global picture of the white matter bundle. Consider two voxels in the brain, i.e., the green and blue voxels that are shown in Fig. 8.8a. The DTI data can be used to estimate tensors in every voxel. Recall that these tensors can be represented by an ellipsoid whose longest axis represents the direction of maximal diffusion. For visualization purposes, only the relevant tensors between the green and blue voxels are displayed, as shown in Fig. 8.8b. As explained in Section 2 of this book (Chaps 3–5), the orientation of the estimated tensor is assumed to relate to the underlying white matter architecture, as the amount of diffusion along the axonal bundles will be greater compared to the amount of diffusion perpendicular to them. DTI tractography is based on the assumption that by following the maximal amount of diffusion in a given direction (i.e., the longitudinal axis of the ellipsoid) in each voxel, the orientation of axon bundles can be followed, and hence the tensors provide an indirect, simplistic, discrete representation of white matter fibre pathways, as shown in Fig. 8.8c. In practice, these assumptions suffer major flaws, which are discussed in detail in several other chapters (see especially Chaps. 5, 11 and 21).

If the tractography process is started in the green voxel A (referred to as the seed voxel), the main direction of diffusion is followed, until a new voxel is reached (voxel B in Fig. 8.8d). This process is then repeated until a certain stop criterion is reached. Typical tracking initiation and termination criteria are based on selection and exclusion ROIs, and FA, fibre length and curvature thresholds. For example, tracking may be stopped when the FA in a voxel is below 0.2, to prevent streamlines going into low anisotropy grey matter or CSF. These ROIs and thresholds determine the number of streamlines and how

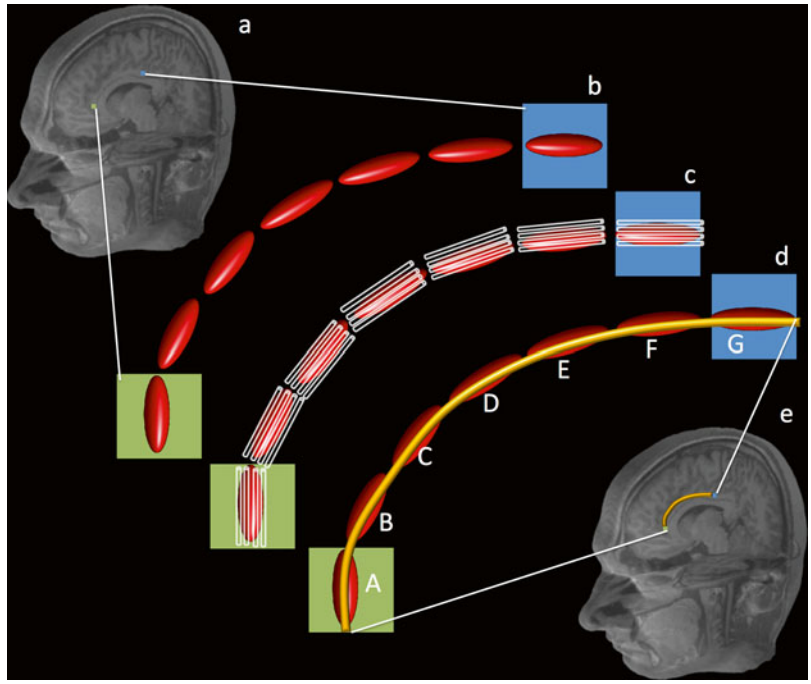

Fig. 8.8 A simplified example or diffusion tensor tractography. Two voxels are selected in the brain (**a**) and the relevant tensors in between the voxels are visualized (**b**). As these tensors are representations of the underlying white matter axonal bundles (**c**), they can be used to mathematically reconstruct virtual representations of these bundles (**d** and **e**) [Courtesy of A. Leemans]

they travel through the data, and hence the final tract reconstruction. It is therefore important to realize that tractography is both operator and parameter dependent, and there is no 'ground-truth' solution to validate tracking results.

In the example of Fig. 8.8, tracking ends in the blue voxel, as shown in Fig. 8.8d. The pathway from seed voxel to end point can be represented by a streamline. In this simplified case, a single the streamline represents a fibre tract (see the orange line in Fig. 8.8e, representing part of the cingulum); however in practice, many streamlines make up a fibre tract.

It is worth noting that some of the terminology used in tractography can be confusing. In tractography, a fibre, streamline or track is *not* synonymous with an actual nerve fibre in the biological sense, and a fibre tract is not synonymous with an anatomical fibre bundle (even in the case of fibre bundles that include "tract" in their anatomical name, such as the corticospinal tract!). These concepts are explained in more detail in Chap. 11. In this context, it is very important to understand that the resulting fibre tracts are virtual mathematical reconstructions that bear some resemblance to parts of axonal bundles. Therefore the thickness, length or number of these reconstructed tracts cannot be *directly* related to the underlying microstructure or anatomy.

As tractography uses directional diffusion information to reconstruct connections in the brain, it is an elegant technique for obtaining diffusion measures from specific white matter bundles. One of the most useful and common applications of tractography is the noninvasive, virtual dissection of fibre bundles in 3D, i.e., segmentation. The segmented tract is equivalent to a 3D ROI from which diffusion measures can be calculated. This obviates the need to delineate the bundle manually by using 2D ROIs on different slices or to apply segmentation methods to anatomical MR images, which contain less specific white matter tract information. Typically, the average of the DTI measure, e.g., FA, is calculated from all voxels that are part of the delineated tract. A less commonly used, but useful strategy is to also measure the value at predefined points or along the length of the bundle. Such

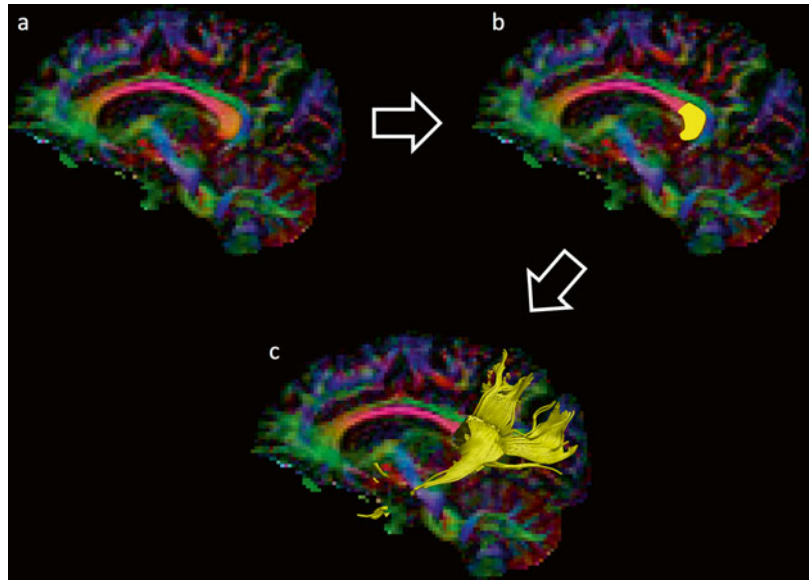

Fig. 8.9 An example of a tractography analysis. A sagittal slice is selected (**a**) to draw a seed region for tractography (**b**). Diffusion measures can then be calculated from the resulting tracts (**c**)

tract profiles or distributions may reveal more localized differences that are lost when averaging over the length of the tract. Some people refer to this as "tractometry" [4].

An example of a tractography analysis is shown in Fig. 8.9. Starting from a sagittal color-encoded FA slice (Fig. 8.9a), a region of interest is drawn as a seed region for tractography (Fig. 8.9b). The resulting tracts, in this case a representation of the splenium of the corpus callosum, are shown in Fig. 8.9c. Diffusion measures can then be extracted from these tracts and compared across subject groups or correlated with clinical or neuropsychological scores.

Region specific analysis of DTI data using tractography has the following strengths and limitations:

Strengths

- In comparison to whole brain tractography or histogram analyses, more regionally specific information is obtained.
- Tractography provides an intuitive way of reconstructing 3D virtual representations of white matter bundles in vivo using diffusion information.
- As typically only very few ROIs are necessary to calculate the tracts, it is in general more reproducible compared to ROI-based methods.

Limitations

- Requires a prior hypothesis about where differences could be found as DTI measures will only be analyzed in the tracts that are reconstructed.
- Tract reconstructions depend on many parameters.
- Tractography results are often affected by the "crossing-fibre" problem.
- In non-automated methods, the use of manually defined ROIs for tract selection means that tractography results are observer dependent. Ideally, clear guidelines should be followed regarding ROI placement.
- Noise and other artifacts affect tract reconstruction, and therefore the selection of voxels that will be used in the analysis.
- The selection of many tracts increases the number of statistical tests that are performed and therefore correction for multiple comparisons is required.

- Pathology can affect the tractography result, again potentially creating a bias.
- There is no ground truth to validate tractography results.

Note that region-specific analyses can also be performed using automated approaches and templates/atlases. This will be discussed in the next section on voxel-based analysis.

Voxel-Based Analysis

One of the advantages of region-specific analyses compared to a whole-brain analysis is that information can be obtained from specific brain areas of interest. As such, the obtained DTI measures have the potential of being more sensitive (not averaged out over the whole brain) as well as specific (localized changes might be related to a certain pathology). Voxel-based analysis techniques take this idea further by evaluating and comparing DTI measures at the smallest imaging scale possible, i.e., the individual voxel. At the same time, DTI measures are compared in all voxels, so this analysis method could also be regarded as a whole-brain analysis technique.

One of the main challenges of any group analysis, and particularly voxel-based analysis, is selecting spatially corresponding voxels across subjects to compare the DTI values. If this condition is not satisfied, it does not make sense to compare the voxel measures. The process of aligning corresponding voxels in different data sets is referred to as image registration, and is an important step in the voxel-based analysis pipeline. Between-subject image registration is especially challenging because the brains of different subjects can vary in size and shape at the global as well as local level. However, when correspondence between images can be achieved at the voxel level, voxel-based analysis is a powerful tool to analyze DTI data. Since it is highly automated, there is no need for an a priori hypothesis about the location of anticipated changes, and the observer dependence of the results is minimized.

Typically, a voxel-based analysis pipeline consists of the following steps:

1. Selection of the atlas/template space to which all data will be aligned
2. Alignment of all data to this atlas using global and local registration methods
3. Smoothing of the aligned data sets
4. Statistical analysis in every voxel

For each of these steps, there are a number of choices to be made, both in terms of selecting the appropriate approach as well as choosing the specific parameters that will be used. As it has been shown that voxel-based analysis results depend on these choices, every step of the pipeline should be considered with care and parameter selections should be justified.

An overview of VBA is provided in Fig. 8.10. Voxel-based comparison of FA values is performed for two groups of subjects, each consisting of five subjects. In Fig. 8.10c, d. Although these images are warped during spatial alignment, the registration process ensures that voxels in the spatially aligned images retain the same quantitative diffusion values as in the original data, thereby allowing statistical comparisons to be made. Depending on the type of VBA implementation used, the warped images may be smoothed, for example to increase signal-to-noise in the parameter maps (smoothing is discussed in detail in Chap. 10). A specific voxel with the same x, y, and z coordinates in the atlas space is then selected across subjects and subject groups (as shown by the blue and green lines in Fig. 8.10c, d). The FA values from the different subjects in that voxel can be visualized by a histogram (as shown in Fig. 8.10e). FA values in that specific voxel can then be compared statistically between the groups. When statistical significance is reached, the voxel can be given a colour, as shown in white in Fig. 8.10f). This process of statistical testing of FA values between groups is repeated for every voxel, resulting in a VBA map that displays the voxels and regions in which a statistical difference is found between the groups.

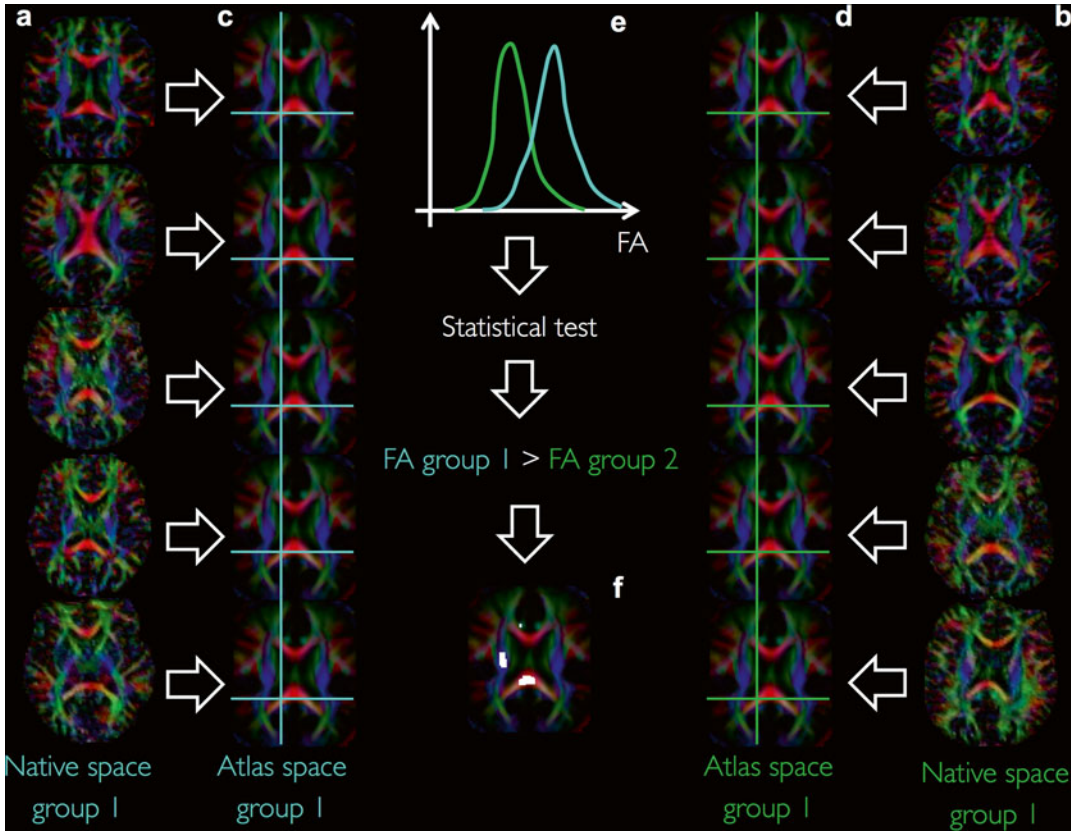

Fig. 8.10 An example of a voxel-based analysis of two groups of five subjects. The original data sets (**a** and **b**) are transformed from their native space to the atlas space (**c** and **d**). Within each voxel of the registered data sets the diffusion measures, such as the FA value, can be evaluated statistically (**e**). Statistically significant voxels are then highlighted, for example by labeling with a specific color (here, *white*) or by coloring according to a test statistic. This provides a visual map of group differences (**f**)

As there are many thousands of voxels in a typical DTI parameter image, many thousands of statistical tests need to be performed in VBA, making it necessary to perform some sort of correction for multiple comparisons, to reduce the number of false positive findings. The number of statistical tests can be reduced by limiting the analysis to, for example:

- White matter
- Manually drawn regions in atlas space
- Specific regions, as derived from atlas parcellations
- Specific white matter tracts, by performing tractography in atlas space (tensor information should then be available in the atlas)

These "hybrid" analysis methods combine the strengths of the different analysis techniques and try to avoid specific limitations of them.

Voxel-based analysis of DTI data has the following advantages and limitations:

Advantages

- The data is analyzed at the smallest scale, i.e., at the voxel level.
- The whole brain is evaluated as all voxels are included in the analysis.
- No a priori hypothesis about the location of the expected differences is needed.
- The manual observer interaction and therefore the observer dependence of the results is minimized.

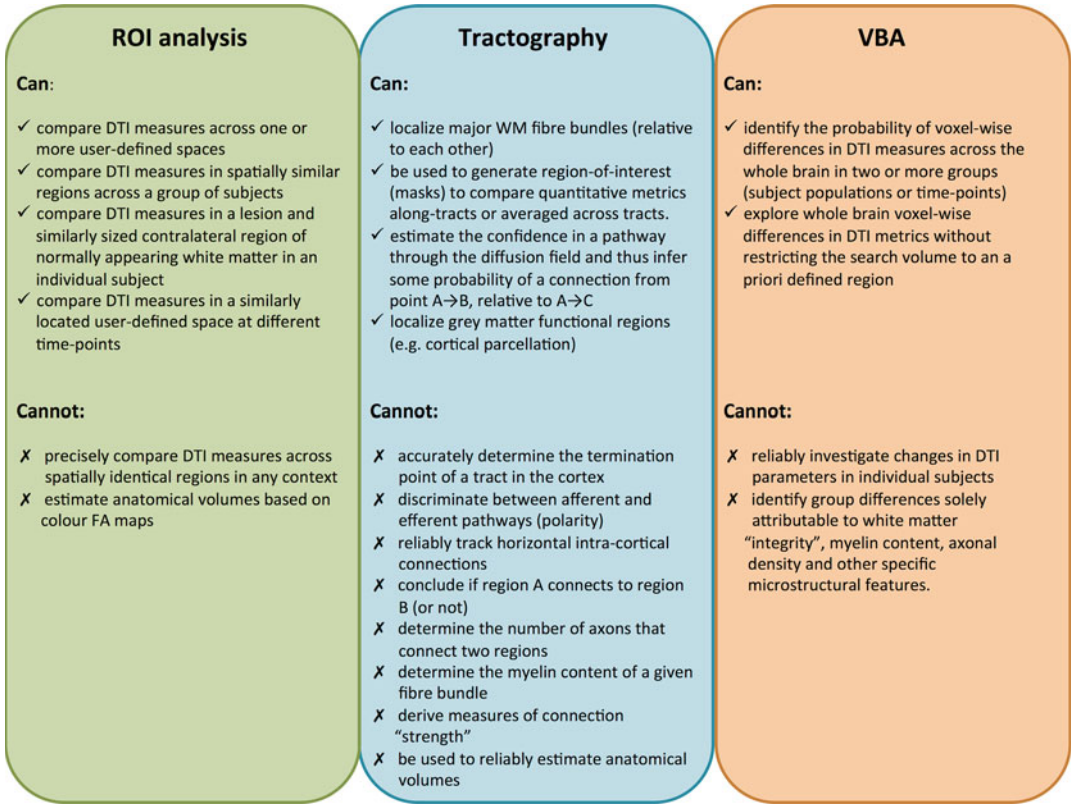

Fig. 8.11 Capabilities and limitations of different analysis approaches

Limitations

- Results depend on the parameters that are chosen in the voxel-based analysis pipeline.
- As statistical analysis is performed in every voxel, there is a chance of false positive findings and multiple comparison correction should be applied.
- Diffusion measures are compared in every voxel, not in specific tracts.
- Results are only meaningful when accurate image registration can be achieved.
- Pathology and lesions can affect the results, especially when the location of the lesions is variable across subjects.

Choosing an Optimal Analysis Approach

Unfortunately, there is no single DTI analysis approach that is optimal for evaluating diffusion MRI measures for all studies and purposes. As different analysis techniques each have their own strengths and weaknesses, and rely on various assumptions, choosing the most optimal analysis approach for a given purpose is an important step in the DTI pipeline. For example, Fig. 8.11 provides a summary of what can and cannot be done using different analysis approaches.

In this section, a short and non-exhaustive overview of factors and guidelines is provided to help select the best analysis technique(s) for different applications. Ideally, these considerations should be made *before* acquiring the data. A much more detailed overview of factors that need to be considered when using DTI in clinical populations can be found in Chap. 13. It is important to stress that these guidelines are not prescriptive and the choice of which methodology to choose ultimately rests with the DTI user. The important point is that each choice should be appropriately reasoned and justified.

Things to Consider before Starting DTI Data Analysis

Goal and Hypothesis

The choice of which DTI analysis technique to apply will depend on the *general goal* of using DTI, i.e. whether the data will be used for a group study in a research setting or for individual patient analysis in clinical practice. For example:

- In research studies, typically, a longer DTI acquisition can be performed compared to the clinical routine, which can impact the selection of a DTI analysis approach. For example, some of the more advanced tractography techniques (see Chaps. 11 and 20) require the acquisition of a large number of diffusion-weighted images acquired along different gradient directions.
- Not all DTI analysis techniques can be easily applied in individual patients, e.g., voxel-based analyses.
- The use of DTI for an individual patient in clinical practice requires the use of CE/FDA approved software, thereby limiting the possible DTI analysis options.

The presence or absence of a *specific hypothesis* about the nature and/or location of the expected diffusion changes can also influence the selection of an appropriate analysis technique.

- *Region-specific DTI analysis* methods can be used to evaluate the diffusion measures in areas where changes are expected. When differences are hypothesized to be present in specific white matter bundles, fibre tractography can be used to reconstruct virtual approximations of these pathways. To evaluate the diffusion measures in lesions or specific parts of a white matter bundle, region of interest analysis can be applied.
- *Voxel-based analysis* can be used for exploratory studies or if no clear hypothesis can be made about the location of the expected differences in diffusion parameters. Recall that in a voxel-based analysis, it is assumed that the changes in the diffusion measures occur in similar regions of the brain in different patients. This is unlikely to be the case in many clinical populations, e.g., traumatic brain injury.
- *Whole-brain analysis* methods can be applied if more global diffusion changes are expected or if the location of diffusion changes is heterogeneous between patients.

The Study Population

With regard to the study population, the following factors should be considered:

- *Population composition*: Can the patient group be regarded as one homogeneous group, or does it need to be subdivided into different subgroups? Is there a need for a matched healthy control group?
- *Population size*: How many subjects should be included in each group in order to be able to draw meaningful conclusions? This will depend on the magnitude of expected differences or changes in diffusion parameters. For example is the amount of change likely to be statistically or visually detectable given the unavoidable presence of noise or artifacts in the data?
- *Population characteristics*: Different factors, such as age, gender, IQ, handedness, etc. may affect the diffusion measures. Different subject

groups should therefore be carefully matched with respect to these factors. For example, if children or elderly subjects are scanned, the choice of which DTI analysis technique to apply can be affected, because:
  - The DTI acquisition time may be shorter and data quality may be affected by increased subject motion.
  - Of differential rates of brain structural change due to development or neurodegeneration.
  - Image registration of DTI data from children or elderly to an adult atlas can introduce errors, which will therefore impact analysis techniques that don't make use of appropriate population atlases [5].
- *Population pathology*: The presence and nature of brain lesions can complicate DTI analysis by distorting normal anatomy (see Fig. 8.6), and hindering image registration and tractography. The degree to which analysis will be affected or the affect on method selection will depend on:
  - If the lesions are focal or diffuse
  - The size and location of the lesion/s
  - The number of lesions
  - Variability of location across patients
- In addition to the presence of lesions, neurodegeneration can affect DTI analysis and interpretation, because of:
  - The increased presence of partial volume effects
  - The challenges associated with image registration to a healthy adult atlas

The Data Acquisition

Data quality and data analysis are affected by the choice of *DTI acquisition* parameters such as the:

- Number of diffusion directions
- Image resolution
- *b*-Value
- Number of *b*-values
- Number of averages

For example, the tensor estimation, tractography result and image registration result depend on the data quality, which depends on which DTI acquisition parameters are chosen. Some types of analysis techniques, such as tractography are indeed more suited to acquisition schemes with more gradient directions. In longitudinal or multicenter studies, the scanner performance and acquisition parameters should be monitored. A DTI hardware phantom is useful for quantifying data quality over time and across centers.

The Resources

The following resources should be considered with regard to DTI analysis:

- *People*: Which clinical and technical/software expertise is present or needed to perform the analysis and interpret the results?
- *Time*: How much scan time is available to obtain the DTI data? Is there time to evaluate different analysis approaches and compare the results, or perform labour-intensive analysis methods such as a region of interest analysis or non-automated fibre-tracking? Is there time to run complex computational processes that may take hours or several days to complete, or are results required immediately?
- *Software and hardware for analysis*: Will the data be processed on the scanner or off-line on a separate computer or server? Which software will be used?
- *Money*: Is there money available to buy specific software packages or licenses, to acquire enough data sets, or to outsource part of the analysis?

Selecting an Optimal DTI Analysis Approach

When faced with so many factors to consider, it is easy to become overwhelmed with choices and lose sight of the reason for acquiring DTI data in the first place. The decision scheme in Fig. 8.12 therefore aims to guide the DTI user in choosing which type of analysis technique to

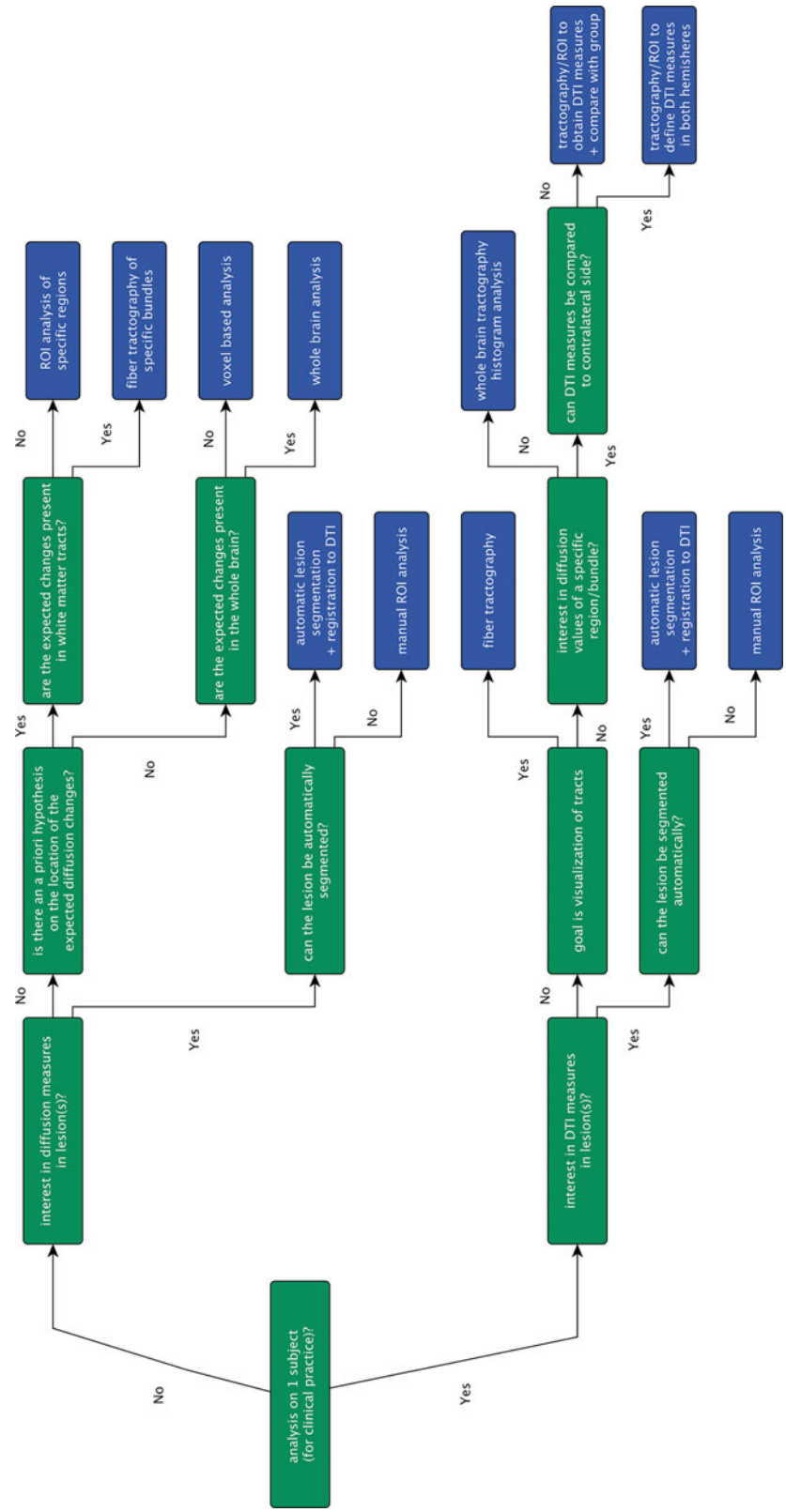

Fig. 8.12 A decision scheme to assist with DTI analysis method selection based on the aim of the DTI study

use according to the initial goal of the DTI investigation.

It is important to stress that this decision scheme does not provide a complete and comprehensive overview of all the relevant questions that could be asked when choosing a DTI analysis method, nor does it provide formal solutions or strict answers. Figure 8.12 should be interpreted as an example of how knowledge about the different analysis options and their pitfalls can be incorporated into an informed decision process, which can assist in the selection of a specific analysis approach.

Selecting a Software Package to Analyze the Data

Many DTI software packages are available, all with different functionalities, ranging from data import, basic image viewing and processing, image quality correction, registration, automatic segmentation, and DTI tractography to higher order diffusion modeling and advanced tractography. Most of the packages can perform the fundamental pre-processing needed for DTI analysis, such as tensor estimation, and visualization of scalar diffusion maps and glyphs. However, the specific approaches for preprocessing, e.g., the mathematical model for tensor estimation, and motion and artifact correction methods, can differ. In addition, there are a wide range of different options and approaches for tractography, which vary according to the algorithms used in the software package and the parameters that can be chosen to control them.

This inconsistency between different DTI analysis tools is further complicated by the use of different terminology for both the same and different operations across packages. It is (unfortunately) possible to perform (apparently) the same analysis using (apparently) the same parameters on the same dataset and obtain different results when using different packages [6], or even using different software versions of the same package. This is because of (sometimes subtle) differences in the way the software developers have integrated the continuously evolving theoretical methods that underlie DTI data processing into their applications, as well as the way their code interacts with different software programs and operating systems. Not only does this add to the challenges of interpreting findings, but means that it is extremely important to use the same package and software version for the analysis of all the datasets in the same study. This is particularly important in longitudinal investigations and may require analyzing new data with older software, or preferably, all the data with the most up-to-date software version.

In this context, it is also important to become familiar with the different parameter settings and how changing them affects the final results. Although most packages provide reasonable default settings, the most optimal results may require some empirical parameter adjustment. This is particularly relevant in VBA and tractography-based analysis, and indeed in any analysis employing image registration (including data correction strategies). Chapter 11 provides some compelling visual examples of how changing just a single parameter can drastically alter tractography results.

New DTI software packages and tools are continuously being released whilst older ones are being developed to incorporate new features, bug fixes, and enhancements. For this reason, specific DTI software tools and their functionality are not listed in this chapter. Instead, we recommend consulting The Neuroimaging Informatics Tools and Resources Clearinghouse (www.nitrc.org) and 'I do Imaging' (www.idoimaging.com) websites which list many of the latest noncommercially developed DTI software. Details about proprietary DTI vendor software can be obtained from the respective MRI scanner manufacturer applications specialists. Further details about DTI analysis software can be found in Chap. 13, including topics such as data storage, export/import and file formats, version control, and licensing. Figure 8.13 provides a summary checklist of considerations related to choosing DTI analysis software.

- Is it approved for clinical use? (e.g. FDA approved)
- Has its use been validated scientifically? (e.g. in peer-reviewed publications)
- Is it easy to install and run?
- What system requirements does it need? (e.g. operating system, memory, processer etc.)
- Does it require additional software (including specific libraries/scripts etc.) to run?
- How much does it cost?
- Is there any technical support available? (e.g. instruction manual, mailing list, contact person or helpdesk)
- How much technical support is available? (e.g. level of detail in manual, activity on mailing list, responsiveness of development team)
- Are change-logs provided that document changes to the source code and software functionality between versions or following software upgrades?
- Is it compatible with or does it generate files that are compatible with other commonly used software packages?
- Is it command-line based or use a graphical user interface?
- Is the source code available to view or modify? (e.g. for trouble-shooting, development and to customize for in-house use or public distribution)
- Is it possible to check the data at each stage of the analysis pipeline?
- Does it include any of the following features?
    - Image viewer (2D / 3D)
    - DICOM or Vendor format file import
    - Data quality assessment and / or correction tools
    - A choice of tensor estimation strategies
    - Histogram analysis tools
    - Region-of-interest analysis tools
    - Tractography analysis tools
    - Group analysis tools (e.g. VBA, atlas-based tractography)
    - Other image processing tools (e.g. registration, editing etc.)

Fig. 8.13 Checklist of considerations and features to DTI analysis software

Conclusion

In conclusion, the analysis of DTI data sets forms only one part of a DTI study. In each phase of a DTI investigation, choices and decisions have to be made. The most optimal analysis approach will therefore depend on the decisions made in earlier stages of the DTI pipeline.

There are many options available for analyzing DTI data sets, ranging from whole brain to regional and voxel-based analysis. Knowing the

advantages and pitfalls of each analysis technique can help with selecting the best strategy for a given application.

The following chapters in this section provide a more detailed overview of the most commonly used DTI analysis techniques.

Acknowledgments We would like to thank Ann Van De Winckel, Thibo Billiet, Alexander Leemans, and Dirk Smeets for providing us with some of the images and data sets that were used to create the figures in this chapter.

Appendix: Memory Game Solution

In Fig. 8.14, the solution to the memory game in Fig. 8.2 is provided. Was it possible to match the pathologies with the FA maps?

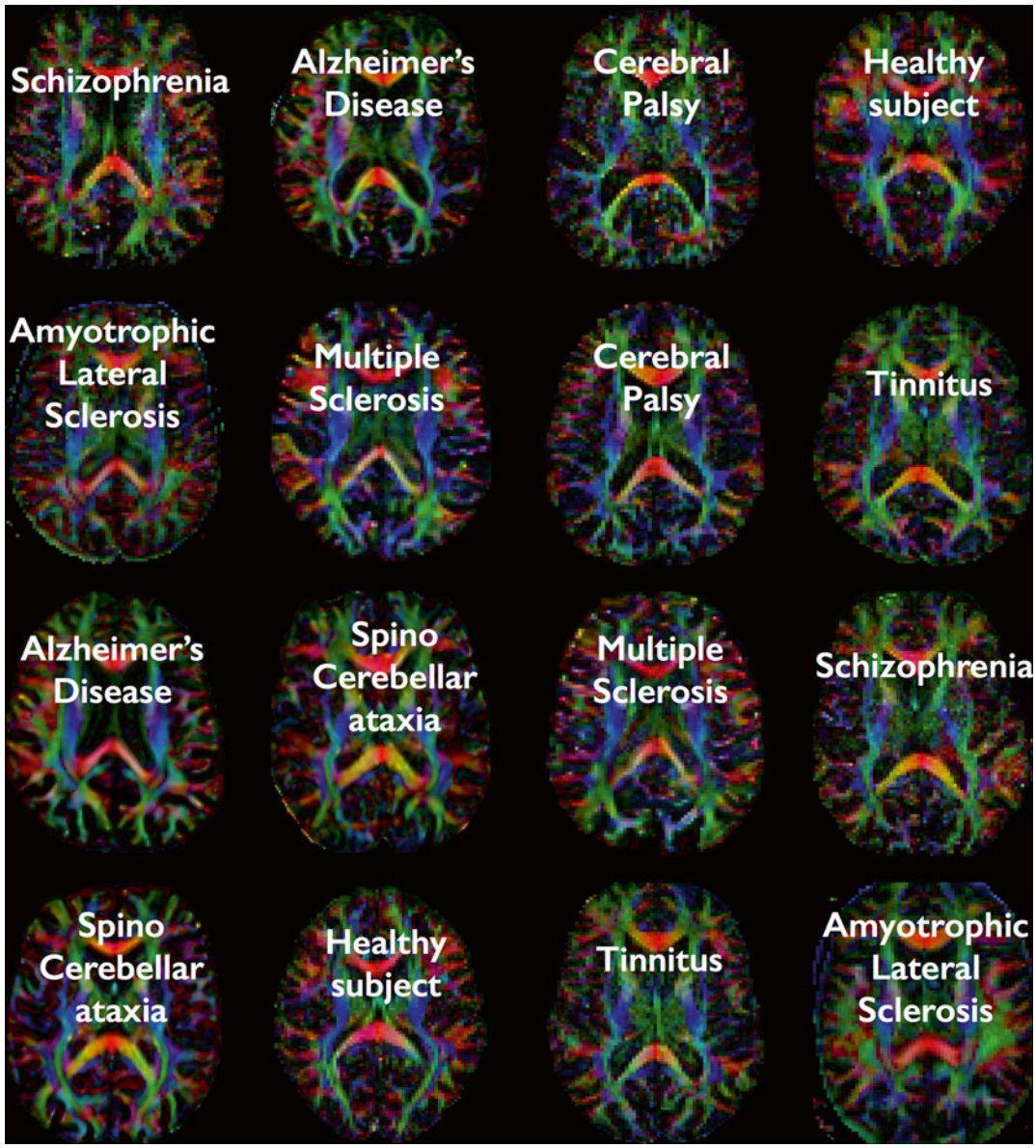

Fig. 8.14 Solution to the DTI memory game

References

1. Soares JM, Marques P, Alves V, Sousa N. A hitchhiker's guide to diffusion tensor imaging. Front Neurosci. 2013;7:31.
2. Mukherjee P, Berman JI, Chung SW, Hess CP, Henry RG. Diffusion tensor MR imaging and fiber tractography: theoretic underpinnings. AJNR Am J Neuroradiol. 2008;29(4):632–41.
3. Jones DK, Cercignani M. Twenty-five pitfalls in the analysis of diffusion MRI data. NMR Biomed. 2010;23(7):803–20.
4. Jbabdi S, Johansen-Berg H. Tractography: where do we go from here? Brain Connect. 2011;1(3):169–83.
5. Van Hecke W, Leemans A, Sage CA, Emsell L, Veraart J, Sijbers J, et al. The effect of template selection on diffusion tensor voxel-based analysis results. Neuroimage. 2011;55(2):566–73.
6. Burgel U, Madler B, Honey CR, Thron A, Gilsbach J, Coenen VA. Fiber tracking with distinct software tools results in a clear diversity in anatomical fiber tract portrayal. Cent Eur Neurosurg. 2009;70(1):27–35.

Suggested Reading

7. Jones DK, Knösche TR, Turner R. White matter integrity, fibre count, and other fallacies: the do's and don'ts of diffusion MRI. NeuroImage. 2013;73:239–54.
8. Cercignani M. Ch 29: Strategies for patient-control comparison of diffusion MRI Data. In: Jones DK, editor. Diffusion MRI: theory, methods & applications. New York, NY: Oxford University Press; 2010. p. 485–99.

DTI Analysis Methods: Region of Interest Analysis

9

Martijn Froeling, Pim Pullens, and Alexander Leemans

Learning Points

- Different strategies to define regions of interest (ROI)
- Advantages and limitations of a ROI analysis
- Effects of ROI size, co-registration, and statistical analysis methods on results

Introduction

The region of interest (ROI) analysis method is based on the delineation of predefined areas of the image and is a commonly used method for quantitative analysis of diffusion tensor imaging data. A ROI is defined as a selected area of an image from which the individual or average pixel values are extracted for further analysis. The ROI commonly has to be manually drawn, but in some cases it can be obtained by (semi-)automated segmentation. The chosen region can be a geometrical shape (i.e., sphere, cube) or be defined by the shape of the anatomical structure of interest. The first is faster but less precise, whereas the second option is more time consuming but in general gives more accurate results, as will be discussed further on.

Overall the ROI analysis method is relatively easy to use and is supported by most diffusion tensor imaging data analysis software [1]. Its main benefit is the high sensitivity to small changes of the parameters of interest [2]. Additionally the method requires only little technical know-how compared to other techniques discussed later on in this and following chapters. However, it also has numerous drawbacks. ROI analysis is very time consuming and a clear hypotheses about the location of pathology is needed. Therefore it does not allow for full brain coverage and requires at least a moderate knowledge of the anatomy. Furthermore, even with expert knowledge of the anatomy and precise ROI definition the technique is very susceptible to inter- and intra-user variability.

This section covers the basis of ROI analysis, when to use and more importantly when not to use the technique. When applying ROI analysis a clear hypotheses is needed and the ROIs have to be accurately defined. Important considerations

M. Froeling, PhD (✉)
Image Sciences Institute, University Medical Center Utrecht, Heidelberglaan 100, 3584 CX Utrecht, The Netherlands
e-mail: m.froeling@umcutrecht.nl

P. Pullens, PhD
icometrix, Leuven, Belgium

Department of Radiology, Antwerp University Hospital, University of Antwerp, Antwerp, Belgium

A. Leemans, PhD
PROVIDI Lab, Image Sciences Institute, University Medical Center Utrecht, Utrecht, The Netherlands

W. Van Hecke et al. (eds.), *Diffusion Tensor Imaging*, DOI 10.1007/978-1-4939-3118-7_9

that will be discussed are the effect of the position and size, ROI normalization, image registration, and statistical analysis.

When to Use ROI Analysis

Because of its good sensitivity, ROI analysis is best performed when a clear hypothesis is present about the expected differences in white matter in a well-defined region of the brain. As stated in the introduction, the region can be defined by anatomical structure (e.g., corpus callosum, amygdala), pathology (stroke, lesion, tumor, etc.), geometry (sphere, cube, etc.) or input from another modality, e.g., fMRI. The ROI should not be too large in size, because of statistical reasons explained further on in this chapter. ROI analysis is especially useful in regions where there are lesions, e.g., tumors. In these cases tract based analysis (TBA) might be impossible due to the lack of normal fiber pathways. Furthermore, registration of a brain with lesions to a standard brain atlas may be difficult or flawed due to deviations from the normal anatomy.

When Not to Use ROI Analysis

ROI analysis can clearly not been used if there is no hypothesis about the location of the effects in the brain. If structural data are absent or of poor quality, other methods such as extraction of diffusion metrics from fiber bundles, histogram analysis [3, 4], voxel-based analysis [5], or TBSS [6] might be better suited, as will be discussed in the next chapters.

Well-Defined Regions

To define a ROI usually the region is drawn by hand on a structural MRI image (T1/T2 weighted). To the investigator ("anatomist") it should be clear what the borders of the regions are and to what extent it should be included. For example, the corpus callosum could be outlined on a mid-sagittal slice and extended 2–3 slices laterally in both directions.

ROIs can also be defined on FA or ADC images, especially when white matter structures are being investigated, where contrast is minimal on a T1- or T2-weighted image. In this approach care must be taken not to fall into the trap of circular reasoning, because drawing of the ROI is not independent of the studied data. This approach can also be taken when investigating pathologies on ipsi- and contralateral sides of the brain as is shown in the next paragraph.

Some pathologies, stroke for instance, are clearly visible on a trace or ADC map, but not on other modalities, as is shown in Fig. 9.1. In this case the trace or ADC map is the obvious choice for ROI definition. By mirroring the ROI to the contralateral side of the brain, DW metrics can be studied in both affected and healthy tissue.

When the researcher is interested in a sub-part of a certain structure and wants to have control over the size of the ROI, a geometrical ROI (circle/sphere, square/cube, etc.) could be used. The ROI is then placed in the center of the structure and has the same size in each subject, in contrast

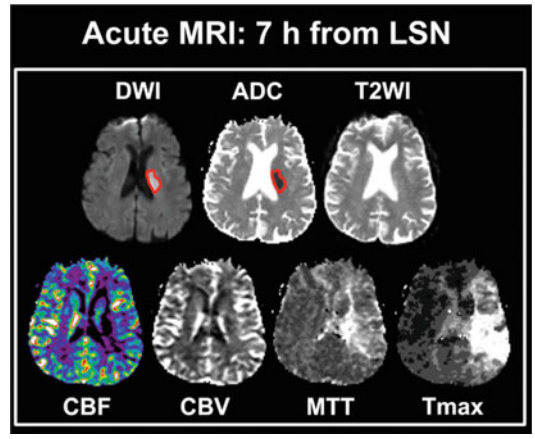

Fig. 9.1 Multimodality data from a stroke patient, 7 h since last seen normal (LSN). Note the difference in contrast between different modalities. In this case, the DWI and ADC maps provide excellent contrast for ROI definition of the stroke area: hyperintense on DWI, hypointense on ADC. *DWI* diffusion-weighted image, *ADC* apparent diffusion coefficient, *T2WI* T2-weighted image, *CBF* cerebral blood flow, *CBV* cerebral blood volume, *MTT* mean transit time, *Tmax* time to max in perfusion [adapted from Wu et al. [7]. With permission from Wolters Kluwer Health]

to manual ROI delineation where ROI size is different for each subject.

The sites of activation of a BOLD fMRI study can also serve as a ROI, for example to start tractography, and it may lead to a very-well-localized ROI in each subject. Because the main signal is in the gray matter, it may be necessary to dilate the ROI into the white matter [8–10].

Atlas-Based ROIs

There are multiple predefined atlases of white matter available, and these may serve as good starting points for ROI analysis. Well-known atlases are the JHU atlas [11] and the probabilistic Juelich atlas [12]. Data from multiple subjects is used to create a 3-D overview of well-defined brain regions. A key advantage of using an atlas is that it is created in a standard space (i.e., MNI, Talaraich), which makes it easy to compare between subjects or studies. A common approach is therefore to register the subject's data to the atlas data, or vice versa. When using atlases, care must be taken to check overlap of the regions with the data under study, as misalignment may obscure region location. Once the data is correctly aligned, diffusion measures such as FA or ADC can be easily extracted from predefined regions such as corpus callosum, fornix etc.

ROI Definition

While relatively easy to implement, there are some important things to keep in mind when performing ROI analysis. As mentioned before, a ROI can be best defined on high quality T1 or T2 weighted anatomical reference images. This is to avoid bias of defining the ROI on the parameter map of interest, which may influence the position and boundaries or the ROI. However, when choosing this approach one has to take great care that the ROI position on the reference images and the parameter map of interest are aligned as illustrated in Fig. 9.2. In this figure the contour of the brain derived from the reference scan is overlaid on the diffusion weighted images and the FA map. Both images were acquired during the same scanning session, which should assure

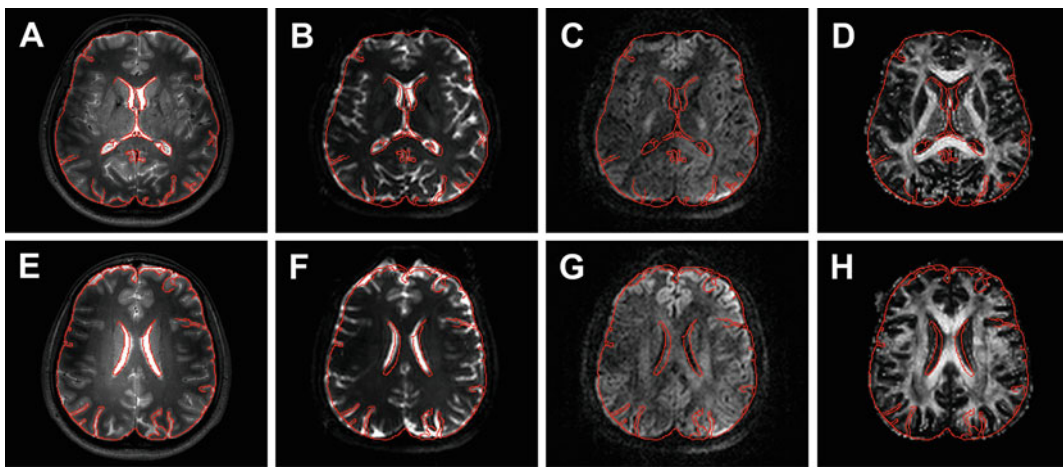

Fig. 9.2 Examples of misalignment between different image types. *Panels* (**a**) and (**e**) show high-resolution T2-weighted images with the contour of the brain outlined in *red*. This contour is overlaid on the corresponding unweighted ($b=0$, (**b**) and (**f**)) and diffusion weighted ($b=1000$ s/mm^2, (**c**) and (**g**)) images and the FA map (**d** and **h**)

a good alignment. At first sight, the un-weighted and the diffusion-weighted images seem to match well with the reference image. However, closer examination clearly shows misalignment. This same misalignment may not be so apparent when just looking at the corresponding FA map (see Fig. 9.2d, h).

The origin of the discrepancy between the different images can have multiple reasons but can have a great effect on parameter quantification and fiber tractography [13]. One common reason for misalignment is that the diffusion images are usually acquired with a single-shot EPI readout, which commonly has nonrigid geometric distortions due to its sensitivity to susceptibility artifacts (see Chap. 6). Furthermore, there can be patient motion in between acquisition of the reference image and diffusion data within the same scan protocol. This motion causes rigid misalignment of the images

Effect of Motion and Size

Although the distortions and offset might seem negligible, one has to realize that only a small misalignment can have serious impact on the parameter estimation. To illustrate this point, two regions of interest in the corpus callosum were defined. Both the regions were based on the anatomical reference image as well as the FA map (see Fig. 9.3). Furthermore, the size of the two different ROIs was varied to illustrate the effect of partial volume effects and user bias in defining the regions of interest. The results for the average FA and MD values from these different ROIs are given in Table 9.1. The variation of the parameters clearly emphasizes the sensitivity of the technique to ROI definition and positioning [14]. Small ROIs will typically be more sensitive to erroneous voxels within the ROI. Increasing the ROI size will generally decrease the sensitivity to these errors, but will increase contamination by other structures, also known as partial volume effects, decreasing the sensitivity [15].

This implies that the definition of the ROIs should be done with great care and accuracy. Although the positioning of circles or rectangles is fast and easy it is generally better to accurately outline the ROI according to the shape of the structure. The latter is more time consuming but can greatly help minimize the inclusion of other structures [16]. Another way to exclude different types of tissue is to exclude pixels based on diffusion parameters. For example one can exclude cerebrospinal fluid by excluding pixels with high

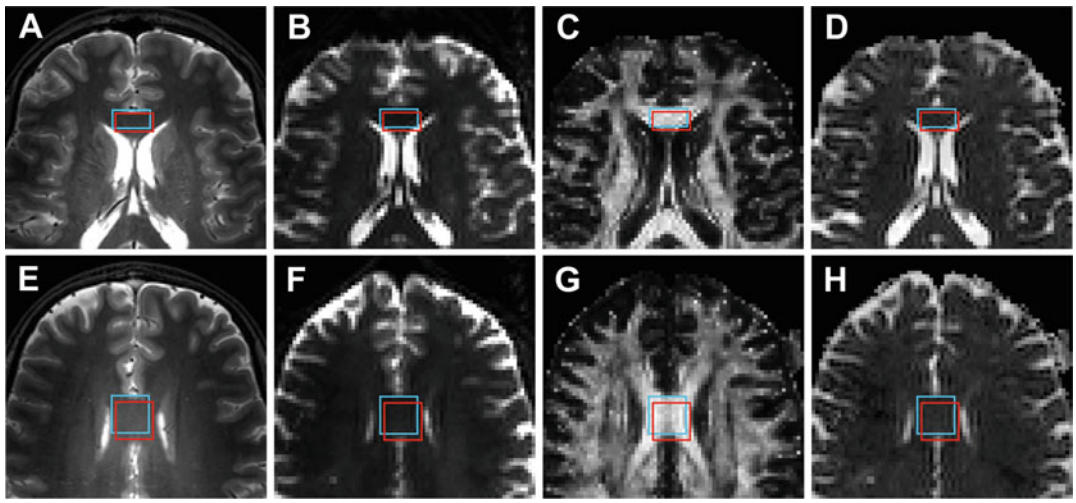

Fig. 9.3 Two examples of a rectangular ROI selecting the frontal and middle part of the corpus callosum. For each region one ROI was drawn based on the high-resolution reference scan (*red*) and one ROI was drawn based on the FA map (*blue*). The selections are shown on the T2-weighted anatomical image (**a** and **e**), the un-weighted diffusion image (**b** and **f**), the FA map (**c** and **g**), and the MD map (**d** and **h**)

Table 9.1 Average values for two part of the corpus callosum for different sizes of manually drawn rectangular regions of interest. The ROIs were drawn both on the anatomical reference images and the FA maps

		Anatomy		FA map	
	Size (pixels)	FA	MD ($\times 10^{-3}$ mm^2/s)	FA	MD ($\times 10^{-3}$ mm^2/s)
Front	3×5	0.71±0.20	0.82±0.44	0.81±0.11	0.77±0.17
	5×7	0.59±0.33	1.19±0.82	0.77±0.20	0.85±0.49
	7×9	0.52±0.35	1.34±0.87	0.63±0.28	0.96±0.58
Mid	7×7	0.75±0.13	0.79±0.11	0.80±0.10	0.76±0.13
	9×9	0.75±0.16	0.80±0.17	0.75±0.16	0.85±0.32
	11×11	0.75±0.19	0.81±0.23	0.71±0.22	0.93±0.47

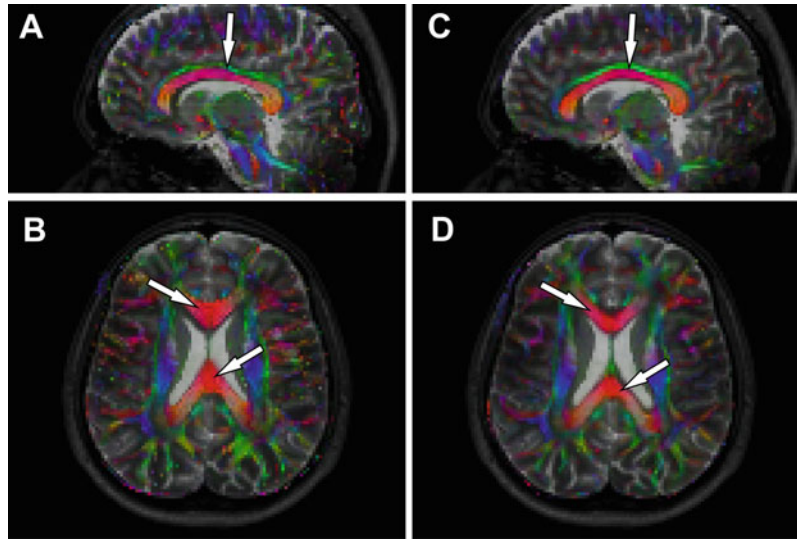

Fig. 9.4 Color coded FA maps overlaid on high resolution anatomical images to illustrate the result of non-rigid registration for EPI distortion correction. The images on the *left* (**a** and **b**) show the uncorrected data, whereas the images on the *right* (**c** and **d**) show the corrected data. The *white arrows* indicate locations where the correction of the misalignment is clearly visible

MD and low FA. However, with this method it is also possible to exclude the tissue of interest with pathology and thus affected parameters.

Registration

There are multiple strategies to correct for the distortions of the EPI images, e.g., B0 field mapping [17, 18], point spread function mapping [19, 20], or reversed gradient acquisition [21, 22]. However, these correction methods demand an extra data acquisition prolonging scan time. Another commonly available method is image registration (see Chap. 10). This technique is widely available in data processing software [1]. Figure 9.4 shows an example of nonrigid registration to correct for the misalignment between the diffusion tensor imaging data and the corresponding anatomical reference data. In panel A and B one can clearly see the misalignment between the corpus callosum, shown in red on the color-coded FA map, and the lateral ventricles, shown in white on the anatomical reference image. After nonrigid registration using *ExploreDTI* [23] one can appreciate the correct alignment of these structures as shown in panel C

Table 9.2 Average values for two part of the corpus callosum based on three manually drawn regions of interest in the corpus callosum based on T1 images before and after registration

	Normal		Corrected	
	FA	MD ($\times 10^{-3}$ mm^2/s)	FA	MD ($\times 10^{-3}$ mm^2/s)
ROI1	0.70±0.20	0.82±0.33	0.76±0.14	0.77±0.14
ROI2	0.70±0.18	0.81±0.24	0.78±0.12	0.76±0.14
ROI3	0.67±0.23	0.95±0.38	0.70±0.20	0.95±0.34

and D. The effect of registration on parameters estimated from ROIs drawn on the anatomical image are shown in Table 9.2. The ROIs were drawn in the regions indicated by the white arrows. In this example the FA increases and MD decreases after registration. For all parameters the standard deviation decreased.

Spatial Normalization

Spatial normalization is the process of bringing the study data into a common stereotaxic space. It is a crucial step for group analysis of MRI data and it allows for use of a standard 3D coordinate space for analysis and reporting of neuroimaging data [24]. It consists of mapping the individual subject data to a template, for instance to the well-known Talairach brain [25] or the MNI template [26]. Once the data is in common space, ROIs can be easily compared and checked for accuracy in size and location. An example is shown in Fig. 9.5. It is recommended not to transfer tensor data into a common space, because interpolation of tensor data is not straightforward and data will be corrupted [28]. Consequently, one should only use scalar maps (FA, ADC, etc.) for conversion into a standard space.

Statistical Analysis

The choice of which statistical method to use depends on the hypotheses and experimental set up [29]. When there is a clear hypothesis and a corresponding well-defined anatomical region, the ROI analysis can be very sensitive. However, when the hypothesis is less strong and multiple regions are investigated, a correction for multiple comparisons should be carried out to reduce false positives [30]. More specifically, when there is no effect of the null hypothesis, and a p-value of 0.05 is used, 5 out of each of 100 comparisons will falsely reject the null hypothesis (known as alpha error or type 1 error). There are numerous possibilities to correct for the multiple comparison problem. One of the most commonly used but also the most conservative is the Bonferroni correction, which treats each comparison as an independent experiment. This implies that the p-value at which the null hypothesis is rejected has to be divided by the number of comparisons. So for ten different ROIs the p-value will be 0.005 instead of 0.05, i.e., 0.05/10. The p-value becomes even lower when multiple parameters are compared. If FA and MD are evaluated in these ten regions, the Bonferroni threshold of significance will even decrease to 0.0025, i.e., 0.05/20.

As stated before, ROI analysis is highly user dependent as variability in ROI placement is easily introduced by different observers. Secondly, variability might be introduced when multiple datasets from the same subject are analyzed by a single observer at different time points. It is therefore good practice to calculate inter- and intra-observer agreement (for instance, using the κ-statistic) [31]. Agreement can be calculated on the basis of extracted DTI metrics (FA, ADC) but also, as percent overlap, on the actual ROI coordinates. The demonstrated overlap in Fig. 9.5 for multiple subjects should then be replaced by the inter- or intra-observer overlap.

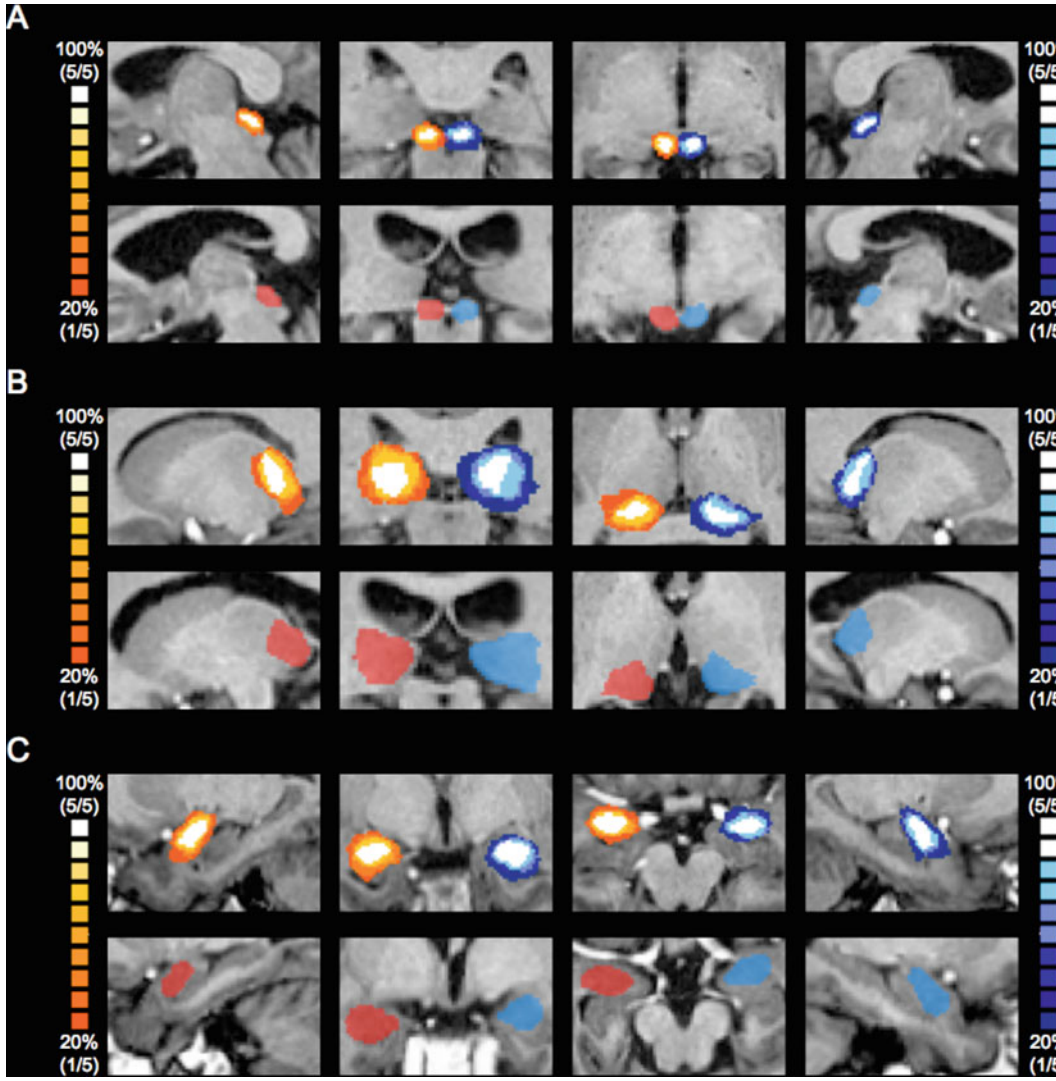

Fig. 9.5 An example of ROI overlap in ten healthy controls (*top rows* in each *panel* **a**–**c**) and patient (*bottom rows*). The ROIs were drawn in native space first, and then mapped into Talairach space and combined to form probabilistic maps of ROI overlap [adapted from Tamietto et al. [27]. With permission from Elsevier]

Summary: The Pros and Cons of ROI Analysis

In conclusion, ROI analysis is a simple and effective means to investigate white matter changes in small, well defined regions on good quality data. However, the technique is prone to error and not suitable for the investigation of structures with complex boundaries or poorly defined changes in white matter microstructure. This particularly applies for areas of compromised data quality. The delineation of ROIs can be very time consuming and both intra and inter-rater measures are poorly reproducible which impacts on both cross-sectional and longitudinal studies [32–34]. Furthermore, ROI placement without any prior knowledge can lead to inaccurate ROI segmentation which will result in different degrees of partial voluming. Therefore ROI analysis is highly user dependent and reliability measures need to be calculated to assess the quality of the results.

References

1. Soares JM, Marques P, et al. A hitchhiker's guide to diffusion tensor imaging. Front Neurosci. 2013;7:31.
2. Cercignani M. Strategies for patient–control comparison of diffusion MR data. In: Jones DK, editor. Diffusion MRI theory, methods, and applications. New York, NY: Oxford University Press; 2011.
3. Law M, Young R, et al. Histogram analysis versus region of interest analysis of dynamic susceptibility contrast perfusion MR imaging data in the grading of cerebral gliomas. AJNR Am J Neuroradiol. 2007;28(4):761–6.
4. Young R, Babb J, et al. Comparison of region-of-interest analysis with three different histogram analysis methods in the determination of perfusion metrics in patients with brain gliomas. J Magn Reson Imaging. 2007;26(4):1053–63.
5. Snook L, Plewes C, et al. Voxel based versus region of interest analysis in diffusion tensor imaging of neurodevelopment. Neuroimage. 2007;34(1): 243–52.
6. Smith SM, Jenkinson M, et al. Tract-based spatial statistics: voxelwise analysis of multi-subject diffusion data. Neuroimage. 2006;31(4):1487–505.
7. Wu O, Dijkhuizen RM, et al. Multiparametric magnetic resonance imaging of brain disorders. Top Magn Reson Imaging. 2010;21(2):129–38.
8. Kleiser R, Staempfli P, et al. Impact of fMRI-guided advanced DTI fiber tracking techniques on their clinical applications in patients with brain tumors. Neuroradiology. 2010;52(1):37–46.
9. Mazerolle EL, Beyea SD, et al. Confirming white matter fMRI activation in the corpus callosum: co-localization with DTI tractography. Neuroimage. 2010;50(2):616–21.
10. Preti MG, Makris N, et al. A novel approach of fMRI-guided tractography analysis within a group: construction of an fMRI-guided tractographic atlas. Conf Proc IEEE Eng Med Biol Soc. 2010;2012:2283–6.
11. Oishi K, Zilles K, et al. Human brain white matter atlas: identification and assignment of common anatomical structures in superficial white matter. Neuroimage. 2008;43(3):447–57.
12. Eickhoff SB, Stephan KE, et al. A new SPM toolbox for combining probabilistic cytoarchitectonic maps and functional imaging data. Neuroimage. 2005;25(4): 1325–35.
13. Irfanoglu MO, Walker L, et al. Effects of image distortions originating from susceptibility variations and concomitant fields on diffusion MRI tractography results. Neuroimage. 2012;61(1):275–88.
14. Pajevic S, Basser PJ. Parametric and non-parametric statistical analysis of DT-MRI data. J Magn Reson. 2003;161(1):1–14.
15. Vos SB, Jones DK, et al. Partial volume effect as a hidden covariate in DTI analyses. Neuroimage. 2011;55(4):1566–76.
16. Jones DK, Cercignani M. Twenty-five pitfalls in the analysis of diffusion MRI data. NMR Biomed. 2010;23(7):803–20.
17. Chen NK, Wyrwicz AM. Correction for EPI distortions using multi-echo gradient-echo imaging. Magn Reson Med. 1999;41(6):1206–13.
18. Jezzard P, Balaban RS. Correction for geometric distortion in echo planar images from B0 field variations. Magn Reson Med. 1995;34(1):65–73.
19. Robson MD, Gore JC, et al. Measurement of the point spread function in MRI using constant time imaging. Magn Reson Med. 1997;38(5):733–40.
20. Zeng H, Constable RT. Image distortion correction in EPI: comparison of field mapping with point spread function mapping. Magn Reson Med. 2002;48(1): 137–46.
21. Andersson JL, Skare S. A model-based method for retrospective correction of geometric distortions in diffusion-weighted EPI. Neuroimage. 2002;16(1):177–99.
22. Chang H, Fitzpatrick JM. A technique for accurate magnetic resonance imaging in the presence of field inhomogeneities. IEEE Trans Med Imaging. 1992;11(3):319–29.
23. Leemans A, Jeurissen B, et al. ExploreDTI: a graphical toolbox for processing, analyzing, and visualizing diffusion MR data. Proceedings 17th Scientific Meeting, International Society for Magnetic Resonance in Medicine, Honolulu; 2009.
24. Evans AC, Janke AL, et al. Brain templates and atlases. Neuroimage. 2012;62(2):911–22.
25. Talairach J, Tournoux P. Co-planar stereotaxic atlas of the human brain: 3-dimensional proportional system - an approach to cerebral imaging. New York, NY: Thieme Medical Publishers; 1988.
26. Evans AC, Collins DL, et al. 3D statistical neuroanatomical models from 305 MRI volumes. Nuclear Science Symposium and Medical Imaging Conference, 1993. 1993 IEEE Conference Record; 1993.
27. Tamietto M, Pullens P, et al. Subcortical connections to human amygdala and changes following destruction of the visual cortex. Curr Biol. 2012;22(15): 1449–55.
28. Arsigny V, Fillard P, et al. Log-Euclidean metrics for fast and simple calculus on diffusion tensors. Magn Reson Med. 2006;56(2):411–21.
29. Dupont WD, editor. Statistical modeling for biomedical researchers. Cambridge: Cambridge University Press; 2009.
30. Miller RG, editor. Simultaneous statistical inference. New York, NY: Springer; 1981.
31. Ozturk A, Sasson AD, et al. Regional differences in diffusion tensor imaging measurements: assessment of intrarater and interrater variability. AJNR Am J Neuroradiol. 2008;29(6):1124–7.
32. Astrakas LG, Argyropoulou MI. Shifting from region of interest (ROI) to voxel-based analysis in human brain mapping. Pediatr Radiol. 2010;40(12): 1857–67.
33. Chanraud S, Zahr N, et al. MR diffusion tensor imaging: a window into white matter integrity of the working brain. Neuropsychol Rev. 2010;20(2):209–25.
34. Mukherjee P, Chung SW, et al. Diffusion tensor MR imaging and fiber tractography: technical considerations. AJNR Am J Neuroradiol. 2008;29(5):843–52.

DTI Analysis Methods: Voxel-Based Analysis

10

Wim Van Hecke, Alexander Leemans, and Louise Emsell

Learning Points

- VBA is a technique that evaluates local voxel-wise differences across the whole brain based on a multistep pipeline, which includes spatial normalization (or image registration) to a template or atlas, smoothing, and statistical analysis.
- VBA is most useful for investigating group differences in DTI measures in an exploratory manner, without the need for specific a priori hypotheses about the location of potential alterations in DTI measures.
- VBA assumes that the spatial location of voxels is equivalent between subjects and is therefore fundamentally dependent on image registration to correct the inherent mismatch between individual images due to anatomical variation and pathology.
- Tract-based spatial statistics (TBSS) is a popular type of VBA that evaluates changes in a skeleton comprising a limited amount of white matter, in order to increase sensitivity by reducing registration error and partial volume effects.

W. V. Hecke, PhD (✉)
icometrix, Tervuursesteenweg 244, Leuven 3001, Belgium

Department of Radiology, Antwerp University Hospital, Wilrijkstraat 10, Edegem, 2650 Antwerp, Belgium
e-mail: wim.vanhecke@icometrix.com

A. Leemans, PhD
PROVIDI Lab, Image Sciences Institute, University Medical Center Utrecht, Utrecht, The Netherlands

L. Emsell, PhD
Translational MRI and Radiology, University Hospital Leuven, KU Leuven, Leuven, Belgium

Universitair Psychiatrisch Centrum (UPC), KU Leuven, Leuven, Belgium

An Introduction to Voxel-Based Analysis

Voxel-based analysis (VBA) of diffusion tensor imaging (DTI) data is an exploratory technique to evaluate differences/changes of diffusion metrics in every voxel of a brain data set. In essence, VBA investigates DTI measures at the smallest scale possible, i.e., the voxel level, and as these measures are compared in every voxel, VBA also simultaneously evaluates the data at the largest scale, i.e., the whole brain. As a result, unlike with region-of-interest (ROI) analysis, VBA does not require an "a priori" hypothesis about precisely where in the brain differences may be found. This makes it an interesting analysis approach when there is a clear hypothesis that there are potential differences in DTI parameters somewhere in the brain, but the location of such differences is not known in advance. Although VBA indeed has many advantages compared to standard ROI or

W. Van Hecke et al. (eds.), *Diffusion Tensor Imaging*, DOI 10.1007/978-1-4939-3118-7_10

tractography-based approaches, it also has many limitations, which one should be aware of before embarking on any VBA study.

The aim of this chapter is to provide the reader with an overview of the different processing steps that need to be performed for a voxel-based analysis of DTI data, whilst emphasizing potential sources of error or specific challenges associated with each step. Along the way we will address common questions posed by those wishing to start their first DTI VBA, for example: When is VBA a good option for the analysis of your data? What assumptions underlie the method? What are the potential pitfalls in each processing step? Why is image registration and template selection so important? What is smoothing? What is multiple hypothesis testing?, and do I *really* need to worry about it? (yes you *really* do!) What is the difference between VBA and tract-based spatial statistics (TBSS)? And how do I interpret the resulting findings?

It is important to remember that the most optimal results will only by obtained by considering the many possible options that are inherent in conducting a VBA study of DTI data, *before you start the analysis*.

Summary Points

- VBA is a technique that evaluates local voxelwise differences across the whole brain.
- It is most useful for investigating group differences in DTI measures.
- It can be used in an exploratory manner, without the need for specific a priori hypotheses about the location of differences in DTI measures.

From Individual Data Sets to VBA Group Results: The Different Steps

As VBA compares diffusion metrics, such as fractional anisotropy (FA) or mean diffusivity (MD), between subjects at the voxel level, one of the main assumptions of VBA is that the DTI information located at a specific voxel is compared equivalently in each individual. In other words, the anatomical location of a particular voxel should be the same for each subject. In general, the gross anatomy of the brain is very similar across the (healthy) population, and all brain regions are present in more or less the same spatial position across individuals. Nevertheless, as a result of natural anatomical variation, there remain clear differences in the size and shape of different brain regions (e.g., due to age, gender, or pathology). Therefore, if we attempt to compare the same voxel in one person to the equivalent location in another person without accounting for this normal variation, we will fail. And if we fail, we also violate one of the main assumptions of the VBA method. Luckily, we can try and overcome this problem.

The image processing technique that aims to correct for differences in brain structure by changing the size and shape of the brain image as well as its local structure is called **image registration**. The end result of the image registration step is thus a brain image that has been *warped* to match another image, and in which voxels with the same spatial coordinates represent the same voxel of the same brain structure of both images. If images cannot be aligned to each other well, it makes no sense comparing quantitative DTI values on a voxel level.

Now one may pose the question: to which image will we align all our data sets? This image to which all data sets are registered is called the atlas or template, and many strategies and options exist for this **template selection**.

Once all data sets are located in the same atlas space, **smoothing** is typically applied, in order to increase the power of the statistical tests that are subsequently performed in each voxel. There are other reasons why you may wish to smooth the data and different choices have to be made regarding the type and extent of smoothing used. This will be discussed later in this section.

Statistical analysis is then performed on these warped, smoothed images. The results of these statistical tests, with or without correction for multiple comparisons, are then displayed with a color on the different slices of the atlas image, thus providing a global view of where in the brain the DTI measures are statistically different between groups of subjects.

In the following sections we will dive a bit deeper into these different steps of the VBA pipeline and highlight some options and limitations.

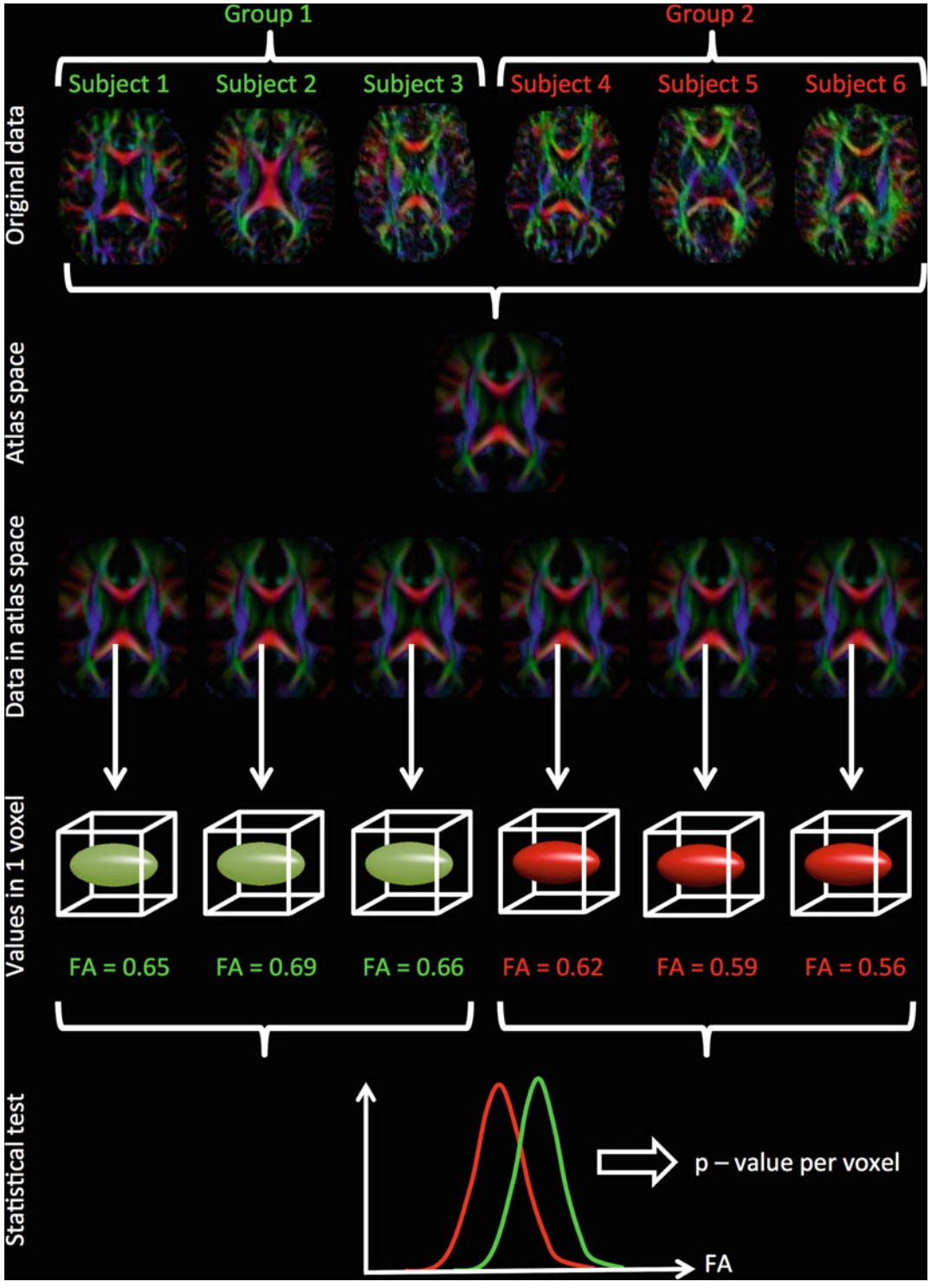

Fig. 10.1 Overview of different steps in the VBA pipeline of DTI data

A theoretical example of the VBA pipeline is displayed in Fig. 10.1. The DTI data of six subjects, three in each group, are registered to a DTI atlas. Once all data sets are located in the same space, FA values can be compared between both groups in each voxel. Note that in this example, all data sets are perfectly aligned to the atlas, which is an important assumption, but also an ideal situation that is not realistic.

Summary Points

- VBA assumes that the spatial location of voxels is equivalent between subjects,
- Natural variation in anatomy and pathology causes an inherent mismatch between individual images that can be corrected by registration to a template,
- The VBA pipeline contains three main steps: spatial normalization (or image registration), smoothing, and statistical analysis.

Image Registration

Introduction

One of the main assumptions of VBA is that the same voxels in different images are aligned to each other. Only in this case, can DTI measures, such as FA or MD, be compared between the same voxels of different subjects. Note that the process of spatially matching different images is frequently described using different terms, such as normalization, warping, aligning, registration, coregistration, etc. But in the end, although these terms may differ slightly in their technical definition, essentially they refer to the same concept.

A simplified example of the registration concept is shown in Fig. 10.2. The data set we want to register is shown on the top left of Fig. 10.2 and is also referred to as the *float image*, as this image will change during the registration process. On the top right of Fig. 10.2, the *reference image*, usually the atlas, is displayed. This is our target

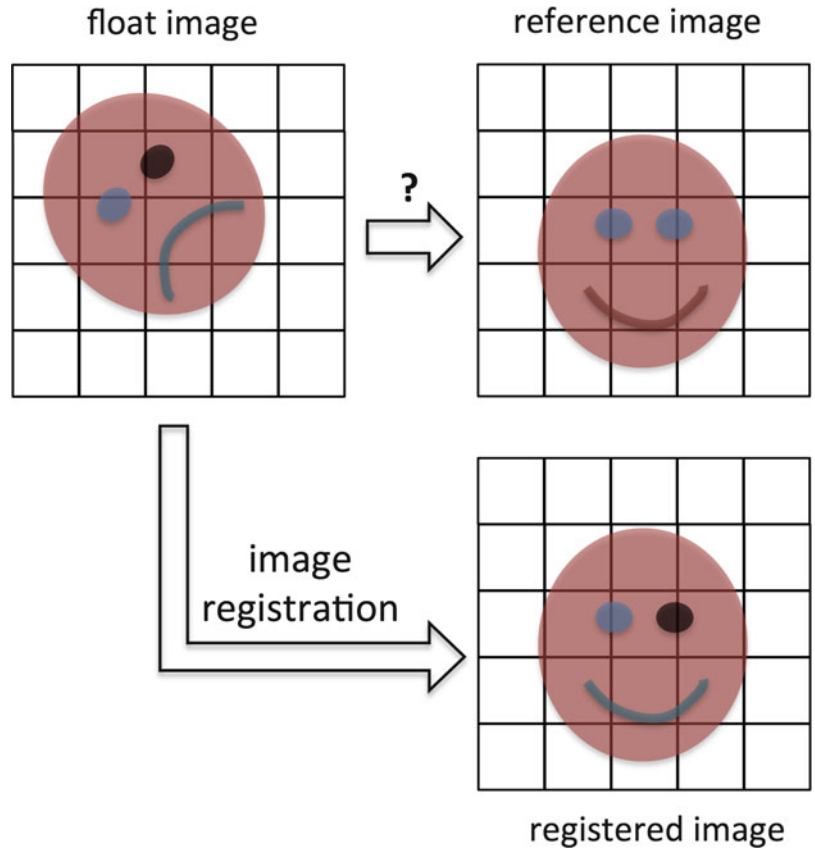

Fig. 10.2 The goal of image registration is to match a float image to the same coordinate space as the reference image. This can be done by applying global warping together with local alignment of structures

image for registration, i.e., we want to warp the float image so that it looks like the reference image. The result of the registration process is shown on the right bottom of Fig. 10.2. This registered image is the original float image, but warped into the space of the reference image. You can note two important characteristics of registration. First, you can see that the float image is translated (i.e., shifted in position along the cardinal axes, up/down, forward/back, and left/right) and rotated, but also that local structures of the float image, such as the mouth in this case, are deformed to match the reference image. Second, you can note from this example that the float image is spatially transformed, but that the colors—in DTI these are the values of the metrics, such as FA or MD—are not changed after registration. Thus, the goal of image registration is to spatially warp images in a way that corresponding voxels are in the same location, without changing the original image values of these voxels [1].

As the global as well as local morphology of the brain can significantly vary between different subjects, image registration is a challenging task. In addition to natural inter-subject brain variability, brain morphology can depend for example, on age, gender, and ethnicity. To make image registration even more challenging in the VBA setting, brain morphology can be significantly altered by the pathologies in patients that are studied.

Image Registration Techniques

The goal of this section is to provide some basic background knowledge of image registration. Image registration can be considered as an optimization problem, for which the similarity between two or more images needs to be maximized iteratively [2]. The image registration problem can thus be subdivided into:

- a method or algorithm used to find a maximal similarity
- an approach to measure similarity between images

Image registration algorithms can be subdivided into two broad categories: **global** and **local** registration techniques.

- **Global image registration techniques** apply the same deformation field (the matrix of numbers that defines how much a point is shifted), which transforms one data set to another, to all voxels of that data set. This can be done by rotating and translating the data set, referred to as a **rigid-body** transformation. In addition, global shearing ("stretching") and scaling parameters can be added, then resulting in an **affine** transformation.
- **Local registration techniques** determine a local deformation field for every voxel of the data set, in order to match every voxel with its corresponding voxel in the other data set.

A simplified example is given in Fig. 10.3, in which sagittal views of the brain, including the corpus callosum, are shown. In this example, the brain of subject X (shown in red) needs to be transformed to the template or atlas brain shown in blue. As a first step, the whole brain data set of subject X can be rotated and translated globally, in order to increase the similarity with the template brain. This registration technique, visualized in Fig. 10.3 by the purple box, is referred to as a **rigid-body transformation**. Subsequently, the resulting brain image can be scaled and skewed globally. The combination of the rigid-body transformation with additional global scaling and skewing is referred to as an **affine registration** (the purple and green boxes in Fig. 10.3). However, in order to obtain a better match of corresponding voxels in different data sets, local deformation fields need to be applied to the globally registered data set of subject X. This transformation is referred to as a **non-rigid or non-affine registration** and aims at aligning corresponding voxels of different data sets.

As aforementioned, an accurate image registration result is of paramount importance for a reliable VBA result. For example, if a non-affine registration would not be performed, the final registration result of subject X to the template would include a mismatch around the corpus

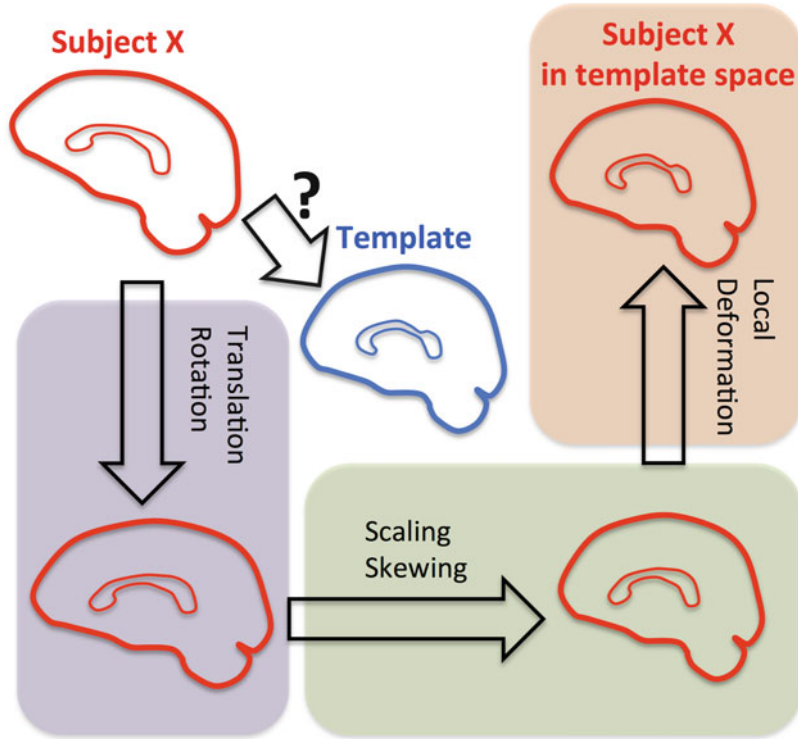

Fig. 10.3 Overview of the combination of global and local image registration techniques. To transform the brain of subject X to the template brain, both global and local image registration techniques are necessary. The *purple box* shows the rigid-body transformation, including global rotation and translation. In the *green box*, global scaling and skewing are added to the transformation, referred to as the affine transformation. The use of local deformations, as shown in the *orange box* and referred to as non-affine transformations, allows one to align both images on a local level

callosum in this example (see Fig. 10.4). Because similar registration errors would be present for the other subjects, it is clear that a voxel-wise comparison of DTI measures would lead to unreliable results. Indeed, the DTI measures in voxels of subject X are then compared with the same measures in non-corresponding voxels of subject Y, which might be more similar to the atlas or contain different registration errors.

In order to optimize the image registration algorithms, appropriate **image similarity measures** need to be defined. In the end, it will be this image similarity measure that will be optimized to obtain the most optimal image alignment. Examples of similarity measures are the sum of squared intensity differences (SSD), cross correlation, and mutual information (MI). In the SSD approach, the intensity in corresponding voxels of two images is subtracted and the absolute value of the result is squared. The SSD is then calculated as the sum of this squared difference over all voxels in the image. A schematic example is shown in Fig. 10.5. The sagittal views of the affine registration result, which was shown

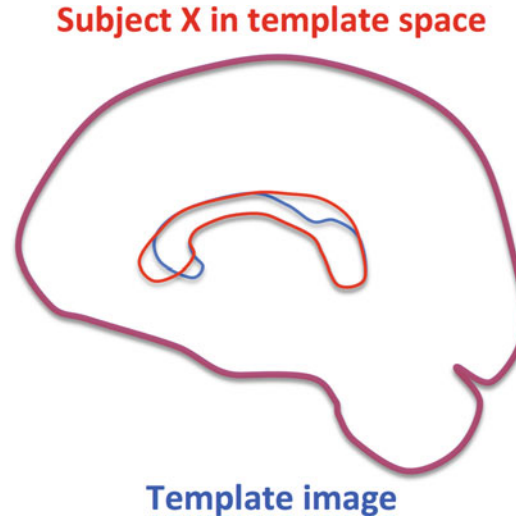

Fig. 10.4 Example of an affine registration result. Although both data sets are globally aligned, significant local image registration errors can be seen in the region of the corpus callosum

in Fig. 10.4, are visualized in grayscale intensities. On the top row, the image X that was registered to the template, the template image, and the overlay between both are displayed, showing

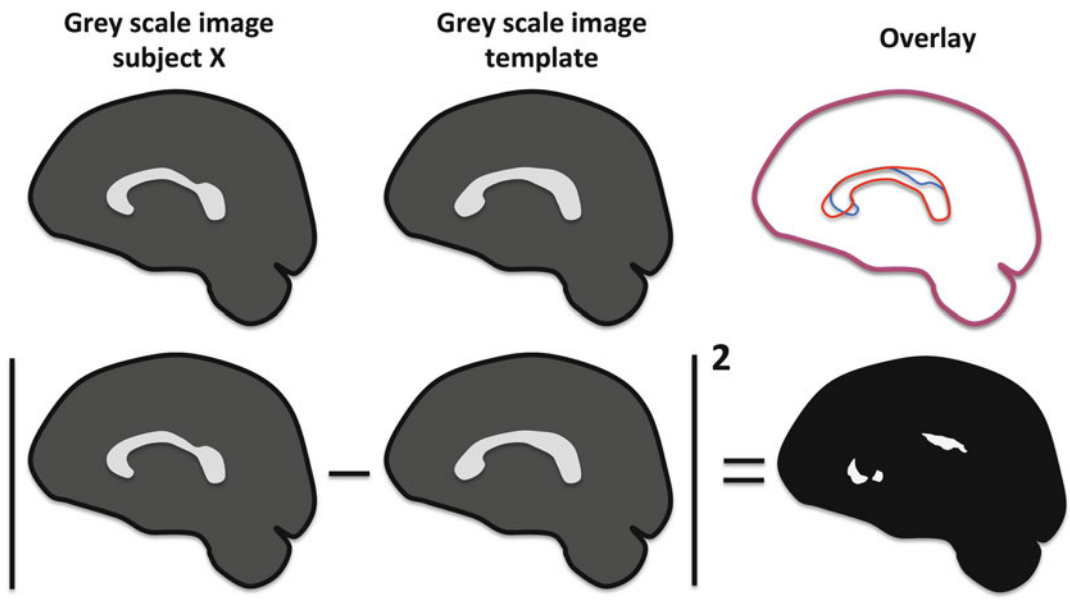

Fig. 10.5 An example of the sum of squared differences technique to measure image similarity. The intensities of the registered image and template are subtracted in every voxel and subsequently squared. Then, the total sum in every voxel is taken. When both images would be perfectly aligned, the sum of squared differences would be zero

some misregistration of the corpus callosum. In the second row, the calculation of the SSD is schematically depicted, highlighting the mismatch regions. If a perfect registration could be performed, the SSD measure would be zero, demonstrating optimal image similarity.

The SSD is a simple approach to evaluate similarity between images. More advanced methods that can take into account different intensity values of similar structures in different images, such as mutual information, generally produce better results. In addition, some specific image similarity methods have been developed for DTI data, using information on tensors, statistical relationships between measures, or anatomical information. In contrast to typical grayscale MRI images, DTI data contain more information in each voxel; therefore similarity measures can be optimized to make use of this additional information [3, 4].

Summary Points

- To register two images you need (a) a model (global and/or local) to warp the floating image to the reference image, and (b) a way to measure how well both images are aligned, in order to find an optimal registration.
- Rigid-body registration involves only translations and rotations, whilst affine registration also includes scaling and shearing.
- Examples of similarity measures include sum of squared intensity differences (SSD), cross correlation, and mutual information (MI).

Registration of DTI Data

The registration of DTI data is especially challenging. This is mainly caused by the fact that DTI data, unlike anatomical MRI or CT data, contain a tensor in each voxel, which also represents orientational information. Taking this tensor information into account can improve the registration result (an overview of DTI registration methods is provided in [5]). In the following paragraphs, we will describe several challenges in more detail.

DTI Registration Challenge 1: Reorientation

The tensor is directionally dependent and contains orientational information about the underlying

white matter microstructure. When transformations are applied to align data sets, a correction (i.e., a tensor reorientation strategy) needs to be applied to ensure that the directional DTI information is still accurate.

The need for tensor reorientation after image alignment of DTI data or during iterative registration processes is explained in Fig 10.6. To simplify things, the concept of reorientation is explained for only one white matter fiber bundle, containing three voxels. Consider that in the original DTI data set of subject X, this bundle runs vertically. The DWI image intensities of the three voxels in that bundle are high for the DWI that was acquired with a diffusion sensitized gradient perpendicular to the bundle, and low for the DWI acquired with a diffusion sensitized gradient parallel to the bundle. For simplicity, only two DWIs are considered here. The corresponding white matter bundle of the template image, however,

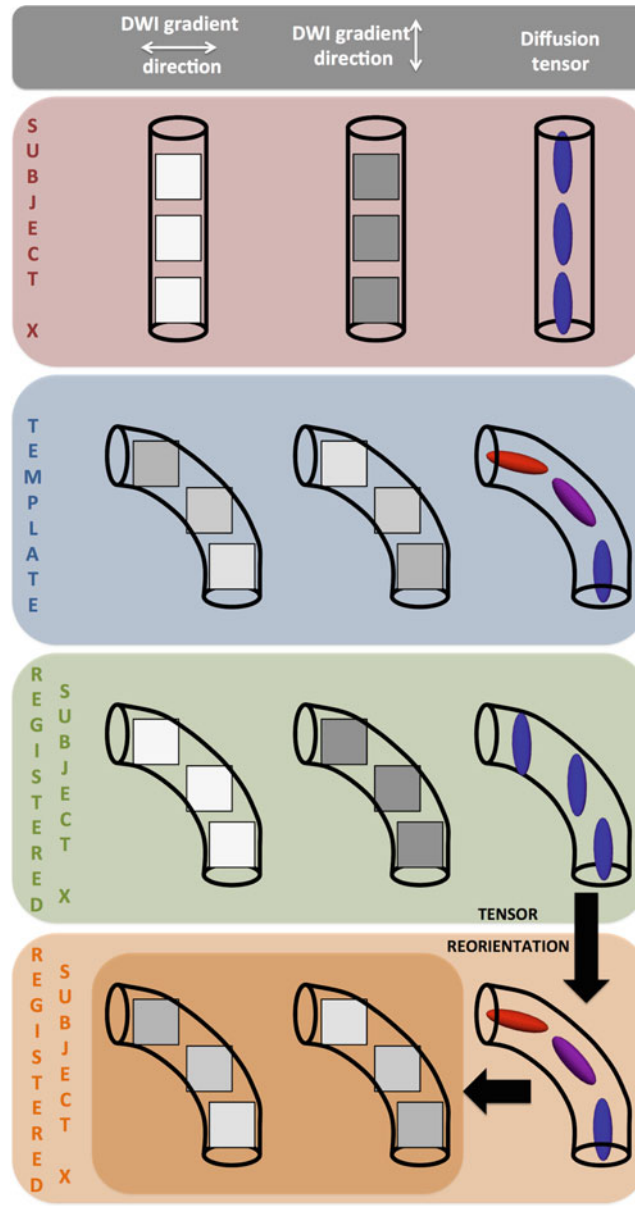

Fig. 10.6 Simplified overview of the tensor reorientation problem in DTI. Tensors indeed need to be reoriented after image registration in order to be aligned with the underlying microstructure

contains some curvature. As a result, the DWI intensities for the different gradients are different in these voxels.

It is now assumed that we can align both white matter bundles perfectly, i.e., the corresponding voxels of the white matter bundle are perfectly registered. The resulting deformation field is then applied to the DWIs and the tensor is recalculated. Now, if we refer to Fig. 10.6 again, we see that the registration process changes the spatial location of voxels in order for them to match, but not their values or image intensity. However, if only the spatial location of the voxels is changed, and not their image intensities, the directional diffusion information, and therefore the tensor, are not changed compared to the information in native space. Indeed, as explained in Chaps. 4 and 6, the image intensities of the different DWIs and the values of the tensor are related to the orientation of the white matter bundle.

As a result, the tensor information of the registered data set of subject X to template space thus no longer reflects the underlying microstructural white matter information, as can be observed in Fig 10.6. In order to correct for this, Alexander and Gee [4] proposed different methods, referred to as the "finite strain" and the "preservation of principle directions" approach. The finite strain method decomposes the transformation matrix in a deformation and a rotation component, whereafter only the latter is used to reorient the tensors. However, shearing, nonuniform scaling, and stretching factors affect the orientation as well. Together with the rotational component, they are taken into account in the preservation of principal direction strategy.

When a global, i.e., rigid-body or affine, registration method is applied, the same reorientation is applied to all voxels. However, in the case of non-rigid registrations, the local transformation matrix, which can be different for each voxel, is used to calculate local tensor reorientation.

It is important to note that tensor reorientation approaches do not affect the rotationally invariant quantitative DTI measures, such as the eigenvalues, the FA, or MD. As they are rotationally invariant, reorienting the tensor does not change their values. In a VBA analysis, it is therefore not necessary to reorient the tensors if only the rotationally invariant, quantitative DTI information is used in the subsequent analysis.

DTI Registration Challenge 2: The Tensor Information

DTI image registration can be optimized by using information from other modalities, such as anatomical MRI, or by incorporating scalar and tensor information. Park et al. [6] compared the use of different input images on the overall registration result of DTI data. They evaluated registration results after using T2-weighted images, FA images, the difference of the first and second tensor eigenvalues, FA and the tensor trace, all three tensor eigenvalues, and finally the six independent tensor components [6]. In this study, it was demonstrated that the use of the six independent tensor components as input channels performed most optimal in aligning the tract morphology and tensor orientation. This was further confirmed by other studies [7].

Scalar Anatomical MRI Information, Such as 3D T1-Weighted Images

Using scalar anatomical MRI information to determine the deformation field between DTI data sets is similar to the approach used in functional MRI analysis. First, the DTI data set is transformed to the 3D T1-weighted image of the same subject, using a rigid-body or affine transformation. The DTI information used for this registration is normally the b0 or non-diffusion weighted image, as this image mostly resembles the anatomical image. Thereafter, the 3D T1-weighted image is aligned to a T1-weighted atlas, such as the Montreal Neurological Institute (MNI) template. The resulting deformation field is then applied to the DWIs, which were transformed into the space of the T1, or to the transformed quantitative DTI maps directly.

The advantages of this approach are:

- T1-weighted atlases can be used.
- Many open-source software packages support this type of algorithms, such as SPM (www.fil.ion.ucl.ac.uk/spm), FSL (www.fmrib.ox.ac.uk/fsl), AFNI (afni.nimh.nih.gov/afni).

However, using this approach is not optimal for DTI data, for several reasons:

- The unique white matter DTI information is not used to guide the registration. The image intensity of white matter is uniform on T1-weighted images, which can result in mismatching of different fiber bundles [6, 8].
- As DTI data sets are usually acquired using an EPI sequence, different artifacts are present compared to the T1 image. For example, geometric distortions due to eddy currents and susceptibility. This results in misregistration between the b0 image and T1-weighted image.

Scalar DTI Information, Such as FA or MD Maps

In this approach, the scalar DTI information, such as contained in FA or MD maps, is used as input information to guide the registration. As a result, no anatomical data sets are involved, and registration is directly performed based the DTI information. Compared to using anatomical information, this method has several advantages:

- Some white matter information (as present in FA or MD maps) is used to increase the registration accuracy.
- The DTI information is directly aligned to an atlas and no anatomical MRI image is needed.

Although this will increase registration accuracy, this approach has some drawbacks:

- FA and MD values do not always discriminate fiber bundles that are located close to one another, potentially resulting in misregistration of these bundles.
- There needs to be an FA template to align the subject data to.

Diffusion Tensor Information

Many approaches have been proposed that incorporate the specific DTI information into the registration process in order to increase registration quality. For example:

- By including several channels of scalar image information. Guimond et al. [9] and Park et al. [6] have used different channels of input information, such as the T2-weighted image intensity, fractional anisotropy, trace of tensor, and eigenvalues.
- By using the scalar information from the whole tensor to align two DTI data sets and detect correspondences between them [6, 7, 10–13]. In addition to using the tensor elements, DTI feature vectors can be derived and used to drive the registration ([14–16]).
- By using DTI tractography or other connectivity information to guide image alignment [17–20].

It has been demonstrated that the use of DTI-specific information with multiple channels results in more accurate registration of DTI data. As an accurate image alignment is one of the most important assumptions in VBA, including DTI information during the registration will increase the reliability of the VBA results [6, 7]. However, some drawbacks of this approach should be mentioned:

- As this approach is more complex compared to the scalar registration methods, computation time is increased.
- There is a need for tensor information in atlas space, as this tensor information is needed to drive the registration.

Summary Points

- In order to achieve successful DTI registration, the orientational dependence of the diffusion data needs to be accounted for, i.e., any rotation of the DWIs should be corrected for, e.g., by using tensor reorientation during affine registration.
- Registration can be improved by incorporating diffusion information, such as scalar DTI measures (e.g., FA/MD), tensor information, or a combination of different data types.

Atlas or Template

The atlas or template is the reference frame to which all data are registered and which is used to report the results. It has been demonstrated that the choice of this atlas or template can affect the VBA results [21–23]. As a result, the atlas selection is an important step in the VBA processing pipeline for DTI data. An overview of possible DTI atlas selection approaches is provided in Zhang and Arfanakis [23].

DTI templates can be subdivided into two broad categories:

- a standard template,
- a population-/study-specific template

A population- or study-specific template is usually constructed based on the data sets that are analyzed. As a result, in theory, this atlas is the best representation of these data sets, and should thus result in minimizing the registration errors. A standard template, on the other hand, is an atlas that was created from a group of healthy subjects and is independent from the subject data sets that need analyzing. However, these atlases usually contain anatomical labels and predefined region of interests, which might be of interest for the study. So, again, there is no single correct approach of selecting an optimal template for your study. The optimal choice will depend on your study and data (i.e., goals, hypothesis, patient population, data quality). In the following paragraphs, a more detailed description of the template selection choice is provided, including some advantages and limitations of the different approaches.

Standard Template

Standard templates are typically constructed by averaging data from a group of healthy subjects that have been registered to a stereotaxic atlas. For example, anatomical T1-weighted templates were constructed by the Montreal Neurological Institute (MNI) and the International Consortium of Brain Mapping (ICBM) [24–26], and are widely used in functional MRI research. Mori et al. created the first standard DTI atlas in the ICBM space, containing fiber orientation maps and white matter parcellation maps [27]. Peng et al. [28] and Zhang et al. [21] created a DTI atlas in the ICBM-152 space by registering high quality DTI data sets of 67 healthy subjects using a non-affine registration procedure.

One of the main **advantages** of using standard templates is that they provide the possibility to make use of predefined anatomical regions for subsequent region-of-interest analysis in atlas space. Furthermore, as the standard templates are widely used, results, and coordinates of significant findings in particular, can be easily compared across studies.

However, there are some **drawbacks** when using a standard template. First, as most standard templates are created from healthy subject data, they do not necessarily represent an average brain of the subjects of your study, especially when pathology is present in some subjects. A simplified example is given in Fig. 10.7. Assume again that DTI measures are compared between healthy subjects and patients with Alzheimer's disease. Although some atrophy can be present in the healthy control group, it will be more severe in the Alzheimer's group. As a result, when all data is transformed to a standard atlas of a healthy brain, the registration result will be much better for the healthy subject data compared to the Alzheimer subject data. This is especially notable at borders with CSF (shown in black in Fig. 10.7), where the groups will not be matched correctly. Not only will there be registration errors (something we don't want in VBA), there is also a bias towards a certain subject group. As a result, this will create false positive findings, caused by more significant misregistration in one of the subject groups in specific brain regions.

Another limitation of some standard templates is that the diffusion tensor information is not always present, hence limiting the information that can be used to drive the registration process to this atlas.

Population-Specific Atlas

The general idea of population- or study-specific atlases is to use the data sets that are studied to determine an atlas space, to which all data sub-

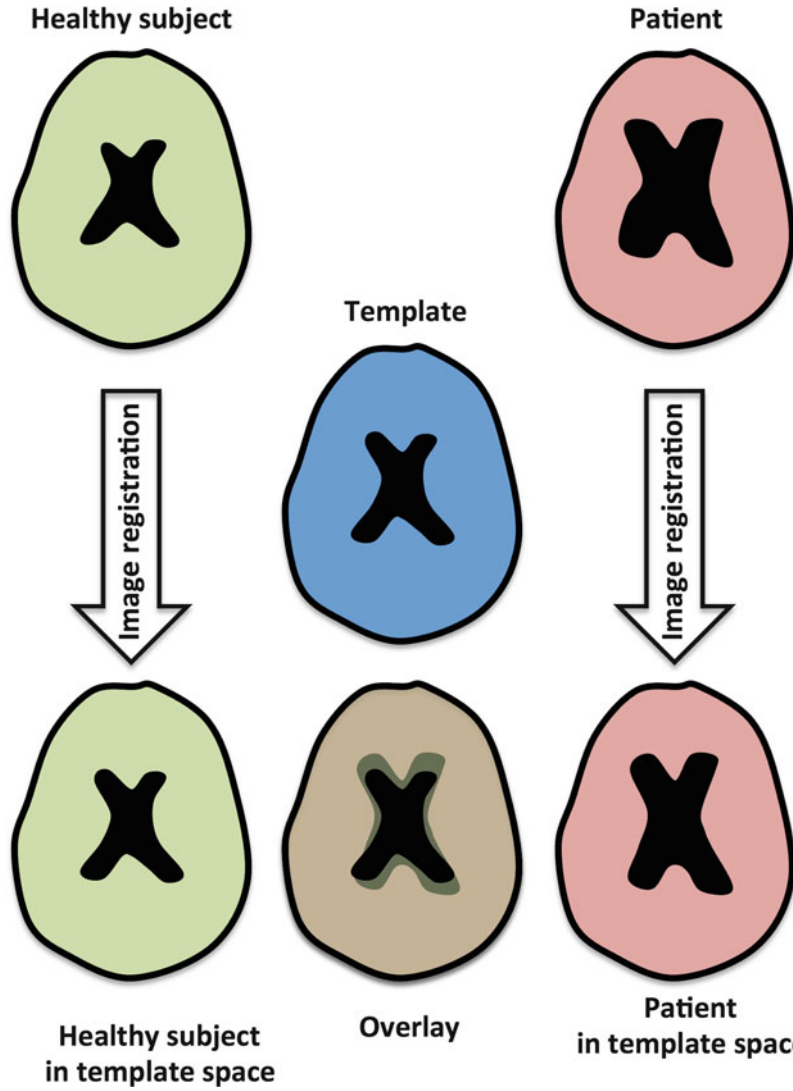

Fig. 10.7 A simplified example of image registration of healthy subjects and subjects with enlarged ventricles to a healthy subject atlas. Registration errors can occur in the group with enlarged ventricles, thereby introducing a potential bias in the VBA results

sequently are registered. The simplest way to construct a study-specific atlas is to select **one DTI data set** from the study population as the template. This subject can be chosen randomly, based on visual inspection of all data or based on calculations that determine which subject is most representative for the population. In the latter case, all data sets are registered to each other and the deformation fields from one subject to all others are averaged. The subject with the smallest average deformation field to all other subjects can then be regarded as the most representative subject of the population under study.

The **advantage** of selecting an individual subject of the study as the template is that the data quality of the template image is similar to the data quality of all other subjects. In addition, tensor information is present in this atlas and can therefore be used during the registration of all data sets to this atlas. However, this approach also has some **limitations**. As discussed, selecting the most representative subject is not trivial. In addition, in the case of an individual subject atlas, there is information on predefined anatomical regions, as is the case in standard template spaces. Similar as with the standard templates, a

bias can be introduced as the selected subject can be a patient or a control subject.

Instead of selecting an individual subject as the atlas space, population-specific atlases can be constructed based on the whole population that is studied [29, 30]. The resulting atlas should then be the best average representation of all the data that is being analyzed. Van Hecke et al. [22] demonstrated that the accuracy of VBA results can be improved when using a population-specific atlas compared to the use of a standard template.

As mentioned, the main **advantage** of the population- or study-specific atlas is that it is the best representation possible of the data sets that are studied (when the appropriate approach and registration techniques are used). As a result, image registration accuracy will be maximized and unbiased to the subject group. By constructing a study-specific atlas, registration errors to the atlas can still be present, but they will be unbiased towards the subject groups. Another advantage of a study-specific data set is that it can be made with all tensor information present. This provides the opportunity to use the tensor-based information during registration, again improving registration accuracy; or to perform tractography in the atlas space.

As with the individual subject atlas, an important **limitation** of the population-specific atlas is that it does not contain anatomical labels and delineated regions, in contrast to the standard templates. In addition, as it is made from the data of a specific study, it is usually (though not necessarily) constructed from fewer data sets compared to the standard templates.

Summary Points

- In order to compare DTI values between groups, individual datasets need to be registered to a common template space or atlas
- Standard atlases are created from large numbers of subjects and are useful for reporting results in a commonly used and well-defined space. Standard atlases are less suitable for subjects with gross morphological differences to the standard template.
- A population-specific atlas is created only from subjects under investigation and is less subject to misregistration bias.

Smoothing

What Is Smoothing?

Smoothing involves blurring the data using a filter, typically a Gaussian kernel. As a result, the image value in each voxel is recalculated, based on the weighted values of neighborhood voxels, as determined by the kernel. Typically, the size of this kernel is defined by the full width at half maximum (FWHM). The FWHM is an indication of the distribution of the kernel values, meaning that when the FWHM is 4 mm, the kernel is 4 mm wide at 50 % of its peak value. Consider the example given in Fig. 10.8.

In Fig. 10.8a, an axial FA slice is shown that will be smoothed by a Gaussian kernel. As an example, we focus on a row of voxels, as shown in Fig. 10.8b. Note that in this example, we explain Gaussian smoothing in a single row of voxels in the x direction, whereas in practice the voxels in the y and z direction will also be taken into account. In Fig. 10.8b, the FA values of the 9 voxels of interest are displayed. The FA value of the middle voxel is depicted in red, as the value of this voxel will be changed during the smoothing in this example. Of course, in practice this process is repeated for all voxels. The Gaussian kernel that will be used for smoothing is shown in Fig. 10.8b. Note that the FWHM of this kernel is 6 mm, as we assume a voxel to have a width of 2 mm. The FA values of the different voxels will be weighted, whereby the weighting factor is determined by the Gaussian kernel. The total sum of the weighting factors thereby equals 1. The resulting weighting factors for the different voxels for this Gaussian kernel are shown in Fig. 10.8c. Next, the FA value of every voxel is multiplied by the corresponding weighting factor (see Fig. 10.8d), and the resulting sum of these values will be the FA value middle voxel in the smoothed image, in this case an FA of 0.664. As mentioned, this process is repeated for all voxels, thereby taking all neighboring voxels (in all dimensions)

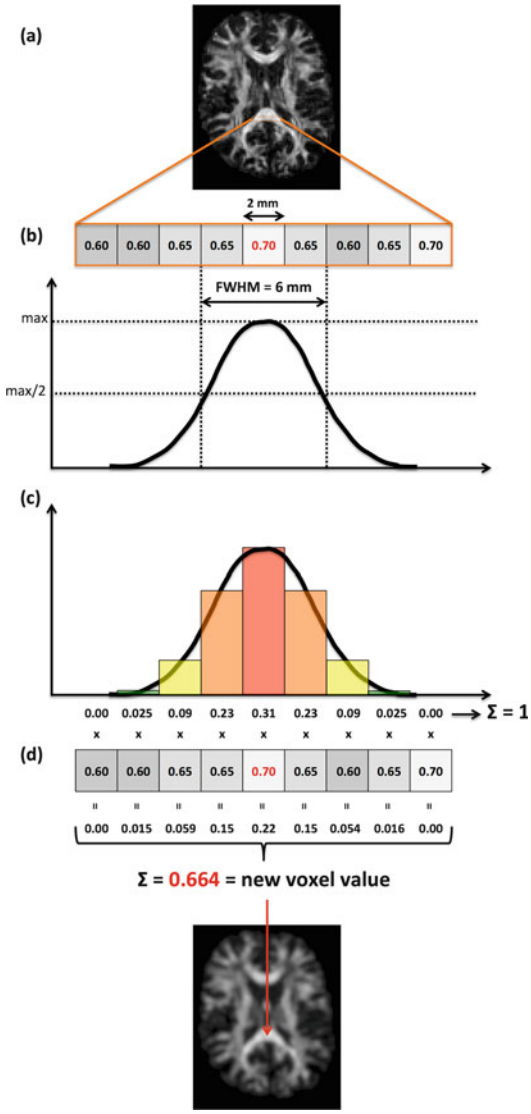

Fig. 10.8 A simplified example of the process of image smoothing in one dimension. An FA map (**a**) is smoothed by a Gaussian kernel with an FWHM of 6 mm (**b**). In (**c**) the different weighting factors are shown. Finally, the resulting FA value after smoothing is calculated (**d**) and the smoothed FA map is displayed

into account. The resulting smoothed FA map is also shown in Fig. 10.8d.

Why Should You Smooth (and Why Not)?

In Fig. 10.8, the process of smoothing was explained. In this simplified example, an isotropic Gaussian smoothing kernel was used. But why would you smooth your data? Why would you bother blurring images when you pushed your scanner and patients to the limits to acquire high resolution data sets? There are several reasons why DTI data sets are smoothed before statistical testing in VBA:

- It helps to accommodate for imperfect registration.
- It reduces the noise and increases SNR.
- It makes the data more normally distributed.

However, an obvious limitation of smoothing is that the resulting data is blurred. In addition, by smoothing the data, information of different white matter structures and tissue types (white matter vs. gray matter vs. CSF) will be averaged. Although it does make sense to integrate information from different neighboring voxels of the same white matter structure, averaging information from other structures or tissue types can introduce false positive as well as false negative results.

Determining the Smoothing Kernel Size

An important parameter related to smoothing is the smoothing kernel size. However, it is not straightforward to determine the optimal size of the smoothing kernel for a specific study. To complicate matters further, it has been demonstrated that the choice of the kernel size can significantly affect the VBA results [31, 32]. This stresses the importance of selecting the optimal kernel size, or at least having a clear argument for using a specific smoothing kernel width.

So, is there a way of determining an optimal smoothing kernel size? According to the matched filter theorem, the optimum smoothing kernel width should be similar to the expected extent of the signal difference, as the SNR then reaches its maximum [33]. In other words, for DTI, an "a priori" hypothesis is needed on the extent of change in the diffusion metrics that are expected. But this shifts the problem from not knowing how to choose the optimal kernel size to the problem of predicting the size of the hypothesized differences. After all, one of the strengths of VBA is

that it is an exploratory approach to search in the whole brain for unknown group differences.

Although similar problems exist with functional MRI analysis, they may be more straightforward to address, as the expected differences relate to the extent of GM brain activity in fMRI and the size of anatomical structures in VBM.

Smoothing in DTI

The problems related to smoothing DTI data are similar to problems in ROI analysis, as for both methods, the size of the expected differences should be known for an optimal result. However, in ROI analysis the location of the differences should also be known, which is not necessary for VBA, as all the voxels of the whole brain are evaluated simultaneously. On the other hand, smoothing of DTI data in VBA has some specific issues. These are related to the specific nature of DTI information, i.e., white matter tract information. These white matter tracts are aligned along a specific orientation and can significantly vary in size and width. Smoothing with isotropic Gaussian kernels will therefore introduce widespread averaging of information across different white matter bundles and tissue types. This is not desirable, as we know for example that white matter degeneration is not present in CSF. An example of how different kernel sizes would average information from different structures is shown in Fig. 10.9.

Not only can an isotropic Gaussian smoothing kernel average out signals from different structures and/or tissue types, this effect will also depend on their location, as white matter tracts and brain structures vary in size, shape, and width across the brain.

To address these problems, anisotropic smoothing kernels were introduced in DTI-based VBA [32, 34]. In these methods, the smoothing kernel shape is not isotropic and can vary across the brain. For example, the kernel shape can be determined based on an FA map. At edges of the FA image, for example between the white matter structure and CSF, the smoothing kernel will stop, as shown in Fig. 10.10. As a result, the chance of averaging signal in the white matter structure alone is increased. In addition, this approach can cope with the variations between shape, size and width of white matter tracts across the brain, as the shape of the smoothing kernel is locally adapted.

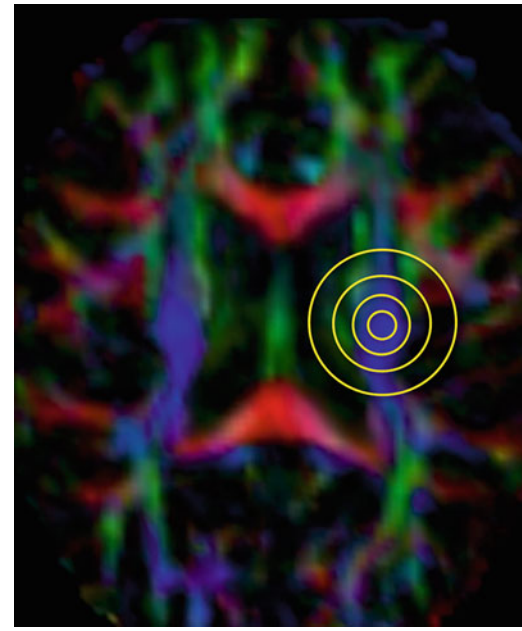

Fig. 10.9 An example of how voxel values from different structures and tissue types are taken into account during smoothing with an isotropic Gaussian smoothing kernel with different widths. In this example, the diameter of the *yellow circles* reflects the FWHM of the Gaussian smoothing kernels. As can be observed, different information is included during smoothing for different FWHM of the smoothing kernels

However, signal can still be averaged between adjacent white matter structures. In addition, this still relies on a prior hypothesis of the size and shape of the expected differences in diffusion metrics between groups of subjects.

Summary Points

- Smoothing is typically performed after image registration to accommodate for imperfect registration, to reduce the noise and increase SNR, and to obtain more normally distributed data.

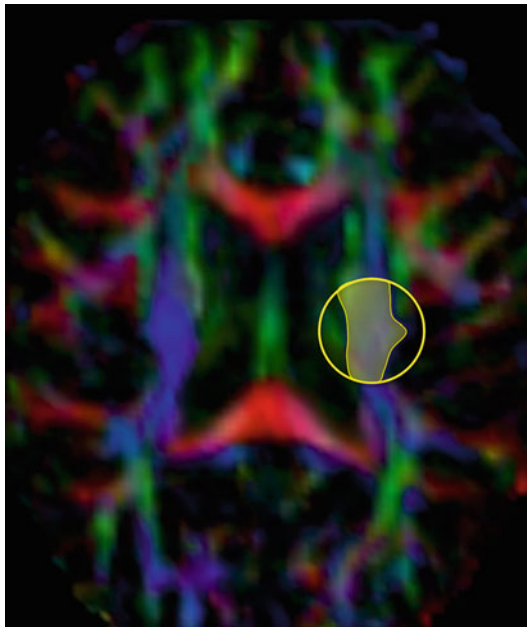

Fig. 10.10 Example of an anisotropic smoothing kernel. As can be seen, the information that is included during smoothing is limited to the white matter structure that is delineated in *yellow*. The FWHM of the smoothing kernel will affect the information included during smoothing, and thus the results, less

- The FWHM reflects the smoothing kernel size of the Gaussian kernel.
- VBA results can be affected by the smoothing that is performed and the FWHM of the smoothing kernel.
- Anisotropic smoothing methods were introduced to average out information within white matter structures during smoothing.

Statistical Analysis

As with all VBA approaches, such as VBM and functional MRI, statistical comparison of DTI metrics is performed in every voxel. Although this is one of the strengths of the technique, i.e., an exploratory whole brain analysis at the smallest scale, it also introduces a "multiple comparisons" problem.

The "Multiple Comparisons" Problem

When a statistical test is performed, a threshold—for example $p<0.05$—is used to assess whether the result is statistically significant or not. However, for a threshold of 0.05, there is still 5 % chance that a type I error—i.e., a false positive result—occurs. Although this is reasonable for a single statistical test, it becomes problematic when thousands of statistical tests are performed, all with a 5 % chance of a type I error. This is known as the multiple comparisons problem. In order to reduce the type I error in VBA, some correction for multiple comparisons should be performed. When very strict corrections, such as the Bonferroni correction (dividing the statistical threshold by the number of statistical tests that are performed), are applied, typically no statistically significant differences are found. However, there is a whole range of other less strict methods to correct for multiple comparisons, the most popular being the theory of Gaussian Random Fields [35], false discovery rate [36], and permutation-based approaches [37]. Unfortunately, there is no consensus on the most optimal technique to correct for multiple comparisons. Different techniques are used in literature, which makes it difficult to compare results, and in many studies no significant findings are reported after correction for multiple comparisons. For the latter reason, many studies report uncorrected values. It is therefore important to interpret the results of studies in the context of the statistical analysis and correction for multiple comparisons that was used.

There are several options to reduce the number of statistical tests that need to be performed in a VBA setting. For example, one can apply a white matter mask and only evaluate the voxels within this mask. In many studies this would make sense, as the quantitative DTI measures are best characterized in white matter and researchers are typically only interested in white matter when DTI is used. Other approaches can be even more limiting in the amount of voxels analyzed, by deriving masks in atlas space from:

- Predefined anatomical labels
- Manually drawn regions of interest
- Tractography results in atlas space

Parametric or Nonparametric Statistics?

Parametric statistical tests, such as the typically used *t*-test or regression tests, require the residuals of the model to be normally distributed. However, Jones et al. demonstrated that this assumption only holds in around 60 % of the voxels [31]. Most of the voxels in which the residuals were not normally distributed were situated in the gray matter. When DTI metrics of smaller groups of subjects are compared, nonparametric statistics, such as permutation or bootstrap based testing, should be strongly considered. Jones et al. [31] also demonstrated that Gaussian smoothing reduces the amount of voxels with non-normally distributed residuals, but the number of voxels with non-normally distributed residuals remained high.

Summary Points

- As statistical tests are performed in all voxels, false positive results can be reported. A correction for multiple comparisons should be performed to reduce the number of false positive findings.
- Nonparametric statistical analysis should be considered, especially when the subjects groups that are studied are small.

To VBA or Not to VBA?

Pros and Cons

So, given all the aforementioned limitations, should we use VBA at all? The answer is not straightforward. VBA has many **advantages**:

- It is an exploratory technique.
- DTI metrics are evaluated in the whole brain and at the same time at the smallest scale with which one can obtain diffusion measures, i.e., the voxel level.
- It doesn't need a lot of manual interaction, making it less observer dependent.

However, VBA also has some significant **limitations**:

- Results are only relevant when perfect image registration is achieved.
- Results are less observer dependent, but are significantly parameter dependent.

The latter point is very important. In every step of the VBA pipeline, choices have to be made, for example, regarding:

- the registration technique and its parameter settings
  - which affine technique?
  - which non-affine technique?
  - which information to drive the registration?
  - which similarity measure for registration?
- the atlas to use
  - standard vs. population specific?
- the smoothing method and the kernel width
  - anisotropic vs. isotropic smoothing?
  - kernel width?
- the statistical test and method to correct for multiple comparisons
  - parametric vs. nonparametric tests?
  - correction for multiple comparison? Which method?

Note that this is a non-exhaustive list of examples, and at each level there are even more parameter settings to consider!

Why Parameter Settings Are Important?

The importance of the choices made at different steps of the VBA pipeline has been demonstrated by Jones et al. [38]. In this study, the same DTI data sets were sent to nine different research groups. Each of these groups performed a voxel-based analysis of the same DTI data set, using their own selected set of methods and parameters. The nine research groups reported different clusters in various anatomical locations despite analyzing identical DTI datasets. This demonstrates the sensitivity of VBA to choices in the pipeline.

Although most VBA studies follow the prototypical pipeline, i.e., image registration, smoothing, and voxel-based statistical analysis, there is currently no standardization with regard to the methods and parameters that should be used. As a result, different VBA approaches and parameter settings are used in different studies. In light of the Jones et al. [38] study, comparison of results across studies is very difficult.

Tract-Based Spatial Statistics, an Alternative to VBA

With the goal of optimizing VBA for DTI data sets, tract-based spatial statistics (TBSS) was introduced by Smith et al. [39]. Although this approach can also be regarded as a voxel-based analysis, some modifications from the standard VBA pipeline were introduced in TBSS. The main difference between TBSS and standard VBA is the construction of "a skeleton." First, all FA images are aligned to a template by using a non-affine transformation and are subsequently averaged to result in a group mean FA map. From this image, a skeleton is created by selecting the locally maximal FA values, which are assumed to form the center of the white matter tracts. TBSS then projects the FA values of each registered data set onto the skeleton. More specifically, the locally highest FA value perpendicular to the skeleton in each registered FA map is then projected onto the skeleton. The projection on the FA skeleton can, to a certain extent, compensate for potential registration errors. In addition, as statistical tests are performed on the skeleton, there is no need for smoothing and less statistical tests are performed compared to a standard VBA.

Although the skeleton projection step in TBSS can indeed correct for some local misregistration, it cannot compensate for larger registration errors that might occur. As the projection procedure must search locally for the highest FA value, in order to avoid finding spurious correspondences, it will not be able to correct for larger misregistrations [40]. Indeed, the study of Zalesky and colleagues [40] used synthetic deformations of ground truth images to demonstrate that the skeleton projection only recovers less than 10 % of the registration errors. As an accurate image registration is as important in TBSS as in classical VBA, similar care must be taken with respect to the use of a non-affine registration method, tensor information during registration, and population-specific atlases in case subjects are studied with significant pathology or atrophy. It was indeed demonstrated by Keihaninejad et al. [41] that the use of a population-specific atlas outperformed the standard template or individual subject template in the study of Alzheimer's disease.

Although TBSS is an elegant way of trying to overcome some of the drawbacks of VBA, as for all methods, there are some limitations, which should be taken into account when performing a TBSS analysis. For example, as only the local maximal FA values are projected on to the skeleton and therefore evaluated, an inherent assumption is made that pathology will mainly affect the local maximal FA values, which is not necessarily the case. TBSS is also more sensitive to changes in DTI measures in diagonally oriented tracts, as their skeleton contains more voxels than horizontal or vertical ones [42]. In addition, the presence of white matter lesions that reduce FA values will affect the results, as it is possible that some voxels that do not belong to the core of the tract have larger FA than those in the core because of the presence of the lesion [43]. Furthermore, by limiting the analysis to local FA maxima on the skeleton, which comprises a relatively small percentage of the total image, a lot of potentially valuable information is not used in the analysis. Sometimes this may not be apparent as some authors choose to display their findings on an artificially thickened skeleton which appears to encompass more white matter voxels than were actually analyzed. This is typically done to emphasize findings, but as with tractography visualizations, it can be misleading to those unfamiliar with the techniques (see Chap. 8). Finally, in regions of crossing fibers, the FA skeleton cannot be determined reliably as the FA in these regions is typically very low. With 60–90 % of white matter voxels containing multiple fiber populations, this may complicate the interpretation of TBSS findings significantly [44].

How Do TBSS and Classical VBA Approaches Compare?

Given the fact that TBSS and classical VBA approaches differ with regard to core aspects of voxel-based analysis, i.e., registration and smoothing, and given we know that parameter selection significantly affects VBA results, it is worth exploring how TBSS results compare with those from classical VBA. Although most studies choose to apply one method or the other, a few studies have directly compared results of the typical VBA approach with those of TBSS when analyzing the same dataset. Sage et al. [8], for example, reported very similar results to TBSS when an optimized VBA (in terms of registration method and atlas building) was performed. It was also demonstrated that the VBA results were more reliable compared to the results of a non-optimized VBA. Preti et al. [45] compared TBSS results with an atlas-based approach to obtain DTI measures in specific tracts of healthy subjects and subjects with mild cognitive impairment and Alzheimer's disease. They concluded that the comparison of the healthy subjects with the patients was similar for the atlas-based approach and TBSS, but that the atlas-based approach was more sensitive to detecting changes between patients with mild cognitive impairment and Alzheimer's disease.

Schwarz et al. [46] evaluated the use of more advanced group-wise registration methods on the accuracy of VBA and TBSS. Using synthetic data sets as well as comparing healthy subject data with data from Alzheimer's patients, they showed that the TBSS skeleton projection step *lowered* the overall accuracy of the results when the image registration was optimized.

In summary, both classical VBA and TBSS can be successfully applied to study voxel-wise differences in DTI parameters at a group level. Despite the widespread adoption of TBSS as a gold standard VBA approach, it is not without significant shortcomings. There have been insufficient studies that have compared the accuracy of TBSS results with classical VBA results on the same datasets to determine if one approach should be used in preference to the other. Regardless of which technique is applied however, the quality of the inter-subject registration is central to determining the sensitivity and accuracy of VBA results.

VBA in Clinical Practice?

When applied responsibly, with due consideration for its limitations, VBA can be a powerful tool to analyze DTI data from patient populations with neurological and psychiatric disorders. However, is it the most appropriate tool to use in clinical practice, when a DTI data set from an individual patient needs to be analyzed and interpreted? Although the most appropriate use of VBA is for group analysis, some authors have applied the technique to analyze individual patient data. For example, in traumatic brain injury patients, Lipton et al. [47] used the enhanced Z-score microstructural assessment of pathology (EZ-MAP) approach to evaluate regional FA abnormalities. In this VBA approach, a patient's FA value is compared to the FA values of a normal reference group in every voxel. However, this requires a large reference group and the results can depend on this reference group. Kim et al. [48] suggested some improvements to overcome these problems. Patel et al. [49] used VBA to detect FA changes in lesions and normal appearing white matter in individual MS patients. Although FA reductions were observed in many regions, the authors also reported abnormal FA values due to misregistration. Given its underlying assumptions and limitations, we would not advocate the use of standard VBA (or TBSS) to analyze individual patient data at the present time.

Conclusion

The aim of this chapter was to introduce the VBA approach for DTI data, to elaborate on the different steps involved, and to outline its advantages and limitations. Compared to a standard ROI or even tractography-based analysis, VBA is a more automated approach and therefore less observer

dependent. However, many choices have to be made in the VBA pipeline with regard to image registration, template selection, smoothing, and statistical analysis, which the final VBA results will ultimately depend on. VBA should not be viewed as a generic DTI analysis technique that can be applied without any hypothesis. Whether or not VBA is a suitable way to analyze your data will depend on your specific study, the questions you hope to answer, on the number and type of patients that are studied, the type of DTI data acquisition and data quality, etc. Although VBA has been applied in many DTI studies, the lack of a standard approach means that it remains primarily a research tool, rather than a technique that can be used clinically to assess individual patients.

References

1. Fitzpatrick J, Hill DLM, Maurer Jr C. Chapter 8. Image registration. In: Medical image processing and analysis, Handbook of medical image registration, vol. 2. Bellingham, WA: SPIE Press; 2000. p. 447–513.
2. Maintz JBA, Viergever MA. A survey of medical image registration. Med Image Anal. 1998;2:1–36.
3. Peeters THJM, Rodrigues PR, Vilanova A, ter Haar Romeny BM. Analysis of distance/similarity measures for diffusion tensor imaging, visualization and processing of tensor fields. New York, NY: Springer; 2006.
4. Alexander DC, Gee JC. Elastic matching of diffusion tensor MRIs. Comput Vis Image Underst. 2000;77:233–50.
5. Muñoz-Moreno E, Cárdenes-Almeida R, Martin-Fernandez M. Review of techniques for registration of diffusion tensor imaging, tensors in image processing and computer vision. New York, NY: Springer; 2009.
6. Park HJ, Kubicki M, Shenton ME, Guimond A, McCarley RW, Maier SE, Kikinis R, Jolesz FA, Westin CF. Spatial normalization of diffusion tensor MRI using multiple channels. Neuroimage. 2003;20:1995–2009.
7. Van Hecke W, Leemans A, D'Agostino E, De Backer S, Vandervliet E, Parizel PM, Sijbers J. Nonrigid coregistration of diffusion tensor images using a viscous fluid model and mutual information. IEEE Trans Med Imaging. 2007;26:1598–612.
8. Sage CA, Van Hecke W, Peeters R, Sijbers J, Robberecht W, Parizel P, Marchal G, Leemans A, Sunaert S. Quantitative diffusion tensor imaging in amyotrophic lateral sclerosis: revisited. Hum Brain Mapp. 2009;30(11):3657–75.
9. Guimond A, Guttmann CRG, Warfield SK, Westin CF. Deformable registration of DT MRI data based on transformation invariant tensor characteristics. In: International symposium on biomedical imaging. Washington, DC: IEEE; 2002. p. 761–4.
10. Ruiz-Alzola J, Westin CF, Warfield SK, Alberola C, Maier S, Kikinis R. Nonrigid registration of 3D tensor medical data. Med Image Anal. 2002;6:143–61.
11. Rohde GK, Pajevic S, Pierpaoli C, Basser PJ. A comprehensive approach for multichannel image registration. Biomedical image registration. Berlin: Springer; 2003. p. 214–23.
12. Zhang H, Yushkevich PA, Alexander DC, Gee JC. Deformable registration of diffusion tensor MR images with explicit orientation optimization. Med Image Anal. 2006;10:764–85.
13. Chiang MC, Leow AD, Klunder AD, Dutton RA, Barysheva M, Rose SE, McMahon KL, de Zubicaray GI, Toga AW, Thompson PM. Fluid registration of diffusion tensor images using information theory. IEEE Trans Med Imaging. 2008;27:442–56.
14. Verma R, Davatzikos C. Matching of diffusion tensor images using Gabor features. In: IEEE international symposium on biomedical imaging: nano to macro, vol. 391. Washington, DC: IEEE; 2004. p. 396–9.
15. Yap PT, Wu G, Zhu H, Lin W, Shen D. TIMER: tensor image morphing for elastic registration. Neuroimage. 2009;47:549–63.
16. Yap PT, Wu G, Zhu H, Lin W, Shen D. F-TIMER: fast tensor image morphing for elastic registration. IEEE Trans Med Imaging. 2010;29:1192–203.
17. Leemans A, Sijbers J, Vandervliet E, Parizel PM. Multiscale white matter fiber tract coregistration: a new feature-based approach to align diffusion tensor data. Magn Reson Med. 2006;55:1414–23.
18. Goodlett C, Davis B, Jean R, Gilmore J, Gerig G. Improved correspondence for DTI population studies via unbiased atlas building. In: MICCAI, 2006. Berlin: Springer; 2006. p. 260–7.
19. Li H, Xue Z, Guo L, Wong SC. Simultaneous consideration of spatial deformation and tensor orientation in diffusion tensor image registration using local fast marching patterns. In: Prince J, Pham D, Myers K, editors. Information processing in medical imaging. Berlin: Springer; 2009. p. 63–75.
20. O'Donnell LJ, Westin CF, Golby AJ. Tract-based morphometry for white matter group analysis. Neuroimage. 2009;45(3):832–44.
21. Zhang S, Peng H, Dawe JR, Arfanakis K. Enhanced ICBM diffusion tensor template of the human brain. Neuroimage. 2011;54:974–84.
22. Van Hecke W, Leemans A, Sage CA, Emsell L, Veraart J, Sijbers J, Sunaert S, Parizel PM. The effect of template selection on diffusion tensor voxel-based analysis results. Neuroimage. 2011;55(2):566–73.
23. Zhang S, Arfanakis K. Role of standardized and study-specific human brain diffusion tensor templates in inter-subject spatial normalization. J Magn Reson Imaging. 2013;37(2):372–81.

24. Collins DL, Neelin P, Peters TM, Evans AC. Automatic 3D intersubject registration of MR volumetric data in standardized Talairach space. Comput Assist Tomogr. 1994;18(2):192–205.
25. Evans AC, Collins DL, Mills SR, Brown ED, Kelly RL, Peters TM. 3D statistical neuroanatomical models from 305 MRI volumes. In: IEEE nuclear science symposium and medical imaging conference. Washington, DC: IEEE; 1993. p. 1813–7.
26. Mazziotta JC, Toga AW, Evans A, Fox P, Lancaster J. A probabilistic atlas of the human brain: theory and rationale for its development. The International Consortium for Brain Mapping (ICBM). Neuroimage. 1995;2(2):89–101.
27. Mori S, Oishi K, Jiang H, et al. Stereotaxic white matter atlas based on diffusion tensor imaging in an ICBM template. Neuroimage. 2008;40:570–82.
28. Peng H, Orlichenko A, Dawe RJ, Agam G, Zhang S, Arfanakis K. Development of a human brain diffusion tensor template. Neuroimage. 2009;46(4):967–80.
29. Zhang H, Yushkevich PA, Rueckert D, Gee JC. Unbiased white matter atlas construction using diffusion tensor images. Med Image Comput Comput Assist Interv. 2007;10(Pt 2):211–8.
30. Van Hecke W, Sijbers J, D'Agostino E, Maes F, De Backer S, Vandervliet E, Parizel PM, Leemans A. On the construction of an inter-subject diffusion tensor magnetic resonance atlas of the healthy human brain. Neuroimage. 2008;43(1):69–80.
31. Jones DK, Symms MR, Cercignani M, Howard RJ. The effect of filter size on VBM analyses of DT-MRI data. Neuroimage. 2005;26(2):546–54.
32. Van Hecke W, Leemans A, De Backer S, Jeurissen B, Parizel PM, Sijbers J. Comparing isotropic and anisotropic smoothing for voxel-based DTI analyses: a simulation study. Hum Brain Mapp. 2010;31(1):98–114.
33. Rosenfeld A, Kak AC. Digital picture processing 2. Orlando, FL: Academic; 1982. p. 42.
34. Lee JE, Chung MK, Lazar M, DuBray MB, Kim J, Bigler ED, Lainhart JE, Alexander AL. A study of diffusion tensor imaging by tissue-specific, smoothing-compensated voxel-based analysis. Neuroimage. 2009;44(3):870–83.
35. Worsley KJ, Evans AC, Marrett S, Neelin P. A three-dimensional statistical analysis for CBF activation studies in human brain. J Cereb Blood Flow Metab. 1992;12:900–18.
36. Genovese CR, Lazar NA, Nichols T. Thresholding of statistical maps in functional neuroimaging using the false discovery rate. Neuroimage. 2002;15:870–8.
37. Nichols TE, Holmes AP. Nonparametric permutation tests for functional neuroimaging: a primer with examples. Hum Brain Mapp. 2002;15:1–25.
38. Jones DK, Chitnis XA, Job D, Khong PL, Leung LT, Marenco S, Smith SM, Symms MR. In Proceedings of the 15th Annual Meeting ISMRM. Berlin, 2007; 74.
39. Smith SM, Jenkinson M, Johansen-Berg H, Rueckert D, Nichols TE, Mackay CE, Watkins KE, Ciccarelli O, Cader MZ, Matthews PM, et al. Tract-based spatial statistics: voxelwise analysis of multisubject diffusion data. Neuroimage. 2006;31:1487–505.
40. Zalesky A. Moderating registration misalignment in voxelwise comparisons of DTI data: a performance evaluation of skeleton projection. Magn Reson Imaging. 2011;29:111–25.
41. Keihaninejad S, Ryan NS, Malone IB, Modat M, Cash D, Ridgway GR, Zhang H, Fox NC, Ourselin S. The importance of group-wise registration in tract based spatial statistics study of neurodegeneration: a simulation study in Alzheimer's disease. PLoS One. 2012;7(11):e45996.
42. Edden RA, Jones DK. Spatial and orientational heterogeneity in the statistical sensitivity of skeleton-based analyses of diffusion tensor MR imaging data. J Neurosci Methods. 2011;201:213–9.
43. Jones DK, Cercignani M. Twenty-five pitfalls in the analysis of diffusion MRI data. NMR Biomed. 2010;23(7):803–20.
44. Jeurissen B, Leemans A, Tournier JD, Jones DK, Sijbers J. Investigating the prevalence of complex fiber configurations in white matter tissue with diffusion magnetic resonance imaging. Hum Brain Mapp. 2013;34(11):2747–66.
45. Preti MG, Laganà MM, Baglio F, Griffanti L, Nemni R, Cecconi P, Baselli G. Comparison between skeleton-based and atlas-based approach in the assessment of corpus callosum damages in Mild Cognitive Impairment and Alzheimer Disease. Conf Proc IEEE Eng Med Biol Soc. 2011;2011:7808–11.
46. Schwarz CG, Reid RI, Gunter JL, Senjem ML, Przybelski SA, Zuk SM, Whitwell JL, Vemuri P, Josephs KA, Kantarci K, Thompson PM, Petersen RC, Jack Jr CR, Alzheimer's Disease Neuroimaging Initiative. Improved DTI registration allows voxel-based analysis that outperforms Tract-Based Spatial Statistics. Neuroimage. 2014;94:65–78.
47. Lipton ML, Kim N, Park YK, Hulkower MB, Gardin TM, et al. Robust detection of traumatic axonal injury in individual mild traumatic brain injury patients: intersubject variation, change over time and bidirectional changes in anisotropy. Brain Imaging Behav. 2012;6:329–42.
48. Kim N, Branch CA, Kim M, Lipton ML. Whole brain approaches for identification of microstructural abnormalities in individual patients: comparison of techniques applied to mild traumatic brain injury. PLoS One. 2013;8(3):e59382.
49. Patel SA, Hum BA, Gonzalez CF, Schwartzman RJ, Faro SH, et al. Application of voxelwise analysis in the detection of regions of reduced fractional anisotropy in multiple sclerosis patients. J Magn Reson Imaging. 2007;26:552–6.

DTI Analysis Methods: Fibre Tracking and Connectivity

11

Matthan W.A. Caan

Learning Points

- Tractography does not represent individual axons but average trajectories of macroscopic white matter bundles.
- Different tractography methods are available, each with its own strengths and weaknesses.
- Prior knowledge on the trajectory of pathways is indispensable and is utilized by drawing seeding and masking ROIs.
- Data quality and tracking parameters highly influence the tracking results.
- Tracking of major pathways can be automated, but may require significant processing time.
- DTI tractography may offer indirect measurements of brain structural connectivity, but quantification based on such metrics is challenging and requires cautious interpretation.

M.W.A. Caan, PhD (✉)
Brain Imaging Center, Academic Medical Center
Amsterdam, 22660, 1100 DD Amsterdam,
The Netherlands
e-mail: m.w.a.caan@amc.uva.nl

From Local to Global

One of the unique properties of diffusion weighted MRI (DWMRI) is its ability to measure the microscopic orientation of white matter tissue on a macroscopic scale. The axonal diameter is in the order of 1–10 μm [1]. A single voxel in a DWMRI scan of $2\times2\times2$ mm^3 thus comprises a diffusion measurement on an ensemble in the order of 10^5 axons. The compactness and organization of white matter bundles enable the measurement of anisotropic diffusion on a macroscopic scale. This property of white matter organisation is exploited in **tractography**, or **fibre tracking**, which is a post-processing technique that is used to virtually dissect white matter fibre bundles in vivo.

White matter bundles are macroscopic structures facilitating communication between brain regions over varying distances. *Association fibres* connect gyri within one hemisphere and can be both short and long [2]. Short association fibres connecting adjacent gyri are termed U-fibres. Connections between both hemispheres are called *commissural fibres*. The largest commissural fibre bundle is the corpus callosum, which connects the hemispheres. *Projection fibres* connect the cortex of the cerebrum to lower brain parts, as well as the spinal cord. An example is the corticospinal tract, which is mainly associated with motor function. Its fibres arise in the precentral gyrus (the primary motor cortex) and

W. Van Hecke et al. (eds.), *Diffusion Tensor Imaging*, DOI 10.1007/978-1-4939-3118-7_11

travel through the brainstem and spinal cord, where they synapse and connect with peripheral nerves travelling to the limbs.

Detailed analysis of neuronal network architecture can only be performed ex vivo, e.g., by individual fluorescent staining of axons [3]. Tractography aims to reconstruct white matter bundles traversing through multiple voxels, in vivo. Estimated fibre tracts are, in contrast to microscopic staining, *in no way a direct representation of single axons*. They merely represent an integrative pathway of continuous smoothly curved diffusion orientation information. Fortunately, validation in macaques has demonstrated good correspondence between tractography and histology in a number of white matter bundles [4]. Nevertheless, there are a number of caveats that leave a high chance of obtaining either false positive or false negative findings, as will be shown in this chapter. Note, in this context "false positives" and "false negatives" represent incorrect estimations of streamline trajectories, not the classical statistical concept. Tractography should hence be performed with care and adequate prior anatomical knowledge, such as available in text books [5].

One of the main applications of tractography is the segmentation of tracts in individual subjects. In the clinic, critical pathways in the neighborhood of a brain tumor may be reconstructed [6]. In a research setting, tractography allows the effect of a pathological process on particular white matter bundles to be studied. In a way, tracking serves to define a region of interest in which changes in (tensor-derived) measures such as fractional anisotropy (FA) and mean diffusivity (MD) (Chap. 5) are assessed. Some authors refer to this type of analysis as "tractometry" [7].

In this chapter, a *bundle* refers to the ground truth, i.e., the anatomical substrate, while a *tract* reflects a reconstructed pathway.

Principles of Deterministic Tractography

Fibre tracts are estimated from measured DWMRI data using computing algorithms. Tractography takes advantage of the fact that both the orientation and shape of the diffusion profile are estimated from the diffusion data. In *deterministic tractography*, pathways are integrated in the principal eigenvector field, which can be computed from the diffusion tensor field (Chap. 4). Tractography is dependent on user input to specify locations in the brain through which tracts are to be reconstructed and that, dependent on the choice, are known to be anatomically connected.

Consider a starting point, called a *seed point*, defined in a particular voxel of interest. From this seed point a tract is generated along both directions of the diffusion orientation in the seed voxel. The tract direction is continuously updated according to the local eigenvector orientation. As a result, a curved tract will be found, representing a part of a white matter bundle of interest (see Fig. 11.1 for an example). By seeding from multiple points distributed over an imaginary bundle intersection, the entire bundle may be represented by a series of streamlines.

Certain criteria are required to generate anatomically plausible tracking results. Tracking is terminated once a voxel is reached that is unlikely to belong to the bundle of interest. A curvature threshold prevents sharp bending of a tract and possible propagation in an adjacent bundle. Thresholding on fractional anisotropy (FA) limits tracking to white matter regions where FA is higher. Curvature thresholds of between 30 and 70° are typically used (examples are illustrated in Fig. 11.2), while FA is typically limited to values >0.2 (as can be seen in Fig. 11.3) [9]. Parameter values are best empirically chosen, balancing between false positive and negative tracking results and accounting for the complexity of the structure. By starting at more conservative values and slowly proceeding to a more liberal regime, optimal parameter values may be determined empirically. Importantly, when multiple datasets or tracking results need to be compared, identical settings must be applied to avoid a biased result.

Additional masking may be applied to restrict tracking to specific regions. Most algorithms allow a minimal and maximal tract length to be set, as well as a seed point density, i.e., multiple seed points per voxel.

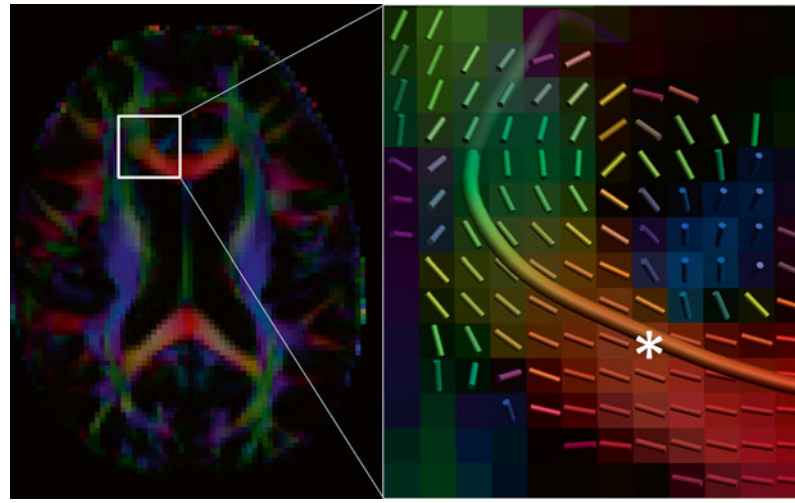

Fig. 11.1 In vivo illustration of a single streamline created in thecorpus callosum, superimposed on the principal orientation field. The seed point is denoted by an *asterisk*. Image created with ExploreDTI software [8]

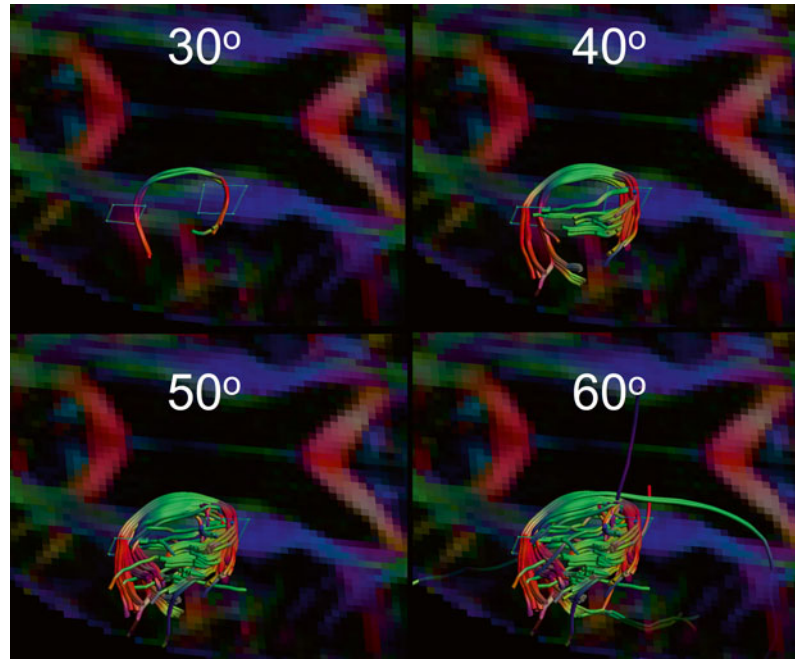

Fig. 11.2 Effect of the curvature threshold on the reconstruction of highly curved U-fibres (language pathways). No single optimal curvature threshold exists, the optimal value depends on the tract of interest and software and must be heuristically determined. In this case, 40° or 50° may be chosen

Data Requirements

Reliable tractography can only be obtained in data of sufficient quality. A correct setting of specific scanning parameters of the diffusion weighted imaging protocol is therefore crucial. The spatial resolution and the sensitivity of orientation encoding (specified by the *b*-value [10]) must be sufficiently high for accurate tract reconstruction, with minimal systematic errors. In addition, a high signal-to-noise ratio (mainly determined by the field strength, coil design, number of gradient directions, and parallel or multiband imaging settings) ensures that the tracking will be precise, with minimal variation. We will now discuss critical parameters and their influence on tract reconstruction.

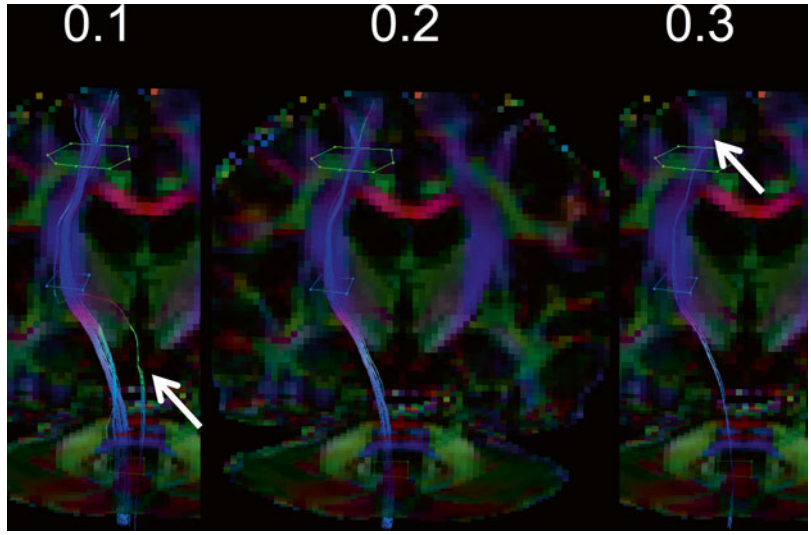

Fig. 11.3 Effect of the FA threshold on the reconstruction of the left corticospinal tract. A low threshold of FA = 0.1 results in more cortical tract with the cost of false positive tracts (indicated by the *red arrow*), which may be removed using an addition AND-ROI. A high FA = 0.3 threshold appears to be too strict, with only few tracts remaining (see the *red arrow*). A threshold of FA = 0.2 is considered optimal and is commonly adopted for most bundles

Resolution

Diffusion-weighted MRI is limited by a relatively low spatial resolution, compared to other MR modalities. At 3 T, a resolution of 2 mm in- and through-plane can reasonably be achieved. In initial work on multislab imaging, higher isotropic resolutions of 1.3 mm [11] and 1 mm at 7 T [12] were reported.

The low resolution has a number of limiting factors on tractography. First, most white matter bundles have a thickness of only a few millimeters resulting in a coarse sampling and partial voluming. As a result, one voxel may constitute of two or more adjacent but perpendicular tracts. It was shown that up to 70 % of white matter voxels contain fibre crossings [13]. Estimating the principal diffusion orientation is then no longer possible using the diffusion tensor model. This problem was recognized more than a decade ago [14] and is known in the field as the "crossing fibre" issue. In practice however, it refers not just to configurations where fibre tracts literally cross, but several other configurations where bundles fan, bend or "kiss." This problem and solutions to overcome it are introduced below and covered in more detail in Chap. 21.

Second, the low resolution limits the maximum curvature of a tract that can be reconstructed. U-fibres or other connections between gyri curve over 180° within the distance of a few voxels (see Fig. 11.2). A tract thus needs to propagate by steps of 45° or more between adjacent voxels. Such strong bends may easily be ignored by tracking algorithms in favour of continuous straight connections. In addition, the chance of false positive tracking results increases by applying a liberal curvature threshold. This manifests as tracts "stepping over" or "jumping" between different adjacent bundles. A careful ROI placement is essential for accurate tract selection (see Fig. 11.4).

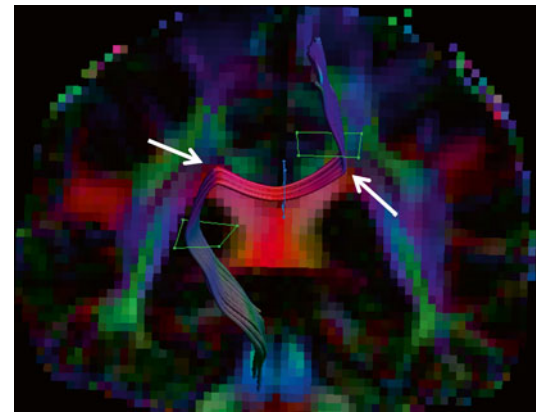

Fig. 11.4 False-positive tracking result. The *white arrows* point to crossing fibre regions where incorrect modeling results in corticospinal fibres traversing via the corpus callosum, contralaterally to the cortex. Anatomical prior knowledge is a prerequisite for correct tracking results

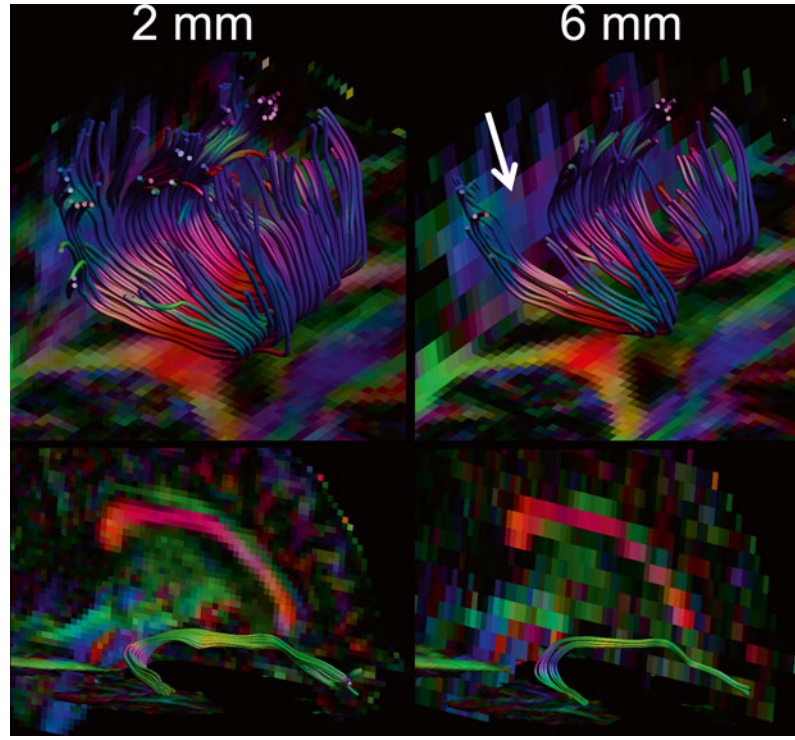

Fig. 11.5 The effect of anisotropic resolution on tractography: an increased slice thickness from 2 to 6 mm with a constant in-plane resolution of 2×2 mm introduces voids in the body of the corpus callosum (*top*, *white arrow*) and reduces the tract volume in the right uncinate fasciculus (*bottom*)

Tracking algorithms require data to be acquired at isotropic resolution, i.e. identical along all three axes. Data generated with sufficient in-plane resolution but a higher slice thickness does not support accurate tract reconstruction, as illustrated in Fig. 11.5 [15]. Given the current hardware supplied by most vendors, an isotropic voxel size of 2.0–3.0 mm is recommended [16].

b-Value

The strength of diffusion weighting as quantified by the *b*-value (Chap. 3), should be sufficiently high for a precise orientation estimation. Although a low *b*-value of 600 s/mm^2 enables the reconstruction of large, uniform white matter tracts (see Fig. 11.6), a value of $b = 1000$ s/mm^2 is advised for obtaining reliable results in the majority of bundles [17].

In case of crossing fibre tracts, an even stronger diffusion weighting is required to unravel multiple diffusion orientations within one voxel (see Fig. 11.7). In simulations it was shown that increasing the *b*-value from 1000 to 3000 s/mm^2 reduced the minimally resolvable angle from 45° to 30° [20]. In addition to acquiring data at a higher *b*-value, a higher order diffusion model must be employed to resolve crossing fibres. Multi-tensor models and constrained spherical deconvolution (CSD) are examples of approaches to this problem [19, 21, 22] (Chap. 21).

Increasing the *b*-value reduces the measured signal value such that multiple signal averages need to be acquired, or sequences with more gradient directions must be chosen, to achieve sufficient data quality for performing reliable tractography (Chap. 6).

Gradient Directions/Signal Averages

DWMRI measures diffusion in a limited number of orientations, which are combined to estimate an arbitrarily oriented diffusion profile. Still, the angular resolution depends on the number and configuration of the gradient directions chosen. Figure 11.8 illustrates that the uncertainty in the

estimated orientation decreases when increasing the number of gradient directions from 12 to 46. Unbiased tractography requires an optimal distribution of gradient directions over the unit sphere [23]. Different methods exist for doing so, e.g., by tessellations of an icosahedron [24], or a distribution of charges. Some vendors provide predefined sets of gradient directions of different numbers (e.g., 12, 32, or 64 directions). Note that these sets may not be optimized for tractography, in which case, if possible, a user-defined gradient set should be entered.

Theoretically, six directions are required to estimate the diffusion tensor. Practically, more directions are chosen for improved precision in the estimation. In Fig. 11.9, the uncinate fasciculus can be tracked with at least 24 gradient directions. In literature, a minimal set of 30 gradient directions is advised [23], while 60–80 directions are recommended for minimal variance in tractography [16].

In addition, the number of signal averages (NSA) can be increased. Note that both doubling the number of gradient directions and choosing NSA = 2 increase scanning time by a factor of 2. Generally speaking, a higher number of gradient directions slightly increases the angular resolution and is preferable over multiple signal averages. Clearly, if time permits choosing NSA = 2 will improve the tracking precision even more. However, increasing the scanning time also increases the likelihood of motion artifacts, which may detract from the image quality gain achieved by increasing the NSA.

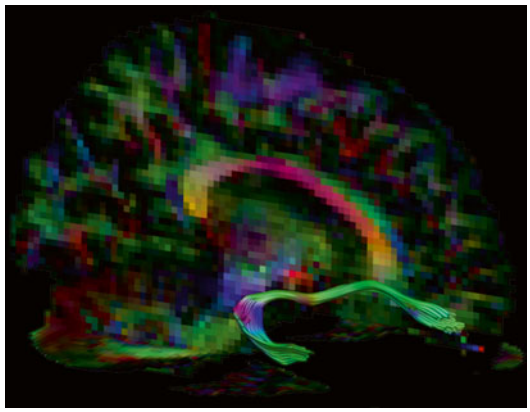

Fig. 11.6 Tracking in a dataset with a lower *b*-value of 600 s/mm^2. The uncinate fasciculus can be accurately delineated in this dataset

Field Strength

Imaging at higher field strengths increases the measured signal, which in turn reduces the uncertainty in the estimated diffusion orientation. A field strength of 3.0 T is currently common practice in tractography-based clinical research studies. Tractography can successfully

Fig. 11.7 Tractography through fibre crossings in a patient with abnormal pathway development in the pons [18]. In addition to non-diffusion-weighted images, 92 gradient directions with a *b*-value of 1600 s/mm^2 were acquired. Deterministic tractography with a constrained spherical deconvolution (CSD) clearly shows crossing pathways [19]. Tracking performed in ExploreDTI software

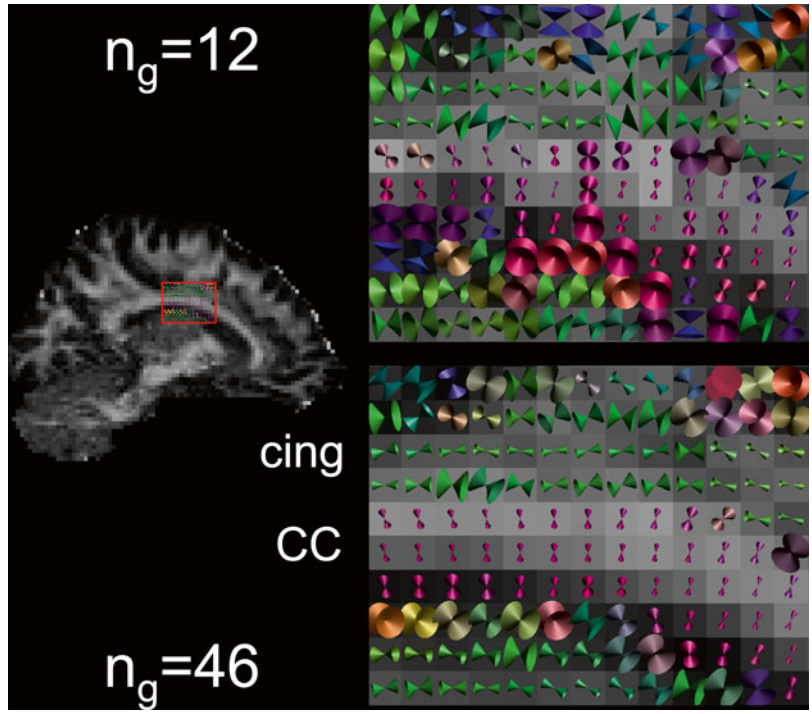

Fig. 11.8 Cones of uncertainty of the estimated diffusion orientation superimposed on the FA of a sagittal slice through the cingulum (cing) and corpus callosum (CC) for datasets with 12 and 46 gradient directions (n_g). Notice increased uncertainty for $n_g = 12$ and in voxels with low FA

performed at 1.5 T, e.g., by acquiring two signal averages (NSA = 2), acquiring data along a greater number of diffusion gradient directions and by using multichannel phased-array head-coils (see Chap. 6). In a prospective evaluation of the depiction of fibre tracts at 1.5 and 3.0 T, higher visual scores, larger numbers of fibres, and a higher asymmetry index in the CST were obtained at 3.0 T [25].

High-field scanners (7.0 T and above) enable smaller anatomical structures to be identified [12]. Diffusion-weighted imaging at 7.0 T compared to 1.5 and 3.0 T showed an increased SNR that was larger than what could be expected from field strength alone: improved receive coil hardware largely contributes to higher image quality [26].

As a downside, imaging artifacts will have a higher impact at higher field strength. Inhomogeneities of the static field (B_0) spatially distort the images. Increasing the acceleration factor partly compensates this effect. Additionally, variations in the radiofrequency field (B_1) increase signal heterogeneity at 7.0 T [27].

Tract Selection

In tractography, prior anatomical knowledge on the trajectory of the bundle of interest is indispensable. Based on this knowledge, one of more regions of interest (ROIs) through which a bundle traverses need to be defined. By means of logic combinations, a set of fibre tracts representing the bundle can be obtained. See Section 4, "DTI Tractography Atlas" for further details on how to track specific white matter bundles.

Seeding

Fibre tracking is initiated from so-called seed points (see Fig. 11.1). These points may be manually annotated by the user in a single voxel or ROI. A drawback of this approach is that fibre tracking is a non-commutative procedure [28], meaning that tracking from a tract end point will not automatically result in a pathway back to the initial seed region, as is illustrated in Fig. 11.10. An alternative approach to single ROI seeding is

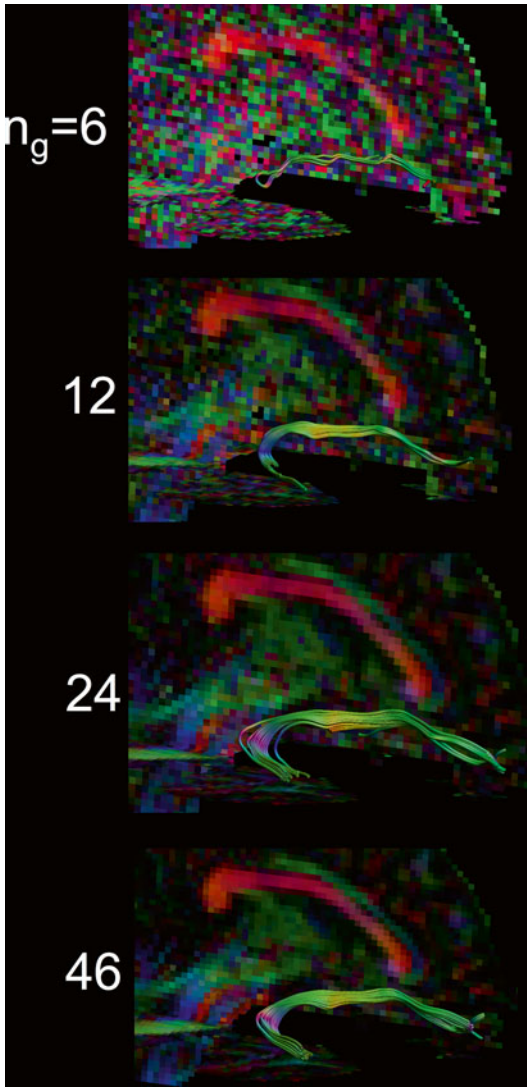

Fig. 11.9 Tractography of theuncinate fasciculus (UF) for increasing number of gradient directions. With the theoretical minimum of six directions, the UF cannot be reconstructed

whole-brain tractography, in which an algorithm initiates seeding in all voxels that satisfy certain criteria, e.g., all white-matter voxels with FA>0.2 act as seed points, as displayed in Fig. 11.11. From this whole-brain tractography, the user can select a set of tracts using an ROI. The advantage of this approach is its symmetry, whereby tracts starting in the ROI and tracts from other brain regions passing through the ROI are found. This does not result in commutative tracking, but will at least result in a more robust tracking of separate branches (see Fig. 11.12). If whole-brain tractography is not supported or practically cumbersome such as in probabilistic tractography (see "Tract Selection"), multiple seed ROIs in all possible branches need to be defined as will be explained in the next section.

Logic Combination: OR/AND/NOT

Logic combination applied to multiple ROIs is commonly needed to delineate a bundle. The OR-operator on two ROIs returns fibres traversing through one or two ROIs. Applying the AND-operator is stricter and only returns fibres passing through both ROIs (see Fig. 11.13 for an example). The NOT-operator, removing fibres entering a specific ROI, must be used sparingly to obtain a reproducible tracking result.

Good Practice for ROI-Drawing

Tractography requires spatial awareness and interpretation of a 3D representation on a 2D screen (although some packages support stereo-viewing). Hence it requires a number of trial-and-error experiments before an accurate result is achieved. Direct feedback from the software aids in speeding up the training phase. A number of programs support interactive exploration, providing instant tracking results after the user updates selection regions. There are currently methods available, which allow interactive positioning of a single seed point or one or more selection boxes (Fig. 11.14).

More accurate tracking may be achieved by delineating arbitrarily shaped ROIs on anatomical scans. The fractional anisotropy (FA) map color-coded for orientation provides a good reference for annotation. Essentially, this map encodes all information employed during tracking. Most accurate tracking is achieved by annotating on a plane perpendicular to the (local) tract orientation. The color information aids the user to identify such a plane. Including low-intensity voxels representing low FA will not affect tractography, since these

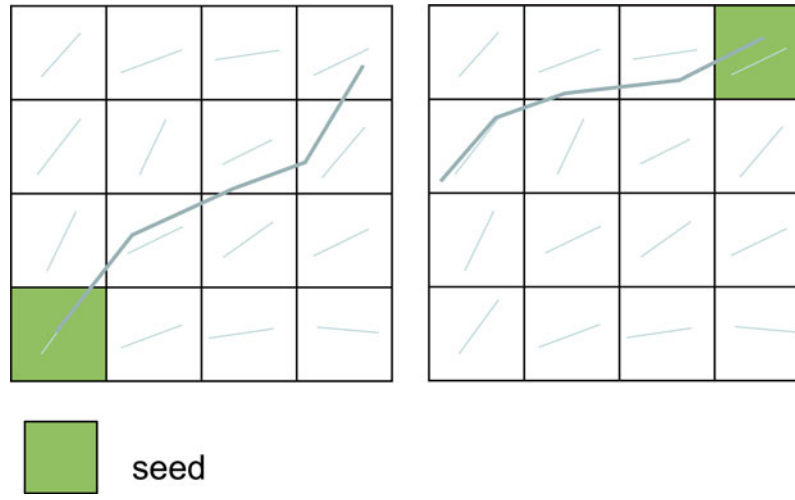

Fig. 11.10 Illustration of the non-commutative property of fibre tracking: seeding from the end voxel of the left tract results in a different pathway

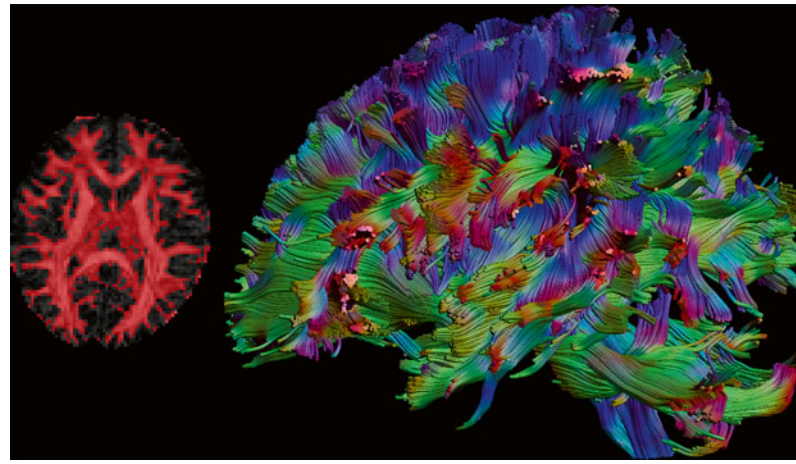

Fig. 11.11 Whole-brain tractography (sagittal view), obtained by seeding from all voxels with FA>0.2, colored *red* on the *left image*

voxels are automatically disregarded based on an FA threshold by the algorithm (see Box 11.1)

Be aware that annotating ROIs on the FA map may create a bias, since the ROIs are drawn on the same maps that will be used for statistical comparison.

A high-resolution structural scan provides additional anatomical reference and can be used in addition to the color-coded FA map. One must keep in mind that the spatial resolution of the diffusion data is commonly a factor of two lower. Also, it is necessary to verify that the scans are spatially aligned and a correction for possible head motion will typically be needed. In addition, a spatial distortion correction of the diffusion data may be required by means of acquiring a B_0-map or performing nonrigid registration (see Chap. 7).

The tractography result is dependent on the selection criteria as imposed by the user. Procedures for reproducible reconstruction of major white matter tracts with deterministic tractography have therefore been proposed [31]. Even when following synchronized tracking procedures, the inter-observer agreement in practice has been reported as not exceeding 90 % [32]. This means that some variability exists in the tract volume obtained from ROIs drawn by different users. This variability is illustrated in Fig. 11.15, sum-

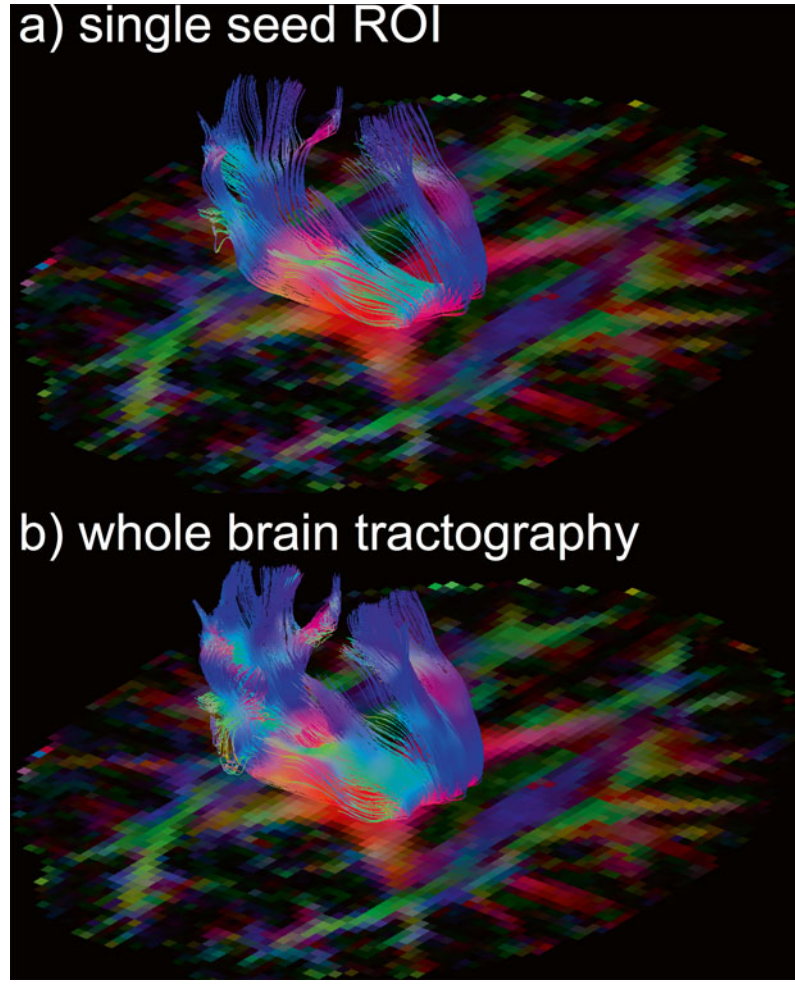

Fig. 11.12 Different seeding strategies: (**a**) single-seed ROI versus (**b**) whole-brain tractography, in which case all brain white matter voxels serve as seeds. A more dense tracking is obtained using whole-brain tractography. One sagittal ROI was drawn in the body of the corpus callosum (not shown)

Box 11.1: On Estimating Tract Volumeand FA (Consideration Box for Researchers)

In a research study, there may be hypotheses of microstructural damage, resulting in reduced FA in a tract or white matter atrophy resulting in reduced tract volume on macroscopic level. Figure 11.15 shows results of a tractography training session of students and suggests that tract volume is measured with less precision compared to the mean FA within a tract, considering the large variation in the number of obtained voxels by the students. Indeed, in literature larger variations in tract volume than tract FA were reported [59]. This work also showed that traumatic volume loss confounds FA estimates, since FA was reduced in smaller volume tracts, likely caused by partial volume effects. Including tract volume as covariate in the statistical model is one way of overcoming this issue [60].

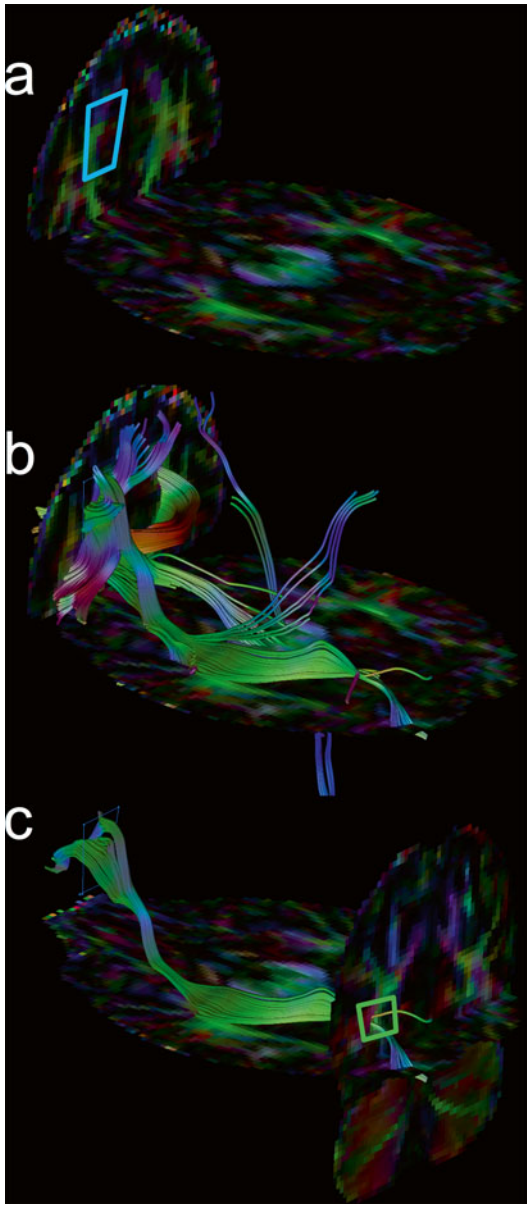

Fig. 11.13 Accurate delineation of a longitudinal fasciculus. A single-seed ROI (**a**) results in many false positive fibres (**b**). Adding a second AND ROI (**c**) removes these fibres from the selection, resulting in the desired pathway

marizing a training session in which students were assigned to reconstruct the forceps major and cingulum tracts. Large variations in tract volume are observed, resulting from differences in ROI size and positioning. One can conclude that training on multiple datasets is required to converge to reproducible findings. Also note that the inter-observer variability in average FA is relatively low.

The following guidelines may aid in achieving a reproducible tracking:

- Draw ROIs as large as possible. This may seem counter-intuitive, but ensures that any possible fibre belonging to a bundle will be included.
- Annotate 2D ROIs in the plane perpendicular to the bundle orientation.
- Apply as few ROIs as possible. In most situations, two or three ROIs suffice, i.e., one OR ROI at one end of the tract, an AND ROI at another end and another AND ROI along the pathway to exclude any deviating tracts.
- Use NOT-ROIs sparingly. Only fibres appearing as clear outliers may be removed.
- In case whole-brain tractography is unavailable, generate two overlapping seed and AND ROIs at both sides of a tract. By doing so a symmetric tracking result is obtained (see Fig. 11.17).
- Section 4 of this book discusses normal anatomy described by a DTI atlas.

Probabilistic Tractography

The principal orientation of diffusion can only be estimated with a certain limited precision [33]. The uncertainty increases both with higher noise levels or fewer gradient directions and lower diffusion anisotropy (see Fig. 11.8).

Tractography is highly sensitive to uncertainty in the orientation estimation. By each tracking step into an adjacent voxel, the pathway will further deviate from the truth. In other words, the uncertainties *propagate* or accumulate, such that tracts may terminate prematurely and the target pathway may not be found. One must be aware that this uncertainty is invisible in conventional deterministic tractography visualizations, which tend to be perceived as precise segmentation while in reality this may not be the case, as is illustrated in Fig. 11.4.

Fortunately, knowledge on the amount of uncertainty in the orientation estimation can be used to obtain potentially precisely delineated pathways. Tractography as it has been introduced thus far is characterized as *deterministic*. Repeated

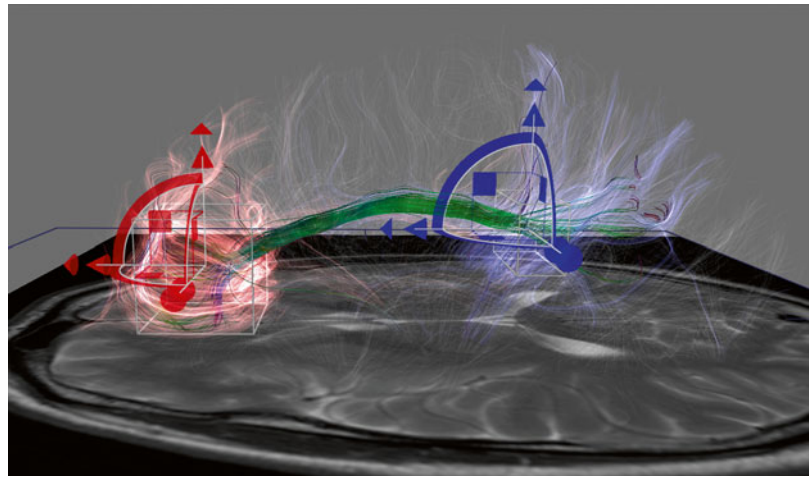

Fig. 11.14 Interactive tractography of the cingulum bundle using two boxes. Transparent colored fibres reflect fibres originating from the corresponding box. *Solid green fibres* represent the cingulum tract, connecting both boxes. Image created with DTI interactive (DTIi) software [29]

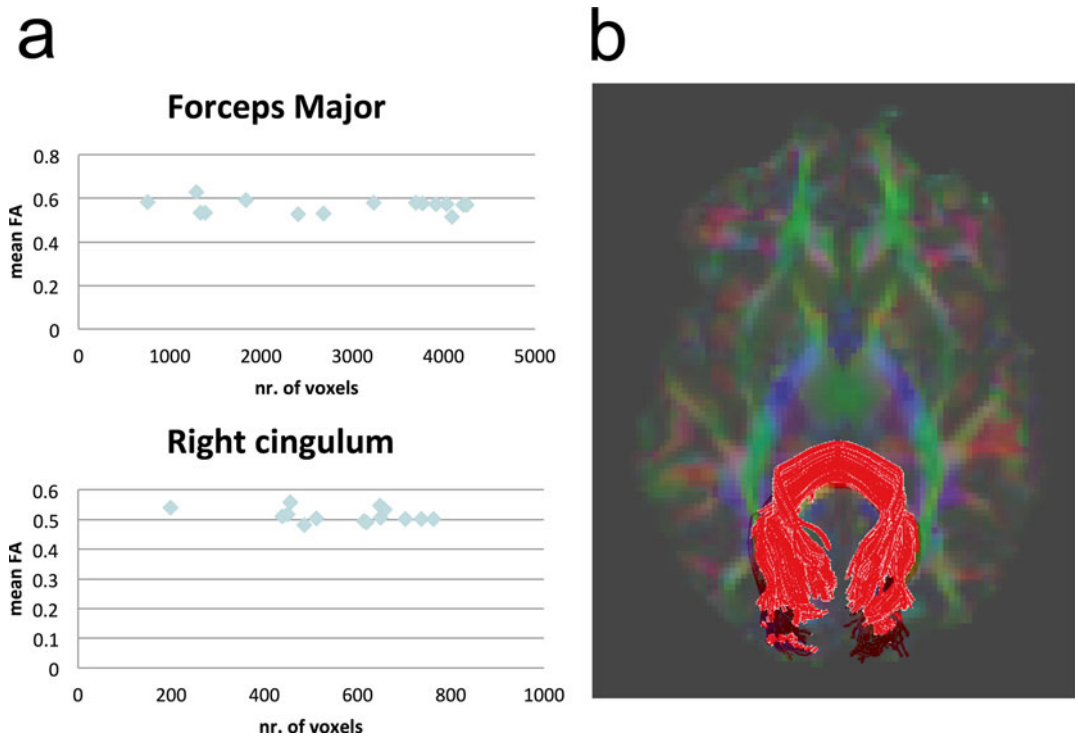

Fig. 11.15 Results of a training session of a group of 15 students. (**a**) Mean FA and number of voxels of two tracts created by the students. (**b**) Illustrative image of a correct tracking of the Forceps Major, containing approximately 4000 voxels. Tracking performed in DTI-Studio software [30]

tracking instances from a single seed point will return identical tracking results, based on an average orientation estimate per voxel (Fig. 11.16).

Probabilistic tractography instead estimates the orientation *distribution* in each voxel [21, 34] (see Fig. 11.8). The mean of this distribution equals the orientation used in deterministic tractography. The width of the distribution is proportional to the uncertainty. Once the distribution is known, multiple tracts in the order of

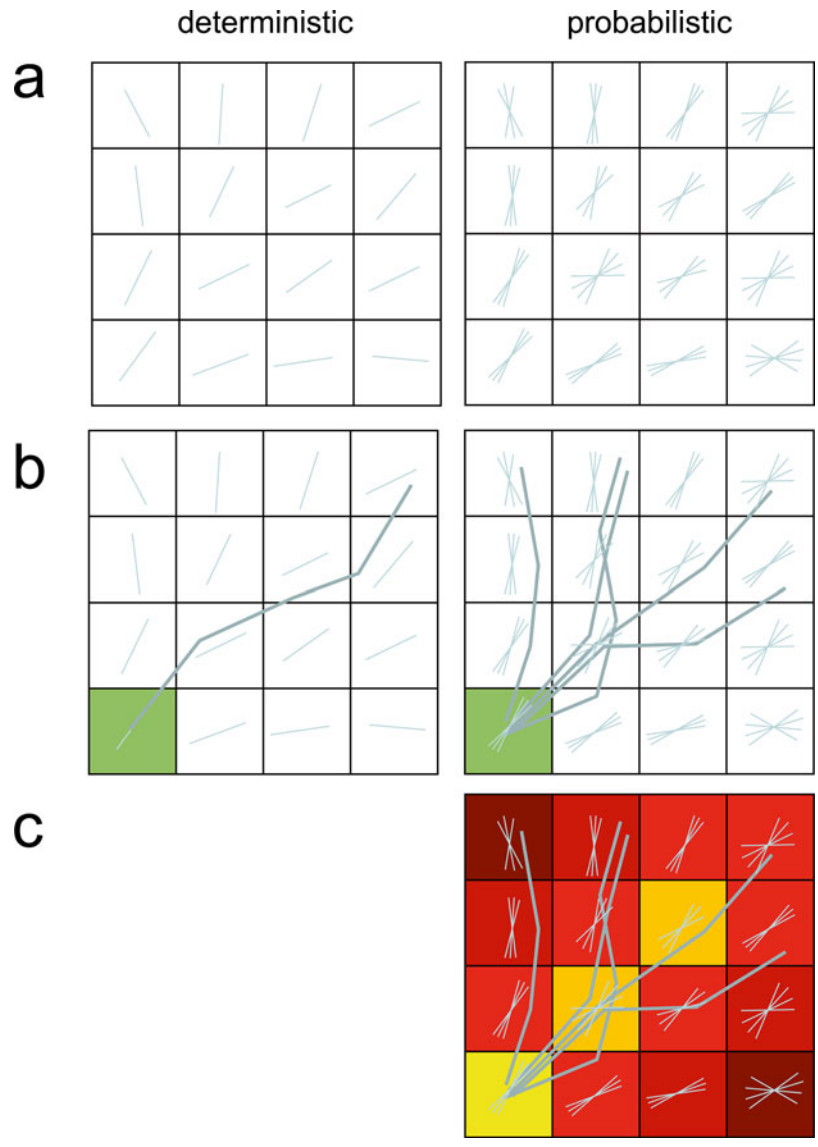

Fig. 11.16 Deterministic and probabilistic tractography. (**a**) Deterministic tractography is based on the principal eigenvector, while probabilistic tractography is based on a distribution of estimated possible orientations. (**b**) From a seed voxel, a single tract is computed in deterministic tracking. Probabilistic tracking proceeds along one randomly selected orientation per voxel. (**c**) After probabilistic tracking, a tract probability map is computed for the relative number of tracts passing through a voxel

10,000 are seeded from each seed point. A tract is computed on an orientation estimate drawn from the distribution in all voxels. Each tract thus follows a different pathway. From the average number of visits of the tracts to each voxel, a tract probability map can be derived. When the orientation uncertainty is low, all tracts will traverse along a similar pathway. Tracts passing through a single area with high uncertainty will spread and show a diffuse pattern afterwards.

Mapping connections from gray matter regions such as the thalamus to the cortex is challenging. Deterministic tractography will be unable to find tracts due to the large distance to be tracked and the uncertainty in the principal orientation in gray matter. By using probabilistic tractography, specific distinct subregions within the thalamic gray matter have been identified, which correspond to histological studies [35].

Probabilistic tractography is computationally much more demanding than deterministic tractography. Estimating the initial orientation distribution, e.g., by Bayesian estimation of diffusion parameters implemented in FSL

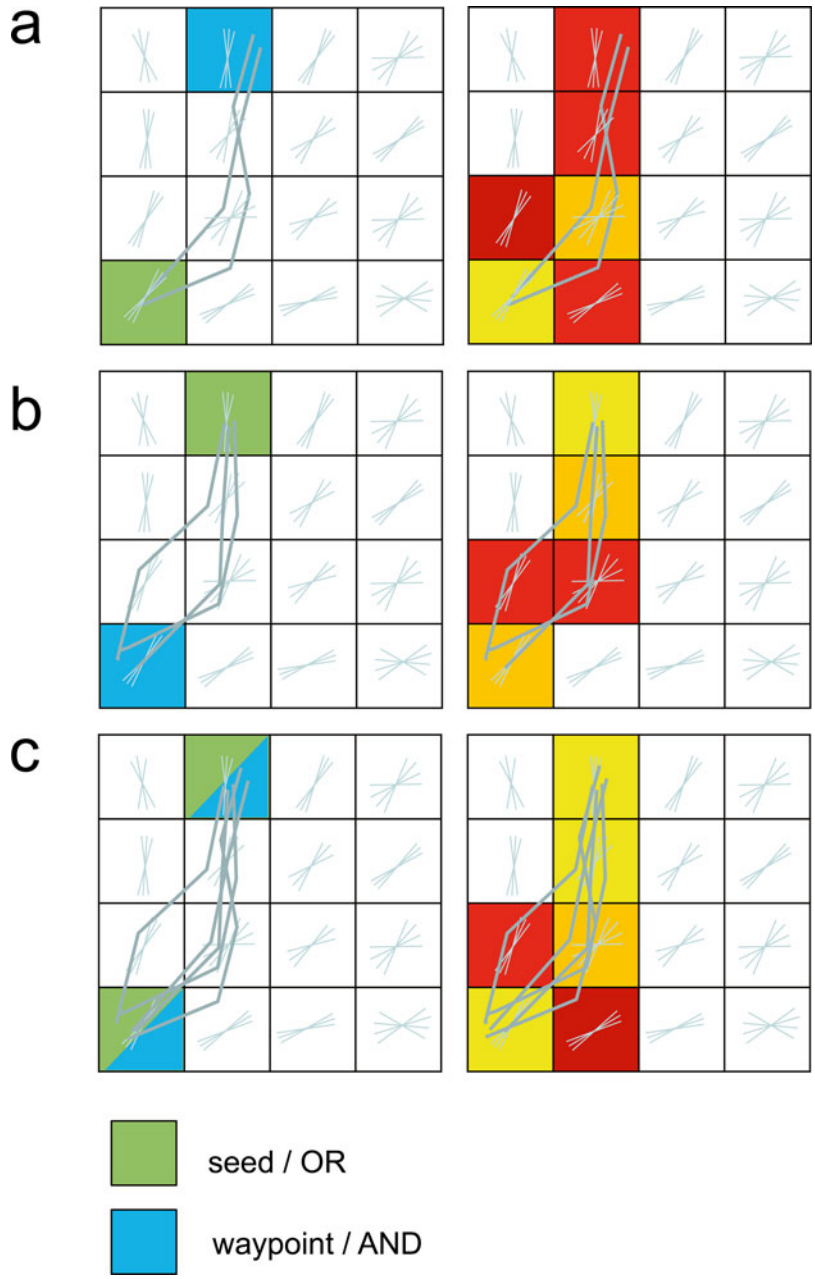

Fig. 11.17 (**a**) In probabilistic tractography, more accurate tract selection is possible by adding a waypoint mask, returning only fibres passing through this mask. (**b**) This type of selection is asymmetrical, swapping the seed and waypoint mask will generate a different outcome, with the highest probability in the seed mask. (**c**) Using both ROIs as seeds and waypoints results in a more representative probability map

BedpostX [21] takes approximately 15 h to complete. There are however, other (non-Bayesian) based methods available that can perform whole-brain probabilistic tractography in a shorter time-frame (see [36] for a review). Due to the many seeds per voxel, computational demands and less intuitive visualization, whole-brain probabilistic tracking is less commonly performed than deterministic tracking. To obtain symmetric and precise tracking results, using combined seed and waypoint masks is advised as illustrated in Fig. 11.17. The obtained probability map may be visualized in 3D using a volume rendering such as in

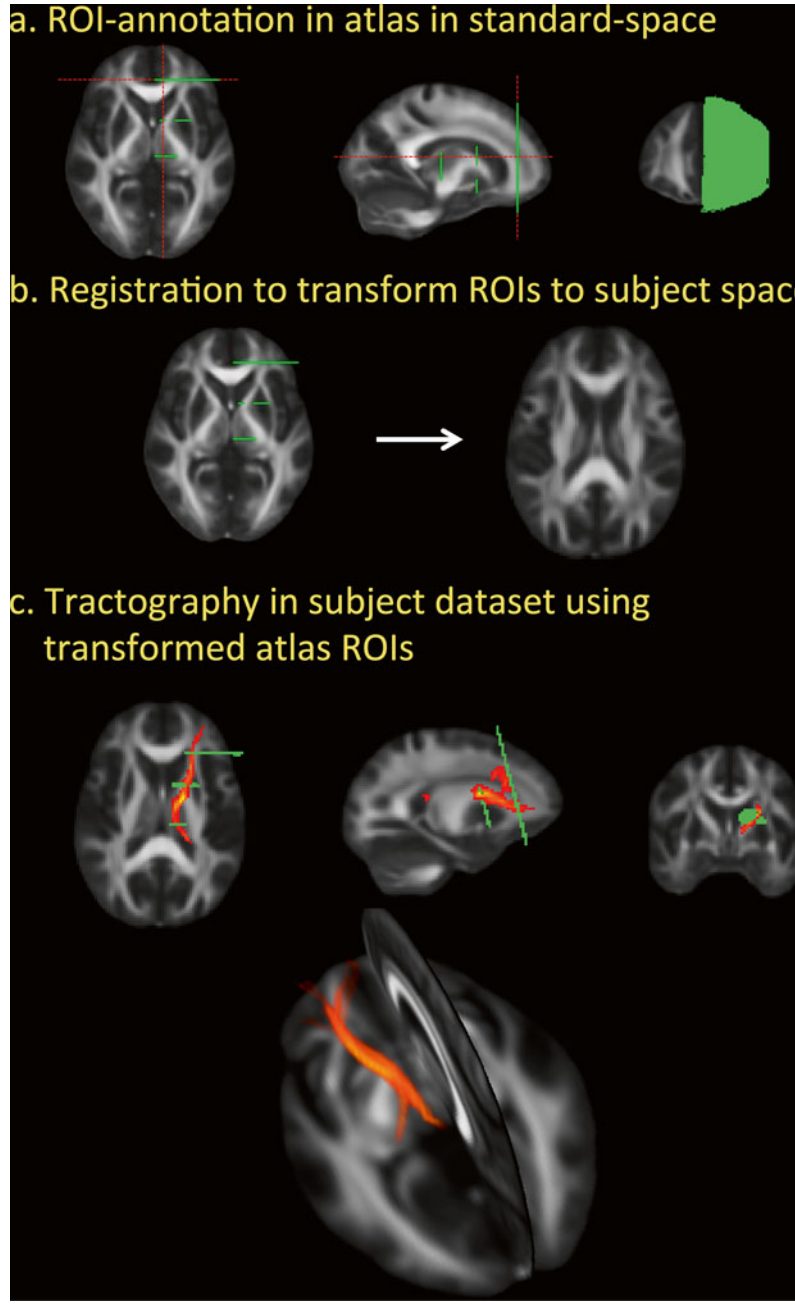

Fig. 11.18 Automated atlas-based tractography. Here, ROIs are manually annotated in standard-space (**a**, cross sections shown in *dashed red*). Then, the atlas FA volume is registered to the subject's FA volume (**b**). The ROIs are transformed accordingly. (**c**) In the subjects' dataset, frontostriatal-thalamic fibres are reconstructed using probabilistic tractography, using all three ROIs both as seed and waypoint masks. Registration and tractography is performed using FSL software. A 3D volume rendering is created in 3D-Slicer software

Fig. 11.18c or a volume isosurface such as in Fig. 11.19. Dependent on the application, deterministic tractography remains the first method for interactive exploration and selection, while probabilistic tractography can add robustness if required.

Higher Order Model Tractography

The diffusion tensor model assumes a single-fibre bundle traversing through a voxel. It has however been estimated that up to 70 % of all white matter voxels contain contributions of at

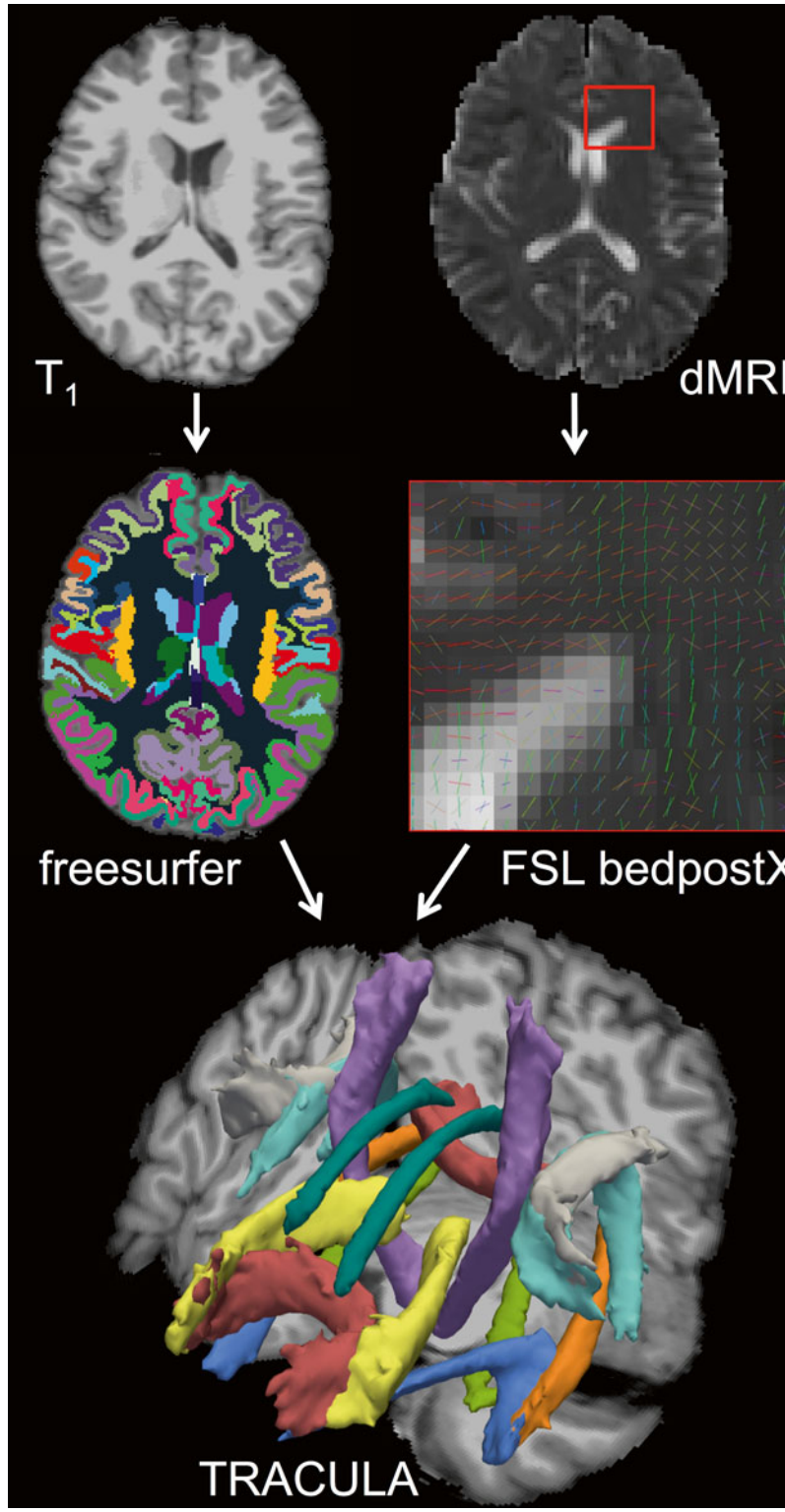

Fig. 11.19 Automated tractography by means of TRACULA [37]. A T_1-weighted scan is segmented by freesurfer software, the resulting labels serve as ROIs in the tractography. Diffusion weighted MRI data are processed by FSL bedpostX software to compute multiple diffusion orientations per voxel (to model fibre crossings). TRACULA combines these data to reconstruct 18 fibre pathway probability maps

least two bundles [13]. Fortunately, despite this model error, it is possible to successfully reconstruct the core structure of major bundles, which is sufficient for preclinical research studies investigating groups of subjects. Note however, this important limitation means that DTI tractography is not the most appropriate method for presurgical planning (see Chaps. 15 and 21).

As stated in Chap. 21, a large number of higher order models for complex fibre configurations have been proposed. Estimating higher order models requires higher quality data with a greater number of diffusion gradient directions and higher b-values compared to classical DTI (see Chap. 6). This type of acquisition is commonly referred to as *high angular resolution diffusion imaging* or HARDI. A higher b-value of $b > 1500$ s/mm^2 and >60 gradient directions are preferred, compared to the typical $b = 1000$ s/mm^2 and 30 directions for DTI. This increases the scan time beyond 8 min per average. Previously this has proved an obstacle for clinical research; however, it is now possible to obtain good quality HARDI data in under 15 min.

Figure 11.7 presents an example of tractography using CSD in the pons of a patient with an embryonic defect in axonal guidance [38]. The patient showed symptoms of reduced coordination of muscle movements (ataxia), eye movements (nystagmus), sensory deafness and episodes of hypothermia. Common interhemispherical connections were diminished in this patient (data not shown); instead an additional transversal bundle was observed, connected to an abnormal projection out of the brain stem.

Automated Tractography

Fibre reconstruction relies on manual identification of anatomical landmarks of a tract of interest. This subjective judgment is a potential source of experimental variability. In addition, manual reconstruction in a large number of datasets is time consuming. Several methods have therefore been proposed for automated tractography.

White Matter Atlas

Stereotaxic human brain atlases are often employed in neuroimaging research as an anatomical reference. Based on an existing anatomical template averaged over 152 subjects (ICBM-152), a hand-segmented white matter parcellation map was created, based on fibre orientation information [39]. Instead of performing tractography, such a map may be used to segment a novel dataset after spatial alignment by means of registration. The accuracy of the segmentation relies on registration errors, mainly caused by inter-subject anatomical variation. As an extension, a white matter parcellation atlas was created by populating tract probability maps of multiple subjects [40]. This atlas allows for automated tract-specific quantification of DTI measures.

Atlas-Based Tractography

A disadvantage of using white matter atlases is that not all inter-subject morphologic variations can be modeled. Alternatively, seeding and masking ROIs may be selected from an atlas for tracking in specific datasets, which is named *atlas-based tracking* [41, 42]. While minor spatial offsets in the ROIs may be expected, the tracking results obtained potentially more accurately describe the anatomy in the datasets compared to atlas-based segmentation alone, as described in the previous section.

In the atlas, a set of reference regions of interest (rROIs) is defined that allow the bundle of interest to be tracked. Next, spatial correspondence needs to found between the atlas and the dataset in which tracking needs to be performed. In Fig. 11.18, this is achieved by linear (affine) registration. The rROIs are transformed accordingly and tracking in the target dataset is performed using the rROIs. Following this approach, sufficient agreement with a manual approaches was obtained ($\kappa > 0.8$) [42], showing that atlas-based automated tracking is relatively robust to registration errors between the atlas and the dataset of interest. See Chaps. 10 and 12 for further details about DTI atlases and spatial alignment.

Additional prior information for tractography may be obtained from a high-resolution structural T_1-weighted scan. An automated segmentation and parcellation of subcortical and cortical structures [43] provides accurately defined ROIs for seeding and masking.

A method was proposed that allows the automated delineation of 18 "tracts constrained by underlying anatomy" (TRACULA). The method takes T_1- and diffusion-weighted images as input. Spatial distortions that appear in DWIs need to be corrected by including an additional B0-scan or by registration. The T_1-scan is segmented using Freesurfer software [43, 44] and diffusion orientation distributions are estimated by means of BedpostX (see "Tract Selection"). Based on these data tractography is performed resulting in subject-specific tract probability maps. These are displayed in Fig. 11.19 at a threshold of 20 %. In case of gross anatomical variation, automated tractography might fail, in which case it is advisable to manually define more ROIs than are definedby default.

Connectivity

The human brain is a highly interconnected organ in which different brain regions are mutually dependent on one another. This leverages a high potential for studies into large-scale connectivity that may provide novel insight into complex brain disorders. DW-MRI has been enthusiastically adopted by neuroscientists as a tool for assessing structural connectivity in the human brain. One goal is to associate this structural connectivity with measures of functional connectivity, e.g., derived from correlation measures in functional MRI data. As an example, in a study into Major Depressive Disorder, a negative structure-function relation was identified that was positively associated with depression severity [45].

The purpose of studying white matter connectivity is to gain insight into the function of the brain [28]. The challenging task is to quantify connectivity using certain measures that may be compared over time or between individuals. One structural aspect of connectivity is defined by the number of axonal projections: the more axons traverse between two brain regions, the stronger the connection is. Additionally, changes in the local microstructural composition of the myelin sheath and cell membranes may affect connectivity. Rather than quantifying these neurobiological features, connectivity in the context of tractography refers to the probability of reconstructing a pathway based on diffusion [46]. The question to be answered is if tractography-derived measures can be used as markers of connectivity. If so, then variations in these measures must be related to changes in the known (or hypothesized) connectivity and be minimally driven by measurement and reconstruction errors. We will briefly touch upon aspects the reader may encounter when considering a tractography-based connectivity study.

What Were We Measuring Again?

It is important to stress that the signal measured with diffusion MRI is really distant from what connectivity aims to capture. Random Brownian motion of water molecules causes an orientation dependent signal attenuation. As discussed before, diffusion MRI is measuring at limited resolution, orders of magnitude higher than the axonal scale. For the purpose of tractography, the principal orientations of diffusion are obtained from the data using any number of modeling schemes, among which CSD [19] and compartment models [47]. One must be aware that these are the available measures based on which research questions are to be defined and answered.

What Not to Do

Streamline deterministic tractography as introduced in this chapter answers the question if a connection between regions can be reconstructed from the given data with a clear "yes" or "no." Any other inferences on quality or confidence of the connection cannot be made. Anatomically implausible connections such as given in Fig. 11.4 are displayed with equally solid streamlines as other connections that are known to be

present. Probabilistic tractography by no means overcomes this issue of inaccuracy: nonexisting connections are shown with equally large reproducibility as for deterministic tractography [28]. Consequently, one cannot bluntly track fibres between any pair of brain regions and obtain massive connectivity matrices without at least introducing anatomical prior knowledge on connections that are known are there. This is not to state that, if carefully designed, such matrices cannot be reconstructed, as is shown in [48].

Fibre Count

It is tempting to interpret streamline or *fibre count* as a measure for the number of axons. However, as has been made clear, tractography is measured on an entirely different measurement scale. Also, a number of factors affect the fibre count:

- Increasing length and curvature will decrease the fibre count, since tracts 'bend off' and are early terminated.
- Brain diseases may locally affect white matter bundles such that tractography may primarily follow other pathways. It is likely that in such a situation an increased number of fibres are found in these other pathways, which clearly does not reflect the underlying configuration.
- Brain atrophy is highly correlated with DTI measures [49] and tract volume [50] and needs to be accounted for in statistical analyses.
- The fibre count is highly dependent on the uncertainty in the estimated diffusion orientation, which in turn is dependent on FA and data quality (see Fig. 11.8). FA is directly related to the diffusion profile and must be assessed if appropriate.
- Track-weighted imaging or tract density imaging and allied techniques uses a sophisticated form of interpolation to visualize diffusion data at a higher resolution than the acquired resolution by locally integrating the number of visiting streamlines [51, 52]. While visually attractive (see Fig. 11.20) and reproducible [53], these maps are primarily qualitative and still subject to similar limitations as other probabilistic tractography based methods.

Other Connectivity Measures?

Probabilistic tractography outputs the reproducibility of tracking in a tract visitation map. These numbers must not be interpreted as a probability of the local existence of a connection, but instead as a measure of variation in the obtained result. Figure 11.17 shows that the tracking variation is minimal close to the seeding area and thus operator dependent. Also other topology-induced variation is present. This makes it clear that these probabilistic outcomes cannot be directly interpreted as connectivity estimates.

Global tractography (not to be confused with "whole-brain tractography") is a more recent development in the field based on HARDI data, which models the problem of estimating the tractogram in a different way to the other techniques discussed so far. In classical approaches, algorithms try and find a close match between the local diffusion signal and underlying microstructure in each voxel, and propagate streamlines based on the principal direction(s) of diffusion. This means they are sensitive to cumulative errors along the fibre trajectory. In global approaches, algorithms reconstruct the whole tractogram simultaneously by finding the most optimal paths through the diffusion field that best fit the underlying data. In contrast to classical, local approaches, in global tractography, neighboring pathways influence each other as part of the optimization process. The advantage of such global approaches is that they are less influenced by local perturbations in the diffusion signal (e.g., due to artefacts, noise) and the accumulation of errors. This may make them more appropriate for investigating global connectivity than classical approaches. The disadvantage however, is that they are computationally very demanding and are therefore presently used only in a research context. For further information, the reader is directed to [54].

Foresight

How to proceed in assessing connectivity based on diffusion MRI? There is increasing evidence that tractography-derived measures correlate with independent modalities, such as fMRI. Future

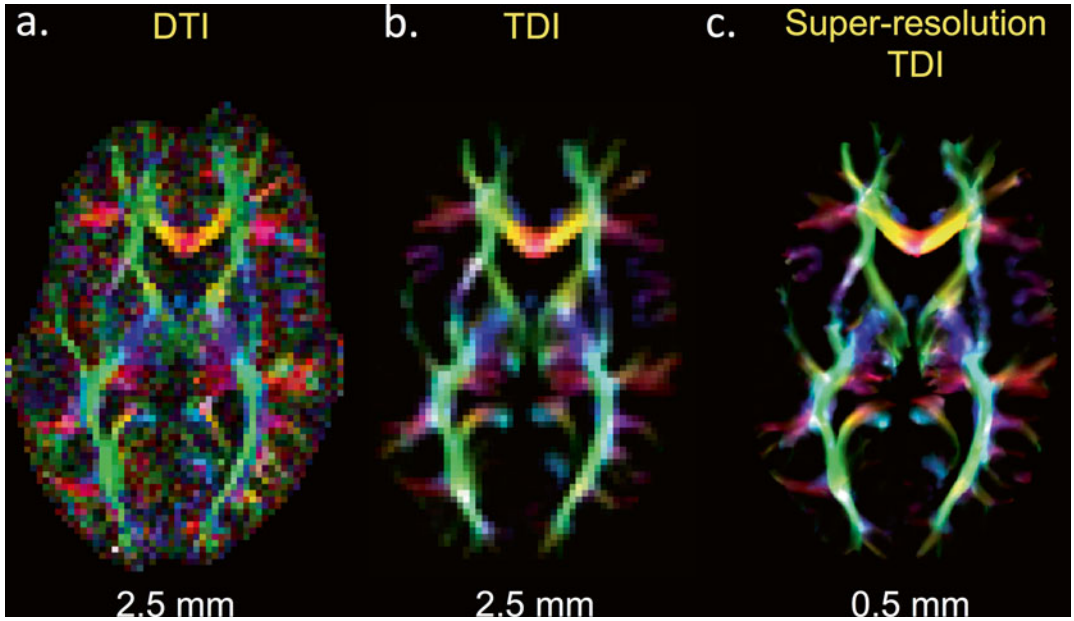

Fig. 11.20 (**a**) Axial FA map colorcoded by orientation (Fac) at original resolution of 2.5 mm (isotropic). (**b**) Color-coded track-density image (TDI) generated from the same data as (**a**) using probabilistic tractography (constrained spherical deconvolution), with 20 million streamlines on a 2.5 mm isotropic grid (i.e., original resolution). (**c**) Color-coded super-resolution TDI generated from the same data as (**a**), with 20 million streamlines on a 0.5 mm isotropic grid. Note the enhanced detail in deep white matter structures, but the apparent loss of detail in the cortex due to higher uncertainty in long-range connections in these regions. Images generated using MRTrix software. Courtesy of Thijs Dhollander

research should identify the underlying processes that co-occur in these data. Novel imaging modalities such as mapping myelin density [55] may shed new light on this highly interesting debate. Meanwhile, tractography-derived measures may be adopted, as long as the strong underlying assumptions are recognized and not violated in analysis and interpretation [56].

Discussion

In this chapter, a number of different tractography methods have been presented, each with its own strengths and weaknesses. Data quality and tracking parameters highly influence the tracking results. Unfortunately, no ground truth is available to the user for validation. Prior knowledge on the global trajectory of pathways is indispensable in drawing seeding and masking ROIs.

Different software packages exist for performing tractography. The software that has been used for creating figures is mentioned in the captions wherever appropriate. The reader is referred to Chap. 13 for further discussion on practical issues related to the analysis of DTI data using presently available software. Some vendors provide software for online tracking on the scanner console or a connected computer. The advantage is that data do not have be transferred and processed off-line (requiring time and expertise) but can be analyzed on the fly, and results can easily be integrated in the acquired dataset to be archived in the hospital PACS. An example of online tracking is given in Fig. 11.21.

In conclusion, tractography is a powerful method to obtain estimates of global structural connections between brain regions from local measurements of diffusion. If performed and interpreted correctly, it may provide useful complementary information in preclinical research and has potential future utility in routine clinical practice (Fig. 11.22).

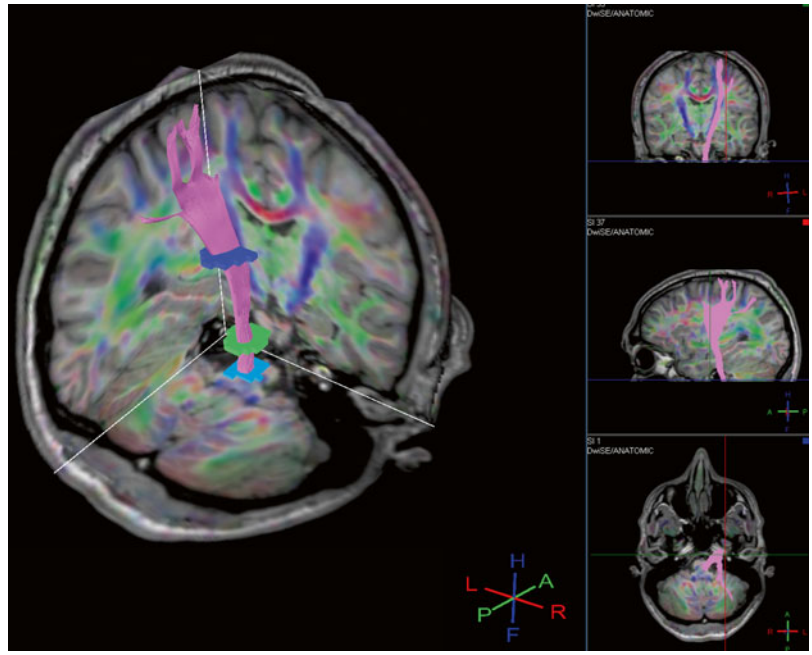

Fig. 11.21 Online tracking result with scanner software (Fibretrak, Philips Medical Systems) of the corticospinal tract. Multiple ROIs were defined by the user to obtain the left corticospinal tract. An FA map color coded for orientation is blended with a T_1-weighted structural scan to aid in delineating the tract. A short diffusion weighted protocol was chosen: resolution 2.5 mm isotropic, 30 gradient directions, $b = 1000$ s/mm^2, total scanning time 3 min and 30 s. Head motion was corrected for prior to tractography

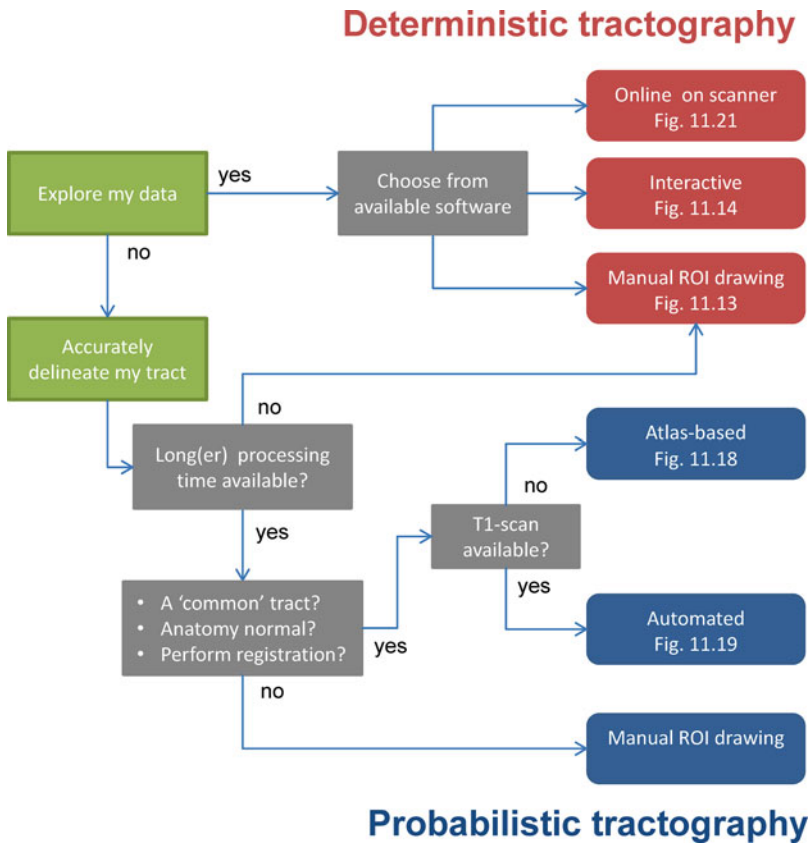

Fig. 11.22 What is my tractography goal?

Must Reads

1. One of the first articles that introduced tractography [57].
2. Principles and limitations of tractography [15].
3. Discussion on connectivity and tractography [28, 36].
4. Overview paper discussing challenges to be addressed in the future [7].
5. A paper providing a distinctive mapping between thalamic and cortical regions using probabilistic tractography [35].

References

1. Waxman SG, Kocsis JD, Stys PK. The axon: structure, function and pathophysiology. Oxford: Oxford University Press; 1995.
2. Jellison BJ, Field AS, Medow J, Lazar M, Salamat MS, Alexander AL. Diffusion tensor imaging of cerebral white matter: a pictorial review of physics, fiber tract anatomy, and tumor imaging patterns. AJNR Am J Neuroradiol. 2004;25(3):356–69.
3. Livet J, Weissman TA, Kang H, Draft RW, Lu J, Bennis RA, Sanes JR, Lichtman JW. Transgenic strategies for combinatorial expression of fluorescent proteins in the nervous system. Nature. 2007;450(7166):56–62.
4. Dauguet J, Peled S, Berezovskii V, Delzescaux T, Warfield SK, Born R, Westin C-F. Comparison of fiber tracts derived from in-vivo DTI tractography with 3D histological neural tract tracer reconstruction on a macaque brain. Neuroimage. 2007;37(2):530–8.
5. Nieuwenhuys R, Voogd J, Van Huijzen C, van Huijzen C, Voogd J. The human central nervous system. New York: Springer; 2008.
6. Stadlbauer A, Nimsky C, Buslei R, Salomonowitz E, Hammen T, Buchfelder M, Moser E, Ernst-Stecken A, Ganslandt O. Diffusion tensor imaging and optimized fiber tracking in glioma patients: histopathologic evaluation of tumor-invaded white matter structures. Neuroimage. 2007;34(3):949–56.
7. Jbabdi S, Johansen-Berg H. Tractography: where do we go from here? Brain Connect. 2011;1(3):169–83.
8. Leemans A, Jeurissen B. ExploreDTI: a graphical toolbox for processing, analyzing, and visualizing diffusion MR data. 17th Annual Meeting …, vol. 245, no. 2, p. 3300, 2009.
9. Tournier JD, Mori S, Leemans A. Diffusion tensor imaging and beyond. Magn Reson Med. 2011;65(6):1532–56.
10. Le Bihan D. Molecular diffusion nuclear magnetic resonance imaging. Magn Reson Q. 1991;7(1):1–30.
11. Engström M, Skare S. Diffusion-weighted 3D multislab echo planar imaging for high signal-to-noise ratio efficiency and isotropic image resolution. Magn Reson Med. 2013;1514:1507–14.
12. Heidemann RM, Anwander A, Feiweier T, Knösche TR, Turner R. k-space and q-space: combining ultra-high spatial and angular resolution in diffusion imaging using ZOOPPA at 7 T. Neuroimage. 2012;60(2):967–78.
13. Jeurissen B, Leemans A, Tournier J-D, Jones DK, Sijbers J. Investigating the prevalence of complex fiber configurations in white matter tissue with diffusion magnetic resonance imaging. Hum Brain Mapp. 2013;34(11):2747–66.
14. Tuch DS, Reese TG, Wiegell MR, Wedeen VJ. Diffusion MRI of complex neural architecture. Neuron. 2003;40(5):885–95.
15. Chung H-W, Chou M-C, Chen C-Y. Principles and limitations of computational algorithms in clinical diffusion tensor MR tractography. AJNR Am J Neuroradiol. 2011;32(1):3–13.
16. Jones DK, Knösche TR, Turner R. White matter integrity, fiber count, and other fallacies: the do's and don'ts of diffusion MRI. Neuroimage. 2013;73:239–54.
17. Jones DK, Basser PJ. 'Squashing peanuts and smashing pumpkins': how noise distorts diffusion-weighted MR data. Magn Reson Med. 2004;52(5):979–93.
18. Barth PG, Majoie CB, Caan MWA, Weterman MAJ, Kyllerman M, Smit LME, Kaplan RA, Haas RH, Baas F, Cobben J-M, Poll-The BT. Pontine tegmental cap dysplasia: a novel brain malformation with a defect in axonal guidance. Brain. 2007;130(Pt 9):2258–66.
19. Jeurissen B, Leemans A, Jones DK, Tournier JD, Sijbers J. Probabilistic fiber tracking using the residual bootstrap with constrained spherical deconvolution. Hum Brain Mapp. 2011;32(3):461–79.
20. Ghosh A, Descoteaux M, Deriche R. Riemannian framework for estimating symmetric positive definite 4th order diffusion tensors. Med Image Comput Comput Assist Interv. 2008;11(Pt 1):858–65.
21. Behrens TE, Berg HJ, Jbabdi S, Rushworth MF, Woolrich MW. Probabilistic diffusion tractography with multiple fibre orientations: what can we gain? Neuroimage. 2007;34(1):144–55.
22. Caan MWA, Khedoe HG, Poot DHJ, den Dekker AJ, Olabarriaga SD, Grimbergen KA, van Vliet LJ, Vos FM. Estimation of diffusion properties in crossing fiber bundles. IEEE Trans Med Imaging. 2010;29(8):1504–15.
23. Jones DK. The effect of gradient sampling schemes on measures derived from diffusion tensor MRI: a Monte Carlo study. Magn Reson Med. 2004;51(4):807–15.
24. Akkerman EM. The direct tensor solution and higher-order acquisition schemes for generalized diffusion tensor imaging. J Magn Reson. 2010;206(1):9–19.
25. Okada T, Miki Y, Fushimi Y, Hanakawa T, Kanagaki M, Yamamoto A, Urayama S, Fukuyama H, Hiraoka M, Togashi K. Diffusion-tensor fiber tractography:

intraindividual comparison of 3.0-T and 1.5-T MR imaging. Radiology. 2006;238(2):668–78.
26. Polders DL, Leemans A, Hendrikse J, Donahue MJ, Luijten PR, Hoogduin JM. Signal to noise ratio and uncertainty in diffusion tensor imaging at 1.5, 3.0, and 7.0 Tesla. J Magn Reson Imaging. 2011;33(6):1456–63.
27. Choi S, Cunningham DT, Aguila F, Corrigan JD, Bogner J, Mysiw WJ, Knopp MV, Schmalbrock P. DTI at 7 and 3 T: systematic comparison of SNR and its influence on quantitative metrics. Magn Reson Imaging. 2011;29(6):739–51.
28. Jones DK. Challenges and limitations of quantifying brain connectivity in vivo with diffusion MRI. Imaging Med. 2010;2(3):341–55.
29. Blaas J, Botha CP, Peters B, Vos FM, Post FH. Fast and reproducible fiber bundle selection in DTI visualization. IEEE Vis. 2005, pp. 59–64.
30. Jiang H, van Zijl PCM, Kim J, Pearlson GD, Mori S. DtiStudio: resource program for diffusion tensor computation and fiber bundle tracking. Comput Methods Programs Biomed. 2006;81(2):106–16.
31. Wakana S, Caprihan A, Panzenboeck MM, Fallon JH, Perry M, Gollub RL, Hua K, Zhang J, Jiang H, Dubey P, Blitz A, van Zijl P, Mori S. Reproducibility of quantitative tractography methods applied to cerebral white matter. Neuroimage. 2007;36(3):630–44.
32. van der Graaff MM, Sage CA, Caan MW, Akkerman EM, Lavini C, Majoie CB, Nederveen AJ, Zwinderman AH, Vos F, Brugman F, van den Berg LH, de Rijk MC, van Doorn PA, Van Hecke W, Peeters RR, Robberecht W, Sunaert S, de Visser M. Upper and extra-motoneuron involvement in early motoneuron disease: a diffusion tensor imaging study. Brain. 2011;134(Pt 4):1211–28.
33. Jones DK. Determining and visualizing uncertainty in estimates of fiber orientation from diffusion tensor MRI. Magn Reson Med. 2003;49(1):7–12.
34. Parker GJM, Alexander DC. Probabilistic anatomical connectivity derived from the microscopic persistent angular structure of cerebral tissue. Philos Trans R Soc Lond B Biol Sci. 2005;360(1457):893–902.
35. Behrens TEJ, Johansen-Berg H, Woolrich MW, Smith SM, Wheeler-Kingshott CAM, Boulby PA, Barker GJ, Sillery EL, Sheehan K, Ciccarelli O, Thompson AJ, Brady JM, Matthews PM. Non-invasive mapping of connections between human thalamus and cortex using diffusion imaging. Nat Neurosci. 2003;6(7):750–7.
36. Lazar M. Mapping brain anatomical connectivity using white matter tractography. NMR Biomed. 2010;23(7):821–35.
37. Yendiki A, Panneck P, Srinivasan P, Stevens A, Zöllei L, Augustinack J, Wang R, Salat D, Ehrlich S, Behrens T, Jbabdi S, Gollub R, Fischl B. Automated probabilistic reconstruction of white-matter pathways in health and disease using an atlas of the underlying anatomy. Front Neuroinform. 2011;5:23.
38. Caan MWA, Barth PG, Niermeijer J-M, Majoie CB, Poll-The BT. Ectopic peripontine arcuate fibres, a novel finding in pontine tegmental cap dysplasia. Eur J Paediatr Neurol. 2014;18(3):434–8.
39. Mori S, Oishi K, Jiang H, Jiang L, Li X, Akhter K, Hua K, Faria AV, Mahmood A, Woods R, Toga AW, Pike GB, Neto PR, Evans A, Zhang J, Huang H, Miller MI, van Zijl P, Mazziotta J. Stereotaxic white matter atlas based on diffusion tensor imaging in an ICBM template. Neuroimage. 2008;40(2):570–82.
40. Hua K, Zhang J, Wakana S, Jiang H, Li X, Reich DS, Calabresi PA, Pekar JJ, van Zijl PCM, Mori S. Tract probability maps in stereotaxic spaces: analyses of white matter anatomy and tract-specific quantification. Neuroimage. 2008;39(1):336–47.
41. Nucifora PGP, Wu X, Melhem ER, Gur RE, Gur RC, Verma R. Automated diffusion tensor tractography: implementation and comparison to user-driven tractography. Acad Radiol. 2012;19(5):622–9.
42. Zhang W, Olivi A, Hertig S, Van Zijl P, Mori S. Automated fiber tracking of human brain white matter using diffusion tensor imaging. Neuroimage. 2008;42(2):771–7.
43. Fischl B. Automatically parcellating the human cerebral cortex. Cereb Cortex. 2004;14(1):11–22.
44. Fischl B, Salat DH, Busa E, Albert M, Dieterich M, Haselgrove C, van der Kouwe A, Killiany R, Kennedy D, Klaveness S, Montillo A, Makris N, Rosen B, Dale AM. Whole brain segmentation: automated labeling of neuroanatomical structures in the human brain. Neuron. 2002;33(3):341–55.
45. de Kwaasteniet B, Ruhe E, Caan M, Rive M, Olabarriaga S, Groefsema M, Heesink L, van Wingen G, Denys D. Relation between structural and functional connectivity in major depressive disorder. Biol Psychiatry. 2013;74(1):40–7.
46. Kaden E, Knösche TR, Anwander A. Parametric spherical deconvolution: inferring anatomical connectivity using diffusion MR imaging. Neuroimage. 2007;37(2):474–88.
47. Panagiotaki E, Schneider T, Siow B, Hall MG, Lythgoe MF, Alexander DC. Compartment models of the diffusion MR signal in brain white matter: a taxonomy and comparison. Neuroimage. 2012;59(3):2241–54.
48. Honey CJ, Sporns O, Cammoun L, Gigandet X, Thiran JP, Meuli R, Hagmann P. Predicting human resting-state functional connectivity from structural connectivity. Proc Natl Acad Sci U S A. 2009;106(6):2035–40.
49. Vernooij MW, de Groot M, van der Lugt A, Ikram MA, Krestin GP, Hofman A, Niessen WJ, Breteler MMB. White matter atrophy and lesion formation explain the loss of structural integrity of white matter in aging. Neuroimage. 2008;43(3):470–7.
50. Fink F, Klein J, Lanz M, Mitrovics T, Lentschig M, Hahn HK, Hildebrandt H. Comparison of diffusion tensor-based tractography and quantified brain atrophy for analyzing demyelination and axonal loss in MS. J Neuroimaging. 2010;20(4):334–44.
51. Calamante F, Tournier J-D, Jackson GD, Connelly A. Track-density imaging (TDI): super-resolution

white matter imaging using whole-brain track-density mapping. Neuroimage. 2010;53(4):1233–43.
52. Dhollander T, Emsell L, Van Hecke W, Maes F, Sunaert S, Suetens P. Track orientation density imaging (TODI) and track orientation distribution (TOD) based tractography. Neuroimage. 2014;94:312–36.
53. Willats L, Raffelt D, Smith RE, Tournier J-D, Connelly A, Calamante F. Quantification of track-weighted imaging (TWI): characterisation of within-subject reproducibility and between-subject variability. Neuroimage. 2013;87:18–31.
54. Mangin J-F, Fillard P, Cointepas Y, Le Bihan D, Frouin V, Poupon C. Toward global tractography. Neuroimage. 2013;80:290–6.
55. Wilhelm MJ, Ong HH, Wehrli SL, Li C, Tsai P-H, Hackney DB, Wehrli FW. Direct magnetic resonance detection of myelin and prospects for quantitative imaging of myelin density. Proc Natl Acad Sci U S A. 2012;109(24):9605–10.
56. Behrens TEJ, Sporns O. Human connectomics. Curr Opin Neurobiol. 2012;22(1):144–53.
57. Basser PJ, Pajevic S, Pierpaoli C, Duda J, Aldroubi A. In vivo fiber tractography using DT-MRI data. Magn Reson Med. 2000;44(4):625–32.
58. Kurki TJI, Laalo JP, Oksaranta OM. Diffusion tensor tractography of the uncinate fasciculus: pitfalls in quantitative analysis due to traumatic volume changes. J Magn Reson Imaging. 2013;38(1):46–53.
59. Vos SB, Jones DK, Viergever MA, Leemans A. Partial volume effect as a hidden covariate in DTI analyses. Neuroimage. 2011;55(4):1566–76.

Part IV

Normal Diffusion Tensor Imaging Anatomy

Normal Diffusion Tensor Imaging-Based White Matter Anatomy

12

Bram Stieltjes

Learning Points

- Normal diffusion tensor imaging-based anatomy of the healthy brain.
- The identification of several major white matter fiber bundles on 2D directionally encoded color fractional anisotropy maps in axial, coronal, and sagittal views.
- The identification of common 3D virtual reconstructions of DTI-based white matter fiber tracts.
- Region-of-interest placement in order to virtually reconstruct commonly identified DTI-based white matter fiber tracts.

B. Stieltjes, MD, PhD (✉)
Department of radiology and nuclear medicine,
University Hospital Basel,
Basel, Switzerland
e-mail: B.Stieltjes@dkfz-heidelberg.de

Representation of White Matter Anatomy Using Diffusion Tensor Imaging

As diffusion tensor imaging permits estimation of the main nerve fiber direction within a voxel, a natural extension is to reconstruct the course of whole nerve tracts [1–7]. Figure 12.1 shows a sketch of a brain with diffusion tensor ellipsoids plotted in several brain voxels. The considered person is watching a red-leaved flower. This information is caught by the eye and passed to the visual brain cortex through the optical tract. This tract is observable in the tensor ellipsoids: they are elongated in tract voxels and reflect the main fiber direction. In the sketch, the diffusion is isotropic in voxels not containing the optic tract.

Figure 12.1b illustrates a straightforward approach to reconstruct tracts from the tensor ellipsoids, the so-called FACT algorithm (FACT = fiber assignment by continuous tracking) [4, 5]. The tract is started in one voxel and it follows the orientation of the ellipsoid in this voxel until it hits the border of the voxel. Then, this process is iterated in the adjacent voxel. Usually several starting points—which are also called seeds—are chosen. For example, in

W. Van Hecke et al. (eds.), *Diffusion Tensor Imaging*, DOI 10.1007/978-1-4939-3118-7_12

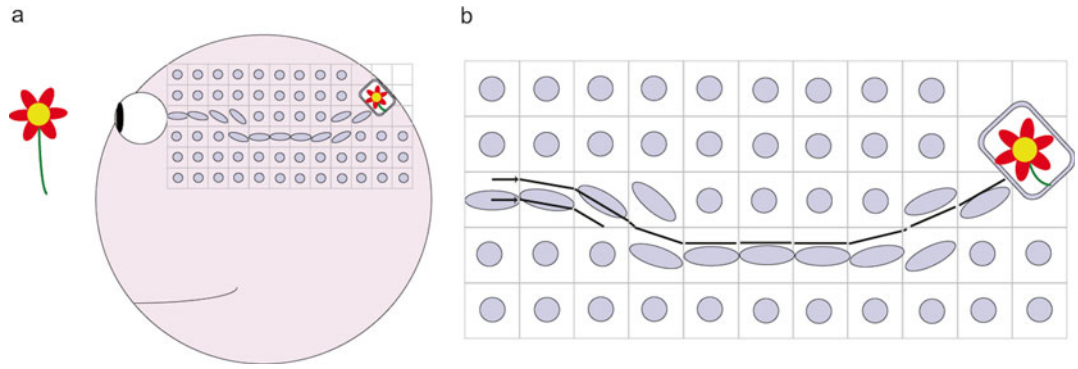

Fig. 12.1 The principle of fiber tracking. (**a**) Schematic view of a person watching a flower. Information is transported from the eye to the visual cortex at the back of the head. (**b**) Close-up of the voxel-wise diffusion measurement. The optical tract shows anisotropic (ellipsoid) water displacement and the tract can be reconstructed using diffusion tensor imaging

Fig. 12.1b, the tract starting in the center of the initial voxel does not reach the end of the optic nerve tract, since the tract is interrupted when it reaches a voxel with isotropic diffusion. The other tract, which starts in the upper part of the initial voxel, reaches the visual brain cortex. Thus, by choosing several seeds instead of only one seed, the chance is increased that the actual tract is reconstructed.

In Fig. 12.1b, an important property of fiber tracking results can be appreciated: the strong dependency on the chosen algorithm and its parameters. The termination criterion of the algorithm depicted in Fig. 12.1b is to stop the tract if an isotropic voxel is reached. However, if the tract were allowed to maintain its direction in an isotropic voxel under the condition that the next voxel is anisotropic, then the broken fiber would make it to the end of the optic tract. In practice, of course, voxels are usually not perfectly isotropic, so one would rather choose a certain anisotropy threshold to terminate the fiber. The final tracking result will in any case depend strongly on this threshold. As there is often no unique and perfect choice of algorithm and parameters, the obtained results should not be regarded as a perfect ground truth. Nonetheless, it has been shown that the main fiber tracts can be reconstructed correctly.

Since the initial works on fiber tracking, many fiber tracking algorithms and strategies have been developed. Since a detailed review of these techniques is beyond the scope of this introduction and covered in Chap. 11 of this book, here we only present an in-depth description of the algorithm used for the fiber tracking in the "Three-Dimensional Tract Representation" section.

Protocol

Data Acquisition

The data were acquired using a 3 T scanner (TIM Trio, Siemens, Erlangen, Germany) equipped with a 32-channel head coil. A single-shot echo-planar imaging (EPI) sequence was applied for DTI assessment (TR 6400 ms, TE 91 ms, 96×96 matrix size, field of view 240 mm). Fifty axial slices with a thickness of 2.5 mm and no gap, 60 gradient directions, and two *b*-values (0 and 1000 s/mm^2) were obtained.

Data Preprocessing

Eddy currents and head motion were corrected using *FSL flirt* (www.fmrib.ox.ac.uk/fsl/) by affine registration of the baseline and diffusion weighted volumes to the first baseline volume. Gradient directions were corrected according to the transformation. FSL bet was used in order to estimate brain masks. Tensors were fit using the teem library (teem.sourceforge.net). Negative Eigenvalues were corrected by adding (to all Eigenvalues) the amount by which the smallest is negative (corresponding to increasing the non-diffusion weighted image value).

Tracking Algorithm

The tractography algorithm that was used to generate the fiber tracking results was originally introduced by Reisert et al. [8] and is a so-called global tracking algorithm [9, 10]. This algorithm ranked first in an evaluation study by Fillard et.al. on the performance of tractography algorithms [11] and is implemented in MITK-Diffusion ([12], www.mitk.org/Difusion). The complete procedure is described in more detail in [13].

Two-Dimensional Tract Representation

Introduction (2D)

Here we present a diffusion tensor imaging derived color map produced using MITK-Diffusion ([12], www.mitk.org/Difusion). In these maps, the directional orientation of fiber tracts is color coded in the following fashion: tracts moving left-right are coded red (e.g., the Corpus callosum), anterior-posterior tracts are coded green (e.g., the Cingulum), and cranio-caudal tracts are coded blue (e.g., the cortico-spinal tract). The intensity or hue indicates the fractional anisotropy, a measure of fiber density. The most important, central parts of the brain are displayed in the three main radiological planes, axial, coronal, and sagittal.

Two-Dimensional Anatomy

Axial slices (Figs. 12.2, 12.3, 12.4, 12.5, 12.6, 12.7, 12.8, 12.9, and 12.10)

Coronal slices (Figs. 12.11, 12.12, 12.13, 12.14, 12.15, 12.16, 12.17, 12.18, and 12.19)

Sagittal slices (Figs. 12.20, 12.21, 12.22, 12.23, 12.24, 12.25, 12.26, and 12.27)

Three-Dimensional Tract Representation

Introduction (3D)

The three-dimensional part covers the most prominent white matter connections within the cerebral hemispheres. The complete reconstruction process is covered in a consistent, step-by-step fashion. First the relevance and anatomy of the tract is discussed and an initial region of interest (ROI) is shown. This ROI is chosen as to yield an optimal final result. By using inclusion (green) and exclusion (red) ROIs, the result is further refined. The final result is represented without the ROIs to optimally appreciate the anatomical location. The color coding of these tracts is identical to the two-dimensional color maps (section, Introduction 2D). The intricate anatomy of important adjacent tracts is further illustrated in combined overviews. Here each individual tract is represented in unicolor to enhance the visualization of the complex, interwoven anatomy.

Three-Dimensional Anatomy

The Corpus Callosum

Fiber tracking of the corpus callosum is relatively straightforward. Select a midsagittal on the sagit-

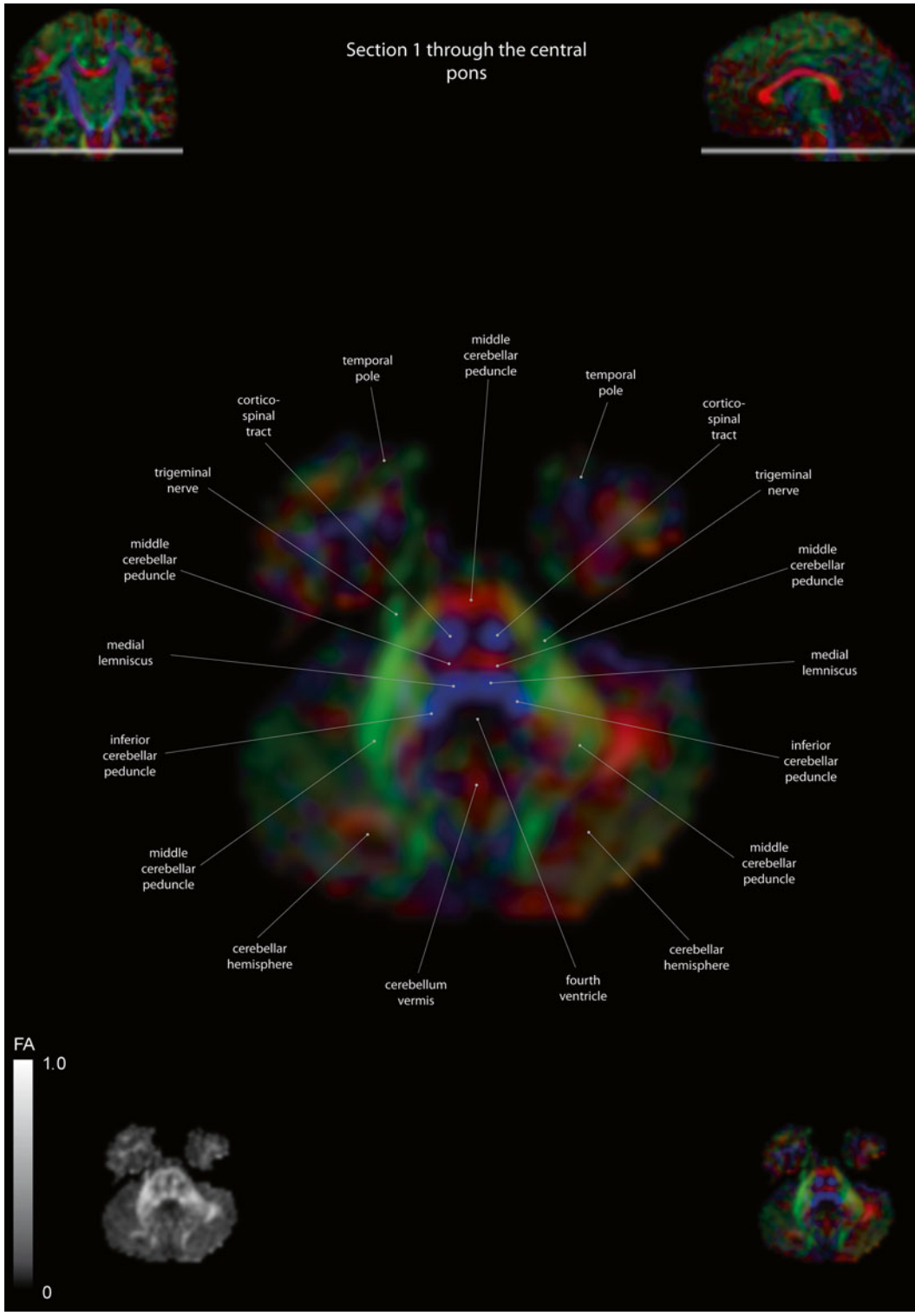

Fig. 12.2 Axial slices of a color-coded diffusion tensor image. The colors represent fiber direction; *red* = left to right, *blue* = cranio-caudal, and *green* = anterior-posterior. The intensity represents the fractional anisotropy (FA) also indicated in the *lower corner*. In the *upper corners*, the slice section is indicated in the coronal and sagittal plane

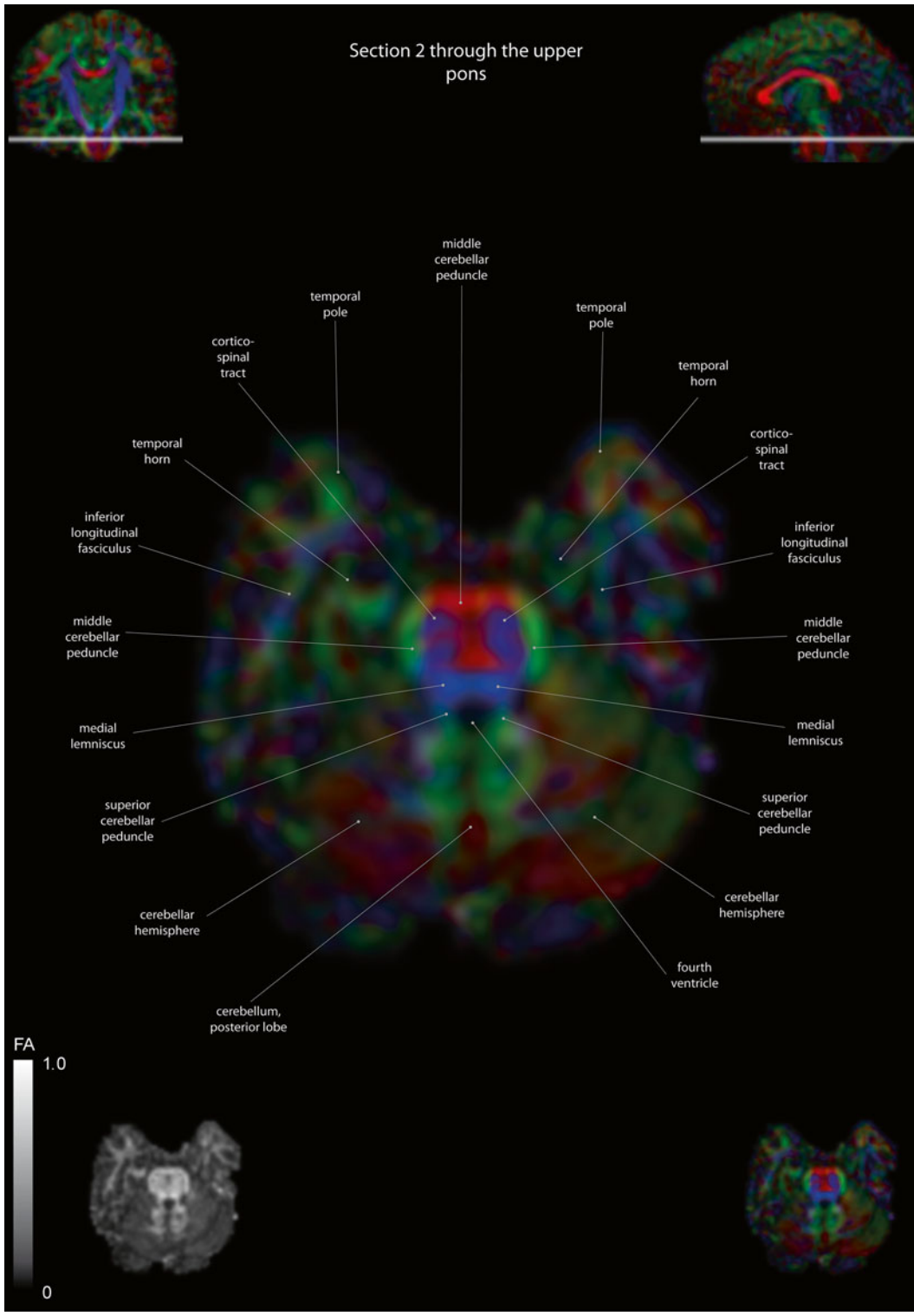

Fig. 12.3 Axial slices of a color-coded diffusion tensor image. The colors represent fiber direction; *red* = left to right, *blue* = cranio-caudal, and *green* = anterior-posterior. The intensity represents the fractional anisotropy (FA) also indicated in the *lower corner*. In the *upper corners*, the slice section is indicated in the coronal and sagittal plane

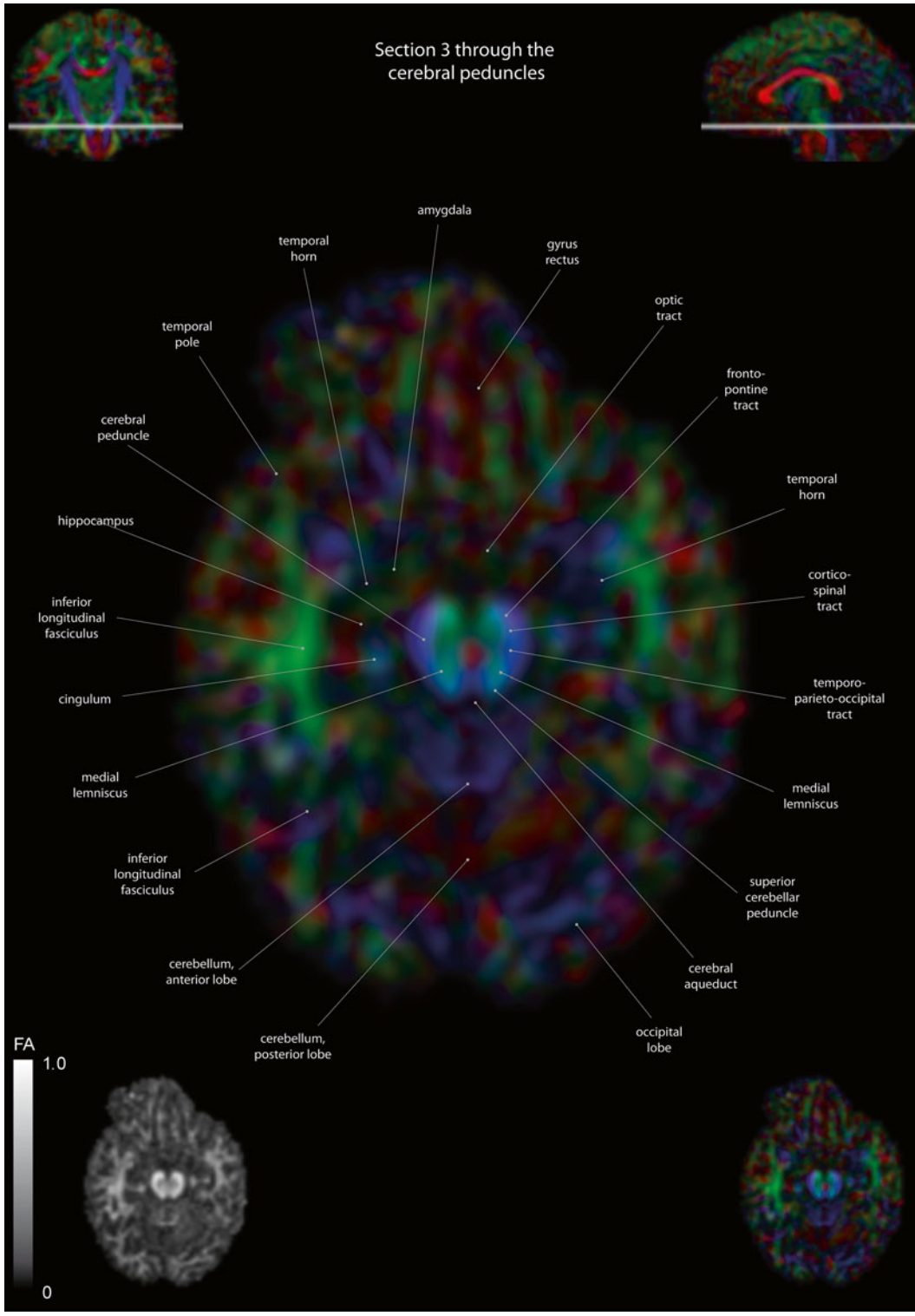

Fig. 12.4 Axial slices of a color-coded diffusion tensor image. The colors represent fiber direction; *red* = left to right, *blue* = cranio-caudal, and *green* = anterior-posterior. The intensity represents the fractional anisotropy (FA) also indicated in the *lower corner*. In the *upper corners*, the slice section is indicated in the coronal and sagittal plane

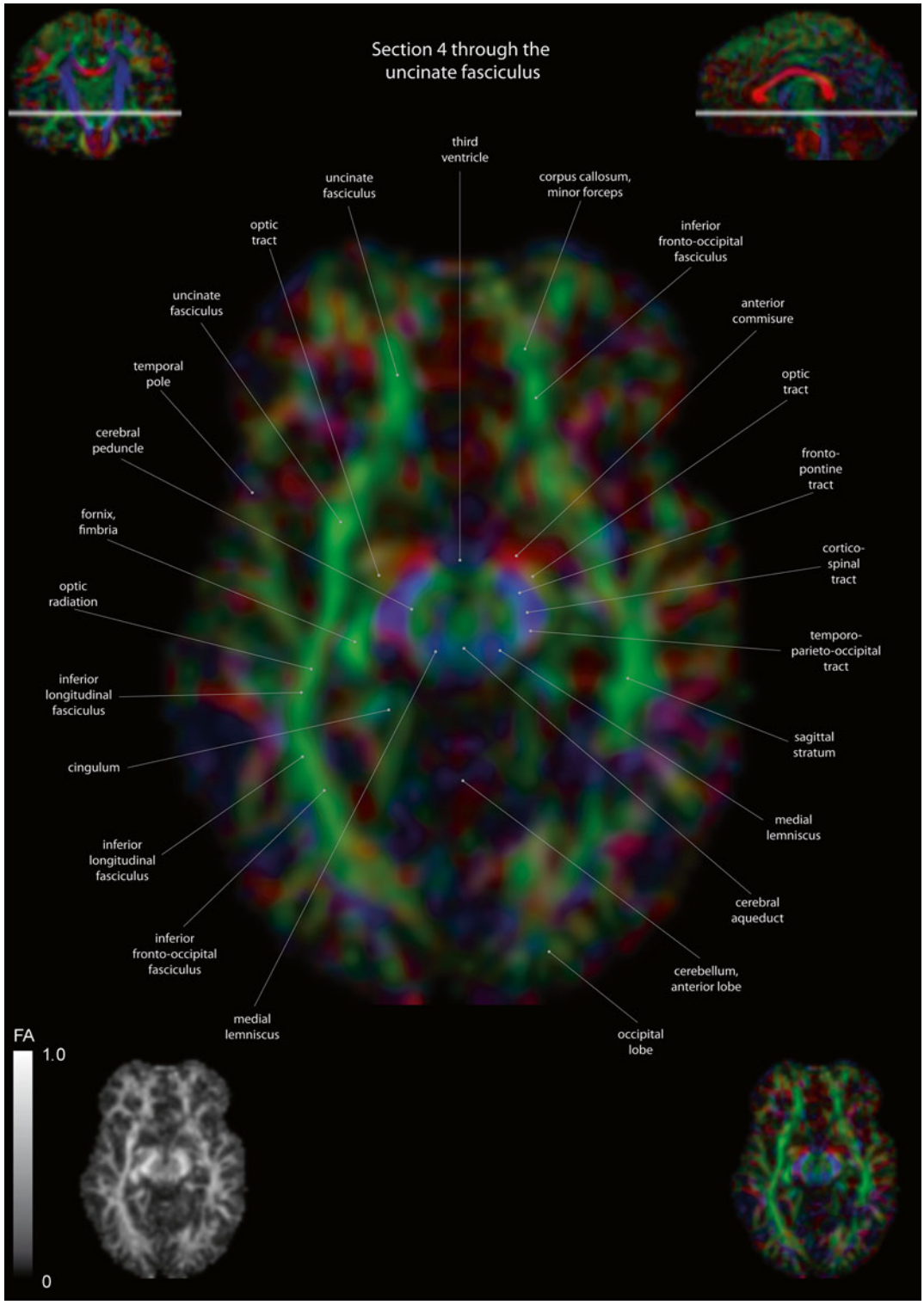

Fig. 12.5 Axial slices of a color-coded diffusion tensor image. The colors represent fiber direction; *red* = left to right, *blue* = cranio-caudal, and *green* = anterior-posterior. The intensity represents the fractional anisotropy (FA) also indicated in the *lower corner*. In the *upper corners*, the slice section is indicated in the coronal and sagittal plane

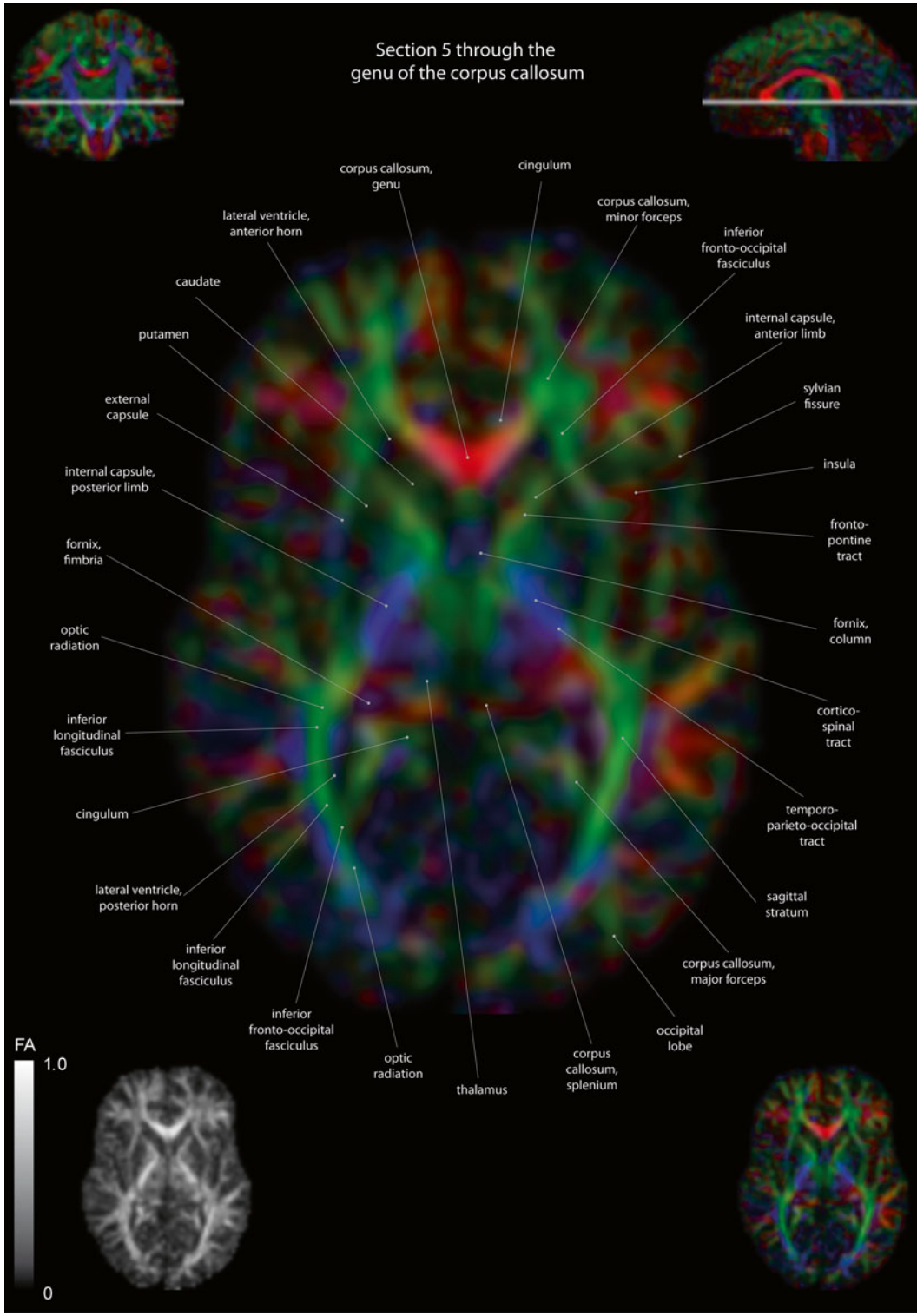

Fig. 12.6 Axial slices of a color-coded diffusion tensor image. The colors represent fiber direction; *red* = left to right, *blue* = cranio-caudal, and *green* = anterior-posterior. The intensity represents the fractional anisotropy (FA) also indicated in the *lower corner*. In the *upper corners*, the slice section is indicated in the coronal and sagittal plane

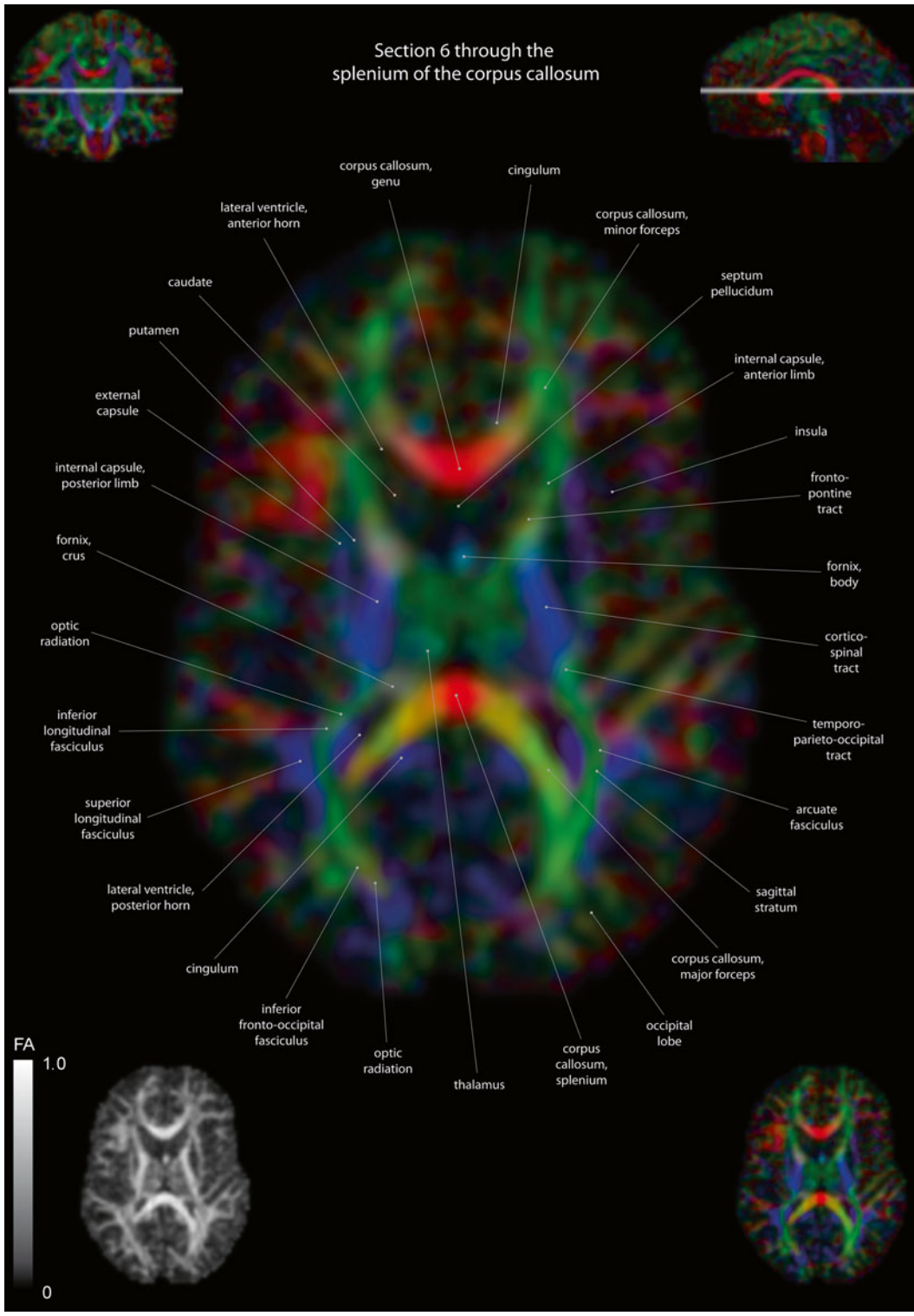

Fig. 12.7 Axial slices of a color-coded diffusion tensor image. The colors represent fiber direction; *red* = left to right, *blue* = cranio-caudal, and *green* = anterior-posterior. The intensity represents the fractional anisotropy (FA) also indicated in the *lower corner*. In the *upper corners*, the slice section is indicated in the coronal and sagittal plane

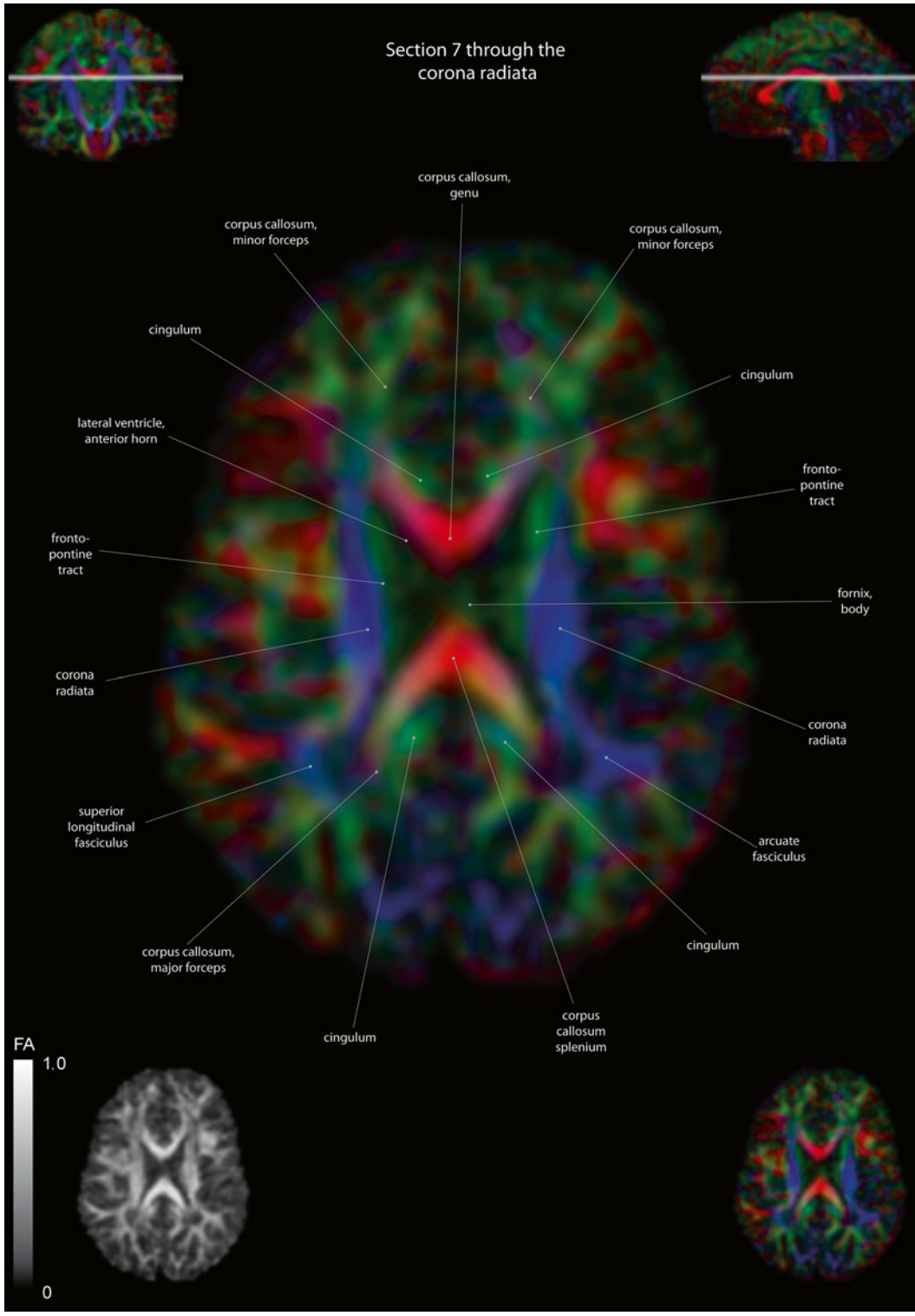

Fig. 12.8 Axial slices of a color-coded diffusion tensor image. The colors represent fiber direction; *red* = left to right, *blue* = cranio-caudal, and *green* = anterior-posterior. The intensity represents the fractional anisotropy (FA) also indicated in the *lower corner*. In the *upper corners*, the slice section is indicated in the coronal and sagittal plane

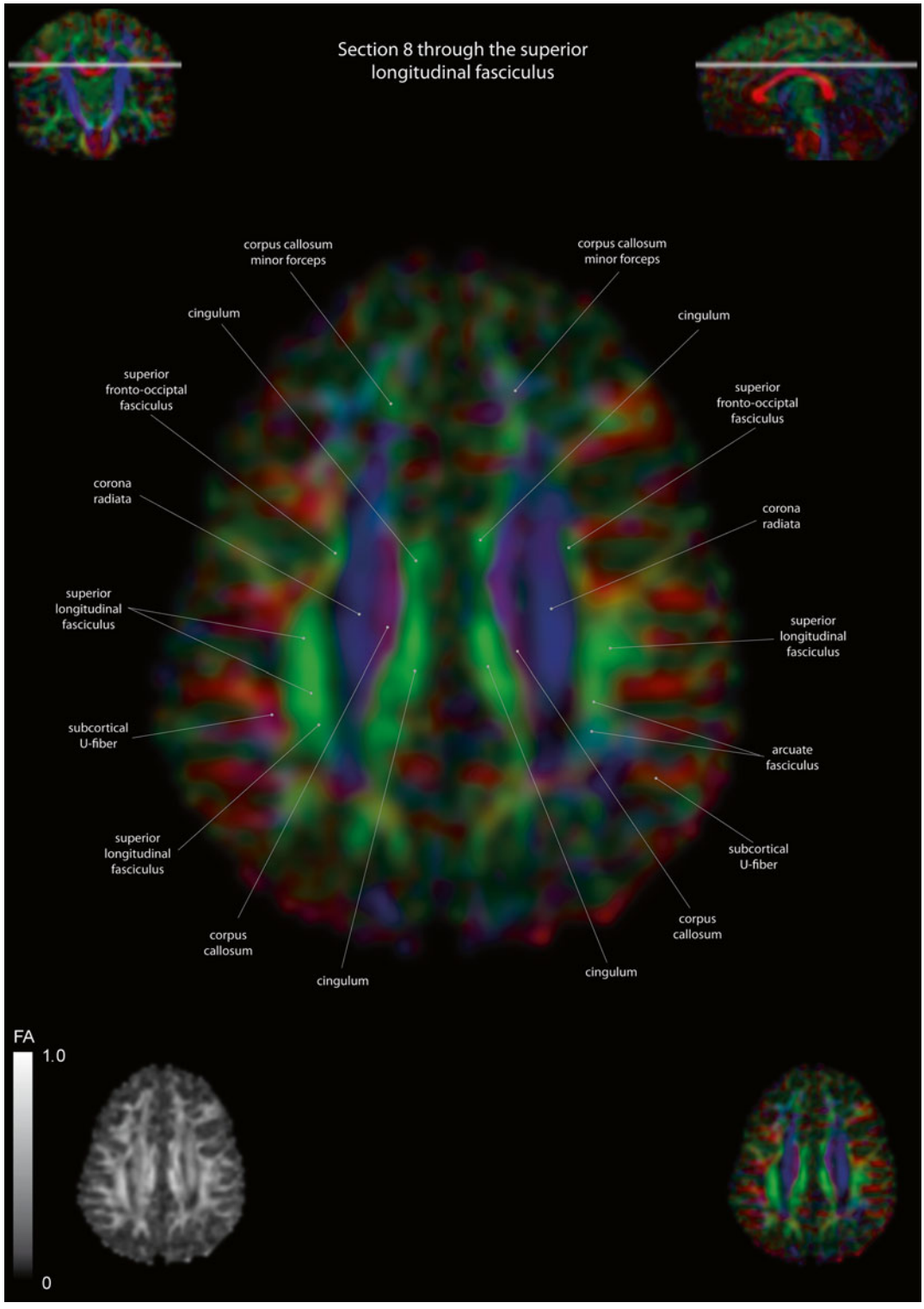

Fig. 12.9 Axial slices of a color-coded diffusion tensor image. The colors represent fiber direction; *red* = left to right, *blue* = cranio-caudal, and *green* = anterior-posterior. The intensity represents the fractional anisotropy (FA) also indicated in the *lower corner*. In the *upper corners*, the slice section is indicated in the coronal and sagittal plane

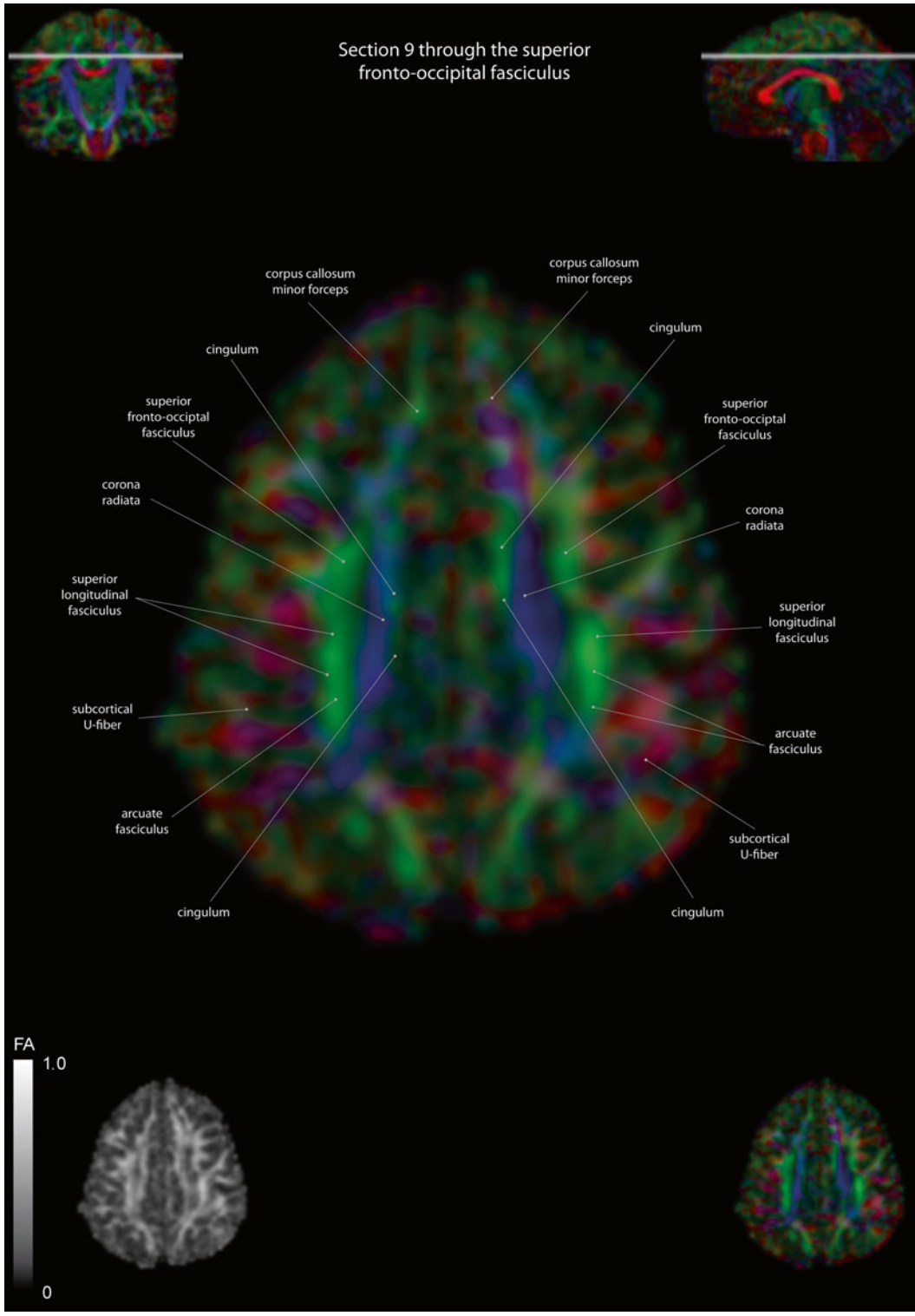

Fig. 12.10 Axial slices of a color-coded diffusion tensor image. The colors represent fiber direction; *red* = left to right, *blue* = cranio-caudal, and *green* = anterior-posterior. The intensity represents the fractional anisotropy (FA) also indicated in the *lower corner*. In the *upper corners*, the slice section is indicated in the coronal and sagittal plane

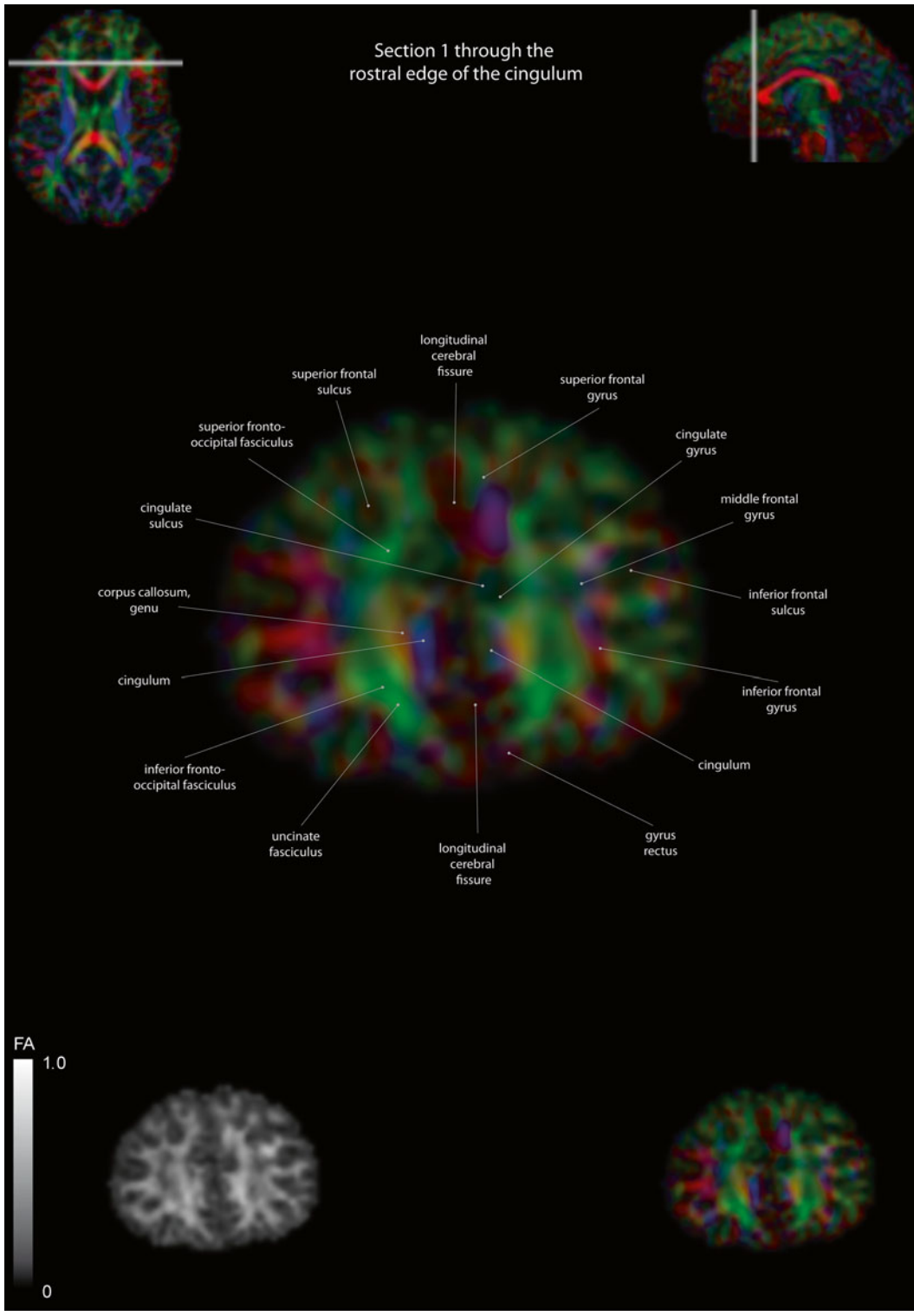

Fig. 12.11 Coronal slices of a color-coded diffusion tensor image. The colors represent fiber direction; *red* = left to right, *blue* = cranio-caudal, and *green* = anterior-posterior. The intensity represents the fractional anisotropy (FA) also indicated in the *lower corner*. In the *upper corners*, the slice section is indicated in the axial and sagittal plane

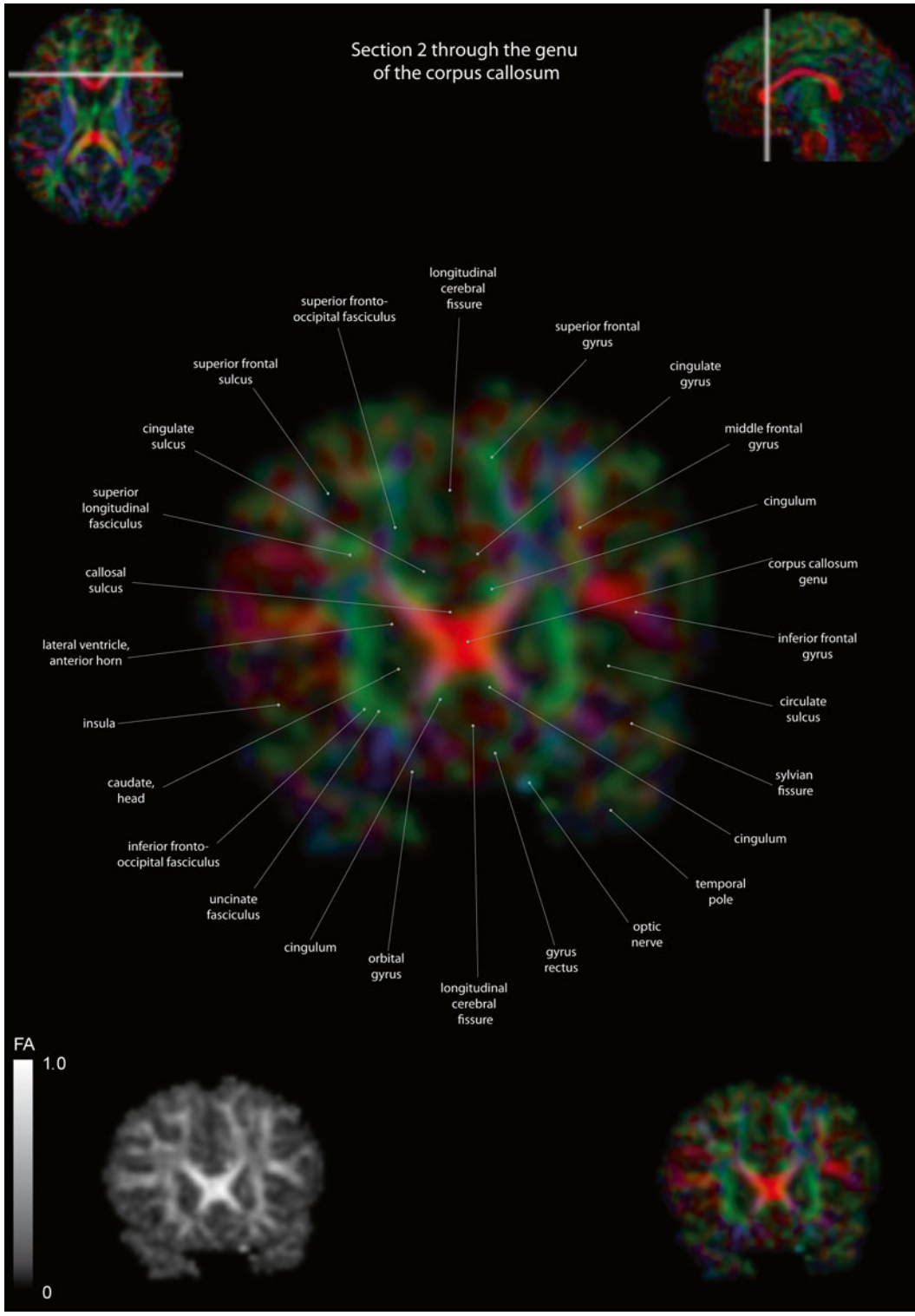

Fig. 12.12 Coronal slices of a color-coded diffusion tensor image. The colors represent fiber direction; *red* = left to right, *blue* = cranio-caudal, and *green* = anterior-posterior. The intensity represents the fractional anisotropy (FA) also indicated in the *lower corner*. In the *upper corners*, the slice section is indicated in the axial and sagittal plane

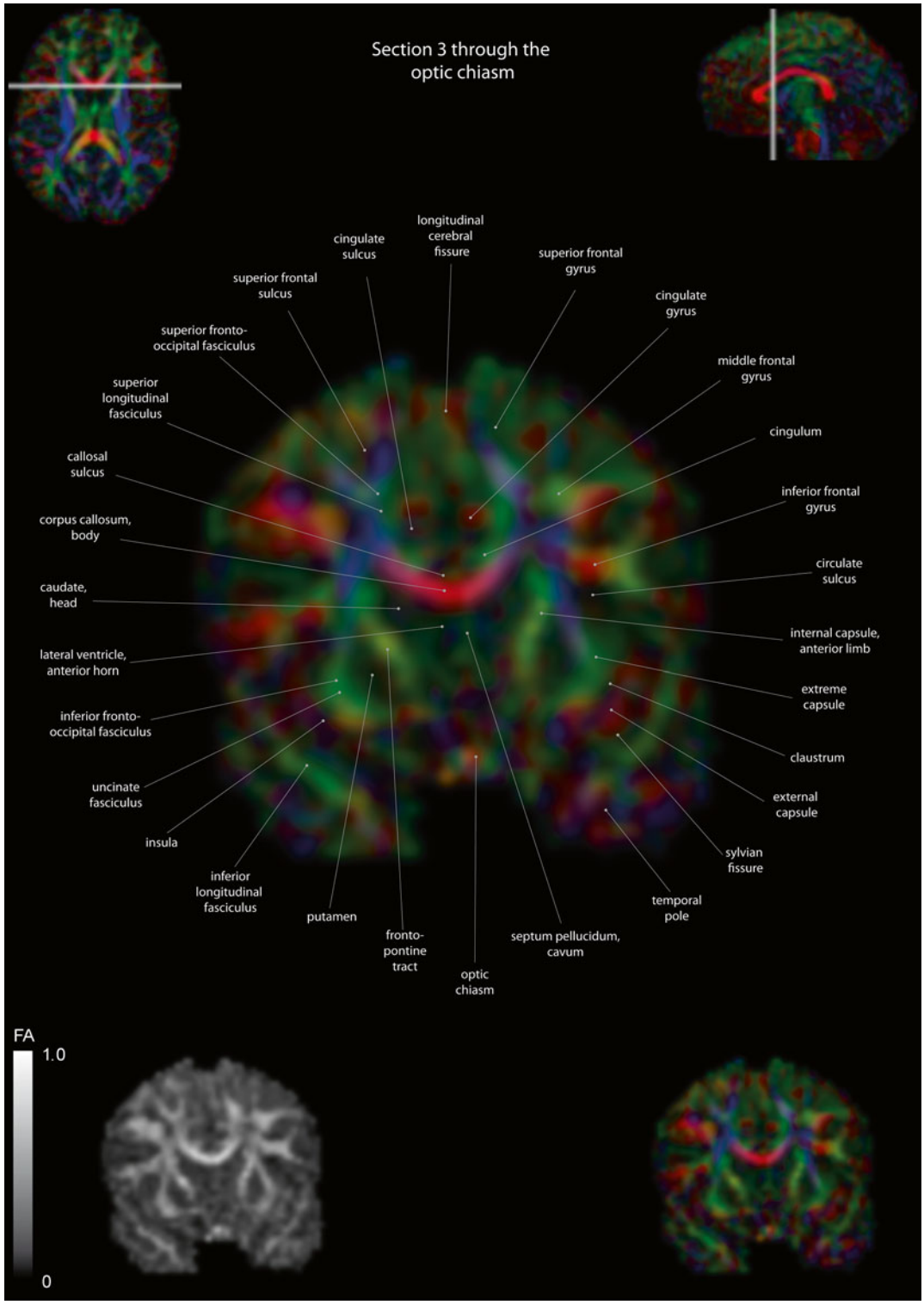

Fig. 12.13 Coronal slices of a color-coded diffusion tensor image. The colors represent fiber direction; *red* = left to right, *blue* = cranio-caudal, and *green* = anterior-posterior. The intensity represents the fractional anisotropy (FA) also indicated in the *lower corner*. In the *upper corners*, the slice section is indicated in the axial and sagittal plane

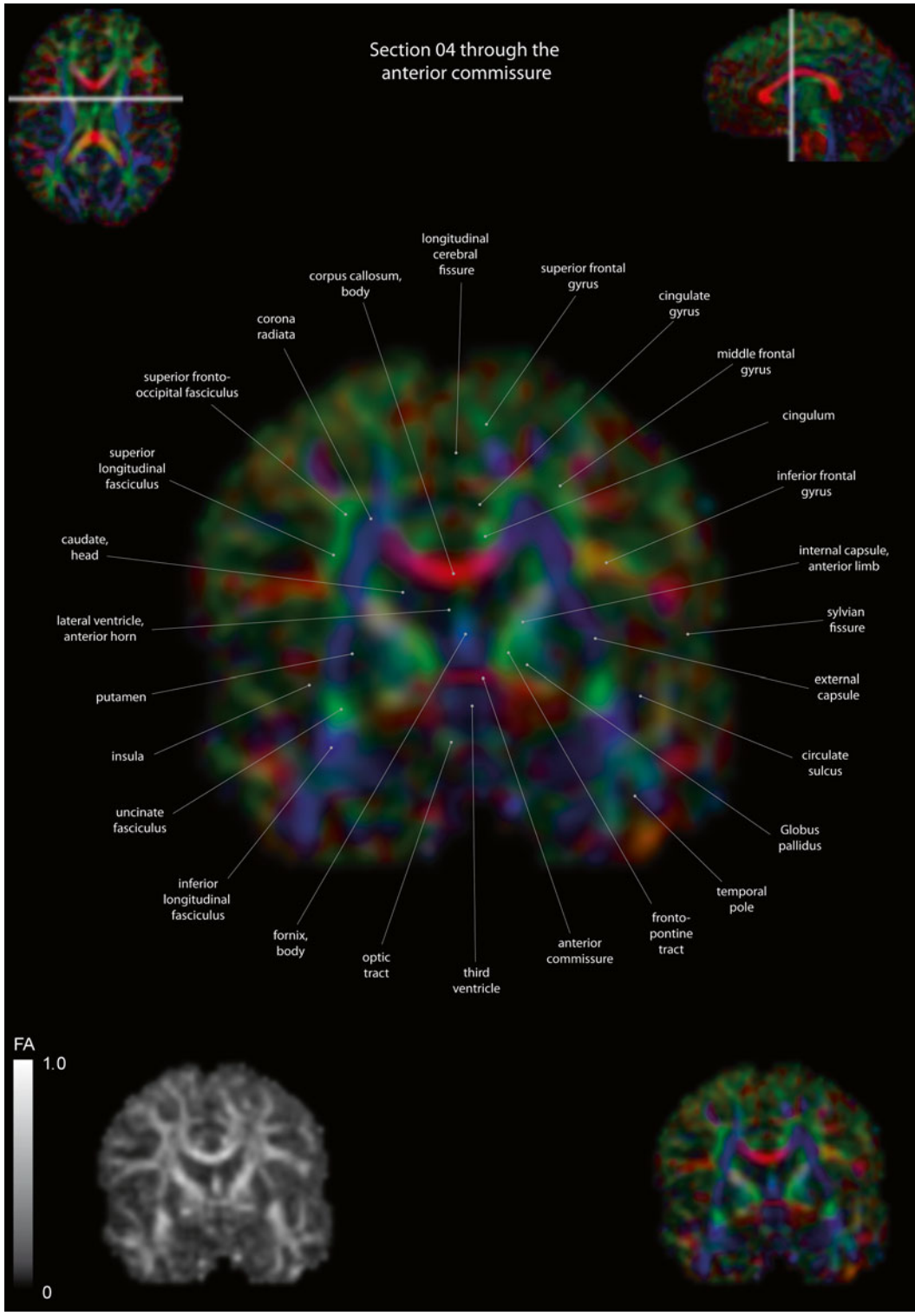

Fig. 12.14 Coronal slices of a color-coded diffusion tensor image. The colors represent fiber direction; *red* = left to right, *blue* = cranio-caudal, and *green* = anterior-posterior. The intensity represents the fractional anisotropy (FA) also indicated in the *lower corner*. In the *upper corners*, the slice section is indicated in the axial and sagittal plane

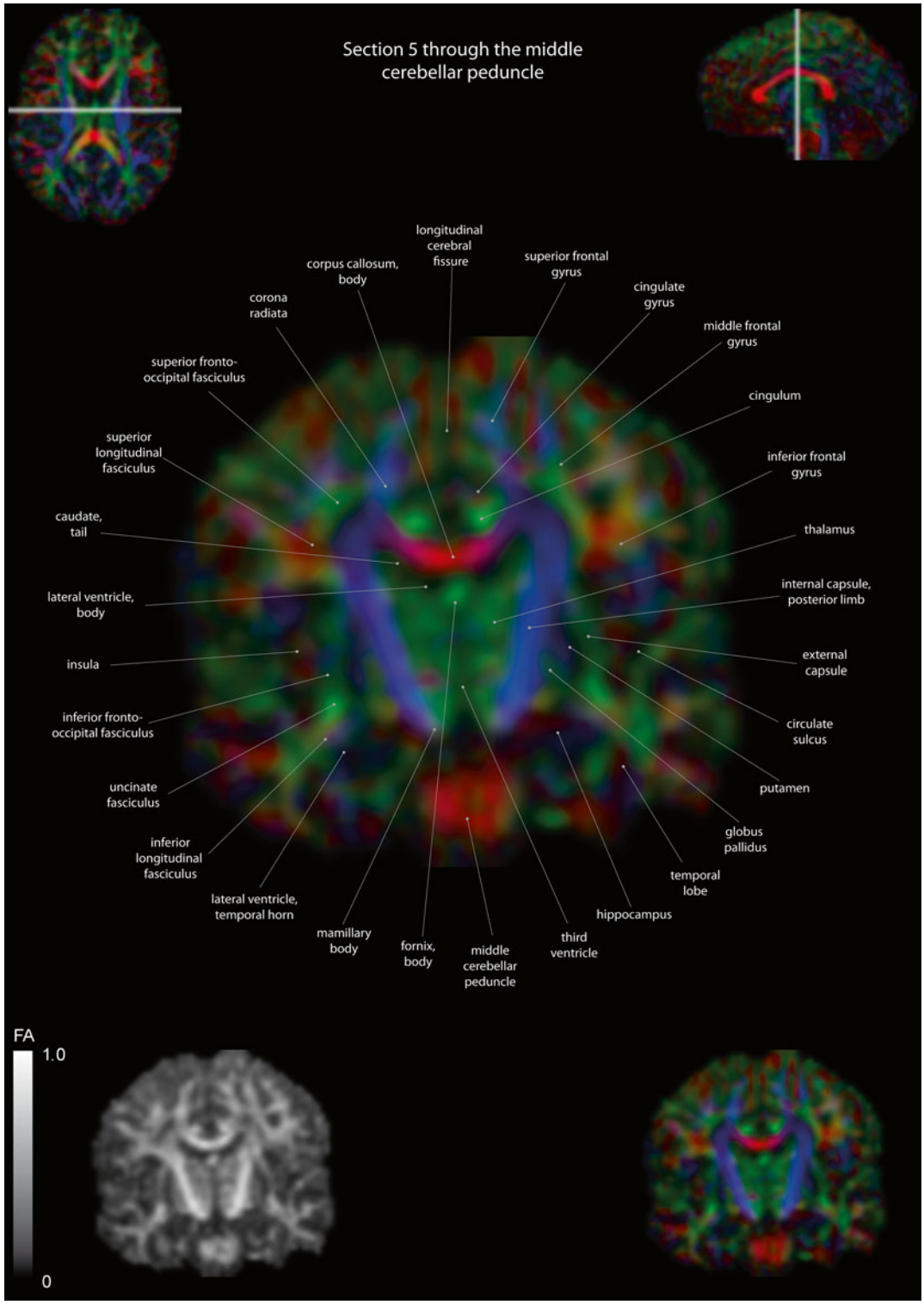

Fig. 12.15 Coronal slices of a color-coded diffusion tensor image. The colors represent fiber direction; *red* = left to right, *blue* = cranio-caudal, and *green* = anterior-posterior. The intensity represents the fractional anisotropy (FA) also indicated in the *lower corner*. In the *upper corners*, the slice section is indicated in the axial and sagittal plane

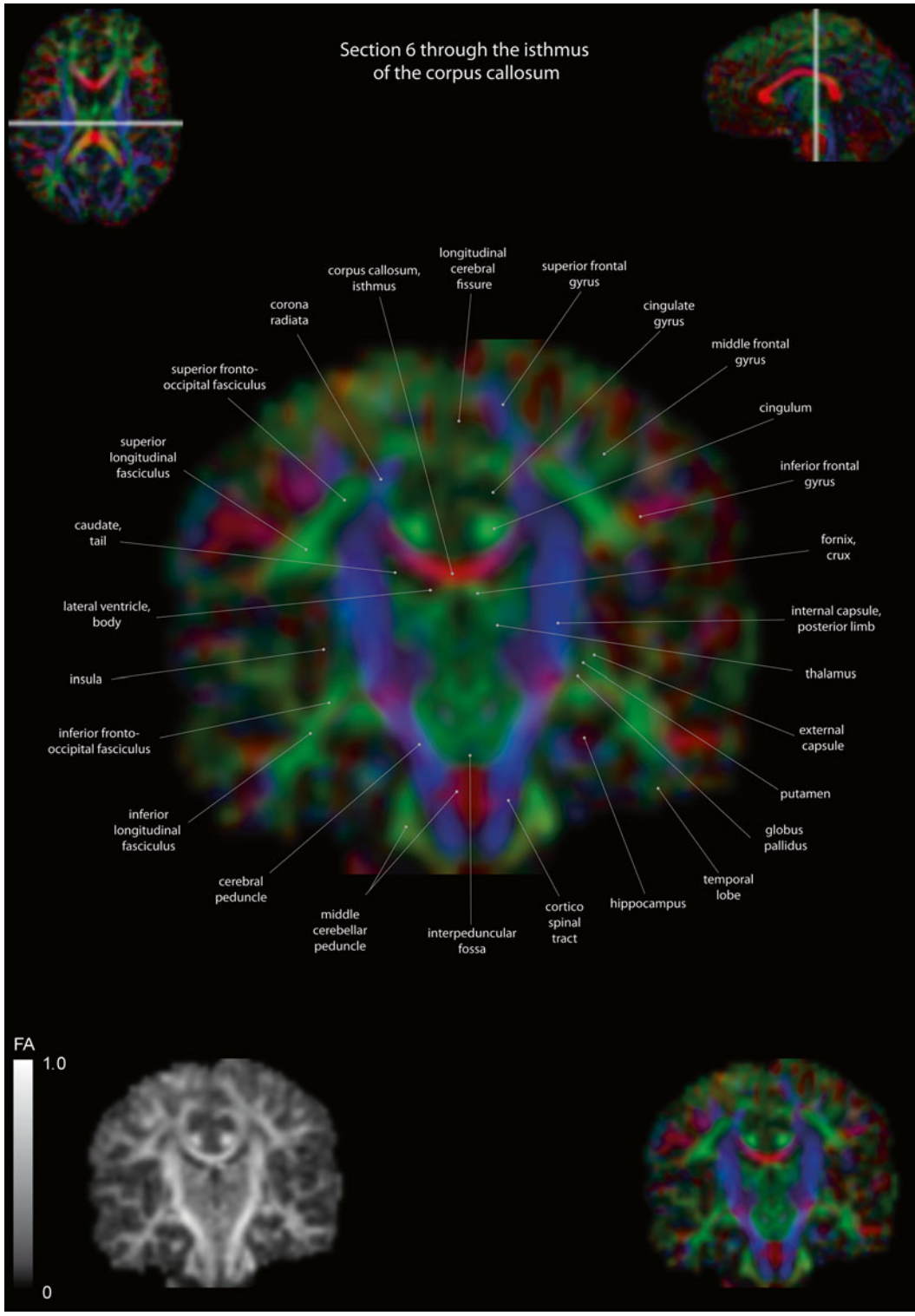

Fig. 12.16 Coronal slices of a color-coded diffusion tensor image. The colors represent fiber direction; *red* = left to right, *blue* = cranio-caudal, and *green* = anterior-posterior. The intensity represents the fractional anisotropy (FA) also indicated in the *lower corner*. In the *upper corners*, the slice section is indicated in the axial and sagittal plane

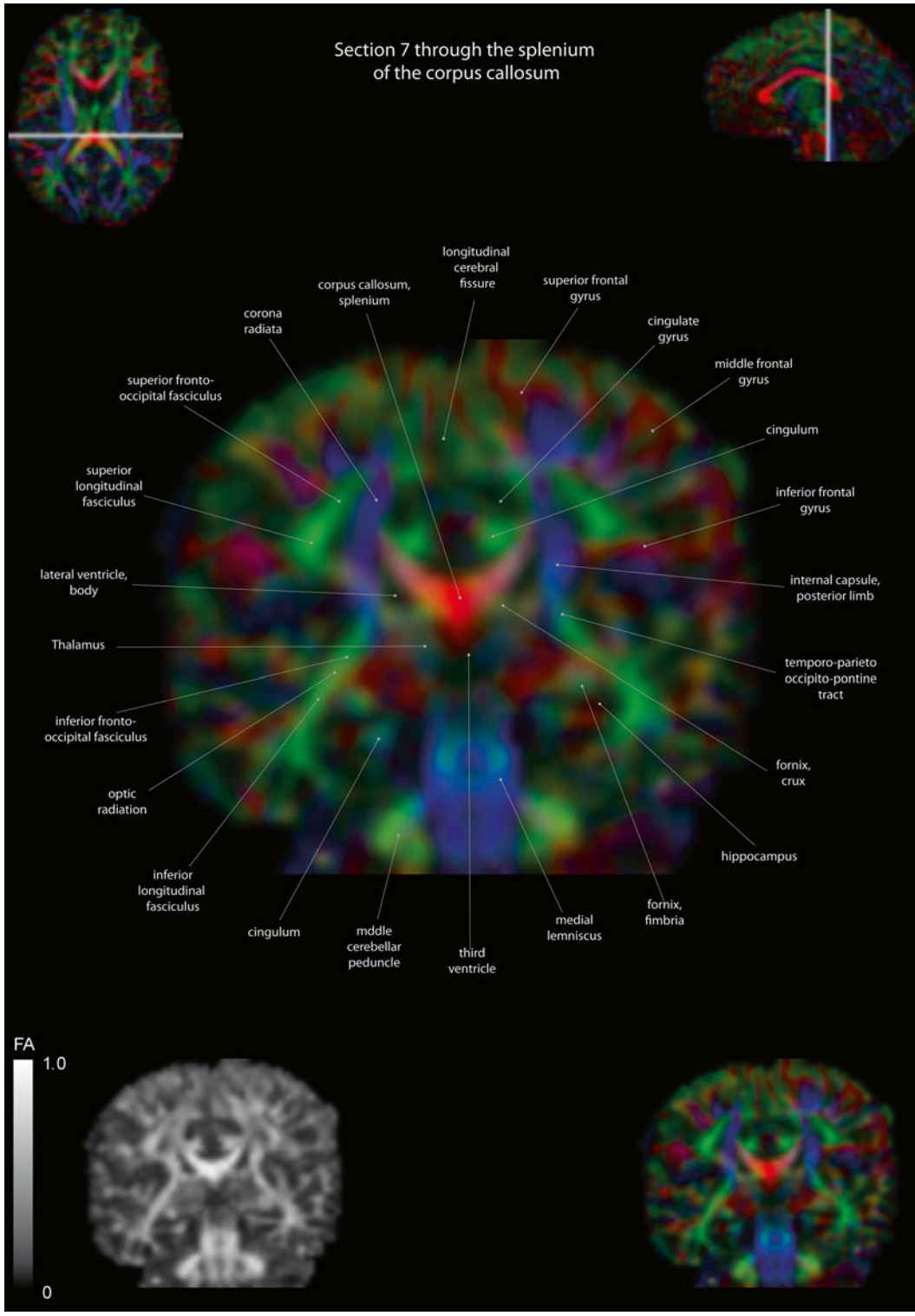

Fig. 12.17 Coronal slices of a color-coded diffusion tensor image. The colors represent fiber direction; *red* = left to right, *blue* = cranio-caudal, and *green* = anterior-posterior. The intensity represents the fractional anisotropy (FA) also indicated in the *lower corner*. In the *upper corners*, the slice section is indicated in the axial and sagittal plane

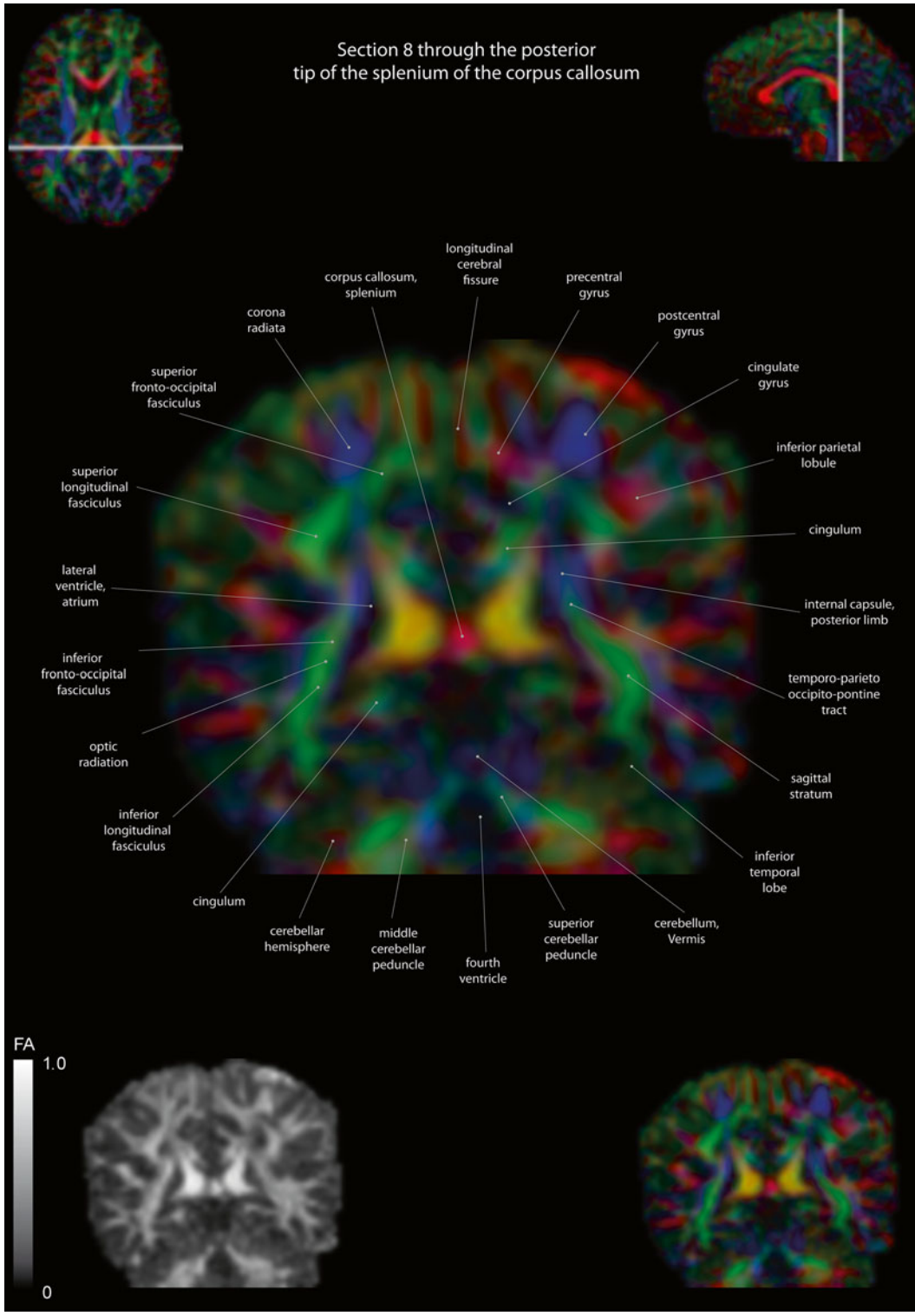

Fig. 12.18 Coronal slices of a color-coded diffusion tensor image. The colors represent fiber direction; *red* = left to right, *blue* = cranio-caudal, and *green* = anterior-posterior. The intensity represents the fractional anisotropy (FA) also indicated in the *lower corner*. In the *upper corners*, the slice section is indicated in the axial and sagittal plane

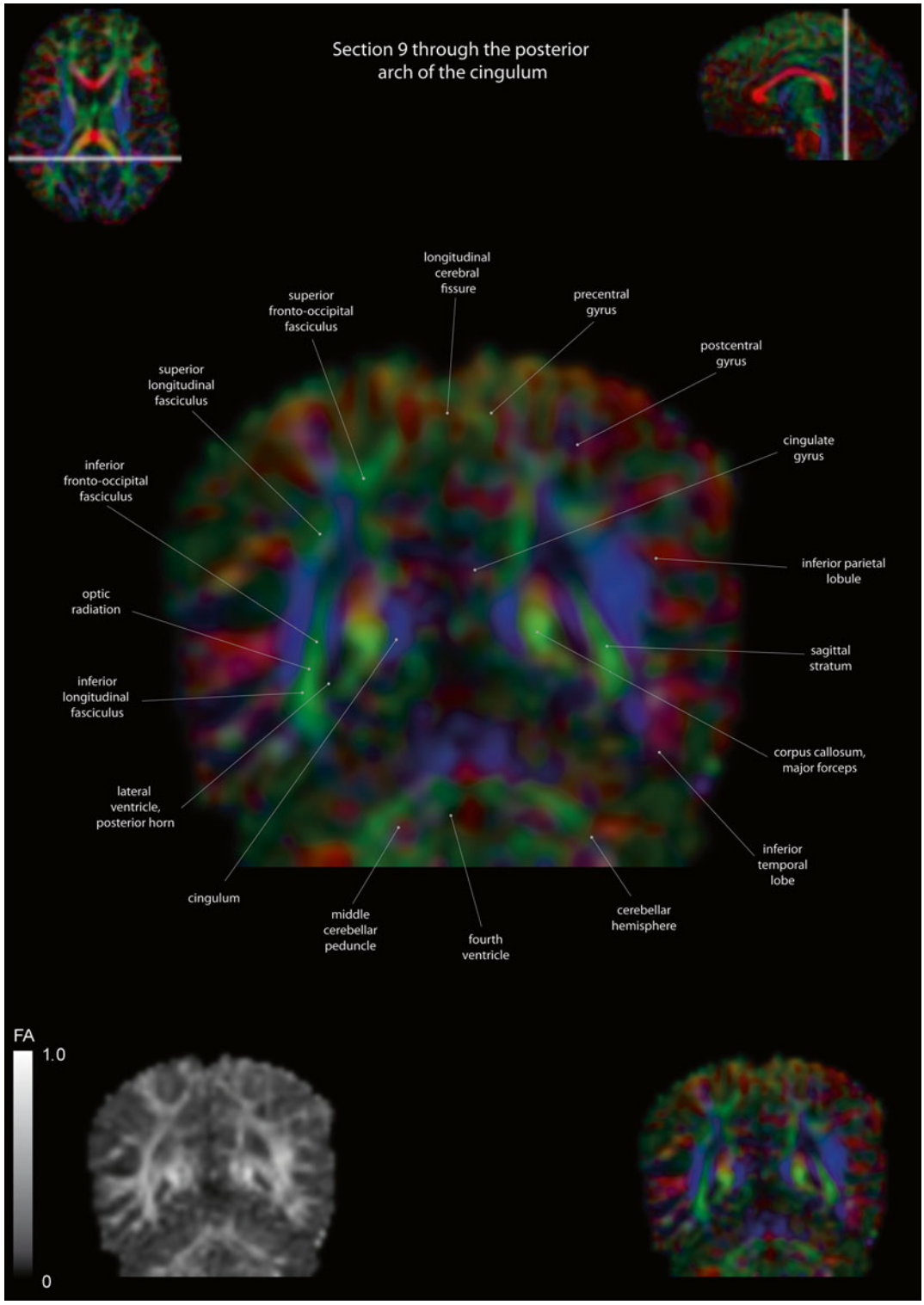

Fig. 12.19 Coronal slices of a color-coded diffusion tensor image. The colors represent fiber direction; *red* = left to right, *blue* = cranio-caudal, and *green* = anterior-posterior. The intensity represents the fractional anisotropy (FA) also indicated in the *lower corner*. In the *upper corners*, the slice section is indicated in the axial and sagittal plane

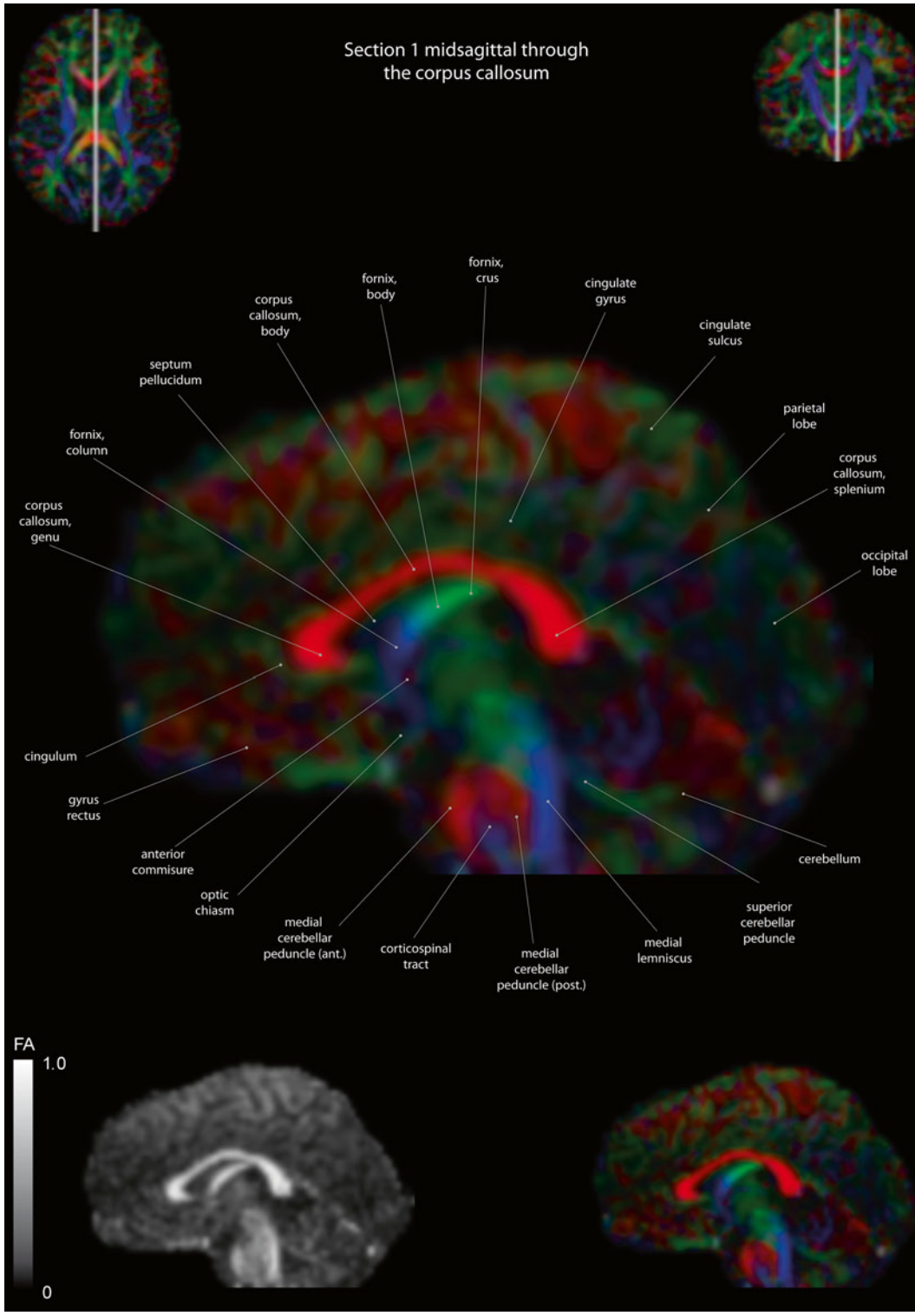

Fig. 12.20 Sagittal slices of a color-coded diffusion tensor image. The colors represent fiber direction; *red* = left to right, *blue* = cranio-caudal, and *green* = anterior-posterior. The intensity represents the fractional anisotropy (FA) also indicated in the *lower corner*. In the *upper corners*, the slice section is indicated in the axial and coronal plane

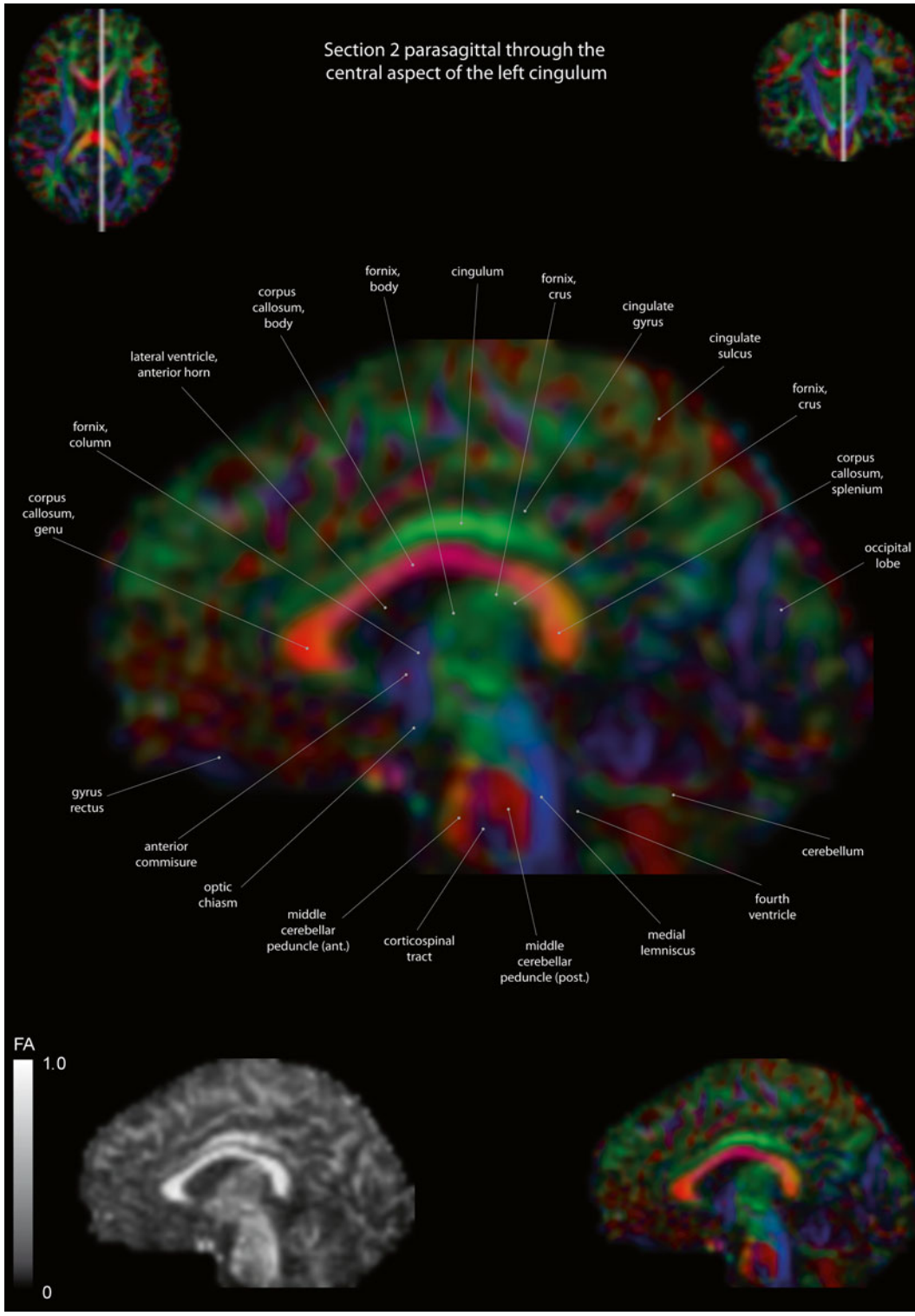

Fig. 12.21 Sagittal slices of a color-coded diffusion tensor image. The colors represent fiber direction; *red* = left to right, *blue* = cranio-caudal, and *green* = anterior-posterior. The intensity represents the fractional anisotropy (FA) also indicated in the *lower corner*. In the *upper corners*, the slice section is indicated in the axial and coronal plane

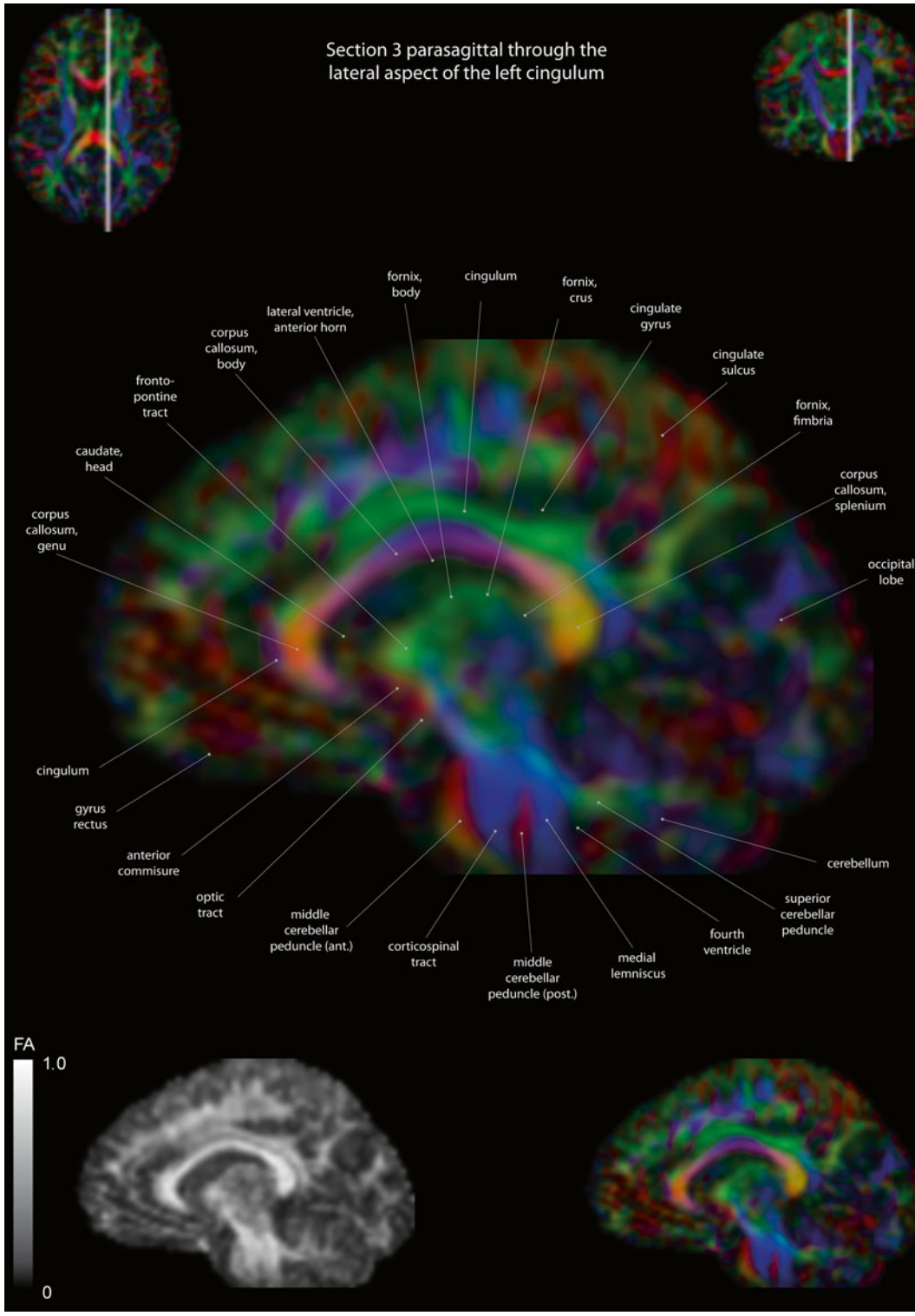

Fig. 12.22 Sagittal slices of a color-coded diffusion tensor image. The colors represent fiber direction; *red* = left to right, *blue* = cranio-caudal, and *green* = anterior-posterior. The intensity represents the fractional anisotropy (FA) also indicated in the *lower corner*. In the *upper corners*, the slice section is indicated in the axial and coronal plane

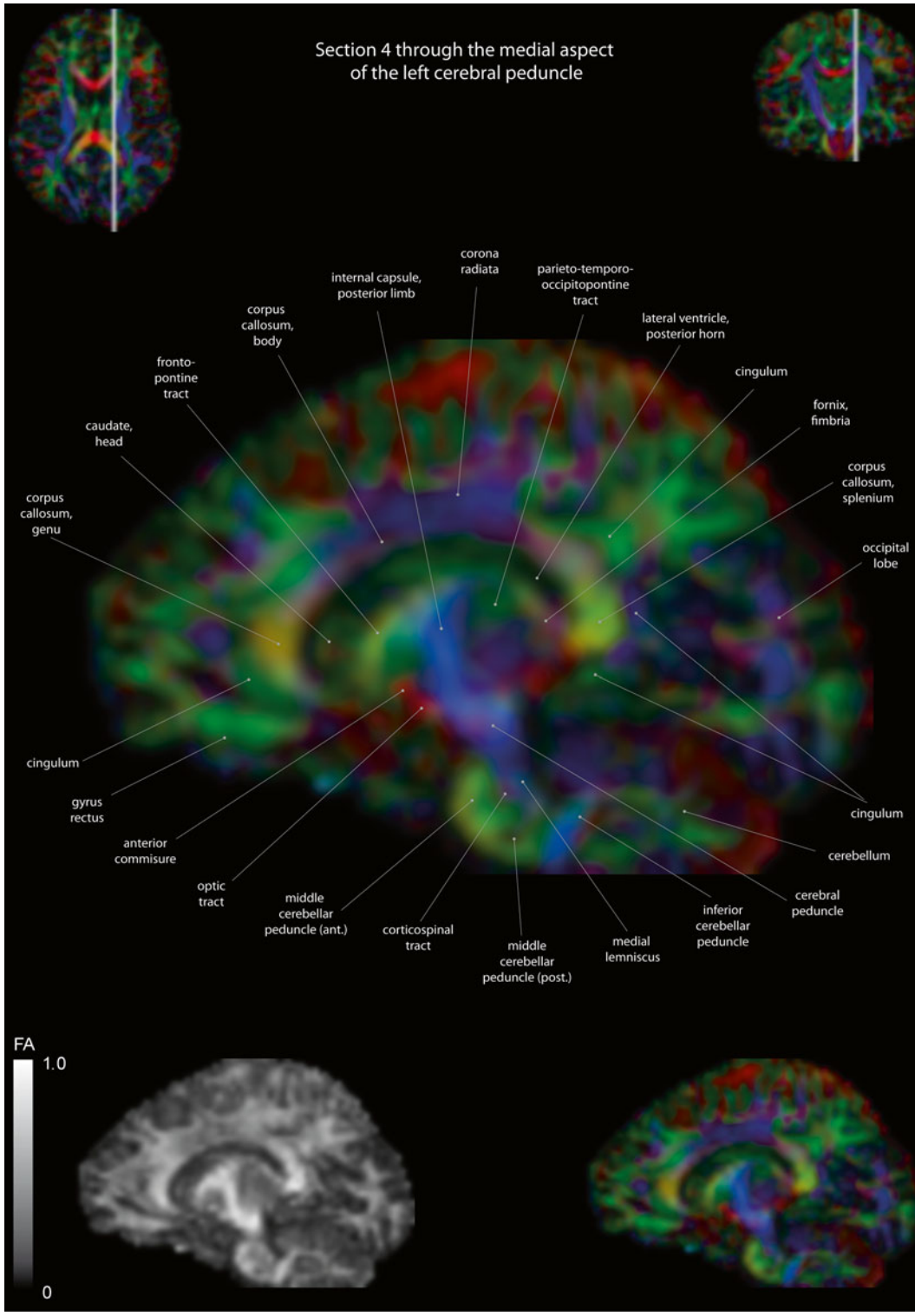

Fig. 12.23 Sagittal slices of a color-coded diffusion tensor image. The colors represent fiber direction; *red* = left to right, *blue* = cranio-caudal, and *green* = anterior-posterior. The intensity represents the fractional anisotropy (FA) also indicated in the *lower corner*. In the *upper corners*, the slice section is indicated in the axial and coronal plane

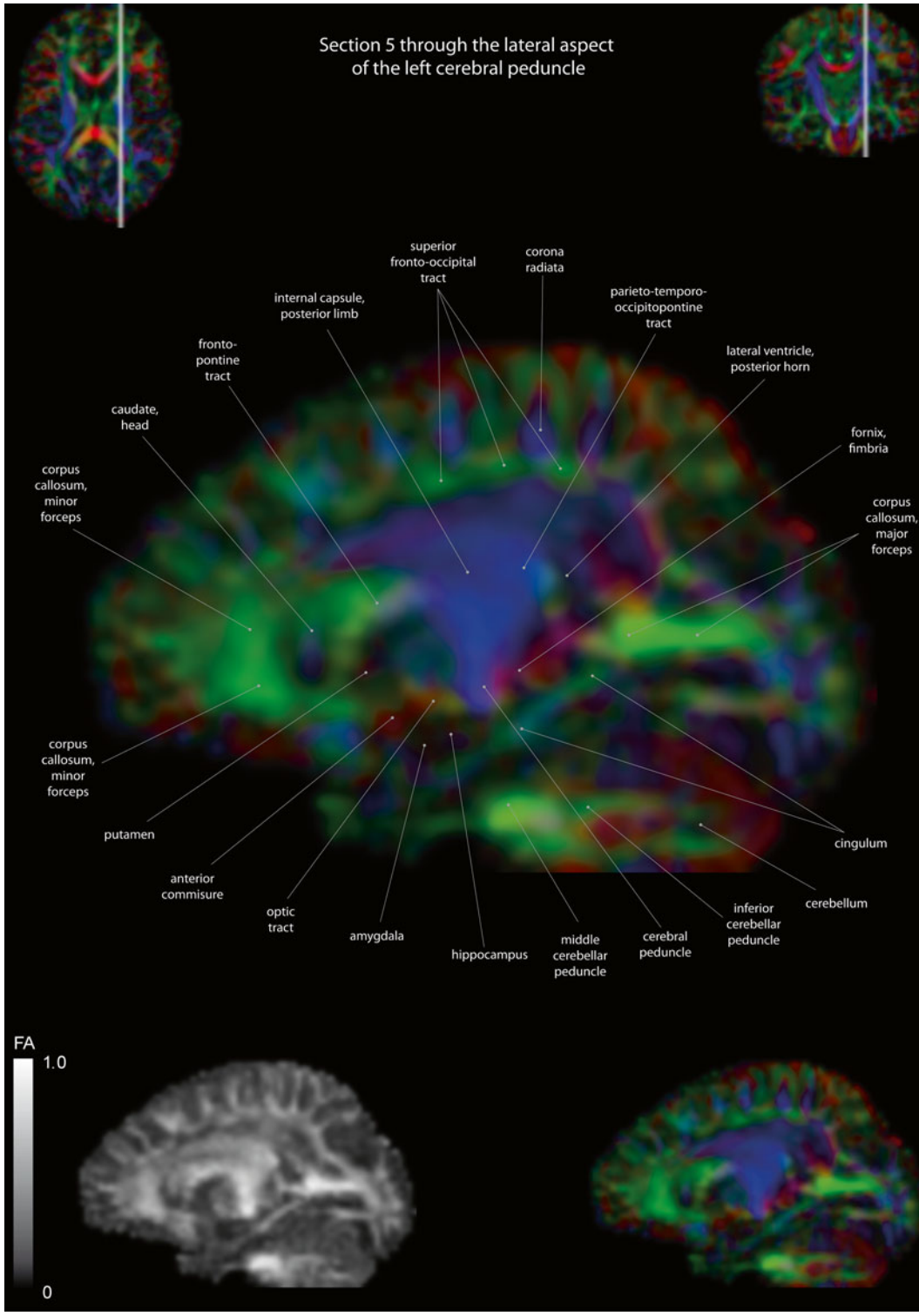

Fig. 12.24 Sagittal slices of a color-coded diffusion tensor image. The colors represent fiber direction; *red* = left to right, *blue* = cranio-caudal, and *green* = anterior-posterior. The intensity represents the fractional anisotropy (FA) also indicated in the *lower corner*. In the *upper corners*, the slice section is indicated in the axial and coronal plane

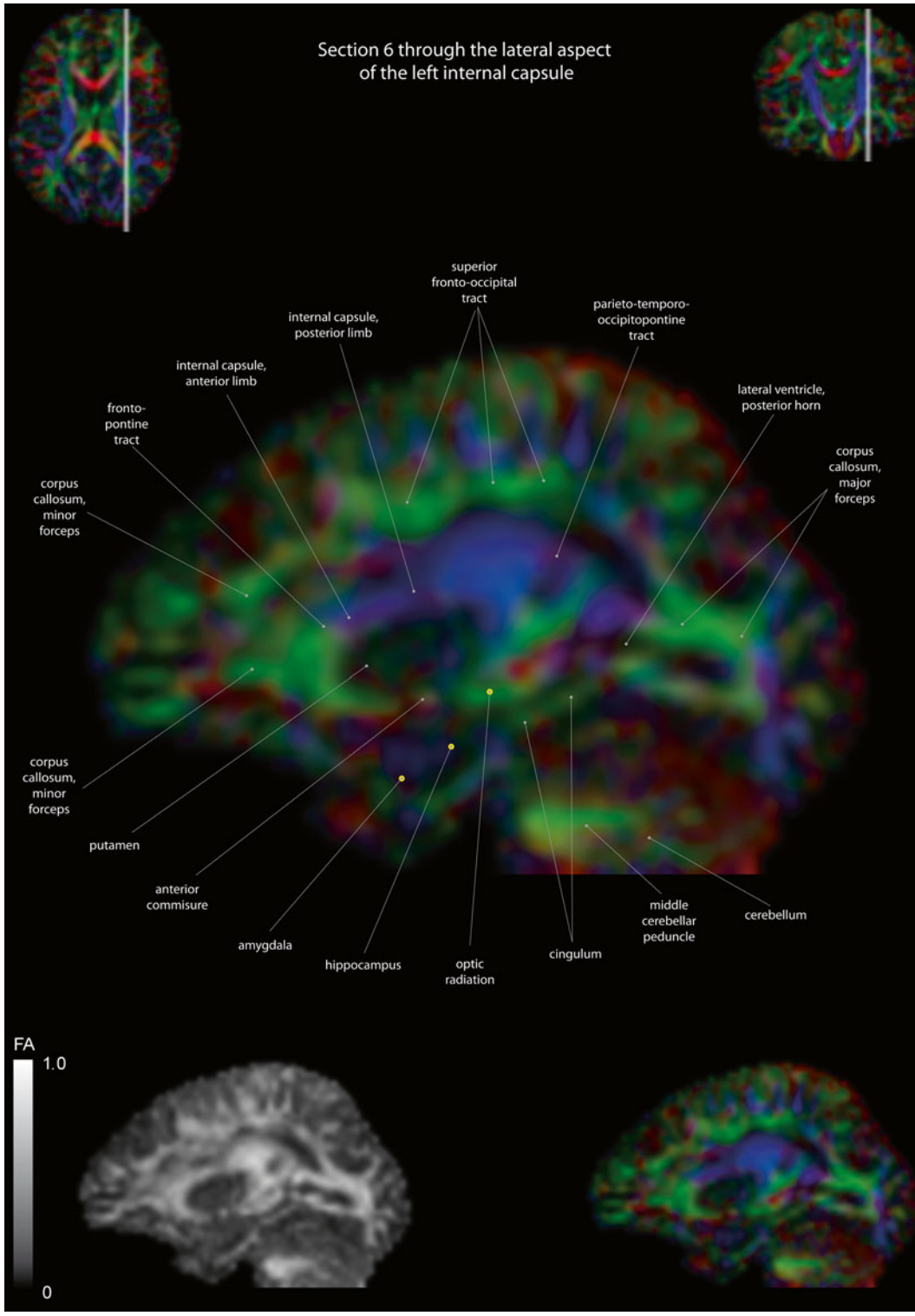

Fig. 12.25 Sagittal slices of a color-coded diffusion tensor image. The colors represent fiber direction; *red* = left to right, *blue* = cranio-caudal, and *green* = anterior-posterior. The intensity represents the fractional anisotropy (FA) also indicated in the *lower corner*. In the *upper corners*, the slice section is indicated in the axial and coronal plane

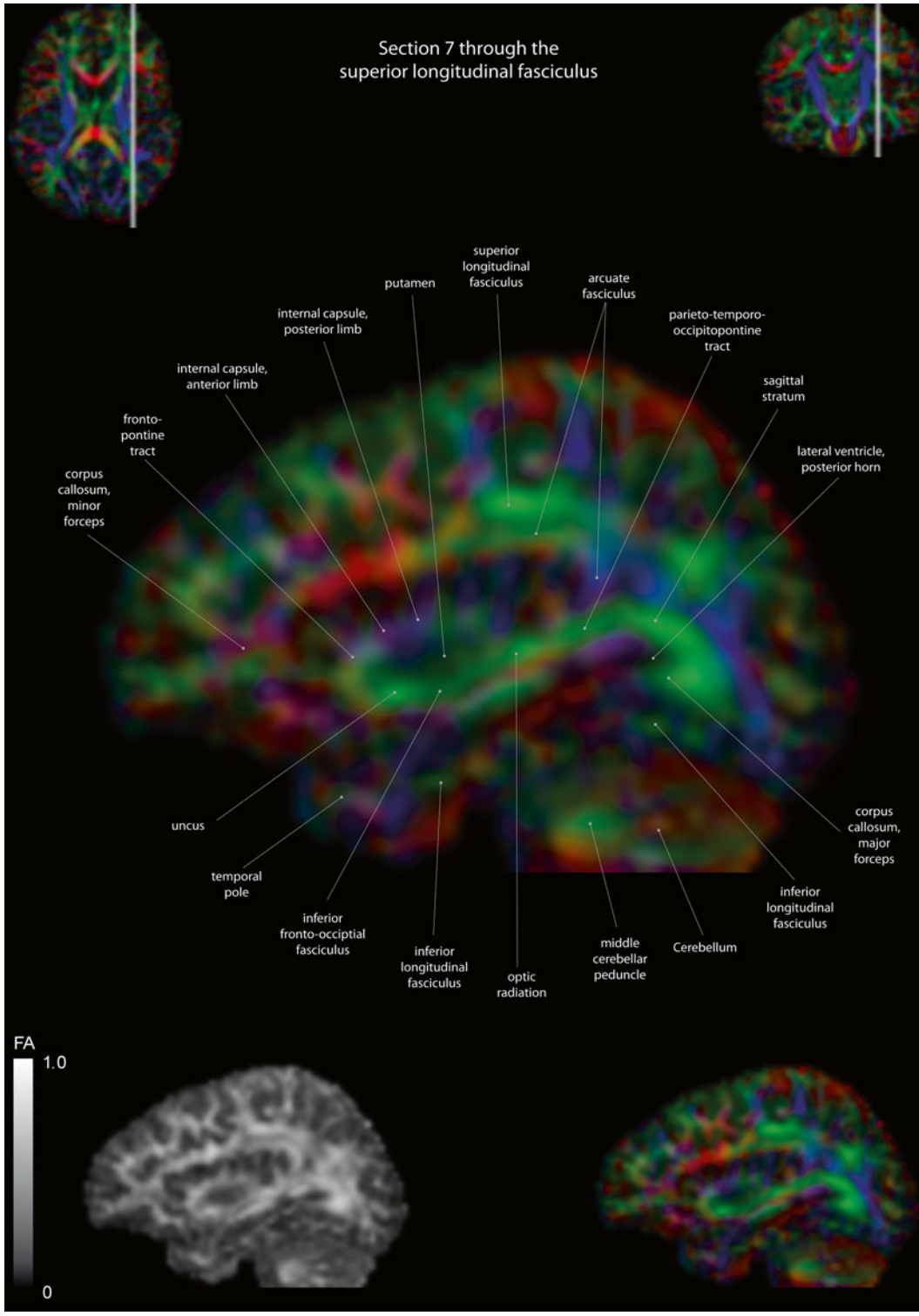

Fig. 12.26 Sagittal slices of a color-coded diffusion tensor image. The colors represent fiber direction; *red* = left to right, *blue* = cranio-caudal, and *green* = anterior-posterior. The intensity represents the fractional anisotropy (FA) also indicated in the *lower corner*. In the *upper corners*, the slice section is indicated in the axial and coronal plane

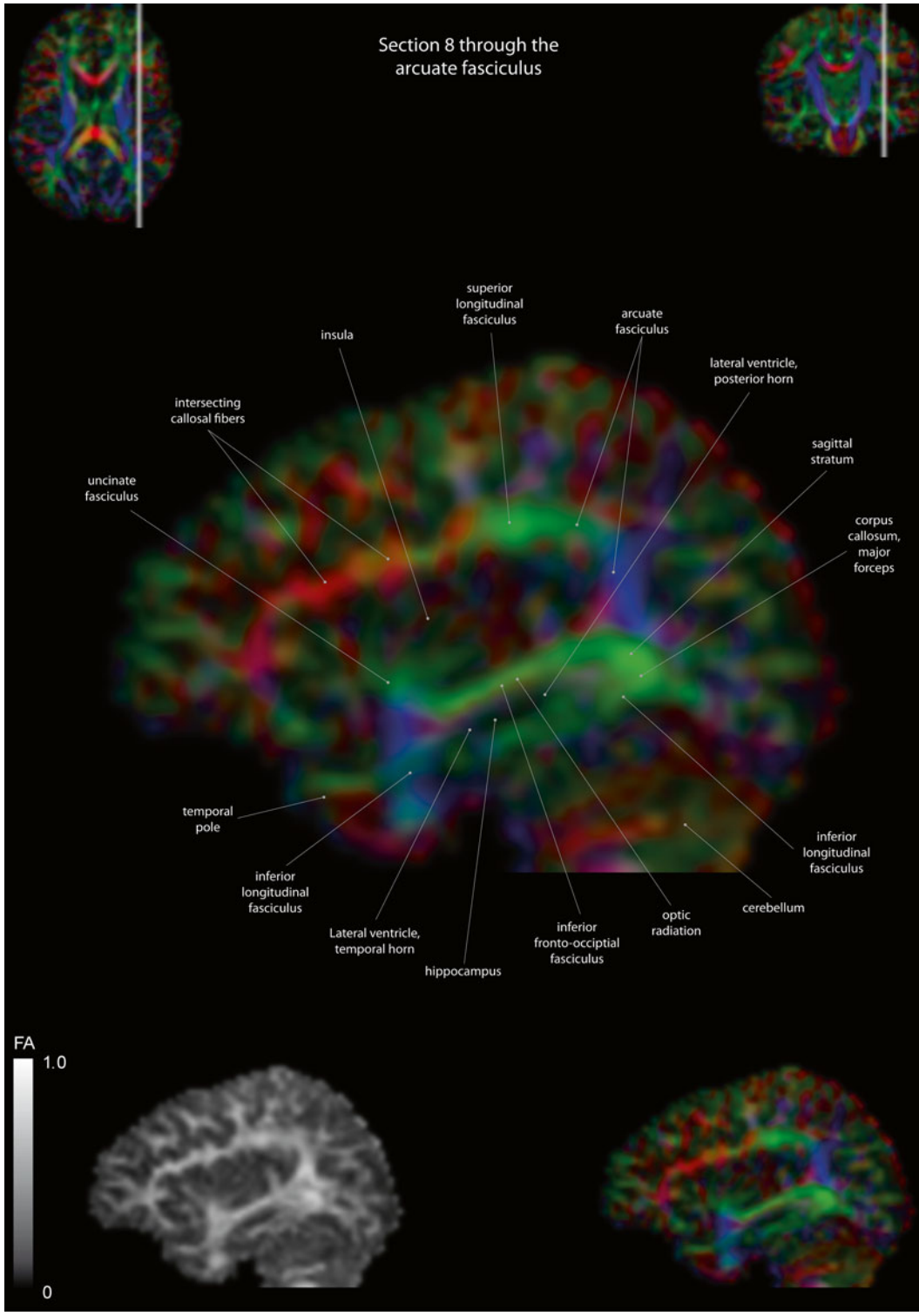

Fig. 12.27 Sagittal slices of a color-coded diffusion tensor image. The colors represent fiber direction; *red* = left to right, *blue* = cranio-caudal, and *green* = anterior-posterior. The intensity represents the fractional anisotropy (FA) also indicated in the *lower corner*. In the *upper corners*, the slice section is indicated in the axial and coronal plane

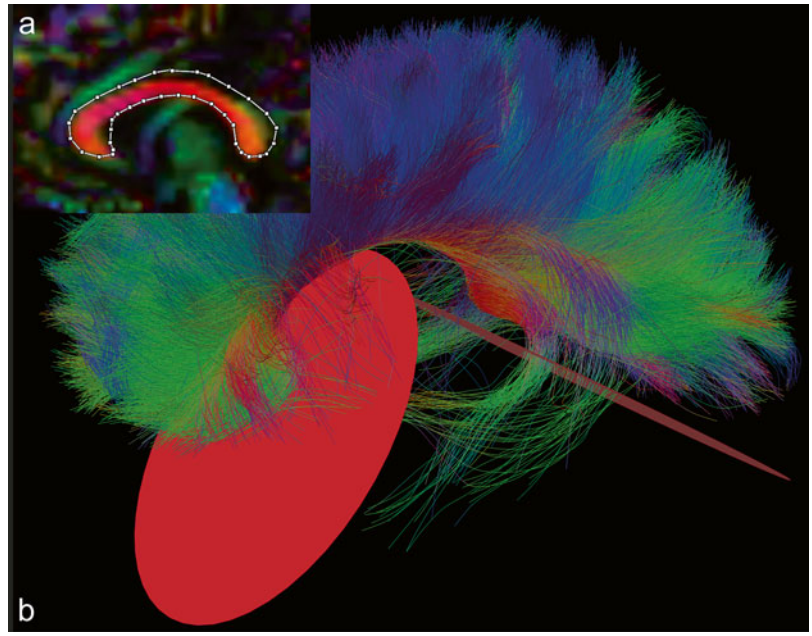

Fig. 12.28 Tracking of the Corpus callosum (CC), first step. (**a**) Midsagittal view of the CC with the initial starting region of interest (ROI) in *white*. (**b**) Removal of spurious fibers mainly from the cingulum using exclusion ROIs (*red*)

tal plane (Fig. 12.28a). The corpus callosum appears as a central large red structure. Outline the structure (white outline) and you should yield an initial tracking result that appears similar to Fig. 12.28b. Since the cingulum and the fornix run directly adjacent to the corpus callosum in the midsagittal plane, parts of these tracts are included in the initial result. These spurious tracts can be removed by placement of two ROIs (red ROIs, Fig. 12.28b). The first ROI is placed just posteriorly of the caudal tip of the genu of the corpus callosum (left red ROI) and the cingulum fibers from this ROI are excluded. The second ROI is placed anteriorly of the caudal tip of the splenium of the corpus callosum (right red ROI). This ROI excludes fibers from the fornix and the posterior aspect of the cingulum.

The previous result can be segmented further into three distinct areas of the corpus callosum, the anterior part or genu, the central part or body, and the posterior aspect or splenium. To achieve this segmentation, the first tracking result is taken and three new ROIs are drawn (Fig. 12.29a). The red ROI delineates the midsagittal aspect of the genu, the yellow ROI the body, and the green ROI the splenium. In Fig. 12.29b, the results from this fiber tracking are shown in corresponding colors.

The Cingulum

The cingulum is a paired parasagittal structure that extends from the septal area to the uncus region of the temporal lobe. Due to its close proximity to the corpus callosum, especially while in proximity of the cingulate gyrus, callosal fibers are invariably included in the starting ROI. The ROI outlined in white includes the left and right cingulum. The appropriate coronal plane is found when the large green structure above the corpus callosum is selected in the sagittal plane (Fig. 12.30a). The callosal fibers can be easily removed by using the midsagittal ROI previously used as starting ROI for tracking of the corpus callosum. The final result is in Fig. 12.30b.

The Fornix

Fiber tracking of the fornix is quite challenging. First, it is a very thin structure with a relatively low fractional anisotropy, most probably due to substantial partial volume effects of the surrounding gray matter and cerebrospinal fluid. This low anisotropy may cause fiber tracking to

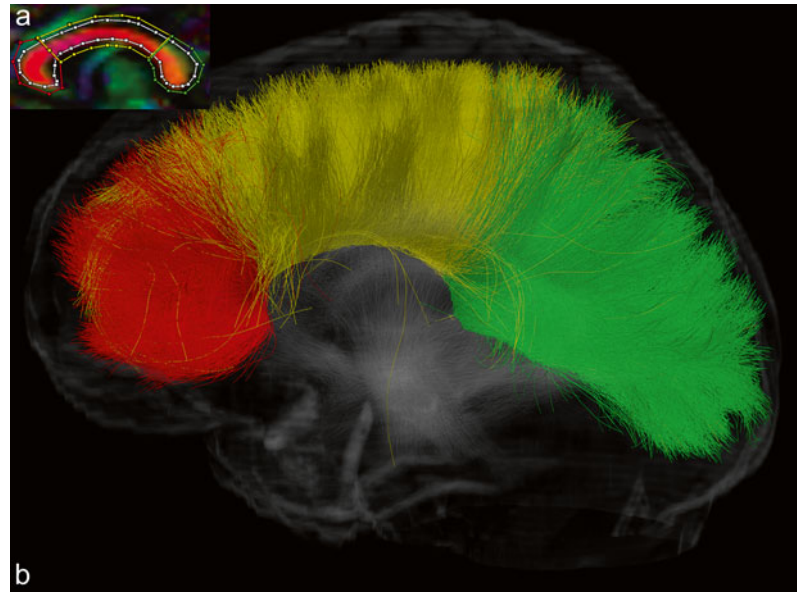

Fig. 12.29 Tracking of the Corpus callosum, second step. (**a**) Midsagittal view of the CC with the initial starting ROI in *white* and the subsegmentation in *red*, *yellow*, and *green*. (**b**) Tracking result in colors corresponding to the initial ROIs

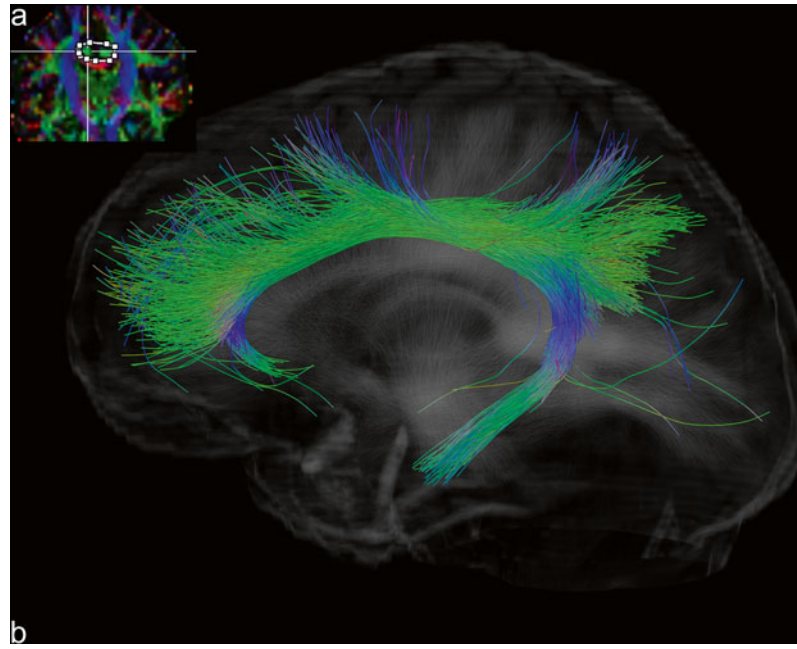

Fig. 12.30 Tracking of the bilateral cingulum bundle (CB). (**a**) Initial ROI encompassing the CB bilaterally (*white*) in the coronal plane. (**b**) Tracking result overlaid on a sagittal fiber density map

be aborted. Second, it is a highly curved structure that poses additional difficulties for fiber tracking algorithms. And finally, the fornix lies in close proximity to other fiber bundles such as the corpus callosum and the anterior commissure that further hamper fiber reconstruction. The fornix is of great interest, especially in psychiatric research on Alzheimer's, since it is one of the major tracts related to the hippocampus and memory function. Its fibers run along the medial aspect of the hippocampus, forming the fimbria, that project posterosuperiorly. The bilateral fibria form the crus, run over the thalamus, and then join to form the body. Running frontally, the corpus separates again to form the column and the majority of the fibers terminate in the mammil-

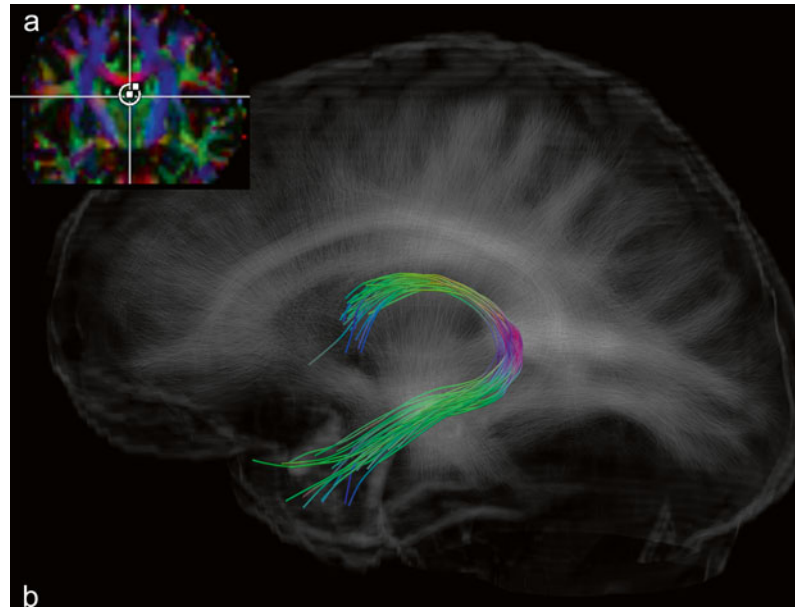

Fig. 12.31 Unilateral tracking of the fornix (FX). (**a**) Initial ROI (*white circle*) encompassing the FX in the coronal plane. (**b**) Tracking result overlaid on a sagittal fiber density map

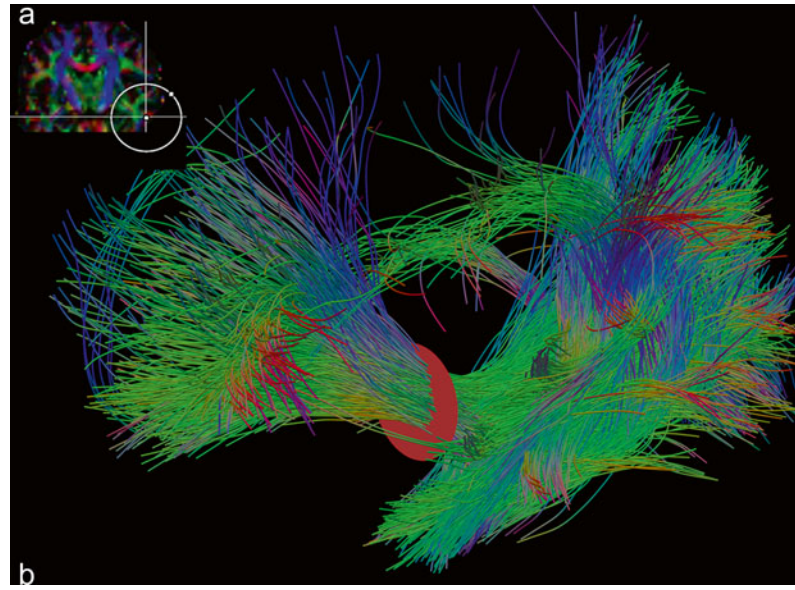

Fig. 12.32 (**a**) Initial ROI (*white circle*) for all the following tracts. (**b**) Through the red exclusion ROI, the Uncinate Fasciculus (UF) is excluded

lary body. The body of the fornix is a good starting region best found in the midsagittal plane. Then, the full fornix can be delineated on the corresponding coronal slice (Fig. 12.31a). The initial result contains spurious fibers from the corpus callosum and the anterior commissure that can be removed subsequently. The final result as shown in Fig. 12.31b is somewhat fragile and, depending on your data, may look less well defined.

The Inferior Longitudinal-, Inferior Fronto-Occipital- and Uncinate Fasciculus

Fiber tracking of the inferior longitudinal fasciculus can be started from the temporal lobe. As indicated in Fig. 12.32a, a large, somewhat nonspecific starting region can be chosen to encompass the temporal lobe on the coronal slice (right). This yields a large complex of fiber bundles (Fig. 12.32b) that can be further dissected.

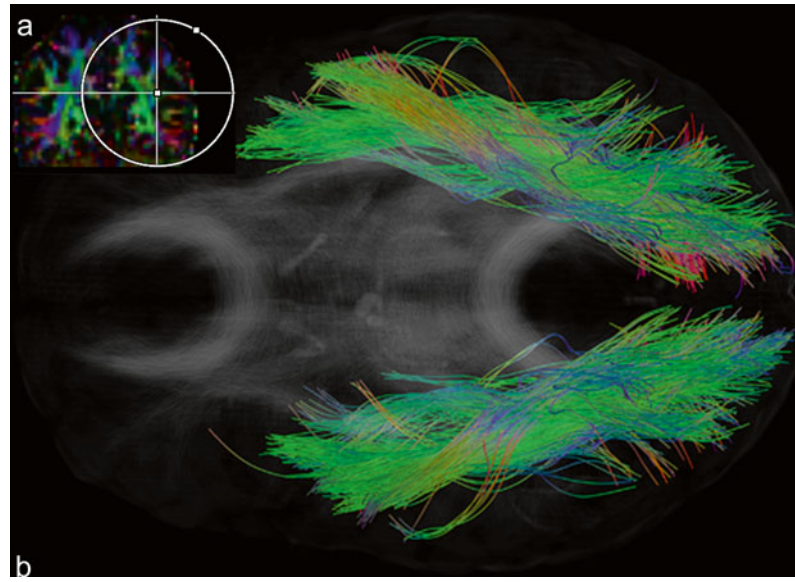

Fig. 12.33 Tracking of the inferior longitudinal fasciculus (ILF). (**a**) Placement of large occipital inclusion ROI (*white circle*). (**b**) Depiction of the ILF overlaid on a fiber density map

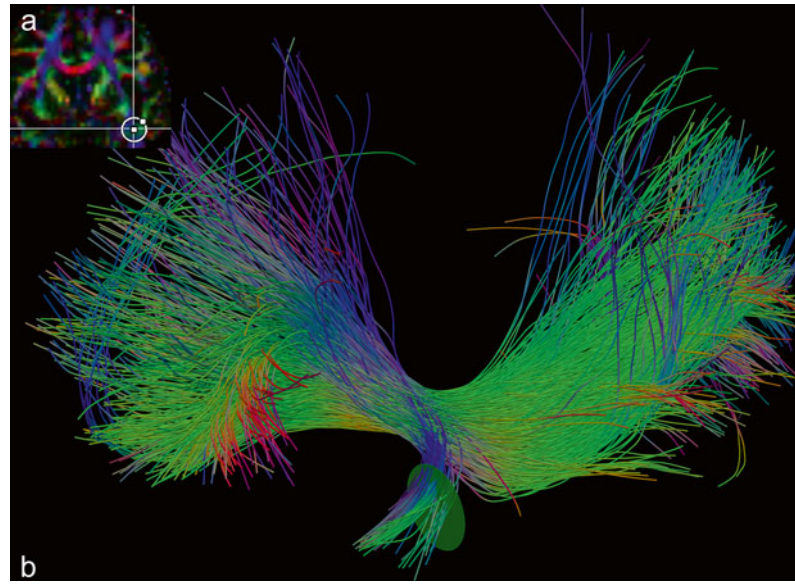

Fig. 12.34 Tracking of the uncinate fasciculus (UF). (**a**) Starting ROI at the fronto-temporal junction. (**b**) Initial tracking result and green inclusion ROI

The inferior longitudinal fasciculus is the main bundle connecting the temporal and occipital lobes. The two other major fiber bundles that are part of the initial complex (Fig. 12.32b) are the uncinate- and the inferior fronto-occipital fasciculus. These two bundles can be easily excluded by the exclusion ROI (red) indicated in Fig. 12.32b at the fronto-temporal junction. This is also a perfect starting ROI for these two structures. This is described in the next section on these two structures. Additional spurious fibers, mainly stemming from the anterior commissure and the corpus callosum, can be excluded by a large parieto-occipital inclusion ROI (Fig. 12.33a). Figure 12.33b shows the inferior longitudinal fasciculus bilaterally.

As mentioned in the previous section on the inferior longitudinal fasciculus, a coronal ROI at the fronto-temporal junction (Fig. 12.32b) is the ideal starting region for the reconstruction of the inferior fronto-occipital and uncinate fas-

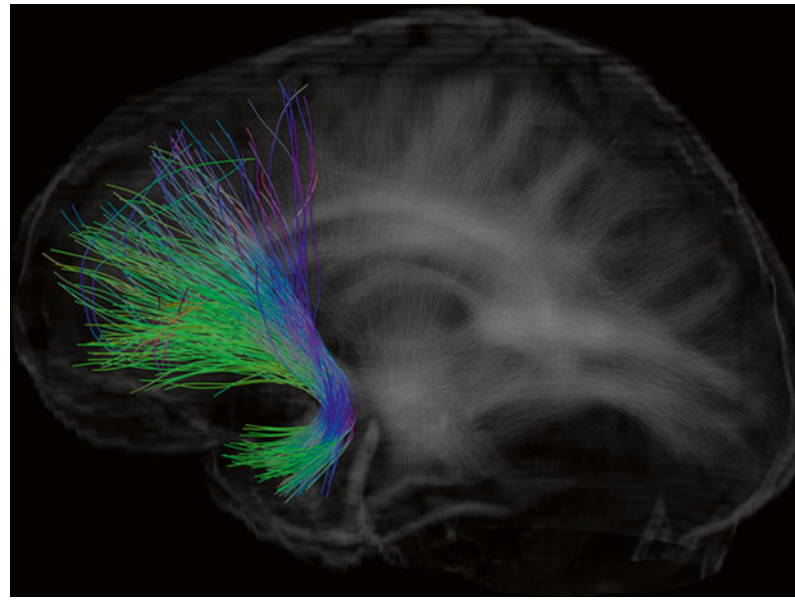

Fig. 12.35 Depiction of the UF overlaid on a sagittal fiber density map

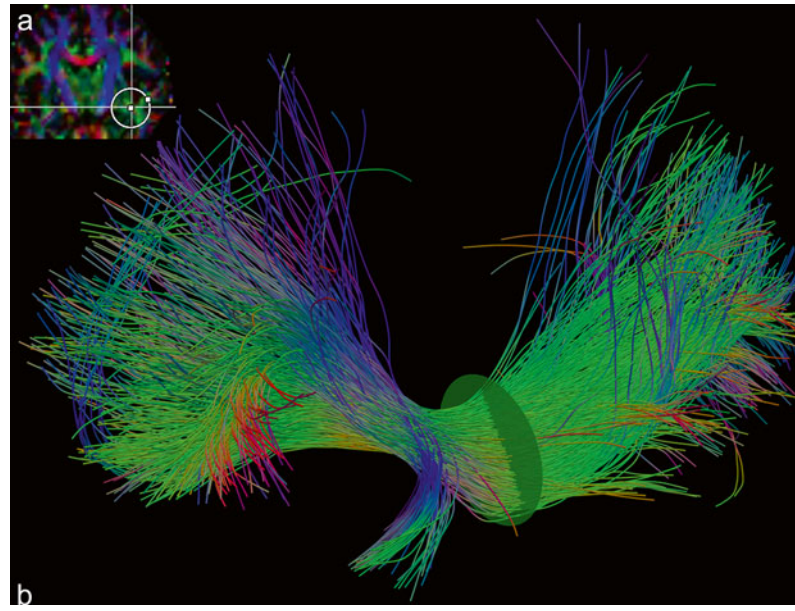

Fig. 12.36 Tracking of the inferior fronto-occipital fasciculus (IFOF). (**a**) Initial ROI as in Fig. 12.34. (**b**) Initial tracking result and green inclusion ROI

ciculus. As can be seen in the initial result in Fig. 12.34b, no spurious fibers are present, and in two easy steps the two bundles can be isolated. To better appreciate the intricate interwoven structure of the above named three fiber bundles, this section is concluded with a combined overview. Since the uncinate fasciculus connects the frontal and temporal lobe whereas the inferior fronto-occipital fasciculus connects the frontal and occipital lobe, a second inclusion ROI, as depicted in Fig. 12.34a, b (green ROI) within the temporal lobe, effectively isolates the uncinate fasciculus. The results can be seen in Fig. 12.35. Note that no additional ROIs are required to remove spurious fibers. Likewise, the inferior fronto-occipital fasciculus can be isolated by placing an inclusion ROI directly posterior to the point where both bundles join

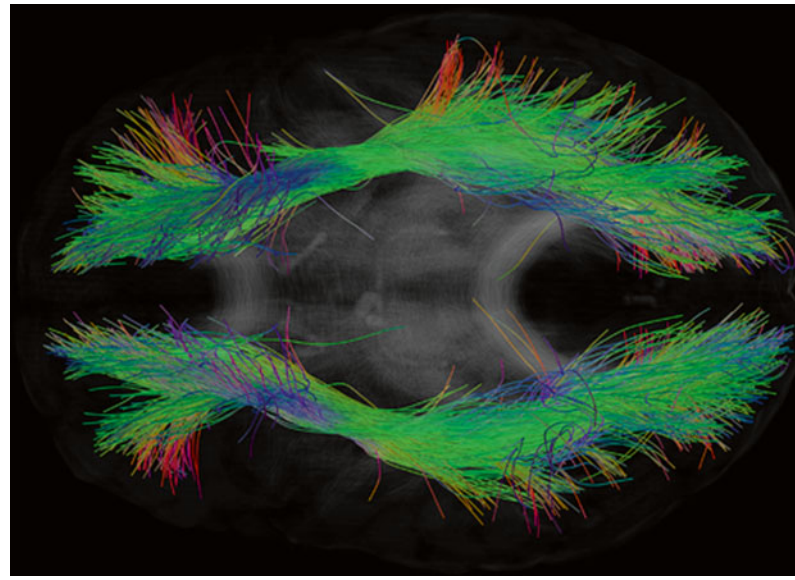

Fig. 12.37 Depiction of the IFOF overlaid on an axial fiber density map

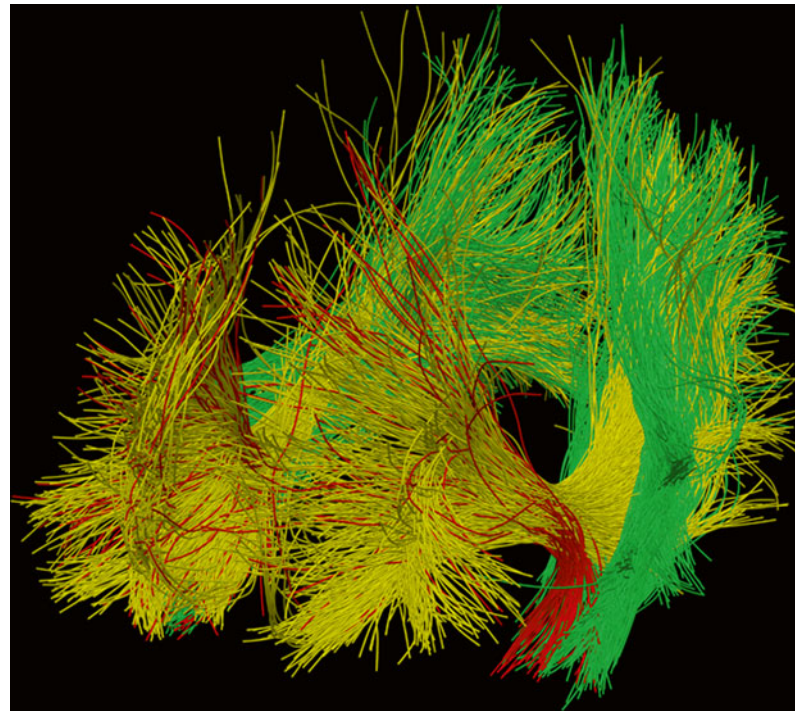

Fig. 12.38 Combined bilateral view of the UF (*red*), the IFOF (*yellow*), and the ILF (*green*)

(Fig. 12.36a, b) and the final result is shown in Fig. 12.37.

Figure 12.38 is an overview where the previously reconstructed tracts are shown in a combined array. The uncinate fasciculus is colored red, the inferior longitudinal fasciculus is colored green, and the inferior fronto-occipital fasciculus is colored yellow.

The Superior Longitudinal-, Superior Fronto-Occipital- and Arcuate Fasciculus

The superior longitudinal, superior fronto-occipital and arcuate fasciculus can all be isolated from one starting ROI (Fig. 12.39a). The arcuate fasciculus especially is of great interest in neuroscience and neurosurgery alike, since it

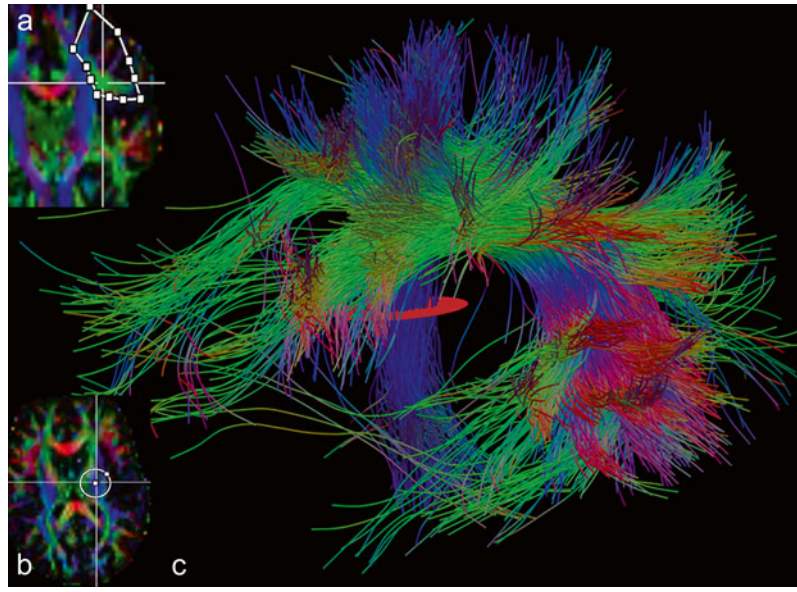

Fig. 12.39 Initial ROI including the superior longitudinal fasciculus (SLF), the arcuate fasciculus (AF), and the superior fronto-occipital fasciculus (SFOF). (**a**) Initial unilateral ROI placement. (**b**) Removal of spurious fibers from the internal capsule (*white ROI*). (**c**) 3D overview of the initial tracking result and the exclusion ROI as in (**b**) (*red circle*)

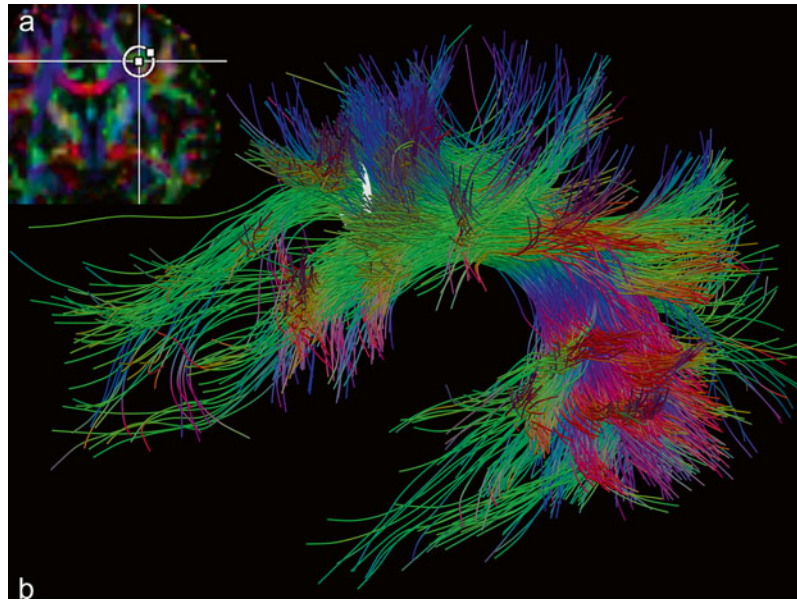

Fig. 12.40 Selection of the SFOF. (**a**) Initial ROI displayed on the coronal color map. (**b**) Depiction of the same inclusion ROI (*white circle*) on the 3D tracking result after removal of the fibers from the internal capsule

connects the speech areas of Broca and Wernicke in the dominant (mostly left) hemisphere.

Spurious fibers from the uncinate and inferior fronto-occipital fasciculus can be removed by using the starting ROI for these two bundles, as described in the previous section, as exclusion ROI. Spurious fibers from the cortico-spinal tract can be removed by placing a large ROI in the posterior limb of the internal capsule (Fig. 12.39b). The final result shown in Fig. 12.39c can be used as a starting point to isolate the individual fiber bundles.

The superior fronto-occipital fasciculus runs slightly more medial and superiorly of the superior longitudinal fasciculus. Thus, by choosing the bundle that follows this course from the initial result, the superior fronto-occipital fasciculus can be isolated. A ROI drawn on a coronal section ensures the complete inclusion of the tract (Fig. 12.40a, b) and the result is shown in Fig. 12.41.

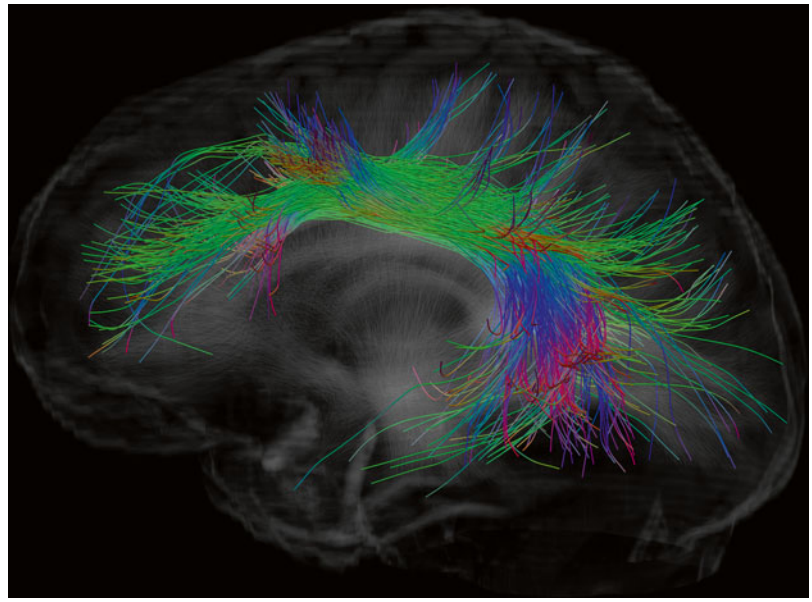

Fig. 12.41 Depiction of the SFOF overlaid on a sagittal fiber density map

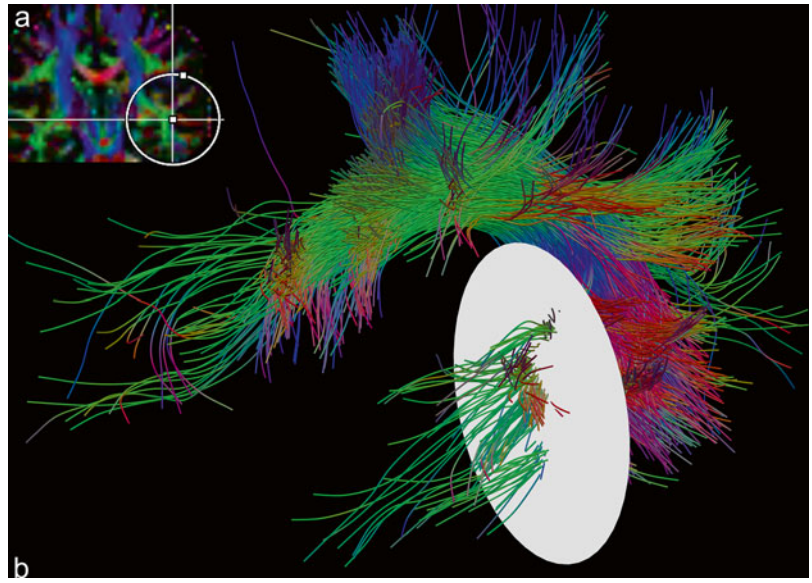

Fig. 12.42 Selection of the AF. (**a**) Initial ROI displayed on the coronal color map. (**b**) Depiction of the same inclusion ROI (*white circle*) on the 3D tracking result after removal of the fibers from the SFOF

After isolation and exclusion of the superior fronto-occipital fasciculus, the result shown in Fig. 12.42b includes the arcuate and superior longitudinal fasciculus. Since the arcuate fasciculus is the only bundle of the two entering the temporal plane, a ROI placed to include this region (Fig. 12.42a, b) will effectively isolate the arcuate fasciculus. The results of this dissection are displayed in Fig. 12.43. The superior longitudinal fasciculus can be obtained by excluding both the arcuate and the superior fronto-occipital fasciculus from the initial result and it is displayed in Fig. 12.44.

In Fig. 12.45, the previously reconstructed tracts are shown in a combined array. The superior fronto-occipital fasciculus is colored red, the arcuate fasciculus is colored green, and the superior longitudinal fasciculus is colored yellow.

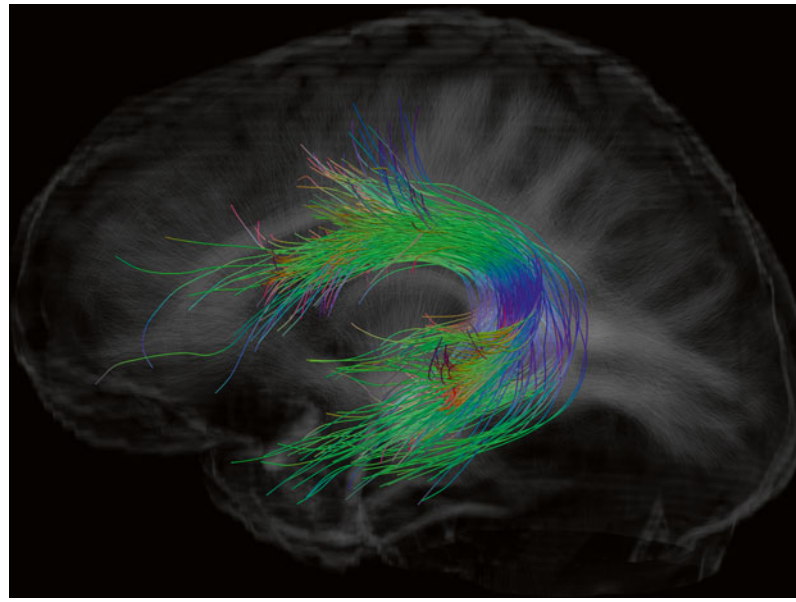

Fig. 12.43 Depiction of the AF overlaid on a sagittal fiber density map

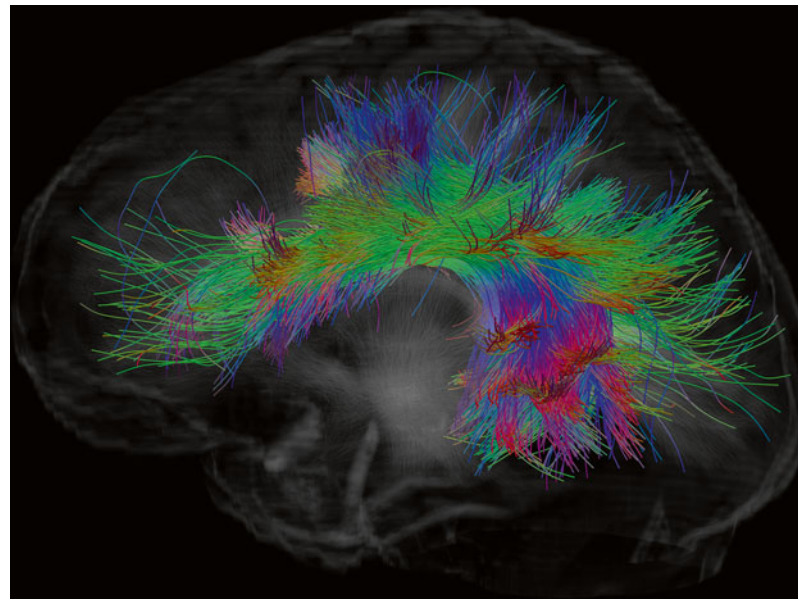

Fig. 12.44 Depiction of the SLF overlaid on a sagittal fiber density map. This image was obtained by removing the AF and the SFOF from the initial tracking result

The Cerebral Peduncles

The cerebral peduncles contain three major fiber bundles, the fronto-pontine, the cortico-spinal, and the temporo-parieto-occipito-pontine tract. The most renowned of the three is the cortico-spinal tract, as it is the main connection from the motor cortex to the spinal cord and of critical importance for motor function in humans. The initial result as shown below can be obtained by encompassing the cerebral peduncle on an axial slice as indicated in Fig. 12.46a. The initial result (Fig. 12.46b) includes all three tracts.

The fronto-pontine tract can be selected by placing a relatively large ROI in the frontal lobe.

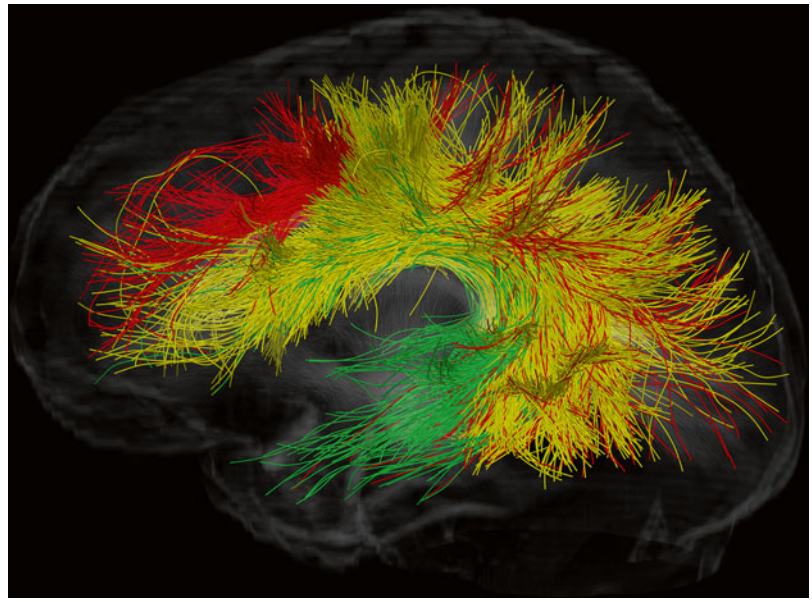

Fig. 12.45 Combined unilateral view of the SFOF (*red*), the SLF (*yellow*), and the AF (*green*)

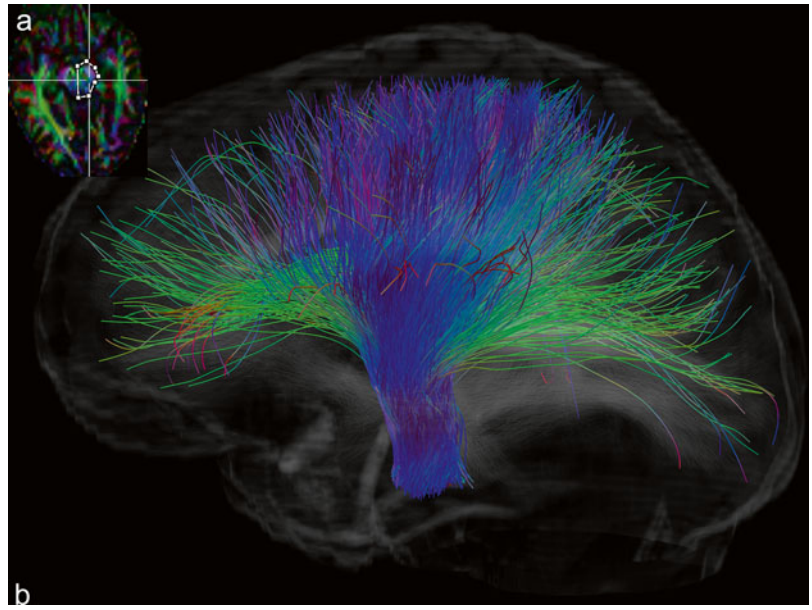

Fig. 12.46 Initial tracking of the fronto-pontine-, the cortico-spinal-, and the parieto-occipito-pontine tract (FPT, CST, and POPT respectively). (**a**) Initial ROI overlaid on an axial color map. (**b**) Initial tracking result with a combined representation of the FPT, the CST, and the POPT overlaid on a sagittal fiber density map

To include all tracts, the coronal plane should be used. The cortico-spinal tract can be selected by placing a relatively large ROI to encompass the corona radiata. To include all tracts, the axial plane should be used. The temporo-parieto-occipito-pontine tract can be selected by placing a relatively large ROI in the parieto-occipital area. To include all tracts, the coronal plane should be used. In the overview, the previously reconstructed tracts are shown in a combined array (Fig. 12.47). The fronto-pontine tract is colored red, the temporo-parieto-occipital-pontine tract is colored green, and the cortico-spinal tract is colored yellow.

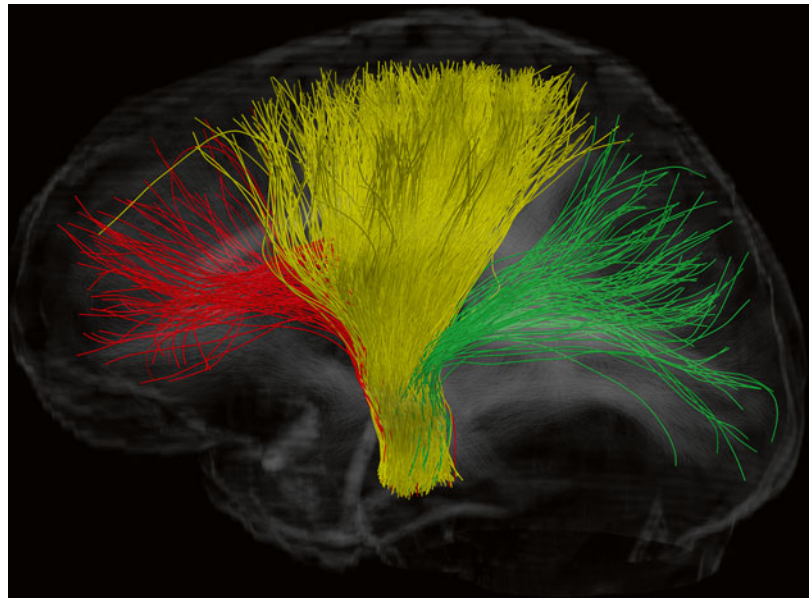

Fig. 12.47 Combined unilateral view of the FPT (*red*), the CST (*yellow*), and the POPT (*green*)

References

1. Mori S, van Zijl PC. Fiber tracking: principles and strategies - a technical review. NMR Biomed. 2002;15(7-8):468–80.
2. Mori S, Kaufmann WE, Davatzikos C, Stieltjes B, Amodei L, Fredericksen K, Pearlson GD, Melhem ER, Solaiyappan M, Raymond GV, Moser HW, van Zijl PC. Imaging cortical association tracts in the human brain using diffusion-tensor-based axonal tracking. Magn Reson Med. 2002;47(2):215–23.
3. Stieltjes B, Kaufmann WE, van Zijl PC, Fredericksen K, Pearlson GD, Solaiyappan M, Mori S. Diffusion tensor imaging and axonal tracking in the human brainstem. NeuroImage. 2001;14(3):723–35.
4. Xue R, van Zijl PC, Crain BJ, Solaiyappan M, Mori S. In vivo three-dimensional reconstruction of rat brain axonal projections by diffusion tensor imaging. Magn Reson Med. 1999;42(6):1123–7.
5. Mori S, Crain BJ, Chacko VP, van Zijl PC. Three-dimensional tracking of axonal projections in the brain by magnetic resonance imaging. Ann Neurol. 1999;45(2):265–9.
6. Hahn HK, Klein J, Nimsky C, Rexilius J, Peitgen HO. Uncertainty in diffusion tensor based fibre tracking. Acta Neurochir Suppl. 2006;98:33–41.
7. Conturo TE, Lori NF, Cull TS, Akbudak E, Snyder AZ, Shimony JS, McKinstry RC, Burton H, Raichle ME. Tracking neuronal fiber pathways in the living human brain. Proc Natl Acad Sci U S A. 1999; 96(18):10422–7.
8. Reisert M, Mader I, Anastasopoulos C, Weigel M, Schnell S, Kiselev V. Global fiber reconstruction becomes practical. NeuroImage. 2011;54(2): 955–62.
9. Kreher BW, Mader I, Kiselev VG. Gibbs tracking: a novel approach for the reconstruction of neuronal pathways. Magn Reson Med. 2008;60(4):953–63.
10. Mangin JF, Poupon C, Cointepas Y, Riviere D, Papadopoulos-Orfanos D, Clark CA, Regis J, Le Bihan D. A framework based on spin glass models for the inference of anatomical connectivity from diffusion-weighted MR data - a technical review. NMR Biomed. 2002;15(7-8):481–92.
11. Fillard P, Descoteaux M, Goh A, Gouttard S, Jeurissen B, Malcolm J, Ramirez-Manzanares A, Reisert M, Sakaie K, Tensaouti F, Yo T, Mangin JF, Poupon C. Quantitative evaluation of 10 tractography algorithms on a realistic diffusion MR phantom. NeuroImage. 2011;56(1):220–34.

MITK Diffusion Imaging

12. Fritzsche KH, Neher PF, Reicht I, van Bruggen T, Goch C, Reisert M, Nolden M, Zelzer S, Meinzer HP, Stieltjes B. MITK Diffusion Imaging. Methods Inf Med. 2012;51(5):441–8.

13. Stieltjes B, Brunner R, Fritzsche KH, Laun FB. Diffusion tensor imaging; introduction and atlas. Heidelberg: Springer; 2012.

Suggested Reading

Nieuwenhuys R, Voogd J, Van Huijzen C. The human central nervous system; a synopsis and atlas. New York: Springer; 1988. A great anatomical work of reference for brain anatomy.

Johansen-Berg H, Behrens TEJ. Diffusion MRI; from quantitative measurement to in vivo neuroanatomy. Amsterdam: Academic; 2009. Chapters 5-7 give a great overview of the relationship between microstructure and DTI-derived parameters.

Stieltjes B, Brunner R, Fritzsche KH, Laun FB. Diffusion tensor imaging; introduction and atlas. New York: Springer; 2012. Gives a more detailed introduction to diffusion imaging and rich anatomical reference.

Part V

Clinical Applications of Diffusion Tensor Imaging

DTI in Clinical Practice: Opportunities and Considerations

13

Louise Emsell and Stefan Sunaert

Learning Points

- DTI can be used in a variety of clinical situations and is not limited to neurological applications.
- DTI is used to varying degrees in clinical practice and despite its utility, remains primarily a preclinical research tool.
- There are a number of special considerations that need to be taken into account when using DTI in clinical practice.

L. Emsell, PhD (✉)
Translational MRI, Department of Imaging and Pathology, KU Leuven, and Radiology, University Hospitals Leuven, Herestraat 49, 3000 Leuven, Belgium

Universitair Psychiatrisch Centrum (UPC)- KU Leuven, Leuven, Belgium
e-mail: louise.emsell@med.kuleuven.be

S. Sunaert, MD, PhD
Translational MRI, Department of Imaging and Pathology, KU Leuven, and Radiology, University Hospitals Leuven, Herestraat 49, 3000 Leuven, Belgium

DTI in Clinical Practice and Research

The utility of DWI in clinical practice is well established and it is routinely used in the investigation of suspected acute ischaemic stroke, to differentiate vasogenic versus cytotoxic oedema and to characterize intracranial lesions such as pyogenic abscess, infections, tumors, and trauma [1]. DTI, however, remains predominantly a tool for preclinical research. Presently, one clinical application of DTI with potential clinical value, is for the planning of neurosurgical and radiotherapeutic procedures where it can be used in combination with invasive electrophysiological monitoring and functional MRI to locate essential motor and eloquent functional pathways. In this context, DTI and/or tractography may also have a future role in the placement of electrodes for deep brain stimulation. As a preclinical research tool, DTI has been applied widely to study a broad range of neurological and psychiatric disorders (Fig. 13.1). A selection of such clinical applications and the special issues that are associated with them is provided in the following chapters. Although, the topic is not covered explicitly in detail in this book, DTI also has been used to investigate nonbrain tissue, including the spinal cord [2, 3], peripheral nerves [4, 5], heart (myocardium) [6], breast [7, 8], skeletal muscle

W. Van Hecke et al. (eds.), *Diffusion Tensor Imaging*, DOI 10.1007/978-1-4939-3118-7_13

Fig. 13.1 Nonexhaustive selection of preclinical applications

CNS-related applications of DTI:
Neurosurgical planning
Dementias, including Alzheimer's Disease, Parkinson's Disease
Multiple sclerosis and other demyelinating diseases
Assessment of brain tumours
Epilepsy
Psychiatric disorders
Spinal cord pathology e.g demyelinating disease, tumors, trauma
Traumatic brain injury
Healthy brain development & neurodevelopmental disorders
Healthy ageing and neurodegeneration
Optic nerve assessment

Non-CNS tissue that has been assessed using DTI:
Cranial nerves
Peripheral nerves: including, spinal, forearm & lower limb nerves
Skeletal muscle
Heart (myocardium)
Uterus
Kidney
Breast
Prostate

[5, 9], kidney [10, 11], prostate [12, 13], and uterus [14], and may be relevant for the investigation of allied disorders.

Special Considerations in the Clinic

When embarking on DTI data collection in a clinical setting or in the context of clinical research, there are a number of considerations that could be taken into account that will guide the way data will be acquired and how it is analyzed. Each of these is summarized below.

Scan Population: Whom Are We Going to Scan?

Nature of Patient Group/Pathology

Different clinical groups present specific challenges. For example, acquiring DTI data on neonates is clearly different in practice to acquiring data on adults. Similarly, acquiring DTI data in the presence of substantial traumatic brain damage will present more challenges than scanning patients with more subtle organic pathology, such as in prodromal schizophrenia. These are extreme cases, however, they illustrate the importance of considering the nature of the patient group and their pathology, when acquiring and analyzing DTI data. Some specific examples are provided in the following chapters, however, more generally, you may consider the following.

Age

The brain changes significantly over the course of the lifespan, and this in turn is reflected by alterations in DTI parameters that are modulated by structural changes as the brain develops and ages. Such changes are not uniform across the brain, and throughout each stage of life fiber pathways are developing and degenerating at different rates [15, 16]. Understanding when these changes occur is useful both when considering the design of DTI research studies and when interpreting clinical findings in the context of other imaging or histopathological data.

Developmental Phase

Although the possibility of acquiring in vivo DTI data and performing tractography in utero has been demonstrated [17], the numerous challenges associated with acquiring such data limits the techniques use in clinical practice. Nevertheless, several groups have applied DTI to study fetal brain development both ex-vivo, using postmortem brains [18, 19] and in-vivo, by scanning preterm infants [20]. As DTI provides contrast in the absence of myelination, these fascinating studies have been able to build on prior histological knowledge to provide further insight into brain development. Far from being small, simplified versions of the adult brain, the fetal brain is a unique, and continuously changing with transient structures such as the ganglionic eminence [21] and fiber bundles that may disappear during fetal life, at term or in early childhood. Others bundles, such as the superior longitudinal fasiculus, may not be detectable until the third trimester or even at birth [22]. Unlike in later developmental stages where DTI is most useful in delineating white matter structure, in the fetal brain, the organization of the cerebral wall is also apparent. Notably, the presence of radially oriented structures that guide neuronal migration to the cortical surface between the second and third trimesters, give rise to anisotropy perpendicular to the cortical surface, which results in high FA in the cortex. As anisotropy decreases with increasing microstructural laminar and columnar complexity in later development, FA, in turn, becomes much lower in the cortex.

Knowledge of such variations in anatomical organization and DTI parameters during fetal life will become increasingly valuable in future clinical applications involving preterm and newborn infants [23].

Typically, as myelination progresses, anisotropy within the white matter continues to increase and diffusivity decreases rapidly during the course of brain development, with the most dramatic changes occurring in the first 2 years of life. After this period, the rate of change decreases as the brain approaches adult proportions in mid-childhood [24]. For a detailed review on the topic of white matter development during the fetal, neonate and infant stages, see Dubois et al. [25].

In order to investigate DTI changes during development, various groups have proposed a series of age-specific population atlases including data from neonates, infants, and children through to adolescence [15, 26]. Although different studies are broadly in agreement with respect to the identification of increases in anisotropy followed by decreases in diffusivity during development, the precise trajectory of such changes remains to be confidently elucidated owing to the myriad challenges associated with DTI data collection and analysis.

Senescent Phase

It is generally accepted that the age-related decline in white matter volume in late adulthood is an indicator of senescence. Precisely when this phase begins and development end is unclear, however DTI data suggests it may occur as early as the fourth decade [27]. In line with heterogenous DTI changes during development, FA and diffusivity changes during senescence are equally regionally variable. One prevailing view is that of retrogenesis, which describes how fiber tracts that are myelinated the latest, are the most vulnerable to neurodegenerative processes. Such early myelinated fibers, which reach maturation in utero or perinatally (e.g. primary motor fibers) are thought to be more robust than those maturing later (e.g. SLF). An allied phenomenum is the concept of an anterior-posterior gradient of diffusion changes, whereby age-related decline in FA is greatest in frontal and parietal WM compared to occipital WM [28].

Advancing age is associated with a loss of white matter volume, FA decrease, and increase in diffusivity measures. There are also other age-related phenomena that may impact upon DTI metrics, which deserve consideration. A common feature of elderly MRI scans are hyperintense lesions on T2-weighted fluid-attenuated inversion recovery (FLAIR) images. These “white matter hyperintensities” (WMH) reflect regional leukaraiosis arising from multiple histopathologic processes, including ischemia/infarction, demyelination, inflammation, gliosis and rarefaction, and amyloid angiopathy [29]. WMH typically occur in a regionally characteristic pattern, with focal or punctuate lesions that may become

confluent, occurring in the deep and subcortical white matter; and periventricular WMH characterized by smooth, confluent bands and periventricular caps. The former are thought to arise from primarily vascular pathology, whilst the latter periventricular lesions are believed to have a non-ischaemic origin [30]. Historically, the boundaries of WMH have been defined by a sharp change in intensity on FLAIR images allowing relatively trivial qualitative clinical ratings and automated segmentation. However, a more contemporary view is that WMH reflect a late, severe stage of damage that extends beyond the hyperintense boundary; a view supported by recent work combining DTI and FLAIR to investigate the evolution of WMH [29, 31]. In this context, DTI studies in populations that include subjects with WMH, should take into account not just the clearly delineated WMH, but also consider potential broader microstructural changes and partial volume effects.

A less widely considered factor in the context of DTI, is the change in brain iron content with advancing age. Ferritin, a protein controlling the storage and release of iron, decreases in white matter and increases in subcortical gray matter [32, 33]. As iron changes MR-signal intensity and causes susceptibility artifacts, any increase in iron-content will influence DTI metrics.

Effect on Brain Structure

Different clinical groups will share both overlapping and distinct neuroanatomical features. For example, infants will share similar features to other infants, but will have markedly different brains to older typically developing children and adults. Similarly, healthy adults of comparable age will share similar gross anatomy, but adults within that age category who have multiple sclerosis, will have brains with regionally altered white matter composition. It is important to recognize and consider such differences in the context of DTI as the size, shape, and composition of the brain impacts DTI parameters in a number of ways. For example, by differentially changing the homogeneity of the magnetic field, particularly at tissue interfaces such as the frontal and temporal sinuses, there will be differential degrees of gradient susceptibility distortions and signal loss. In such regions, the measured diffusion signal will be corrupt and therefore any derived DTI metrics will be inaccurate. Although it may be possible to recover some information by applying offline postprocessing correction strategies such as informed RESTORE [34] or field-map-based techniques [35], attempting to reduce these effects during data acquisition are encouraged.

Brain geometry will also determine the extent of partial volume effects (PVE). For example, larger brains may be expected to have larger fiber bundles and therefore less PVE-contaminated voxels relative to smaller fiber bundles. As DTI parameters represent a voxel-average scalar measure, PVE modulate DTI parameters [36]. It follows that systematic differences in PVE may introduce bias into tract-based statistics.

Almost all DTI processing will be performed in another reference space than the native image space. This is because image quality correction techniques that attempt to reduce the effect of eddy currents and motion, require the image to be transformed using image registration techniques. For example, by mapping the DWIs to the non-DWI (b0), or to an anatomical scan. Image registration is also required for any sort of group analysis where equivalent voxels/anatomy needs to be compared between subjects equitably. In simple terms, registration algorithms seek to find common features between images in order to match them. In the presence of large differences in brain structure such as gross atrophy or lesions, the registration will perform more poorly. In the case of individual datasets with atypical anatomy and/significant pathology, special attention should be paid to assessing the quality of correction strategies. In the case of group comparisons, the template space should match the study population as closely as possible (e.g. pediatric). Ideally, a population atlas derived from combining all the subjects data, should be used, or alternatively, a high quality template developed by the neuroimaging community (see Chap. 10 for further details).

Effect on Patient Mobility

The sequences used to acquire DTI data (e.g. EPI), are particularly susceptible to motion. In the absence of real-time motion correction, it is therefore preferable for the subject to remain as still as possible for the duration of the scan. There are a number of clinical groups where this may be more challenging. For example: children, patients with motor disorders or hyperkinesia due to other pathology or medication, and patients that are particularly restless, agitated, or anxious (including patients with active psychiatric symptomatology). When such subjects are included in group studies, it is particularly important to recognize the potential for bias if there are more motion artifacts in the patient data compared to the control data.

Aside from increased motion, patients may also present with reduced or restricted mobility. In such cases, patients may not be positioned optimally within the scanner, or suffer discomfort.

In both cases of increased and decreased mobility, it may be sensible to consider limiting scan time, using optimized sampling of diffusion gradients [37, 38] and/or allowing breaks between sequences in order to ensure optimal data acquisition and patient comfort.

Degree of Patient Compliance

The patient's motivation for having a DTI scan and their understanding of the procedure may impact on the success of data collection. A significant number of patients may refuse or terminate scanning early due to anxiety, typically arising out of claustrophobia [39]. Aside from the risk of incomplete data collection, data quality may be reduced by motion artifacts arising from gross patient movement, increased respiration and swallowing. DTI sequences involving EPI are characterized by a persistent, loud high frequency repetitive beep and strong gradients that may vibrate the scanner table. These features may startle or unnerve anxious patients. However, careful explanation and the provision of realistic expectations of the scanning process has been shown to reduce patient anxiety and increase compliance, and therefore reduce unwanted motion effects or early termination of scans [40].

DTI in Children

Aside from the analytical challenges associated with changes in brain development described above, there are other practical factors that should be considered when acquiring DTI data in children (for a detailed review, see [41]). These considerations can be broadly divided into the following themes.

Child-Centered Approach to Scanning

Acquiring DTI data on children is challenging across all age groups, as the scanning procedure requires that they lay still in an unfamiliar, noisy restrictive space for a relatively long period of time. This can be challenging enough for adults, let alone for younger children who may not comprehend what is happening and why. At best, this may result in poor quality data due to excessive bulk motion artifacts, at worst; it will result in significant distress and termination of the scan and thus incomplete data acquisition. Approaches to avoid these scenarios are therefore necessary, both for the sake of clinical care and the child's well-being, and also to prevent potential bias due to motion artifacts in case–control group studies. The most appropriate approach will be guided by the age of the child and the context of the scanning protocol. For example, if the DTI scan is required for clinical purposes, such as for presurgical planning, where good quality data is essential to clinical care, the child will typically be sedated. If the child is voluntarily taking part in a clinical research study, a different approach will be required. Babies are encouraged to sleep and pre-school or school-aged children are typically awake.

Broadly, a child-centered approach involving parents and carers is recommended, both in the scanning environment and in communication. This could involve a decorated waiting area, the provision of child-size furniture and toys, and child-friendly uniforms for medical staff. Some institutions have a mock scanning facility, which can be used to introduce the child to the scanner by replicating the scanning experience in a safe, controlled manner. Child-appropriate scanning equipment is useful, for example, a smaller head coil, foam padding and blankets, ear-plugs/headphones

to reduce scanner background noise (SBN), and the opportunity to stream children's music/videos within the scanner.

With regard to communication, it is important to engage both parents/carers and children, as parental anxiety and misunderstanding will translate to the child. Furthermore, parents are required to provide written informed consent in addition to verbal consent from the child, and should therefore fully comprehend the purpose and procedures surrounding the DTI scan. Some ethical committee regulations may also require written consent from children, typically over 12 years of age. Appropriate communication can take many forms but should always make use of child-specific and/lay terminology and be presented in a calm, unhurried, and friendly manner. Aside from general verbal instructions, it is useful to offer illustrated information booklets, brochures, and videos. Beyond these basic approaches, a variety of other methods can be used, for example drawing on behavioral and situational training techniques [41]. Further technical details about acquiring DTI data in children can be found in Chap. 6.

Ethical Considerations

A complete discussion of ethical considerations associated with the use of DTI data is beyond the scope of this book. However, a few points deserve mention. Firstly, the same fundamental principles apply to DTI scanning as to any other noninvasive imaging procedure. Informed consent should be obtained and the DTI examination should conform to local institutional regulatory ethical standards and those required within broader national and international frameworks e.g. International Code of Medical Ethics, Declaration of Helsinki and The Belmont Principles.

Secondly, the decision to use DTI in a clinical setting should not be undertaken without due consideration of the limitations of the technique, particularly with regard to risk-assessment. The question arises as to whether or not to use DTI data if it is available i.e. *is suboptimal, potentially incorrect data about white matter anatomy better than no information at all*? This is especially pertinent in the context of surgical planning. For example, it has been clearly demonstrated that DTI-based fiber tractography does not provide a complete representation of anatomy and underestimates the size and cortical extent of white matter tracts [42], therefore using the technique without due regard to this limitation is potentially harmful. In practice however, surgeons typically draw on a range of imaging and electrophysiological techniques for presurgical risk assessment and planning. They are also more likely to use the color FA maps in the first instance, with DTI-based tract reconstructions providing a coarse assessment of tract displacement (see Chap. 20). When used responsibly, this complementary information may improve surgical outcomes [43]. Surgical planning is an illustrative example, however, the decision to use DTI data in other clinical settings should be guided by the acting physicians duty of care.

Thirdly, there are different ethical issues associated with acquiring data for clinical care and for preclinical research, and due attention such be paid to this distinction. Of particular note are issues associated with managing incidental findings [44] and the difficulty patients may experience distinguishing between a diagnostic brain scan and one used for research purposes i.e. the "therapeutic misconception" (e.g. clinical study participants may incorrectly assume the scan forms part of their medical record and will be used to identify pathology) [45]. Finally, there is an increasing trend towards data-sharing within the neuroimaging research community and a concerted effort to understand brain connectivity, often incorporating DTI data. This sharing of clinical research data for secondary analysis presents additional ethical challenges, particularly relating to informed consent (see Brakewood and Poldrack [46], for a detailed review).

Scanner Resources: What Equipment Is Available?

Hardware

Magnetic Field Strength

Clinical MR systems typically used for routine DTI scanning of humans are 1.5 T or 3 T, although a small number of specialist research centers

offer the possibility of scanning (predominantly healthy) subjects at 7 T. As DTI parameters should not be dependent on the static magnetic field strength, the reproducibility of measures at different field strengths is largely dependent on signal-to-noise ratio and the effect of artifacts [47]. It is commonly accepted that scanning at higher field strengths provides increased signal-to-noise, therefore one would expect higher fields to equate with higher quality. Although this is the case for conventional imaging, the competing decreases in T2 time and increased b0 inhomogeneity associated with increasing field strength, coupled with increased distortions due to eddy currents, magnetic susceptibility, and chemical shift artifacts, off-set the gain in image quality in DTI. Nevertheless, it has been shown that the uncertainty of fitted DTI parameters decreases with increasing field strength, which may impact positively on fiber-tracking results [47]. Additionally, the use of multichannel phased-array head radio-frequency coils in place of a traditional birdcage coil allows the use of parallel imaging techniques such as sensitivity encoding (SENSE), array spatial sensitivity encoding technique (ASSET), and generalized auto-calibrating partially parallel acquisition (GRAPPA) to improve DTI data quality. At moderate acceleration factors (e.g. 2 or 3) these techniques may reduce susceptibility-induced geometric warping artifacts and T2 effects by allowing a reduced EPI echo train and TE time [48].

Gradient System

Aside from the static field, the number and strength of transmit and receive gradient coils contributes significantly to DTI data quality. Additionally, the gradient duty cycle determines how many 2D images can be acquired per TR. Modern scanners will have larger duty cycles and therefore allow more data to be collected in less time. Increasing gradient strength allows stronger diffusion weighting and read-out in a shorter period of time. In turn, this means TE can be reduced, which improves data quality by decreasing susceptibility effects. The rate at which the gradients can be turned on and off, the *slew rate*, is also important. Fast slew rates are preferable for DTI. However, the rapid rise and fall of strong gradients can induce image distorting eddy currents and mechanical vibrations. More significantly for the patient, rapid gradient switching can cause peripheral nerve stimulation leading to involuntary muscle contractions. For safety reasons, the maximal gradient amplitude and slew rate are therefore limited. Typical clinical systems operating within these safety limits use gradients in the order of 40–80 mT/m maximal gradient amplitude and 150–200 mT/m per millisecond maximal slew rate, although new systems with stronger gradients and faster slew rates are emerging on the market and in specialist research centers.

Peripheral Equipment

DTI data quality may be improved by using non-standard equipment provided by the scanning manufacturer or developed by and for researchers. For example, using multi-channel phased array coils instead of birdcage coils to boost SNR and to allow parallel imaging a simple way to improve DTI data quality. However, it should be noted that increasing the number of component coils may introduce a bias field which favors cortical coverage over deep white matter and therefore may be less optimal for DTI in these regions. Peripheral cardiac-gating is commonly supplied by MRI vendors and enables DTI data to be acquired only during the diastole phase of the cardiac cycle, thereby reducing pulsation artifacts. At the other end of the spectrum, prospective motion correction using real-time tracking with external devices such as cameras is gaining ground in high-field research centers [49]. When such advanced equipment is available, the choice remains as to whether or not it would be appropriate to use it. For example, cardiac-gating increases scan time and may not be useful in restless subjects or when data must be acquired quickly.

Number of Scanners

This will determine to a great extent, the relative availability of DTI scanning time. Consider, how many people are using the scanner/s and how frequently. In a primary clinical setting, consider the patient turnover of the department. DTI sequences can vary in length from a few minutes to half an

hour or more depending on the amount of data acquired and number of gradient directions sampled. In a small clinic with only one scanner and a high patient turnover, it is clearly more sensible to consider short sequences, and the possibility of performing long, complex longitudinal data collection may be limited. The need for standardization of protocols and effective quality assurance procedures is particularly important within a center with multiple scanners.

Software

Data Management

An often-overlooked issue when managing DTI data is how it will be stored and transferred from the scanner to other platforms. Typical DTI datasets are much larger than standard clinical scans and therefore present additional storage issues, greater burden on PACS (Picture Archiving and Communication System) and extended transfer time.

Data Storage

It is beyond the scope of this chapter to discuss DTI data storage options in detail; however, those working with DTI data should consider how and in what form it will be stored. For example, will the data be archived on PACS? Or stored off-line on a secure server? Or within a cloud computing framework? Will there be a back-up? Who will have access to this data? How will it be accessed? Who will manage the data? Will the raw DICOM data be stored, or also processed data? These are examples of issues common to all types of imaging data. The difference with DTI data however is that DTI datasets are larger and thus present a more disproportionate storage burden than other data.

Data Format

There are different data formats that can be exported from the scanner. The DICOM (Digital Information and Communication in Medicine) format is the industry standard. As this format is constantly being revised to match the pace of technological developments, there may be subtle differences in the way DTI data is coded in the DICOM headers, which should contain all the relevant information about the scan (such as patient details, date and location of acquisition, scan parameters etc.). These differences can present issues for DICOM conversion software, which attempt to use specific tags in the DICOM header to work out the image type, orientation, size, and diffusion gradient directions. These issues present real challenges with regard to left-right switching and incorrect gradient vectors, and should not be ignored. Nevertheless, DICOM remains the preferred format for data export and most DTI analysis packages support DICOM file conversion.

In addition to DICOM, MRI vendors have their own file formats that conform to the DICOM standard. However, these formats are not typically compatible across different vendor platforms and are supported to varying degrees by noncommercial image analysis software.

In order to address these issues, another standard has been developed by the neuroimaging community called NIFTI (Neuroimaging Informatics Technology Initiative), with an associated file format that is compatible across noncommercial DTI analysis software applications, represented with the file extension ".nii". Some vendors are now also including a nifti export function. There are also a variety of freely available tools that can convert DICOM data to nifti format.

The choice of file format to export will therefore depend on the users available storage/transfer capacity resources. DICOM format is the option of choice as it is the most cross-platform compatible and can easily be converted to other formats. However, cautious users and those wishing to use vendor firmware to analyze their data should consider exporting DTI data in both vendor and DICOM formats.

Data Security

When considering clinical data management, confidentiality and data security are important considerations. When data is used in clinical

practice, patient identification is crucial and should be readily accessible. However, in clinical research, personal identifiers such as the patients name, such be removed, i.e. the data should be anonymised. This can be done relatively trivially using software tools to remove the relevant information from the DICOM header.

Aside from issues of confidentiality, data protection extends to the secure storage and transfer of data. Data that is being transferred within and between hospital environments and research institutions outside of PACS may be controlled by firewalls. This important barrier protects sensitive data, however, it may also present an obstacle to DTI data transfer. The institution network administrator should be consulted for advice on this issue as using a secure shell file transfer protocol (sftp) is one of the safest and most efficient ways of transferring DTI data.

Data Transfer

Aside from sftp, another method of data transfer is by exporting data to an external device such as a portable hard drive or CD/DVD. Using portable devices such as USB sticks carries additional risks for MRI vendors in the form of potential malware or virus transfer to the scanner, and in some institutions is not recommended. If you are interested in using this method of transfer, you should consult the recommended protocol for your institution for advice. Aside from potential malware issues, portable devices may not be optimal for transferring large amounts of DTI data due to the speed at which they operate. There are also added risks associated with losing small portable devices and for data loss due to cross-platform incompatibility.

Licensing Issues

When choosing software, the user should consider the type of software license associated with it, both in the context of liability and terms of use. For example, different software will have different degrees of approval for clinical use that will dependent on the purpose for which it is used and the geographical region in which it is used (e.g. Does the software fall within the scope of the Federal Drugs Agency (FDA) regulations or to any other national or international regulatory standard). Typically Vendor software will be approved for clinical use, however, users should check to what degree and under what conditions this approval extends to DTI data. Noncommercial and open-source DTI software almost universally contains a disclaimer stating that the software is not approved for clinical use.

Aside from liability issues, there are financial considerations associated with software licenses. For example, commercial software, by definition, invariably has associated costs. This may be justified in terms of its conformation to the required clinical/regulatory standards, multi-platform compatibility, security, and the availability of dedicated technical support. Noncommercial and open-source software is freely available and constantly in development making it an attractive option for those interested in using the most advanced methods available and for tailoring processing and analysis pipelines to their data. The disadvantage to this approach however, is that the newest methods are unlikely to be clinically validated thereby introducing an element of risk. Some noncommercial software also makes use of licensed software such as "Matlab" (The MathWorks, Inc., Natick, Massachusetts, United States) in order to run. Also, there may be platform compatibility issues, a higher rate of software bugs and less technical support than for commercial software. Typically, technical support for freeware is found in mailing lists and online support forums, as well as in manuals. The degree of support varies widely depending on the software package. The most commonly used packages tend to have the most active mailing lists and support forums, whilst more specialized packages often (but not always) rely on the provision of support by a small development team who provide technical advice on an ad hoc basis alongside their normal research commitments.

Version Control

Both scanner software and DTI analysis software is in continuous development in order to keep

apace of scientific and technical developments, and to address technical issues/problems with the software code (e.g. bug fixes/patches). This means that all software will require upgrading at some point. Although in practice this may seem a relatively trivial procedure, there may be unintended consequences that users should be aware of. For example, scanner software upgrades may result in alterations to data acquisition parameters and image quality. Some specialist research sequences, such as "work in progress" or "WIP" protocols may only function with specific software versions. These issues are normally addressed by the local MR physicist(s) and Vendor applications specialist, however, being aware of the timing of scanner software upgrades is useful when planning data acquisition and an important part of DTI data quality control.

Upgrades to analysis software are usually more explicit for end-users as changes are typically documented in release notes. However *major* software upgrades can significantly alter the way data is processed or how the software interfaces with other software and hardware. In such cases, data processed with two different versions of the same software package may not be truly comparable. This is important when the DTI data will be used longitudinally, such as for patient follow-up or in a group analysis investigating treatment effects or illness evolution. It is also important in cross-sectional group analysis where data is being collected over a long time frame, such that some preliminary analysis is completed using a different software version. In all these situations, it is better to analyze all the data using the same software version, and when practical, this means using the latest official release (not the beta version). If this is not practical, then the software version may need to be included as a nuisance variable in statistical analyses.

Software Features

Just as there is no standard way of acquiring or analyzing DTI data, there is no standard DTI software application. However, most software packages will share some core features, typically: a raw data/DICOM reader/converter, a viewer to visualize the data, a diffusion tensor estimation tool and derivative FA maps, color FA maps and MD or ADC maps, deterministic and/or probabilistic fiber-tracking and region-of-interest analysis, and a user-manual. Beyond these fundamental features, there are a variety of add-ons and advanced modeling tools available which are incorporated to varying degrees into different packages. These are summarized in Fig. 13.2.

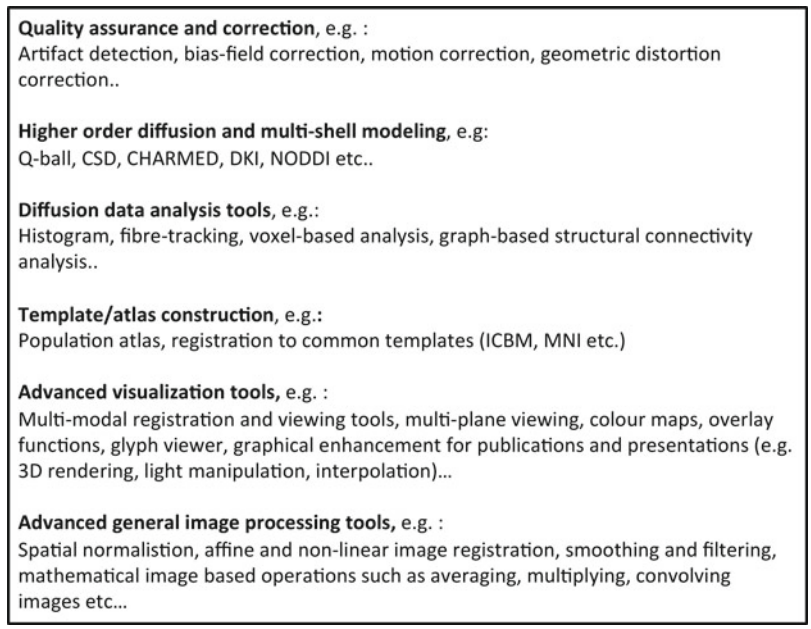

Fig. 13.2 Nonexhaustive list of features available in different DTI software packages

Multimodal Viewing and Analysis

It is useful to be able to combine different kinds of data in order to maximally benefit from the complementary information they provide. For example, clinical neuronavigation software typically integrates neurophysiological and imaging data such as from EEG, MEG, fMRI, sMRI, and DTI, for the purpose of presurgical assessment and planning. Vendor supplied software has the advantage of being intuitive to use and specifically designed for clinical use. However, the "one-size fits all" approach may not always be the most appropriate, particularly in the context of DTI analysis. Off-line processing offers the benefit of flexibility and the possibility to use more advanced image processing and analysis strategies. However, this added customizability makes it difficult to establish the industry standards required for comparability across clinical groups. This lack of standardization presents a significant challenge for both software developers and users. A recent study highlights the point. It compared 4 DTI software packages, two commercial and two freeware, and found significantly divergent reconstructions of the corticospinal tract in the same individual across the packages, even when using the same or similar tracking algorithms (FACT) [50] and single regions of interest (ROIs), as well as background threshold, fractional anisotropy (FA) threshold, maximum fiber angulation, and fiber length [51].

Essentially, combining multimodal data is an image registration issue. This is discussed in more detail in Chap. 10.

Human Resources: Who Can Help?

Availability and Expertise of Support Staff

A number of people with various roles are involved in MRI-based operations. For example physicists, radiographers, specialist nurses, technicians, radiologists, and imaging scientists. The availability and expertise of these individuals will vary widely from one setting to the next, and will determine the degree of support available for DTI scanning. Consider for example, is there a physicist available to optimize acquisition protocols, program the scanner, perform specialist quality assurance, and trouble-shoot data quality? Who will acquire the data? Are they familiar with DTI sequences and the special issues associated with them? Who will analyze the data? Are there trained radiologists or imaging scientists available to process, analyze and interpret the data?

Time

As always with medical imaging, there needs to be a balance that aims to minimize scan time whilst maximizing image quality and obtaining sufficient relevant data to provide useful information. In a clinical setting, DTI scan time may need to be reduced, for example, to accommodate a busy schedule, for financial reasons, for improved patient tolerance or due to the nature of the patients medical condition. In this context, consideration must be paid not only to the length of the scan itself, but also peripheral, allied activities.

Preparation

Consider how much time is needed to register the patient, perform safety checks, gain informed consent, explain procedures, set up the patient in the scanner, set-up any auxiliary equipment etc.

Acquisition

Consider not only the duration of data DTI acquisition (see Chap. 6), but the duration in the context of the entire protocol, e.g. how many other scans are being acquired, are there preparatory/in-line correction routines; what is the motivation for the DTI scan, e.g. is it the most important part or an add-on? Etc.

Analysis/Off-Line Processing

Consider whether the data is going to be analyzed immediately on the scanner using vendor software, if there will be immediate data quality checks (recommended!), or if the data needs to be exported for off-line processing using specialist software. If it will be exported, consider the type of postprocessing and analysis, who will perform this and how long it will take.

Radiological Reporting

Is the data going to be assessed clinically or used in the context of preclinical research? Who will do this and how will it be integrated into their clinical or research schedule?

Outsourcing

It is possible to outsource complex advanced radiological data, such as DTI data, for processing and analysis by third parties. This can be in the form of an academic collaboration whereby clinicians recruit and scan a clinical population of interest which is then analyzed by expert biomedical imaging scientists or students, under the supervision of such scientists, and then jointly published. Alternatively, a commercial image analysis services provider is paid to analyze the data and provide a report of the results for a fee. Both options have advantages and disadvantages. For example, academic collaboration is useful for long-term training and for fostering strategic partnerships to boost long-term research output and project financing. Commercial service providers offer a more short-term solution that can be attractive to clinicians and clinical researchers needing more immediate results or who require a more standardized or regulated approach (for example, ISO certification, FDA-approval).

Cost

The amount of DTI data acquired may be determined by the availability of financial resources, and the various costs associated with MRI scanning should be considered. The following are examples.

Costs Associated with Scanning

Consider access to the scanner—can you collect data routinely? Do you need to rent time on the hospital scanner? Are you able to rent time on a research scanner? Who pays for scanning? For example, are the scanning costs covered by local departmental funds, a third-party funding agency, a governmental body or by national or private health insurance providers? Clearly, with limited financial resources, less data can be collected. You may need to think about acquiring a greater amount of high quality data on fewer subjects, or using shorter sequences on a greater number of subjects. These decisions will be informed by your rationale for acquiring DTI data in the first place.

Costs Associated with Analysis

Consider*who* will analyze the data (see above section "Availability and Expertise of Support Staff") and whether or not there are costs associated with this e.g. Do you need to hire or train specialized staff? Are you planning on outsourcing the data analysis? Consider *how* you will analyze the data. Do you need to purchase any software? (see above section "Software").

Summary

In this introductory chapter we have presented a high-level overview of clinical DTI applications and the types of things that could be considered before embarking on DTI data-collection and analysis in clinical populations. These considerations are illustrated in Figs. 13.3, 13.4, and 13.5. Although we have presented what may seem like an exhaustive list, our aim in providing such an overview is primarily to raise awareness of issues related to the implementation of DTI in clinical populations that are often over-looked by the DTI novice. In this way, we hope to encourage both the thoughtful implementation of future DTI investigations, and also to provide the reader with a broader appreciation of the many issues underlying clinical research studies.

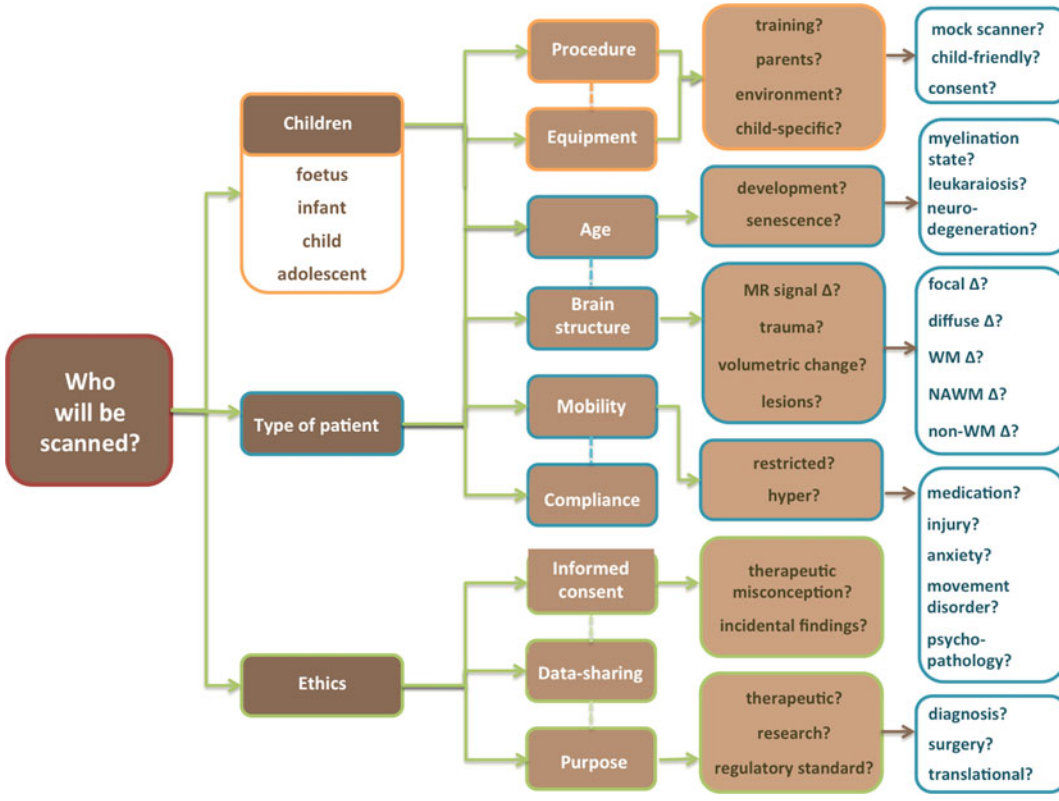

Fig. 13.3 Who will be scanned? (characteristics of the patient population)

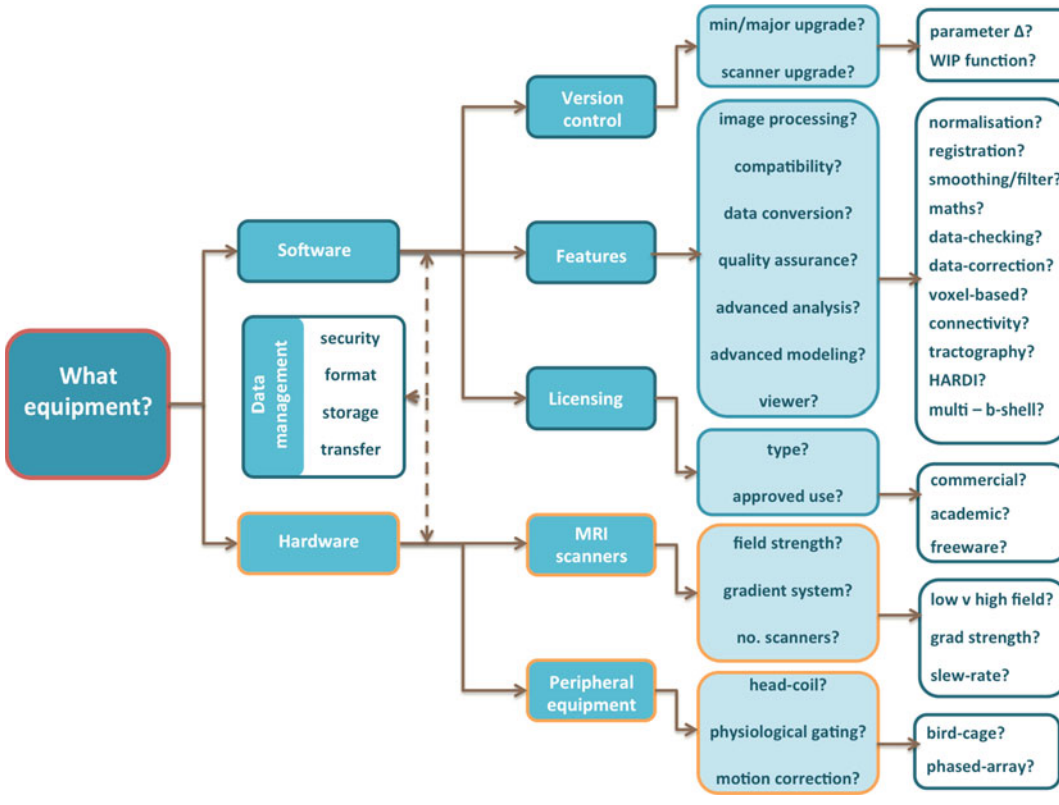

Fig. 13.4 How will they be scanned? (scanning, hardware and software resources)

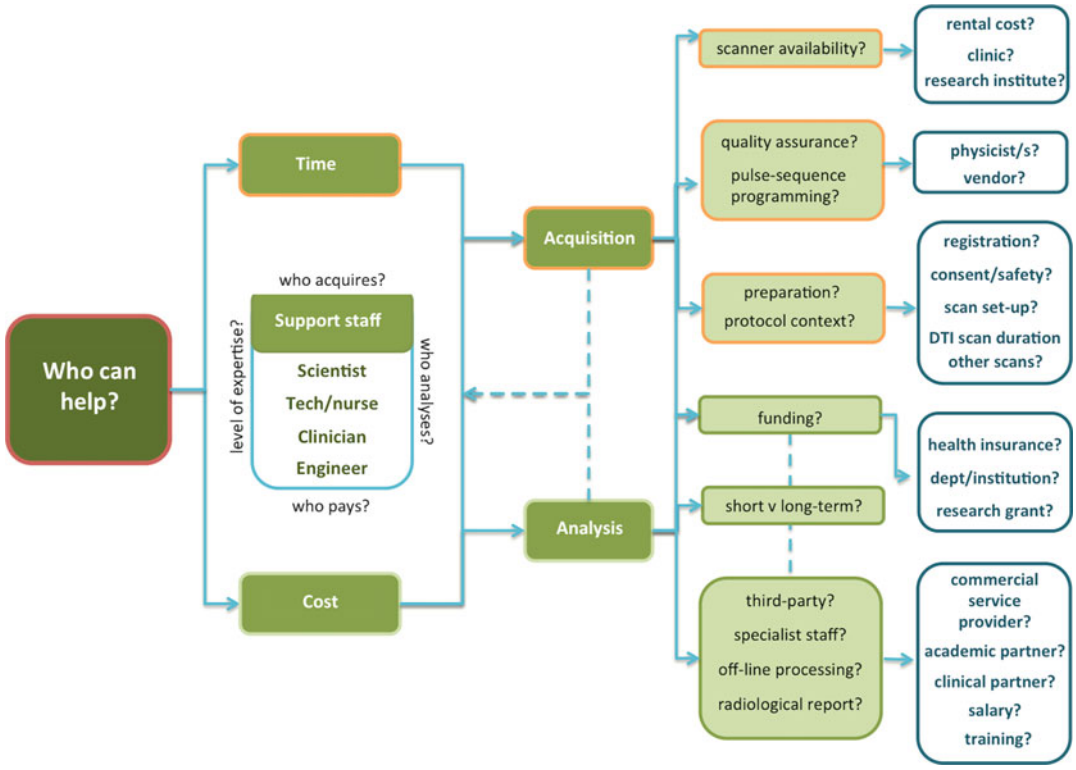

Fig. 13.5 Who can help? (human resources)

References

1. Mukherjee P, Berman JI, Chung SW, Hess CP, Henry RG. Diffusion tensor MR imaging and fiber tractography: theoretic underpinnings. AJNR Am J Neuroradiol. 2008;29(4):632–41 [Review].
2. van Hecke W, Nagels G, Emonds G, Leemans A, Sijbers J, van Goethem J, et al. A diffusion tensor imaging group study of the spinal cord in multiple sclerosis patients with and without T2 spinal cord lesions. J Magn Reson Imaging. 2009;30(1):25–34 [Evaluation Studies].
3. Vedantam A, Jirjis MB, Schmit BD, Wang MC, Ulmer JL, Kurpad SN. Diffusion tensor imaging of the spinal cord: insights from animal and human studies. Neurosurgery. 2014;74(1):1–8.
4. Zhou Y, Narayana PA, Kumaravel M, Athar P, Patel VS, Sheikh KA. High resolution diffusion tensor imaging of human nerves in forearm. J Magn Reson Imaging. 2014;39(6):1374–83.
5. Khalil C, Budzik JF, Kermarrec E, Balbi V, Le Thuc V, Cotten A. Tractography of peripheral nerves and skeletal muscles. Eur J Radiol. 2010;76(3):391–7 [Review].
6. Wei H, Viallon M, Delattre BM, Wang L, Pai VM, Wen H, et al. Assessment of cardiac motion effects on the fiber architecture of the human heart in vivo. IEEE Trans Med Imaging. 2013;32(10):1928–38 [Research Support, Non-U.S. Gov't].
7. Furman-Haran E, Eyal E, Shapiro-Feinberg M, Nissan N, Grobgeld D, Weisenberg N, et al. Advantages and drawbacks of breast DTI. Eur J Radiol. 2012;81 Suppl 1:S45–7.
8. Tagliafico A, Rescinito G, Monetti F, Villa A, Chiesa F, Fisci E, et al. Diffusion tensor magnetic resonance imaging of the normal breast: reproducibility of DTI-derived fractional anisotropy and apparent diffusion coefficient at 3.0 T. Radiol Med. 2012;117(6):992–1003.
9. Froeling M, Nederveen AJ, Nicolay K, Strijkers GJ. DTI of human skeletal muscle: the effects of diffusion encoding parameters, signal-to-noise ratio and T2 on tensor indices and fiber tracts. NMR Biomed. 2013;26(11):1339–52.
10. Jaimes C, Darge K, Khrichenko D, Carson RH, Berman JI. Diffusion tensor imaging and tractography of the kidney in children: feasibility and preliminary experience. Pediatr Radiol. 2014;44(1):30–41.
11. Notohamiprodjo M, Dietrich O, Horger W, Horng A, Helck AD, Herrmann KA, et al. Diffusion tensor imaging (DTI) of the kidney at 3 tesla-feasibility, protocol evaluation and comparison to 1.5 Tesla. Invest Radiol. 2010;45(5):245–54 [Comparative Study].

12. Kim CK, Jang SM, Park BK. Diffusion tensor imaging of normal prostate at 3 T: effect of number of diffusion-encoding directions on quantitation and image quality. Br J Radiol. 2012;85(1015):e279–83 [Comparative Study].
13. Gurses B, Kabakci N, Kovanlikaya A, Firat Z, Bayram A, Ulug AM, et al. Diffusion tensor imaging of the normal prostate at 3 Tesla. Eur Radiol. 2008;18(4): 716–21.
14. Fiocchi F, Nocetti L, Siopis E, Curra S, Costi T, Ligabue G, et al. In vivo 3 T MR diffusion tensor imaging for detection of the fibre architecture of the human uterus: a feasibility and quantitative study. Br J Radiol. 2012;85(1019):e1009–17.
15. Verhoeven JS, Sage CA, Leemans A, Van Hecke W, Callaert D, Peeters R, et al. Construction of a stereotaxic DTI atlas with full diffusion tensor information for studying white matter maturation from childhood to adolescence using tractography-based segmentations. Hum Brain Mapp. 2010;31(3):470–86 [Research Support, Non-U.S. Gov't].
16. Lebel C, Gee M, Camicioli R, Wieler M, Martin W, Beaulieu C. Diffusion tensor imaging of white matter tract evolution over the lifespan. Neuroimage. 2012;60(1):340–52 [Research Support, Non-U.S. Gov't].
17. Kasprian G, Brugger PC, Weber M, Krssak M, Krampl E, Herold C, et al. In utero tractography of fetal white matter development. Neuroimage. 2008;43(2):213–24.
18. Huang H, Xue R, Zhang J, Ren T, Richards LJ, Yarowsky P, et al. Anatomical characterization of human fetal brain development with diffusion tensor magnetic resonance imaging. J Neurosci. 2009;29(13): 4263–73 [Research Support, N.I.H., Extramural Research Support, Non-U.S. Gov't].
19. Zhan J, Dinov ID, Li J, Zhang Z, Hobel S, Shi Y, et al. Spatial-temporal atlas of human fetal brain development during the early second trimester. Neuroimage. 2013;82:115–26 [Research Support, N.I.H., Extramural Research Support, Non-U.S. Gov't].
20. Deipolyi AR, Mukherjee P, Gill K, Henry RG, Partridge SC, Veeraraghavan S, et al. Comparing microstructural and macrostructural development of the cerebral cortex in premature newborns: diffusion tensor imaging versus cortical gyration. Neuroimage. 2005;27(3):579–86 [Comparative Study Research Support, N.I.H., Extramural Research Support, U.S. Gov't, P.H.S.].
21. Judas M. Prenatal development of the human fetal telencephalon. In: Prayer D, editor. Fetal MRI. Heidelberg, Germany: Springer; 2011. p. 81–146.
22. Huang H, Zhang J, Wakana S, Zhang W, Ren T, Richards LJ, et al. White and gray matter development in human fetal, newborn and pediatric brains. Neuroimage. 2006;33(1):27–38 [Research Support, N.I.H., Extramural].
23. Hüppi P. Diffusion tensor imaging in brain development. In: Jones DK, editor. Diffusion MRI: theory, methods, and applications. New York, NY: Oxford University Press, Inc.; 2010.
24. Lenroot RK, Giedd JN. Brain development in children and adolescents: insights from anatomical magnetic resonance imaging. Neurosci Biobehav Rev. 2006;30(6):718–29 [Review].
25. Dubois J, Dehaene-Lambertz G, Kulikova S, Poupon C, Huppi PS, Hertz-Pannier L. The early development of brain white matter: a review of imaging studies in fetuses, newborns and infants. Neuroscience. 2014; 276:48–71.
26. Faria AV, Zhang J, Oishi K, Li X, Jiang H, Akhter K, et al. Atlas-based analysis of neurodevelopment from infancy to adulthood using diffusion tensor imaging and applications for automated abnormality detection. Neuroimage. 2010;52(2):415–28 [Comparative Study Research Support, N.I.H., Extramural].
27. Brickman AM, Meier IB, Korgaonkar MS, Provenzano FA, Grieve SM, Siedlecki KL, et al. Testing the white matter retrogenesis hypothesis of cognitive aging. Neurobiol Aging. 2012;33(8):1699–715 [Research Support, N.I.H., Extramural Research Support, Non-U.S. Gov't].
28. Sullivan EV, Pfefferbaum A. DTI in aging and age-related neurodegenerative disorders. In: Jones DK, editor. Diffusion MRI: theory, methods and applications. New York: Springer; 2011.
29. Maillard P, Carmichael O, Harvey D, Fletcher E, Reed B, Mungas D, et al. FLAIR and diffusion MRI signals are independent predictors of white matter hyperintensities. AJNR Am J Neuroradiol. 2013;34(1):54–61 [Research Support, N.I.H., Extramural Research Support, Non-U.S. Gov't].
30. Fazekas F, Schmidt R, Scheltens P. Pathophysiologic mechanisms in the development of age-related white matter changes of the brain. Dement Geriatr Cogn Disord. 1998;9 Suppl 1:2–5 [Review].
31. de Groot M, Verhaaren BF, de Boer R, Klein S, Hofman A, van der Lugt A, et al. Changes in normal-appearing white matter precede development of white matter lesions. Stroke. 2013;44(4):1037–42 [Research Support, Non-U.S. Gov't].
32. Bartzokis G, Tishler TA, Lu PH, Villablanca P, Altshuler LL, Carter M, et al. Brain ferritin iron may influence age- and gender-related risks of neurodegeneration. Neurobiol Aging. 2007;28(3):414–23 [Comparative Study Research Support, N.I.H., Extramural Research Support, Non-U.S. Gov't Research Support, U.S. Gov't, Non-P.H.S.].
33. Pfefferbaum A, Adalsteinsson E, Rohlfing T, Sullivan EV. Diffusion tensor imaging of deep gray matter brain structures: effects of age and iron concentration. Neurobiol Aging. 2010;31(3):482–93 [Research Support, N.I.H., Extramural].
34. Chang LC, Walker L, Pierpaoli C. Informed RESTORE: a method for robust estimation of diffusion tensor from low redundancy datasets in the presence of physiological noise artifacts. Magn Reson Med. 2012;68(5):1654–63 [Research Support, N.I.H., Intramural Research Support, U.S. Gov't, Non-P.H.S.].
35. Gholipour A, Kehtarnavaz N, Scherrer B, Warfield SK. On the accuracy of unwarping techniques for the

correction of susceptibility-induced geometric distortion in magnetic resonance Echo-planar images. Conf Proc IEEE Eng Med Biol Soc. 2011;2011:6997–7000 [Research Support, N.I.H., Extramural].
36. Vos SB, Jones DK, Viergever MA, Leemans A. Partial volume effect as a hidden covariate in DTI analyses. Neuroimage. 2011;55(4):1566–76 [Research Support, Non-U.S. Gov't].
37. Cook PA, Symms M, Boulby PA, Alexander DC. Optimal acquisition orders of diffusion-weighted MRI measurements. J Magn Reson Imaging. 2007;25(5):1051–8 [Research Support, Non-U.S. Gov't].
38. Dubois J, Poupon C, Lethimonnier F, Le Bihan D. Optimized diffusion gradient orientation schemes for corrupted clinical DTI data sets. MAGMA. 2006;19(3):134–43 [Evaluation Studies].
39. Thorpe S, Salkovskis PM, Dittner A. Claustrophobia in MRI: the role of cognitions. Magn Reson Imaging. 2008;26(8):1081–8.
40. Grey SJ, Price G, Mathews A. Reduction of anxiety during MR imaging: a controlled trial. Magn Reson Imaging. 2000;18(3):351–5 [Clinical Trial Controlled Clinical Trial Research Support, Non-U.S. Gov't].
41. Raschle N, Zuk J, Ortiz-Mantilla S, Sliva DD, Franceschi A, Grant PE, et al. Pediatric neuroimaging in early childhood and infancy: challenges and practical guidelines. Ann N Y Acad Sci. 2012;1252:43–50 [Research Support, Non-U.S. Gov't Review].
42. Farquharson S, Tournier JD, Calamante F, Fabinyi G, Schneider-Kolsky M, Jackson GD, et al. White matter fiber tractography: why we need to move beyond DTI. J Neurosurg. 2013;118(6):1367–77 [Case Reports Comparative Study Research Support, Non-U.S. Gov't].
43. Bello L, Gambini A, Castellano A, Carrabba G, Acerbi F, Fava E, et al. Motor and language DTI Fiber Tracking combined with intraoperative subcortical mapping for surgical removal of gliomas. Neuroimage. 2008;39(1):369–82 [Clinical Trial Research Support, Non-U.S. Gov't].
44. Illes J, Kirschen MP, Edwards E, Bandettini P, Cho MK, Ford PJ, et al. Practical approaches to incidental findings in brain imaging research. Neurology. 2008;70(5):384–90 [Research Support, N.I.H., Extramural Research Support, Non-U.S. Gov't Review].
45. Rangel EK. The management of incidental findings in neuro-imaging research: framework and recommendations. J Law Med Ethics. 2010;38(1):117–26.
46. Brakewood B, Poldrack RA. The ethics of secondary data analysis: considering the application of Belmont principles to the sharing of neuroimaging data. Neuroimage. 2013;82:671–6.
47. Polders DL, Leemans A, Hendrikse J, Donahue MJ, Luijten PR, Hoogduin JM. Signal to noise ratio and uncertainty in diffusion tensor imaging at 1.5, 3.0, and 7.0 Tesla. J Magn Reson Imaging. 2011;33(6):1456–63.
48. Mukherjee P, Chung SW, Berman JI, Hess CP, Henry RG. Diffusion tensor MR imaging and fiber tractography: technical considerations. AJNR Am J Neuroradiol. 2008;29(5):843–52 [Review].
49. Maclaren J, Herbst M, Speck O, Zaitsev M. Prospective motion correction in brain imaging: a review. Magn Reson Med. 2013;69(3):621–36 [Research Support, Non-U.S. Gov't Review].
50. Mori S, Crain BJ, Chacko VP, van Zijl PC. Three-dimensional tracking of axonal projections in the brain by magnetic resonance imaging. Ann Neurol. 1999;45(2):265–9 [Research Support, Non-U.S. Gov't].
51. Burgel U, Madler B, Honey CR, Thron A, Gilsbach J, Coenen VA. Fiber tracking with distinct software tools results in a clear diversity in anatomical fiber tract portrayal. Cent Eur Neurosurg. 2009;70(1):27–35 [Case Reports Research Support, Non-U.S. Gov't].

DTI in Neurosurgical Planning

14

Ronald L. Wolf, Paolo G. Nucifora,
and Elias R. Melhem

Learning Points

- Functional MRI provides information regarding cortical function, but DTI provides complementary information about important subcortical structures and may thus have utility in neurosurgical and radiotherapeutic planning when applied correctly.
- Neurosurgical application of DTI has special challenges, including the effects of pathophysiology and intraoperative procedures on fiber pathways as well as the integration of DTI data with other modalities in neuronavigation software.
- Standard deterministic DTI tractography may not be the most reliable method to map eloquent fiber pathways and alternative approaches such as HARDI should be considered in neurosurgical applications.

R.L. Wolf, MD, PhD (✉) • P.G. Nucifora, MD, PhD
Neuroradiology Section, Department of Radiology,
University of Pennsylvania Medical Center,
3400 Spruce St., Philadelphia, PA 19104, USA
e-mail: Ronald.Wolf@uphs.upenn.edu

E.R. Melhem, MD, PhD
Department of Diagnostic Radiology and Nuclear
Medicine, University of Maryland Medical Center,
Baltimore, MD, USA

Introduction

While noninvasive and invasive cortical and subcortical electrophysiologic measurements for clinical mapping of brain function have been available for decades [1], multiple noninvasive techniques are now increasingly available for routine neurosurgical planning. These include cortical mapping using magnetoencephalography (MEG) and BOLD functional magnetic resonance imaging (fMRI) and subcortical mapping using diffusion-based methods such as diffusion tensor imaging (DTI). Intraoperative electrophysiologic mapping remains the gold standard for most applications, but limitations do exist including intraindividual and interindividual variability and inaccuracy from penetration of current; and thus, noninvasive mapping provides at least complementary information [2–4]. The purpose of this chapter is to focus on practical aspects of DTI in neurosurgical planning.

Role of DTI in Neurosurgical Planning

DTI methods provide not only microstructural information on local cellular environment and organization, but also macrostructural information regarding white matter tracts and connections between important cortical and subcortical functional regions in the brain.

W. Van Hecke et al. (eds.), *Diffusion Tensor Imaging*, DOI 10.1007/978-1-4939-3118-7_14

Microstructural elements including cellularity, intraaxonal organization and fiber density, myelination, and fiber diameter combine with macrostructural organization of fibers to affect diffusion anisotropy, the basis for the color fractional anisotropy (FA) and tractography maps primarily used in neurosurgical planning. The color FA maps provide a 3D image data set showing direction and degree of anisotropy on a voxel by voxel level, while fiber tractography (FT) depicts likely "connections" from voxel to voxel and thus from one region (or regions) of the brain to another. It is important to remember that visualization strategies create virtual tracts and do not represent nerves or real fibers, but these can be used to provide a macrostructural guide for preoperative planning and intraoperative navigation [5–10] and for the purpose of the chapter will be collectively referred to as DTI FT. Currently, this and other techniques based on diffusion (e.g., high-angular resolution diffusion MRI-HARDI-techniques) are the only means to perform in vivo, noninvasive localization of important white matter tracts. There is growing evidence supporting the role of fMRI and fiber tracking in the presurgical setting not only for formulating a surgical plan but also with regard to safety, postsurgical treatment and outcome.

Prevention of Injury to Eloquent WM Pathways

There is enough interindividual anatomic variation such that standard landmarks are not always reliable for motor or language functional cortex [11, 12], hence the need for preoperative mapping. Primary goals are to determine feasibility of resection and to maximize extent of resection while avoiding injury to eloquent cortical and subcortical structures. To visualize a tract of interest with DTI FT, a region or volume of interest (ROI) is chosen as the origin (seed) and typically combined with additional inclusion (target, 'AND') and exclusion (non-target, 'OR') ROIs. Activation maps from fMRI can be incorporated to improve specificity, which is particularly helpful when mass effect distorts anatomy of cortical or subcortical structures such that standard landmarks are obscured [13, 14]. If fMRI fails, in some cases DTI can provide sufficient information to localize functional cortex [15] (Figs. 14.1 and 14.2). The anatomy of subcortical white matter tracts is of course very complex, but there are

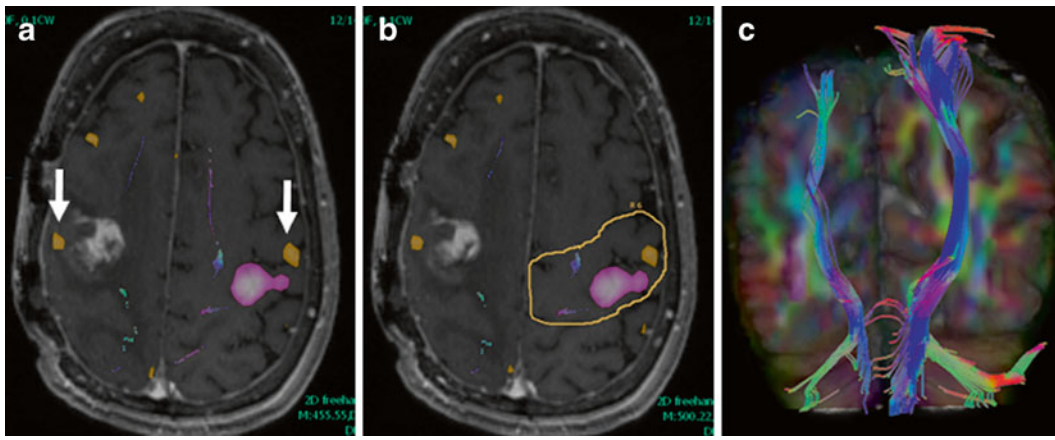

Fig. 14.1 Corticospinal tract (CST) mapping with fMRI guidance. Seed ROIs in the cerebral peduncles showed multiple fiber tracts in addition to CST, left more than right. Hand (*magenta*) and face (*orange*) activation maps (**a** and **b**, enhanced T1 images) were used to select an inclusion ROI around sensorimotor cortex. The patient could not move their left hand and no hand activation was elicited, but face motor activation was identified in the right hemisphere (*arrows*). A generous ROI similar to that in (**b**) was chosen for both sides, showing left greater than right CST tracking (**c**, 3D cut plane view). Lower extremity function was still partially intact at this time, and the ROI included this cortical region as well (fMRI not shown)

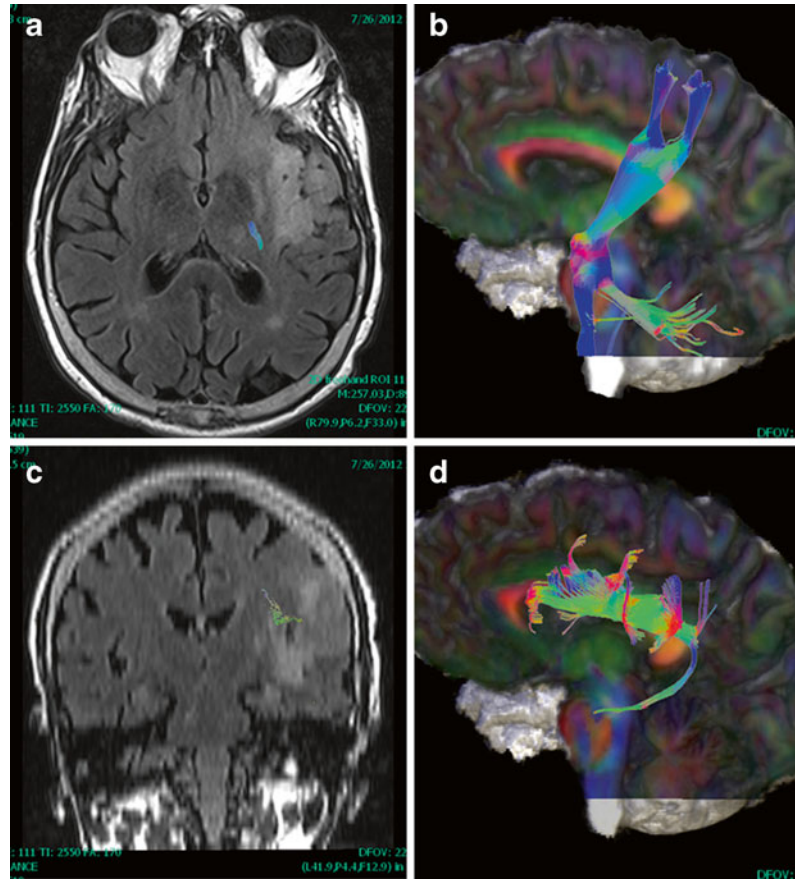

Fig. 14.2 Corticospinal tract (CST) and superior longitudinal fasciculus (SLF). For a patient with gliomatosis, fMRI failed because the tumor interfered with language such that the patient could not follow commands, even for motor tasks; however, fiber tracking was adequate. Left CST (**a**, **b**) and SLF (**c**, **d**) are shown on FLAIR (**a**, **c**) and 3D cut plane views (**b**, **d**)

three main categories: association, projection, and commissural. This chapter focuses on association (language) and projection (motor and vision) pathways.

Motor

Preservation of motor function is critical and mapping of the corticospinal (pyramidal) tract (CST) and motor cortex is most commonly requested. There are multiple reports of its utility in preoperative planning [13, 16–20]. If pathology has not sufficiently altered the tract, basic single tensor DTI FT for the CST in general works well for trunk and in some cases hand and lower extremity; however, it is less successful for cortical regions like the face because intervening tracts like the SLF interfere with continuous tracking in critical voxels due to crossing fibers in these locations. Some detail in somatotopic mapping is possible [6, 13]. Yamada et al. [21] used cortical ROIs for lower extremity, trunk, hand, face, and tongue and found robust tracking only for the trunk with a single tensor approach while a HARDI-based multitensor approach was more successful in tracking for other cortical regions including face and tongue. Techniques such as HARDI will be required if detailed somatotopic mapping is desired [3, 21].

Multiple studies have addressed validation of cortical and subcortical motor mapping with DTI FT [3, 15, 22–24]. Berman et al. [22] used seed points identified during intraoperative stimulation mapping (ISM) to retrospectively map ipsilateral CST in 11 glioma patients using the preoperative imaging data after the surgery was complete. Though not used for surgery, they showed appropriate tracking to the central cerebral peduncle based on the seed points verified intraoperatively; however, there were some failures in tracking depending on the extent of pathologic alterations in or near the CST. Kamada et al. reported studies confirming CST mapping

with subcortical [23] and cortical mapping [15]. The latter included 30 patients with lesions in proximity to the motor system, with central sulcus and sensorimotor cortex identified using DTI FT and verified with intraoperative cortical somatosensory evoked potential (SEP) measurements. Functional MRI or MEG identification of primary motor cortex failed in nine patients while DTI FT was successful in all.

Accuracy of CST localization with DTI FT compared with subcortical stimulation appears to be within 10 mm [3, 24, 25]. Berman et al. [3] reported a mean distance of 8.7 mm (±3.1 mm standard deviation) for 16 sites in 9 patients. Mikuni et al. [24] found consistent motor evoked potentials (MEP) at 7 mm or less and absent MEP over 13 mm when stimulating near the mapped CST fibers at the inferior aspect of the mass. Between 8 and 12 mm, stimulation near the mapped CST at the level of the corona radiata consistently elicited MEPs. Another study of 40 patients with masses within 2 cm of CST found MEPs elicited at less than 1 cm from mapped CST in 18 of 21, negative MEPs in 5 at stimulation points greater than 2 cm, and negative MEPs in 12 of 15 at 1–2 cm from mapped CST [26]. Motor function was ultimately preserved in all, improved in five cases with weakness prior to surgery, and two of the cases with negative MEP at 1–2 cm distance developed SMA syndrome, which subsequently resolved.

Other studies have also addressed impact on surgical plan and/or outcomes [16, 25, 27–31], in general with preserved or improved clinical function postoperatively. Bello et al. [27] reported high correlation of DTI FT for CST (and multiple language tracts) with intraoperative subcortical mapping (ISM). With low grade gliomas, fibers tracking through the neoplasm were often found. A combination of DTI FT and ISM decreased surgery time, patient fatigue and intraoperative seizure rate.

With increased extent of resection, postoperative deficits have been reported to increase transiently but with improvement over time [25, 32, 33]. The concept of a safety margin of about 5–10 mm has been introduced, but with careful intraoperative mapping this boundary may be minimized [32]. In a prospective randomized study by Wu et al. [30], 238 patients with suspected primary supratentorial glioma (214 ultimately proven gliomas) not previously treated and near the pyramidal tract with at least 1/5 motor strength were randomized to surgery with conventional neuronavigation versus neuronavigation with integrated DTI data. Only FA maps were used for intraoperative mapping, although in the later stages of the study tractography was added for preoperative planning and postoperative assessment (23 of the cases). Those in the neuronavigation plus DTI group were more likely to have complete resection of high grade tumors (74.4 % vs. 33.3 %), although low grade gliomas had similar extent of resection. Decline in motor function postoperatively was less likely overall (15.3 % versus 32.8 %) and 6 month Karnofsky scores were better (86 ± 20 vs. 74 ± 28). They also reported improved survival for high grade gliomas (21.2 months vs. 14.0 months).

Vision and Language

The optic radiations (OR) and in particular Meyer's loop pose difficulties for DTI FT. Problems include not only the anatomy with tight turns, but location along medial temporal lobe where susceptibility-related artifacts can affect image quality with DTI sequences using EPI [34, 35]. Crossing fibers can create problems here as elsewhere. There are early reports using DTI FT to map visual pathways with integrity of OR on DTI FT linked to deficits pre- and/or postoperatively [29, 35–38], and intraoperative correlation also described in at least one case [36]; however, results remain preliminary and further validation is required and caution warranted in this setting [35].

Validation of language tractography is also ongoing and though reports are less extensive than for CST mapping, experience is growing. Co-localization with intraoperative mapping seems to be similar to CST; that is, distance between DTI FT prediction and subcortical mapping is in the range of 5–10 mm. For example, Kamada et al. [39] studied 22 lesions near the superior longitudinal/arcuate fasciculus (SLF/

AF) in the dominant hemisphere, using fMRI or MEG to choose seed and target ROIs. For two of these cases, functional mapping was integrated into neuronavigation and validated by cortical and subcortical mapping during awake surgery with stimulation near AF leading to paranomia without speech arrest at a distance of 6 mm. Leclercq et al. [40] studied multiple language tracts in ten patients with low grade gliomas or dysplasia, reporting positive subcortical stimulation responses 6 mm or less from DTI FT prediction in 81 %, but they also reported four false negative results (positive stimulations away from any mapped fiber tract). Of course, understanding of language functional cortical regions and connections remains incomplete, and important fiber tracts not anticipated and thus not mapped are considerations as well [41].

False positives for DTI FT based on subcortical mapping have also been described [27], with DTI FT mapping of SLF larger than identified on subcortical mapping in some cases such that ISM did not evoke a response in some tracked fibers, and there were also false negatives in this study which could be addressed in part by adjusting ROI placement. For low grade gliomas, tracts could be identified within the neoplasm and in some cases ISM evoked a response within the mass even when tracts appeared interrupted. IFOF and UF were also evaluated in this study. The majority of patients where motor or language tracts were identified with ISM had decline immediately after surgery, in general improving after 1 week (about 90 % normal at 1 month).

Zhao et al. [42] used preoperative as well as intraoperative DTI FT for the SLF/AF in 20 patients, 9 of which had no preoperative deficit and 11 with variable conduction aphasia. They monitored intraoperative shifts of the tract from −5 to 2 mm. After surgery, follow up within 1 month revealed one previously normal patient with new conduction aphasia while those with language deficit had improved. Many of the studies discussed here have integrated DTI FT data with neuronavigation systems, but not all scenarios necessarily require it. Review of preoperative data may be sufficient for confirming or altering an operative approach. Powell et al. [43] used a probabilistic fiber tracking method for hemisphere dominance prior to anterior temporal lobe resection, finding a significant correlation between frontotemporal tract lateralization to dominant hemisphere resections and postoperative naming deficits. Romano et al. [29] performed tractography for CST, OR, and AF in 25 patients, and for 35 of 75 tracts analyzed which were in proximity to a given neoplasm reported a change in surgical plan in 16 % and a change in extent of resection in 68 %.

Reduction in Radiation Damage to Eloquent WM Pathways

The concepts for sparing eloquent structures in surgery extend also to radiosurgery and to an extent to other therapeutic radiation strategies. Koga et al. [44] for example integrated tractography for CST, OR, and AF with navigation for AVM Gamma Knife radiosurgery in 71 of 155 treatments for 144 patients, optimizing dose such that the maximum dose to CST, OR, and AF was 20 Gy, 8 Gy, and 8 Gy respectively. Of the 71/155 treatments planned with this approach, 60 % had less than 5 mm separation from these WM tracts. Maruyama [45] integrated tractography for OR with navigation in ten patients receiving Gamma Knife near OR, reporting 8 Gy or more single dose to be associated with neurological changes such as visual field deficit and new (or improved) migraine symptoms. Another study included 24 patients (9 retrospective and 15 prospective) [46], reporting maximum dose to CST of 23 Gy with 5 % complication risk and 20 Gy and 25 Gy volumes for 5 % complication risk were 58 mm^3 and 21 mm^3, respectively.

There is also an interest in using DTI metrics for microstructural assessment not only to estimate extent of infiltration [47–50] but also to improve accuracy in diagnosis, assess grade or prognosis, evaluate treatment response, and potentially predict recurrence patterns. Jena et al. [48] described the use of a DTI-based "high risk volume" or IHV_{DTI} which allowed a 35 % reduc-

tion in planning target volume and a dose escalation such that complications did not exceed conventional plan.

Targeted DBS Electrode Placement

Conventional imaging is often inadequate for visualization of important functional anatomy; for example, the subthalamic nucleus (STN) is difficult to demonstrate with high image contrast and targeting is not trivial [51]. DTI data can be used to improve localization of functional anatomy relevant to deep brain stimulation (DBS) placement. Simple integration of color FA maps has been utilized to augment identification of STN and globus pallidus interna (GPi)targets [52].

Other studies have shown proof of concept for use of DTI FT in this setting. Pouratian et al. [53] retrospectively studied cases where DBS had been placed using traditional methods for tremor control. The procedure was efficacious in 11/12 electrodes placed (six patients), and postoperative CT or MR fused with preoperative probabilistic tractography for thalamic voxel connectivity to primary, premotor, and prefrontal cortex showed thalamic sites with connectivity to premotor and supplemental motor regions were most efficacious in controlling tremor. A postoperative study of white matter tracts in proximity to leads placed in GPi, STN, and ventral intermediate nucleus (VIM) was useful in understanding side effects related to stimulator setting [54]. Tracts of interest in proximity to these targets included motor, premotor, supplemental motor, and frontal eye fields. Coenen et al. [55] also used a retrospective approach for DTI FT, showing unilateral refractory tremor control in a patient with Parkinson disease with DBS placement involving the dentate-rubral-thalamic tract (DRT), subsequently prospectively targeting the DRT for DBS implantation bilaterally with excellent control of head tremor in a patient with myoclonus dystonia [56]. Other fields of interest where tractography may be potentially useful in this setting include neuropsychiatric problems [57, 58] including OCD and depression [59, 60], headache and chronic pain [61, 62].

Practical Considerations in Neurosurgery

Clinical Implementation

Image Acquisition and Postprocessing

There are multiple sources of potential image degradation related to patient and technique. Bulk and physiologic motion including cardiac and respiratory can degrade image quality. Additionally, the imaging sequence typically used (single shot spin echo EPI) has limitations which include eddy current distortion, mechanical vibrations related to large amplitude and rapidly switching gradients, Nyquist ghosting, chemical shift, magnetic field inhomogeneity, local susceptibility effects near bone and paranasal sinus interfaces, and limitations in spatial resolution and SNR [9]. Pathologic and postsurgical changes can also be problematic (e.g., hemorrhage and surgical hardware). There are strategies for solving or at least minimizing these problems including fat saturation techniques, cardiac gating, parallel imaging, and phased array coils. Improvements in image quality need to be balanced with the need for efficient implementation in this clinical setting such that data are adequate for presurgical planning but acquisition or processing times do not exceed a patient's ability to cooperate or a clinician's ability to obtain processed data integrated with other imaging data for surgical planning and intraoperative navigation.

An example of a standard acquisition at 3 T is provided in Table 14.1. While at least six diffusion encoding directions plus one baseline ($b=0$ s/mm^2 or low b-value) are needed to generate the diffusion tensor, a minimum of 30 directions are recommended for good quality DTI in this setting with at least 3–6 low-b acquisitions if possible [9, 63]. Acquisition time under 10 min is a reasonable target for integration into a full planning protocol and for patient compliance. Cardiac gating is not routinely used at our institution due to increased scan time, but this can improve image quality [64]. Small isotropic voxels with no gaps between imaging sections, on the order of 2 mm at 3 T, helps minimize partial volume effects and thus extent of crossing fibers in a given voxel [9].

Table 14.1 Sample DTI parameters at 3 T

Resolution (mm)	1.72 × 1.72 × 3.0[a]
Matrix	128
FOV (cm)	22 cm
Encoding directions	30 (plus baseline)
NEX	2–3
b-value (s/mm^2)	1000
TR/TE	5000/86 ms
Acquisition time	8 min
Parallel imaging acceleration	2

[a]Isotropic voxels may be better for multiplanar reformatting of tractography, e.g., on the order of 2 mm for 3 T or 2.5 mm for 1.5 T [9], but acquisition time and coverage will need to be balanced

Post-processing may include motion correction and eddy current distortion as well as registration with structural imaging data. Post-processed DTI data include scalar and directional data which can be used for fiber tracking, usually with a fiber assignment by continuous tracking (FACT) approach (most of the vendor supplied algorithms currently in use are based on this strategy). At least one "seed" ROI must be chosen, but typically at least one seed and target (inclusion) ROI are most commonly used (see below). Additional inclusion or exclusion ROIs are useful to minimize stray tracked fibers. Typical starting FA thresholds might be greater than 0.1–0.15 and turning angle less than 40–70°, and these can be adjusted for optimal display of desired tracts.

Preparation of multiple fiber tracts can be time-consuming and requires an understanding of neuroanatomy. A knowledgeable support staff is needed. Judicious selection of fiber tracts chosen and displayed for intraoperative navigation is important; for example, some navigation software can display only binary imported tract maps and though independent colors can be assigned, the amount of information can become confusing and counterproductive. Another approach is to generate all tracts based on a chosen threshold FA and curvature around the anatomic region of interest with subsequent selection of specific tracts of interest using ROIs [9]. Automated or semiautomated fiber tracking strategies are not routinely used for preoperative planning, but a technique allowing atlas-based segmentation would be of obvious utility for preoperative or radiation planning [65].

Both color FA maps and tractography should be used in interpretation [66, 67]. FA maps can be more reliable in proximity to a mass distorting local anatomy, while tractography is helpful for visualizing major tracts travelling in proximity to each other though less successful and potentially misleading when anatomy is substantially distorted and/or when anisotropy is altered such that fibers can no longer be tracked [68] (Fig. 14.3). Some institutions currently integrate only the color FA map for intraoperative navigation.

Incorporation into Navigation Software for Multimodal Data

Functional MRI, MEG and DTI with or without tractography are complementary techniques for assessing feasibility and extent of resection, predicting risk, and planning operative approach and they are also helpful intraoperatively for shortening cortical and subcortical intraoperative mapping times [68–70]. Many of the studies using DTI and/or tractography in preoperative planning discussed so far have also integrated results into neuronavigation systems prospectively, and while not yet universal across institutions this is becoming more widespread as validation improves. Tractography can show variable results with different software packages and with differences in user selection of tracking ROIs [66, 71], and of course pathology in and around a brain neoplasm can also lead to suboptimal or failed fiber tracking.

DTI and fMRI data can be integrated into commonly used navigation packages, in some instances the DTI/tractography software is integrated with the navigation software. In our current implementation, fMRI and DTI/tractography data are processed separately and functional activation maps and selected fiber tracts are uploaded to the navigation computer in DICOM format pre-registered with structural images, but there are many possible solutions which can be customized for each institution's needs (Fig. 14.4).

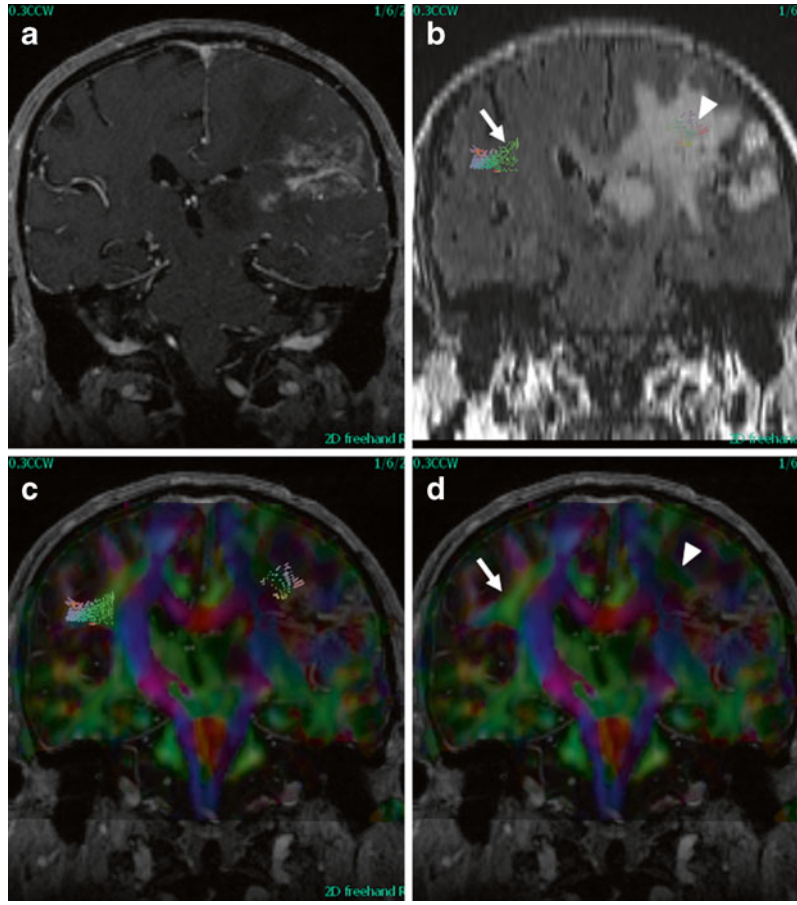

Fig. 14.3 Fiber tracking and color fractional anisotropy (FA) maps. Coronal enhanced T1 (**a**), reformatted FLAIR (**b**), and color FA maps with and without superior longitudinal fasciculus (SLF) tracts displayed (**c**, **d**). Fiber tracking on left was incomplete and did not extend anterior to enhancing mass, color FA maps show decreased intensity and loss of directional information (**d**, *arrowhead*) compared to normal hemisphere (**d**, *arrow*)

Clinical Examples

Atlases of white matter tracts including proposed ROIs for tract generation are available [72–75]. These only provide guidelines since factors such as location and size of mass, degree of infiltration or destruction of fibers, presence of blood products or surgical hardware causing susceptibility, motion, or other factors affecting image quality may necessitate one or more approaches for a given patient. Alternatively, tractography may have to be abandoned if inadequate or potentially misleading.

Corticospinal (Pyramidal) Tract

A simple approach is to choose a seed ROI in the cerebral peduncle and display all tracts passing through this region. Other fiber tracts will be incorporated including thalamocortical fibers and other tracts in proximity in the peduncle, so increased specificity can be accomplished by using inclusion ROIs in the posterior limb of the internal capsule and/or subcortical ROIs in proximity to the precentral gyrus based on standard neuroanatomic landmarks. Alternatively, one may choose seed ROIs adjacent to the precentral gyrus and use inclusion ROIs corresponding to the posterior limb of the internal capsule (PLIC) and/or cerebral peduncle. Unwanted fibers can be further eliminated by choosing inclusion or exclusion ROIs above and/or below the tentorium.

Mapping of the CST is most frequently requested since preservation of motor function is paramount. Depending on extent of fiber disruption and where it occurs, motor impairment can be devastating and also more enduring than at the cortical level. The basic strategies outlined here are not sufficient for mapping the more lateral primary motor cortex for the face and sometimes

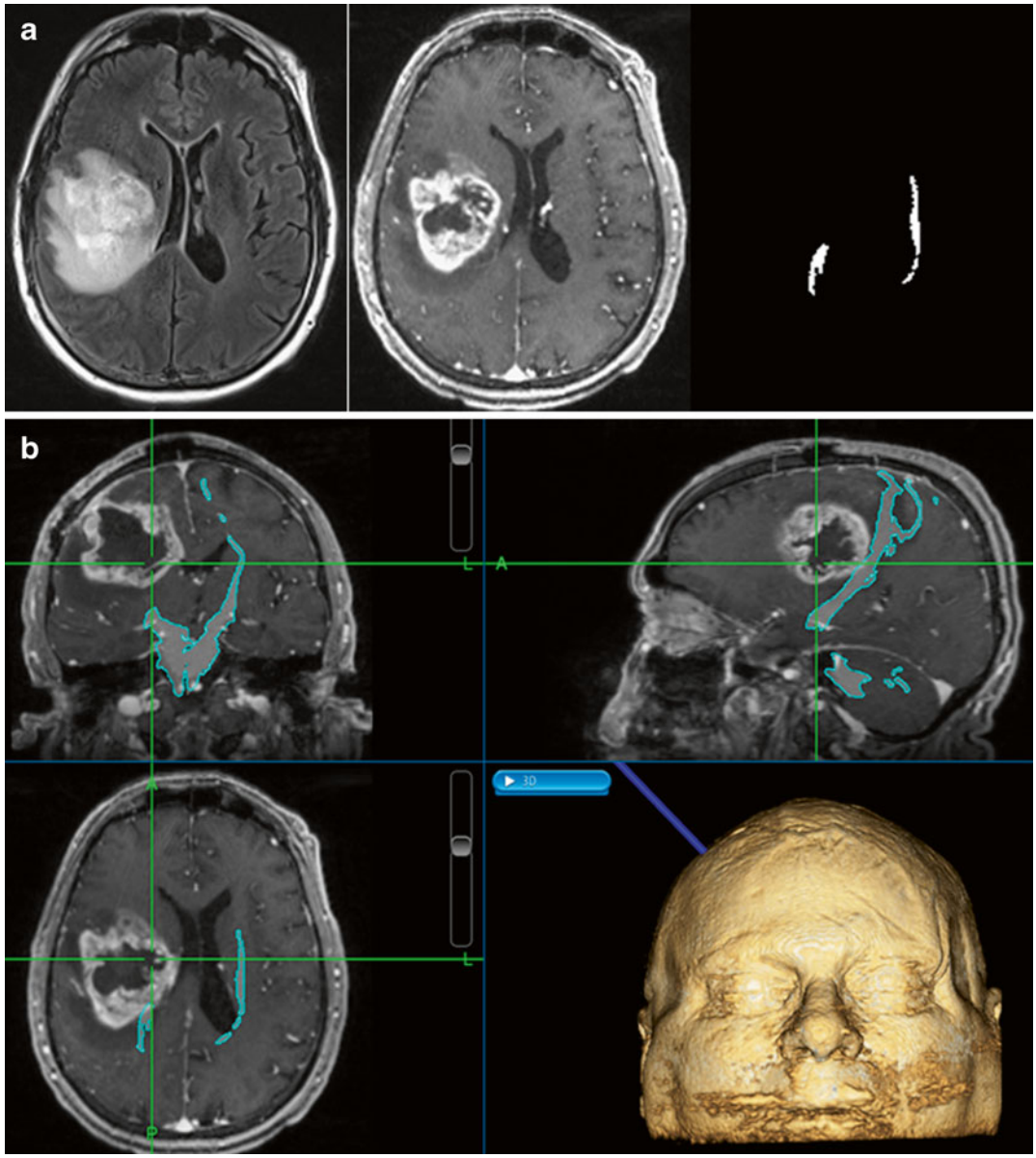

Fig. 14.4 Incorporation of fiber tracking into navigation software. Registered FLAIR, 3D T1 post-contrast and fiber bilateral corticospinal tract masks (**a**) were uploaded to the intraoperative navigation computer (**b**). Fiber tracts were less selective in this case to show cut-off anteriorly near the enhancing mass, a glioblastoma. The patient had facial paralysis on the left, but upper and lower extremity motor function was intact (although there was left upper extremity numbness)

for the hand and foot, but is usually robust for fiber tracking corresponding to the locus for trunk. Better tracking can ultimately be obtained with more complex techniques with longer acquisitions such as HARDI. The primary goal is to preserve contralateral motor function and so the focus here was on the CST, but of course other important tracts pass through the internal capsule in the anterior limb, the genu as well as in the PLIC (e.g., thalamocortical sensory fibers intermingle and are tracked with motor fibers). Other deficits may also occur with injuries to PLIC near the CST, including sensory deficits and ataxia [72] (Fig. 14.5).

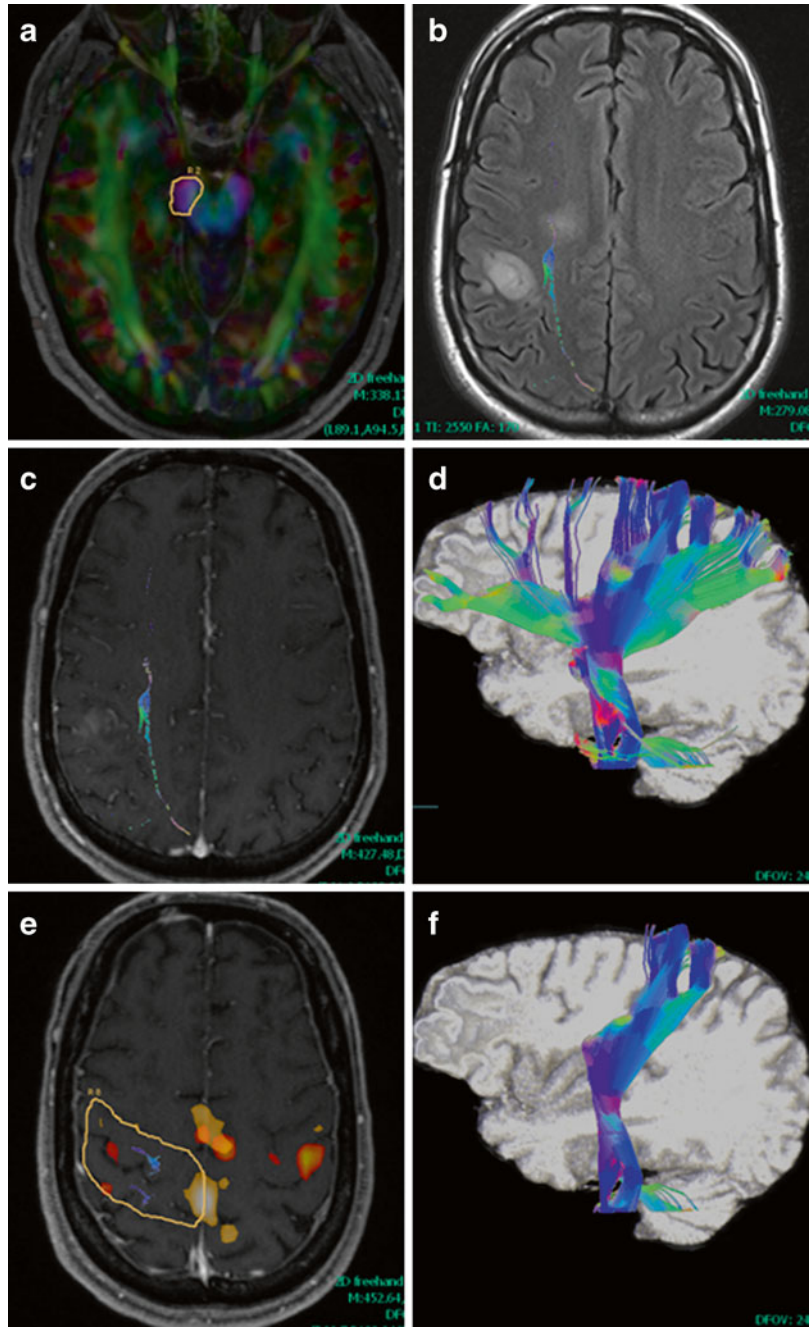

Fig. 14.5 Corticospinal tract (CST). A seed ROI was chosen to include the cerebral peduncle (**a**), leading to multiple fiber tracts in addition to CST displayed (**b**, **c** FLAIR and T1 post-contrast and **d**, 3D cut plane view). Fibers pass between nonenhancing (anteromedial) and enhancing (posterolateral) parts of a multicentric glioblastoma (**b**, **c**). An inclusion ROI chosen based on fMRI (**e**) around precentral and postcentral gyri was used in this case, resulting in (**f**). For the fMRI in (**e**), the *red*/*yellow* color scale corresponds to hand motor activation (weaker in right precentral gyrus) and *orange*/*white* corresponds to left foot tapping. Both tasks show supplemental motor area as well

Superior Longitudinal/Arcuate Fasciculus

Though not strictly accurate, SLF and AF are commonly used to represent the same fiber tract(s) linking frontal, parietal and temporal perisylvian cortex, and for the purposes of this chapter they are used interchangeably. Typically one triangular ROI places on coronal views is sufficient (Fig. 14.6), though specificity and image quality can be improved by adding a target or inclusion ROI. Disruption of this tract in the dominant hemisphere may lead to not only con-

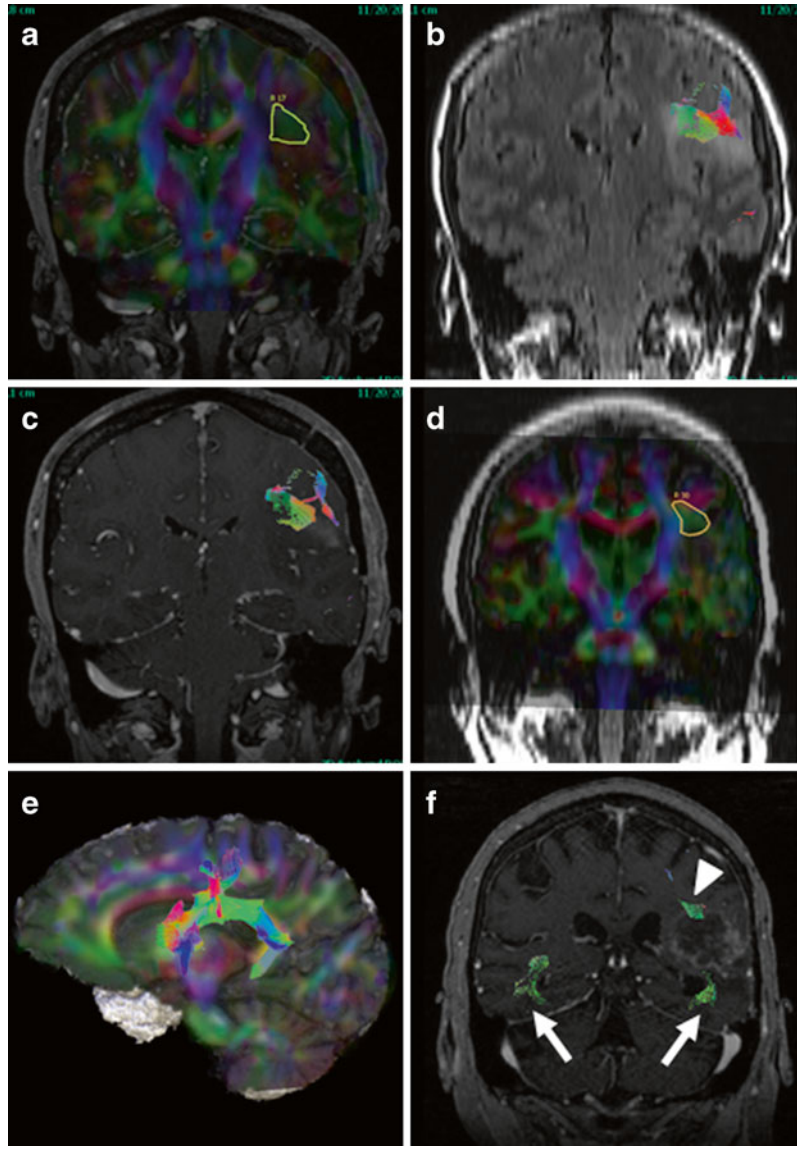

Fig. 14.6 Superior longitudinal fasciculus (SLF). Two cases are shown, one patient with anaplastic astrocytoma (AA, **a-c**) and the other patient with breast cancer metastasis after whole brain radiation and subsequent stereotactic radiosurgery now with primarily treatment related necrosis (TRN, **d-f**). Seed ROIs are shown for the left SLF in each case (**a**, **d**). For the patient with AA (**a-c**), decreased FA compared to contralateral side is noted (**a**), likely reflecting infiltration of SLF fibers by the neoplasm. Fiber tracking was suboptimal anterior and posterior to the mass. For the patient with TRN (**d-f**), color FA in SLF is more symmetric and tracking was more complete (**e**, 3D cut plane view), but fibers of inferior longitudinal fasciculus (ILF) and inferior frontal occipital fasciculus (IFOF) were asymmetric (**f**, *arrows*). Both SLF and ILF/IFOF tracked in proximity to edge of enhancing mass (*arrowhead* and *arrow*, respectively)

duction aphasia but also other deficits including ideational apraxia [72]. In the nondominant hemisphere, injury to the SLF may result in contralateral neglect.

Inferior Longitudinal Fasciculus, Inferior Frontal Occipital Fasciculus

These can be seeded together from an ROI in the occipital region when tracts are intact, with inclusion ROIs in the mid temporal lobe and anterior frontal lobe for ILF and IFOF, respectively (Fig. 14.7). If this fails (e.g., extensive occipital lobe pathology), one could use seed ROIs in the mid temporal lobe and anterior frontal lobe instead, tracking posteriorly and using appropriate inclusion ROIs. Injury to the ILF may result in visual agnosia, alexia, and deficits in naming and visual memory. Examples of deficits related to the IFOF include semantic paraphasias and problems with visuospatial processing and visual recognition [72] (Figs. 14.7, 14.8, and 14.9).

Uncinate Fasciculus

The inclusionROI for the IFOF in the anterior frontal lobe can be used again as the target or as a

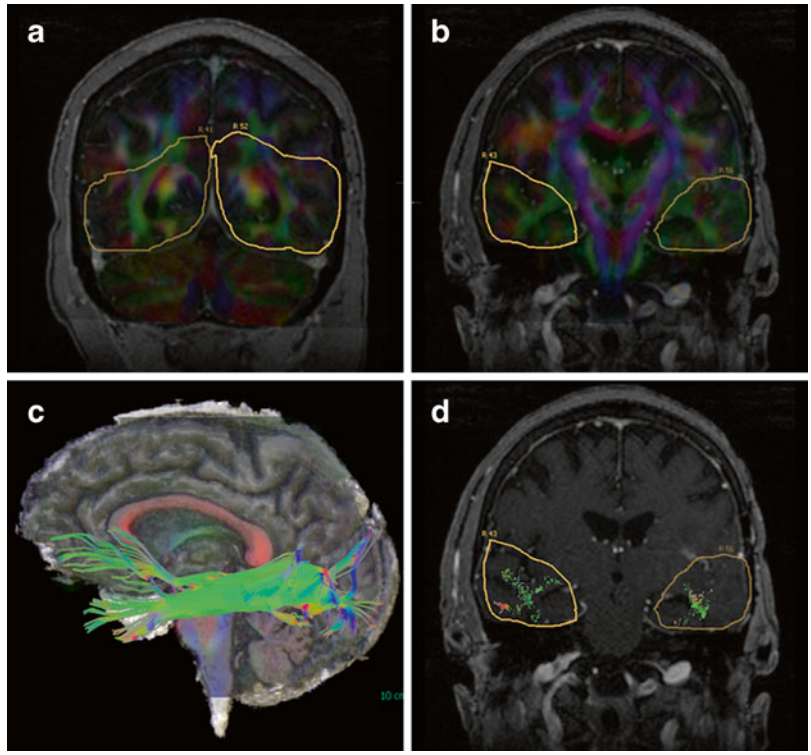

Fig. 14.7 Inferior longitudinal fasciculus (ILF) and inferior frontal occipital fasciculus (IFOF). For a patient with treatment related necrosis (TRN, same case as in Fig. 14.6, **d-f**), seed ROI was placed in the occipital lobe (**a**), with inclusion ROI in mid temporal lobe (**b**–**d**) to include both ILF and IFOF. Fibers of ILF and IFOF track together posteriorly and separate anteriorly, ROIs can be chosen to separate these (see below), but for practical neurosurgical implementation they can often be displayed together

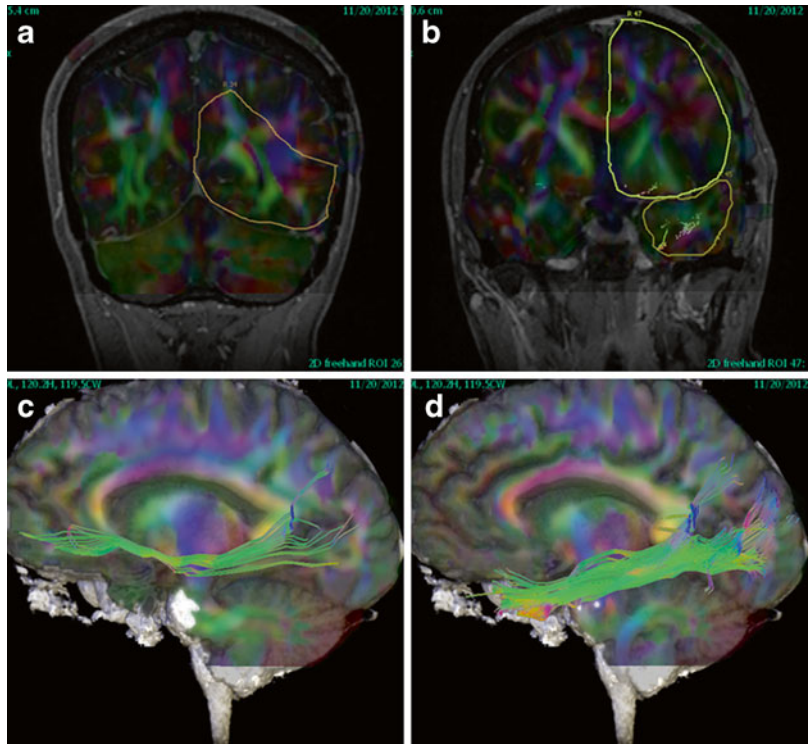

Fig. 14.8 Separating inferior longitudinal fasciculus (ILF) from inferior frontal occipital fasciculus (IFOF). For a patient with anaplastic astrocytoma (AA, same patient as in Fig. 14.6, **a-c**), seed ROI in left occipital lobe (**a**) with inclusion ROI left frontal ROI (**b**) can be used to select IFOF (**c**) or an anterior temporal inclusion ROI chosen to select ILF (**d**)

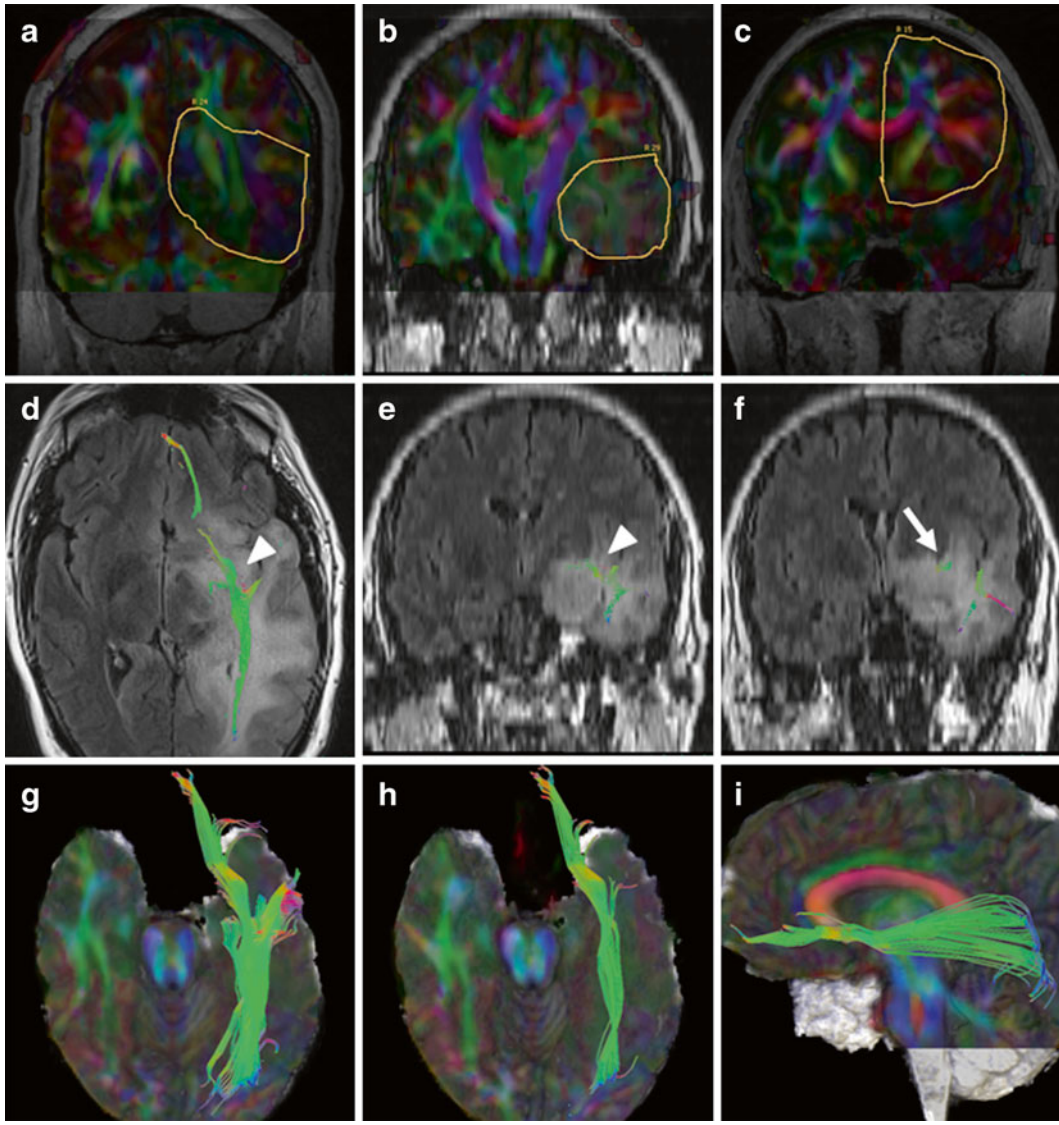

Fig. 14.9 Inferior frontal occipital fasciculus (IFOF). For a patient with gliomatosis, histologically anaplastic astrocytoma (AA, WHO grade III), a left occipital seed ROI was chosen (**a**), a mid temporal ROI (**b**) posterior to separation of ILF and IFOF (**d, e** on FLAIR, *arrowheads*, and **g** on 3D cut plane views) selected both tracts (**d**, **e**, **g**). A seed ROI in left frontal lobe (**c**) could be used instead of the mid temporal ROI to select the IFOF alone shown on 3D cut plane views (**h**, **i**) and coronal FLAIR (**f**, *arrow*)

seed for generating the UF, with the other ROI in the anterior temporal lobe (Fig. 14.10). Disruption of this tract may lead to specific memory deficits depending on side; for example deficits in memories of personal experiences on the right and in general knowledge of facts on the left or dominant side [72].

Pitfalls and Sources of Error

Misregistration and Intraoperative Shift

Discrepancies between tractography and true anatomic and functional localization may of course occur. Though DTI FT may be imperfect,

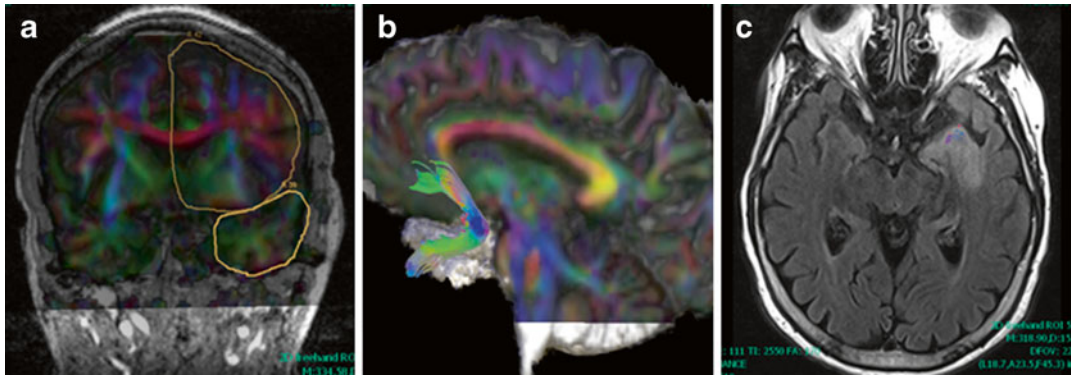

Fig. 14.10 Uncinate fasciculus (UF). Seed and inclusion ROIs in frontal lobe and anterior temporal lobe (**a**) were used to select the UF (**b**). For this patient with grade II infiltrating astrocytoma, the UF passes through infiltrating neoplasm (**c**). The same ROIs can be used with an occipital seed ROI as shown earlier for selecting IFOF and ILF

subcortical stimulation is not a perfect reference standard and may also have error in localization [68]. Ultimately, misregistration is often a combination of effects many of which have already been introduced, including those related to stereotactic localization error and brain shift, DTI FT uncertainty and registration error, and stimulation errors related to current penetration [3]. There can also be intra- and inter-user variability as well as variability between institutions and different fiber tracking software and/or navigation systems.

Overall error in registration of DTI/tractography data with structural images for navigation can be reduced to about 2 mm or less, which is on a par with errors in an optical navigation system with structural images alone [3, 20, 71]. Despite intraoperative checks on landmarks in navigation and surgical approach to minimize anticipated shifts, major shifts may render preoperative mapping inaccurate. Nimsky et al. [19] reported maximum tract shift of the CST or CC ranging from −8 to +15 mm, outward more frequent than inward. Zhao et al. [42] reported AF shifts of −5 to 2 mm, with the direction or pattern of shift more complex. Intraoperative MRI with updated tractography can adjust for this [19, 76, 77]. In spite of these problems, concordance of subcortical intraoperative mapping with fiber tracts has been reported to be within 10 mm in multiple studies [3, 23–26, 40, 69].

Pathophysiology and Effect on White Matter Tracts and Tractography

Pathology can alter fiber tracts by displacement, infiltration and disruption. An early report by Holodny et al. showed infiltration of the CST by an oligodendroglioma confirmed intraoperatively [78], and others have also demonstrated apparent neoplastic infiltration of white matter tracts by gliomas [50, 79]. Stadlbauer et al. [50], for example, retrospectively studied 25 cases of grade II and III gliomas, correlating biopsy sites with fiber tracking at different FA thresholds. Histopathology showed neoplastic infiltration of visualized fiber tracts in 9 of 25 cases with FA threshold at 0.2 or less while tracking at 0.25 or higher in these regions was not successful, pathology thus affecting performance of DTI FT.

DTI FT can show intact but displaced fiber tracts, and should fail if tracts are disrupted [80]. Intact but infiltrated fibers can be tracked to an extent, but neoplastic infiltration, edema and blood can have variable effects on successful tracking in this regard [80, 81]. If FA is unaffected or only minimally decreased, displaced fibers can usually still be tracked. Vasogenic edema may lead to a decrease in FA while leaving underlying architecture more or less intact such that fibers may still be followed through edematous regions, but one may have to adjust FA threshold to optimize tracking. Neoplastic infiltration may alter not only FA but also fiber

orientation and this may have a variable effect on tractography depending on the neoplasm. As discussed above, DTI FT can show different results depending on the quality of image data, software employed, and thresholds and ROIs chosen. Pathologic alteration adds another level of complexity, and postoperative evaluation may show improvement in tract visualization [82].

For these reasons, false positives and negatives can occur [83]. Inability to follow a particular tract with DTI FT does not necessarily indicate disruption, vasogenic edema and infiltrating tumors can lead to interruption in tracking without pathologic disruption [17, 22, 84, 85]. Normal structures can interrupt tracking with standard techniques due to crossing fibers [24]. On the other hand, DTI FT demonstration of interruption can be of use even when incorrect, if only to indicate that sufficient pathologic interruption is present such that intraoperative mapping becomes even more important [18]. Apparent vasogenic edema with mild decreased FA and preservation of appropriate orientation and ability to track fibers does not exclude neoplastic infiltration [50]. Errant fibers often occur and could mimic connectivity.

Pathophysiological Effects on Diffusion Properties: beyond Tractography

While pathology may interfere with tractography, potentially useful information may still be available from the microstructural information DTI provides. DTI metrics including trace or mean diffusivity, FA, and others are potentially helpful in the assessment of margins and degree of infiltration, differential diagnosis of glioma versus defined lesions like metastases, glioma grading, prognosis, and treatment response monitoring [86–88]. A detailed review is beyond the scope of this chapter, but see reviews by Gupta et al. [47] and Cruz LC Jr et al. [81] as well as a wealth of references therein.

Conclusion

DTI with or without tractography (DTI FT) provides complementary information about important subcortical structures for neurosurgical and radiotherapeutic planning, but DTI-FT has special challenges for these applications, including the effects of pathophysiology and intraoperative procedures on fiber pathways as well as the integration of DTI data with other modalities in neuronavigation software. Though validation is improving, the technique is still a relatively young one and caution is still warranted in implementation [35, 83].

References

1. Engel AK, Moll CK, Fried I, Ojemann GA. Invasive recordings from the human brain: clinical insights and beyond. Nat Rev Neurosci. 2005;6:35–47.
2. Pouratian N, Cannestra AF, Bookheimer SY, Martin NA, Toga AW. Variability of intraoperative electrocortical stimulation mapping parameters across and within individuals. J Neurosurg. 2004;101:458–66.
3. Berman JI, Berger MS, Chung SW, Nagarajan SS, Henry RG. Accuracy of diffusion tensor magnetic resonance imaging tractography assessed using intraoperative subcortical stimulation mapping and magnetic source imaging. J Neurosurg. 2007;107:488–94.
4. Berman J. Diffusion MR, tractography as a tool for surgical planning. Magn Reson Imaging Clin N Am. 2009;17:205–14.
5. Hagmann P, Jonasson L, Maeder P, Thiran JP, Wedeen VJ, Meuli R. Understanding diffusion MR imaging techniques: from scalar diffusion-weighted imaging to diffusion tensor imaging and beyond. Radiographics. 2006;26 Suppl 1:S205–23.
6. Melhem ER, Mori S, Mukundan G, Kraut MA, Pomper MG, van Zijl PC. Diffusion tensor MR imaging of the brain and white matter tractography. AJR Am J Roentgenol. 2002;178:3–16.
7. Mori S, van Zijl PC. Fiber tracking: principles and strategies - a technical review. NMR Biomed. 2002;15:468–80.
8. Mukherjee P, Berman JI, Chung SW, Hess CP, Henry RG. Diffusion tensor MR imaging and fiber tractography: theoretic underpinnings. AJNR Am J Neuroradiol. 2008;29:632–41.
9. Mukherjee P, Chung SW, Berman JI, Hess CP, Henry RG. Diffusion tensor MR imaging and fiber tractography: technical considerations. AJNR Am J Neuroradiol. 2008;29:843–52.
10. Yang E, Nucifora PG, Melhem ER. Diffusion MR imaging: basic principles. Neuroimaging Clin N Am. 2011;21:1–25. vii.
11. Duffau H. Introduction. Surgery of gliomas in eloquent areas: from brain hodotopy and plasticity to functional neurooncology. Neurosurg Focus 2010; 28: Intro
12. Pouratian N, Bookheimer SY. The reliability of neuroanatomy as a predictor of eloquence: a review. Neurosurg Focus. 2010;28:E3.

13. Holodny AI, Ollenschleger MD, Liu WC, Schulder M, Kalnin AJ. Identification of the corticospinal tracts achieved using blood-oxygen-level-dependent and diffusion functional MR imaging in patients with brain tumors. AJNR Am J Neuroradiol. 2001;22: 83–8.
14. Smits M, Vernooij MW, Wielopolski PA, Vincent AJ, Houston GC, van der Lugt A. Incorporating functional MR imaging into diffusion tensor tractography in the preoperative assessment of the corticospinal tract in patients with brain tumors. AJNR Am J Neuroradiol. 2007;28:1354–61.
15. Kamada K, Sawamura Y, Takeuchi F, et al. Functional identification of the primary motor area by corticospinal tractography. Neurosurgery. 2005;56:98–109. discussion 198-109.
16. Chen X, Weigel D, Ganslandt O, Buchfelder M, Nimsky C. Diffusion tensor imaging and white matter tractography in patients with brainstem lesions. Acta Neurochir (Wien). 2007;149:1117–31. discussion 1131.
17. Laundre BJ, Jellison BJ, Badie B, Alexander AL, Field AS. Diffusion tensor imaging of the corticospinal tract before and after mass resection as correlated with clinical motor findings: preliminary data. AJNR Am J Neuroradiol. 2005;26:791–6.
18. Mikuni N, Okada T, Enatsu R, et al. Clinical significance of preoperative fibre-tracking to preserve the affected pyramidal tracts during resection of brain tumours in patients with preoperative motor weakness. J Neurol Neurosurg Psychiatry. 2007;78: 716–21.
19. Nimsky C, Ganslandt O, Hastreiter P, et al. Preoperative and intraoperative diffusion tensor imaging-based fiber tracking in glioma surgery. Neurosurgery. 2005;56:130–7. discussion 138.
20. Nimsky C, Grummich P, Sorensen AG, Fahlbusch R, Ganslandt O. Visualization of the pyramidal tract in glioma surgery by integrating diffusion tensor imaging in functional neuronavigation. Zentralbl Neurochir. 2005;66:133–41.
21. Yamada K, Sakai K, Hoogenraad FG, et al. Multitensor tractography enables better depiction of motor pathways: initial clinical experience using diffusion-weighted MR imaging with standard b-value. AJNR Am J Neuroradiol. 2007;28:1668–73.
22. Berman JI, Berger MS, Mukherjee P, Henry RG. Diffusion-tensor imaging-guided tracking of fibers of the pyramidal tract combined with intraoperative cortical stimulation mapping in patients with gliomas. J Neurosurg. 2004;101:66–72.
23. Kamada K, Todo T, Masutani Y, et al. Combined use of tractography-integrated functional neuronavigation and direct fiber stimulation. J Neurosurg. 2005;102: 664–72.
24. Mikuni N, Okada T, Nishida N, et al. Comparison between motor evoked potential recording and fiber tracking for estimating pyramidal tracts near brain tumors. J Neurosurg. 2007;106:128–33.
25. Gonzalez-Darder JM, Gonzalez-Lopez P, Talamantes F, et al. Multimodal navigation in the functional microsurgical resection of intrinsic brain tumors located in eloquent motor areas: role of tractography. Neurosurg Focus. 2010;28:E5.
26. Mikuni N, Okada T, Enatsu R, et al. Clinical impact of integrated functional neuronavigation and subcortical electrical stimulation to preserve motor function during resection of brain tumors. J Neurosurg. 2007;106: 593–8.
27. Bello L, Gambini A, Castellano A, et al. Motor and language DTI Fiber Tracking combined with intraoperative subcortical mapping for surgical removal of gliomas. Neuroimage. 2008;39:369–82.
28. Ulmer JL, Salvan CV, Mueller WM, et al. The role of diffusion tensor imaging in establishing the proximity of tumor borders to functional brain systems: implications for preoperative risk assessments and postoperative outcomes. Technol Cancer Res Treat. 2004;3: 567–76.
29. Romano A, Ferrante M, Cipriani V, et al. Role of magnetic resonance tractography in the preoperative planning and intraoperative assessment of patients with intra-axial brain tumours. Radiol Med. 2007;112: 906–20.
30. Wu JS, Zhou LF, Tang WJ, et al. Clinical evaluation and follow-up outcome of diffusion tensor imaging-based functional neuronavigation: a prospective, controlled study in patients with gliomas involving pyramidal tracts. Neurosurgery. 2007;61:935–48. discussion 948-939.
31. Keles GE, Lundin DA, Lamborn KR, Chang EF, Ojemann G, Berger MS. Intraoperative subcortical stimulation mapping for hemispherical perirolandic gliomas located within or adjacent to the descending motor pathways: evaluation of morbidity and assessment of functional outcome in 294 patients. J Neurosurg. 2004;100:369–75.
32. Gil-Robles S, Duffau H. Surgical management of World Health Organization Grade II gliomas in eloquent areas: the necessity of preserving a margin around functional structures. Neurosurg Focus. 2010;28:E8.
33. Kamada K, Houkin K, Takeuchi F, et al. Visualization of the eloquent motor system by integration of MEG, functional, and anisotropic diffusion-weighted MRI in functional neuronavigation. Surg Neurol. 2003;59:352–61. discussion 361-352.
34. Hofer S, Karaus A, Frahm J. Reconstruction and dissection of the entire human visual pathway using diffusion tensor MRI. Front Neuroanat. 2010;4:15.
35. Mandelstam SA. Challenges of the anatomy and diffusion tensor tractography of the Meyer loop. AJNR Am J Neuroradiol. 2012;33:1204–10.
36. Kamada K, Todo T, Morita A, et al. Functional monitoring for visual pathway using real-time visual evoked potentials and optic-radiation tractography. Neurosurgery. 2005;57:121–7. discussion 121-127.
37. Kikuta K, Takagi Y, Nozaki K, et al. Early experience with 3-T magnetic resonance tractography in the surgery of cerebral arteriovenous malformations in and around the visual pathway. Neurosurgery. 2006;58: 331–7. discussion 331-337.

38. Powell HW, Parker GJ, Alexander DC, et al. MR tractography predicts visual field defects following temporal lobe resection. Neurology. 2005;65:596–9.
39. Kamada K, Todo T, Masutani Y, et al. Visualization of the frontotemporal language fibers by tractography combined with functional magnetic resonance imaging and magnetoencephalography. J Neurosurg. 2007;106:90–8.
40. Leclercq D, Duffau H, Delmaire C, et al. Comparison of diffusion tensor imaging tractography of language tracts and intraoperative subcortical stimulations. J Neurosurg. 2010;112:503–11.
41. Henry RG, Berman JI, Nagarajan SS, Mukherjee P, Berger MS. Subcortical pathways serving cortical language sites: initial experience with diffusion tensor imaging fiber tracking combined with intraoperative language mapping. Neuroimage. 2004;21:616–22.
42. Zhao Y, Chen X, Wang F, et al. Integration of diffusion tensor-based arcuate fasciculus fibre navigation and intraoperative MRI into glioma surgery. J Clin Neurosci. 2012;19:255–61.
43. Powell HW, Parker GJ, Alexander DC, et al. Imaging language pathways predicts postoperative naming deficits. J Neurol Neurosurg Psychiatry. 2008;79:327–30.
44. Koga T, Maruyama K, Kamada K, et al. Outcomes of diffusion tensor tractography-integrated stereotactic radiosurgery. Int J Radiat Oncol Biol Phys. 2012;82:799–802.
45. Maruyama K, Kamada K, Shin M, et al. Optic radiation tractography integrated into simulated treatment planning for Gamma Knife surgery. J Neurosurg. 2007;107:721–6.
46. Maruyama K, Kamada K, Ota T, et al. Tolerance of pyramidal tract to gamma knife radiosurgery based on diffusion-tensor tractography. Int J Radiat Oncol Biol Phys. 2008;70:1330–5.
47. Gupta A, Shah A, Young RJ, Holodny AI. Imaging of brain tumors: functional magnetic resonance imaging and diffusion tensor imaging. Neuroimaging Clin N Am. 2010;20:379–400.
48. Jena R, Price SJ, Baker C, et al. Diffusion tensor imaging: possible implications for radiotherapy treatment planning of patients with high-grade glioma. Clin Oncol (R Coll Radiol). 2005;17:581–90.
49. Krishnan AP, Asher IM, Davis D, Okunieff P, O'Dell WG. Evidence that MR diffusion tensor imaging (tractography) predicts the natural history of regional progression in patients irradiated conformally for primary brain tumors. Int J Radiat Oncol Biol Phys. 2008;71:1553–62.
50. Stadlbauer A, Nimsky C, Buslei R, et al. Diffusion tensor imaging and optimized fiber tracking in glioma patients: histopathologic evaluation of tumor-invaded white matter structures. Neuroimage. 2007;34:949–56.
51. Brunenberg EJ, Platel B, Hofman PA, Ter Haar Romeny BM, Visser-Vandewalle V. Magnetic resonance imaging techniques for visualization of the subthalamic nucleus. J Neurosurg. 2011;115:971–84.
52. Sedrak M, Gorgulho A, Bari A, et al. Diffusion tensor imaging (DTI) and colored fractional anisotropy (FA) mapping of the subthalamic nucleus (STN) and the globus pallidus interna (GPi). Acta Neurochir (Wien). 2010;152:2079–84.
53. Pouratian N, Zheng Z, Bari AA, Behnke E, Elias WJ, Desalles AA. Multi-institutional evaluation of deep brain stimulation targeting using probabilistic connectivity-based thalamic segmentation. J Neurosurg. 2011;115:995–1004.
54. Barkhoudarian G, Klochkov T, Sedrak M, et al. A role of diffusion tensor imaging in movement disorder surgery. Acta Neurochir (Wien). 2010;152:2089–95.
55. Coenen VA, Madler B, Schiffbauer H, Urbach H, Allert N. Individual fiber anatomy of the subthalamic region revealed with diffusion tensor imaging: a concept to identify the deep brain stimulation target for tremor suppression. Neurosurgery. 2011;68:1069–75. discussion 1075-1066.
56. Coenen VA, Allert N, Madler B. A role of diffusion tensor imaging fiber tracking in deep brain stimulation surgery: DBS of the dentato-rubro-thalamic tract (drt) for the treatment of therapy-refractory tremor. Acta Neurochir (Wien). 2011;153:1579–85. discussion 1585.
57. Henderson JM. "Connectomic surgery": diffusion tensor imaging (DTI) tractography as a targeting modality for surgical modulation of neural networks. Front Integr Neurosci. 2012;6:15.
58. Sedrak M, Gorgulho A, De Salles AF, et al. The role of modern imaging modalities on deep brain stimulation targeting for mental illness. Acta Neurochir Suppl. 2008;101:3–7.
59. Lakhan SE, Callaway E. Deep brain stimulation for obsessive-compulsive disorder and treatment-resistant depression: systematic review. BMC Res Notes. 2010;3:60.
60. Lujan JL, Chaturvedi A, Malone DA, Rezai AR, Machado AG, McIntyre CC. Axonal pathways linked to therapeutic and nontherapeutic outcomes during psychiatric deep brain stimulation. Hum Brain Mapp. 2012;33:958–68.
61. Grover PJ, Pereira EA, Green AL, et al. Deep brain stimulation for cluster headache. J Clin Neurosci. 2009;16:861–6.
62. Owen SL, Heath J, Kringelbach M, et al. Pre-operative DTI and probabilisitic tractography in four patients with deep brain stimulation for chronic pain. J Clin Neurosci. 2008;15:801–5.
63. Jones DK. The effect of gradient sampling schemes on measures derived from diffusion tensor MRI: a Monte Carlo study. Magn Reson Med. 2004;51:807–15.
64. Skare S, Andersson JL. On the effects of gating in diffusion imaging of the brain using single shot EPI. Magn Reson Imaging. 2001;19:1125–8.
65. Nucifora PG, Wu X, Melhem ER, Gur RE, Gur RC, Verma R. Automated diffusion tensor tractography: implementation and comparison to user-driven tractography. Acad Radiol. 2012;19:622–9.

66. Burgel U, Madler B, Honey CR, Thron A, Gilsbach J, Coenen VA. Fiber tracking with distinct software tools results in a clear diversity in anatomical fiber tract portrayal. Cent Eur Neurosurg. 2009;70:27–35.
67. Hattingen E, Rathert J, Jurcoane A, et al. A standardised evaluation of pre-surgical imaging of the corticospinal tract: where to place the seed ROI. Neurosurg Rev. 2009;32:445–56.
68. Young RJ, Brennan N, Fraser JF, Brennan C. Advanced imaging in brain tumor surgery. Neuroimaging Clin N Am. 2010;20:311–35.
69. Bello L, Castellano A, Fava E, et al. Intraoperative use of diffusion tensor imaging fiber tractography and subcortical mapping for resection of gliomas: technical considerations. Neurosurg Focus. 2010;28:E6.
70. Rasmussen Jr IA, Lindseth F, Rygh OM, et al. Functional neuronavigation combined with intraoperative 3D ultrasound: initial experiences during surgical resections close to eloquent brain areas and future directions in automatic brain shift compensation of preoperative data. Acta Neurochir (Wien). 2007;149:365–78.
71. Nimsky C, Ganslandt O, Fahlbusch R. Implementation of fiber tract navigation. Neurosurgery. 2006;58:ONS-292–303. discussion ONS-303–294.
72. Aralasmak A, Ulmer JL, Kocak M, Salvan CV, Hillis AE, Yousem DM. Association, commissural, and projection pathways and their functional deficit reported in literature. J Comput Assist Tomogr. 2006;30:695–715.
73. Mori S, Kaufmann WE, Davatzikos C, et al. Imaging cortical association tracts in the human brain using diffusion-tensor-based axonal tracking. Magn Reson Med. 2002;47:215–23.
74. Wakana S, Jiang H, Nagae-Poetscher LM, van Zijl PC, Mori S. Fiber tract-based atlas of human white matter anatomy. Radiology. 2004;230:77–87.
75. Catani M, Howard RJ, Pajevic S, Jones DK. Virtual in vivo interactive dissection of white matter fasciculi in the human brain. Neuroimage. 2002;17:77–94.
76. Mamata Y, Mamata H, Nabavi A, et al. Intraoperative diffusion imaging on a 0.5 Tesla interventional scanner. J Magn Reson Imaging. 2001;13:115–9.
77. Nimsky C, Ganslandt O, Hastreiter P, et al. Intraoperative diffusion-tensor MR imaging: shifting of white matter tracts during neurosurgical procedures--initial experience. Radiology. 2005;234:218–25.
78. Holodny AI, Schwartz TH, Ollenschleger M, Liu WC, Schulder M. Tumor involvement of the corticospinal tract: diffusion magnetic resonance tractography with intraoperative correlation. J Neurosurg. 2001;95:1082.
79. Talos IF, Zou KH, Kikinis R, Jolesz FA. Volumetric assessment of tumor infiltration of adjacent white matter based on anatomic MRI and diffusion tensor tractography. Acad Radiol. 2007;14:431–6.
80. Jellison BJ, Field AS, Medow J, Lazar M, Salamat MS, Alexander AL. Diffusion tensor imaging of cerebral white matter: a pictorial review of physics, fiber tract anatomy, and tumor imaging patterns. AJNR Am J Neuroradiol. 2004;25:356–69.
81. Hygino da Cruz LC, Jr VIG, Domingues RC. Diffusion MR imaging: an important tool in the assessment of brain tumors. Neuroimaging Clin N Am. 2011;21:27–49. vii.
82. Lazar M, Alexander AL, Thottakara PJ, Badie B, Field AS. White matter reorganization after surgical resection of brain tumors and vascular malformations. AJNR Am J Neuroradiol. 2006;27:1258–71.
83. Johansen-Berg H, Behrens TE. Just pretty pictures? What diffusion tractography can add in clinical neuroscience. Curr Opin Neurol. 2006;19:379–85.
84. Kinoshita M, Yamada K, Hashimoto N, et al. Fiber-tracking does not accurately estimate size of fiber bundle in pathological condition: initial neurosurgical experience using neuronavigation and subcortical white matter stimulation. Neuroimage. 2005;25:424–9.
85. Schonberg T, Pianka P, Hendler T, Pasternak O, Assaf Y. Characterization of displaced white matter by brain tumors using combined DTI and fMRI. Neuroimage. 2006;30:1100–11.
86. Lu S, Ahn D, Johnson G, Law M, Zagzag D, Grossman RI. Diffusion-tensor MR imaging of intracranial neoplasia and associated peritumoral edema: introduction of the tumor infiltration index. Radiology. 2004;232:221–8.
87. Wang S, Kim S, Chawla S, et al. Differentiation between glioblastomas, solitary brain metastases, and primary cerebral lymphomas using diffusion tensor and dynamic susceptibility contrast-enhanced MR imaging. AJNR Am J Neuroradiol. 2011;32:507–14.
88. Tsuchiya K, Fujikawa A, Nakajima M, Honya K. Differentiation between solitary brain metastasis and high-grade glioma by diffusion tensor imaging. Br J Radiol. 2005;78:533–7.

DTI in Diagnosis and Follow-Up of Brain Tumors

15

Frank De Belder, Sophie Van Cauter, Luc van den Hauwe, Wim Van Hecke, Louise Emsell, Maya De Belder, Matthias Spaepen, Stefan Sunaert, and Paul M. Parizel

Learning Points

- Both DWI and DTI may have utility in the assessment of brain tumors.
- Surgical planning is currently the most useful clinical application of DTI in the context of brain tumor neuroradiology.
- DTI parameters such as apparent diffusion coefficient (ADC) and fractional anisotropy (FA) may be useful to differentiate between mass lesions in the brain and different types of brain tumor.
- Methodological inconsistency and challenges associated with tumor delineation and DTI tractography limit the applicability of DTI for assessing patients in clinical practice.
- The most optimal use of DTI in the diagnosis, treatment, and follow-up of brain tumors should incorporate multiple imaging, surgical and clinical assessment strategies.

F. De Belder, MD (✉) • L. van den Hauwe, MD
M. Spaepen, MD • P.M. Parizel, MD, PhD
Department of Radiology, Antwerp University Hospital, Wilrijkstraat 10, Edegem, 2650 Antwerp, Belgium
e-mail: Frank.DeBelder@uza.be

S. Van Cauter, MD, PhD • S. Sunaert, MD, PhD
Departments of Translational MRI and Radiology, KU Leuven and University Hospitals Leuven, Leuven, Belgium

W. V. Hecke, PhD
icometrix, Leuven, Belgium

Department of Radiology, Antwerp University Hospital, Wilrijkstraat 10, Edegem, 2650 Antwerp, Belgium

L. Emsell, PhD
Departments of Translational MRI and Radiology, KU Leuven and University Hospitals Leuven, Leuven, Belgium

Department of Old Age Psychiatry, Universitair Psychiatrisch Centrum (UPC) - KU Leuven, Leuven, Belgium

M. De Belder, M.Sc.
Department of Experimental Psychology, University of Ghent, Ghent, Belgium

Introduction

Diffusion Tensor Imaging (DTI) maps the diffusion process of water molecules in tissue. The technique is mainly used to visualize brain connectivity and the relation between lesions such as brain tumors and the surrounding white matter tracts. DTI can also be used to characterize brain tumor microstructure, which makes it potentially useful in the differential diagnosis of mass lesions in the brain. For example, apparent diffusion coefficient (ADC) derived from DWI or DTI may be used to differentiate an abscess with low ADC from a necrotic brain tumor and an epidermoid from an arachnoid cyst with high ADC (Fig. 15.1), or to assess cell density and nucleus/cytoplasma ratio which can be used to differentiate

W. Van Hecke et al. (eds.), *Diffusion Tensor Imaging*, DOI 10.1007/978-1-4939-3118-7_15

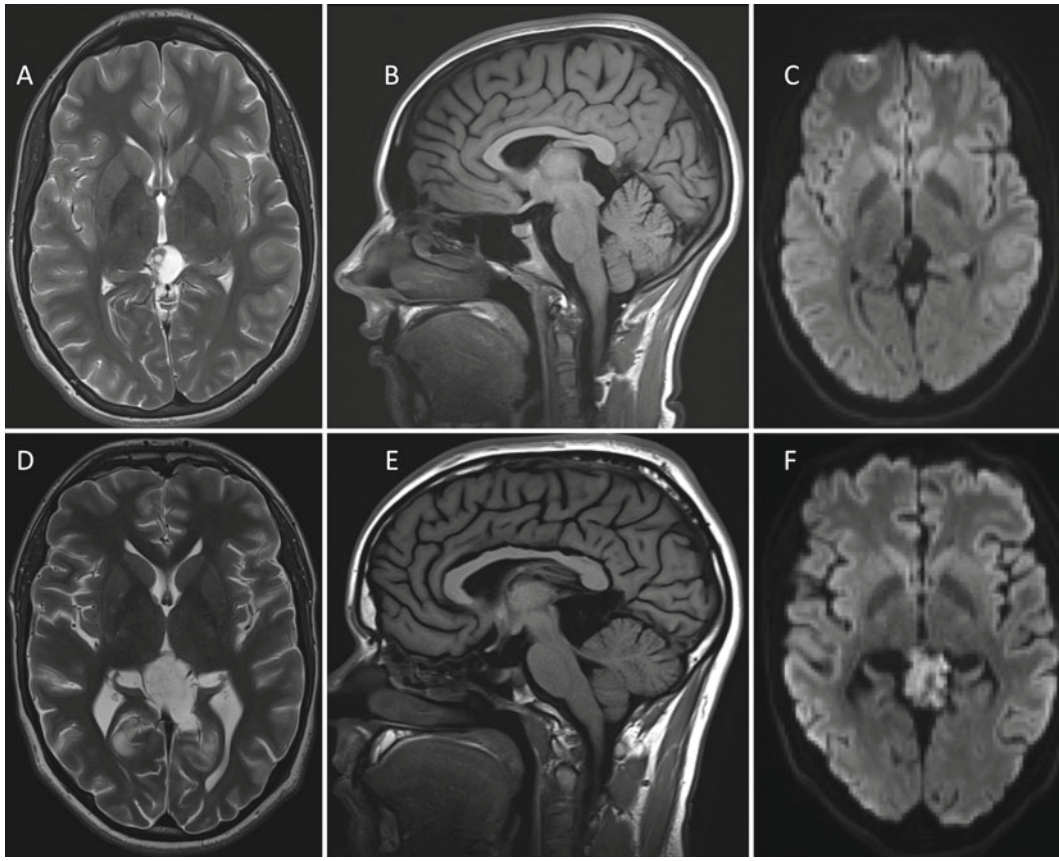

Fig. 15.1 Differentiation between arachnoid cyst and epidermoid cyst using DWI. A 19-year-old female patient (**a**–**c**) and a 27-year-old male patient (**d**–**f**), each with a lesion located in the quadrigeminal cistern. Both lesions show a high signal intensity on T2-weighted images (**a**, **d**) and low signal intensity on T1-weighted images (**b**, **e**). The axial diffusion-weighted trace images ($b = 1000$) demonstrate no restricted diffusion in the 19-year-old female patient (**c**). The lesion was a histologically proven arachnoid cyst. In the 27-year-old male, the trace image (**f**) showed restricted diffusion. He had a histologically proven epidermoid cyst

tumors with high cellularity, such as lymphoma, from tumors with lower cellularity, such as glioma. Other examples include the differentiation of tumor recurrence from pseudoprogression and vasogenic edema from tumor-infiltrated edema, or to differentiate suckable (low fractional anisotropy, FA) from non-suckable tumors (high FA) (e.g., pituitary adenoma versus meningioma) [1].

In addition to standard DTI derived parameters such as ADC (or mean diffusivity, MD) and FA, other indices have been proposed, which may provide additional complementary information when characterizing brain tumors, such as the $FA_{tumor}/FA_{normal\ appearing\ white\ matter}$ ratio, fiber coherence index, and tumor infiltration index [2, 3].

It is important to understand however that although the utility of DTI has been demonstrated in clinical studies, there remains a wide range of findings, which are sometimes contradictory and which may be due to differences in methodology. This limits the clinical applicability of such DTI findings in individual patients. This topic is addressed in more detail in this chapter. Supplemented with illustrative case studies, the remainder of the chapter reviews the role of DTI in the differential diagnosis and follow-up of brain tumors, and includes detailed sections on surgical planning, tumor grading, and characterizing posterior fossa tumors in children.

The Role of DWI and DTI in the Characterization and Differential Diagnosis of Mass Lesions in the Brain

Imaging findings in brain tumors are frequently nonspecific on conventional MRI. Both low-grade (LGGs) and high-grade gliomas (HGGs), metastases, and lymphomas show variable high signal on FLAIR and T2-weighted images, and are hypo- to isointense on T1-weighted images, whilst all lesions may show some degree of enhancement on contrast-enhanced T1-weighted images. Also non-tumoral lesions, such as acute and subacute infarcts, tumefactive demyelinating lesions, abscesses, and hematomas may sometimes be difficult to differentiate. More advanced neuroimaging techniques such as DWI and DTI, in combination with MR spectroscopy and perfusion and permeability MR imaging, may be helpful in obtaining a specific diagnosis.

Differentiating between Tumors, Cysts, and Abscesses

Abscess pus is a creamy and viscous fluid containing inflammatory cells, bacteria, mucoid proteins, and cell debris. The high cellularity of pus represents the main biological parameter leading to a diminution of the extracellular space and to decreased diffusion. Ebisu et al. [4] were the first to report on the difference in ADC value between abscess fluid and necrotic or cystic tumors, and to highlight the capability of DWI to discriminate between these two types of mass lesions. Marked hyperintensity on DWI was observed in the abscess cavity, which was associated with an extremely low ADC (0.31×10^{-3} mm^2/s). Restricted diffusion might be characteristic but is not pathognomonic for abscesses, as low ADC values also may be found in brain metastases. Rare cases of glioblastoma multiforme (GBM) that show restricted diffusion, i.e., hyperintense on trace DW images and hypointense on ADC maps, have been also reported in the literature [5]. The application of MR spectroscopy and MR perfusion may be helpful in these patients. Additionally, there are cases of cerebral abscess cavities showing hypointensity on DWI and high ADC values which overlapped with findings of neoplastic cysts. The cause of increasing diffusion in abscess cysts might be due to changes in pus composition and probably reflects increasing pus liquefaction as a result of adequate antibiotic therapy [6].

Conventional MRI does not allow an adequate differentiation between an abscess, a glioblastoma, and a solitary metastasis. The three entities generally present as rim-enhancing, central necrotic, expansive lesions with distinct perilesional edema.

At histopathological examination, the cystic parts of glioblastoma and metastases contain necrotic tumor tissue, while the enhancing rim on conventional MRI represents viable tumor cells. In a brain abscess, the cavity contains necrotic debris, neutrophils, and bacteria whereas the enhancing rim is a fibrous capsule formed by collagen [7, 8]. The role of DWI in the differential diagnosis of tumoral lesions versus abscesses, with the ADC typically low in abscess cavities and high in tumor cysts, has been widely demonstrated. However, high diffusivity similar to that found in necrotic tumors has been reported in abscesses. Brain tumors with infected or hemorrhagic material can show similar ADC in the cystic core compared to brain abscesses. Several studies addressed the role of DTI in optimizing the differential diagnosis of tumoral from non-tumoral infectious lesions.

Although results vary greatly among different studies, the consistent findings are reported regarding the FA values in the immediate perilesional edema of abscesses versus tumors. Elevated FA values are reported in the perilesional edema of the GBM and metastases [8–10]. In contrast, brain abscesses are associated with a lower FA in the peritumoral edematous zone. The elevated FA value in the immediate peritumoral edematous region of tumors is probably a result of a compressive effect, as well as gliosis. The gliotic response, an astrocytic reaction in response to any central nervous system injury, usually exists for a shorter duration in an abscess compared to a tumor. Consequently, the gliosis

may be in an earlier stage with more irregular glial fibers, explaining the lower FA value.

Higher FA values in the core of abscesses compared to GBM and metastases are reported [10, 11]. The higher FA in the abscess cavity is postulated to reflect a combination of cells, necrotic debris, viscosity, and macromolecules present in the pus due to upregulation of various adhesion surface molecules [8].

Elevated FA values are also reported in the enhancing rim of abscesses, which probably reflect the concentric layers of collagen fibers that intermix with the neutrophils and macrophages [8, 12, 13].

Although absolute FA values vary greatly among studies due to different acquisition schemes, field strengths and processing methods, some guidelines can be deducted. FA values measured in the necrotic and solid enhancing parts of glioblastoma and metastases are typically lower than those in normal white matter. FA in the cystic cavity and enhancing rim of an abscess can be as high as values found in normal white matter.

Differentiating between Epidermoid and Arachnoid Cysts

Epidermoid cysts are slow-growing lesions derived from ectodermal tissue that are hypothesized to have been inwardly displaced from the ectodermal surfaces during embryologic development. These cysts represent 1–2 % of all intracranial tumors, and occur typically as extra-axial lesions, most commonly in the cerebellopontine angle [14], fourth ventricle, parasellar region, and subarachnoid spaces of the basal cisterns. Less common locations include the middle cranial fossa, the lateral ventricles [15], diploe, and the spinal canal [16]. Epidermoid cysts that are exclusively intraparenchymal are very rare [17]. Most are asymptomatic but may occasionally result in mass effect, cranial neuropathy, or seizure. Occasionally, epidermoid cysts rupture and may elicit a granulomatous meningitis [18]. Most epidermoid cysts are isointense to CSF, although close inspection often shows they are not precisely identical in signal intensity to CSF [18]. The differential diagnosis with arachnoid cysts is usually made with FLAIR and DWI [19]. Epidermoid cysts do not suppress completely on FLAIR images and show high signal intensity on DW images [18–21]. The usefulness of DWI in distinguishing epidermoid tumors from arachnoid cysts was first reported by Tsuruda et al. in 1990. They showed that the ADC of epidermoid tumors is clearly lower than that of arachnoid cysts. Epidermoid cysts display much lower ADC values than the CSF, and little higher ADC values when compared with normal gray or white matter [21, 22]. So, whether the high signal on DW images in epidermoid cysts is due to diffusion restriction or T2 shine-through remains controversial [20–22]. Reduced ADC is not the only explanation of the epidermoid cysts bright signal intensity on the DW trace images [20]. The mechanisms of signal intensity generation in epidermoid appear to be different in various sequences and the additive effect of diffusion anisotropy and T2 shine-through may be the cause for bright signal on DWI [22]. On exponential DW images, epidermoid cysts have similar intensity with brain parenchyma showing that hyperintensity of these lesions on trace images is caused by increased T2 effect rather than the decrease in ADC values [23].

The high signal intensity on DWI of epidermoid tumors also serves as a useful feature for the detection of any residual tumor on postoperative follow-up examinations (Fig. 15.2).

Differentiating between High-Grade Gliomas and Tumefactive Demyelinating Lesions

Tumefactive demyelinating lesions (TDL) are demyelinating lesions larger than 2 cm, often indistinguishable from high-grade gliomas with conventional MRI. Incorrect diagnosis leads to unnecessary treatment such as radiotherapy, which could exacerbate demyelinating disease. Conventional imaging features of TDL include a relative lack of mass effect, less substantial perilesional edema, and open ring enhancement. These findings were proven to be nonspecific [24]. Very few studies have focused on the role of DTI in the characterization of TDL [25, 26]. Intralesional elevated FA values in the peripheral

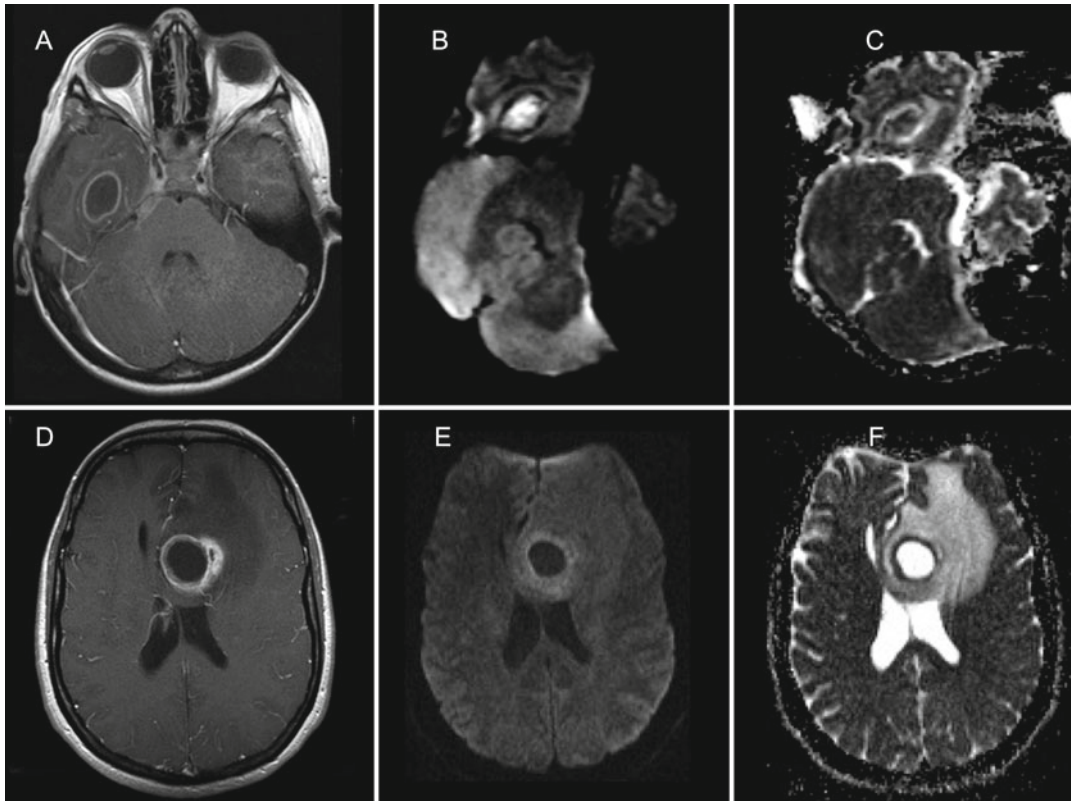

Fig. 15.2 A 7 year old boy (**a**–**c**) and a 51-year-old woman (**d**–**f**) both presented with headache and fever. Contrast-enhanced CT (not shown) displayed a solitary ring-enhancing lesion in the brain. MRI was performed to further characterize the lesions. Gd-enhanced T1-weighted images (**a**, **d**) show smooth ring enhancement in the right temporal lobe lesion (**a**) and a slightly irregular ring enhancement in the deep frontal white matter of the left cerebral hemisphere (**d**). The axial diffusion-weighted trace images ($b = 1000$) show high signal intensity (**b**) with corresponding low signal on the ADC map (**c**) indicative for restricted diffusion in the 7-year-old boy. Facilitated diffusion (low signal on DWI trace image (**e**), and high signal on ADC (**f**)) is observed in the 51-year-old woman. Final diagnosis was bacterial abscess and necrotic solitary metastasis of a primary lung cancer

enhancing portions as well as in the central portion have been reported to differentiate TDL from high-grade gliomas, although differences were very small (average FA: 0.07 versus 0.06) [25]. Therefore we conclude that quantitative DTI is not useful in the differential diagnosis of TDL and high-grade glioma in individual patients.

Characterizing Brain Tumors

Glioblastoma Multiforme versus Solitary Metastasis

Intracranial metastases and glioblastoma are the most common intra-axial brain tumors in adults with gliomas representing 40 % of all primary brain tumors and brain metastases occurring in almost 15 % of all cancer patients [27]. In the typical setting of an oncological patient presenting with multiple lesions, the diagnosis of brain metastasis is straightforward using conventional MRI and clinical history. However, in the patient with unknown primary malignancies and a solitary brain lesion, differentiation may often be difficult. On conventional MR imaging, both HGGs and solitary metastasis display similar signal intensity characteristics and contrast enhancement patterns [2, 28–30] and anatomical MRI is not able to accurately characterize the extent of tumor infiltration.

Chiang et al. found the mean ADC values in contrast-enhancing areas of metastases to be significantly higher than those in HGGs [31]. However, the ADC values for metastases and enhancing gliomas overlap and most studies in the literature have suggested that the tumoral ADC value is not useful for discriminating metastatic tumors from HGGs [32–40]. HGGs and metastatic tumors often display heterogeneous signal intensity secondary to necrosis and susceptibility artifacts. As a result of this heterogeneity, DWI metrics obtained from the tumor can be imprecise or inaccurate [39].

Most tumors are surrounded by a high T2 signal area indicative of vasogenic edema. In general, the nonenhancing area of signal abnormalities that surrounds the enhancing tumor is referred to as peritumoral edema. In metastatic brain tumors or non-infiltrative primary tumors such as meningioma, peritumoral edema is synonymous with vasogenic edema. In HGGs, however, peritumoral edema is better referred to as "infiltrative edema" because it represents vasogenic edema and infiltrating tumor cells that invade newly formed or pre-existing blood vessels and white matter tracts [39]. Therefore, the key to distinguishing between these two entities appears to lie in detecting the changes within the peritumoral area—that is, the area beyond the enhancing margin [39].

Several studies have suggested that DTI can aid in the distinction of vasogenic edema surrounding metastases from nonenhancing tumor infiltration in gliomas [3, 10, 41–43]. A number of studies have demonstrated the utility of ADC in the peritumoral region for differentiating HGGs and solitary metastasis, and have found that the mean or minimum ADC values in peritumoral edema of metastases are significantly higher than those in HGGs [31, 37–39, 44]. Other groups, however, believe that ADC measurements in the peritumoral areas of GBM and metastasis cannot be used to distinguish between these groups, as a large overlap is often demonstrated [34, 40].

In metastasis, the peritumoral region does not contain infiltrating tumor cells. FA values have been reported to be negatively correlated with cellular density and tumor infiltration. In addition to FA, less commonly used scalar measures: p, q, and L exist, which represent pure isotropic, anisotropic diffusion, and the total magnitude of the diffusion tensor, respectively [42]. Wang et al. [45] argued that the integration of multiple measures would provide insights in tumor infiltration. In several studies, Price et al. demonstrated that increased isotropic diffusion correlates with tumor infiltration [43, 46]. The extent of the abnormality of pure isotropic diffusion was a predictor for tumor spread at the time of progression [43] (Fig. 15.3).

Glioblastoma Multiforme versus Lymphoma

Primary central nervous system lymphoma (PCNSL) is a manifestation of extranodal non-Hodgkin's lymphoma, which accounts for 6 % of all intracranial malignant tumors. 90 % of PCNSLs are histologically diffuse large B-cell lymphomas, and the remaining 10 % are poorly characterized low-grade, Burkitt's or T-cell lymphomas. An increase in the incidence of PCNSL has been reported both in immune-compromised and immune-competent individuals in the last decades, especially among the elderly [47]. The peak prevalence is between the fifth and sixth decades of life. Histologically, PCNSLs are typically angiocentric tumors that form perivascular cuffs of tumor cells, which infiltrate brain parenchyma either as individual diffusely infiltrating cells or as a compact aggregates of tightly packed cells [48]. Because of their high degree of cellularity, PCNSLs are frequently hyperattenuating to gray matter on CT and hypointense to gray and white matter on T2-wi. Usually these tumors show homogeneous and intense contrast enhancement. Both tumors can primarily affect or secondarily extend across the corpus callosum with a characteristic butterfly pattern of infiltration [49] (Fig. 15.4).

Differentiation between PCNSL and other primary brain tumors, such as GBM, can however sometimes be difficult or even impossible because conventional MR imaging findings may

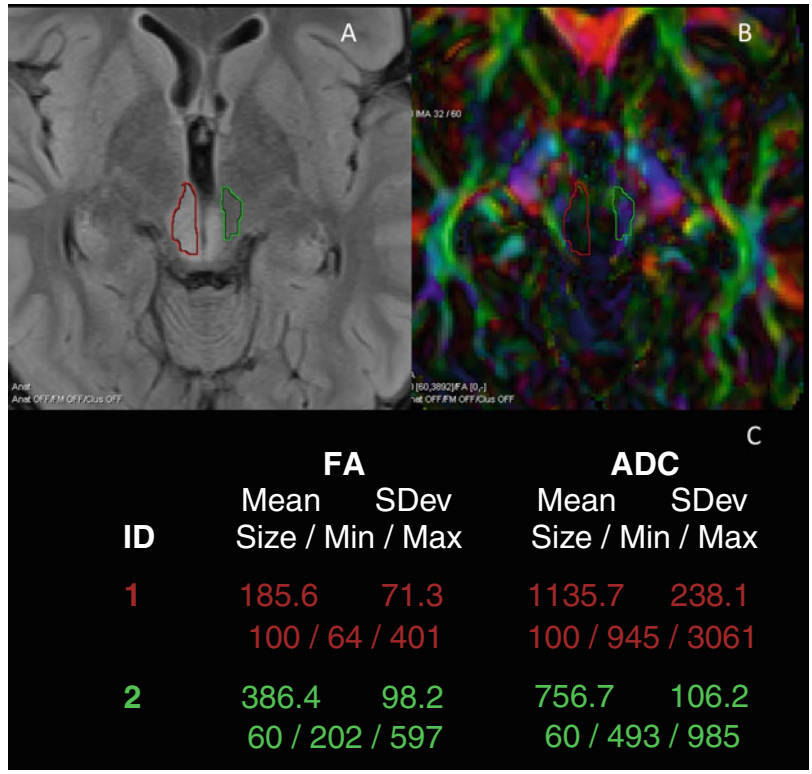

Fig. 15.3 Low-grade glioma in the midbrain of a 28-year-old male. The axial Flair (**a**) demonstrates a diffuse infiltrating tumor in the midbrain around the aqueduct. The lesion has a high T2-signal intensity. The color-coded FA map (**b**) and measurements of FA and ADC calculated on a Siemens Leonardo (Erlangen) workstation values (**c**) in the tumor (*red*) and NAWM (*green*) illustrating that $FA_{tumor} < FA_{NAWM}$ and $ADC_{tumor} > FA_{NAWM}$

overlap [47]. Accurate preoperative differentiation between these two tumor types is important. Primary therapy for HGGs/GBMs almost always includes neurosurgical resection, whereas PCNSL is managed primarily with chemotherapy or radiation therapy after stereotactic biopsy [47].

PCNSLs are generally hyperintense to gray matter on trace DW images and isointense to hypointense on ADC maps, findings consistent with restricted diffusion due to high cellularity [33, 35, 48]. In contrast, HGGs are generally hyperintense to gray matter on both trace DW images and ADC maps, findings consistent with the so-called T2 shine-through phenomenon, rather than low diffusivity [48]. Guo et al. were the first to publish quantitative data regarding water diffusivity (i.e., ADC values) in PCNSL and to correlate these values directly with the cellularity of the tumor [48]. Strongly reduced ADC values have been described as being typical for PCNSL [33, 48–50]. However, rare cases of GBMs that show restricted diffusion, i.e., hyperintense on trace DW images and hypointense on ADC maps, have been reported in the literature [5]. The application of MR spectroscopy and MR perfusion may be helpful in these patients. In a series of PCNSLs and astrocytic tumors infiltrating the corpus callosum, Horger et al. observed lower (17 %) ADC values for both tumor types when compared to other previous studies. The lower ADCs in their cohort may be the result of mixed inhibition of water diffusivity caused by both tumor tissue and the underlying white matter fibers of the corpus callosum [49] (Fig. 15.5).

Meningiomas

Meningiomas account for 30 % of all intracranial neoplasms, with up to 20 % of these lesions being atypical (WHO grade II) or anaplastic (WHO grade III) [51]. These are more aggressive tumors with high morbidity, mortality, and recurrence

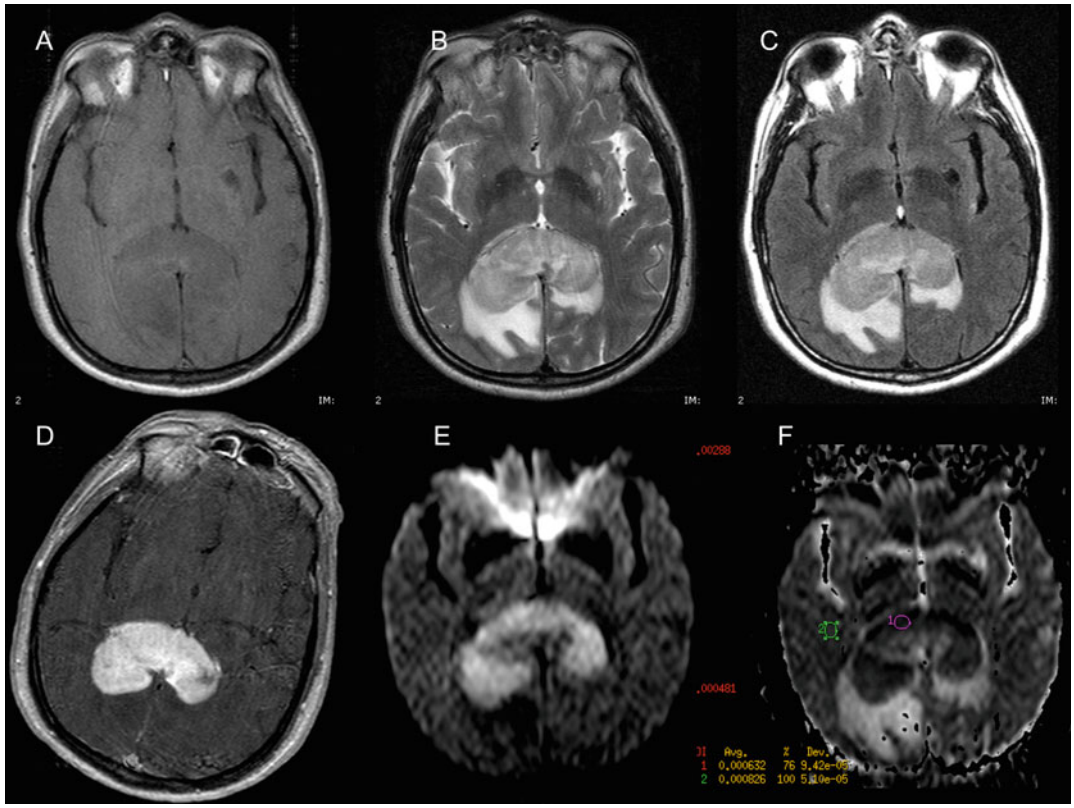

Fig. 15.4 Primary central nervous system lymphoma (PCNSL) characterized by DWI. A 54-year-old man with an expansile lesion within the splenium of the corpus callosum. Low signal intensity on T1-weighted image (**a**) and intermediate signal intensity (almost isointense with cortical gray matter) on T2-weighted (**b**) and FLAIR (**c**) images. Moderate vasogenic edema can also be observed. After gadolinium injection, homogeneous and intense contrast enhancement is seen (**d**). The axial diffusion-weighted trace image ($b = 1000$) shows high signal intensity (**e**) with corresponding low signal on the ADC map (**f**) indicative of restricted diffusion. The proposed diagnosis of PCNSL was confirmed by stereotactic biopsy

rates. The incidence and prevalence of meningiomas are twice as high in women compared to men, and higher in middle-aged patients. Most meningiomas are benign, but some may cause edema in the adjacent brain parenchyma depending on their size, subtype, or hormone receptors present in the lesion. The edema surrounding meningiomas is purely vasogenic. In most cases diagnosis of meningioma is straightforward given their extra-axial location. In some cases it may be difficult to differentiate meningiomas from large intra-axial tumors. Most meningiomas are well organized, from which the organization may differ between subtypes. Meningiothelial meningiomas, the most common meningioma, consist of cells arranged in lobules or whorls. The fibroblastic meningiomas consist of spindle cells with nuclei arranged in fascicules or storiform pattern. Atypical and malignant meningiomas show discohesion of the tumor cells with loss of histologic structure. Distinctions in microstructure are reflected on DTI in differing FA values, which appear to be helpful to differentiate fibroblastic meningiomas from other benign subtypes [52] and atypical or malignant meningiomas from the benign ones [53]. Preoperative planning for meningiomas requires information about tumor location, size, and tumor consistency and in grade I meningioma, lesion consistency is an important factor determining surgical outcome.

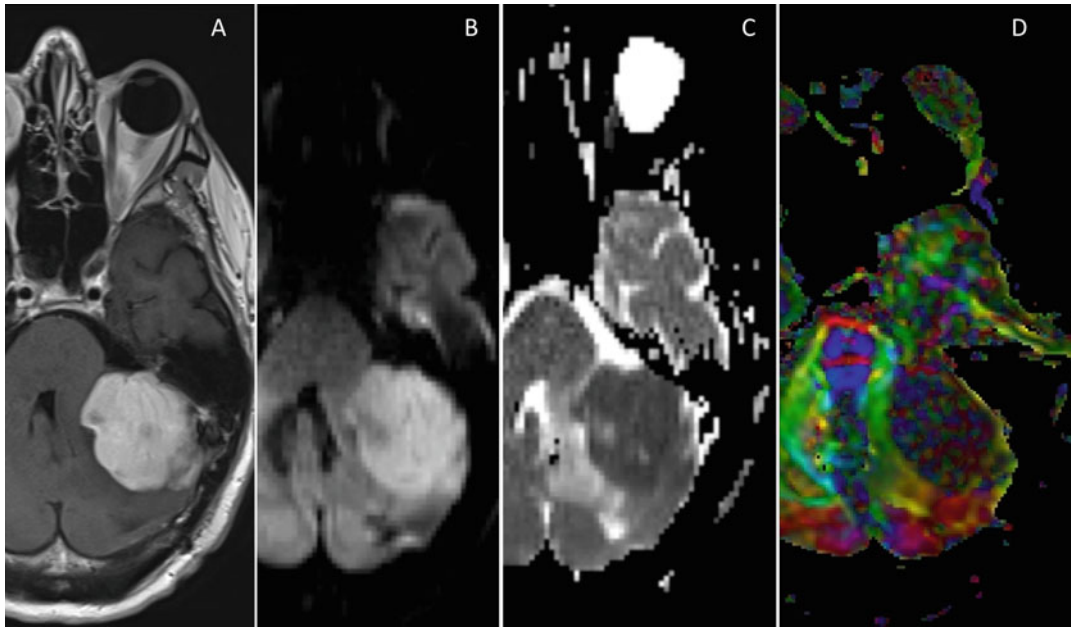

Fig. 15.5 (**a**) A 46-year-old male with a strong enhancing lesion in the left cerebellar hemisphere on the axial T1-weighted images. The lesion has a restricted diffusion with a very low ADC value as demonstrated on the trace images (**b**) and the ADC maps (**c**). The color-coded FA maps a low FA value of the lesion, which is a histological proven B-cell lymphoma (**d**)

For example, a hard consistency, as seen in fibroblastic subtypes, makes the removal difficult [54], whereas soft tumors are suckable and therefore more easy to resect than hard tumors, especially if there is an encasement of nerves or blood vessels. This means they require a shorter operating time and have a better outcome than hard meningiomas. Conventional MRI is unable to differentiate subtypes and grades, based on signal intensity value on T1- and T2-weighted images. An elevated FA is observed in fibroblastic meningiomas compared to meningothelial meningiomas. Fibroblastic meningiomas present with a fascicular orientation of long spindle-shaped tumor cells with a high content of intracellular collagen and reticulin, which is believed to be responsible for the hard consistency of these tumors. Transitional meningiomas showed no differences with either type [45, 52, 54, 55]. Although literature reports concerning the added value of DTI in predicting meningioma consistency are fairly consistent, studies regarding the differentiation of typical versus atypical and anaplastic meningiomas using DTI show substantially less agreement [2, 53, 56]. Further studies are warranted to address this issue. Conventional MRI features with cystic changes, hemorrhage, ischemic necrosis, and extracranial extension through the skull are more indicative of rapid growth and thus of an aggressive nature, although this reflects already advanced stages of disease [1, 57] (Fig. 15.6).

Posterior Fossa Tumors in Children

Brain tumors are the most common solid tumors in children, with an estimated incidence between 1 and 3 per 100,000. Whereas in infants most brain tumors are located at the supratentorial level, in children over the age of 4, infratentorial tumors are more frequent. Most common posterior fossa tumors in children include pilocytic astrocytoma (PA), medulloblastoma (MB), ependymoma (EP), and brain stem glioma [58]. Other tumor types such as atypical teratoid–rhabdoid tumor, hemangioblastoma, schwannoma, and choroid plexus papilloma are less frequently

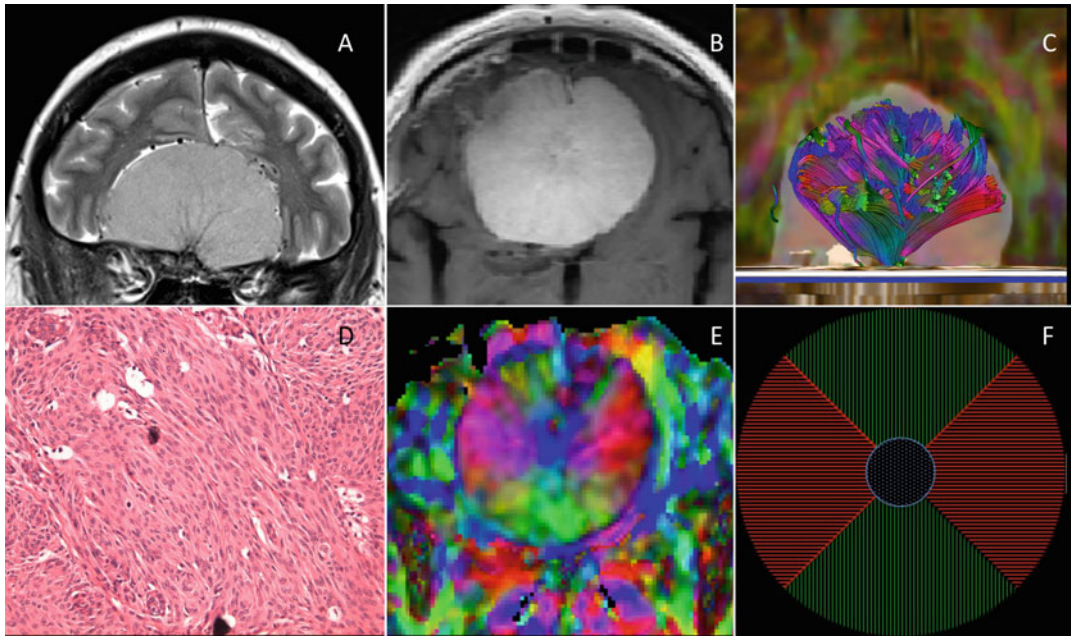

Fig. 15.6 Midline meningothelial meningioma in the anterior cranial fossa in a 61-year-old woman. A coronal TSE T2 (**a**) and Gadolinium-enhanced axial TSE T1 (**b**) demonstrate a large well-circumscribed midline tumor, which displays the typical characteristics of a meningioma. Hematoxylin and eosin staining, original magnification×200, demonstrates the fascicular arrangement of the tumor cells (**d**). This more organized structure is reflected in the axial color-coded FA map (**e**). A schematic representation of the FA map is shown in (**f**). *Green* indicates a predominantly anteroposterior direction of fibers (as seen in the anterior and posterior quadrant of the lesion), whereas *red* indicates fibers with a predominantly left-right orientation (as seen in the left and right lateral quadrants of the tumor). A *blue* area, in the center of the tumor, indicates vertically oriented fibers. The architecture of this tumor with high FA values can be displayed using diffusion tensor tractography (**c**), which nicely illustrates the spoke-wheel pattern

observed. Accurate preoperative diagnosis is important, because the most common tumors in this location and age group, benign PA and highly malignant MB, not only have different treatment approaches but also different natural histories and outcomes [59].

DWI distinguishes tumor types and histological grades, because higher-grade tumors have increasingly restricted diffusion (high signal intensity on DWI, low ADC values) [59, 60]. Kotsenas et al. were the first to describe the high signal intensity of MB on DWI. They postulated that the densely packed tissue, the high cellularity, and small *extracellular* space of MB restrict the extracellular diffusion of water protons, and that the high nuclear-to-cytoplasmic ratio of these tumor cells limits *intracellular* motion. The combination of these factors leads to a marked increase in signal on DWI (Fig. 15.7). Indeed, MBs are highly cellular WHO grade IV neoplasms, with little cytoplasm and extracellular matrix (i.e., small extracellular spaces). On the other hand, PAs (WHO grade I) are paucicellular tumors with abundant extracellular spaces. EPs (classic and anaplastic, WHO grades II and III, respectively) are between these two ends of the cellularity spectrum [51]. The significant differences in cellularity between these group of tumors—particularly between PAs and MBs—indicate that these lesions could potentially be distinguished by DWI and their ADC values. Rumboldt et al. observed significantly higher ADC values in PAs than in EPs and MBs, and EPs demonstrated higher ADC values than MBs [59]. They concluded that assessment of ADC values of enhancing solid tumor is a simple and reliable technique for preoperative differentiation of cerebellar tumors in children [59]. These

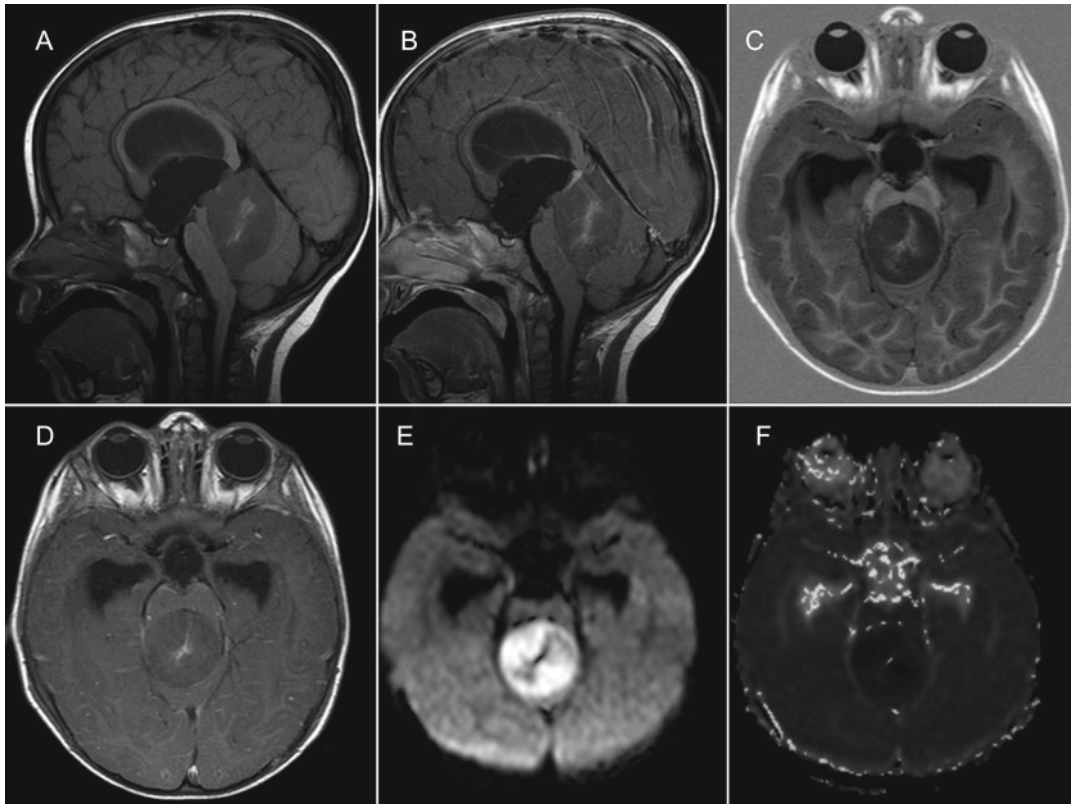

Fig. 15.7 Medulloblastoma characterized by DWI. An 18-month-old boy presented with headaches, nausea, and vomiting, Sagittal and axial T1-weighted images before (**a**, **c**) and after (**b**, **d**) Gd injection show a large tumor obstructing the fourth ventricle. Only very mild contrast enhancement in the center of the tumor is observed. Obvious obstructive hydrocephalus with dilatation of the third ventricle and temporal horns of the lateral ventricles and transependymal migration of CSF can be seen. The tumor is "bright" on the DW images (**e**), and "black" on the ADC maps (**f**), i.e., restricted diffusion. Final diagnosis after total resection was medulloblastoma, classic subtype

observations were confirmed by other group [61, 62]. Other groups, however, observed overlap in ADC values between the different groups of tumors [60, 63–65]. Overlap was observed between the ADC values of the PAs and EPs, and the ADC values of EPs and MBs. There was, however, no overlap between the ADC values of PAs and MBs [66]. This overlap in ADC values between tumor types may be due to technical factors (especially in small, heterogeneous, calcified or hemorrhagic lesions) but also likely reflects true histologic variability [60]. Both MBs and EPs are heterogeneous tumors, and this heterogeneity presumably contributes to the possible overlap of their ADC values. MB consists of a classic type and four variants according to the latest WHO classification [67]. Desmoplastic MB is one of these variants that has a more favorable prognosis compared to the classical MB. Remarkable finding in this subgroup is the lower ADC values due to the presence of dense reticulin fiber networks within the extracellular space of the tumor [64, 68]. Rare cases of classic MB that show normal or even increased ADC values have been published; reticulin deposition was absent in these lesions [64]. Conversely, the large cell or anaplastic MB subtype which is associated with a high relapse risk and poor outcome may show increased ADC values since tumor cells are much larger when compared to classic MBs [68, 69]. Similarly, EPs have two distinct types, presumably contributing to their heterogeneity.

DWI is also a valuable tool in early detection of metastatic disease and treatment monitoring of MB patients. DWI may show recurrent tumor and/or metastatic deposits that are not seen on contrast-enhanced MRI [68, 70]. DWI is more sensitive than contrast-enhanced MRI alone in the early diagnosis of recurrent disease. It should therefore be included in the follow-up of patients with MB, especially when gross total resection of the tumor could not be achieved.

Determination of Tumor Grade

Diffusely infiltrating gliomas are the most common primary tumors of the brain in adults, ranging from low grade (WHO grade II) to high grade (WHO grade III and IV). Grading is based on the histopathological findings of the tumor, and differentiation between HGGs and LGGs is important for therapeutic planning, and assessing prognosis and response to therapy [71]. The presence of contrast enhancement on CT and conventional MRI as a marker of tumor angiogenesis has been an important criterion in predicting the malignancy of gliomas for many years. However, this is not a reliable finding since tumoral enhancement is mainly due to disruption of the blood brain barrier and not tumor angiogenesis [72]. Localized astrocytomas such as pilocytic astrocytoma (WHO grade I), subependymal giant cell astrocytoma (WHO grade I), and pleiomorphic xanthoastrocytoma (WHO grade II) typically show contrast enhancement. In a series by Kono et al., abnormal contrast enhancement was observed in 50 % of patients with diffuse astrocytoma grade II. Conversely, in a large series of supratentorial gliomas one third of the nonenhancing tumors proved to be malignant [73]. Other findings in HGGs on conventional MRI include the presence of peritumoral edema, mass effect, tumor heterogeneity, central necrosis, and intratumoral hemorrhage [74].

Previous reports have shown that the histopathological grade of glial tumors is inversely correlated with ADC, with lower ADCs found in higher-grade tumors in comparison with lower-grade tumors [32, 35, 59, 74]. Regions with minimum ADCs have been suggested to reflect the highest tumor cell density, or the most proliferative portion of the tumor, within heterogeneous tumors. Recent studies have shown that minimum ADCs may facilitate accurate grading of astrocytic tumors because regions exhibiting the minimum ADC correspond to the highest-grade glioma foci within heterogeneous tumors [74–76].

The higher the tumor cellularity and grade are, the lower the ADC is because of decreased water diffusivity [31, 32]. However, other factors may be complicating this relationship: ADC increases with increased edema and increased edema is seen in high-grade tumors [71].

Although the ADC is thought to be inversely correlated with tumor cellularity, and hence glioma grade, its clinical effect remains limited because of substantial overlap in the regional ADCs between gliomas of differing grades [72].

Several studies focused on the potential added value of FA in grading gliomas. However, the relationship between tumor cell density and FA is still controversial, as both positive and negative correlations between these parameters have been reported [52, 77–79] [80, 81]. An increased amount of cellular membranes and intracellular viscosity as well as relatively decreased extracellular space in high-grade glioma compared to low-grade gliomas induces an increase in the extent of directionality of water diffusion, resulting in a relative increase in FA value. On the other hand, other structural factors than cell density affect the interpretation of FA (Fig. 15.3). For example, increased vascularity, edema, the presence of microcysts, and larger tumor cell sizes result in an overall decrease in FA. The latter features are listed in the World Health Organization (WHO) classification in order to differentiate low- from high-grade gliomas [51]. Microscopically, GBM shows high cellularity, cellular and nuclear anaplasia, increased mitoses, microvascular proliferation, and necrosis, which are factors with mixed effects on FA. Altogether, the value of FA measurements in glioma grading remains controversial. In that view, recently developed imaging techniques have become of interest to address this issue of glioma grading.

Diffusion kurtosis imaging (DKI) is a relatively new MRI technique that has been developed as an extension of the DTI model. DKI provides additional parameters to the DTI model, which relate to the complexity of the biological environment determined by the cytoarchitecture, e.g., cell membranes, intracellular organelles, and the rapid exchange of protons between different cellular compartments [55, 82, 83]. To date, two studies were published on the role of DKI in grading gliomas. In these studies, diffusion kurtosis parameters were assigned as potential biomarkers for the grading of gliomas, this because of a better separation between high- and low-grade gliomas using kurtosis parameters compared to conventional DTI and DWI parameters [84, 85].

Diffusion-Weighted Imaging in Surgical Planning

Determination of Tumor Boundaries

In preoperative planning it is important for the surgeon to know the relationship between the tumor and the surrounding white matter tracts. To minimize the postoperative neurological deficit, the surgeon needs to know the exact tumor boundaries. Jellison et al. [7, 8] described four major patterns in affected WM tracts, categorized on the basis of anisotropy and fiber direction or orientation (Fig. 15.8). Pattern 1 (Figs. 15.8a and 15.9) consists of normal or only slightly decreased FA with abnormal location resulting from tumor mass effect. This means that white matter tracts

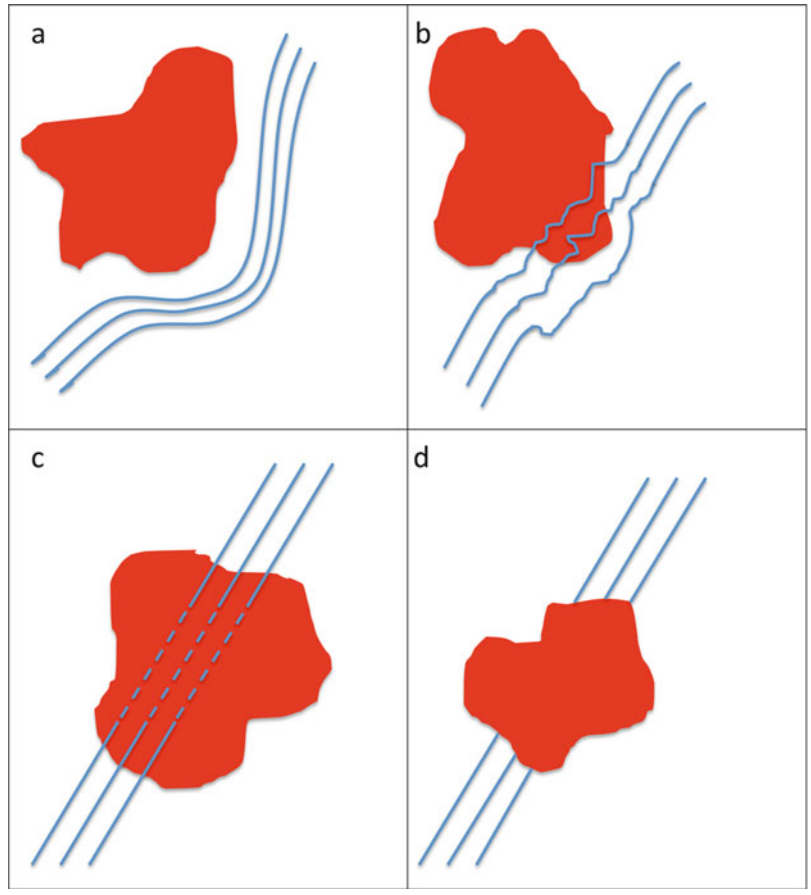

Fig. 15.8 Potential patterns of WM fiber tract alteration by cerebral neoplasms. (**a**) Displaced but intact white matter tracts resulting in a normal to slightly decreased FA in tumor boundaries of low-grade gliomas, anaplastic astrocytomas, and metastasis [7]. (**b**) Normally located white matter tracts in edematous white matter with decreased FA around metastasis. (**c**) Tumor-infiltrated, but identifiable white matter tracts with decreased FA in tumor boundaries of anaplastic astrocytoma and glioblastoma. (**d**) Disrupted non-identifiable white matter tracts with decreased FA in tumor boundaries of anaplastic astrocytoma and glioblastoma

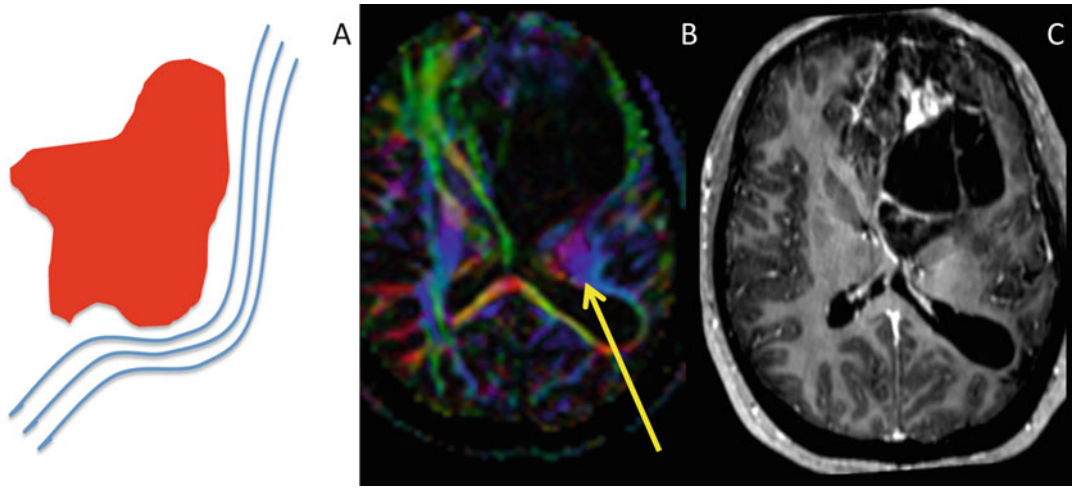

Fig. 15.9 (**a**) A 32-year-old female with a low-grade glioma in the left frontal lobe [7]. The color-coded FA map (**b**) demonstrates the displacement of the fibers of the corticospinal tract (*blue*; *yellow arrow*) compared to the normal appearing white matter (NAWM) of the right corticospinal tract (**c**)

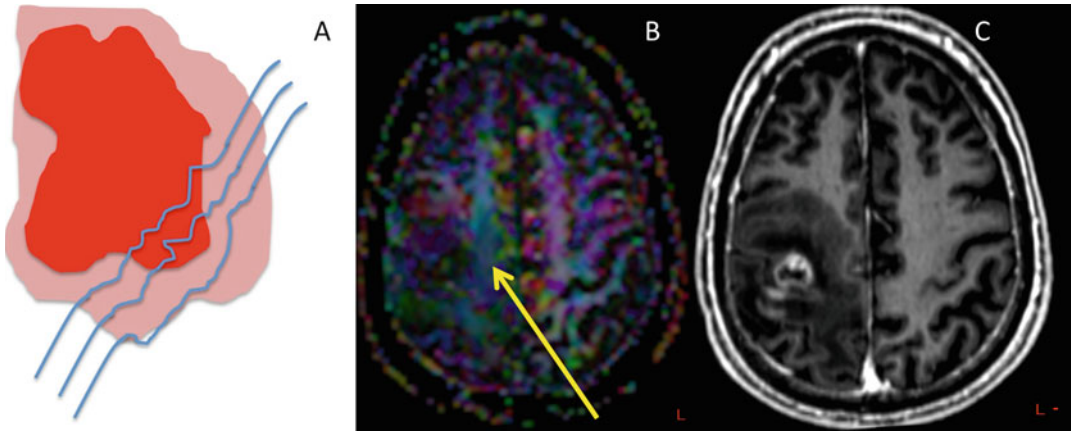

Fig. 15.10 (**a**) A 45-year-old male with a metastasis in the right frontal lobe [7]. The color-coded FA map (**b**) shows a decrease of FA value in the peritumoral edema represented by a less pronounced color (*yellow arrow*) as compared to the normal appearing white matter (NAWM) in the left frontal lobe (**c**)

are intact and that they can be preserved during surgery. Pattern 2 (Figs. 15.8b and 15.10) shows substantially decreased FA with a normal location and direction. This pattern is observed in vasogenic edema surrounding tumors such as metastases of meningiomas. Pattern 3 (Figs. 15.8c and 15.11) displays a substantially decreased FA with abnormal hues on directional color maps. This pattern can be identified in a small number of infiltrating gliomas in which the bulk mass effect appeared to be insufficient to account for the abnormal hues on directional maps. Jellison et al. [7] speculated that an infiltrating tumor disrupts the directional organization of fiber tracts to cause altered color patterns on directional maps. Pattern 4 (Figs. 15.8d and 15.12) consists of isotropic (or near-isotropic) diffusion such that the tract cannot be identified on directional color maps. This pattern is observed when a part of a tract is completely disrupted by a tumor. Combinations of the above patterns may occur.

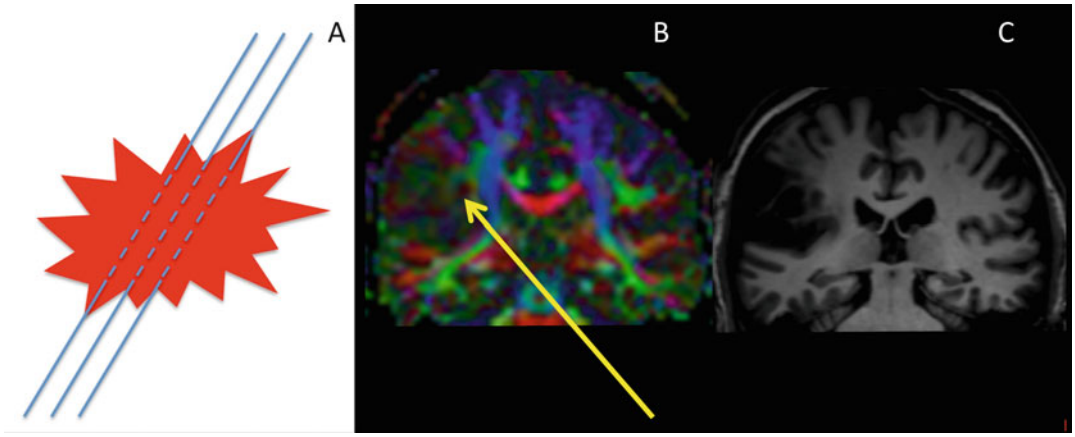

Fig. 15.11 (**a**–**c**) A 44-year-old male with a glioblastoma in the left frontal lobe, which infiltrates the left arcuate fasciculus [7]. The color-coded FA map shows a color loss and abnormal color hues for the left arcuate fasciculus (*yellow arrow*) as compared to the right one. The normal arcuate fasciculus is colored green due to the anteroposterior alignment of the white matter tracts

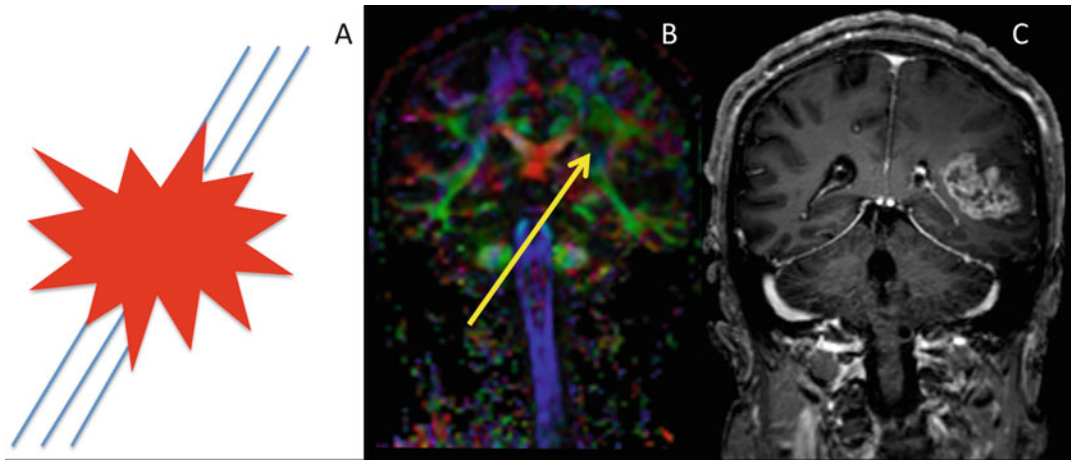

Fig. 15.12 (**a**–**c**) A 76-year-old female with a glioblastoma in the left frontal lobe [7]. The color-coded FA maps demonstrate a complete disruption of the arcuate fasciculus, represented by a complete loss of its green color (*yellow arrow*), compared to the right frontal lobe

Assessment of Tumor Extension

Contrary to the findings of previous studies [86], Stadnik et al. found no clear advantage of DWI in the evaluation of tumor extension [33]. This poor delineation between gliomas, edema, and normal white matter in DW images may be easily explained by the conjoined effect of T2 and ADC values as the different ADC values of white matter, gliomas, and edema are counter-compensated by T2 values [33]. Therefore, ADC cannot depict peritumoral neoplastic cell infiltration in HGGs [40, 87].

Determining the Ideal Site for Biopsy

Regions of minimum ADC in glial tumors correspond to the highest-grade foci in heterogeneous tumors. Measuring the lowest ADC within a tumor might aid in selecting an appropriate site for biopsy [39].

Monitoring Progression and Treatment Effects

The follow-up of patients with high-grade gliomas is routinely performed with serial MRI scans. However, the differentiation between therapy-induced inflammatory reactions and early tumor relapse remains challenging as the radiological characteristics of both entities are similar [9–11]. Radiation injury may exhibit morphologic changes such as a "soap-bubble" pattern, but these morphologic changes are nonspecific. Both therapy-induced inflammatory reactions and early tumor relapse can present as contrast-enhancing lesions with a variable degree of perilesional edema and mass effect. The inability to differentiate tumor relapse from therapy-induced inflammation is a commonly encountered problem in the therapy follow-up of high-grade glioma patients who are treated with the standard therapy, surgery, and radiochemotherapy, as well as patients treated using more innovative therapies such as anti-angiogenic therapy and immune therapy [9, 88]. The ultimate diagnosis is more often the result of the clinical course, follow-up exams, and brain biopsy, more than conventional MRI alone. Multiparametric MRI sequences, such as MRI spectroscopy and MRI perfusion, are helpful to differentiate a recurrent tumor from treatment-related changes.

Only limited and preliminary reports have been published on the role of DTI in the distinction between radiation-induced injury and tumor recurrence [89] [90–92]. The contribution of anisotropy measures remains to be explored. Studies which found FA to be a suitable marker for the follow-up of patients with high-grade gliomas showed results with only marginal statistical significance in small patient samples [54] In practice, DTI is not very useful in the differentiation of tumor recurrence and therapy-induced inflammation, as cutoff values vary with different acquisition schemes. ADC measurements are easier to interpret both quantitatively and qualitatively [93]. Sundgren et al. [90] found ADC values in the contrast-enhancing lesions to be significantly higher in the case of tumor recurrence than for non-recurrence. The ADC ratios in the white matter tracts in perilesional edema showed a trend towards higher values in treatment-related injury compared to in recurrent neoplasm. Assessment of ADC values and ADC ratios, in contrast-enhancing lesions, perilesional edema, and NAWM adjacent to the edema in the follow-up of new contrast-enhancing lesions at the site of previously treated brain tumors, may be helpful to differentiate recurrent tumor from radiation necrosis (Fig. 15.13).

Challenges Specific to Using DTI in the Diagnosis and Follow-Up of Brain Tumors

DTI is readily available on most recent MRI scanners with powerful gradient coil systems. A routine based "DTI sequence" measuring diffusion in 30 directions on a 3 T scanner requires an examination time of about 4–8 min. This short sequence provides all data for the calculation of DWI and DTI parameters.

The calculation of ADC and FA ratios and corresponding visualizations of tumor morphology on DTI is not straightforward and requires co-registration with other complementary imaging data, such as anatomical images. The calculation of FA_{tumor}/FA_{NAWM} and ADC_{tumor}/ADC_{NAWM} ratios requires the delineation of contralateral normal appearing white matter (NAWM), as demonstrated in Fig. 15.5. This requires (typically) manually outlining the tumor, NAWM, and edema, which is a time-consuming and challenging process that relies primarily on subjective assessment of tumor borders. Moreover, because white matter adjacent to glioma generally contains different proportions of vasogenic edema and tumor infiltrations, it is difficult to define an unbiased region of interest for valid grouped data analysis (see Chap. 9 for further information). This difficulty is superimposed on the challenge of obtaining a pathological "gold standard," because extensive biopsy of grossly intact white matter in tumors is ethically unacceptable (Fig. 15.14).

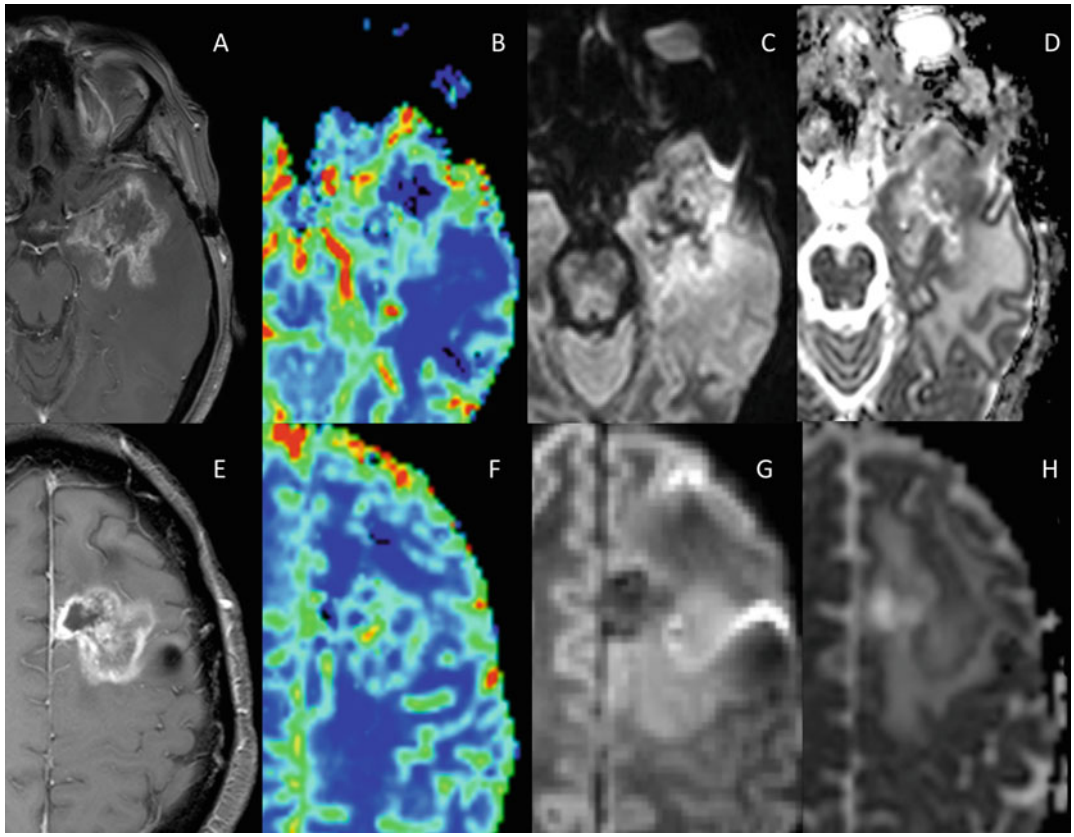

Fig. 15.13 Radionecrosis (**a**–**d**) versus a recurrent high-grade glioma (**e**, **f**). A 62-year-old female (**a**–**d**), with a ring-enhancing lesion in the left temporal lobe after resection and radiation therapy of a myoepithelioma on the axial T1-weighted images (**a**). rCBV maps show no elevated rCBV (**b**). Diffusion-weighted imaging ($b = 1000$) shows no restricted diffusion on trace images (**c**) and ADC maps (**d**). Surgical resection and pathology proved it to be the sequelae of radiation therapy with radionecrosis. A 41-year-old female (**e**–**h**) with a ring-enhancing lesion in the left frontal lobe on the axial T1-weighted images (**e**) after surgical resection, radiotherapy, and chemotherapy. rCBV maps demonstrate elevated rCBV in the lesion. Diffusion-weighted imaging: trace images (**g**) and ADC maps (**h**) display restricted diffusion in the lesion, which was proved histologically to be a recurrent tumor

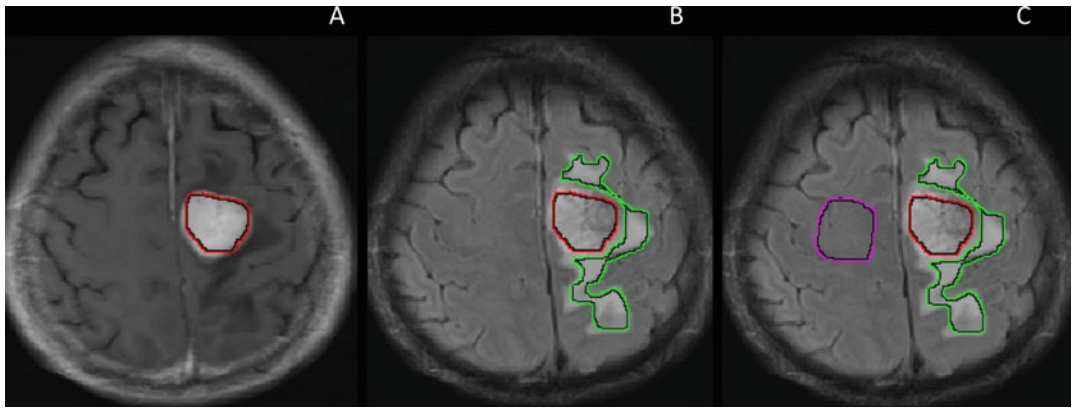

Fig. 15.14 Example of co-registration. Left frontal meningioma in a 71-year-old female. Axial gadolinium (Gd)-enhanced turbo spin echo (TSE) T1-weighted image (**a**) and precontrast fat-saturated fluid-attenuated inversion recovery (FLAIR) images (**b**, **c**), illustrating the methodology of co-registration. On the Gd-enhanced T1-weighted image, the outline of the enhancing part of the tumor is drawn (*red line*; **a**). This contour has to be transferred to the fat-saturated FLAIR image (**b**) on which the outline of the peritumoral edema (*green line*) and NAWM on the contralateral side (*purple line*) is drawn (**c**)

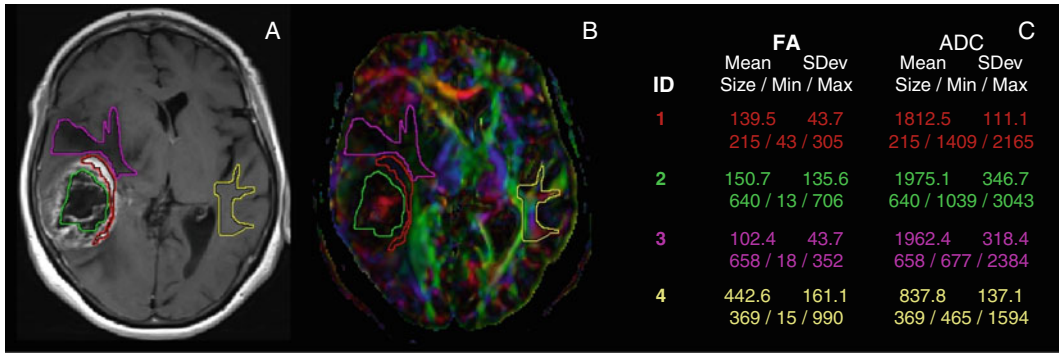

Fig. 15.15 A 70-year-old female with a glioblastoma in the right temporal lobe. Gadolinium-enhanced axial TSE T1 (**a**) demonstrates a ring-enhancing mass lesion with central necrosis surrounded by edema in the left temporal lobe. Axial color-coded FA map (**b**) and associated DTI parameter values obtained on a Siemens (Erlangen) Leonardo workstation (**c**), after registration of tumor (*red*), necrosis (*green*), peritumoral edema (*purple*), and NAWM (*yellow*) demonstrate that $FA_{edema} < FA_{tumor} < FA_{necrosis} < FA_{NAWM}$ and $ADC_{necrosis} > ADC_{edema} > ADC_{tumor} > ADC_{NAWM}$

DTI results are indicative for the differential diagnosis of brain tumors, and several studies have demonstrated statistical significant differences between values extracted from DTI-based analyses of different types of brain tumor [10, 56, 81]. However, significant overlap between these values is commonly observed and findings are not always consistent. This suggests that methodological issues may play a significant role. For example, imaging parameters (*b*-value, signal-to-noise ratio) could be critical determinants for the concentration of the tumor within the white matter [94], whilst inconsistent ROI delineation may introduce bias and inaccurate measurements. This lack of specificity makes DTI less suitable to use as a single technique in the context of routine clinical diagnostic work-up of brain tumors. DTI data have to be interpreted in the context of complementary information from conventional MR images and other multiparametric techniques as MR perfusion (relative cerebral blood volume; rCBV) and MR spectroscopy. In combination with these techniques DTI demonstrates to be helpful (Fig. 15.15).

Conclusion

This chapter has highlighted the utility and challenges associated with using DTI in the assessment of brain tumors and how it can be used to improve surgical planning. Studies investigating the use of different DTI-derived parameters to differentiate between different types of tumorous and non-tumorous lesions in the brain have yielded promising, but sometimes conflicting findings. Differences in methodological strategies, a lack of standardization, and normative values continue to confound the interpretation of DTI-based results, limiting its utility for assessing the individual patient. Further research using improved analysis and tractography techniques should help to overcome some of these issues in the future.

References

1. Pierallini A, Caramia F, Falcone C, Tinelli E, Paonessa A, Ciddio AB, et al. Pituitary macroadenomas: preoperative evaluation of consistency with diffusion-weighted MR imaging--initial experience. Radiology. 2006;239(1):223–31.
2. Lu S, Ahn D, Johnson G, Cha S. Peritumoral diffusion tensor imaging of high-grade gliomas and metastatic brain tumors. AJNR Am J Neuroradiol. 2003;24(5):937–41.
3. Zhou X, et al. A DTI study of glioma infiltration using fractional anisotropy and fiber coherence index. Proc Intl Soc Mag Reson Med. 2007;15:344.
4. Ebisu T, et al. Discrimination of brain abscess from necrotic or cystic tumors by diffusion-weighted echo planar imaging. Magn Reson Imaging. 1996;14(9):1113–6.
5. Hakyemez B. Glioblastoma multiforme with atypical diffusion-weighted MR findings. Br J Radiol. 2005;78(935):989–92.

6. Reiche W, Schuchardt V, Hagen T, II'yasov KA, Billmann P, Weber J. Differential diagnosis of intracranial ring enhancing cystic mass lesions-role of diffusion-weighted imaging (DWI) and diffusion-tensor imaging (DTI). Clin Neurol Neurosurg. 2010;112(3):218–25.
7. Jellison BJ, Field AS, Medow J, Lazar M, Salamat MS, Alexander AL. Diffusion tensor imaging of cerebral white matter: a pictorial review of physics, fiber tract anatomy, and tumor imaging patterns. AJNR Am J Neuroradiol. 2004;25(3):356–69.
8. Toh C, et al. Differentiation of brain abscesses from necrotic glioblastomas and cystic metastatic brain tumors with diffusion tensor imaging. AJNR Am J Neuroradiol. 2011;32(9):1646–51.
9. Brandsma D, van den Bent MJ. Pseudoprogression and pseudoresponse in the treatment of gliomas. Curr Opin Neurol. 2009;22(6):633–8.
10. Wang S, Kim S, Chawla S, Wolf RL, Zhang W-G, O'Rourke DM, et al. Differentiation between glioblastomas and solitary brain metastases using diffusion tensor imaging. Neuroimage. 2009;44(3):653–60.
11. Sinha S, Bastin ME, Whittle IR, Wardlaw JM. Diffusion tensor MR imaging of high-grade cerebral gliomas. AJNR Am J Neuroradiol. 2002;23(4):520–7.
12. Gupta RK, Hasan KM, Mishra AM, Jha D, Husain M, Prasad KN, et al. High fractional anisotropy in brain abscesses versus other cystic intracranial lesions. AJNR Am J Neuroradiol. 2005;26(5):1107–14.
13. Kumar M, Gupta RK, Nath K, Rathore RKS, Bayu G, Trivedi R, et al. Can we differentiate true white matter fibers from pseudofibers inside a brain abscess cavity using geometrical diffusion tensor imaging metrics? NMR Biomed. 2008;21(6):581–8.
14. Bonneville F, Savatovsky J, Chiras J. Imaging of cerebellopontine angle lesions: an update. Part 2: intra-axial lesions, skull base lesions that may invade the CPA region, and non-enhancing extra-axial lesions. Eur Radiol. 2007;17(11):2908–20.
15. Koot RW, Jagtap AP, Akkerman EM, Den Heeten GJ, Majoie CBLM. Epidermoid of the lateral ventricle: evaluation with diffusion-weighted and diffusion tensor imaging. Clin Neurol Neurosurg. 2003;105(4):270–3.
16. Thurnher MM. Diffusion-weighted MR, imaging (DWI) in two intradural spinal epidermoid cysts. Neuroradiology. 2012;54(11):1235–6.
17. Lian K, Schwartz ML, Bilbao J, Perry J, Aviv RI, Symons SP. Rare frontal lobe intraparenchymal epidermoid cyst with atypical imaging. J Clin Neurosci. 2012;19(8):1185–7.
18. Osborn AG, Preece MT. Intracranial cysts: radiologic-pathologic correlation and imaging approach 1. Radiology. 2006;239(3):650–64.
19. Chen S, Ikawa F, Kurisu K, Arita K, Takaba J, Kanou Y. Quantitative MR evaluation of intracranial epidermoid tumors by fast fluid-attenuated inversion recovery imaging and echo-planar diffusion-weighted imaging. AJNR Am J Neuroradiol. 2001;22(6):1089–96.
20. Annet L, Duprez T, Grandin C, Dooms G, Collard A, Cosnard G. Apparent diffusion coefficient measurements within intracranial epidermoid cysts in six patients. Neuroradiology. 2014;44(4):326–8.
21. Hakyemez B, Aksoy U, Yildiz H, Ergin N. Intracranial epidermoid cysts: diffusion-weighted, FLAIR and conventional MR findings. Eur J Radiol. 2005;54(2):214–20.
22. Santhosh K, Thomas B, Radhakrishnan VV, Saini J, Kesavadas C, Gupta AK, et al. Diffusion tensor and tensor metrics imaging in intracranial epidermoid cysts. J Magn Reson Imaging. 2009;29(4):967–70.
23. Hakyemez B, Erdogan C, Bolca N, Yildirim N, Gokalp G, Parlak M. Evaluation of different cerebral mass lesions by perfusion-weighted MR imaging. J Magn Reson Imaging. 2006;24(4):817–24.
24. Lucchinetti CF, Gavrilova RH, Metz I, Parisi JE, Scheithauer BW, Weigand S, et al. Clinical and radiographic spectrum of pathologically confirmed tumefactive multiple sclerosis. Brain. 2008;131(7):1759–75.
25. Toh C, et al. Differentiation of tumefactive demyelinating lesions from high-grade gliomas with the use of diffusion tensor imaging. AJNR Am J Neuroradiol. 2012;33(5):846–51.
26. Masu K, Beppu T, Fujiwara S, Kizawa H, Kashimura H, Kurose A, et al. Proton magnetic resonance spectroscopy and diffusion-weighted imaging of tumefactive demyelinating plaque. Neurol Med Chir. 2009;49(9):430–3.
27. Barnholtz-Sloan JS. Incidence proportions of brain metastases in patients diagnosed (1973 to 2001) in the metropolitan detroit cancer surveillance system. J Clin Oncol. 2004;22(14):2865–72.
28. Law M, Cha S, Knopp EA, Johnson G, Arnett J, Litt AW. High-grade gliomas and solitary metastases: differentiation by using perfusion and proton spectroscopic MR imaging. Radiology. 2002;222(3):715–21.
29. Tang YM, Ngai S, Stuckey S. The solitary enhancing cerebral lesion: can FLAIR aid the differentiation between glioma and metastasis? AJNR Am J Neuroradiol. 2006;27(3):609–11.
30. Maurer M, Synowitz M, Badakshi H, Lohkamp L, Wüstefeld J, Schäfer ML, et al. Glioblastoma multiforme versus solitary supratentorial brain metastasis: differentiation based on morphology and magnetic resonance signal characteristics. Fortschr Röntgenstr. 2013;185(03):235–40.
31. Chiang IC, Kuo Y-T, Lu C-Y, Yeung K-W, Lin W-C, Sheu F-O, et al. Distinction between high-grade gliomas and solitary metastases using peritumoral 3-T magnetic resonance spectroscopy, diffusion, and perfusion imagings. Neuroradiology. 2004;46(8):619.
32. Kono K, Inoue Y, Nakayama K, Shakudo M, Morino M, Ohata K, et al. The role of diffusion-weighted imaging in patients with brain tumors. AJNR Am J Neuroradiol. 2001;22(6):1081–8.

33. Stadnik TW, Chaskis C, Michotte A, Shabana WM, van Rompaey K, Luypaert R, et al. Diffusion-weighted MR imaging of intracerebral masses: comparison with conventional MR imaging and histologic findings. AJNR Am J Neuroradiol. 2001;22(5): 969–76.
34. Bulakbasi N, Kocaoglu M, Ors F, Tayfun C, Uçöz T. Combination of single-voxel proton MR spectroscopy and apparent diffusion coefficient calculation in the evaluation of common brain tumors. AJNR Am J Neuroradiol. 2003;24(2):225–33.
35. Yamasaki F, Kurisu K, Satoh K, Arita K, Sugiyama K, Ohtaki M, et al. Apparent diffusion coefficient of human brain tumors at MR imaging. Radiology. 2005;235(3):985–91.
36. Calli C, Kitis O, Yunten N, Yurtseven T, Islekel S, Akalin T. Perfusion and diffusion MR imaging in enhancing malignant cerebral tumors. Eur J Radiol. 2006;58(3):394–403.
37. Rollin N, Guyotat J, Streichenberger N, Honnorat J, Tran Minh V-A, Cotton F. Clinical relevance of diffusion and perfusion magnetic resonance imaging in assessing intra-axial brain tumors. Neuroradiology. 2006;48(3):150–9.
38. Pavlisa G, Rados M, Pavlisa G, Pavic L, Potocki K, Mayer D. The differences of water diffusion between brain tissue infiltrated by tumor and peritumoral vasogenic edema. J Clin Imaging. 2009;33(2):96–101.
39. Lee EJ, terBrugge K, Mikulis D, Choi DS, Bae JM, Lee SK, et al. Diagnostic value of peritumoral minimum apparent diffusion coefficient for differentiation of glioblastoma multiforme from solitary metastatic lesions. Am J Roentgenol. 2011;196(1):71–6.
40. Server A, Kulle B, Mæhlen J, Josefsen R, Schellhorn T, Kumar T, et al. Quantitative apparent diffusion coefficients in the characterization of brain tumors and associated peritumoral edema. Acta Radiol. 2009;50(6):682–9.
41. Kallenberg K, Goldmann T, Menke J, Strik H, Bock HC, Stockhammer F, et al. Glioma infiltration of the corpus callosum: early signs detected by DTI. J Neurooncol. 2013;112(2):217–22.
42. Price SJ, Peña A, Burnet NG, Pickard JD, Gillard JH. Detecting glioma invasion of the corpus callosum using diffusion tensor imaging. Br J Neurosurg. 2004;18(4):391–5.
43. Price SJ, Jena R, Burnet NG, Carpenter TA, Pickard JD, Gillard JH. Predicting patterns of glioma recurrence using diffusion tensor imaging. Eur Radiol. 2007;17(7):1675–84.
44. Lee EJ, Ahn KJ, Lee EK, Lee YS, Kim DB. Potential role of advanced MRI techniques for the peritumoural region in differentiating glioblastoma multiforme and solitary metastatic lesions. Clin Radiol. 2013;68:e689.
45. Wang W, Steward C, Desmond P. Diffusion tensor imaging in glioblastoma multiforme and brain metastases: the role of p, q, L, and fractional anisotropy. AJNR Am J Neuroradiol. 2008;30(1):203–8.
46. Price SJ, Jena R, Burnet NG, Hutchinson PJ, Dean AF, Peña A, et al. Improved delineation of glioma margins and regions of infiltration with the use of diffusion tensor imaging: an image-guided biopsy study. AJNR Am J Neuroradiol. 2006;27(9):1969–74.
47. Partovi S, Karimi S, Lyo JK, Esmaeili A, Tan J, Deangelis LM. Multimodality imaging of primary CNS lymphoma in immunocompetent patients. Br J Radiol. 2014;87(1036):20130684.
48. Guo AC, Cummings TJ, Dash RC, Provenzale JM. Lymphomas and high-grade astrocytomas: comparison of water diffusibility and histologic characteristics. Radiology. 2002;224(1):177–83.
49. Horger M, Fenchel M, Nägele T, Moehle R, Claussen CD, Beschorner R, et al. Water diffusivity: comparison of primary CNS lymphoma and astrocytic tumor infiltrating the corpus callosum. Am J Roentgenol. 2009;193(5):1384–7.
50. Toh C-H, Castillo M, Wong AMC, Wei K-C, Wong H-F, Ng S-H, et al. Primary cerebral lymphoma and glioblastoma multiforme: differences in diffusion characteristics evaluated with diffusion tensor imaging. AJNR Am J Neuroradiol. 2008;29(3):471–5.
51. Louis DN, Ohgaki H, Wiestler OD, Cavenee WK, Burger PC, Jouvet A, et al. The 2007 WHO classification of tumours of the central nervous system. Acta Neuropathol. 2007;114(2):97–109.
52. Tropine A, Dellani PD, Glaser M, Bohl J, Plöner T, Vucurevic G, et al. Differentiation of fibroblastic meningiomas from other benign subtypes using diffusion tensor imaging. J Magn Reson Imaging. 2007; 25(4):703–8.
53. Toh C-H, Castillo M, Wong A-C, Wei K-C, Wong H-F, Ng S-H, et al. Differentiation between classic and atypical meningiomas with use of diffusion tensor imaging. AJNR Am J Neuroradiol. 2008;29(9): 1630–5.
54. Kashimura H, Inoue T, Ogasawara K, Arai H, Otawara Y, Kanbara Y, et al. Prediction of meningioma consistency using fractional anisotropy value measured by magnetic resonance imaging. J Neurosurg. 2007;107(4):784–7.
55. Le Bihan D, Turner R, Douek P, Patronas N. Diffusion MR imaging: clinical applications. AJR Am J Roentgenol. 1992;159(3):591–9.
56. Jolapara M, Kesavadas C, Radhakrishnan VV, Thomas B, Gupta AK, Bodhey N, et al. Role of diffusion tensor imaging in differentiating subtypes of meningiomas. J Neuroradiol. 2010;37(5):277–83.
57. Horsfield MA, Jones DK. Applications of diffusion-weighted and diffusion tensor MRI to white matter diseases - a review. NMR Biomed. 2002;15(7-8):570–7.
58. Poretti A, Meoded A, Huisman TAGM. Neuroimaging of pediatric posterior fossa tumors including review of the literature. J Magn Reson Imaging. 2011;35(1): 32–47.
59. Rumboldt Z, Camacho DLA, Lake D, Welsh CT, Castillo M. Apparent diffusion coefficients for differentiation of cerebellar tumors in children. AJNR Am J Neuroradiol. 2006;27(6):1362–9.
60. Jaremko JL, Jans LBO, Coleman LT, Ditchfield MR. Value and limitations of diffusion-weighted

imaging in grading and diagnosis of pediatric posterior fossa tumors. AJNR Am J Neuroradiol. 2010;31(9):1613–6.
61. Kan P, Liu JK, Hedlund G, Brockmeyer DL, Walker ML, Kestle JRW. The role of diffusion-weighted magnetic resonance imaging in pediatric brain tumors. Childs Nerv Syst. 2006;22(11):1435–9.
62. Poretti A, Meoded A, Cohen KJ, Grotzer MA, Boltshauser E, Huisman TAGM. Apparent diffusion coefficient of pediatric cerebellar tumors: a biomarker of tumor grade? Pediatr Blood Cancer. 2013;60:2036.
63. Schneider JF, Confort-Gouny S, Viola A, Le Fur Y, Viout P, Bennathan M, et al. Multiparametric differentiation of posterior fossa tumors in children using diffusion-weighted imaging and short echo-time 1H-MR spectroscopy. J Magn Reson Imaging. 2007;26(6):1390–8.
64. Pillai S, Singhal A, Byrne AT, Dunham C, Cochrane DD, Steinbok P. Diffusion-weighted imaging and pathological correlation in pediatric medulloblastomas—"They are not always restricted!". Childs Nerv Syst. 2011;27(9):1407–11.
65. Bull JG, Saunders DE, Clark CA. Discrimination of paediatric brain tumours using apparent diffusion coefficient histograms. Eur Radiol. 2011;22(2):447–57.
66. Gimi B, et al. Utility of apparent diffusion coefficient ratios in distinguishing common pediatric cerebellar tumors. Acad Radiol. 2020;19(7):794–800.
67. Kotsenas AL, Roth TC, Manness WK, Faerber EN. Abnormal diffusion-weighted MRI in medulloblastoma: does it reflect small cell histology? Pediatr Radiol. 1999;29(7):524–6.
68. Yeom KW, Mobley BC, Lober RM, Andre JB, Partap S, Vogel H, et al. Distinctive MRI features of pediatric medulloblastoma subtypes. Am J Roentgenol. 2013;200(4):895–903.
69. Fruehwald-Pallamar J, Puchner SB, Rossi A, Garre ML, Cama A, Koelblinger C, et al. Magnetic resonance imaging spectrum of medulloblastoma. Neuroradiology. 2011;53(6):387–96.
70. Schubert MI, Wilke M, Müller-Weihrich S, Auer DP. Diffusion-weighted magnetic resonance imaging of treatment-associated changes in recurrent and residual medulloblastoma: preliminary observations in three children. Acta Radiol. 2006;47(10):1100–4.
71. Hilario A, Ramos A, Perez-Nunez A, Salvador E, Millan JM, Lagares A, et al. The added value of apparent diffusion coefficient to cerebral blood volume in the preoperative grading of diffuse gliomas. AJNR Am J Neuroradiol. 2012;33(4):701–7.
72. Maia A. MR cerebral blood volume maps correlated with vascular endothelial growth factor expression and tumor grade in nonenhancing gliomas. AJNR Am J Neuroradiol. 2005;26(4):777.
73. Scott JN, Brasher PMA, Sevick RJ, Rewcastle NB, Forsyth PA. How often are nonenhancing supratentorial gliomas malignant? A population study. Neurology. 2002;59(6):947–9.
74. Lee EJ, Lee SK, Agid R, Bae JM, Keller A, terBrugge K. Preoperative grading of presumptive low-grade astrocytomas on MR imaging: diagnostic value of minimum apparent diffusion coefficient. AJNR Am J Neuroradiol. 2008;29(10):1872–7.
75. Kitis O, Altay H, Calli C, Yunten N, Akalin T, Yurtseven T. Minimum apparent diffusion coefficients in the evaluation of brain tumors. Eur J Radiol. 2005;55(3):393–400.
76. Murakami R, Hirai T, Sugahara T, Fukuoka H, Toya R, Nishimura S, et al. Grading astrocytic tumors by using apparent diffusion coefficient parameters: superiority of a one- versus two-parameter pilot method 1. Radiology. 2009;251(3):838–45.
77. Beppu T, Inoue T, Shibata Y, Kurose A, Arai H, Ogasawara K, et al. Measurement of fractional anisotropy using diffusion tensor MRI in supratentorial astrocytic tumors. J Neurooncol. 2003;63(2):109–16.
78. Stadlbauer A, Ganslandt O, Buslei R, Hammen T, Gruber S, Moser E, et al. Gliomas: histopathologic evaluation of changes in directionality and magnitude of water diffusion at diffusion-tensor MR imaging. Radiology. 2006;240(3):803–10.
79. Zikou AK, Alexiou GA, Kosta P, Goussia A, Astrakas L, Tsekeris P, et al. Diffusion tensor and dynamic susceptibility contrast MRI in glioblastoma. Clin Neurol Neurosurg. 2012;114(6):607–12.
80. Beppu T, Inoue T, Shibata Y, Yamada N, Kurose A, Ogasawara K, et al. Fractional anisotropy value by diffusion tensor magnetic resonance imaging as a predictor of cell density and proliferation activity of glioblastomas. Surg Neurol. 2005;63(1):56–61.
81. Lee HY, Na DG, Song I-C, Lee DH, Seo HS, Kim J-H, et al. Diffusion-tensor imaging for glioma grading at 3-T magnetic resonance imaging: analysis of fractional anisotropy and mean diffusivity. J Comput Assist Tomogr. 2008;32(2):298–303.
82. Hui ES, Cheung MM, Qi L, Wu EX. Towards better MR characterization of neural tissues using directional diffusion kurtosis analysis. Neuroimage. 2008;42(1):122–34.
83. Jensen JH, Helpern JA, Ramani A, Lu H, Kaczynski K. Diffusional kurtosis imaging: the quantification of non-gaussian water diffusion by means of magnetic resonance imaging. Magn Reson Med. 2005;53(6):1432–40.
84. Raab P, Hattingen E, Franz K, Zanella FE, Lanfermann H. Cerebral gliomas: diffusional kurtosis imaging analysis of microstructural differences. Radiology. 2010;254(3):876–81.
85. Van Cauter S, Veraart J, Sijbers J, Peeters RR, Himmelreich U, De Keyzer F, et al. Gliomas: diffusion kurtosis MR imaging in grading. Radiology. 2012;263(2):492–501.
86. Brunberg JA, Chenevert TL, McKeever PE, Ross DA, Junck LR, Muraszko KM, et al. In vivo MR determination of water diffusion coefficients and diffusion anisotropy: correlation with structural alteration in gliomas of the cerebral hemispheres. AJNR Am J Neuroradiol. 1995;16(2):361–71.
87. Castillo M, Smith JK, Kwock L, Wilber K. Apparent diffusion coefficients in the evaluation of high-grade

cerebral gliomas. AJNR Am J Neuroradiol. 2001; 22(1):60–4.
88. De Vleeschouwer S, et al. Transient local response and persistent tumor control in a child with recurrent malignant glioma: treatment with combination therapy including dendritic cell therapy. Case report. J Neurosurg. 2004;100:492–7.
89. Sundgren PC, Fan XY, Dong Q, Weybright P, Welsh RC, Chenevert TL. Discriminating of brain tumor recurrence from radiation induced injury using diffusion tensor imaging. Proc Intl Soc Mag Reson Med. 2005;13:661.
90. Sundgren PC, Fan X, Weybright P, Welsh RC, Carlos RC, Petrou M, et al. Differentiation of recurrent brain tumor versus radiation injury using diffusion tensor imaging in patients with new contrast-enhancing lesions. Magn Reson Imaging. 2006;24(9):1131–42.
91. Xu J-L, Li Y-L, Lian J-M, Dou S-W, Yan F-S, Wu H, et al. Distinction between postoperative recurrent glioma and radiation injury using MR diffusion tensor imaging. Neuroradiology. 2010;52(12):1193–9.
92. Weybright P. Differentiation between brain tumor recurrence and radiation injury using MR spectroscopy. Am J Roentgenol. 2005;185(6):1471–6.
93. Shah R, Vattoth S, Jacob R, Manzil FFP, O'Malley JP, Borghei P, et al. Radiation necrosis in the brain: imaging features and differentiation from tumor recurrence. Radiographics. 2012;32(5):1343–59.
94. Young GS. Advanced MRI, of adult brain tumors. Neurol Clin. 2007;25(4):947–73. viii.

The Role of DTI in Multiple Sclerosis and Other Demyelinating Conditions

16

Massimo Filippi, Elisabetta Pagani, Paolo Preziosa, and Maria Assunta Rocca

Learning Points

- Multiple sclerosis (MS) white matter (WM) lesions show increased mean diffusivity (MD) and decreased fractional anisotropy (FA), with the most severe abnormalities seen in nonenhancing T1-hypointense lesions. No clear-cut differences have been detected between enhancing and nonenhancing lesions. Increased MD may precede the development of MS lesions visible on conventional magnetic resonance imaging (MRI).
- In MS, DTI abnormalities are detected in the normal-appearing WM, gray matter, optic nerves, and spinal cord.
- MS-related DTI abnormalities are more severe in patients with the progressive forms of the disease, correlate with clinical manifestations (locomotor disability and cognitive impairment), and tend to worsen over time.
- Fiber tracking based on DTI and voxel-based approaches for the definition of regional distribution of damage hold promise for the assessment of specific WM tracts, whose damage might be critical for the development of irreversible disability.
- The role of DTI in the diagnostic workup of patients with different demyelinating conditions deserves further investigation.

Introduction

Multiple sclerosis (MS) is the most common chronic inflammatory demyelinating disease affecting the central nervous system (CNS) of young adults in Western countries leading, in most cases, to severe and irreversible clinical disability. Due to its sensitivity in the detection of white matter (WM) lesions, conventional magnetic resonance imaging (MRI) has become a paraclinical tool central to the diagnosis of MS and to monitor its evolution. Despite this, the correlation between patients' clinical status and MRI measures is often weak to moderate. Diffusion tensor (DT) MRI is a quantitative technique with a higher specificity toward the heterogeneous pathological substrates of MS than conventional MRI. Indeed, correlative MR/pathological studies

M. Filippi, MD (✉) • P. Preziosa, MD
M.A. Rocca, MD
Neuroimaging Research Unit, and Department of Neurology, Institute of Experimental Neurology, Division of Neuroscience, San Raffaele Scientific Institute, Vita-Salute San Raffaele University, Via Olgettina 60, 20132 Milan, Italy
e-mail: filippi.massimo@hsr.it

E. Pagani, PhD
Neuroimaging Research Unit, Institute of Experimental Neurology, Division of Neuroscience, San Raffaele Scientific Institute, Vita-Salute San Raffaele University, Via Olgettina 60, 20132 Milan, Italy

W. Van Hecke et al. (eds.), *Diffusion Tensor Imaging*, DOI 10.1007/978-1-4939-3118-7_16

have shown that the main pathological correlates of diffusivity abnormalities in MS are demyelination and axonal loss [1, 2], which show a stronger correlation with anisotropy than with diffusivity indices [1, 2].

DTI has been widely applied to measure and grade MS burden not only within T2 white matter (WM) lesions but also in the normal-appearing WM (NAWM), gray matter (GM), optic nerve, and spinal cord of patients at different stages of the disease [3, 4]. Such an extensive application has markedly contributed to improving our understanding of the different pathophysiological substrates of the disease and the complexity of its clinical manifestations and evolution.

DTI has also been used to quantify CNS involvement in other demyelinating conditions, which may mimic MS, such as neuromyelitis optica (NMO) and acute disseminated encephalomyelitis (ADEM). After discussing the challenges specific to the use of DTI in MS and other demyelinating diseases, this chapter summarizes the main findings derived from the application of DTI in these conditions and future possible developments of the technique.

Special Challenges of DTI in the Assessment of Demyelinating Diseases

The application of DTI for the study of patients with demyelinating conditions presents several challenges related to: (1) the definition of acquisition protocols, both in terms of sequence setting and duration; (2) the selection of the most appropriate method for the analysis of the data; and (3) the interpretation of the results.

Setup of the Acquisition Protocol

Usually, MS patients can tolerate acquisition protocols with a relatively long duration, unless they are in an advanced and disabled stage of the disease. As a consequence, it is reasonable to use optimized DTI sequences (i.e., at least 30 diffusion-weighted directions, b factor $\approx$ 1000, full brain coverage) [5, 6]. The duration of such an acquisition is about 10 min, during which the patient is requested to lie still. Sequences with longer acquisition times, which allow a more sophisticated analysis, can also be used. However, they are not advisable for all patients. Since the effect of demyelinating diseases on the myelinated portions of the CNS is usually diffuse and unevenly distributed, imaging of the cervical cord and optic nerves using DTI is of interest for the clinician. Nevertheless, obtaining reliable DTI estimates from these structures is more challenging than for the brain. Both these structures are small and have a larger surface area to volume ratio than the brain. This leads to a decreased image quality from partial volume contamination from the cerebrospinal fluid (CSF). Moreover, DTI is prone to movement artifacts and this is a major issue especially in the study of the optic nerves which are mobile structures, and of the spinal cord, where image quality may be affected by cardiac pulsation and swallowing. Since an in-plane resolution of at least one square mm is recommended, the available single-shot echo planar imaging (EPI) technique may not be adequate. It would be better to combine this acquisition scheme with methods for reducing the field of view [7, 8], which allow an improved resolution with the same matrix and acquisition time, but avoiding problems of fold over. A multi-shot acquisition scheme can be considered an alternative strategy to achieve a better image resolution with less geometric distortions. However, these techniques require longer acquisition times and are prone to image ghosting, if not adequately corrected. To this end, other methods have been developed, which are not based on a Cartesian reading of the *k*-space and consider other trajectories. One of these methods is the so-called PROPELLER technique [9] that acquires, at each diffusion preparation, a central strip, rotated from time to time at each excitation until the *k*-space is entirely filled. The advantage of using PROPELLER sequences is that each segment can be translated into the *k*-space to correct for variation of the phase. These techniques are now more readily available on clinical scanners and should be considered as a feasible alternative to standard single-shot methods.

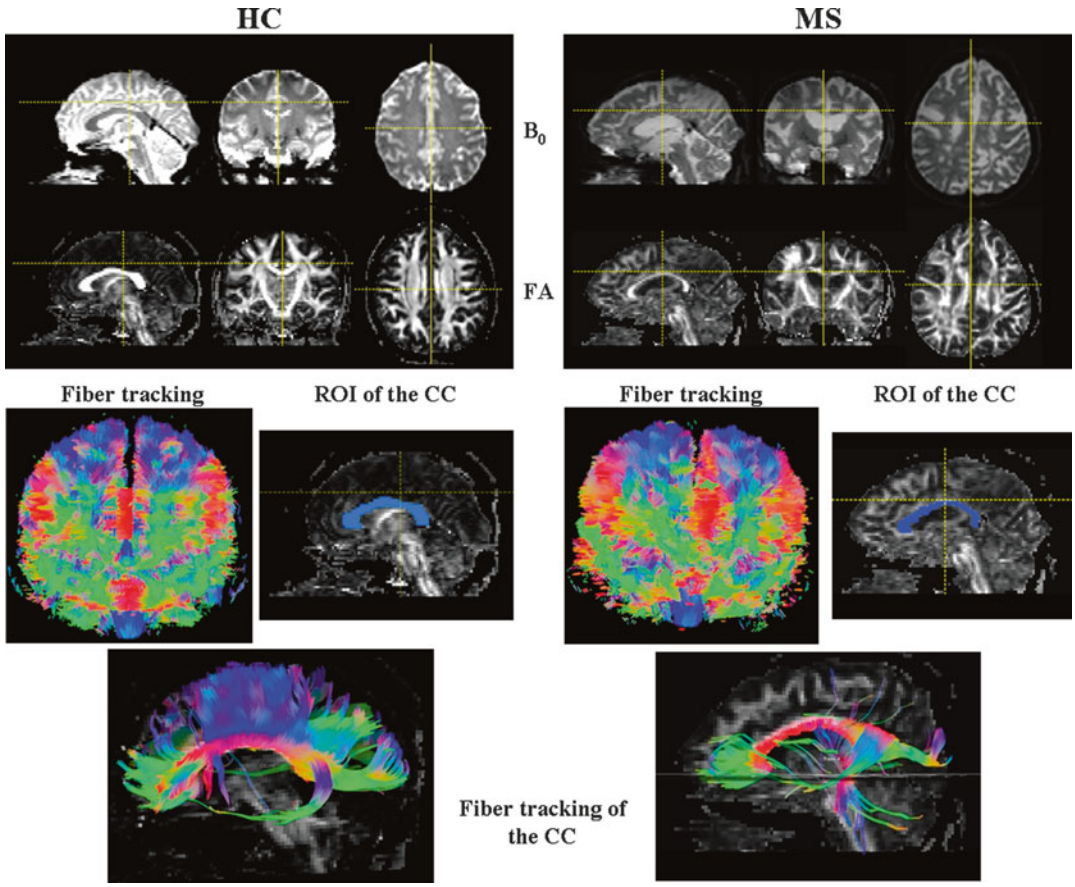

Fig. 16.1 An example of diffusion tensor imaging (DTI) tractography analysis (diffusion toolkit http://trackvis.org/dtk) of a healthy control (HC) (*left side*) and a patient with secondary progressive multiple sclerosis (MS) (*right side*). The B_0 image and fractional anisotropy (FA) map are shown in the *top part* of the figure. In the *middle part*, the global reconstruction of all fibers is shown. After the definition of a region of interest (ROI) for tracking the corpus callosum (CC) on the FA map, the reconstruction of the CC is shown at the *bottom*. In the MS patient, several periventricular lesions, causing a reduction of FA values, are visible on the B_0 image. Diffuse atrophy is also evident (enlargement of the ventricles and thinning of the CC on the midsagittal slice). The reconstruction of the CC shows the interruption of fiber propagation due to the presence of low FA values in lesions. Parameters used for tractography: FA threshold = 0.15, angle threshold = 35°, propagation algorithm: FACT with spline filter applied

Analysis of DTI Data

The main problems associated with the analysis of DTI data from patients with demyelinating conditions, both for the brain and spinal cord, are related to the presence of focal WM lesions and atrophy (Fig. 16.1). At present, one of the main obstacles to the development of DT tractography in vivo, and particularly in diseased states, is secondary to the strategy used in tracking when a fiber tract enters a region of low fractional anisotropy (FA). Low FA can be caused either by multiple crossing fibers in the voxel of interest or by a lesion that damages the tissue. One possibility to overcome this problem is to decouple the use of DTI to segment fiber tracts from its use to calculate measures of tissue damage. To this end, tractography can be used to construct a probability map of a tract of interest from healthy volunteer data and then apply such a map to patients scans to calculate DTI indexes of that tract (Fig. 16.2) [10]. For the construction of tract atlases and their application to single subject data, spatial normalization strategies need to be imple-

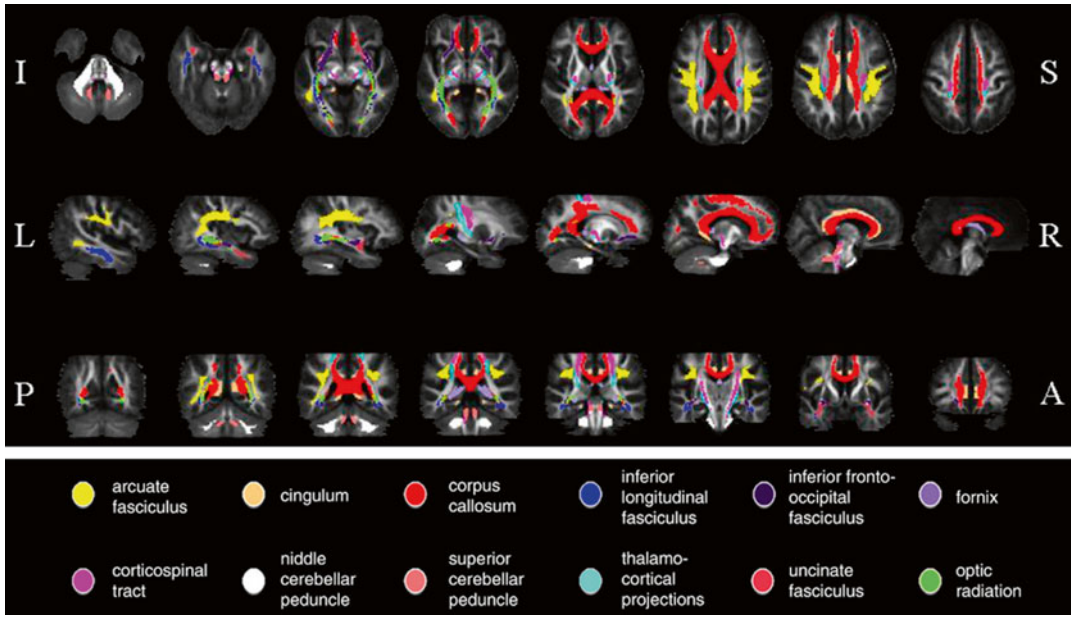

Fig. 16.2 White matter (WM) tract probability maps obtained from a reference group of 24 healthy controls. Probability maps are superimposed on axial (*top row*), sagittal (*middle row*), and coronal (*bottom row*) sections of the fractional anisotropy (FA) atlas. *A* anterior, *I* inferior, *L* left, *P* posterior, *R* right, *S* superior. Images are presented in neurologic convention. [Adapted from Preziosa P, Rocca MA, et al. (2011). "Intrinsic damage to the major white matter tracts in patients with different clinical phenotypes of multiple sclerosis: a voxelwise diffusion-tensor MR study." Radiology 2011;260(2):541–50. With permission from The Radiological Society of North America]

mented, so that morphological and positioning differences between subjects are corrected. The need for nonlinear deformation is particularly important when compensating for differences caused by brain atrophy.

Likewise, voxel-based analysis depends strongly on nonlinear registration methods and on their capability to produce an adequate overlap between subjects. However, the application of a nonlinear deformation introduces new issues related on how to use additional pieces of information on tract morphology in order to drive the registration. This is the consequence of an increased ability of this algorithm to compensate for local morphological differences. It has been shown that the accuracy of registration is higher when the whole DTI acquisition set is used to drive the transformation. For instance, the use of six channels of tensor components allows matching of the shape, magnitude, and orientation of local tensors between images better than that of one channel of FA or one channel of T2-weighted image.

Interpretation of DTI Findings

The interpretation of DTI findings is not straightforward. So far, the actual pathological features underlying diffusion abnormalities in MS are not completely understood. Some pieces of evidence suggest that the various, and often concomitant, pathological abnormalities occurring in MS (i.e., inflammation, demyelination, axonal loss, Wallerian degeneration) can affect diffusivity and anisotropic characteristics of tissues in opposing ways, thereby complicating the interpretation of DTI findings [1, 2, 11].

DTI Features of MS

Focal WM Lesions

DTI can contribute to grade the severity of damage within focal MS lesions, which typically show increased mean diffusivity (MD) and decreased fractional anisotropy (FA). However, abnormalities of DTI indexes are highly heterogeneous among different T2 lesions [3, 4]. The more severe abnormalities are found in T1 hypointense lesions (the so-called black holes) [12–14], which represent areas of irreversible tissue disruption, gliosis, and axonal loss. Conversely, conflicting results have been reported when comparing findings in gadolinium-enhancing vs. nonenhancing lesions [12–15], although most of the studies found lower FA values in enhancing lesions [14, 16]. These findings suggest that DTI might grade intrinsic abnormalities of acute lesions, which in turn are likely to reflect different substrates, some of which are transient (e.g., edema, demyelination, and remyelination) and others, permanent (e.g., neurodegeneration and axonal loss). Moreover, a longitudinal study of enhancing MS lesions followed up for 1–3 months [15] showed that MD values were increased in all lesions, but continued to increase during follow-up only in a subgroup of them. This finding highlights the notion that contrast enhancement does not allow the differentiation of acute MS lesions, which might be characterized by varying degrees of tissue disruption.

Compared to acute vascular neurological diseases such as stroke, a restricted diffusion has been reported in only a few lesions in patients with ADEM and MS in the acute phase of lesion formation [17–19].

NAWM

Using different methods of analysis, increased MD and decreased FA have been consistently found in the NAWM of MS patients [3, 4], even before the formation of new focal lesions [20]. Such abnormalities can be detected from the earliest stages of the disease, also in patients with clinically isolated syndrome (CIS) suggestive of MS [21, 22], and become more pronounced with increasing disease duration and neurological impairment [3, 4]. NAWM damage in MS patients is distributed but tends to be more severe in perilesional areas [23, 24] and at sites where MS lesions are typically located [14, 25].

NAWM damage is only partially correlated with the extent of T2 lesions and the severity of intrinsic lesion damage [3], which suggests that diffusivity changes in NAWM are not entirely dependent on retrograde degeneration of axons transected in focal lesions, but they rather represent diffuse abnormalities beyond the resolution of conventional MRI. A study [26] correlated diffusivity with perfusion findings in the corpus callosum of patients with relapsing-remitting (RR) MS. These results are more consistent with a primary ischemia than a secondary hypoperfusion due to Wallerian degeneration. These findings suggest a potentially reversible substrate of tissue damage, related to vascular impairment, whereas hypometabolism from axonal degeneration would represent an advanced and irreversible condition.

DTI is also useful for assessing the evolution of MS damage over time [21, 27]. Changes of DTI metrics seem to be independent of the concomitant accumulation of focal lesions and reduction in brain volume [27]. Thus, the application of DTI in monitoring the evolution of MS-related tissue damage over time looks promising for possible future trials of neuroprotective therapies.

GM

DTI abnormalities have been demonstrated also in the GM of MS patients [3, 4, 25, 28, 29]. They tend to be more pronounced in patients with the progressive forms of the disease [4, 29, 30], especially in those with secondary progressive (SP) MS [29]. In patients with SPMS and primary progressive (PP) MS [31, 32], as well as in those with RRMS [33] and CIS [34], such DTI abnor-

malities worsen over time. The severity of GM damage has been correlated with the degree of cognitive impairment in mildly disabled RRMS patients [35] and has been found to predict accumulation of disability over a 5-year period in patients with PPMS [32].

Despite the presence of conflicting results, higher MD values have been detected in deep GM nuclei of MS patients, especially in the thalamus [36]. Such abnormalities are more pronounced in SPMS than in RRMS patients [36]. In another study, average NAWM MD and FA thalamic changes over 1 year follow-up were predictors of clinical deterioration after 5 years in PPMS patients [37].

Possible explanations for the observed changes in GM diffusivity include a retrograde degeneration of neurons caused by injury to WM fiber tracks [38] and the presence of otherwise undetected MS lesions in the GM. These hypotheses are supported by the observation that GM damage is only partially correlated with the extent of focal WM lesions and the severity of their intrinsic damage [3, 4].

Cortical Lesions

Pathologic and MRI studies have shown that cortical lesions (CLs) are frequent in MS, especially in the progressive forms of the disease. Two DTI studies have demonstrated that, compared to patients' GM, intracortical MS lesions have increased FA values [39, 40], which might reflect an intralesional loss of dendrites, neuronal damage, and activation of microglial cells. One of these studies [40] also found that quantifying CL damage using DTI can help to distinguish the different MS clinical phenotypes, particularly benign (B) MS from SPMS patients (Fig. 16.3).

Optic Nerve

Early DTI studies of the optic nerve measured diffusivity in a few directions [41]. With the introduction of high-resolution fat- and CSF-suppressed zonal oblique multisection echo planar imaging (ZOOM-EPI) sequence [7, 42, 43], full DTI measurements from the optic nerve have been obtained.

It has been shown that in patients in the chronic phase following optic neuritis, MD of the diseased optic nerve is significantly higher than in either the fellow eye or those from healthy individuals [42]. DTI abnormalities were found to be correlated with abnormal visual evoked potentials (VEPs) latencies [42], loss of visual acuity [42, 44], and retinal nerve fiber layer thinning at optic coherence tomography, particularly at high contrast and in nerves previously affected by optic neuritis [44]. A multiparametric MRI study showed that, 4 years after a unilateral optic neuritis, decreased optic nerve FA and volume are factors independently associated with visual dysfunction [45].

Spinal Cord

With the development of sophisticated MR receiver coils and fast imaging techniques, it has been possible to obtain more reliable imaging of the spinal cord, which also allows the acquisition of quantitative data, such as DTI. Clark et al. [46] found higher MD values in spinal cord lesions of MS patients than in spinal cord from healthy controls. Abnormal DTI quantities from the cervical cord have been shown in patients with established MS [47, 48] and NMO [49] but not in those with CIS [50]. Cervical cord damage outside focal lesions is diffuse in SPMS, while it is more limited in BMS patients [51]. Several studies highlighted that brain and cord DTI metrics are independently associated with MS disability [27, 48, 49], thus calling for an aggregate use of these measures to improve the understanding of disease progression.

One longitudinal study which obtained DTI from relapse-onset MS patients at baseline and after a mean period of 2.4 years showed that baseline cord cross-sectional area and FA correlate with increased disability at follow-up [27].

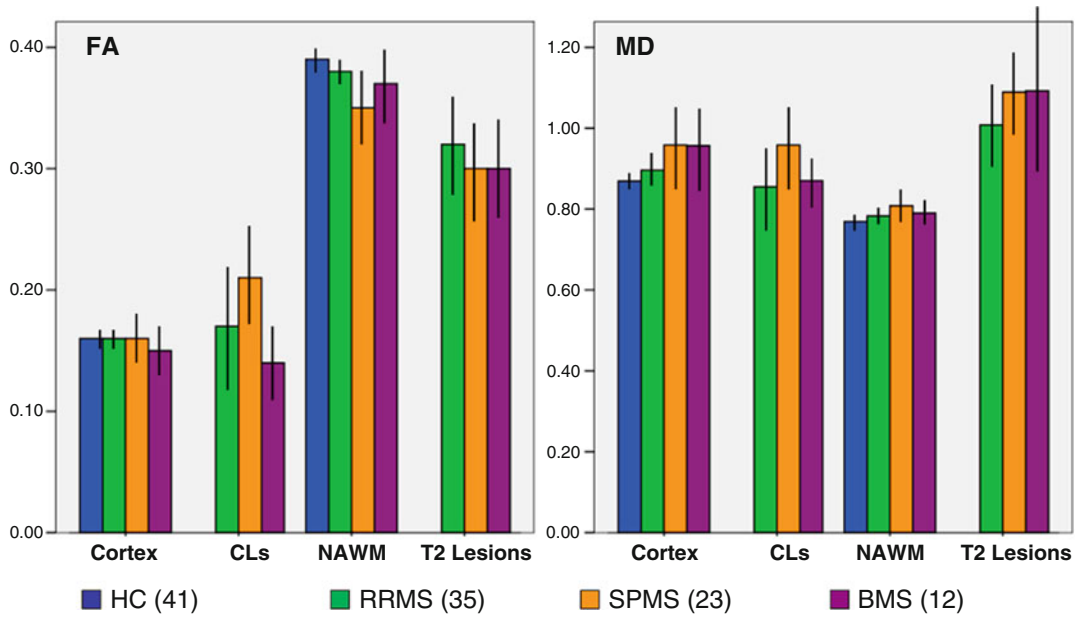

Fig. 16.3 Diffusion tensor imaging (DTI) values from cortical lesions (CLs), normal-appearing white matter (NAWM), and T2 lesions in multiple sclerosis (MS) patients with different disease clinical phenotypes and a group of healthy controls (HC). Compared to relapsing-remitting (RR) MS patients, those with secondary progressive (SP) MS had a higher T2 lesion volume and a more severe damage to the cortex, NAWM, T2 lesions, and CLs. With the exception of CLs, damage to all these compartments was similar in SPMS and benign (B) MS patients. Conversely, compared to SPMS, BMS patients had a lower fractional anisotropy (FA) and mean diffusivity (MD) of CLs. No difference was detected between RRMS and BMS patients. MD is expressed in units of $mm^2/s \times 10^{-3}$, FA is dimensionless index. [Adapted from Filippi M, Preziosa P, et al. Microstructural MR imaging of cortical lesion in multiple sclerosis. Mult Scler. 2013;19(4):418–26. With permission from Sage Publications]

Novel Strategies of Analysis

Tractography

Thanks to the ability of DTI to depict anisotropic tissues [52] and to detect their intrinsic structural abnormalities, several approaches have been developed to investigate damage to selected WM tracts, with the ultimate goal of improving the correlation with clinical measures. DTI tractography can be used to segment clinically eloquent WM pathways involved in different functions, such as the corticospinal tract (CST) [10, 53–55], the corpus callosum (CC) [56], optic radiations (OR) [57], and many others [22, 58–60]. In line with studies performed using histogram or regions-of-interest analysis, these studies have detected higher MD and lower FA of WM tracts in MS patients compared to healthy controls. Moreover, tract-derived DTI metrics correlate with several measures of locomotor disability and cognitive impairment [10, 22, 53–62]. For instance, MD and FA values of the CST correlated with clinical measures of locomotor disability or the pyramidal functional system score of the expanded disability status scale (EDSS) more than T2 lesion volume and the overall extent of diffusivity changes of the brain [53–55]. CIS patients with motor impairment had increased MD and T2 lesion volume in the CST compared to patients without pyramidal symptoms [10].

Increased MD of the CC has been associated with MS cognitive dysfunction [54, 63]. Compared to cognitively unimpaired BMS patients, those with cognitive impairment had significantly higher NAWM MD of the CC [56].

By applying a random forest analysis to measures derived from DTI tractography, damage to "critical" WM tracts, such as the cingulum, was shown to contribute significantly to the cognitive impairment of MS patients [62].

Using DTI tractography of the ORs, one study showed that patients with optic neuritis had reduced connectivity values (as assessed by the number of reconstructed streamlines via tractography) in both ORs compared to healthy controls, suggesting the occurrence of transsynaptic degeneration secondary to optic nerve damage [57]. In another study, OR DTI abnormalities correlated with retinal injury, assessed using optical coherence tomography, and visual impairment [61].

Advances in DTI and tractography have spurred the development of brain neuroconnectivity techniques, which define and quantify anatomical links between remote brain regions by axonal fiber pathways [64]. The use of these approaches has revealed reduced network efficiency in the WM structural networks of MS patients [65], including those at the earliest stages of the disease [66].

Voxel-Wise Approaches

Voxel-wise approaches to the analysis of quantitative MRI data, such as voxel-based morphometry [67], hold promise for improving our ability to study the structural features of MS damage, since they assess the topographical distribution of brain damage at a voxel level. Despite voxel-based MRI studies of MS patients having mainly focused on measures of atrophy [68], this approach can also be used for the analysis of DTI data. A voxel-based study [69] showed that patients with RRMS and BMS differ in terms of topographical distribution of WM damage, while no between-group differences were found when the overall extent of WM diffusivity abnormalities was assessed.

By combining tractography and voxel-based analysis, another study evaluated damage to several WM tracts, in terms of focal lesions and NAWM, from the main clinical phenotypes of MS [22]. Compared to healthy controls, diffusivity abnormalities were found in PPMS and CIS patients. The progressive MS forms showed the most severe and distributed diffusivity abnormalities, whereas BMS patients had only a limited WM damage. These findings support the notion that the assessment of regional damage using DTI may be more rewarding than that of "global" brain damage in order to gain insight into the relation between clinical status and disease burden in MS.

Tract-based spatial statistics (TBSS) is a technique that allows voxel-wise analysis of multi-subject DTI data. Using such a technique, compared to healthy controls, MS patients had reduced FA values of several WM tracts, which were related to deficits of specific cognitive domains [70, 71]. A voxel-based method has been developed to obtain estimates of WM tract volumes using DTI [72]: an index of volume change is derived from the differences between an FA atlas based on the morphological characteristics of a reference population and an individual subject FA map. This approach has been successfully applied to assess the topographical distribution of age-related WM volume changes in healthy subjects [73] and may be helpful to improve our understanding of MS abnormalities.

Other Inflammatory Demyelinating Diseases

NMO

NMO is an inflammatory demyelinating condition clinically characterized by optic neuritis and transverse myelitis and by the presence of a serum autoantibody (NMO-IgG) found to specifically target aquaporin-4 (AQP4). A DTI study revealed more severe cervical cord damage in NMO than in MS patients [49]. The assessment of brain NAWM and GM damage in NMO patients gave conflicting results: some authors found an isolated involvement of the GM [74],

while others described an involvement of several WM tracts [75], which was more severe in the ORs and CSTs [76].

ADEM

ADEM is classically defined as a monophasic dysimmune demyelinating disease, commonly affecting children, generally preceded by infections or vaccinations. A large effort has been invested in trying to define MRI parameters that are able to differentiate MS from ADEM. Using DTI, no abnormalities of the normal-appearing brain tissue and spinal cord have been detected in ADEM patients after the acute phase of the disease [77], whereas mild DTI abnormalities of the basal ganglia have been described [78].

Conclusions

Conventional MRI is limited by its lack of specificity to the heterogeneous pathological substrates of inflammatory and demyelinating diseases of the CNS. DTI has proved to be able to quantify the amount of intrinsic tissue damage of focal lesions and to detect more subtle abnormalities occurring in NAWM, GM, spinal cord, and optic nerve. DTI is contributing to improving the understanding of the mechanisms associated with the development of locomotor and cognitive impairment in patients with MS as well as the heterogeneity of the disease clinical phenotypes. The role of DTI in the diagnostic workup of patients with different demyelinating conditions deserves further and more extensive investigation.

Several approaches have been applied to analyze DTI data. Each of them has demonstrated the potential to provide useful pieces of information to improve our understanding of MS pathophysiology. However, the best acquisition and postprocessing strategies for MS studies remain a matter of debate, and the contribution of newer and more sophisticated DTI techniques in the study of demyelinating conditions needs to be evaluated further.

References

1. Mottershead JP, Schmierer K, et al. High field MRI correlates of myelin content and axonal density in multiple sclerosis—a post-mortem study of the spinal cord. J Neurol. 2003;250(11):1293–301.
2. Schmierer K, Wheeler-Kingshott CA, et al. Diffusion tensor imaging of post mortem multiple sclerosis brain. Neuroimage. 2007;35(2):467–77.
3. Rovaris M, Gass A, et al. Diffusion MRI in multiple sclerosis. Neurology. 2005;65(10):1526–32.
4. Rovaris M, Agosta F, et al. Diffusion tensor MR imaging. Neuroimaging Clin N Am. 2009;19(1):37–43.
5. Jones DK, Horsfield MA, et al. Optimal strategies for measuring diffusion in anisotropic systems by magnetic resonance imaging. Magn Reson Med. 1999;42(3):515–25.
6. Jones DK. The effect of gradient sampling schemes on measures derived from diffusion tensor MRI: a Monte Carlo study. Magn Reson Med. 2004;51(4):807–15.
7. Wheeler-Kingshott CA, Parker GJ, et al. ADC mapping of the human optic nerve: increased resolution, coverage, and reliability with CSF-suppressed ZOOM-EPI. Magn Reson Med. 2002;47(1):24–31.
8. Saritas EU, Cunningham CH, et al. DWI of the spinal cord with reduced FOV single-shot EPI. Magn Reson Med. 2008;60(2):468–73.
9. Pipe JG. Motion correction with PROPELLER MRI: application to head motion and free-breathing cardiac imaging. Magn Reson Med. 1999;42(5):963–9.
10. Pagani E, Filippi M, et al. A method for obtaining tract-specific diffusion tensor MRI measurements in the presence of disease: application to patients with clinically isolated syndromes suggestive of multiple sclerosis. Neuroimage. 2005;26(1):258–65.
11. Rosso C, Remy P, et al. Diffusion-weighted MR imaging characteristics of an acute strokelike form of multiple sclerosis. AJNR Am J Neuroradiol. 2006;27(5):1006–8.
12. Bammer R, Augustin M, et al. Magnetic resonance diffusion tensor imaging for characterizing diffuse and focal white matter abnormalities in multiple sclerosis. Magn Reson Med. 2000;44(4):583–91.
13. Filippi M, Iannucci G, et al. A quantitative study of water diffusion in multiple sclerosis lesions and normal-appearing white matter using echo-planar imaging. Arch Neurol. 2000;57(7):1017–21.
14. Filippi M, Cercignani M, et al. Diffusion tensor magnetic resonance imaging in multiple sclerosis. Neurology. 2001;56(3):304–11.
15. Castriota-Scanderbeg A, Sabatini U, et al. Diffusion of water in large demyelinating lesions: a follow-up study. Neuroradiology. 2002;44(9):764–7.
16. Werring DJ, Clark CA, et al. Diffusion tensor imaging of lesions and normal-appearing white matter in multiple sclerosis. Neurology. 1999;52(8):1626–32.

17. Tievsky AL, Ptak T, et al. Investigation of apparent diffusion coefficient and diffusion tensor anisotropy in acute and chronic multiple sclerosis lesions. AJNR Am J Neuroradiol. 1999;20(8):1491–9.
18. Bernarding J, Braun J, et al. Diffusion- and perfusion-weighted MR imaging in a patient with acute demyelinating encephalomyelitis (ADEM). J Magn Reson Imaging. 2002;15(1):96–100.
19. Abou Zeid N, Pirko I, et al. Diffusion-weighted imaging characteristics of biopsy-proven demyelinating brain lesions. Neurology. 2012;78(21):1655–62.
20. Rocca MA, Cercignani M, et al. Weekly diffusion-weighted imaging of normal-appearing white matter in MS. Neurology. 2000;55(6):882–4.
21. Gallo A, Rovaris M, et al. Diffusion-tensor magnetic resonance imaging detects normal-appearing white matter damage unrelated to short-term disease activity in patients at the earliest clinical stage of multiple sclerosis. Arch Neurol. 2005;62(5):803–8.
22. Preziosa P, Rocca MA, et al. Intrinsic damage to the major white matter tracts in patients with different clinical phenotypes of multiple sclerosis: a voxelwise diffusion-tensor MR study. Radiology. 2011;260(2):541–50.
23. Guo AC, Jewells VL, et al. Analysis of normal-appearing white matter in multiple sclerosis: comparison of diffusion tensor MR imaging and magnetization transfer imaging. AJNR Am J Neuroradiol. 2001; 22(10):1893–900.
24. Hasan KM, Gupta RK, et al. Diffusion tensor fractional anisotropy of the normal-appearing seven segments of the corpus callosum in healthy adults and relapsing-remitting multiple sclerosis patients. J Magn Reson Imaging. 2005;21(6):735–43.
25. Cercignani M, Bozzali M, et al. Magnetisation transfer ratio and mean diffusivity of normal appearing white and grey matter from patients with multiple sclerosis. J Neurol Neurosurg Psychiatry. 2001;70(3): 311–7.
26. Saindane AM, Law M, et al. Correlation of diffusion tensor and dynamic perfusion MR imaging metrics in normal-appearing corpus callosum: support for primary hypoperfusion in multiple sclerosis. AJNR Am J Neuroradiol. 2007;28(4):767–72.
27. Agosta F, Absinta M, et al. In vivo assessment of cervical cord damage in MS patients: a longitudinal diffusion tensor MRI study. Brain. 2007;130(Pt 8):2211–9.
28. Bozzali M, Cercignani M, et al. Quantification of brain gray matter damage in different MS phenotypes by use of diffusion tensor MR imaging. AJNR Am J Neuroradiol. 2002;23(6):985–8.
29. Rovaris M, Bozzali M, et al. Assessment of normal-appearing white and gray matter in patients with primary progressive multiple sclerosis: a diffusion-tensor magnetic resonance imaging study. Arch Neurol. 2002;59(9):1406–12.
30. Pulizzi A, Rovaris M, et al. Determinants of disability in multiple sclerosis at various disease stages: a multiparametric magnetic resonance study. Arch Neurol. 2007;64(8):1163–8.
31. Rovaris M, Gallo A, et al. Short-term accrual of gray matter pathology in patients with progressive multiple sclerosis: an in vivo study using diffusion tensor MRI. Neuroimage. 2005;24(4):1139–46.
32. Rovaris M, Judica E, et al. Grey matter damage predicts the evolution of primary progressive multiple sclerosis at 5 years. Brain. 2006;129(Pt 10):2628–34.
33. Oreja-Guevara C, Rovaris M, et al. Progressive gray matter damage in patients with relapsing-remitting multiple sclerosis: a longitudinal diffusion tensor magnetic resonance imaging study. Arch Neurol. 2005;62(4):578–84.
34. Rovaris M, Judica E, et al. A 3-year diffusion tensor MRI study of grey matter damage progression during the earliest clinical stage of MS. J Neurol. 2008;255(8):1209–14.
35. Rovaris M, Iannucci G, et al. Cognitive dysfunction in patients with mildly disabling relapsing-remitting multiple sclerosis: an exploratory study with diffusion tensor MR imaging. J Neurol Sci. 2002;195(2):103–9.
36. Fabiano AJ, Sharma J, et al. Thalamic involvement in multiple sclerosis: a diffusion-weighted magnetic resonance imaging study. J Neuroimaging. 2003; 13(4):307–14.
37. Mesaros S, Rocca MA, et al. Thalamic damage predicts the evolution of primary-progressive multiple sclerosis at 5 years. AJNR Am J Neuroradiol. 2011;32(6):1016–20.
38. Evangelou N, Konz D, et al. Regional axonal loss in the corpus callosum correlates with cerebral white matter lesion volume and distribution in multiple sclerosis. Brain. 2000;123(Pt 9):1845–9.
39. Poonawalla AH, Hasan KM, et al. Diffusion-tensor MR imaging of cortical lesions in multiple sclerosis: initial findings. Radiology. 2008;246(3):880–6.
40. Filippi M, Preziosa P, et al. Microstructural MR imaging of cortical lesion in multiple sclerosis. Mult Scler. 2013;19(4):418–26.
41. Iwasawa T, Matoba H, et al. Diffusion-weighted imaging of the human optic nerve: a new approach to evaluate optic neuritis in multiple sclerosis. Magn Reson Med. 1997;38(3):484–91.
42. Hickman SJ, Wheeler-Kingshott CA, et al. Optic nerve diffusion measurement from diffusion-weighted imaging in optic neuritis. AJNR Am J Neuroradiol. 2005;26(4):951–6.
43. Trip SA, Wheeler-Kingshott C, et al. Optic nerve diffusion tensor imaging in optic neuritis. Neuroimage. 2006;30(2):498–505.
44. Smith SA, Williams ZR, et al. Diffusion tensor imaging of the optic nerve in multiple sclerosis: association with retinal damage and visual disability. AJNR Am J Neuroradiol. 2011;32(9):1662–8.
45. Kolbe S, Chapman C, et al. Optic nerve diffusion changes and atrophy jointly predict visual dysfunction after optic neuritis. Neuroimage. 2009;45(3):679–86.
46. Clark CA, Werring DJ, et al. Diffusion imaging of the spinal cord in vivo: estimation of the principal diffusivities and application to multiple sclerosis. Magn Reson Med. 2000;43(1):133–8.

47. Agosta F, Benedetti B, et al. Quantification of cervical cord pathology in primary progressive MS using diffusion tensor MRI. Neurology. 2005;64(4):631–5.
48. Valsasina P, Rocca MA, et al. Mean diffusivity and fractional anisotropy histogram analysis of the cervical cord in MS patients. Neuroimage. 2005;26(3):822–8.
49. Benedetti B, Valsasina P, et al. Grading cervical cord damage in neuromyelitis optica and MS by diffusion tensor MRI. Neurology. 2006;67(1):161–3.
50. Agosta F, Filippi M. MRI of spinal cord in multiple sclerosis. J Neuroimaging. 2007;17 Suppl 1:46S–9S.
51. Benedetti B, Rocca MA, et al. A diffusion tensor MRI study of cervical cord damage in benign and secondary progressive MS patients. J Neurol Neurosurg Psychiatry. 2010;81(1):26–30.
52. Mori S, van Zijl PC. Fiber tracking: principles and strategies—a technical review. NMR Biomed. 2002;15(7–8):468–80.
53. Wilson M, Tench CR, et al. Pyramidal tract mapping by diffusion tensor magnetic resonance imaging in multiple sclerosis: improving correlations with disability. J Neurol Neurosurg Psychiatry. 2003;74(2):203–7.
54. Lin X, Tench CR, et al. 'Importance sampling' in MS: use of diffusion tensor tractography to quantify pathology related to specific impairment. J Neurol Sci. 2005;237(1–2):13–9.
55. Lin F, Yu C, et al. Diffusion tensor tractography-based group mapping of the pyramidal tract in relapsing-remitting multiple sclerosis patients. AJNR Am J Neuroradiol. 2007;28(2):278–82.
56. Mesaros S, Rocca MA, et al. Corpus callosum damage and cognitive dysfunction in benign MS. Hum Brain Mapp. 2009;30(8):2656–66.
57. Ciccarelli O, Toosy AT, et al. Optic radiation changes after optic neuritis detected by tractography-based group mapping. Hum Brain Mapp. 2005;25(3): 308–16.
58. Audoin B, Guye M, et al. Structure of WM bundles constituting the working memory system in early multiple sclerosis: a quantitative DTI tractography study. Neuroimage. 2007;36(4):1324–30.
59. Rocca MA, Pagani E, et al. Altered functional and structural connectivities in patients with MS: a 3-T study. Neurology. 2007;69(23):2136–45.
60. Rocca MA, Valsasina P, et al. Structural and functional MRI correlates of Stroop control in benign MS. Hum Brain Mapp. 2009;30(1):276–90.
61. Reich DS, Smith SA, et al. Damage to the optic radiation in multiple sclerosis is associated with retinal injury and visual disability. Arch Neurol. 2009; 66(8):998–1006.
62. Mesaros S, Rocca MA, et al. Diffusion tensor MRI tractography and cognitive impairment in multiple sclerosis. Neurology. 2012;78(13):969–75.
63. Lin X, Tench CR, et al. Use of combined conventional and quantitative MRI to quantify pathology related to cognitive impairment in multiple sclerosis. J Neurol Neurosurg Psychiatry. 2008;79(4):437–41.
64. Guye M, Bettus G, et al. Graph theoretical analysis of structural and functional connectivity MRI in normal and pathological brain networks. MAGMA. 2010;23(5–6):409–21.
65. Shu N, Liu Y, et al. Diffusion tensor tractography reveals disrupted topological efficiency in white matter structural networks in multiple sclerosis. Cereb Cortex. 2011;21:2565–77.
66. Li Y, Jewells V, et al. Diffusion tensor imaging based network analysis detects alterations of neuroconnectivity in patients with clinically early relapsing-remitting multiple sclerosis. Hum Brain Mapp. 2013;34(12):3376–91.
67. Ashburner J, Friston KJ. Voxel-based morphometry—the methods. Neuroimage. 2000;11(6 Pt 1): 805–21.
68. Filippi M, Agosta F, et al. Regional assessment of brain atrophy: a novel approach to achieve a more complete picture of tissue damage associated with central nervous system disorders? AJNR Am J Neuroradiol. 2007;28(2):260–1.
69. Ceccarelli A, Rocca MA, et al. The topographical distribution of tissue injury in benign MS: a 3T multiparametric MRI study. Neuroimage. 2008;39(4): 1499–509.
70. Dineen RA, Vilisaar J, et al. Disconnection as a mechanism for cognitive dysfunction in multiple sclerosis. Brain. 2009;132(Pt 1):239–49.
71. Roosendaal SD, Geurts JJ, et al. Regional DTI differences in multiple sclerosis patients. Neuroimage. 2009;44(4):1397–403.
72. Pagani E, Horsfield MA, et al. Assessing atrophy of the major white matter fiber bundles of the brain from diffusion tensor MRI data. Magn Reson Med. 2007;58(3):527–34.
73. Pagani E, Agosta F, et al. Voxel-based analysis derived from fractional anisotropy images of white matter volume changes with aging. Neuroimage. 2008;41(3): 657–67.
74. Rocca MA, Agosta F, et al. Magnetization transfer and diffusion tensor MRI show gray matter damage in neuromyelitis optica. Neurology. 2004;62(3):476–8.
75. Liu Y, Duan Y, et al. A tract-based diffusion study of cerebral white matter in neuromyelitis optica reveals widespread pathological alterations. Mult Scler. 2012;18(7):1013–21.
76. Zhao DD, Zhou HY, et al. Diffusion tensor imaging characterization of occult brain damage in relapsing neuromyelitis optica using 3.0T magnetic resonance imaging techniques. Neuroimage. 2012;59(4): 3173–7.
77. Inglese M, Salvi F, et al. Magnetization transfer and diffusion tensor MR imaging of acute disseminated encephalomyelitis. AJNR Am J Neuroradiol. 2002;23(2):267–72.
78. Holtmannspotter M, Inglese M, et al. A diffusion tensor MRI study of basal ganglia from patients with ADEM. J Neurol Sci. 2003;206(1):27–30.

DTI in Dementing Conditions

17

Massimo Filippi, Federica Agosta,
and Edoardo Gioele Spinelli

Learning Points

- Diffusion-weighted imaging is useful in the early diagnosis of Creutzfeld–Jakob disease.
- Diffusion tensor imaging (DTI) reveals brain microstructural abnormalities associated with the most common neurodegenerative dementing conditions.
- DTI studies in Alzheimer's disease (AD) have consistently found white matter (WM) microstructural damage in temporal and frontal lobes, posterior cingulum, corpus callosum, superior longitudinal fasciculus, and uncinate fasciculus, with a posterior-to-anterior gradient of severity.
- Using DTI, WM abnormalities can be identified, which can be used to follow the progression from normal cognition to mild cognitive impairment (MCI) and from MCI to AD.
- Patterns of DTI abnormalities are likely to discriminate between AD and other dementing conditions, such as frontotemporal lobar degeneration spectrum and dementia with Lewy bodies.

M. Filippi, MD (✉) • E.G. Spinelli, MD
Neuroimaging Research Unit and Department of Neurology, Division of Neuroscience, Institute of Experimental Neurology, San Raffaele Scientific Institute, Vita-Salute San Raffaele University, Via Olgettina 60, 20132 Milan, Italy
e-mail: filippi.massimo@hsr.it

F. Agosta, MD, PhD
Neuroimaging Research Unit, Division of Neuroscience, Institute of Experimental Neurology, San Raffaele Scientific Institute, Vita-Salute San Raffaele University, Via Olgettina 60, 20132 Milan, Italy

Introduction

Although a detailed clinical assessment remains the basis of the evaluation of a patient with suspected dementia, current European [1, 2], UK ((NICE) March [3]), and US [4] guidelines recommend that structural imaging should be used in the assessment of people with suspected dementia to exclude other cerebral pathologies and to help establish subtype diagnosis. In general, the tendency is to move away from simply excluding other (brain) diseases, towards finding specific pointers to a diagnosis [5]. This approach is exemplified by the formal incorporation of biomarkers, including those from neuroimaging, in the most recent revisions of the diagnostic criteria for Alzheimer's disease (AD) [6, 7] and other neurodegenerative forms of dementia [8–10].

W. Van Hecke et al. (eds.), *Diffusion Tensor Imaging*, DOI 10.1007/978-1-4939-3118-7_17

Recent years have also witnessed an impressive advancement in the development of novel imaging approaches, which, with varying degrees of success, have improved our understanding of the pathophysiology of dementing conditions. These new techniques, which include diffusion-weighted (DWI) and diffusion tensor (DTI) imaging, are likely able to fill voids and improve our ability to diagnose, monitor and understand the pathophysiology of these diseases. DWI is commonly used in the diagnostic work up of rapidly progressive dementia cases, particularly when Creutzfeld–Jakob disease (CJD) is suspected [1]. Although, at present, DTI does not have a role in the diagnosis, routine assessment, and monitoring of neurodegenerative dementia [1], significant efforts are underway in order to achieve harmonization of both acquisition and post-processing procedures [11], which are likely to contribute to a dramatic change of the clinical scenario. This chapter provides an overview of the findings obtained using DWI and DTI in patients with neurodegenerative dementing conditions, which support a more extensive use of these techniques to study disease evolution and to monitor drug efficacy in clinical trials.

Creutzfeldt–Jakob Disease

CJD is a rapidly progressive dementing syndrome, eventually leading to death in a few months after disease onset [12]. Typically, the clinical presentation of the disease includes neurological signs, such as ataxia and myoclonus. Most CJD cases are sporadic (sCJD), but some are genetically determined (familial CJD—fCJD) or transmitted through contaminated biological material. The pathogenesis of sCJD remains partly unknown, but it is believed that it is likely due to the conversion of normal prion protein—whose physiologic function remains undetermined—to proteinaceous infectious scrapie particles (PrP^{Sc}) that accumulate in and around neurons, leading to widespread neuronal degeneration [12, 13]. This pathologic process is macroscopically described as spongiform degeneration of the brain. Variant CJD is believed to have occurred as a consequence of the epidemic of bovine spongiform encephalopathy in the UK.

Currently, DWI is more useful for the diagnosis of prion disease than for any other dementia [14, 15]. DWI can show focal changes in CJD not yet apparent on fluid-attenuated inversion recovery (FLAIR) images (up to 20 % of cases) [14, 15]. The better performance of DW MRI over FLAIR in the identification of hyperintensities suggests that diffusion restriction is a crucial feature of CJD pathology, probably due to a process of vacuolation [16]. The combined presence of DWI and/or FLAIR hyperintensities has the highest sensitivity and specificity for the diagnosis of sCJD (83–96 % sensitivity, 83–95 % specificity) [14, 15, 17–19]. The recently updated diagnostic criteria of sCJD include high signal abnormalities on DWI or FLAIR in the caudate nucleus and putamen or in at least two cortical regions as one of the supportive markers for a diagnosis of probable CJD, together with periodic sharp wave complexes on the electroencephalogram and 14-3-3 protein detection in the cerebrospinal fluid [19].

In sCJD, the most common patterns of DW MRI hyperintensities are neocortical, limbic and subcortical (54–68 % of cases), and neocortical and limbic (24–27 % of cases) [14, 15]. No neocortical involvement is detected in 5–11 % of patients with sCJD [14, 15]. In sCJD, cortical areas most commonly involved are the cingulate gyrus, superior and middle frontal gyrus, insula, precuneus, angular gyrus, and parahippocampal gyrus, with a relative sparing of the precentral gyrus [15] (Fig. 17.1). In both sCJD and fCJD, striatal hyperintensity almost always shows an anterior-to-posterior gradient, with prevalent involvement of the caudate and relative sparing of the posterior putamen [15]. Thalamic alterations on DWI are usually bilateral, involving the dorsomedial and posterior (pulvinar) regions [15]. The DWI hyperintensity in subcortical regions almost invariably corresponds to a hypointensity on the apparent diffusion coefficient map, a finding which confirms a pattern of restricted diffusion (Fig. 17.1)

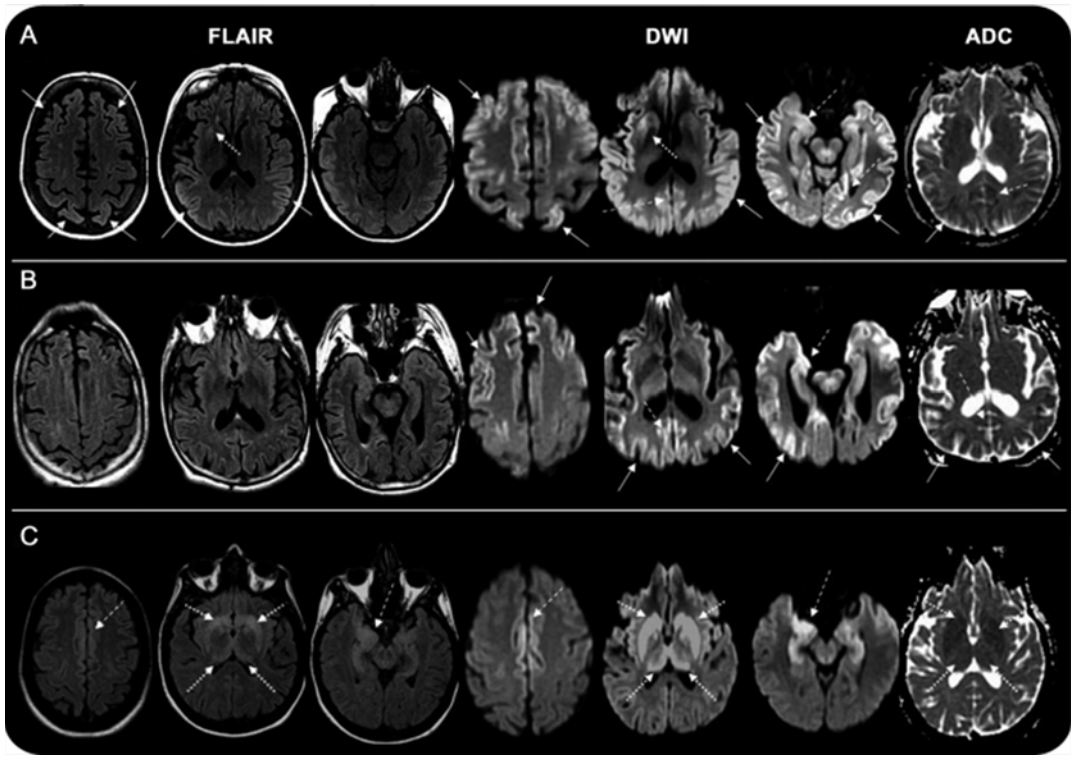

Fig. 17.1 Three common variations of sporadic Creutzfeldt–Jakob disease presentation on MRI. (**a**) Neocortical (*solid arrow*), limbic (*dashed arrow*), and subcortical gray matter hyperintensities (*dotted arrow*) on diffusion weighted imaging (DWI) and fluid attenuated inversion recovery (FLAIR) scans. (**b**) Neocortical and limbic cortex involvement. (**c**) Limbic and subcortical involvement. Note that the DWI shows the hyperintensities much more than the corresponding FLAIR sequences, and that DWI hyperintensities often have corresponding apparent diffusion coefficient (ADC) hypointensity. ADC abnormalities are most easily identified in the basal ganglia. [Reprinted from Vitali, P., E. Maccagnano, et al. (2011). "Diffusion-weighted MRI hyperintensity patterns differentiate CJD from other rapid dementias." Neurology 76(20): 1711–9. With permission from Wolters Kluwer Health.]

[15]. In variant CJD, there is a selective involvement of the medial and dorsal (pulvinar) thalamic nuclei, leading to the so-called hockey stick sign [20].

To our knowledge, only one study evaluated the relationship between DWI alterations and the severity of the clinical course in nine patients with sCJD [21], demonstrating that patients harboring hyperintensities in both the cortex and basal ganglia experience a significantly shorter interval from disease onset to akinetic mutism than those with only cortical ribbon hyperintensity.

Cortical and basal ganglia degeneration is an important feature of CJD pathology. On the contrary, only a very few studies investigated white matter (WM) involvement using DT MRI in these patients [22, 23]. One study, which assessed patients with the E200K familial variant of CJD [22], found a significant decrease of fractional anisotropy (FA) of the corticospinal tract, internal capsule, external capsule, fornix, and posterior thalamic radiation, which was correlated with disease duration. FA alterations of fCJD were mainly due to an increase of radial diffusivity [22], suggesting axonal damage presumably secondary to PrP^{Sc} propagation along WM pathways. A second DTI study in sCJD patients did not find WM abnormalities in the corpus callosum and posterior limb of the internal capsule, but showed a significant mean diffusivity (MD) decrease in the caudate and pulvinar regions relative to healthy controls [23].

Alzheimer's Disease and Mild Cognitive Impairment

The earliest pathologic brain abnormalities associated with AD develop years, if not decades, before the onset of the first memory symptoms [24, 25]. Such alterations include misfolded proteins aggregating into extracellular amyloid β plaques and intracellular neurofibrillary tangles, followed by inflammatory damage, oxidation, excitotoxicity, and cell death in the central nervous system. The prospect of experimental treatment with the potential to slow or prevent AD progression has prompted an increased interest in the identification of individuals with AD early in the course of the disease, even at the mild cognitive impairment (MCI) stage [6].

DTI in AD and MCI Patients

The loss of cortical neurons in AD is invariably accompanied by axonal degeneration along WM pathways. DTI studies of AD have found consistently increased MD and decreased FA compared with controls in several brain regions (Fig. 17.2), most notably in temporal and frontal lobes, posterior cingulum, corpus callosum, superior longitudinal fasciculus (SLF), and uncinate fasciculus [26, 27]. A posterior-to-anterior gradient in the severity of WM abnormalities has been observed, with posterior regions being affected more severely [26]. WM changes in AD generally follow the anatomical pattern of cortical atrophy [26, 28], supporting the theory that Wallerian degeneration may account for WM involvement in this disease.

The clinical relevance of DTI alterations in AD patients is reflected by the association between decreased global cognition, as measured using the Mini-Mental State Examination (MMSE), and reduced FA [29–41] or increased MD [30, 32, 33] values in at least one brain region. Significant correlations between altered DTI metrics of temporo-parietal WM structures and neuropsychological measures of memory performance have also been reported by several studies [42–46]. In addition, a number of studies also showed that decreased FA in the frontal lobe correlates with poor performance at neuropsychological assessment of executive functions of AD patients [35, 47–49], as well as with the severity of neuropsychiatric symptoms [50, 51].

DTI studies have attempted to elucidate the earliest point at which diffusivity abnormalities can be detected by focusing on patients with amnestic MCI [28, 33, 35, 43, 46, 52–63]. Two recent meta-analyses showed that differences between amnestic MCI and controls parallel those between AD and controls, but fewer regions reached statistical significance [26, 27], possibly because MCI consists of an heterogeneous group of individuals and there are no universally recognized criteria to define this condition. Corpus callosum, cingulum, parahippocampal and frontal tracts were found to be affected in the prodromal stages of AD [28, 43, 54, 55, 59, 60, 63]. Interestingly, in patients with amnestic MCI, damage to the majority of WM tracts was not correlated with cortical atrophy [28], thus suggesting that, in the early phases of the disease, WM abnormalities may reflect a primary WM tract damage over and above cortical pathology. Similar findings have been reported in cognitively normal individuals who were later diagnosed with amnestic MCI at 2-year follow-up [64]. WM alterations at baseline in these subjects were predictive of subsequent cognitive decline, in the absence of significant correlation with cortical atrophy [64]. In addition, a number of studies [65–72] showed a similar pattern of WM damage in cognitively normal individuals with high risk for the development of AD (i.e., Apolipoprotein E4 genotype and/or positive family history). Preclinical subjects with familial autosomal dominantly inherited AD also showed decreased WM integrity of the fornix and orbitofrontal lobe [73]. Taking together, these studies suggest that microstructural WM changes may serve as a potential imaging marker of early AD-related brain damage.

DTI tractography can improve the sensitivity and specificity of diffusion measurements by localizing WM changes in specific neuronal pathways of MCI/AD patients. Diffusivity abnormalities have been shown in the splenium

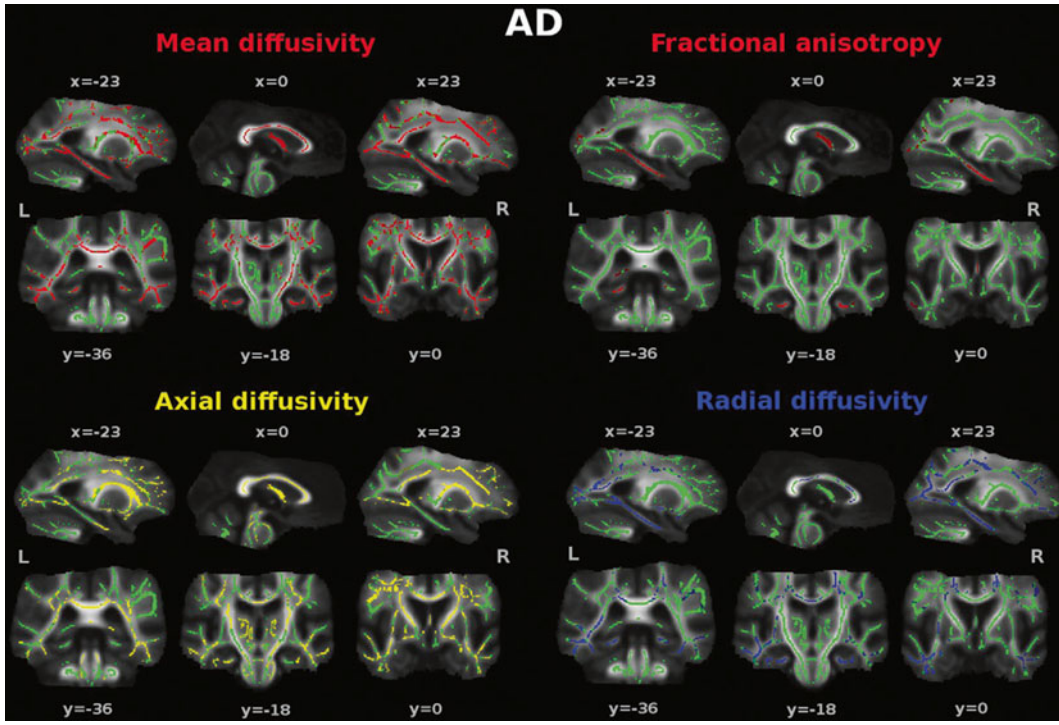

Fig. 17.2 Diffusion tensor imaging (DTI) abnormalities in patients with Alzheimer's disease (AD) compared with healthy controls. Tract-based spatial statistics color maps showing voxel-wise differences between patients and healthy controls are overlaid on a mean fractional anisotropy (FA) skeleton. Voxels of increased mean diffusivity and decreased FA are shown in *red*; voxels of increased axial and radial diffusivity are shown in *yellow* and *blue*, respectively. The results for mean, axial, and radial diffusivity are shown at $p<0.05$ corrected for multiple comparisons (family-wise error). Results from FA are shown at an uncorrected statistical threshold ($p<0.05$) [Reprinted from Agosta F, Pievani M, et al. "White matter damage in Alzheimer disease and its relationship to gray matter atrophy." Radiology 2011;258(3): 853–63. With permission from The Radiological Society of North America.]

of the corpus callosum, posterior cingulum and uncinate fasciculi [74–78] of AD patients. Only a few tractography studies have been carried out in amnestic MCI patients [79–82], and diffusion abnormalities of the posterior cingulum were found in these patients relatively to controls, but not to early AD patients [79]. In amnestic MCI, WM damage was found not only in the limbic pathways (i.e., fornix [82] and cingulum [81]), but also in the major cortico-cortical WM tracts subserving association cortices (i.e., the uncinate fasciculus, the inferior fronto-occipital fasciculus, the inferior longitudinal fasciculus, the superior longitudinal fasciculus and the corpus callosum) [80]. Recently, a novel method to analyze DTI data, called anatomical connectivity mapping (ACM), has been proposed to assess abnormalities of structural brain connectivity. ACM can be easily obtained by initiating diffusion tractography streamlines from all parenchymal voxels, and then counting the number of streamlines passing through each voxel of the brain. An exploratory study employing such an approach in patients with AD and amnestic MCI revealed that ACM provides information that is complementary to that offered by FA with increased sensitivity [83]. Additionally, an unexpected increase of ACM has been found in the putamen of AD (the only group under treatment with cholinesterase inhibitors) but not of MCI patients [83]. An intriguing explanation is that such an increase of ACM in AD patients might reflect brain plasticity driven by cholinesterase inhibitors.

Diagnostic Accuracy of DTI in AD and MCI Patients

For DTI to be useful in the clinical setting, one must be able to make inferences at the level of the individual rather than the group. Adding DTI measurements of the posterior cingulum to hippocampal volume significantly improves the accuracy in separating AD and amnestic MCI subjects from healthy controls (from 63 to 74 % in amnestic MCI, and from 78 to 91 % in AD) [55]. Diffusivity abnormalities of the left posterior cingulum were able to distinguish subjects with amnestic MCI from those with non-amnestic MCI with an accuracy of 85 % [56]. In addition, hippocampal diffusivity measurements were found to be more sensitive than hippocampal volume in predicting conversion to AD in patients with amnestic MCI [33, 52, 53]. The severity of microstructural damage beyond the medial temporal lobe was also associated with an increased short-term risk to develop AD in amnestic MCI patients [58]. A reduction of FA of the fornix has been recently proposed as an imaging sign that may be helpful in order to differentiate AD patients from normal controls with an accuracy of 75 %, as well as to predict conversion from normal cognitive status to amnestic MCI and from amnestic MCI to AD (with an accuracy of 96 % and 92 %, respectively) [41]. An individual classification of MCI cases using support vector machine analysis of DTI data allowed for an individual classification with an accuracy up to 91 % (healthy controls vs. MCI) and 98 % (stable vs. progressive MCI at 1 year) [57]. Furthermore, such an approach resulted in a highly accurate individual classification of stable vs. progressive MCI at 1 year, regardless of the MCI subtype, indicating that it might become a tool for early detection of MCI subjects evolving to overt dementia [57].

Longitudinal DTI Studies

Longitudinal studies of fiber tract injury in neurodegenerative diseases are still scanty. Amnestic MCI subjects experience a significant fractional anisotropy (FA) decline predominantly in the anterior corpus callosum after 13–16 months from a baseline scan [84]. More recently, longitudinal changes of WM microstructural alterations in AD patients with and without treatment with galantamine, a cholinesterase inhibitor, were evaluated over a 12-month follow up [85]. Galantamine slowed the FA decrease of the posterior body of the corpus callosum over a 6-month period compared to placebo, but this effect was not seen anymore after a 6-month open-label treatment of all AD patients [85]. A large-scale application of DTI in multicentre studies may help in the identification of markers that are likely to provide sensitive outcome measures in clinical trials of patients with AD and MCI.

Novel Strategies of Analysis

A correlation between the site of amyloid-β deposition in AD patients and the location of major brain hubs as defined by graph theoretical analysis of functional connectivity in healthy adults has been demonstrated [86]. These regions include the posterior cingulate cortex/precuneus, the inferior parietal lobule, and the medial frontal cortex, implying that the hubs are preferentially affected in the progression of AD. Using structural and DTI, abnormal topological properties were described also in the structural brain networks of patients with AD. In a study that used between-subject covariation in regional measures of cortical thickness to infer anatomical networks from a large structural MRI data set, global clustering and path length were increased in patients with AD relative to controls [87]. This study also found a decreased centrality of the classical hubs, such as the temporal and parietal heteromodal cortices, and an increased centrality of unimodal association cortex, such as the lingual gyrus and lateral occipitotemporal gyrus, as well as paralimbic regions [87]. The global clustering coefficient and path length of MCI structural networks were found to be intermediate between the AD group and normal elderly people [88]. In addition, compared with controls, AD and MCI patients retained their hub regions in the frontal lobe but

showed a loss of such regions in the temporal lobe [88]. Similar to functional MRI data, this study also revealed increased short-range interregional correlations and disrupted long distance interregional correlations in MCI and AD [88]. An abnormal topological organization of large-scale WM networks was found in AD patients using DTI, with increased path length and decreased global efficiency compared with controls [89]. More importantly, WM connectivity patterns were associated with cognitive deficits [89], implying that a disturbed communication between different brain regions is likely to be important in the cognitive decline typical of this condition.

Frontotemporal Lobar Degeneration

Frontotemporal lobar degeneration (FTLD) represents the second most common early-onset neurodegenerative dementia after AD. FTLD is a clinically and pathologically heterogeneous spectrum of disorders, which encompasses distinct clinical syndromes: the behavioral variant of frontotemporal dementia (bvFTD) [10], and the language variant [9]. BvFTD presents with marked changes in personality and behavior [10], and, pathologically, is associated with all the three major FTLD pathologies, characterized by abnormal cellular inclusions containing either tau, TAR DNA-binding protein 43 (TDP-43), or fused-in-sarcoma protein [90]. In the language variant, known as primary progressive aphasia (PPA), a prominent, isolated language deficit is the dominant feature during the initial phase of the disease [91]. Distinct profiles of language impairment define the three clinical phenotypes of PPA [9]: the nonfluent/agrammatic (for convenience hereafter called nonfluent), characterized by agrammatism in language production and effortful speech with motor speech deficits; the semantic, characterized by progressive loss of knowledge about words and objects in the context of relatively preserved fluency of speech; and the logopenic, characterized by impaired naming and repetition in the context of spared syntactic and motor speech abilities. Clinicopathological series suggest that the majority of nonfluent patients exhibit FTLD-tau or, less frequently, FTLD-TDP pathology, while most semantic cases have a TDP-43 proteinopathy [90]. AD is the most likely underlying pathology of the logopenic variant [92].

DTI vs. Pathology and Genetic Background in FTLD

In a single, pathology-proven bvFTD case, DTI detected decreased FA values in WM frontal regions, where histopathology revealed a typical frontal lobe degeneration of non-AD type [93]. Neuropathological [94, 95] and structural MRI [96] observations suggested that FTLD-tau may have a more severe involvement of WM than FTLD-TDP cases. In view of this, DTI metrics were recently evaluated in autopsy- or genetic-proven FTLD patients and showed a 96 % sensitivity and 100 % specificity in distinguishing between the two pathological variants [97]. This could prove to be clinically relevant, as potential disease-modifying treatments emerge that target tau or TDP-43.

Microtubule-associated protein tau (MAPT), progranulin (GRN), and C9orf72 mutations are the major genetic causes of autosomal dominant FTLD [98, 99]. Presymptomatic individuals with these mutations represent the ideal population to assess the initial alterations of FTLD. A DTI study performed in a small sample of subjects with GRN mutation revealed decreased FA of the left uncinate and left inferior occipitofrontal fasciculi, with respect to non-carrier controls [100]. More recently, a larger sample of MAPT or GRN mutation carriers was found to have distributed pattern of reduced FA in frontotemporal WM tracts, in comparison with non-carriers [101].

DTI in bvFTD Patients

Using a regions of interest (ROI)-based approach, a study of bvFTD patients found DTI abnormalities of WM tracts passing through the frontal—anterior

cingulum, genu of the corpus callosum, anterior SLF—and temporal lobes—uncinate fasciculus and inferior longitudinal fasciculus (ILF) [102]. Voxel-based DTI studies in bvFTD patients found FA reduction in frontoparietal regions, which are likely to correspond to the SLF [103, 104], and in frontal and temporal WM regions, including the anterior corpus callosum, anterior cingulum, and uncinate, bilaterally (Fig. 17.3) [75, 104]. Such findings were confirmed by a DTI tractography study, which disclosed a significant FA decrease in all major association WM tracts (ILF, uncinate, and SLF) and genu of the corpus callosum, as well as a sparing of corticospinal tracts and splenium of the corpus callosum [105]. The majority of studies also detected diffusivity abnormalities in posterior WM regions, such as the posterior SLF and the posterior cingulum [75, 102, 104]. Although bvFTD is typically associated with frontal and anterior temporal atrophy [106], patterns of atrophy are known to be heterogeneous in this condition [107]. In addition, even in the classic frontotemporal cases, the lateral and medial parietal lobes usually become affected later in the disease course [108]. It is therefore tempting to speculate that DTI metrics may be viewed as early markers of WM injury in bvFTD patients, which may result at a later stage in detectable volumetric abnormalities.

DTI in PPA Patients

To date, only a few studies to date have investigated the patterns of WM abnormalities in small samples of PPA patients using DTI. Most of these studies were performed in patients with the two major variants (i.e., nonfluent and semantic).

Using ROI-based or tractography DTI to investigate the WM language tracts of these patients, it has been showed that the nonfluent variant is characterized by an involvement of all the left SLF components [102, 109–111] (Fig. 17.4). In contrast, the ventral tracts connecting the temporal lobe with the occipital and the orbitofrontal cortices (i.e., the ILF and uncinate fasciculi) were relatively spared [102, 109, 111]. Studies using a voxel-wise approach showed that nonfluent patients have not only a damage to the fronto-parieto-temporal connections but also an involvement of the corpus callosum, cingulum bundle, external capsule, several regions of the prefrontal and orbitofrontal and parietotemporal WM, mainly in the left hemisphere [104, 112, 113]. A recent tract-based spatial statistics (TBSS) study found a damage to portions of the ILF in nonfluent patients [112].

In the semantic variant, abnormalities of WM tract diffusivity were identified in the major inferior and superior temporal connections of the left hemisphere, thus mirroring the severe atrophy affecting the same regions: the ILF, inferior-fronto-occipital fasciculus, and the uncinate fasciculus within the ventral stream, and the arcuate and the temporo-parietal component of the SLF within the dorsal stream [102, 104, 109, 112, 114, 115] (Fig. 17.4). Although tractography studies have suggested that the fronto-parietal connections are relatively spared in the semantic variant [109, 114], a finding which couples with the absence of syntactic deficits in these patients, a few TBSS reports have shown an involvement of the left prefrontal and parieto-frontal WM contributing to the SLF and corona radiata [104, 112].

DTI measures of the anterior corpus callosum and left SLF differentiated bvFTD from nonfluent cases, while the best predictors of semantic PPA compared with both bvFTD and nonfluent cases were diffusivity abnormalities of the left uncinate and inferior longitudinal fasciculus [104].

Two studies so far applied DTI to patients with the logopenic variant of PPA [104, 109], showing the most consistent abnormalities in the left SLF temporoparietal component; abnormalities were also detected in the left arcuate fasciculus, other components of the left SLF and right temporoparietal SLF (Fig. 17.4). These findings suggest that the logopenic variant is associated with damage to the WM tracts connecting regions important for sentence repetition and phonological short-term memory [116].

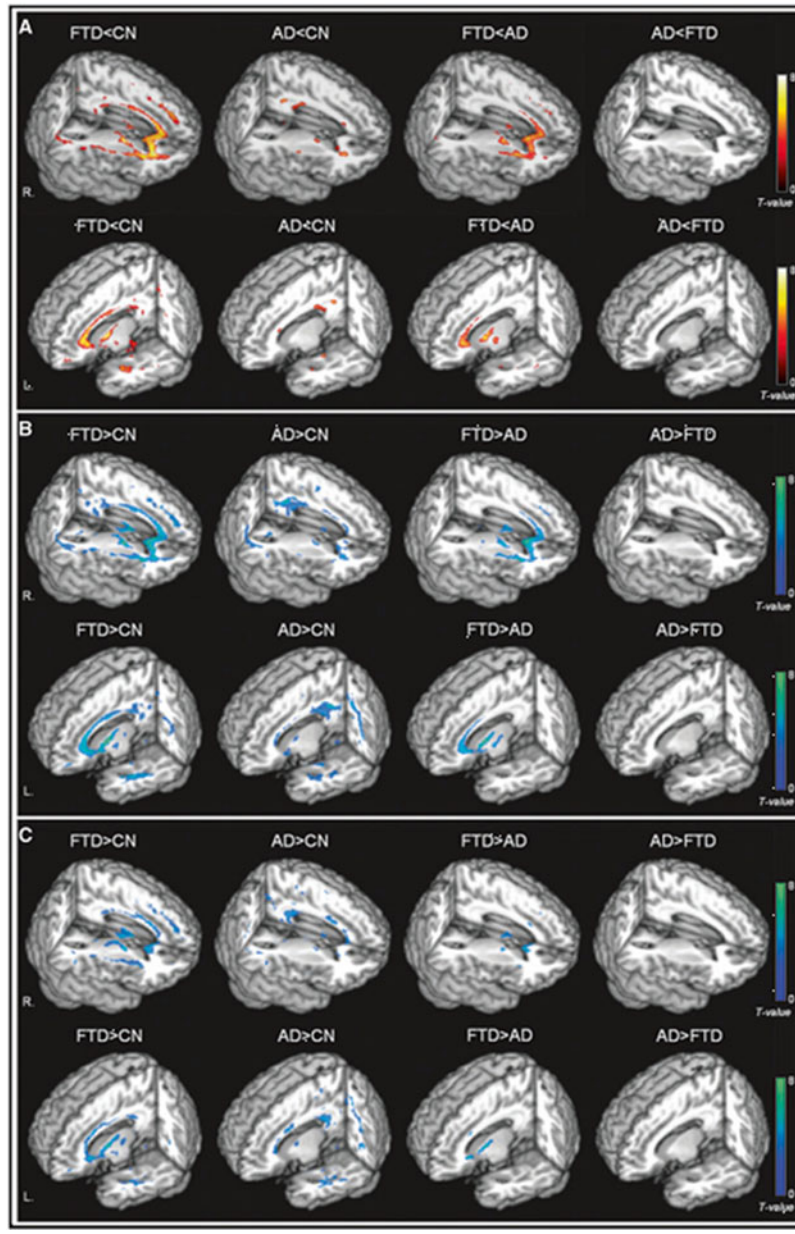

Fig. 17.3 Rendered displays of diffusion tensor imaging (DTI) abnormalities in patients with the behavioral variant of frontotemporal dementia (bvFTD) or Alzheimer's disease (AD) compared with cognitively normal subjects, as well as direct comparisons between bvFTD and AD: (**a**) reduced fractional anisotropy (warm colors); (**b**) increased radial diffusivity (cool colors); (**c**) increased axial diffusivity (cool colors) [Reprinted from Zhang, Y., N. Schuff, et al. "White matter damage in frontotemporal dementia and Alzheimer's disease measured by diffusion MRI." Brain 2009;132(Pt 9): 2579–92. With permission from Oxford University Press.]

Differential Diagnosis: FTLD vs. AD

DTI is increasingly being used to improve the diagnostic differentiation between FTLD and AD. When compared with AD, bvFTD is associated with greater reductions of FA in frontal regions (Fig. 17.3) [75], which suggests that WM injury is more prominent in bvFTD than in AD. One recent study combined cortical thickness measurement and DTI to compare FTLD (both bvFTD and PPA) and AD patients, with autopsy- or cerebrospinal fluid-confirmed disease [117]. The direct comparison of the two groups showed a significantly greater atrophy in inferior

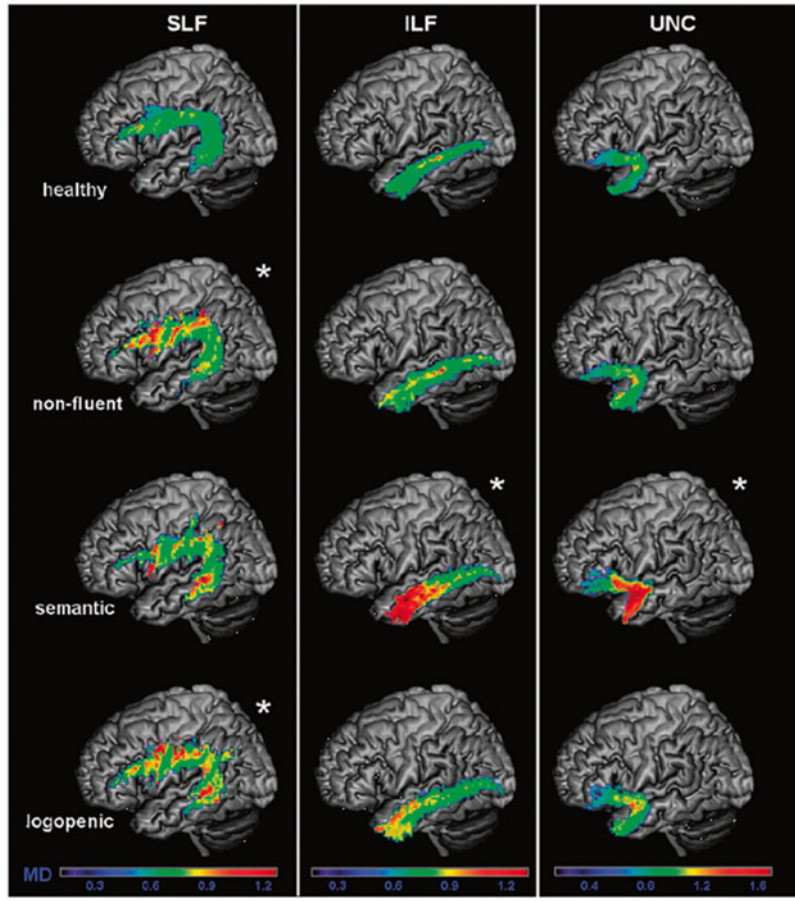

Fig. 17.4 Mean diffusivity (MD) values of healthy controls, nonfluent, semantic, and logopenic variants of primary progressive aphasia are shown on the probability maps for left superior longitudinal fasciculus (SLF), inferior longitudinal fasciculus (ILF), uncinate fasciculus (UNC), overlaid on a standard Montreal Neurological Institute brain. Only voxels that are in common in at least 20 % of the subjects in each group were included in the probability maps. *Asterisks* denote significant difference relative to normal controls at $p<0.05$. The chromatic scale represents average MD values ranging from lower (*violet-blue*) to higher values (*yellow-red*). MD is measured in $mm^2/s \times 10^{-3}$ [Reprinted from Galantucci, S., M. C. Tartaglia, et al. White matter damage in primary progressive aphasias: a diffusion tensor tractography study. Brain 2011;134(Pt 10): 3011–29. With permission from Oxford University Press.]

frontal, medial frontal and prefrontal cortical regions, and a reduced FA of the genu of the corpus callosum, left inferior fronto-occipital fasciculus, cingulum, uncinate and bilateral corona radiata in FTLD cases relative to AD [117]. Conversely, AD patients showed no areas of significant reduction in cortical thickness or WM integrity relative to FTLD patients [117]. Another recent study compared DT MRI alterations and patterns of cortical atrophy between FTLD and AD patients, identifying a significant area of reduced FA in the anterior corpus callosum of FTLD patients, as well as a significantly more severe atrophy of the precuneus and posterior cingulate cortex in AD patients [118]. A combination of WM and cortical data provided a highly accurate classification of these two conditions, with 87 % sensitivity and 83 % specificity [118].

Dementia with Lewy Bodies

Dementia with Lewy bodies (DLB) is the second most common form of neurodegenerative dementia in elderly subjects [8]. Memory impairment is generally less severe in patients with DLB than in those with AD, whereas deficits on tests of attention, executive function, and visuospatial ability can be prominent. In pathological studies, a distributed pattern of Lewy bodies has been observed in the neocortex, limbic structures, subcortical nuclei and brainstem of these patients [119, 120].

DTI in DLB Patients

Only a few studies investigated diffusivity alterations in DLB patients [76, 121–127]. The comparison between DLB patients and controls using DTI resulted in controversial findings, ranging from isolated damage to the ILF [123, 124], uncinate fasciculus [126] or parietal lobe [122] to a distributed pattern of FA reduction [121, 125]. The most consistent finding among studies was a decreased FA in the ILF [121, 123, 124], as well as reduced FA or increased MD in tracts of the parieto-occipital lobes [121, 122, 124, 125, 127], particularly the posterior cingulum and precuneus (Fig. 17.5a). Damage to these regions, which are important for visual information processing, may reflect the prevalent impairment of visuospatial abilities, as well as the presence of visual hallucinations in these patients. One study [124] reported significantly higher diffusivity of the ILF from patients with DLB experiencing visual hallucinations, in comparison with DLB patients who did not.

Differential Diagnosis: DLB vs. AD

Diffusivity abnormalities in the cortex of patients with AD are more distributed and severe than in those with DLB [122, 124]. Patients with AD experience an increased diffusivity and a reduced cortical volume in the medial temporal lobe, posterior cingulate cortex, precuneus, and temporoparietal association cortex compared to both healthy controls and patients with DLB [124]. The addition of diffusivity values of the hippocampus and parahippocampal gyrus to those of cortical volumes improves further the ability to distinguish AD patients from those with DLB [124].

A reduction of FA in the uncinate fasciculus has been shown both in AD and DLB patients [76, 126], with additional more posterior damage in patients with DLB [76]. A recent study [127] showed an involvement of the parieto-occipital and temporal WM tracts both in DLB and AD, but a much greater ratio of posterior-to-anterior suprathreshold voxels was found in DLB—6.5—when compared to AD—1.1 (Fig. 17.5) [127]. Similarly, the few other studies investigating WM damage in DLB showed a more posterior pattern of abnormalities in comparison to AD [122, 123], with a relative sparing of the structures of the temporal and frontal lobes, reflecting the structural preservation of these areas in DLB [128].

Conclusions

DTI is a sensitive tool to detect WM abnormalities in subjects with neurodegenerative dementing conditions. Diffusivity seems to be impaired in several brain regions early in the disease process; then, WM damage increases with disease severity. Since new disease-modifying therapies in AD and other neurodegenerative dementia will likely be most beneficial before substantial neuronal loss and clinical impairment have occurred, DTI holds promise as valuable tool for selecting candidates for clinical trials and as predictive markers of dementia progression in defined risk groups of patients. The reliability and reproducibility of DTI in a large-scale, multicenter setting in patients with these diseases warrant further investigation.

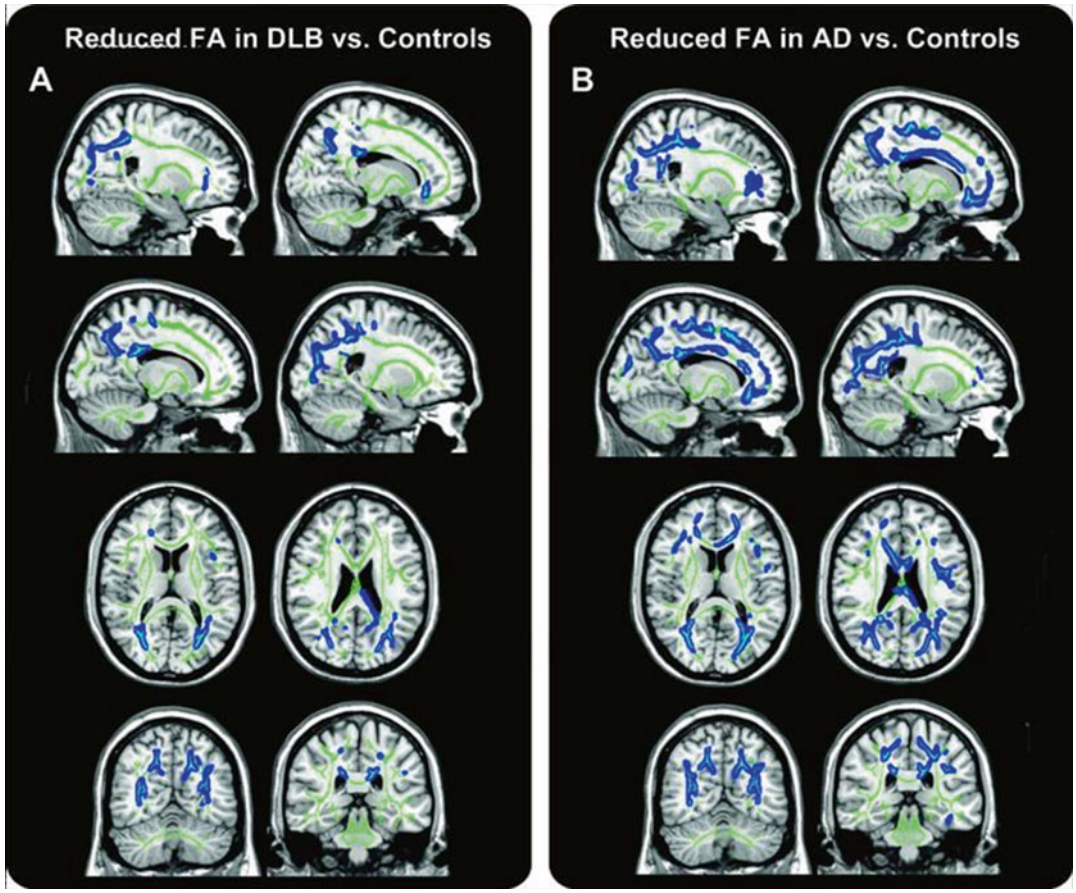

Fig. 17.5 Fractional anisotropy (FA) reduction in patients with dementia with Lewy bodies (DLB) and Alzheimer's disease (AD). Tract-based spatial statistics color maps showing voxel-wise differences in FA (*blue*) between these groups are overlaid on a mean FA skeleton (*green*). (**a**) DLB vs. controls: abnormalities were identified mainly in the parieto-occipital areas (precuneus and cingulate gyrus). Reduced FA in the temporal lobes was detected in a region of the posterior thalamic radiation that included the optic radiation ($p < 0.05$, corrected for multiple comparisons). (**b**) AD vs. controls: the pattern of abnormalities was more distributed than in DLB and included clusters in the temporal, parieto-occipital, and frontal lobes ($p < 0.05$, corrected) [Reprinted from Watson, R., A. M. Blamire, et al. "Characterizing dementia with Lewy bodies by means of diffusion tensor imaging." Neurology 2012;79(9): 906–14. With permission from Wolters Kluwer Health.]

References

1. Filippi M, Agosta F, et al. EFNS task force: the use of neuroimaging in the diagnosis of dementia. Eur J Neurol. 2012;19(12):e131–40. 1487-501.
2. Sorbi S, Hort J, et al. EFNS-ENS Guidelines on the diagnosis and management of disorders associated with dementia. Eur J Neurol. 2012;19(9): 1159–79.
3. (NICE), N. I. f. H. a. C. E. (March 2011). CG42 Dementia: NICE guideline.
4. Knopman DS, DeKosky ST, et al. Practice parameter: diagnosis of dementia (an evidence-based review). Report of the Quality Standards Subcommittee of the American Academy of Neurology. Neurology. 2001;56(9):1143–53.
5. Barkhof F, Fox NC, et al. Neuroimaging in dementia. New York, NY: Springer; 2011.
6. Dubois B, Feldman HH, et al. Revising the definition of Alzheimer's disease: a new lexicon. Lancet Neurol. 2010;9(11):1118–27.
7. McKhann GM, Knopman DS, et al. The diagnosis of dementia due to Alzheimer's disease: recommendations from the National Institute on Aging-Alzheimer's Association workgroups on diagnostic guidelines for Alzheimer's disease. Alzheimers Dement. 2011;7(3):263–9.

8. McKeith IG, Dickson DW, et al. Diagnosis and management of dementia with Lewy bodies: third report of the DLB Consortium. Neurology. 2005;65(12): 1863–72.
9. Gorno-Tempini ML, Hillis AE, et al. Classification of primary progressive aphasia and its variants. Neurology. 2011;76(11):1006–14.
10. Rascovsky K, Hodges JR, et al. Sensitivity of revised diagnostic criteria for the behavioural variant of frontotemporal dementia. Brain. 2011;134(Pt 9): 2456–77.
11. Teipel SJ, Wegrzyn M, et al. Anatomical MRI and DTI in the diagnosis of Alzheimer's disease: a European multicenter study. J Alzheimers Dis. 2012;31 Suppl 3:S33–47.
12. Geschwind MD, Shu H, et al. Rapidly progressive dementia. Ann Neurol. 2008;64(1):97–108.
13. Prusiner SB. Shattuck lecture--neurodegenerative diseases and prions. N Engl J Med. 2001;344(20): 1516–26.
14. Young GS, Geschwind MD, et al. Diffusion-weighted and fluid-attenuated inversion recovery imaging in Creutzfeldt-Jakob disease: high sensitivity and specificity for diagnosis. AJNR Am J Neuroradiol. 2005;26(6):1551–62.
15. Vitali P, Maccagnano E, et al. Diffusion-weighted MRI hyperintensity patterns differentiate CJD from other rapid dementias. Neurology. 2011;76(20): 1711–9.
16. Geschwind MD, Potter CA, et al. Correlating DWI MRI with pathologic and other features of Jakob-Creutzfeldt disease. Alzheimer Dis Assoc Disord. 2009;23(1):82–7.
17. Murata T, Shiga Y, et al. Conspicuity and evolution of lesions in Creutzfeldt-Jakob disease at diffusion-weighted imaging. AJNR Am J Neuroradiol. 2002;23(7):1164–72.
18. Shiga Y, Miyazawa K, et al. Diffusion-weighted MRI abnormalities as an early diagnostic marker for Creutzfeldt-Jakob disease. Neurology. 2004;63(3): 443–9.
19. Zerr I, Kallenberg K, et al. Updated clinical diagnostic criteria for sporadic Creutzfeldt-Jakob disease. Brain. 2009;132(Pt 10):2659–68.
20. Collie DA, Summers DM, et al. Diagnosing variant Creutzfeldt-Jakob disease with the pulvinar sign: MR imaging findings in 86 neuropathologically confirmed cases. AJNR Am J Neuroradiol. 2003;24(8): 1560–9.
21. Yi SH, Park KC, et al. Relationship between clinical course and Diffusion-weighted MRI findings in sporadic Creutzfeldt-Jakob Disease. Neurol Sci. 2008;29(4):251–5.
22. Lee H, Cohen OS, et al. Cerebral white matter disruption in Creutzfeldt-Jakob disease. AJNR Am J Neuroradiol. 2012;33(10):1945–50.
23. Wang LH, Bucelli RC, et al. Role of magnetic resonance imaging, cerebrospinal fluid, and electroencephalogram in diagnosis of sporadic Creutzfeldt-Jakob disease. J Neurol. 2013;260(2): 498–506.
24. Jack Jr CR, Lowe VJ, et al. Serial PIB and MRI in normal, mild cognitive impairment and Alzheimer's disease: implications for sequence of pathological events in Alzheimer's disease. Brain. 2009;132(Pt 5):1355–65.
25. Bateman RJ, Xiong C, et al. Clinical and biomarker changes in dominantly inherited Alzheimer's disease. N Engl J Med. 2012;367(9):795–804.
26. Sexton CE, Kalu UG, et al. A meta-analysis of diffusion tensor imaging in mild cognitive impairment and Alzheimer's disease. Neurobiol Aging. 2011; 32(12):2322.e5–18.
27. Clerx L, Visser PJ, et al. New MRI markers for Alzheimer's disease: a meta-analysis of diffusion tensor imaging and a comparison with medial temporal lobe measurements. J Alzheimers Dis. 2012; 29(2):405–29.
28. Agosta F, Pievani M, et al. White matter damage in Alzheimer disease and its relationship to gray matter atrophy. Radiology. 2011;258(3):853–63.
29. Rose SE, Chen F, et al. Loss of connectivity in Alzheimer's disease: an evaluation of white matter tract integrity with colour coded MR diffusion tensor imaging. J Neurol Neurosurg Psychiatry. 2000;69(4): 528–30.
30. Bozzali M, Falini A, et al. White matter damage in Alzheimer's disease assessed in vivo using diffusion tensor magnetic resonance imaging. J Neurol Neurosurg Psychiatry. 2002;72(6):742–6.
31. Xie S, Xiao JX, et al. Evaluation of bilateral cingulum with tractography in patients with Alzheimer's disease. Neuroreport. 2005;16(12):1275–8.
32. Duan JH, Wang HQ, et al. White matter damage of patients with Alzheimer's disease correlated with the decreased cognitive function. Surg Radiol Anat. 2006;28(2):150–6.
33. Muller MJ, Greverus D, et al. Diagnostic utility of hippocampal size and mean diffusivity in amnestic MCI. Neurobiol Aging. 2007;28(3):398–403.
34. Ukmar M, Makuc E, et al. Evaluation of white matter damage in patients with Alzheimer's disease and in patients with mild cognitive impairment by using diffusion tensor imaging. Radiol Med. 2008;113(6): 915–22.
35. Bai F, Zhang Z, et al. Abnormal integrity of association fiber tracts in amnestic mild cognitive impairment. J Neurol Sci. 2009;278(1-2):102–6.
36. Mielke MM, Kozauer NA, et al. Regionally-specific diffusion tensor imaging in mild cognitive impairment and Alzheimer's disease. Neuroimage. 2009;46(1):47–55.
37. Catheline G, Periot O, et al. Distinctive alterations of the cingulum bundle during aging and Alzheimer's disease. Neurobiol Aging. 2010;31(9): 1582–92.
38. Morikawa M, Kiuchi K, et al. Uncinate fasciculus-correlated cognition in Alzheimer's disease: a diffusion

tensor imaging study by tractography. Psychogeriatrics. 2010;10(1):15–20.
39. Zarei M, Patenaude B, et al. Combining shape and connectivity analysis: an MRI study of thalamic degeneration in Alzheimer's disease. Neuroimage. 2010;49(1):1–8.
40. Zimny A, Szewczyk P, et al. Multimodal imaging in diagnosis of Alzheimer's disease and amnestic mild cognitive impairment: value of magnetic resonance spectroscopy, perfusion, and diffusion tensor imaging of the posterior cingulate region. J Alzheimers Dis. 2011;27(3):591–601.
41. Oishi K, Mielke MM, et al. The fornix sign: a potential sign for Alzheimer's disease based on diffusion tensor imaging. J Neuroimaging. 2012;22(4):365–74.
42. Fellgiebel A, Muller MJ, et al. Color-coded diffusion-tensor-imaging of posterior cingulate fiber tracts in mild cognitive impairment. Neurobiol Aging. 2005;26(8):1193–8.
43. Rose SE, McMahon KL, et al. Diffusion indices on magnetic resonance imaging and neuropsychological performance in amnestic mild cognitive impairment. J Neurol Neurosurg Psychiatry. 2006;77(10): 1122–8.
44. Fellgiebel A, Schermuly I, et al. Functional relevant loss of long association fibre tracts integrity in early Alzheimer's disease. Neuropsychologia. 2008;46(6): 1698–706.
45. Walhovd KB, Fjell AM, et al. Multimodal imaging in mild cognitive impairment: metabolism, morphometry and diffusion of the temporal-parietal memory network. Neuroimage. 2009;45(1):215–23.
46. Bosch B, Arenaza-Urquijo EM, et al. Multiple DTI index analysis in normal aging, amnestic MCI and AD. Relationship with neuropsychological performance. Neurobiol Aging. 2012;33(1):61–74.
47. Huang J, Friedland RP, et al. Diffusion tensor imaging of normal-appearing white matter in mild cognitive impairment and early Alzheimer disease: preliminary evidence of axonal degeneration in the temporal lobe. AJNR Am J Neuroradiol. 2007; 28(10):1943–8.
48. Chen TF, Chen YF, et al. Executive dysfunction and periventricular diffusion tensor changes in amnesic mild cognitive impairment and early Alzheimer's disease. Hum Brain Mapp. 2009;30(11):3826–36.
49. Sjobeck M, Elfgren C, et al. Alzheimer's disease (AD) and executive dysfunction. A case-control study on the significance of frontal white matter changes detected by diffusion tensor imaging (DTI). Arch Gerontol Geriatr. 2010;50(3):260–6.
50. Ota M, Sato N, et al. Relationship between apathy and diffusion tensor imaging metrics of the brain in Alzheimer's disease. Int J Geriatr Psychiatry. 2011;27(7):722–6.
51. Tighe SK, Oishi K, et al. Diffusion tensor imaging of neuropsychiatric symptoms in mild cognitive impairment and Alzheimer's dementia. J Neuropsychiatry Clin Neurosci. 2012;24(4):484–8.
52. Kantarci K, Petersen RC, et al. DWI predicts future progression to Alzheimer disease in amnestic mild cognitive impairment. Neurology. 2005;64(5): 902–4.
53. Fellgiebel A, Dellani PR, et al. Predicting conversion to dementia in mild cognitive impairment by volumetric and diffusivity measurements of the hippocampus. Psychiatry Res. 2006;146(3):283–7.
54. Stahl R, Dietrich O, et al. White matter damage in Alzheimer disease and mild cognitive impairment: assessment with diffusion-tensor MR imaging and parallel imaging techniques. Radiology. 2007; 243(2):483–92.
55. Zhang Y, Schuff N, et al. Diffusion tensor imaging of cingulum fibers in mild cognitive impairment and Alzheimer disease. Neurology. 2007;68(1):13–9.
56. Chua TC, Wen W, et al. Diffusion tensor imaging of the posterior cingulate is a useful biomarker of mild cognitive impairment. Am J Geriatr Psychiatry. 2009;17(7):602–13.
57. Haller S, Nguyen D, et al. Individual prediction of cognitive decline in mild cognitive impairment using support vector machine-based analysis of diffusion tensor imaging data. J Alzheimers Dis. 2010; 22(1):315–27.
58. Scola E, Bozzali M, et al. A diffusion tensor MRI study of patients with MCI and AD with a 2-year clinical follow-up. J Neurol Neurosurg Psychiatry. 2010;81(7):798–805.
59. Shu N, Wang Z, et al. Multiple diffusion indices reveals white matter degeneration in Alzheimer's disease and mild cognitive impairment: a tract-based spatial statistics study. J Alzheimers Dis. 2011;26 Suppl 3:275–85.
60. Alves GS, O'Dwyer L, et al. Different patterns of white matter degeneration using multiple diffusion indices and volumetric data in mild cognitive impairment and Alzheimer patients. PLoS One. 2012; 7(12):e52859.
61. Nowrangi MA, Lyketsos CG, et al. Longitudinal, region-specific course of diffusion tensor imaging measures in mild cognitive impairment and Alzheimer's disease. Alzheimers Dement. 2013;9(5): 519–28.
62. van Bruggen T, Stieltjes B, et al. Do Alzheimer-specific microstructural changes in mild cognitive impairment predict conversion? Psychiatry Res. 2012;203(2-3):184–93.
63. Amlien IK, Fjell AM, et al. Mild cognitive impairment: cerebrospinal fluid tau biomarker pathologic levels and longitudinal changes in white matter integrity. Radiology. 2013;266(1):295–303.
64. Zhuang L, Sachdev PS, et al. Microstructural white matter changes in cognitively normal individuals at risk of amnestic MCI. Neurology. 2012;79(8): 748–54.
65. Nierenberg J, Pomara N, et al. Abnormal white matter integrity in healthy apolipoprotein E epsilon4 carriers. Neuroreport. 2005;16(12):1369–72.

66. Persson J, Lind J, et al. Altered brain white matter integrity in healthy carriers of the APOE epsilon4 allele: a risk for AD? Neurology. 2006;66(7):1029–33.
67. Honea RA, Vidoni E, et al. Impact of APOE on the healthy aging brain: a voxel-based MRI and DTI study. J Alzheimers Dis. 2009;18(3):553–64.
68. Bendlin BB, Ries ML, et al. White matter is altered with parental family history of Alzheimer's disease. Alzheimers Dement. 2010;6(5):394–403.
69. Gold BT, Powell DK, et al. Alterations in multiple measures of white matter integrity in normal women at high risk for Alzheimer's disease. Neuroimage. 2010;52(4):1487–94.
70. Smith CD, Chebrolu H, et al. White matter diffusion alterations in normal women at risk of Alzheimer's disease. Neurobiol Aging. 2010;31(7):1122–31.
71. Heise V, Filippini N, et al. The APOE varepsilon4 allele modulates brain white matter integrity in healthy adults. Mol Psychiatry. 2011;16(9):908–16.
72. Westlye LT, Reinvang I, et al. Effects of APOE on brain white matter microstructure in healthy adults. Neurology. 2012;79(19):1961–9.
73. Ringman JM, O'Neill J, et al. Diffusion tensor imaging in preclinical and presymptomatic carriers of familial Alzheimer's disease mutations. Brain. 2007;130(Pt 7):1767–76.
74. Taoka T, Iwasaki S, et al. Diffusion anisotropy and diffusivity of white matter tracts within the temporal stem in Alzheimer disease: evaluation of the "tract of interest" by diffusion tensor tractography. AJNR Am J Neuroradiol. 2006;27(5):1040–5.
75. Zhang Y, Schuff N, et al. White matter damage in frontotemporal dementia and Alzheimer's disease measured by diffusion MRI. Brain. 2009;132(Pt 9):2579–92.
76. Kiuchi K, Morikawa M, et al. White matter changes in dementia with Lewy bodies and Alzheimer's disease: a tractography-based study. J Psychiatr Res. 2011;45(8):1095–100.
77. Fischer FU, Scheurich A, et al. Automated tractography of the cingulate bundle in Alzheimer's disease: a multicenter DTI study. J Magn Reson Imaging. 2012;36(1):84–91.
78. Preti MG, Baglio F, et al. Assessing corpus callosum changes in Alzheimer's disease: comparison between tract-based spatial statistics and atlas-based tractography. PLoS One. 2012;7(4):e35856.
79. Kiuchi K, Morikawa M, et al. Abnormalities of the uncinate fasciculus and posterior cingulate fasciculus in mild cognitive impairment and early Alzheimer's disease: a diffusion tensor tractography study. Brain Res. 2009;1287:184–91.
80. Pievani M, Agosta F, et al. Assessment of white matter tract damage in mild cognitive impairment and Alzheimer's disease. Hum Brain Mapp. 2010;31(12):1862–75.
81. Bozzali M, Giulietti G, et al. Damage to the cingulum contributes to Alzheimer's disease pathophysiology by deafferentation mechanism. Hum Brain Mapp. 2012;33(6):1295–308.
82. Zhuang L, Wen W, et al. Abnormalities of the fornix in mild cognitive impairment are related to episodic memory loss. J Alzheimers Dis. 2012;29(3):629–39.
83. Bozzali M, Parker GJ, et al. Anatomical connectivity mapping: a new tool to assess brain disconnection in Alzheimer's disease. Neuroimage. 2011;54(3):2045–51.
84. Teipel SJ, Meindl T, et al. Longitudinal changes in fiber tract integrity in healthy aging and mild cognitive impairment: a DTI follow-up study. J Alzheimers Dis. 2011;22(2):507–22.
85. Likitjaroen Y, Meindl T, et al. Longitudinal changes of fractional anisotropy in Alzheimer's disease patients treated with galantamine: a 12-month randomized, placebo-controlled, double-blinded study. Eur Arch Psychiatry Clin Neurosci. 2012;262(4):341–50.
86. Buckner RL, Sepulcre J, et al. Cortical hubs revealed by intrinsic functional connectivity: mapping, assessment of stability, and relation to Alzheimer's disease. J Neurosci. 2009;29(6):1860–73.
87. He Y, Chen Z, et al. Structural insights into aberrant topological patterns of large-scale cortical networks in Alzheimer's disease. J Neurosci. 2008;28(18):4756–66.
88. Yao Z, Zhang Y, et al. Abnormal cortical networks in mild cognitive impairment and Alzheimer's disease. PLoS Comput Biol. 2010;6(11):e1001006.
89. Lo CY, Wang PN, et al. Diffusion tensor tractography reveals abnormal topological organization in structural cortical networks in Alzheimer's disease. J Neurosci. 2010;30(50):16876–85.
90. Mackenzie IR, Neumann M, et al. Nomenclature and nosology for neuropathologic subtypes of frontotemporal lobar degeneration: an update. Acta Neuropathol. 2010;119(1):1–4.
91. Mesulam MM. Primary progressive aphasia. Ann Neurol. 2001;49(4):425–32.
92. Mesulam M, Wicklund A, et al. Alzheimer and frontotemporal pathology in subsets of primary progressive aphasia. Ann Neurol. 2008;63(6):709–19.
93. Larsson EM, Englund E, et al. MRI with diffusion tensor imaging post-mortem at 3.0 T in a patient with frontotemporal dementia. Dement Geriatr Cogn Disord. 2004;17(4):316–9.
94. Forman MS, Zhukareva V, et al. Signature tau neuropathology in gray and white matter of corticobasal degeneration. Am J Pathol. 2002;160(6):2045–53.
95. Geser F, Martinez-Lage M, et al. Clinical and pathological continuum of multisystem TDP-43 proteinopathies. Arch Neurol. 2009;66(2):180–9.
96. Kim EJ, Rabinovici GD, et al. Patterns of MRI atrophy in tau positive and ubiquitin positive frontotemporal lobar degeneration. J Neurol Neurosurg Psychiatry. 2007;78(12):1375–8.
97. McMillan CT, Irwin DJ, et al. White matter imaging helps dissociate tau from TDP-43 in frontotemporal lobar degeneration. J Neurol Neurosurg Psychiatry. 2013;84:949.

98. Seelaar H, Kamphorst W, et al. Distinct genetic forms of frontotemporal dementia. Neurology. 2008; 71(16):1220–6.
99. DeJesus-Hernandez M, Mackenzie IR, et al. Expanded GGGGCC hexanucleotide repeat in noncoding region of C9ORF72 causes chromosome 9p-linked FTD and ALS. Neuron. 2011;72(2):245–56.
100. Borroni B, Alberici A, et al. Brain magnetic resonance imaging structural changes in a pedigree of asymptomatic progranulin mutation carriers. Rejuvenation Res. 2008;11(3):585–95.
101. Dopper EG, Rombouts SA, et al. Structural and functional brain connectivity in presymptomatic familial frontotemporal dementia. Neurology. 2013; 80(9):814–23.
102. Whitwell JL, Avula R, et al. Gray and white matter water diffusion in the syndromic variants of frontotemporal dementia. Neurology. 2011;74(16): 1279–87.
103. Borroni B, Brambati SM, et al. Evidence of white matter changes on diffusion tensor imaging in frontotemporal dementia. Arch Neurol. 2007;64(2): 246–51.
104. Agosta F, Scola E, et al. White matter damage in frontotemporal lobar degeneration spectrum. Cereb Cortex. 2012;22(12):2705–14.
105. Matsuo K, Mizuno T, et al. Cerebral white matter damage in frontotemporal dementia assessed by diffusion tensor tractography. Neuroradiology. 2008;50(7):605–11.
106. Rosen HJ, Gorno-Tempini ML, et al. Patterns of brain atrophy in frontotemporal dementia and semantic dementia. Neurology. 2002;58(2):198–208.
107. Whitwell JL, Przybelski SA, et al. Distinct anatomical subtypes of the behavioural variant of frontotemporal dementia: a cluster analysis study. Brain. 2009;132(Pt 11):2932–46.
108. Brambati SM, Renda NC, et al. A tensor based morphometry study of longitudinal gray matter contraction in FTD. Neuroimage. 2007;35(3):998–1003.
109. Galantucci S, Tartaglia MC, et al. White matter damage in primary progressive aphasias: a diffusion tensor tractography study. Brain. 2011;134(Pt 10):3011–29.
110. Grossman M, Powers J, et al. Disruption of large-scale neural networks in non-fluent/agrammatic variant primary progressive aphasia associated with frontotemporal degeneration pathology. Brain Lang. 2012;127:106–20.
111. Zhang Y, Tartaglia MC, et al. MRI signatures of brain macrostructural atrophy and microstructural degradation in frontotemporal lobar degeneration subtypes. J Alzheimers Dis. 2013;33(2):431–44.
112. Schwindt GC, Graham NL, et al. Whole-brain white matter disruption in semantic and nonfluent variants of primary progressive aphasia. Hum Brain Mapp. 2013;34:973.
113. Mahoney CJ, Malone IB, et al. White matter tract signatures of the progressive aphasias. Neurobiol Aging. 2013;34(6):1687–99.
114. Agosta F, Henry RG, et al. Language networks in semantic dementia. Brain. 2010;133(Pt 1):286–99.
115. Acosta-Cabronero J, Patterson K, et al. Atrophy, hypometabolism and white matter abnormalities in semantic dementia tell a coherent story. Brain. 2011;134(Pt 7):2025–35.
116. Gorno-Tempini ML, Brambati SM, et al. The logopenic/phonological variant of primary progressive aphasia. Neurology. 2008;71(16):1227–34.
117. Avants BB, Cook PA, et al. Dementia induces correlated reductions in white matter integrity and cortical thickness: a multivariate neuroimaging study with sparse canonical correlation analysis. Neuroimage. 2010;50(3):1004–16.
118. McMillan CT, Brun C, et al. White matter imaging contributes to the multimodal diagnosis of frontotemporal lobar degeneration. Neurology. 2012; 78(22):1761–8.
119. McKeith IG, Galasko D, et al. Consensus guidelines for the clinical and pathologic diagnosis of dementia with Lewy bodies (DLB): report of the consortium on DLB international workshop. Neurology. 1996;47(5):1113–24.
120. Spillantini MG, Crowther RA, et al. alpha-Synuclein in filamentous inclusions of Lewy bodies from Parkinson's disease and dementia with Lewy bodies. Proc Natl Acad Sci U S A. 1998;95(11): 6469–73.
121. Bozzali M, Falini A, et al. Brain tissue damage in dementia with Lewy bodies: an in vivo diffusion tensor MRI study. Brain. 2005;128(Pt 7):1595–604.
122. Firbank MJ, Blamire AM, et al. Diffusion tensor imaging in dementia with Lewy bodies and Alzheimer's disease. Psychiatry Res. 2007;155(2): 135–45.
123. Ota M, Sato N, et al. Degeneration of dementia with Lewy bodies measured by diffusion tensor imaging. NMR Biomed. 2009;22(3):280–4.
124. Kantarci K, Avula R, et al. Dementia with Lewy bodies and Alzheimer disease: neurodegenerative patterns characterized by DTI. Neurology. 2010;74(22):1814–21.
125. Lee JE, Park HJ, et al. A comparative analysis of cognitive profiles and white-matter alterations using voxel-based diffusion tensor imaging between patients with Parkinson's disease dementia and dementia with Lewy bodies. J Neurol Neurosurg Psychiatry. 2010;81(3):320–6.
126. Serra L, Cercignani M, et al. White matter damage along the uncinate fasciculus contributes to cognitive decline in AD and DLB. Curr Alzheimer Res. 2012;9(3):326–33.
127. Watson R, Blamire AM, et al. Characterizing dementia with Lewy bodies by means of diffusion tensor imaging. Neurology. 2012;79(9):906–14.
128. Whitwell JL, Weigand SD, et al. Focal atrophy in dementia with Lewy bodies on MRI: a distinct pattern from Alzheimer's disease. Brain. 2007; 130(Pt 3):708–19.

DTI in Psychiatry

18

Josselin Houenou and Louise Emsell

Learning Points

- DTI is not used routinely in clinical practice owing to special challenges inherent to defining psychopathology, the practical issues associated with scanning patients and the lack of sensitivity and specificity of DTI measures. In the future, it could be used to inform invasive neurosurgical treatments of psychiatric illness, such as deep brain stimulation.
- DTI is increasingly used as clinical research tool in psychiatry. It can be used to inform neurobiological models of psychiatric illness, such as those based on "connectivity." DTI metrics can be used in combination with other neuroimaging data as potential biomarkers that may aid patient stratification and improve treatment.
- DTI studies in psychiatry face a number of issues. Specifically, the categorical classification of mental disorders is subjective and definitions are continually evolving. Clinical samples are therefore highly heterogeneous with regard to clinical history, psychiatric and medical comorbidity, active symptoms, and medication. Alcohol misuse may represent a significant confound in studies of psychiatric populations.
- Scanning psychiatric patients presents some practical challenges, including obtaining informed consent, reduced compliance with procedures owing to anxiety or hyperactivity, and increased movement within the scanner compared to healthy subjects.
- DTI has been used to investigate a number of psychiatric disorders, including, but not limited to schizophrenia, mood, anxiety, personality and neurodevelopmental disorders. Findings are largely nonspecific and suggest varying degrees of white matter microstructural abnormality in cortical and subcortical cognitive and limbic networks.

J. Houenou, MD, PhD
INSERM U955 Team 15 "Translation Psychiatry", Fondation Fondamental, APHP, Hôpitaux Universitaires Mondor, Créteil, France

NeuroSpin Neuroimaging Center, UNIACT Lab, Psychiatry Team, CEA Saclay, Gif-Sur-Yvette, France

L. Emsell, PhD (✉)
Translational MRI, Department of Imaging and Pathology, KU Leuven, and Radiology, University Hospitals, Leuven, Belgium

Universitair Psychiatrisch Centrum (UPC), KU Leuven, Leuven, Belgium
e-mail: louise.emsell@med.kuleuven.be

W. Van Hecke et al. (eds.), *Diffusion Tensor Imaging*, DOI 10.1007/978-1-4939-3118-7_18

Role of DTI in Psychiatry

Clinical Research

Presently, DTI is not used routinely in clinical psychiatric practice. There are a number of reasons for this, which broadly relate to both the complex nature of defining psychopathology and the practical challenges associated with scanning patients with mental illness. These issues are discussed in more detail in the body of this chapter. Nevertheless, DTI does have an increasingly significant role in psychiatry, and that is in the field of clinical research.

Early clinical neuroimaging studies in psychiatry used computed tomography (CT) and subsequently classical structural magnetic resonance imaging (MRI) (using T1, T2, and fluid attenuation inversion recovery—FLAIR—sequences) [1]. These studies have allowed us to better understand the volumetric changes present in psychiatric disorders such as schizophrenia, mood disorders (bipolar and unipolar disorders), anxiety disorders, addiction, personality disorders, autism, and attention deficit hyperactivity disorder (ADHD). As an example, in schizophrenia, we now know from these neuroimaging studies that global brain volumes are decreased in patients compared to controls, even before the first clinical episode [2, 3]. Regional volumes are also decreased, especially in the prefrontal cortex [4]. High-risk subjects are also a population of interest in these pathologies and are generally defined as healthy relatives of patients. They thus share some common genetic risk with the patients, but without the expression of the disease *per se* and without some confounding factors such as medication and number of episodes. Usually, these high-risk subjects share most of the same features regarding brain volumes, though at a lower amplitude than patients [5]. However, although such computational morphometry based studies are useful, they are unable to provide information beyond total and regional white matter volume, density, and shape.

Functional MRI has also provided insight into the mechanisms of psychiatric disorders, via the identification of over- or under-active areas during the completion of specific tasks in groups of patients [6].

Strikingly, T1, T2, FLAIR, and fMRI studies point to crucial abnormalities of white matter in major psychiatric disorders. On T1 scans, total white matter volume has been found to be reduced in schizophrenia, whilst regional volumetric reduction (e.g., corpus callosum) has also been reported in schizophrenia and in other conditions such as bipolar disorder [7]. In mood disorders, white matter hyperintensities observed on T2 and FLAIR are the most commonly reported abnormalities, especially in bipolar disorder and late-life depression [1]. Altered functional connectivity between brain areas, as measured by inter-regional BOLD levels correlations, has been reported in schizophrenia, bipolar disorder, and anxiety disorders, both during the completion of specific tasks and at rest [8]. Some authors believe that schizophrenia and even bipolar disorder can be conceptualized as "connectivity disorders." Schizophrenia, for example, is characterized by a global alteration in brain connectivity [9]. This could explain the widespread cognitive deficits characteristic of the disorder. Neurobiological models of mood disorders assume compromised functional regulation of prefrontal-limbic connectivity. As functional connectivity is obviously linked to structural connectivity, there is a need to precisely explore and characterize white matter in the context of psychiatric illness [10].

This is why DTI has steadily gained importance as an investigative tool in psychiatric disorders. Its unique ability to examine WM microstructure in vivo provides a means to build upon findings from previous classical MR studies. When integrated with findings from functional neuroimaging studies and molecular biology, it can be used to refine neurobiological models of psychiatric disorders. A brief review of DTI findings in selected psychiatric conditions is provided at the end of this chapter.

The Development of Imaging Biomarkers

The assessment of psychiatric disorders is currently based entirely on clinical evaluation, without any possibility of laboratory tests. Diagnosis,

prediction of the transition to illness, course, and outcome of major psychiatric illnesses thus continue to be very challenging and remain difficult to predict using classical clinical instruments. The absence of an objective biomarker to assess the evolution and severity of the illnesses leads to mismanagement and increased burden [11]. There is therefore a strong need to develop biomarkers of outcome to perform more personalized healthcare plans. Recent studies have raised hopes of identifying possible biomarkers that are usable at an individual level [12]. The most promising predictive biomarkers include neuroimaging features such as white matter abnormalities. The development and use of such biomarkers of prognosis may help to identify patients that should receive specific targeted interventions [13].

One technique to achieve the development of individual neuroimaging biomarkers usable at the bedside is "Machine learning" [14]. Techniques such as support vector machines have been developed in recent years and have already shown potential to classify patients with psychiatric disorders using neuroimaging data [15–17]. In such machine learning multivariate algorithms, the computer applies a specific mathematical method (e.g., support vector machine algorithms) to find specific patterns in a "learning dataset" (group information supplied to the computer) that form the basis of rules for distinguishing the MRI scans of different groups (e.g., patients from those of healthy controls). The computer then applies these rules to new datasets (e.g., for the automatic classification of patients and healthy subjects within the sample). Therefore, a biomarker is constructed, with measurable metrics such as specificity, sensitivity, positive and negative predictive values, and accuracy.

Proof-of-concept of such approaches in psychiatry has already been demonstrated in schizophrenia and autism. In 2005, Davatzikos and colleagues [18] applied such an automated classification technique to T1 MRI scans from 69 patients with schizophrenia and 79 healthy controls. They achieved a classification accuracy of 81 %.

Such techniques have also proven capable of predicting clinical outcome with MRI data in neuropsychiatric disorders in recent studies. Koutsouleris et al. used multivariate machine learning algorithms to predict disease transition in schizophrenia: using T1 MRI scans from at-risk subjects, they were able to predict transition to psychosis 4 years later, with an accuracy of 82 % [16]. They performed this study with only 15 subjects having a transition to psychosis and 18 without such a transition.

In mood disorders, a recent study has highlighted the utility of such approaches to predict relapses. Farb et al. [19] recruited 16 remitted unipolar depressed patients who underwent fMRI while viewing sad and neutral film clips. They used a receiver operating characteristic analysis to determine signal cutoffs for predicting relapse. Within the depressed group, relapse was predicted by medial prefrontal cortical activity and contraindicated by visual cortical activity with sensitivity and specificity scores all above 80 %. This study clearly demonstrates the feasibility of discovering neuroimaging-based predictors of clinical outcome in mood disorders. It must be noted however that the sample size of this study was quite small.

A few studies have used DTI data as an entry point for such machine learning algorithms in psychiatry [20]. Such studies have achieved very high rates of accuracy, sensitivity, and specificity [21–23] and are a promising application of DTI in future psychiatric research.

Planning Psychosurgical Procedures

Neurosurgical treatments of severe, intractable psychiatric disorders using procedures that destroy or disconnect brain tissue have a controversial history and despite their reported efficacy are not widely used. A major criticism of such procedures is that the pathways involved in psychiatric illness are ill defined and therefore reliable surgical targets are lacking, resulting in widely variable postsurgical outcomes. Nevertheless, four major techniques are in use, which are generally accepted as safe and efficacious: anterior cingulotomy, subcaudate tractotomy, limbic leucotomy, and anterior capsulotomy [24].

All these procedures target the limbic territory and its connections.

Another promising surgical approach, particularly in the treatment of depression, is deep brain stimulation (DBS). This technique involves the targeted stimulation of brain tissue via an electrode in order to modulate neurotransmission. In the case of depression, improvements have been reported when using DBS to target the subcallosal cingulate, ventral striatum, and anterior limb of the internal capsule (ALIC). The ALIC has also been targeted in obsessive-compulsive disorder [25].

Given the ability of DTI to virtually delineate major pathways, it can be used to investigate the connectivity profile of ablation and electrode target sites in order to understand more about the biological basis of the therapeutic and unwanted effects associated with the procedures, and about the neural circuitry involved in different aspects of psychopathology. For example, recent DTI tractography studies have found that typical psychosurgical lesion and DBS sites share similar fiber bundles within various cortical and subcortical circuits involving the prefrontal cortex and limbic networks, including, for example, the medial forebrain bundle and anterior thalamic radiation [26–28].

As the neurocircuitry of psychiatric disorders is unraveled, DTI could also be informative in guiding neurosurgical placement of the electrode in DBS (see Chap. 14) and for refining psychosurgical targets. Although presently such applications are very much in their infancy, in the future, DTI or advanced versions of the technique such as HARDI (see Chap. 21) may rejuvenate modern surgical interventions in psychiatry [29].

Special Challenges in the Application of DTI in Psychiatry

The application of DTI, and neuroimaging in general in psychiatry, is an exciting challenge. Nevertheless, specific caveats must be kept in mind, which are related to the current classification systems in psychiatry and to the psychiatric condition *per se*. These caveats are not all specific to DTI, but are generally common to all neuroimaging studies of patients in psychiatry.

Diagnosis and Patient Stratification Presently Based on Clinical Assessment, Not Biomarkers

To date, diagnoses in psychiatry are solely based on clinical assessment. The classification and definition of the illnesses rely on guidelines and manuals approved by the psychiatry community such as the "Diagnostic and Statistical Manual of Mental Disorders" (DSM; current version DSM-V) of the American Psychiatric Association and the "International Statistical Classification of Diseases and Related Health Problems" (ICD; current version ICD-10) of the World Health Organization.

These classification systems define a mental disorder based on a collection of clinical signs and symptoms ("a syndrome") and their consequences. As an example, the DSM-V defines a mental disorder as a syndrome that occurs in an individual, the consequences of which are clinically significant distress or disability, that must not be merely an expectable response to common stressors and losses or a culturally sanctioned response to a particular event, that reflects an underlying psychobiological dysfunction and is not primarily a result of social deviance or conflicts with society. Other accepted validity criteria for psychiatric disorders include those established by Robins and Güze in 1970 that are a common clinical description, the exclusion of other disorders, longitudinal studies (for stability over time), familial studies, and laboratory tests.

These definitions and the classification systems thus rely largely on statistical clustering of symptoms in individuals. No single pathophysiological process is assumed for a disease definition such as in other medical fields. The "underlying psychobiological dysfunction" is vague and secondary, largely because psychiatry presently has no unitary pathophysiological model for most diseases (schizophrenia, bipolar disorder, autism etc.).

The issue with such a situation is that neuroimaging and DTI studies currently investigate groups of patients based on clinical classifications only. As an example, when we compare a group of 30 patients with "schizophrenia" with "healthy controls," one cannot know if the 30 patients share a common underlying etiological mechanism or various physiopathological processes. This may explain some false negatives (because of the inclusion of patients with heterogeneous neurobiology). This situation may also explain the heterogeneity of the results if different groups studying the same "disease" have included non-comparable groups. Indeed, the DSM-V authors state that an inter-rater kappa for most diagnoses between 0.4 and 0.6 would be a realistic goal, and 0.2 and 0.4 would be acceptable [30]. Therefore, one cannot assume that groups of patients with an identical diagnosis are similar between studies.

In addition, the stability of psychiatric diagnoses over time is also open to debate. A very recent study explored this question in a cohort of 470 first-admission patients with psychotic disorders who were systematically assessed at baseline and during a 10-year follow-up [31]. Diagnoses were based on best-estimate consensus. In this report, 50.7 % of study participants' diagnoses *changed* at some point during the study. Therefore, a study scanning patients with "first-episode schizophrenia" may include patients with first-episode schizophrenia, but also patients with other future diagnoses such as bipolar disorder.

Boundaries of diagnoses are also unclear. The distinction between schizophrenia and bipolar disorder has been debated since 1896, when Emil Kraepelin proposed that a fundamental dichotomy exists between those two diagnoses (the "Kraepelinian dichotomy"). The existence of mixed clinical forms ("schizoaffective disorders"), shared genetic vulnerability, diagnosis instability, and common risk factors have led several authors to consider those two illnesses as belonging to the same fundamental process [32, 33]. Some authors even include autism in this picture (Kanner, himself, firstly described autism as "early-onset schizophrenia").

Finally, an additional layer of complexity comes from the variation in time of the diagnostic criteria used. As an example, diagnoses in the DSM-III and DSM-IV are not strictly identical, and thus, studies using these different manuals cannot be directly compared. Some diagnoses disappear from the classifications, while others arise.

On the other hand, neuroimaging may help to better define homogeneous and valid diagnostic groups, by identifying clear physiopathological processes involved. The initial goal of the DSM-V revision was indeed to define illnesses by using the new knowledge stemming from biological, including neuroimaging studies. To achieve this goal, large studies comparing patients across diagnoses are recommended.

Psychiatric and Medical Comorbidity, including Alcohol and Substance Abuse

Heterogeneous results have been obtained in neuroimaging studies of psychiatric conditions. Several sources of heterogeneity can be identified. Amongst them, the heterogeneity of the clinical samples recruited is a crucial issue. One source of heterogeneity comes from the classification systems used (see previous paragraph). But potential biases are specifically present in neuroimaging of patients with psychiatric illnesses: comorbidity, heterogeneity of the illness, medication, impact of illness duration, and episodes and impact of symptoms.

Comorbidity

Patients suffering from a psychiatric illness often exhibit high rates of psychiatric and somatic comorbidities. In schizophrenia, anxiety and depressive symptoms are very common with an estimated prevalence of 29 % for PTSD and 23 % for OCD. Depression occurs in 50 % of patients with schizophrenia and 47 % also have a lifetime diagnosis of substance abuse [34]. In patients with bipolar disorder, substance use comorbidities are present in up to 72 % of patients, along with anxiety or multiple comorbidities [35].

For somatic conditions, cardiovascular diseases are far more frequent than in general population in patients with bipolar disorder [36]. In schizophrenia, most of the common medical conditions are more frequent than in general vpopulation [37]. The cause for this is unclear. Two hypotheses are proposed: firstly, there is a delay in diagnosis and lack in the care of somatic conditions in patients with psychiatric illnesses. Secondly, some of these somatic conditions are inherent to the pathophysiology of psychiatric diseases [36].

The very high rates of comorbidities in psychiatric illnesses raise two challenges in DTI studies. First of all, the inclusion of patients with comorbidities may introduce a bias in the interpretation of the results. The differences found between patients and controls may be caused by the psychiatric illness itself or by its comorbidity. As an example, DTI differences between patients with bipolar disorder and controls may be linked to alcohol use disorder in these patients. Indeed, even detoxified subjects with alcohol use disorder exhibit DTI abnormalities [38], which are probably of larger magnitude than those of bipolar disorder. Even somatic conditions such as diabetes may bias the DTI results [39]. One solution to this issue may be the inclusion of comorbidity-free patients in DTI studies. However, this approach introduces a sampling bias as most of the patients have comorbidities and therefore, comorbidity-free patients may not be representative of typical patient populations.

Heterogeneity of Illness

Another source of heterogeneity in the results of neuroimaging studies is the heterogeneity of the clinical samples, which probably confounds the observed results. The clinical characteristics of the patients studied are diverse, with, for example, different forms of schizophrenia (with or without hallucinations etc.) or different subtypes of BD (e.g., types I and II, rapid cycling) and differences in age at onset (early, intermediate, late). Unipolar depression is probably even more diverse. In anxiety disorders, PTSD may arise from various types of trauma. Some of these clinical features such as the presence or absence of hallucinations in patients with schizophrenia have already been associated with specific DTI findings [40].

Illness duration, severity, number of episodes, and current symptoms may also vary between samples and are known to have an influence on DTI findings in most conditions.

A last source of heterogeneity is the recruitment mode. Patients recruited via the press, inpatient or outpatient facilities differ on many demographic and clinical characteristics.

Medication

Another major confounding variable is psychotropic medication. For major psychiatric illnesses such as schizophrenia, bipolar disorder, or severe unipolar disorder, virtually all patients are taking one, or more usually, several psychotropic medications such as antipsychotics, mood stabilizers, antidepressants, and benzodiazepines. All these psychotropic medications may affect brain structure. The most common example is the neurotrophic effect of lithium on grey matter volumes. There is presently a lack of knowledge regarding the effect of these medications on brain white matter, but current evidence suggests a limited impact on DTI variables [41].

Similarly to the comorbidity issue, the recruitment of medication-free patients, apart from being very difficult, may lead to sampling issues.

Special Considerations in the Scanner: The Effect of Motion, Active Symptoms, and Informed Consent

Another source of noise and bias that is crucial in DTI studies is the compliance of the patients to the instructions given by the scanning staff. More specifically, head motion is a major source of noise in most neuroimaging studies [42]. Patients are more prone to head motion than controls because of several factors including minor neurological signs associated with the disease itself, medication, motivation, and anxiety. In DTI, head motion is also a source of noise despite motion correction algorithms [43]. In movement

disorders, FA values have proven to be robust despite head motion, which is very encouraging for the psychiatric field [44].

Aside from motion, the nature of psychiatric symptoms that patients present with during scanning may hinder optimal data acquisition. For example, depressed subjects may be less motivated to attend scanning sessions or suffer higher levels of anxiety. Manic or actively psychotic individuals may be too restless or anxious to tolerate scanning. The resulting scans may suffer more motion artifacts or scanning may be terminated before the acquisition is complete. In all these cases, the most optimum results will be obtained by employing strategies to increase patient compliance with the scanning procedures. It is therefore extremely important that staff scanning subjects with active psychiatric disorders pay special attention to ensuring that patients receive clear and complete instructions on the scanning procedure and what they can expect to experience whilst in the scanner. Along these same lines, it is vital that the nontherapeutic investigation of psychiatric patients conforms to an ethical framework that takes into account the ability of the patient to provide informed consent [45].

DTI findings in Psychiatric Disorders

Despite the inherent difficulties in acquiring good comparative data in psychiatric populations, research in psychiatry has greatly benefited from neuroimaging. Earlier work using CT, MRI, and PET fundamentally altered the perception of psychiatric illness from an intangible, unquantifiable, functional disturbance without organic pathology, to a collection of disorders for which measurable neurological changes in brain structure and biochemical function could be identified and visualized. With the ability to investigate white matter, DTI continues to advance our understanding of the nature of these structural changes. Since the advent of the technique, the role of white matter alterations as a core feature of mental illness pathophysiology has become apparent, and the concept of psychiatric disease arising from altered structural connectivity has been strengthened.

Which Fiber Bundles Are of Interest in Psychiatric Disorders?

DTI has been applied to the investigation of a number of psychiatric disorders to varying degrees and using a range of analysis methods to explore whole brain white matter, specific fiber tracts, and tract subregions. The most commonly reported deficits are found in frontal and temporal white matter and tracts that subserve the limbic system. Such tracts include the various subregions of the corpus callosum (CC), cingulum bundle (CB), superior (SLF) and inferior longitudinal fasciculi (ILF), thalamic radiations, and uncinate fasciculus (UF) [1, 46]. Impaired WM microstructure in these regions is hypothesized to contribute to a breakdown in the regulation of higher functions relating to cognition, emotion, and memory, which are typically compromised in psychiatric illness. Some ascending and descending fiber systems such as the corona radiata, internal vcapsules, cerebral and cerebellar peduncles feature more predominantly in neurodevelopmental disorders such as autism and ADHD, and also in schizophrenia, and may underlie the psychomotor features of these illnesses.

Reported alterations are however by no means limited to these areas and neither are such findings universal. This likely reflects the heterogeneity of both the clinical populations studied and the methodology employed to investigate them. Furthermore, several regions such as the WM of the medial temporal lobe and corpus callosum emerge consistently in meta-analyses of different disorders. This illustrates the lack of specificity of DTI changes in psychiatric illnesses and may be reflective of the considerable overlap in symptomatology between them. In this context, DTI metrics in isolation cannot be used diagnostically but provide useful additional data in a multimodal framework incorporating for example, genetic, neuropsychological, psychosocial, and clinical measures.

DTI Findings in Selected Psychiatric Disorders

Schizophrenia

Schizophrenia is a disorder of thought, perception, emotion, and behavior affecting an estimated 1 % of the population. Patients may experience both "positive" symptoms, such as hallucinations, delusions, altered thoughts and feelings of being controlled, and "negative" symptoms characterized by withdrawal, flattened affect, and anhedonia.

It is the most widely studied psychiatric disorder using DTI, with over 300 studies listed on PubMed at the time of writing (early 2015). There are few negative studies, with the majority reporting FA reductions in more than one brain region [47]. Although FA reduction in frontal and temporal WM appears most frequently reported, there are also reports of such decreases in parietal, occipital, and even cerebellar white matter, suggesting widespread diffuse whole brain pathology, consistent with findings of widespread grey matter reductions and functional impairments detected using other imaging modalities [10]. A recent meta-analysis of DTI studies in schizophrenia described two distinct regions where FA was reduced consistently: one in the left perigenual WM of the frontal lobe and a second region, in the medial temporal lobe [48]. The authors postulate that these regions represent two distinct networks that are compromised in schizophrenia, leading to a disconnection of important fronto-temporal grey matter functional areas.

Mood Disorders

The next most widely investigated psychiatric conditions are**major depressive disorder (MDD)** and **bipolar disorder (BD)**. Depression is a common disorder affecting up to one in five people in their lifetime. It is characterized by extended periods of low mood, sadness, anhedonia, impaired concentration, altered sleep and appetite, feelings of guilt and worthlessness, and in severe cases, suicidal thoughts. Bipolar disorder is less common, affecting 1 % of the population, and is characterized by alternating periods of severe depression and hypomania or mania. During (hypo) manic episodes, patients experience elevated mood, increased energy, reduced need for sleep, talk more quickly, may make unrealistic plans, overspend, engage in risky behavior, become irritable, aggressive, and abuse alcohol and drugs. Some patients may also experience psychosis, a state in which their perception of reality becomes distorted. In this context, symptoms of BD and schizophrenia overlap. It is interesting that DTI findings in BD also parallel those in schizophrenia. However, FA reductions are less widely reported across the whole brain in BD and there are considerably more negatives studies. There are also some reports of regional FA increase [49]. Regionally, FA reductions tend to be found in frontal and temporal WM. Corpus callosum deficits feature strongly, particularly anterior (genu) and posterior (splenium) projections [50–52]. FA reductions also predominate in anatomically closely related tracts, such as portions of the SLF, ILF, IFOF, posterior thalamic radiation, and cingulum [53]. Such regions are classically associated with emotional regulation, working memory, and facial processing; functions that are impaired in BD. Interestingly, these regions, which emerged consistently in a meta-analysis of 11 DTI studies [46], parallel the two regions identified in the schizophrenia meta-analysis described above.

Findings in MDD are significantly more heterogeneous and overlap considerably with changes identified in BD. Strikingly, a recent meta-analysis [54] not only identified FA deficits in the callosal genu and body but also found them in precisely the same posterior WM region encompassing the right ILF, IFOF, and posterior thalamic radiation, as the meta-analysis of DTI studies in BD and schizophrenia, all performed by different authors [46, 48]. Findings diverge somewhat from BD and schizophrenia, where FA reductions in MDD are found in more dorsal regions of the PFC, compared to more ventral and perigenual PFC regions in BD and schizophrenia.

Anxiety Disorders

Anxiety disorders are common, affecting one in ten people in their lifetime. They are characterized by both psychological effects, including increased worry, irritability, fear, and impaired sleep; and somatic complaints, such as dizziness, palpitations, trembling, sweating, rapid breathing, and gastrointestinal disruption. Some anxiety disorders are a permanent and disruptive feature of a patient's life such as **generalized anxiety disorder (GAD)**, **obsessive-compulsive disorder (OCD)**, and **posttraumatic stress disorder (PTSD)**. Other forms of anxiety disorder arise only in certain situations, which are typically stressful for the affected individual. For example, **panic disorder** is characterized by intense, isolated "attacks" that come on quickly, and **phobias**, which give rise to feelings of anxiety and fear when the sufferer is exposed to something that is not usually dangerous, such as house spiders or traveling by air. Neurobiological models of anxiety propose a disruption to key networks that modulate fear and attention and involve brain structures such as the medial prefrontal cortex, posterior cingulate cortex, insula, brain stem, hippocampus, and amygdala [55]. The cingulum bundle is central to these networks and features prominently in DTI studies of anxiety.

Most types of anxiety disorder have been investigated using DTI, but studies are less numerous than in the schizophrenia and mood disorders. Two studies have investigated panic disorder. One ROI analysis of the anterior and posterior cingulum reported increased FA in this structure [56]. The other utilized a voxel-based approach and found FA decreases in the right IFOF, left callosal body, and left SLF [57].

DTI studies of PTSD are limited and include investigations into the effect of childhood trauma measured during childhood and during adulthood, and also the effect of adult trauma. A meta-analysis of seven studies investigating trauma-exposed adults identified FA decreases in nine clusters and increases in six clusters, which included different regions of the cingulum. Interestingly, volumetric reductions have also been commonly reported in this structure [58].

The typical behaviors associated with OCD are hypothesized to reflect cortical dysregulation of cortico-thalamo-striatal circuits including the orbitofrontal cortex, cingulate, and caudate [59]. Positive DTI findings predominate, with FA changes, i.e., reductions and also increases reported in tracts associated with these regions, for example, in the cingulum bundle, internal capsule, anterior thalamic radiation, superior longitudinal fasciculus and inferior fronto-occipital fasciculus, as well as in the corpus callosum, frontal and parietal white matter [60, 61].

Personality Disorders

Personality disorders are common, and arise from the abnormal expression of certain character traits that diverge from the sociocultural norm of the individual's environment. Such traits include being overly suspicious, impulsive, overly emotional, and anxious. These traits may lead those with the disorder to engage in destructive and harmful behavior to themselves and/or others, and they may find it difficult to function in healthy relationships and formal educational or employment settings.

Research using DTI to study personality disorders is limited. Two studies report reduced FA in orbitofrontal WM [62, 63], whilst another reports no FA decrease in borderline personality disorder patients compared to a control group [64]. However, interpretation of these findings is compromised by the inclusion of patients with different comorbid psychiatric conditions and analyses based on suboptimal DTI data. Only two studies have examined schizotypal personality disorder. The first used an automated ROI analysis of the uncinate fasciculus and cingulum bundle in DTI linescan data and found reduced FA in the uncinate only [65]. The second investigated a larger sample in a more elaborate analysis examining WM underlying Brodmann regions of the dorsolateral PFC, cingulate gyrus, and temporal lobe, and found both FA reductions in temporal WM and posterior cingulum and FA increase in the subgenual PFC [66].

Neurodevelopmental Disorders

Neuroimaging studies in children have additional challenges beyond those described previously (see Chap. 13). Notably, the effect of age is likely to be an important confound in such studies. Given the different trajectories of white matter development both within and between typically developing children and children affected by psychopathology, cross-sectional studies including different age groups limit comparability between studies and generalizability of findings. In spite of such issues, DTI is providing data supporting dyconnectivity models of two key neurodevelopmental disorders.

Autism

Autism (autism spectrum disorder/ASD) is a pervasive neurodevelopmental disorder emerging in early childhood that is characterized by impaired social and communication skills, repetitive, stereotyped behavior, and increased sensitivity to external stimuli. The dramatic increase in ASD diagnosis in recent years has been mirrored by an increase in neuroimaging research investigating the neurobiological basis of the condition. Studies employing active and resting state fMRI have demonstrated aberrant functional connectivity in ASD, which may be driven by impaired structural connectivity, i.e., WM pathology [67, 68]. However, DTI findings have been heterogeneous with a particular lack of consensus on the location of FA and MD changes in ASD. Most studies have found FA to be reduced; however few studies have reported this reduction in the same region and other studies have failed to find FA reductions in these regions [69]. A relatively large recent study including 39 young autistic children found widespread, minor FA reductions and MD increases in the order of 1–2 % compared to 39 typically developing children [69]. Notably, this study used two different voxel-based approaches and found discrepancies in the level of statistical significance in regions reported between the methods. The authors also identified image artifacts in their data that may have contributed to the results, which they discussed in the context of potential confounds in such DTI studies and to caution against the use of DTI metrics as a biomarker for single-subject diagnosis.

Attention Deficit Hyperactivity Disorder

Attention Deficit Hyperactivity Disorder (ADHD) is a neurodevelopmental, behavioral disorder affecting up to 5 % of school age children, characterized by impaired attention and concentration with increased impulsivity and hyperactivity. One neurobiological theory proposes that the disorder reflects abnormal fronto-striatal-cerebellar circuitry. Findings from DTI appear to support this model with several studies reporting both FA alterations in a range of tracts subserving these regions. For example, a meta-analysis including nine VBA studies of both pediatric and adult populations (173 ADHD patients and 169 healthy controls) identified five foci of altered FA within the callosal genu, anterior corona radiate, internal capsule, and cerebellar white matter [70]. ROI studies have also reported reduced anisotropy in overlapping regions, including the middle cerebellar peduncle [71], corticospinal tract [72], internal capsules, and corpus callosum [73, 74]. Anisotropy increases have also been reported in frontal and temporal white matter [75, 76]. Interestingly, one study of the basal ganglia did not find group differences in FA or MD, but found an increase in FA with age in the ADHD group that was absent in the controls, hinting at delayed WM development that normalizes in adulthood [77]. Indeed, many cases of ADHD resolve with increasing maturity, whilst others persist into adulthood, which may reflect different illness subtypes or pathophysiological mechanisms.

Alcohol Use Disorders

The harmful use of alcohol is widespread across the globe, with many Eastern European countries, Thailand, Korea, and Columbia reporting

prevalence rates of over 10 % in men (WHO). In the context of abuse and dependence, alcohol misuse is a common and significant comorbidity in psychiatric disorders [78]. The damaging effect of alcohol on the brain through acute cytotoxity and the sequelae of chronic overconsumption is well documented [79]. One DTI ROI based study investigating the acute effects of wine consumption on different brain regions at 0.5, 1, 2, and 3 h following consumption reported significant changes in ADC in the cerebral peduncles, thalamus and frontal WM, and in FA in frontal WM over time that may reflect the development of cytotoxic edema and subsequent recovery [80]. Another voxel-based study investigating 14 adolescent binge drinkers (defined as drinking five alcoholic beverages in one sitting) and equally matched controls reported widespread FA reductions that appeared to be dose dependent [81]. Studies of "uncomplicated alcoholics" have aimed to characterize long-term effects of chronic alcohol exposure and have reported regional FA reductions in anterior and superior association bundles and in the corpus callosum [82, 83]. One study investigating mesencephalic fiber tracts in detoxified subjects reported ADC increases and an 18 % reduction in reconstructed tracts per unit volume between the midbrain and pons [38]. Alcohol therefore appears to impact upon DTI metrics, whether consumed in moderate or large amounts, and these effects are measurable in both acute and chronic phases of overuse, as well as in states of detoxification. As such, alcohol use should be accounted for in DTI investigations and may represent an important confound in DTI studies of psychiatric disorders.

In summary, DTI is a valuable tool in the field of psychiatry, particularly in clinical research. It is not without its limitations, and implementing the technique properly in psychiatric populations requires careful attention. In the future, concurrent advances in both neuroimaging and biological psychiatry should converge with advances in allied disciplines in order to inform and improve clinical practice and the care of patients with psychiatric disorders.

References

1. Emsell L, Mcdonald C. The structural neuroimaging of bipolar disorder. Int Rev Psychiatry. 2009;21:297–313.
2. Levitt JJ, Bobrow L, Lucia D, Srinivasan P. A selective review of volumetric and morphometric imaging in schizophrenia. Curr Top Behav Neurosci. 2010;4:243–81.
3. Thermenos HW, Keshavan MS, Juelich RJ, Molokotos E, Whitfield-Gabrieli S, Brent BK, et al. A review of neuroimaging studies of young relatives of individuals with schizophrenia: a developmental perspective from schizotaxia to schizophrenia. Am J Med Genet B Neuropsychiatr Genet. 2013;162B:604–35.
4. Fornito A, Yucel M, Patti J, Wood SJ, Pantelis C. Mapping grey matter reductions in schizophrenia: an anatomical likelihood estimation analysis of voxel-based morphometry studies. Schizophr Res. 2009;108:104–13.
5. Whalley HC, Harris JC, Lawrie SM. The neurobiological underpinnings of risk and conversion in relatives of patients with schizophrenia. Int Rev Psychiatry. 2007;19:383–97.
6. Linden DE. The challenges and promise of neuroimaging in psychiatry. Neuron. 2012;73:8–22.
7. Walterfang M, Malhi GS, Wood AG, Reutens DC, Chen J, Barton S, et al. Corpus callosum size and shape in established bipolar affective disorder. Aust N Z J Psychiatry. 2009;43:838–45.
8. Greicius M. Resting-state functional connectivity in neuropsychiatric disorders. Curr Opin Neurol. 2008;21:424–30.
9. Dauvermann MR, Whalley HC, Schmidt A, Lee GL, Romaniuk L, Roberts N, et al. Computational neuropsychiatry - schizophrenia as a cognitive brain network disorder. Front Psychiatry. 2014;5:30.
10. Fornito A, Zalesky A, Pantelis C, Bullmore ET. Schizophrenia, neuroimaging and connectomics. Neuroimage. 2012;62:2296–314.
11. Kupfer DJ. The increasing medical burden in bipolar disorder. JAMA. 2005;293:2528–30.
12. Singh I, Rose N. Biomarkers in psychiatry. Nature. 2009;460:202–7.
13. Houenou J, d'Albis MA, Vederine FE, Henry C, Leboyer M, Wessa M. Neuroimaging biomarkers in bipolar disorder. Front Biosci (Elite Ed). 2012;4:593–606.
14. Lemm S, Blankertz B, Dickhaus T, Muller KR. Introduction to machine learning for brain imaging. Neuroimage. 2011;56:387–99.
15. Duchesnay E, Cachia A, Boddaert N, Chabane N, Mangin JF, Martinot JL, et al. Feature selection and classification of imbalanced datasets: application to PET images of children with autistic spectrum disorders. Neuroimage. 2011;57:1003–14.
16. Koutsouleris N, Meisenzahl EM, Davatzikos C, Bottlender R, Frodl T, Scheuerecker J, et al. Use of neuroanatomical pattern classification to identify

subjects in at-risk mental states of psychosis and predict disease transition. Arch Gen Psychiatry. 2009;66:700–12.
17. Iwabuchi SJ, Liddle PF, Palaniyappan L. Clinical utility of machine-learning approaches in schizophrenia: improving diagnostic confidence for translational neuroimaging. Front Psychiatry. 2013;4:95.
18. Davatzikos C, Shen D, Gur RC, Wu X, Liu D, Fan Y, et al. Whole-brain morphometric study of schizophrenia revealing a spatially complex set of focal abnormalities. Arch Gen Psychiatry. 2005;62:1218–27.
19. Farb NA, Anderson AK, Bloch RT, Segal ZV. Mood-linked responses in medial prefrontal cortex predict relapse in patients with recurrent unipolar depression. Biol Psychiatry. 2011;70:366–72.
20. Wang P, Verma R. On classifying disease-induced patterns in the brain using diffusion tensor images. Med Image Comput Comput Assist Interv. 2008;11:908–16.
21. Ingalhalikar M, Kanterakis S, Gur R, Roberts TP, Verma R. DTI based diagnostic prediction of a disease via pattern classification. Med Image Comput Comput Assist Interv. 2010;13:558–65.
22. Ardekani BA, Tabesh A, Sevy S, Robinson DG, Bilder RM, Szeszko PR. Diffusion tensor imaging reliably differentiates patients with schizophrenia from healthy volunteers. Hum Brain Mapp. 2011;32:1–9.
23. Besga A, Termenon M, Grana M, Echeveste J, Perez JM, Gonzalez-Pinto A. Discovering Alzheimer's disease and bipolar disorder white matter effects building computer aided diagnostic systems on brain diffusion tensor imaging features. Neurosci Lett. 2012;520:71–6.
24. Mashour GA, Walker EE, Martuza RL. Psychosurgery: past, present, and future. Brain Res Brain Res Rev. 2005;48:409–19.
25. Ward HE, Hwynn N, Okun MS. Update on deep brain stimulation for neuropsychiatric disorders. Neurobiol Dis. 2010;38:346–53.
26. Gutman DA, Holtzheimer PE, Behrens TE, Johansen-Berg H, Mayberg HS. A tractography analysis of two deep brain stimulation white matter targets for depression. Biol Psychiatry. 2009;65:276–82.
27. Schlaepfer TE, Bewernick BH, Kayser S, Madler B, Coenen VA. Rapid effects of deep brain stimulation for treatment-resistant major depression. Biol Psychiatry. 2013;73:1204–12.
28. Schoene-Bake JC, Parpaley Y, Weber B, Panksepp J, Hurwitz TA, Coenen VA. Tractographic analysis of historical lesion surgery for depression. Neuropsychopharmacology. 2010;35:2553–63.
29. Henderson JM. "Connectomic surgery": diffusion tensor imaging (DTI) tractography as a targeting modality for surgical modulation of neural networks. Front Integr Neurosci. 2012;6:15.
30. Kraemer HC, Kupfer DJ, Clarke DE, Narrow WE, Regier DA. DSM-5: how reliable is reliable enough? Am J Psychiatry. 2012;169:13–5.
31. Bromet EJ, Kotov R, Fochtmann LJ, Carlson GA, Tanenberg-Karant M, Ruggero C, et al. Diagnostic shifts during the decade following first admission for psychosis. Am J Psychiatry. 2011;168:1186–94.
32. Burmeister M, McInnis MG, Zollner S. Psychiatric genetics: progress amid controversy. Nat Rev Genet. 2008;9:527–40.
33. Kas MJ, Fernandes C, Schalkwyk LC, Collier DA. Genetics of behavioural domains across the neuropsychiatric spectrum; of mice and men. Mol Psychiatry. 2007;12:324–30.
34. Buckley PF, Miller BJ, Lehrer DS, Castle DJ. Psychiatric comorbidities and schizophrenia. Schizophr Bull. 2009;35:383–402.
35. Bauer MS, Altshuler L, Evans DR, Beresford T, Williford WO, Hauger R. Prevalence and distinct correlates of anxiety, substance, and combined comorbidity in a multi-site public sector sample with bipolar disorder. J Affect Disord. 2005;85:301–15.
36. Leboyer M, Soreca I, Scott J, Frye M, Henry C, Tamouza R, et al. Can bipolar disorder be viewed as a multi-system inflammatory disease? J Affect Disord. 2012;141:1–10.
37. Laursen TM, Munk-Olsen T, Gasse C. Chronic somatic comorbidity and excess mortality due to natural causes in persons with schizophrenia or bipolar affective disorder. PLoS One. 2011;6:e24597.
38. Chanraud S, Reynaud M, Wessa M, Penttila J, Kostogianni N, Cachia A, et al. Diffusion tensor tractography in mesencephalic bundles: relation to mental flexibility in detoxified alcohol-dependent subjects. Neuropsychopharmacology. 2009;34:1223–32.
39. Antenor-Dorsey JA, Meyer E, Rutlin J, Perantie DC, White NH, Arbelaez AM, et al. White matter microstructural integrity in youth with type 1 diabetes. Diabetes. 2013;62:581–9.
40. Allen P, Modinos G, Hubl D, Shields G, Cachia A, Jardri R, et al. Neuroimaging auditory hallucinations in schizophrenia: from neuroanatomy to neurochemistry and beyond. Schizophr Bull. 2012;38:695–703.
41. Hafeman DM, Chang KD, Garrett AS, Sanders EM, Phillips ML. Effects of medication on neuroimaging findings in bipolar disorder: an updated review. Bipolar Disord. 2012;14:375–410.
42. Van Dijk KR, Sabuncu MR, Buckner RL. The influence of head motion on intrinsic functional connectivity MRI. Neuroimage. 2012;59:431–8.
43. Jones DK, Cercignani M. Twenty-five pitfalls in the analysis of diffusion MRI data. NMR Biomed. 2010;23:803–20.
44. Muller HP, Sussmuth SD, Landwehrmeyer GB, Ludolph A, Tabrizi SJ, Kloppel S, et al. Stability effects on results of diffusion tensor imaging analysis by reduction of the number of gradient directions due to motion artifacts: an application to presymptomatic Huntington's disease. PLoS Curr. 2011;3:RRN1292.
45. Gupta UC, Kharawala S. Informed consent in psychiatry clinical research: a conceptual review of issues, challenges, and recommendations. Perspect Clin Res. 2012;3:8–15.

46. Vederine FE, Wessa M, Leboyer M, Houenou J. A meta-analysis of whole-brain diffusion tensor imaging studies in bipolar disorder. Prog Neuropsychopharmacol Biol Psychiatry. 2011;35(8): 1820–6.
47. Kyriakopoulos M, Frangou S. Recent diffusion tensor imaging findings in early stages of schizophrenia. Curr Opin Psychiatry. 2009;22:168–76.
48. Ellison-Wright I, Bullmore E. Meta-analysis of diffusion tensor imaging studies in schizophrenia. Schizophr Res. 2009;108:3–10.
49. Heng S, Song AW, Sim K. White matter abnormalities in bipolar disorder: insights from diffusion tensor imaging studies. J Neural Transm. 2010;117:639–54.
50. Sarrazin S, Poupon C, Linke J, Wessa M, Phillips M, Delavest M, et al. A multicenter tractography study of deep white matter tracts in bipolar I disorder: psychotic features and interhemispheric disconnectivity. JAMA Psychiatry. 2014;71:388–96.
51. Emsell L, Langan C, Van Hecke W, Barker GJ, Leemans A, Sunaert S, et al. White matter differences in euthymic bipolar I disorder: a combined magnetic resonance imaging and diffusion tensor imaging voxel-based study. Bipolar Disord. 2013;15:365–76.
52. Emsell L, Leemans A, Langan C, Van Hecke W, Barker GJ, McCarthy P, et al. Limbic and callosal white matter changes in euthymic bipolar I disorder: an advanced diffusion magnetic resonance imaging tractography study. Biol Psychiatry. 2013;73: 194–201.
53. Emsell L, Chaddock C, Forde N, Van Hecke W, Barker GJ, Leemans A et al. White matter microstructural abnormalities in families multiply affected with bipolar I disorder: a diffusion tensor tractography study. Psychol Med. 2013;10:2139–50
54. Liao Y, Huang X, Wu Q, Yang C, Kuang W, Du M, et al. Is depression a disconnection syndrome? Meta-analysis of diffusion tensor imaging studies in patients with MDD. J Psychiatry Neurosci. 2013;38:49–56.
55. Etkin A. Functional neuroanatomy of anxiety: a neural circuit perspective. Curr Top Behav Neurosci. 2010;2:251–77.
56. Han DH, Renshaw PF, Dager SR, Chung A, Hwang J, Daniels MA, et al. Altered cingulate white matter connectivity in panic disorder patients. J Psychiatr Res. 2008;42:399–407.
57. Lai CH, Wu YT. Fronto-occipital fasciculus, corpus callosum and superior longitudinal fasciculus tract alterations of first-episode, medication-naive and late-onset panic disorder patients. J Affect Disord. 2013;146:378–82.
58. Daniels JK, Lamke JP, Gaebler M, Walter H, Scheel M. White matter integrity and its relationship to PTSD and childhood trauma--a systematic review and meta-analysis. Depress Anxiety. 2013;30:207–16.
59. Fineberg NA, Potenza MN, Chamberlain SR, Berlin HA, Menzies L, Bechara A, et al. Probing compulsive and impulsive behaviors, from animal models to endophenotypes: a narrative review. Neuropsychopharmacology. 2010;35:591–604.
60. Benedetti F, Giacosa C, Radaelli D, Poletti S, Pozzi E, Dallaspezia S, et al. Widespread changes of white matter microstructure in obsessive-compulsive disorder: effect of drug status. Eur Neuropsychopharmacol. 2013;23:581–93.
61. Bora E, Harrison BJ, Fornito A, Cocchi L, Pujol J, Fontenelle LF, et al. White matter microstructure in patients with obsessive-compulsive disorder. J Psychiatry Neurosci. 2011;36:42–6.
62. Carrasco JL, Tajima-Pozo K, Diaz-Marsa M, Casado A, Lopez-Ibor JJ, Arrazola J, et al. Microstructural white matter damage at orbitofrontal areas in borderline personality disorder. J Affect Disord. 2012; 139:149–53.
63. Grant JE, Correia S, Brennan-Krohn T, Malloy PF, Laidlaw DH, Schulz SC. Frontal white matter integrity in borderline personality disorder with self-injurious behavior. J Neuropsychiatry Clin Neurosci. 2007;19:383–90.
64. Rusch N, Weber M, Il'yasov KA, Lieb K, Ebert D, Hennig J, et al. Inferior frontal white matter microstructure and patterns of psychopathology in women with borderline personality disorder and comorbid attention-deficit hyperactivity disorder. Neuroimage. 2007;35:738–47.
65. Nakamura M, McCarley RW, Kubicki M, Dickey CC, Niznikiewicz MA, Voglmaier MM, et al. Fronto-temporal disconnectivity in schizotypal personality disorder: a diffusion tensor imaging study. Biol Psychiatry. 2005;58:468–78.
66. Hazlett EA, Goldstein KE, Tajima-Pozo K, Speidel ER, Zelmanova Y, Entis JJ, et al. Cingulate and temporal lobe fractional anisotropy in schizotypal personality disorder. Neuroimage. 2011;55:900–8.
67. Muller RA, Shih P, Keehn B, Deyoe JR, Leyden KM, Shukla DK. Underconnected, but how? A survey of functional connectivity MRI studies in autism spectrum disorders. Cereb Cortex. 2011;21:2233–43.
68. Verly M, Verhoeven J, Zink I, Mantini D, Peeters R, Deprez S, et al. Altered functional connectivity of the language network in ASD: role of classical language areas and cerebellum. Neuroimage Clin. 2014; 4:374–82.
69. Walker L, Gozzi M, Lenroot R, Thurm A, Behseta B, Swedo S, et al. Diffusion tensor imaging in young children with autism: biological effects and potential confounds. Biol Psychiatry. 2012;72:1043–51.
70. van Ewijk H, Heslenfeld DJ, Zwiers MP, Buitelaar JK, Oosterlaan J. Diffusion tensor imaging in attention deficit/hyperactivity disorder: a systematic review and meta-analysis. Neurosci Biobehav Rev. 2012;36:1093–106.
71. Bechtel N, Kobel M, Penner IK, Klarhofer M, Scheffler K, Opwis K, et al. Decreased fractional anisotropy in the middle cerebellar peduncle in children with epilepsy and/or attention deficit/hyperactivity disorder: a preliminary study. Epilepsy Behav. 2009;15:294–8.
72. Hamilton LS, Levitt JG, O'Neill J, Alger JR, Luders E, Phillips OR, et al. Reduced white matter integrity

in attention-deficit hyperactivity disorder. Neuroreport. 2008;19:1705–8.
73. Pavuluri MN, Yang S, Kamineni K, Passarotti AM, Srinivasan G, Harral EM, et al. Diffusion tensor imaging study of white matter fiber tracts in pediatric bipolar disorder and attention-deficit/hyperactivity disorder. Biol Psychiatry. 2009;65:586–93.
74. Cao Q, Sun L, Gong G, Lv Y, Cao X, Shuai L, et al. The macrostructural and microstructural abnormalities of corpus callosum in children with attention deficit/hyperactivity disorder: a combined morphometric and diffusion tensor MRI study. Brain Res. 2010;1310:172–80.
75. Peterson DJ, Ryan M, Rimrodt SL, Cutting LE, Denckla MB, Kaufmann WE, et al. Increased regional fractional anisotropy in highly screened attention-deficit hyperactivity disorder (ADHD). J Child Neurol. 2011;26:1296–302.
76. Davenport ND, Karatekin C, White T, Lim KO. Differential fractional anisotropy abnormalities in adolescents with ADHD or schizophrenia. Psychiatry Res. 2010;181:193–8.
77. Silk TJ, Vance A, Rinehart N, Bradshaw JL, Cunnington R. Structural development of the basal ganglia in attention deficit hyperactivity disorder: a diffusion tensor imaging study. Psychiatry Res. 2009;172:220–5.
78. Hasin D, Kilcoyne B. Comorbidity of psychiatric and substance use disorders in the United States: current issues and findings from the NESARC. Curr Opin Psychiatry. 2012;25:165–71.
79. Harper C. The neuropathology of alcohol-related brain damage. Alcohol Alcohol. 2009;44:136–40.
80. Kong LM, Zheng WB, Lian GP, Zhang HD. Acute effects of alcohol on the human brain: diffusion tensor imaging study. AJNR Am J Neuroradiol. 2012;33:928–34.
81. McQueeny T, Schweinsburg BC, Schweinsburg AD, Jacobus J, Bava S, Frank LR, et al. Altered white matter integrity in adolescent binge drinkers. Alcohol Clin Exp Res. 2009;33:1278–85.
82. Pfefferbaum A, Rosenbloom M, Rohlfing T, Sullivan EV. Degradation of association and projection white matter systems in alcoholism detected with quantitative fiber tracking. Biol Psychiatry. 2009;65:680–90.
83. Harris GJ, Jaffin SK, Hodge SM, Kennedy D, Caviness VS, Marinkovic K, et al. Frontal white matter and cingulum diffusion tensor imaging deficits in alcoholism. Alcohol Clin Exp Res. 2008;32:1001–13.

Suggested Reading

Thomason ME, Thompson PM. Diffusion imaging, white matter, and psychopathology. Annu Rev Clin Psychol. 2011;7:63–85.

Diffusion Tensor Imaging in Traumatic Brain Injury

19

Süleyman Sener, Paul M. Parizel, and Andrew I.R. Maas

Learning Points

- Challenges in the use of DTI in TBI.
- DTI as a diagnostic tool for severity of TBI.
- DTI as an outcome predictor.

Introduction

Traumatic brain injury (TBI) is defined as an alteration in brain function, or other evidence of brain pathology, caused by an external force [1]. TBI is considered a silent epidemic, giving rise to many new victims each year, and represents a substantial socioeconomic and health problem. Worldwide, the incidence of TBI continues to increase, and the WHO predicts that road traffic incidents will be among the top three causes of death and disability by the year 2020. In Europe, approximately 2.5 million new cases of TBI are diagnosed each year. The epidemiology is, however, changing: in low and middle income countries, injuries are mainly caused by road traffic incidents and involve vulnerable road users (pedestrians, cyclists), who are mostly young men. In higher income countries, injuries are more often caused by falls and involve older patients. These patients more frequently have comorbidities, and often take medication, including anticoagulants and platelet aggregation inhibitors. Both comorbidity and medications may influence the disease process. TBI does not only affect the patient, but also has a direct impact on their families, relatives, caretakers, and social environment. The costs related to TBI are high, not only because of long-term hospitalization and rehabilitation but also because of indirect costs resulting from loss of productivity in previously healthy individuals due to mortality and disability. The financial burden for TBI is estimated at over 60 billion dollars a year in the USA [2].

Despite its frequent occurrence and significant personal and societal impact, our understanding of TBI is still limited. The injured brain is like a black box, from which it is difficult to extract information. Advanced MR Imaging, and in particular Diffusion Tensor Imaging (DTI), offers opportunities to investigate this black box, and to extract information that can be used to better characterize damage, track disease processes, and to establish a more accurate prognosis.

In the acute phase, structural brain damage is best assessed by CT scanning, as this is rapidly

S. Sener, MD (✉) • A.I.R. Maas
Department of Neurosurgery, Antwerp University Hospital and University of Antwerp, Wilrijkstraat 10, 2650 Edegem, Antwerp, Belgium
e-mail: suleyman.sener@uza.be

P.M. Parizel, MD, PhD
Department of Radiology, Antwerp University Hospital and University of Antwerp, Edegem, Antwerp, Belgium

W. Van Hecke et al. (eds.), *Diffusion Tensor Imaging*, DOI 10.1007/978-1-4939-3118-7_19

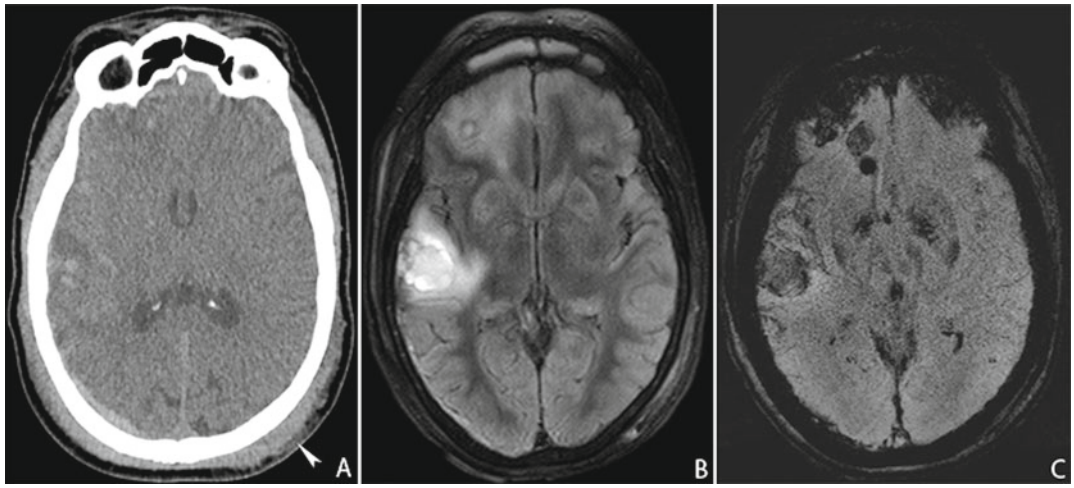

Fig. 19.1 TBI in a 57-year-old man, injured in a car accident. GCS on admission was 11/15 Noncontrast CT of the brain upon admission (**a**) and MRI of the brain on day 7 after the injury, including fat-saturated turbo FLAIR (**b**) and susceptibility weighted imaging (SWI) (**c**) were performed. The coup side is indicated by a left parieto-occipital subgaleal hematoma and infiltration of the subcutaneous fat (*arrow*). On the contre-coup side, there are hemorrhagic contusions in the right frontal and temporal lobes. In addition, there is a small right parietal subdural hematoma, but the midline structures are not displaced. The MRI scan on day 7 reveals hemorrhagic contusions in the right temporal and right frontal lobes, surrounded by edema. On the SWI scan, the hemorrhagic nature of these contre-coup contusions is clearly seen, and there is evidence of multiple other hemorrhagic foci in the brain parenchyma, as well as small amounts of intraventricular blood in the trigone and occipital horns of the lateral ventricles

available and can be performed quickly. This is important, as rapid detection and—if indicated—prompt removal of an intracranial hematoma is one of the major principles upon which care for the TBI patient is based. CT scanning further permits a broad characterization of TBI by the Marshall CT classification [3]. This classification offers a descriptive approach, which is important, as TBI is a very heterogeneous disease encompassing a broad range of pathologies [4]. The Rotterdam CT score was developed from a prognostic perspective and combines different CT features into a sum score. This score has been shown to be more strongly related to outcome than the Marshall CT classification [5]. Prediction of outcome, however, is better performed by combining different variables (clinical, radiological, and laboratory) into a multidimensional model.

TBI is a dynamic process, and pathology evolves over time. In patients with contusions, new lesions may develop in up to 16 % of cases and existing contusions may increase in size in up to 40 % of cases. This lesion progression mainly occurs within 6–9 h after injury [6]. Follow-up imaging is therefore essential.

The disadvantage of CT scanning is that it only captures limited information on the full extent of structural damage and does not provide any insight into function. Magnetic Resonance (MR) imaging can provide better insight into the extent and severity of primary and secondary brain damage (Fig. 19.1).

Specific MRI sequences, i.e., susceptibility weighted imaging (SWI) and diffusion weighted imaging (DWI), are more sensitive for detecting structural changes in the brain, particularly smaller lesions, such as microhemorrhages, diffuse axonal injury (DAI), and traumatic axonal injury (TAI) (Fig. 19.2) [7]. Diffusion tensor imaging (DTI) provides valuable additional information about white matter lesions and structural damage, and is therefore particularly suited

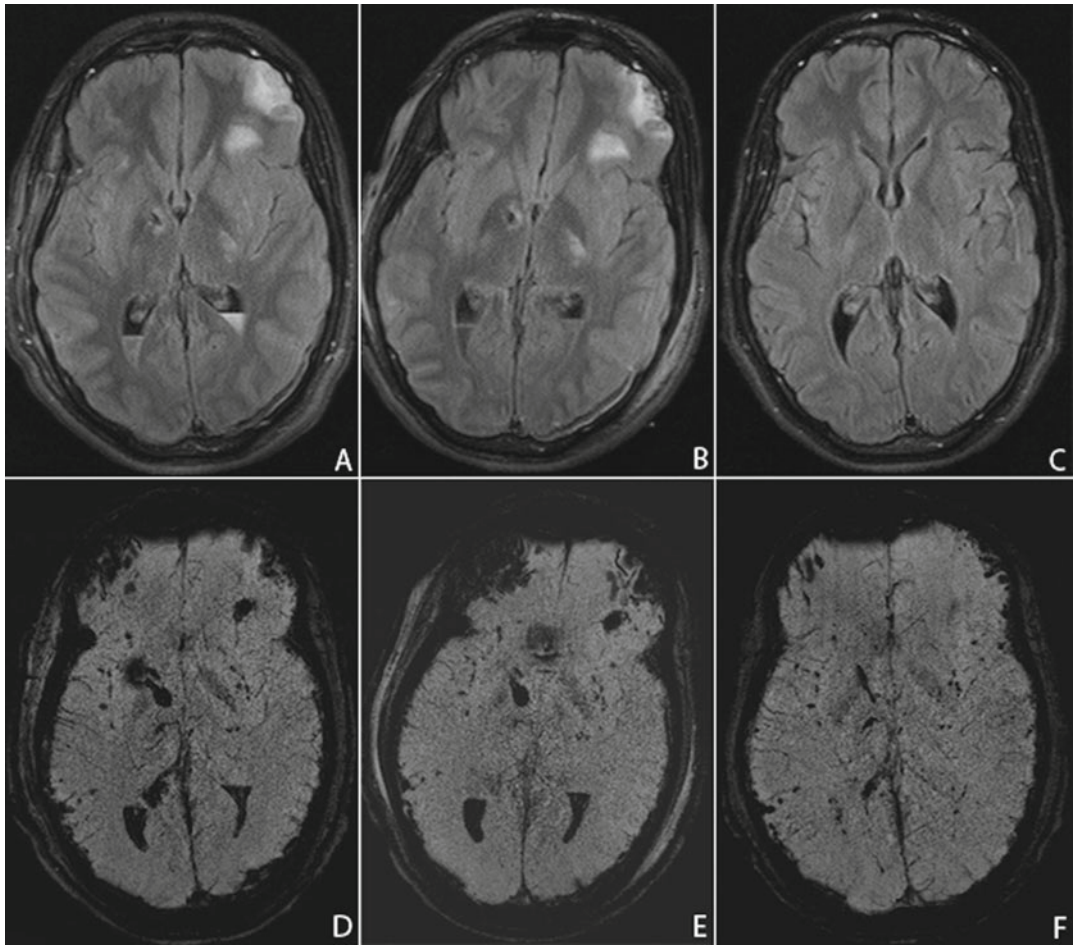

Fig. 19.2 TBI in a 19-year-old man, injured in a motor vehicle accident. The patient was admitted to the emergency department with a GCS of 9/15. MR imaging was performed on day 7 (**a**, **d**), day 12 (**b**, **e**), and after 6 months (**c**, **f**), using fat-saturated turbo FLAIR (**a**, **b**, **c**) and susceptibility weighted imaging (SWI) (**d**, **e**, **f**). The MRI scan on day 7 (**a**, **d**) reveals left frontal and bilateral capsulo-lenticular contusions, as well as intraventricular hemorrhage and multiple scattered hemorrhagic foci. A prominent susceptibility artifact in the right frontal region is caused by the ventricular shunt. Five days later, on day 12, the parenchymal lesions are unchanged, but there is a slight decrease in the amount of intraventricular hemorrhage. After 6 months (**c**, **f**) the intracerebral lesions have regressed on the FLAIR image, but there remain multifocal, punctate microhemorrhagic foci on the SWI sequence. In addition, a mild cortical atrophy has occurred

to characterize the presence and degree of injury and understand pathophysiological mechanisms in neurotrauma.

MR imaging can visualize abnormalities, consistent with axonal injury in up to 30–50 % of patients, in whom CT showed no apparent structural damage (Fig. 19.3) [8–10]. It is important to detect such lesions since TAI is a major cause of cognitive impairment and disability after TBI and thus a determining factor for outcome [11–18]. For example, in mild TBI patients with impaired executive function, reduced FA values were seen in the dorsolateral prefrontal cortex (DLPFC) [19]. A study by the NICER consortium demonstrated that microstructural changes were observed up to 5 years after severe TBI [20].

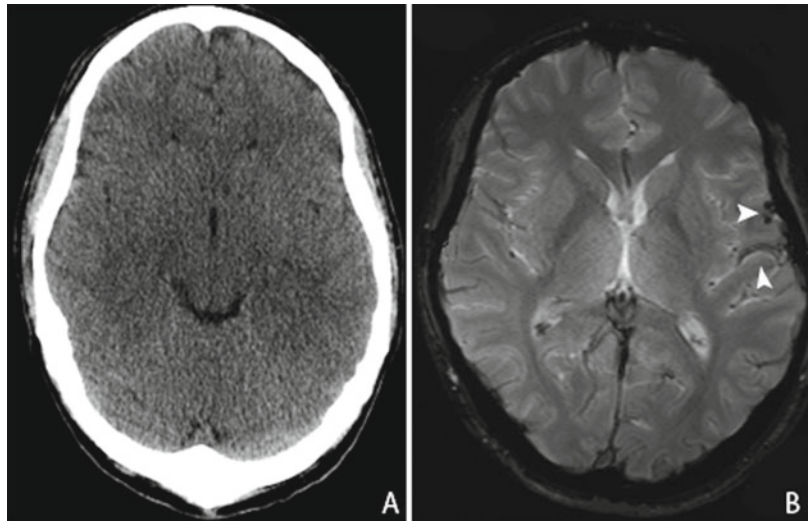

Fig. 19.3 Mild TBI in a 35-years-old patient who fell from the stairs, with GCS of 14/15 (E4M6V4) on admission. CT scan (**a**) upon admission showed no intracranial abnormalities. MR imaging—gradient echo T2 sequence—(**b**) 6 weeks after initial injury shows remnants of subarachnoid hemorrhage in the left parieto-temporal lobe (*arrow*)

This chapter will elaborate on the role of diffusion tensor imaging in traumatic brain injury for research and clinical practice.

Role of DTI in TBI

Pathophysiology

The pathophysiology of TBI is highly complex and involves multiple pathophysiologic processes. Importantly, TBI should not be seen as an event, but as a progressive disease, in which further damage may occur over hours, days, weeks, months, or even years. Secondary damage is preventable and potentially treatable. Detection, quantification, and tracking of such secondary damage is thus of paramount importance. Secondary damage may include brain swelling due to vascular engorgement or brain edema, which may be intracellular (cytotoxic) or vasogenic (extracellular). Cerebral ischemia, considered one of the most common problems after TBI, can occur locally (in the penumbra of a contusion) or more generalized and may be exacerbated by systemic insults, such as low blood pressure or inadequate blood oxygenation. Traumatic axonal injury, formerly considered a mechanical disruption of axons, has now been shown to result from metabolic failure of axonal transport mechanisms. Both hypo- and hypermetabolism may occur at different stages after injury. Disturbances of the mitochondrial transition pore are thought to be a main cause of mitochondrial failure after TBI. Inflammatory cascades are activated, some of which may be protective, others—when in excess—detrimental. Much insight into these mechanisms can be gained from MR Imaging. DWI and apparent diffusion coefficient (ADC) mapping can provide information about ischemia and edema, whilst MR spectroscopy can provide insight into metabolic derangements.

DTI in Diagnosis, Characterization, and Classification of TBI

DTI can provide important indirect information about neuronal integrity, continuity, and connectivity of neural pathways, even when traditional MRI sequences appear normal. The diffusion tensor characterizes the magnitude of water diffusion (ADC and mean diffusivity, MD), its directional nonuniformity (fractional anisotropy, radial and axial diffusivity, FA, RD, AD), and its orientation (the tensor eigenvectors). The exact mechanisms of the nature of water diffusion in both grey and white matter are not completely understood. However the organization of

tissue structure including the presence of myelin, microtubules, and organelles, as well as the contribution of intra- and extracellular water (edema formation) play a significant role. This is illustrated in a study by Newcombe et al. [21] in subjects with moderate to severe head injury where MRI was performed at a median of 32 h after injury. Results showed a decreased FA in the white matter, which was attributed predominantly to increased radial diffusivity, consistent with edema.

In 2012, Shenton et al. published a review of MRI and DTI focusing on mild traumatic brain injury. This article gives a good overview of studies performed on mild TBI, with all analyzed data showing some degree of subtle brain damage in mild TBI. The authors noted a wide range of variability in DTI studies and difficulties in data interpretation, due to the use of different scanning protocols and timings at DTI.

A meta-analysis of 28 studies by Aoki et al. [22] in mild TBI showed that the posterior part of the corpus callosum is more vulnerable to damage compared to the anterior part. Compared to healthy volunteers, there was a significant decrease in FA and increase in mean diffusivity in the corpus callosum in TBI patients.

In a study by Rutgers et al. [23] on 21 patients with mild TBI, in whom MRI was performed at an average of 5.5 months after injury, the cerebral lobar white matter showed regions with reduced FA values in almost 62 % of the study population. Further decrease of FA was observed in 23.6 % of the patients in the cingulum or the corpus callosum. Since abnormalities in the internal capsule, fornix, brain stem, and cerebellum were not frequently seen in their case study of mild TBI, the authors suggest these lesions may be more associated with severe TBI.

Kraus et al. [24] performed a DTI study in chronic traumatic brain injury patients with mild, moderate, and severe injury. The study included a total of 20 patients with mild and 17 patients with moderate/severe TBI as well as 18 healthy controls. DTI was performed at least 6 months after injury (average of 107 months after injury), using both whole brain analysis and region of interest analysis. Results showed an increased radial and axial diffusivity in patients with moderate and severe TBI in both whole brain and ROIs, indicative of potential myelin and axonal damage.

Notably, differences in the effect of TBI severity on AD and RD may reflect different underlying pathophysiological mechanisms related to the degree of tissue injury.

Recently, Van der Eerden and the Neuroimaging for Coma Emergence and Recovery (NICER) consortium [25] published the results of a multicenter study investigating DTI changes in cardiac arrest and TBI patients, using 19 predetermined ROIs. They found a decrease in axial diffusivity in cardiac arrest patients and increase in radial diffusivity in severe TBI patients. In the cardiac arrest patients, abnormalities are mostly seen in the cerebral hemispheres. For the TBI patients the abnormalities were found in both the central brain structures and cerebral hemispheres. The changes in axial diffusivity could be related to primary axonal damage due to energy depletion caused by ischemia. It was hypothesized that the increase in radial diffusivity in TBI patients was related to myelin damage and edema. The moderate decrease in axial diffusivity suggests axonal damage due to direct impact at trauma or ischemic changes due to secondary mechanism caused by intracranial lesions. However, relating changes in the axial and radial diffusivities to specific microstructural features is fraught with challenges, particularly in the context of tissue injury. As a consequence, these hypotheses for the observed DTI changes remain tentative.

Kasahara et al. [26] performed DTI in healthy controls and patients with mild TBI and DAI. Decreased axonal and radial diffusivity was found in the DAI patients. In mild TBI patients, normal radial diffusivity and increased axial diffusivity values were observed, indicating possible axonal abnormality.

DTI and Prognosis in TBI

DTI may also be used as a prognostic predictor in traumatic brain injury.

A DTI voxel-based analysis by Perlbarg et al. [27] investigating the prediction of 1-year outcome in severe TBI showed no significant ADC

differences between the favorable and unfavorable outcome groups. However, significant changes were observed in the FA values between these two groups, with a decrease in the FA value in the unfavorable outcome group.

Tollard and colleagues [28] performed a study with DTI and magnetic resonance spectroscopy (MRS) for outcome prediction in severe traumatic brain injury. Forty-three patients with severe TBI and 15 control subjects underwent MRI with DTI and MRS sequences. The imaging was performed in the subacute phase after trauma (24 ± 11 days after injury). DTI was performed using symmetrical regions of interest (ROI) analysis in the left and right mesencephalon, temporal and occipital white matter, anterior and posterior centrum semiovale, and anterior and posterior part of the pons.

These regions were predetermined regardless of the presence of morphologic lesions.

The results revealed significantly lower FA values in patients with unfavorable outcome (i.e., Glasgow Outcome Scale, GOS 1–3). Lower FA values were also seen in the temporal white matter and the centrum semiovale for patients with favorable outcome (i.e., GOS 4–5) compared to the control group. The authors suggest this may be because these lesions have no effect on the recovery of consciousness.

In this study, MRS was analyzed as single voxel spectroscopy in the posterior pons and axial chemical shift imaging (CSI) at the basal ganglia. Interestingly, using DTI and MRS separately showed lower specificity (85 % and 75 % respectively) and sensitivity (79 % and 75 % respectively) for predicting unfavorable outcome at 1-year post-injury, than combining the techniques (97 % specificity and 86 % sensitivity). This highlights the added value of combining DTI with other imaging modalities to improve its clinical utility.

Challenges for the Use of DTI in TBI

DTI is well suited to provide information related to the continuity and connectivity of neuronal pathways. It can provide insight into microstructural changes, such as fiber disruption and axonal degeneration after injury, and can potentially serve as a prognostic factor and aid the surgeon and the treating physician in their decision-making.

Nevertheless, there are challenges, both in interpreting literature data and in conducting studies on patients following TBI. For example, despite broad interest, most reports on DTI in TBI have been restricted to relatively small case series, have included some selection bias, and have only rarely studied patients early after injury. Furthermore, the multiple assumptions that underpin the algorithms used in post-processing of DTI data are not always applicable. Practical challenges associated with conducting DTI studies in TBI populations include transportation, logistic issues concerning scanning, timing of DTI scanning, and standardization of data acquisition and analysis protocols.

Transportation and Scanning Issues

In the acute phase of TBI, transport and scanning of a critically ill patient poses substantial logistical challenges. Transportation and scanning is thwarted by the need for mechanical ventilation and continuous monitoring. Since these patients are treated on the intensive care unit, transportation itself may carry risks. For instance, the intra-hospital transportation of critically ill patients increases the risk for significant adverse events, such as inadvertent hyperventilation or hypotension with limited options to intervene in case of problems [29]. In addition, installation of an ICU patient on a MRI scan is time consuming. Scanning time for a brain MRI, including DWI, SWI, and DTI, is also significantly longer compared to a CT scan (45 min vs. 2 min).

A major cause for disruption of DTI analysis is motion artifacts, resulting in loss of signal. Correction of the motion artifacts however is complex, but feasible using various methods [30].

Since TBI patients may have been operated on, any surgical material such as titanium clips, fixation materials, hemoclips, and surgical staples can cause loss of signal and will affect DTI analysis.

Timing of DTI Scanning

Since we deal with an evolving pathology, it is important to determine when to perform a MRI scan after TBI. As explained earlier, TBI is a dynamic process and both primary and secondary brain damage will cause brain swelling. In the acute phase after TBI, DTI can be influenced by edema, which imitates fiber disruption [23], and by large intracranial lesions. In the subacute phase, neuronal degeneration and inflammatory reactions due to secondary brain damage are still ongoing. Valuable information can be missed by DTI scanning during this period.

Standardization of DTI Analysis—Analyzing DTI

Two major approaches for analyzing DTI in TBI exist: (1) region of interest (ROI) analysis and (2) whole brain (WB) tractography.

In the region of interest approach, analyses are performed in predetermined regions, generally chosen within the white matter (because of interest in axonal disruption and water content/diffusion). This gives detailed analysis in these selected ROIs, but risks possibly missing areas of decreased FA values outside of these regions.

TBI is a very heterogeneous group and with WB tractography a more complete overview can be achieved. Nevertheless, artifacts such as large intracranial lesions, which can influence DTI analysis, may hinder this technique. In addition, specific regional information is lost by using whole brain tractography results.

It is the combination of all these challenges, i.e., problems due to transportation, timing in DTI scanning, specialized software, and different methods in analysis, that make standardization of the analysis one of the most difficult issues to overcome when using TBI to assess traumatic brain injury.

Conclusion

DTI remains for now mostly a research tool. Even though various studies have yielded promising findings, there are still difficulties to overcome before DTI will be a standard scanning sequence in clinical practice for TBI.

Standardization is the most difficult issue in the use of DTI for TBI since analyzing DTI is complex. Furthermore, studies of larger numbers of patients and multicenter studies that incorporate DTI are needed to evaluate the relevance of DTI as a diagnostic and prognostic tool for TBI in the acute and chronic phase. Nevertheless, DTI holds great promise to better characterize damage, track disease processes, and establish a more accurate prognosis in patients with TBI.

References

1. Menon DK, Schwab K, Maas AIR. Demographics and Clinical Assessment Working Group of the international and interagency initiative toward common data elements for Research on Traumatic Brain Injury and Psychological Health; Position statement: definition of traumatic brain injury. Arch Phys Med Rehabil. 2010;91(11):1637–40.
2. Finkelstein EA, Corso PS, Miller TR. The incidence and economic burden of injuries in the United States. New York, NY, USA: Oxford University Press; 2006. Xiii. p. 187.
3. Marshall LF, Bowers Marshall S, Klauber MR, Van Berkum Clark M, Eisenberg HM, Jane JA, Luerssen TG, Marmarou A, Foulkes MA. A new classification of head injury based on computerised tomography. Spec Suppl. 1991;75(1s):S14–20.
4. Saatman KE, Duhaime A-C, Bullock R, Maas AIR, Valadka A, Manley GT. Workshop scientific team and advisory panel members. Classification of traumatic brain injury for targeted therapies. J Neurotrauma. 2008;25:719–39.
5. Maas AIR, Hukkelhoven CWPM, Marshall LF, Steyerberg EW. Prediction of outcome in traumatic brain injury with computed tomographic characteristics: a comparison between the computed tomographic classification and combinations of computed tomographic predictors. Neurosurgery. 2005;57:1173–82.
6. Sener S, Rozenbeek B, Maas AIR. Surgical management of traumatic brain injury—evidences, controversies and perspectives for the futures. Eur Neurol Rev. 2011;6(3):196–201.
7. Shenton ME, Hamoda HM, Schneiderman JS, Bouix S, Pasternak O, Rathi Y, Vu M-A, Purohit MP, Helmer K, Koerte I, Lin AP, Kikinis R, Kubicki M, Stern RA, Zafonte R. A review of magnetic resonance imaging and diffusion tensor imaging findings in mild traumatic brain injury. Brain Imaging Behav. 2012;6:137–92.
8. Lee B, Newberg A. Neuroimaging in traumatic brain imaging. NeuroRx. 2005;2:372–83.
9. Mittle RL, Grossman RI, Hiehle JF, Hurst RW, Kauder DR, Gennarelli RA, et al. Prevalence of MR

evidence of diffuse axonal injury in patients with mild head injury and normal head CT findings. Am J Neuroradiol. 1994;15:1583–9.
10. Hammoud DA, Wasserman BA. Diffuse axonal injuries: pathophysiology and imaging. Neuroimaging Clin N Am. 2002;12(2):205–16.
11. Ezaki Y, Tsutsumi K, Morikawa M, Nagata I. Role of diffusion-weighted magnetic resonance imaging in diffuse axonal injury. Acta Radiol. 2006;47:733–40.
12. Kelly AB, Zimmerman RD, Snow RB, Gandy SE, Heier LA, Deck MDF. Head trauma: comparison of MR and CT—experience in 100 patients. AJNR Am J Neuroradiol. 1988;9(4):699–708.
13. Murray JG, Gean AD, Evans SJ. Imaging of acute head injury. Semin Ultrasound CT MR. 1996;17:185–205.
14. Shaefer PW, Huisman TAGM, Sorensen AG, Gonzalez RG, Schwamm LH. Diffusion weighted MR Imaging in closed head injury: high correlation with initial Glasgow Coma Scale score and score on Modified Rankin scale at discharge. Radiology. 2004;233(1):58–66.
15. Smith DH, Meaney DF, Shull WH. Diffuse axonal injury in head trauma. J Head Trauma Rehabil. 2003;18:307–16.
16. Scheid R, Walther K, Guthke T, Preul C, von Cramon Y. Cognitive sequelae of diffuse axonal injury. Arch Neurol. 2006;63:418–24.
17. Skandsen T, Kvistad KA, Solheim O, Haavde Strand I, Folvik M, Vik A. Prevalence and impact of diffuse axonal injury in patients with moderate and severe head injury: a cohort study of early magnetic resonance imaging findings and 1-year outcome. J Neurosurg. 2010;113:556–63.
18. Chelly H, Chaari A, Daoud E, Dammak H, Medhioub F, Mnif J, Ben Hamida C, Bahloul M, Bouaziz M. Diffuse axonal injury in patients with head injuries: an epidemiologic and prognosis study of 124 cases. J Trauma. 2011;71:838–46.
19. Lipton ML, Gulko E, Zimmerman ME, Friedman BW, Kim M, Gellella E, Gold T, Shifteh K, Ardekani BA, Branch CA. Diffusion-tensor imaging implicates prefrontal axonal injury in executive function impairment following very mild traumatic brain injury. Radiology. 2009;252(3):816–24.
20. Dinkel J, Drier A, Khalilzadeh O, Perlbarg V, Czernecki V, Gupta R, Gomas F, Sanchze P, Dormont D, Galanaud D, Stevens RD, Puybasset L. for NICER (Neuro Imaging for Coma Emergence and Recovery) Consortium. Long-term white matter changes after severe traumatic brain injury: a 5-year prospective cohort. Am J Neuroradiol. 2014;35:23–9.
21. Newcombe VF, Williams GB, Nortje J, et al. Analysis of acute traumatic axonal injury using diffusion tensor imaging. Br J Neurosurg. 2007;21(4):340–8.
22. Aoki Y, Inokuchi R, Gunshin M, Yahagi N, Suwa H. Diffusion tensor imaging studies of mild traumatic brain injury: a meta-analysis. J Neurol Neurosurg Psychiatry. 2012;83:870–6.
23. Rutgers DR, Toulgoat F, Cazejust J, Fillard P, Lasjaunias P, Ducreaux D. White matter abnormalities in mild traumatic brain injury: a diffusion tensor imaging study. Am J Neuroradiol. 2008;29:514–9.
24. Kraus MF, Susmaras T, Caughlin BP, Walker CJ, Weeney JA, Little DM. White matter integrity and cognition in chronic traumatic brain injury: a diffusion tensor imaging study. Brain. 2007;130:2508–19.
25. Van der Eerden AW, Khalilzadeh O, Perlbarg V, Dinkel J, Sanchez P, Vos PE, Luyt C-E, Stevens RD, Menjot de Champfleur N, Delmaire C, Tollard E, Gupta R, Dormont D, Laureys S, Benali H, Vanhaudenhuyse A, Galanaud D, Puybasset L. For NICER (Neuro Imaging for Coma Emergence and Recovery) Consortium. White matter changes in comatose survivors of anoxic ischemic encephalopathy and traumatic brain injury: comparative diffusion-tensor imaging study. Radiology. 2014;270:506–16.
26. Kasahara K, Hashimoto K, Abo M, Senoo A. Voxel- and atlas-based analysis of diffusion tensor imaging may reveal focal axonal injuries in mild traumatic brain injury—comparison with diffuse axonal injury. Magn Reson Imaging. 2012;30:496–505.
27. Perlbarg V, Puybasset L, Tollard E, Lehéricy S, Benali H, Galanaud D. Relation between brain lesion location and clinical outcome in patients with severe traumatic brain injury: a diffusion tensor imaging study using voxel-based approaches. Hum Brain Mapp. 2009;30:3924–33.
28. Tollard E, Galanaud D, Perlbarg V, Sancez-Pena P, Le Fur Y, Abdennour L, Cozzone P, Lehericy S, Chiras J, Puybasset L. Experience of diffusion tensor imaging and 1H spectroscopy for outcome prediction in severe traumatic brain injury: preliminary results. Crit Care Med. 2009;37:1448–55.
29. Parmentier-Decrucq E, Poissy J, Favory R, Nseir S, Onimus T, Guerry M-J, Durocher A, Mathieu D. Adverse events during intrahospital transport of critically ill patients: incidence and risk factors. Ann Intensive Care. 2013;3:10.
30. Le Bihan D, Poupon C, Amadon A, Lethimonnier F. Artefacts and pitfalls in diffusion MRI. J Magn Reson Imaging. 2006;24:478–88.

Suggested Reading

Yeh P-H, Oakes TR, Riedy G. Diffusion tensor imaging and its application to traumatic brain injury: basic principles and recent advances. Open J Med Imaging. 2012;2:137–61.

Hulkower MB, Poliak DB, Rosenbaum SB, Zimmerman ME, Lipton ML. A decade of DTI in traumatic brain injury: 10 years and 100 articles later. AJNR Am J Neuroradiol. 2013;34(11):2064–74.

Xiong K, Zhu Y, Zhang W. Diffusion tensor imaging and magnetic resonance spectroscopy in traumatic brain injury: a review of recent literature. Brain Imaging Behav. 2014;8(4):487–96. doi:10.1007/s11682-013-9288-2 [Epub ahead of print].

Part VI

Beyond Diffusion Tensor Imaging

High Angular Resolution Diffusion Imaging

20

Shawna Farquharson
and Jacques-Donald Tournier

Learning Points

- The fundamental limitations of the Diffusion Tensor (DTI) model have important implications for the interpretation of anisotropy as a marker of white matter integrity, and for applications such as diffusion-based tractography.
- Over the past decade, more advanced models have been developed to specifically address the limitations of the DTI model, many of which are based on the high angular resolution diffusion-weighted imaging (HARDI) data acquisition strategy.
- These HARDI-based approaches can be combined with appropriate tracking algorithms to provide improved tractography results.
- HARDI data is characterized primarily by two parameters: the number of unique directions, and the *b*-value. HARDI acquisition strategies are essentially identical in nature to the standard DTI acquisition, and differ only in that a larger number of unique diffusion-weighting gradient directions are used, potentially using a larger *b*-value than would be considered optimal for DTI.
- In practice, the number of directions required for HARDI is difficult to ascertain exactly since increasing it will always improve results through increasing the overall SNR of the acquisition. The primary requirement of the angular sampling is to characterize the relevant features of the DW signal. In practice, the optimal set of parameters will need to be determined empirically on a case-by-case basis, based on the intended HARDI reconstruction method and its particular requirements.
- HARDI-based reconstruction methods are now beginning to be used for clinical and neuroscientific investigations with extremely promising results.

S. Farquharson, MSc
Florey Institute of Neuroscience and Mental Health, University of Melbourne, 245 Burgundy Street, Heidelberg, VIC 3084, Australia

J.-D. Tournier, PhD (✉)
Florey Institute of Neuroscience and Mental Health, University of Melbourne, 245 Burgundy Street, Heidelberg, VIC 3084, Australia

Biomedical Engineering, Division of Imaging Sciences & Biomedical Engineering, King's College London, London, UK
e-mail: jacques_donald.tournier@kcl.ac.uk

Why We Need to Move Beyond DTI

The development of diffusion tensor imaging (DTI) and quantitative parameters derived from the diffusion tensor over the past two decades

W. Van Hecke et al. (eds.), *Diffusion Tensor Imaging*, DOI 10.1007/978-1-4939-3118-7_20

was a pivotal moment in the field of diffusion Magnetic Resonance Imaging (MRI). Although DTI is still the most commonly used model to relate the diffusion-weighted MRI signal to the underlying diffusion process, it is now widely acknowledged to be inadequate for this purpose. The limitations of the DTI model have important implications for the interpretation of anisotropy as a marker of white matter integrity and for applications such as diffusion-based tractography. In this chapter we discuss the practical limitations of the DTI model and review recent developments in the field, many of which are based on the high angular resolution diffusion-weighted imaging (HARDI) data acquisition strategy.

Key Points About DTI

The physical basis of the DTI model is that if water molecules encounter highly oriented barriers, then the distance they travel (from a given point for a given time) is on average greater along the structure than across the structure. This introduces a dependence of the measured diffusion signal on the direction along which it is measured, a phenomenon commonly referred to as anisotropy [1]. The diffusion tensor ellipsoid is used to describe in three dimensions the degree of anisotropy within individual voxels, and the principal axes of this ellipsoid (or principal eigenvectors) represent the orientation of the constituent tissue. Scalar measures derived from the diffusion tensor—for example the fractional anisotropy (FA) and mean diffusivity (MD)—are commonly used as measures of "tissue integrity." The principal orientation of the tensor ellipsoid within each voxel is used as an estimate of the fiber orientation, and forms the basis of many diffusion-based tractography methods [2, 3].

The fundamental limitation of the DTI model is that the tensor framework assumes a single straight fiber orientation within each imaging voxel, and is hence inadequate for the purpose of describing diffusion data within voxels containing complex fiber configurations or multiple fiber populations [1–4], an issue commonly referred to as the "crossing fiber problem." The so-called crossing fiber problem refers to any configuration of white matter fibers within a given imaging voxel that is more complex than a single straight fiber population, including fanning, bending, diverging and crossing fibers [5–7], as illustrated in Fig. 20.1. It is well known in the technical diffusion MRI community that using DTI to model complex fiber orientations results in an incorrect characterization of the constituent fiber populations (e.g., [1–4, 7–11]), as illustrated in Fig. 20.2. Given that diffusion-weighted data acquired on clinical scanners are typically limited to a spatial resolution of 2–3 mm and the relatively small size of most white matter tracts, it is not surprising that the so-called "crossing fiber problem" remains a significant issue for DTI.

The fact that the diffusion tensor is affected by the crossing fiber problem has been known since its very invention [12]; however, it is only recently that the scale of this problem has been fully appreciated. Recent work demonstrates that multiple fiber populations can be detected in over 90 % of imaging voxels in the white matter [13]. The scale of this problem has obvious and profound implications for both DTI-based tractogra-

Fig. 20.1 The term "crossing fibers" can refer to any situation where the fiber orientation is not unique. This includes obvious cases where the voxel contains two fiber bundles that cross or pass close to each other (*left*), but also voxels where the fibers themselves are curved, such as curving or diverging configurations (*right*), or any combination of these two (*middle*)

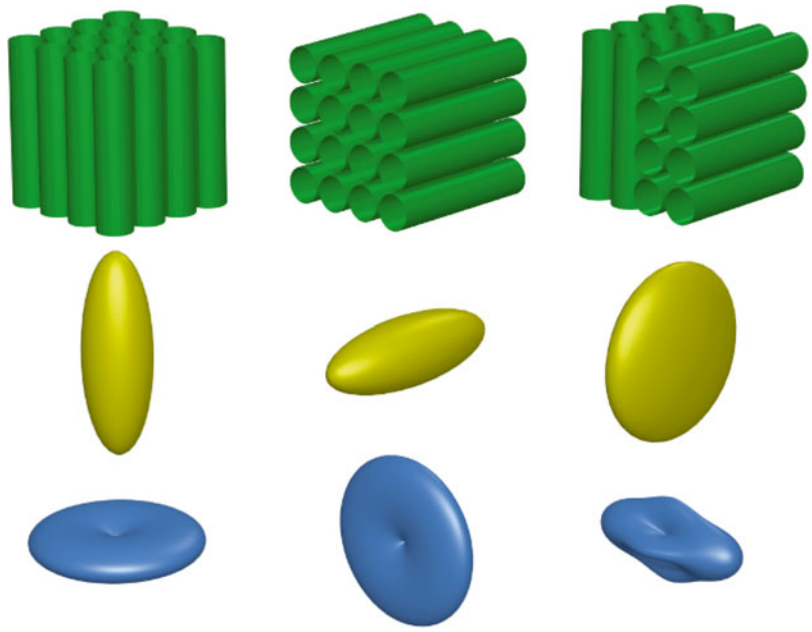

Fig. 20.2 A simple illustration of the effect of crossing fibers in diffusion tensor imaging. The diffusion tensor model is a good fit for voxels that contain a single fiber orientation (*left* and *middle* columns), but fails to capture the orientation information when two distinct orientations are present (*right*); in this case, the major eigenvector will not in general be aligned with either of the populations present, and the anisotropy is also reduced. On the other hand, the DW signal itself (*bottom row*) clearly does contain higher-order information in crossing fiber voxels (*bottom right*), which can be used to resolve the different fiber orientations present

phy techniques and DTI-derived measures used to assess tissue integrity.

The impact of crossing fibers has important ramifications for the application of tractography in particular, as the DTI model provides incorrect fiber orientation estimates in regions containing complex fiber configurations (see Fig. 20.2) [1]. This has important practical implications, as the majority of white matter tracts will traverse regions with multiple fiber orientations at some point along their path. Even a single incorrect orientation estimate (or for that matter, even a relatively small error in orientation estimation) will be enough to cause the algorithm to veer off-course or follow a completely unrelated tract, resulting in the delineation of false negative [13, 14] or false positive delineation of white matter pathways [13, 15]. The severe limitations of using the diffusion tensor model for fiber tractography have consistently been reported in the neurosurgical literature [16–20]. Of particular concern is that studies that have specifically investigated the feasibility of DTI-based tractography for the purpose of visualizing tracts of neurosurgical interest demonstrate that these methods result in systematically unreliable and clinically misleading tractography information [17, 19].

The extent of the crossing fiber problem means that caution also needs to be observed when interpreting DTI-derived diffusion indices such as fractional anisotropy (FA), particularly if the intention is to use them as surrogate markers of white matter "integrity" [11, 21–23]. It is well known that FA values vary greatly over the white matter even in healthy controls where there is no known change in white matter integrity. Such variations are likely due to the presence of crossing fibers in different parts of the white matter leading to reductions in tensor-derived anisotropy, as was originally suggested in the early DTI literature [24]. The profound confounding influence of crossing fibers on the interpretation of DTI-derived diffusion indices in the presence of pathology is demonstrated in clinical studies that

have observed an *increase* in anisotropy in cases where the given pathology or condition would have been expected to result in a reduction in tissue integrity [25]. The diffusion tensor model is increasingly recognized to be a gross over-simplification of the actual anatomy and the simplistic interpretation of DTI derived indices as a marker of white matter "integrity" is fraught with technical challenges [22, 23, 26]. As a consequence, there is a growing interest in finding clinically feasible alternatives to DTI [27].

Over the past decade, more advanced models have been developed to specifically address the limitations of the DTI model ([5–7], see reviews in [8]), many of which are now being used clinically with promising results. In this section, we describe some of the concepts and theory behind approaches that are based on high angular resolution diffusion-weighted imaging (HARDI) data [4], developed specifically to provide more robust fiber orientation estimates for applications such as diffusion tractography, and more recently to provide more biologically accurate measures of tissue microstructure or "integrity."

HARDI Methods

What Is HARDI?

The term HARDI stands for *high angular resolution diffusion imaging*, and was originally coined by Tuch et al. to refer to the particular acquisition strategy employed in their study, namely the use of dense sampling on the sphere using a single *b*-value, as illustrated in Fig. 20.3 [4]. Data acquired in such a way allow the thorough characterization of the angular dependence on the DW signal, with no attempt at characterizing its radial (*b*-value) dependence. For this reason, it is arguably the most efficient acquisition strategy for the purpose of fiber orientation estimation, and hence for tractography.

The HARDI acquisition is essentially identical in nature to the standard DTI acquisition, and differs only in that a larger number of unique diffusion-weighting gradient directions are used, potentially using a larger *b*-value than would be considered optimal for DTI. There is in fact no clear point at which an acquisition strategy

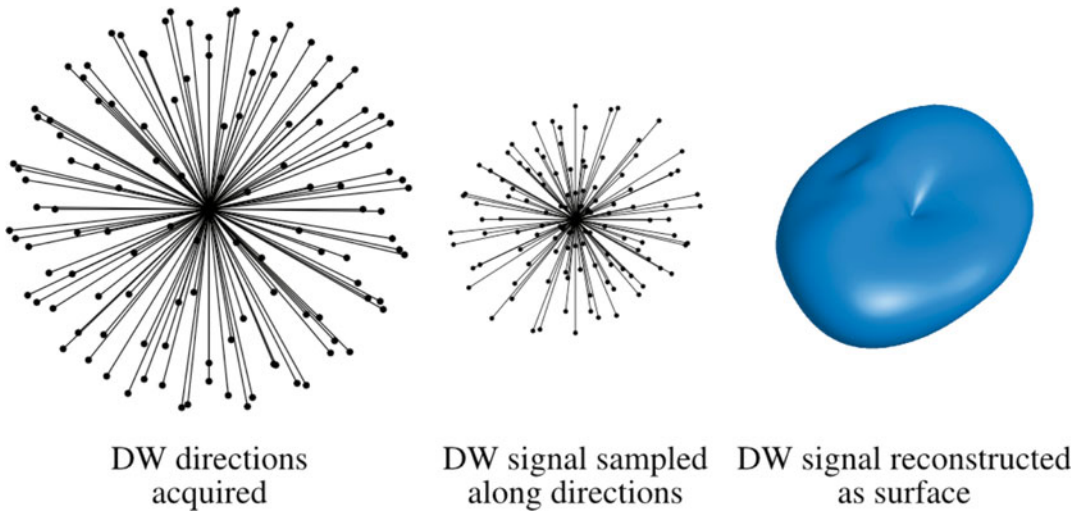

Fig. 20.3 The motivation for HARDI is the need to capture all the features of the DW signal over the sphere. For example, the DW signal shown on the right clearly contains angular features, and these features are key to resolving crossing fibers. The idea behind HARDI is to sample the orientation space as densely and uniformly as is practical, using a suitable set of DW directions such as those shown on the *left*. By measuring the DW signal along these orientations (*middle*), the DW signal can be reconstructed by fitting a surface (*right*), so that these features can be estimated accurately

becomes a HARDI sequence or vice-versa. For example, the current recommended minimum number of directions for robust DTI is 30 [28], while higher-order reconstruction methods have been applied to data acquired using as few as 20 directions [29]. Nonetheless, a sequence will typically be considered HARDI if the number of directions is relatively large (>~40).

It is worth noting that HARDI is *not* in itself a method for estimating fiber orientations; it refers specifically to the acquisition strategy. This can lead to confusion in the literature when authors claim to "perform a HARDI reconstruction"—this statement is ambiguous since it makes no mention of the reconstruction method used: it is in fact perfectly possible to perform a DTI reconstruction using HARDI data. Nonetheless, HARDI is the most common data acquisition strategy required for methods that aim to resolve crossing fibers, and for this reason the term HARDI is often used to refer to more advanced higher-order methods.

Why HARDI?

The simplest and most intuitive approach to understanding HARDI is to consider the example shown in Fig. 20.2, with two fiber populations crossing within a voxel. In this example, it is easy to see that DTI provides a good characterization of each of the two fiber populations separately, but fails when the two are combined. However, if we focus on the DW signal itself, it is clear that there is structure present in this case that the tensor ellipsoid fails to capture. Indeed, the DW signal for the crossing fiber case is to a very good approximation the sum of the DW signals that would be measured for each population independently; even by eye, the two contributions can easily be appreciated in the combined DW signal. The aim of HARDI methods is essentially to separate out these two contributions, and thus to resolve crossing fibers. For this to be possible, the relevant features of the DW signal need to be captured with sufficient accuracy. This requires a larger number of DW directions than typically acquired in DTI, leading directly to the development of HARDI approaches.

The problem of separating the two contributions can in essence be written out as a set of simultaneous equations: M DW measurements are acquired per voxel, and from these a set of N model parameters need to be estimated. What these N parameters represent is dependent on the particular reconstruction approach used: they might represent the orientations and volume fractions of a fixed number of potential fiber populations, or the coefficients of a more continuous representation of the diffusion or fiber configuration, as illustrated in Fig. 20.4. The latter is particularly advantageous from a mathematical perspective, since describing the orientation information using a continuous distribution allows the problem to be expressed and solved using extremely fast linear algebra techniques, with reconstruction times on the order of seconds for whole-brain datasets. Using a more explicit

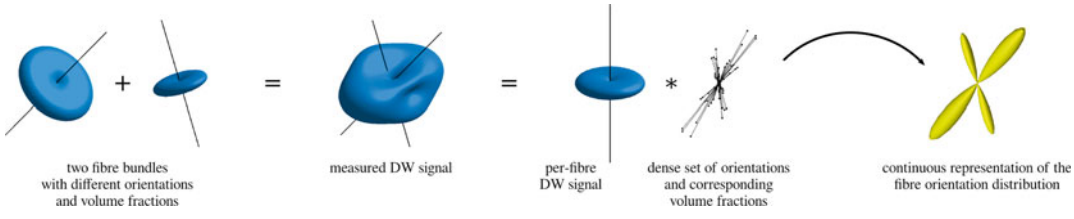

Fig. 20.4 The simplest approach to modelling crossing fibers in HARDI is to assume that the DW signals from the various fiber populations add up to give the total measured DW signal for that voxel (*middle left*). Resolving these crossing fibers is then a matter of finding the fiber configuration that best matches the observed data. One way to represent this configuration is as a set of discrete orientations with associated volume fractions (*left*); this is approach used in multi-tensor fitting methods. Another approach is to represent the fiber configuration as a continuous distribution, which can be approximated by a dense set of fixed orientations and corresponding volume fractions (*right*); this is the approach used in spherical deconvolution methods

parametric representation (for example partial volume and orientation per fiber population) does not lend itself to such convenient linear approaches, and will in general necessitate the use of more computationally expensive nonlinear optimization methods.

Using HARDI to Resolve Crossing Fibers

By far the most common application for HARDI methods is the estimation of the fiber orientations for use in fiber tracking. A number of methods are available to achieve this, but all are based on the same concept: each fiber population (i.e., distinct orientation) adds its own contribution to the measured signal, so that the total measured signal is the sum of the contributions that would have been measured for each bundle in isolation.

Multi-Tensor Fitting

Based on this observation, the most obvious approach to resolving crossing fibers is the *multi-tensor* approach: we assume the voxel contains two fiber populations rather than one, with each population modeled using its own diffusion tensor. In this case, the minimum additional information required is the relative amounts of each fiber population (i.e., their volume fractions) and their respective orientations. The problem is then one of estimating the set of parameters (volume fractions and orientations) that best fit the measured data [4, 30].

It turns out that this is not a simple problem to solve in practice due to the nonlinear formulation of the problem (a sum of exponentials), dictating the use of computationally expensive nonlinear minimization methods. In addition, the problem is generally ill-conditioned, due to the difficulty of differentiating between changes in anisotropy and changes in volume fraction of the constituent fiber populations[1]; to get around this, most implementations enforce the condition that each diffusion tensor be at least axially symmetric, and often hold all their diffusivities constant (i.e., assume a fixed mean diffusivity and anisotropy). Nonetheless, a number of methods are based on this general approach; some allow for larger numbers of fiber populations, some include an isotropic "CSF" compartment, and some use advanced Bayesian Monte Carlo Markhov Chain (MCMC) sampling techniques to characterize the uncertainty about the parameters estimates [14, 30–32].

The **Combined Hindered and Restricted Model of Diffusion** (CHARMED)approach is strongly related to the multi-tensor approach in that it also models each fiber population independently [33, 34]. However, it differs substantially in that it assumes a more biologically plausible model of restricted diffusion in cylinders to represent the DW signal from each fiber populations, rather than a diffusion tensor model. It also includes an extracellular compartment, itself modeled by a diffusion tensor. One limitation is that it requires a more demanding multi-shell (i.e., multiple b-values) HARDI data acquisition, leading to lengthier scan times.

One issue with these methods is that they somehow need to know how many fiber populations to include in the model for each voxel. While a number of approaches have been proposed to do this [2, 14, 31], any errors in this number will inevitably lead to errors in the estimated parameters. Most of these approaches are based on some statistical "goodness of fit" measure, and this will in general lead to underestimation of the number of fiber populations present, particularly in noisy data where any improvements in the model fit will be overwhelmed by the noise. The result is that while the algorithm can be said to be "conservative" in that it only includes additional fiber populations if there is good evidence that these are needed, it will inevitably fail to identify a significant proportion of crossing fiber voxels and therefore model them using the single tensor model, with all the limitations highlighted above.

Spherical Deconvolution

The multi-tensor approach can be extended by switching from a discrete representation (i.e., a small number of distinct fiber populations) to a continuous representation of the fiber orientation

[1] This is discussed in more detail in *the* "*constant anisotropy*" *assumption* section below.

information. One way to understand this is to imagine that rather than trying to estimate the volume fraction and orientation of each fiber population, we are now going to model a large number of fiber populations, each with a fixed orientation. The problem now reduces to figuring out the volume fractions of each of these. If we use a sufficiently dense set of orientations that are uniformly distributed over the sphere, the information can be represented as a distribution of volume fractions over the sphere, as illustrated in Fig. 20.4. This distribution is commonly referred to as the fiber orientation density function (fODF) or simply the fiber orientation distribution (FOD).

Essentially, the FOD is a function defined over the sphere, which represents the amount of fibers at any point on the sphere (i.e., aligned with the corresponding orientation). It is often displayed using orientation plots such as those shown in Fig. 20.5, whereby the distance from the origin represents the "density" along the corresponding orientation. Distinct fiber orientations can clearly be seen as distinct peaks in the FOD.

The advantages of using such a distribution to represent the fiber orientation information are threefold. First, it means that the relationship between the measured DW signal and the FOD is linear, allowing the use of much more efficient reconstruction methods based on linear algebra. Second, there is no need to specify the number of directions that might be present in each voxel; the FOD is continuous, and distinct fiber orientations will simply be reflected as distinct peaks in the FOD. Finally, the FOD is suited to describing fiber configurations containing a range of orientations, such as for example bending or fanning fibers; these are clearly not well characterized using a single orientation, as would be used in multi-tensor approaches. In these cases, the corresponding peak in the FOD will simply be broadened accordingly, as expected. Spherical deconvolution approaches are therefore more computationally efficient, while providing a much more general description of the fiber orientation information. These provide estimates of the FOD that are suitable for fiber-tracking, as illustrated for example in Fig. 20.6.

A number of different spherical deconvolution techniques have been proposed [10, 29, 36–39]. The most stable of these impose a non-negativity constraint to explicitly prevent or minimize negative fiber density values, which are clearly non-physical; this has been shown to dramatically improve the robustness to noise of these methods [29, 37]. Some estimate the per-fiber anisotropy on a per-voxel basis [36], other assume fixed diffusivity values [37–39], while others bypass the diffusion tensor model entirely and measure the actual per-fiber DW signal profile from the data themselves [10, 29].

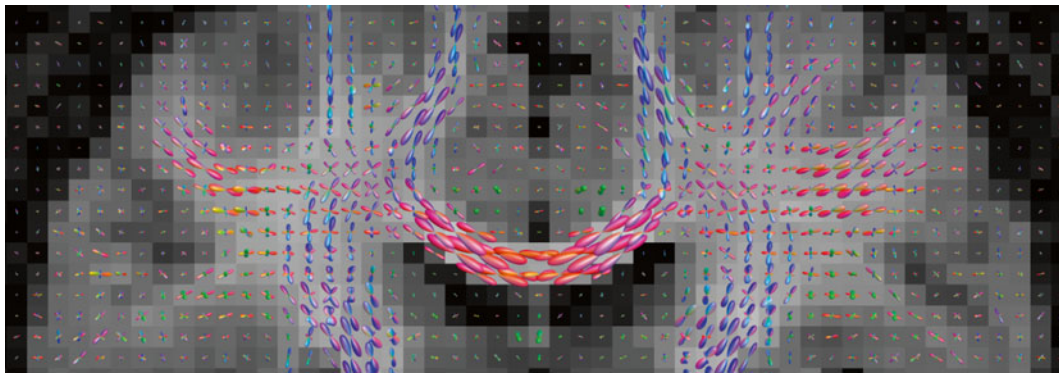

Fig. 20.5 Fiber orientation distributions obtained from a healthy volunteer, estimated using constrained spherical deconvolution [29] as implemented in MRtrix [35]. These are shown as a coronal projection overlaid on the mean DWI image, with the corpus callosum clearly visible in the centre with fibers running left–right (*red lobes*). Its lateral projections can be seen to cross through the fibers of the corona radiata (running inferior–superior; *blue lobes*) and the superior longitudinal fasciculus (running anterior–posterior; *green lobes*)

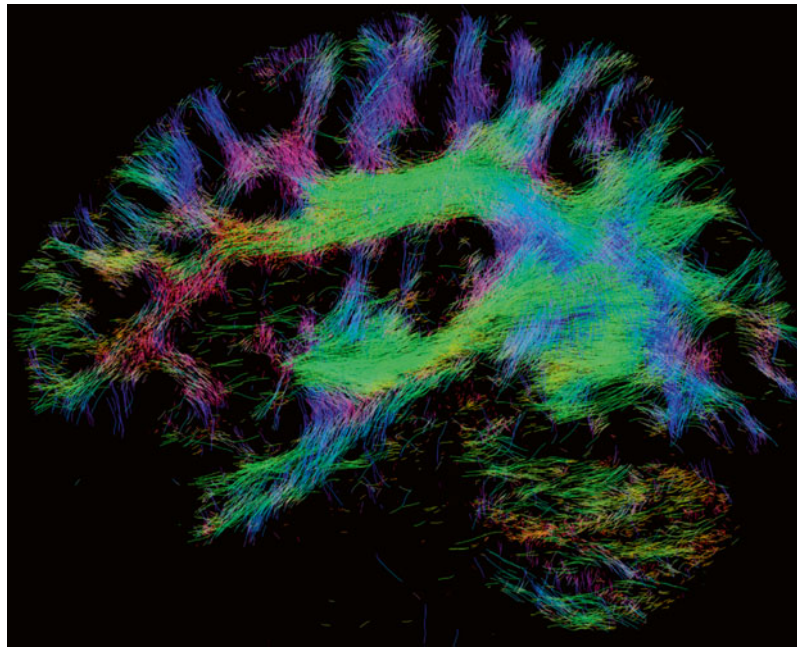

Fig. 20.6 Whole-brain fiber-tracking results obtained from a healthy volunteer, generated using a probabilistic fiber tracking algorithm on orientations estimated using constrained spherical deconvolution [29] as implemented in MRtrix [35]. A 2 mm-thick section through the tracks is shown as a sagittal projection. Amongst other white matter tracts, the superior longitudinal fasciculus can be seen running anterior–posterior (*green*) and then down into temporal and parietal regions. Also visible are the uncinate fasciculus, connecting the temporal pole to the frontal lobes (*blue*), and the inferior fronto-occipital fasciculus running anterior–posterior (*green*), connecting the frontal lobe to the occipital lobe

The "Constant Anisotropy" Assumption

The overwhelming majority of multi-tensor fitting and spherical deconvolution techniques will make the assumption that all fiber bundles can be described by diffusion tensors with the same intrinsic "constant anisotropy" (or at least axial symmetry) to reduce the complexity of the problem. At first sight, this might seem to be a gross over-simplification, particular to those steeped in the more traditional DTI framework, where tensor-derived metrics are often used as surrogate markers of white matter "integrity." Since these new approaches assume fixed values for these metrics over all white matter bundles, it is now impossible to estimate equivalent measures, let alone detect differences between them.

However, there are very good reasons to believe that this approximation holds in most, if not all cases. The assumption of fixed anisotropy inherently implies that all observed anisotropy differences in the brain are due entirely to crossing fiber effects or other partial volume effects (e.g., with CSF). This is in fact in line with the original DTI literature, where the large variations of anisotropy observed in healthy volunteers were attributed to differences in the coherence of fiber tract directions [24]. The relationship between anisotropy (and more recently radial and axial diffusivities) and white matter "integrity" was suggested based on highly controlled single nerve experiments, where any confounding effects of crossing fibers could explicitly be ruled out [40–44]. While these studies undeniably demonstrated changes in various tensor-derived metrics under different conditions (dysmyelination, axonal injury, changes in axonal diameter, etc.), these changes are dwarfed by the changes induced by the presence of crossing fibers [1, 23]. Moreover, and more importantly, while changes in diffusivities and/or anisotropy can be observed in these experiments, they are not of a magnitude sufficient to alter the results dramatically; as

shown in previous studies, while moderate changes in the assumed anisotropy will affect the estimated volume fractions, they have almost no impact on the estimated fiber orientations [10]. In fact, any pathology that would cause severe changes in the anisotropy of the per-fiber DW signal would probably need to involve destruction of the axonal membrane, with a large increase in radial diffusivity and corresponding reduction in the DW signal; this will be interpreted by these models primarily as a dramatic decrease in volume fraction, an interpretation that is in fact fairly accurate given the pathology.

For this reason, this particular assumption is very commonly employed, and with great success. However, the implication is that genuine anisotropy changes are at best extremely difficult to detect from HARDI data (given that they are essentially indistinguishable from partial volume effects), which essentially rules out the possibility of deriving equivalent markers of white matter "integrity"—at least using these approaches. Instead, the current trend is to focus on the estimated partial volume fractions, since these seem to have the most dominant impact on the DW signal, and can be used as estimates of fiber density—a measure that, although different from the more common interpretation of "integrity," is nonetheless clearly clinically very relevant [45–47].

Using HARDI to Characterize Diffusion

Another approach to the crossing fiber problem is to take a step back and focus on characterizing the *diffusion process* itself, rather than the fiber configuration directly. The motivation for such approaches is to avoid over-interpretation of the measured data. The relationship between the measured DW signal and the actual fiber configuration and associated tissue composition is obviously extremely complex: white matter is not made up of neatly arranged impermeable cylinders, but contains a wide range of different cells of different sizes and shapes, each with their own internal microstructure. Clearly, the DW signal depends on a myriad of different factors, and any attempt at extracting specific microstructural information will inevitably require that assumptions and approximations be made. Rather than trying to do this, it might be best to characterize what we can, and avoid making any potentially invalid or unjustified assumptions. For this reason, a number of so-called *model-free* techniques have been proposed to characterize the diffusion process itself.

q-Space and the Spin Propagator

These methods are all in some way based on the theory of *q*-space [48], which describes the relationship between the DW signal and the so-called *averagespin propagator* (also called the *spin displacement probability density function*). In simple terms, the spin propagator is a function describing the probability $P(\underline{r}|\underline{x},\Delta)$ that a water molecule initially at $\underline{x}$ has moved by displacement $\underline{r}$ during the diffusion time Δ of the MR measurement. For free diffusion, this is simply a Gaussian distribution with standard deviation equal to the root mean square displacement of the water molecules (as per Chap. 3). For more complex environments, the propagator will have a more complex shape, as illustrated in Fig. 20.7. This makes no assumption about whether diffusion is free or restricted: it simply characterizes the chances of molecules moving along a given direction by a given amount. In general, this will depend on the diffusion time Δ: with free diffusion, the distances moved will increase with diffusion time. However, in restricted geometries the maximum distance moved will clearly be dictated by the size of the restricting compartment. The relationship between the DW signal and the spin propagator is relatively simple and not subject to any particular biological assumptions.[2] Clearly, the diffusion propagator provides the most complete and accurate description of the diffusion process, and contains all the information that can be extracted from diffusion MRI, which is the reason why a number of methods attempt to estimate it.

[2] Although there are assumptions on the way data are acquired, as discussed in the section entitled *The narrow pulse approximation* below.

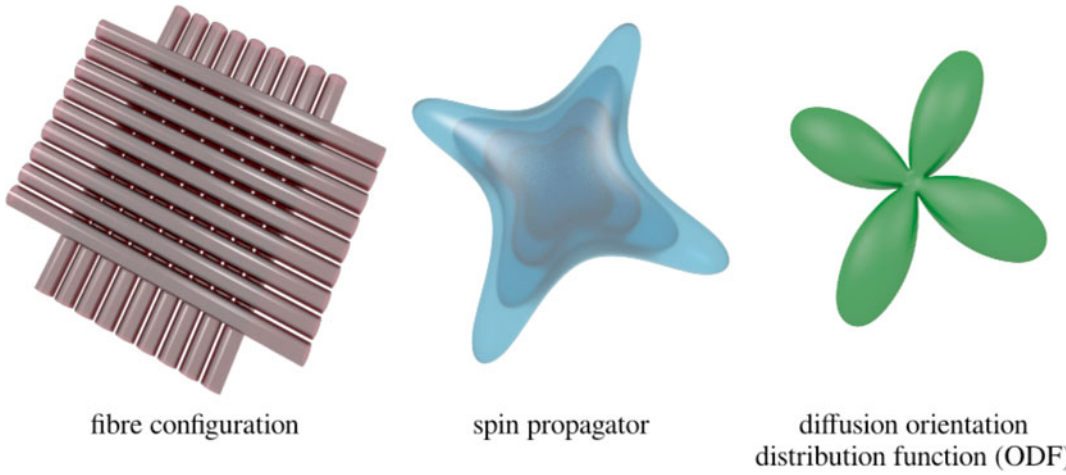

Fig. 20.7 Illustration of the relationship between the fiber configuration (*left*), the average spin propagator (*middle*), and the diffusion ODF (*right*). In a crossing fiber voxel (*left*), water molecules will tend to diffuse more readily along the fiber orientations than across them. This corresponds to a spin propagator with pronounced "ridges" along the fiber orientations (*middle*). This is a full three-dimensional density function, the characterization of which requires a vast amount of data. In contrast, the diffusion ODF (*right*) provides a more condensed version of spin propagator, which essentially describes the probability of a water molecules moving along any given orientation. As expected, the peaks of the dODF point along the fiber orientations

According to q-space, the DW signal is related to the spin propagator via a simple Fourier transform. In practice, this means that to estimate the spin propagator along one dimension, a number of DW images need to be acquired, each with a different q-value.[3] To get an accurate estimate, a sufficient number of distinct q-values need to be acquired, up to a sufficiently large maximum q-value to ensure near-complete nulling of the DW signal. These two requirements alone are difficult to achieve: for a full three-dimensional characterization of the spin propagator, the number of distinct q-vectors (and hence image volumes) required is of the order of 1000 (approx. 10 per image axis). These requirements also dictate the use of very large gradients and/or long echo times (to achieve the very large maximum q-values needed), leading to a reduction in the SNR. Clearly, the full characterization of the spin propagator is extremely challenging.

[3] The q-value is a measure of the strength of the diffusion weighting, akin to the b-value. It is given by $q = (\gamma/2\pi)\delta G$, where δ and G are the DW gradient pulse duration and amplitude respectively, and γ is the magnetogyric ratio.

Nonetheless, this complete characterization is exactly what **Diffusion Spectrum Imaging** (**DSI**) aims to achieve [49]. To do this, 515 image volumes are acquired, each with a distinct *q-vector* with a maximum b-value of 17,000 s/mm^2. This is clearly a much more demanding acquisition than can realistically be accommodated in routine clinical imaging, and for this reason much of the recent development in this area has been focused on obtaining relevant features of the spin propagator (namely the *diffusion orientation density function*; dODF) using the much more clinically achievable HARDI acquisition.

The Diffusion Orientation Density Function (dODF)

Essentially, the dODF is a simplified version of the full spin propagator, which provides only the probability of a water molecule moving along a given direction; any information about how far it moved is discarded. This much more compact version of the spin propagator is obviously still sufficiently informative, especially for the purposes of resolving crossing fibers, motivating the development of these HARDI-based methods.

Q-ball Imaging (QBI) was the first method proposed to estimate the dODF [50]. It performs a *Funk–Radon Transform* on the HARDI data to map the DW signal per-voxel onto the corresponding dODF. This has the advantage of being a linear operation, and was subsequently shown to be much more efficiently and robustly implemented using spherical harmonics [51, 52]. More recently, **Constant Solid Angle Q-ball Imaging** (CSA-QBI) has been proposed to obtain a more accurate, sharper estimate of the dODF [53].

Other techniques based on *q*-space that have been proposed include the **Diffusion Orientation Transform** (DOT), which provides a contour of the spin propagator evaluated at a particular value of the displacement—in other words, it provides the probability of a water molecule moving along any given direction by a fixed distance [54]. Another early technique is **Persistent Angular Structure MRI** (PAS-MRI), which evaluates an ODF from relatively modest data by imposing a maximum entropy constraint [55]. See Fig. 20.8 for an illustration of the results obtained using three different dODF estimation methods.

The Narrow Pulse Approximation

The theory of *q*-space does rely on one approximation: that the duration of the DW gradient pulses is negligible—in other words, the DW gradient pulses can be considered to be infinitesimally narrow. More specifically, the distance moved by molecules during the application of each DW gradient pulse should be much smaller than the distance moved between the pulses. The idea is that each DW gradient pulse respectively "tags" and "untags" water molecules based on their current location, so that the only relevant quantity is their actual displacement between these two events. For this approximation to hold in white matter, water molecules should not be allowed to diffuse by any distance approaching the axonal diameter. Even if we assume an acceptable distance to be 1 μm (which is already larger than many axons) and a diffusion coefficient of 10^{-3} mm^2/s (which is smaller than would typically be assumed), the DW pulse duration would need to be less than 0.5 ms. To achieve any reasonable *b*-value with such a short pulse duration would require gradients strengths and rise-times orders of magnitude larger than can be used in the clinic. In practice, the minimum DW pulse duration than can realistically be achieved on a human system is of the order of 10 ms. Clearly, the narrow pulse approximation cannot hold on a clinical system.

Thankfully, the impact of breaking this assumption is actually relatively trivial for most clinical applications. While this does invalidate some of the quantitative estimates that might otherwise have been derived using these methods, it does not affect the overall angular structure of the spin

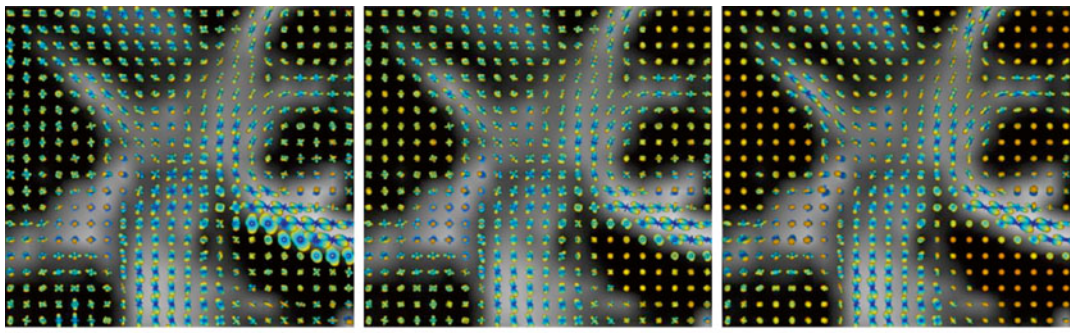

Fig. 20.8 An illustration of the results obtained using three different dODF estimation methods: Q-ball imaging (QBI; *left*), constant solid angle QBI (CSA-QBI; *middle*), and the diffusion orientation transform (DOT; *right*). These are displayed as coronal projections overlaid on the fractional anisotropy map, showing the well-known crossing of the lateral projections of the corpus callosum (left–right) with the corona radiata (inferior–superior) and the superior longitudinal fasciculus (anterior–posterior) [Reprinted from Aganj I, Lenglet C, Sapiro G, Yacoub E, Ugurbil K, Harel N. Reconstruction of the orientation distribution function in single- and multiple-shell q-ball imaging within constant solid angle. Magn Reson Med. 2010 Aug;64(2):554–66. With permission from John Wiley & Sons.]

propagator [49]. In fact, some studies suggest that such long diffusion times might in fact be beneficial when estimating the orientation and density of fiber bundles [47, 56]. The failure to meet the narrow pulse approximation is therefore unlikely to have any detrimental impact, and indeed many successful techniques have been proposed that are based on *q*-space, as described previously.

Extracting Useful Information from the dODF

Methods that aim to characterize the diffusion propagator have the advantage of being "model-free": no assumptions are made with respect to the microstructure, and the only information provided is strictly based only the measurements themselves. While this may seem to be an attractive property, in practice this may actually cause problems when applied in clinical and neuroscientific studies. The reason for this is essentially the very reason that these methods are claimed to be advantageous: being model-free, the information they do provide is not what most researchers are actually interested in. As a consequence, end-users will typically resort to ad-hoc methods to extract the information they need, in ways that are often demonstrably inferior and/or actually involve a model of some sort.

For instance, the extraction of fiber orientations from the dODF is typically done by finding the peaks of the dODF. While this may initially seem sensible, it suffers from a number of limitations. First, the power to resolve closely aligned fiber orientations is typically reduced when using dODF-based methods [6, 7, 57–59]. Second, this introduces a bias in the estimated orientations when the fibers do not cross at 90° [59, 60]. Finally, peak-finding inherently imposes a model on the form of the fiber orientation distribution: it assumes that fiber bundles are arranged in distinct bundles with discrete fiber orientations. It explicitly does not allow for curvature or divergence within a voxel. While tensor-fitting methods admittedly also suffer from this limitation, methods that recover the full fiber ODF do not make any such assumption.

While newer dODF methods such as CSA-QBI and DOT do provide better resolving power than the original QBI approach, they still cannot provide better separation than model-based techniques, since the diffusion ODF is inevitably broader than the corresponding fiber ODF—in other words, the diffusion ODF cannot be sharper than the fiber configuration from which it emanated. In fact, methods have been proposed to "sharpen" the diffusion ODF to recover the fiber ODF using a spherical deconvolution operation, a process shown to be ultimately equivalent to the "standard" model-based spherical deconvolution [58].

Another potential benefit of the dODF is to derive measures of tissue microstructure. However, there is relatively little on that topic in the literature to date. The main scalar index that has been extracted from the dODF is the generalized fractional anisotropy (GFA) index [50], which is essentially the standard deviation of the dODF relative to its RMS amplitude. Unfortunately, it has no clear biological interpretation, depends on the data acquisition parameters and technique used to reconstruct the dODF, and is also sensitive to the fiber configuration: the GFA is inherently lower in crossing fiber regions, making it unsuitable as a measure of white matter "integrity." To date, no readily interpretable metric has been proposed that can be derived directly from the dODF to characterize white matter tissue.

For these reasons, while the "model-free" nature of these approaches does initially seem appealing, it is unclear how these advantages can actually be translated through to routine investigations. The diffusion ODF simply does not provide the information typically desired in routine studies, be it for fiber-tracking or the characterization of white matter "integrity." While there may be cases where the model-free nature of these methods is advantageous, in most cases the fiber ODF is the information required, particularly for fiber-tracking applications—in which case it seems more appropriate to use the model-based techniques introduced in the previous section.

HARDI in Practice

Data Acquisition

HARDI is characterized primarily by two parameters: the number of unique directions, and the *b*-value. The optimal values for both of these

parameters are difficult to ascertain in general, since different reconstruction methods will have different requirements. Nonetheless, it is generally acknowledged that higher *b*-values ($b=2500$–3000 s/mm^2) allow better estimation of fiber orientations [9, 10]. While the DW images undeniably look much noisier at these *b*-values, they actually exhibit near-optimal *contrast* in the angular domain, which is what is required to resolve the different contributions from the various fiber orientations present (Fig. 20.9). Note however that good results can still be obtained using $b=1000$ s/mm^2 data, provided they are of sufficient quality; indeed many HARDI studies have been published using *b*-values in this range [14, 29, 30, 58].

The number of directions required for HARDI is difficult to ascertain exactly since increasing it will always improve results through increasing the overall SNR of the acquisition. The primary requirement of the angular sampling is to characterize the relevant features of the DW signal. At a *b*-value of ~3000 s/mm^2, it can be shown that these angular features can be adequately characterized using a minimum of 45 directions [61]. In practice however, a larger number is generally recommended to increase the overall SNR, since most reconstruction methods will give poor results on such data at a typical spatial resolution of ~2 mm. There is clearly a trade-off between spatial resolution and angular resolution: increasing either will increase the scan time, and increasing the spatial resolution will also lower the SNR, potentially compromising the performance of the HARDI reconstruction. In practice, the optimal set of parameters will need to be determined empirically on a case-by-case basis, based on the intended HARDI reconstruction method and its particular requirements.

Clinical Applications

The advantages of using more advanced HARDI-based methods specifically developed to provide more robust estimates of the fiber orientations are now being realized for applications such as diffusion tractography, and more recently in the assessment of tissue microstructure. Despite the wealth of studies in the technical literature that focus on the validation of the various methods providing illustrative examples of white matter pathways in healthy volunteers, to date, there are comparatively few studies that have utilized HARDI-based methods for clinical applications. It is generally conceded that the lack of translation of HARDI-based methods to the clinical research setting has largely been due to software availability, technical expertise, and in some cases clinically impractical scans times. It may also be due to a lack of awareness of the full

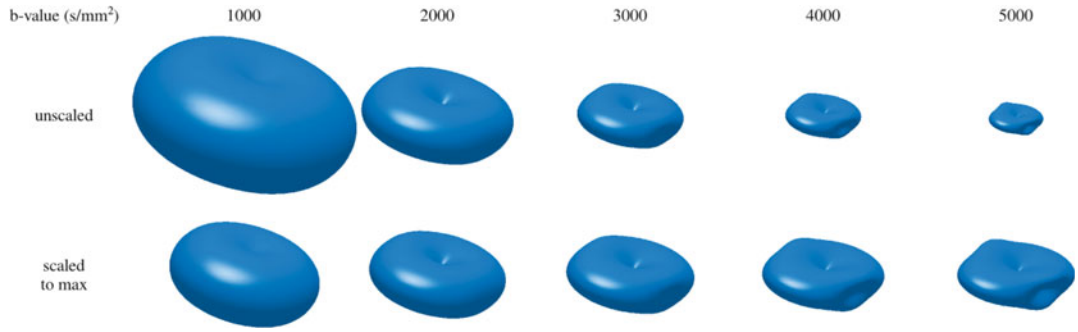

Fig. 20.9 A simple illustration of the influence of *b*-value on the measured DW data. Using low *b*-values (*right*) provides little signal attenuation, and hence good SNR in the DW images. However, there is little contrast in angular domain: the DW signal is very smooth, making is difficult to make out the two fiber orientations present in this example. In contrast, the relevant features of the DW signal are much more clearly depicted at higher *b*-values, and the presence of the multiple fiber orientations is much more obvious, particularly when looking at the scaled-up version of the results (*bottom row*). However, this does come with a significant reduction in the overall DW signal. In practice, the optimal *b*-value is a compromise between angular contrast on the one hand, and signal to noise on the other

impact of the limitations of DTI, of the widespread nature of crossing fiber regions, or of the availability of clinically practical alternatives. In this next section, we describe some of the more recent work focussed specifically on clinical applications of HARDI-based techniques.

Targeted Tractography for Neurosurgery

Development of white matter fiber-tracking techniques more than a decade ago represented an extraordinary achievement in neuroscience, with the potential to have huge impact on the diagnosis and treatment of brain disorders. From a neurosurgical perspective in particular, targeted tractography was expected to become the ultimate tool for surgical planning as it promised the ability to noninvasively map specific structural connections in the human brain in vivo in patients with brain lesions. Since its inception, there have been hundreds of studies presented in the neurosurgical literature demonstrating the potential for mapping white matter pathways that support eloquent function for the purposes of planning and navigation, see Chap. 21 for review. However, over 90 % of the tractography literature to date is based on DTI-based techniques despite its known practical limitations. There have also been more recent appeals by some members of the neurosurgical community to consider DTI-based fiber-tracking techniques obsolete for the purpose of neurosurgical planning [27].

Despite the lack of translation to the clinical setting, a number of studies in the neurosurgical literature have clearly demonstrated the advantages of using various HARDI-based tractography techniques (as opposed to DTI-based methods) specifically for delineating tracts of neurosurgical interest. An early HARDI-based tractography study comparing initial clinical experience using single tensor technique versus the multi-tensor approaches to depict the motor pathways, illustrated that although there were "perceived" advantages of using the single tensor technique (i.e., instantaneous calculation of tractography maps), the multi-tensor appeared to offer better depiction of motor tracts from the face and tongue regions in over half of the patients studied [62] (Fig. 20.10). Whilst this early study highlights improved tractography results even with the earliest of HARDI-based techniques, there was inconsistency in the ability of the multi-tensor model to depict fibers extending laterally to the face region. Yamada et al. [62] attributed this shortfall to the fact that the study relied on relatively low *b*-value data of 1000 s/mm^2, and only 32 directions. Whilst the study may have benefited from the acquisition of higher quality data to improve fiber orientations estimates through increasing the overall SNR, it is likely that the failure of the multi-tensor technique may simply be because the model is limited to fitting only two tensors in voxels through regions, such as the centrum semiovale, which are known to contain more than two fiber populations.

Berman [16] presented a more complete delineation of the corticospinal pathways in a case used to demonstrate the potential capabilities of q-ball tractography for the purpose of neurosurgical navigation. Although this article was limited to the presentation of illustrative cases, it was clear that that the HARDI-based tractography method had the capacity to provide a more accurate description of fiber tracts through regions such as the centrum semiovale than that previously shown using single and multi-tensor based studies [19, 63–69]. The practical advantages of using HARDI-based methods for the delineation of the corticospinal pathways have recently been more systematically evidenced in the neurosurgery literature, in a study based on constrained spherical deconvolution (CSD) [10, 29]. The data presented demonstrated that the CSD-based tractography technique, when directly compared to both deterministic and probabilistic DTI-based tractography techniques, consistently resulted in more biologically reliable tractography information that provided improved estimates of safety margins which may be useful in neurosurgical procedures—see illustrative cases provided in Fig. 20.11 [70].

It should be emphasized that the more accurate representation of the corticospinal pathways using the CSD-based tractography method compared to DTI-based tractography presented in

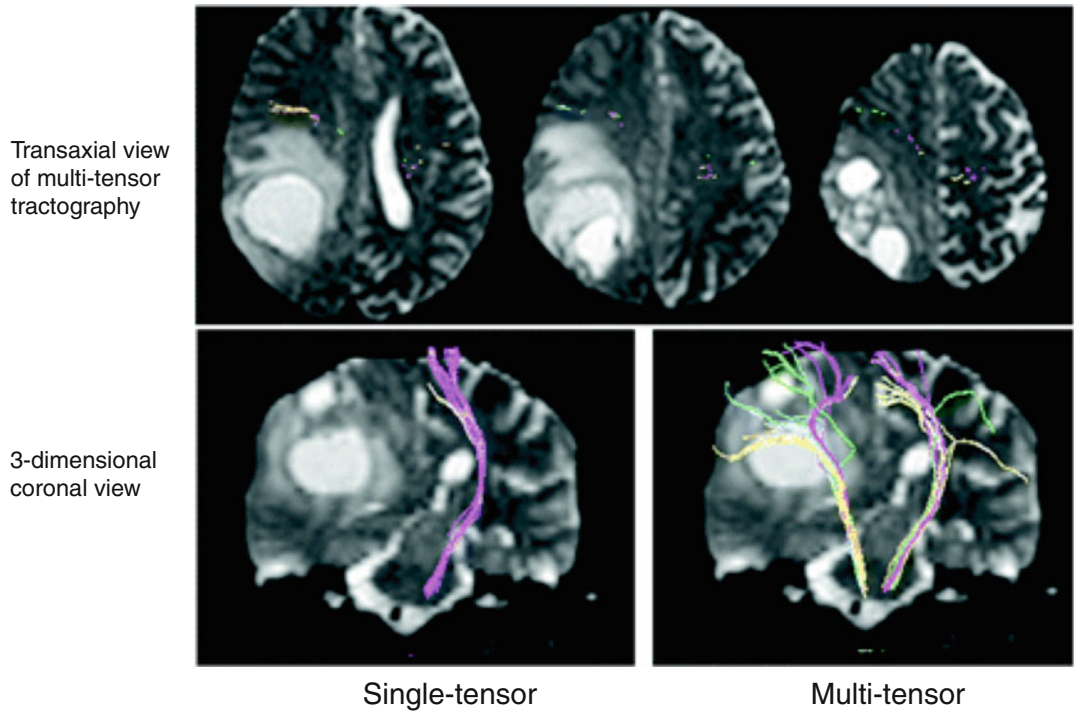

Fig. 20.10 Example of single tensor vs. multi-tensor tractography in a 58-year-old woman with glioblastoma multiforme. Note that the pyramidal fibers of lesional side (*right*) are not depicted using single-tensor tractography, whereas they are well shown by using multitensor tractography. These fibers are noted to have substantial anterior displacement [Reprinted from Yamada K, Sakai K, Hoogenraad FGC, Holthuizen R, Akazawa K, Ito H, et al. Multitensor Tractography Enables Better Depiction of Motor Pathways: Initial Clinical Experience Using Diffusion-Weighted MR Imaging with Standard b-Value. AJNR Am J Neuroradiol. 2007 Oct 1;28(9):1668–73. With permission from American Society of Neuroradiology]

this study was consistent across a range of diffusion acquisition schemes, and included DWI data typically considered optimal for both DTI- and CSD-based methods (Fig. 20.12) [71, 72]. Although the configuration of tracks identified by the CSD-based method appears to be better defined when using higher *b*-value DWI data acquired using a higher number of diffusion directions (as expected—see above), it is clear from the data presented in this study that the application of this HARDI based model to the simpler diffusion acquisition schemes also results in a considerable improvement in tractography results, particularly in crossing fiber regions (Fig. 20.12). While this study was confined to the investigation of the corticospinal pathways, it is likely that the results will apply to most fiber tracts, given that such tracts will inevitably traverse through voxels containing substantial contributions from two of more fiber populations at some point along their path.

Over the past few years, HARDI-based tractography has also been used to demonstrate improvements in the delineation of other functionally important tracts including the optic radiations and the arcuate fasciculus. Recent studies depicting Meyer's loop of the optic radiation using HARDI data and a multi-tensor tractography technique [73] demonstrate that, although there is biological variability in the distance from the temporal pole (TP) to Meyer's loop (ML), multi-tensor tractography can achieve results that are more consistent with anatomical dissection studies [74] than previously reported [75]. These

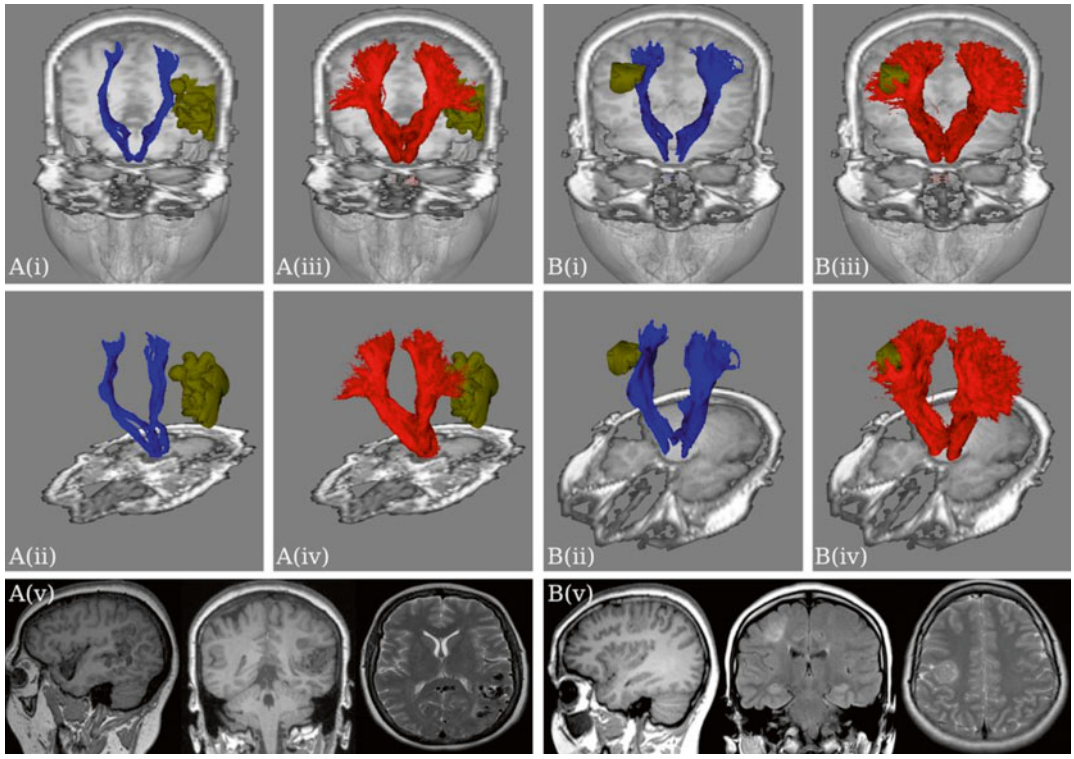

Fig. 20.11 Examples of CSD-based (*red*) vs. DTI-based (*blue*) tractography results with segmented pathology volumes (*green*) overlaid on coronal T1-weighted images in a 49-year-old woman with a large left-sided temporo-parietal AVM (Case A), and a 24-year-old woman with a right focal cortical dysplasia situated in the right posterior frontal lobe (Case B). Note that the DTI-based tractography results in Case A suggest a clear margin surrounding the lesion (i and ii), whereas the CSD-based tractography results indicate that lateral projections of the corticospinal pathway may be at risk (iii and iv). The DTI-based tractography results in Case B suggest that only the medial aspect of the lesion impinges on the corticospinal tracts (i and ii), whereas the CSD-based tractography results suggest that the lesion is enveloped by medial and lateral projections of corticospinal fibers (iii and iv) [Reprinted from Farquharson S, Tournier J-D, Calamante F, Fabinyi G, Schneider-Kolsky M, Jackson GD, et al. White matter fiber tractography: why we need to move beyond DTI: Clinical article. Journal of Neurosurgery. 2013 Jun;118(6):1367–77. With permission from AANS]

findings are important because it had been previously suggested that patients with a shorter TP-ML distance were at greater risk of a visual field deficit (VFD) following anterior temporal lobe resection (ATLR), while the data presented by Winston et al. suggests that there is no difference in TP-ML distance between patients developing a VFD and those who do not [73]. In fact, the direct comparison of visual field deficits prior to, and at 3 and 12 months post-surgery and the preoperative tractography data co-registration with the postoperative anatomical data in the 20 ATLR patients studied suggest that the size of the resection and the degree of damage to ML is a more accurate marker, which could be used to better predict postoperative VFD.

Given the increasing demand for accurate neurosurgical tractography information and the ever-present challenges that complicate tractography in the neurosurgical setting (the variation in anatomy of individual patients, disease-related change, and the inevitable intraoperative shift of anatomy during neurosurgical procedures, to name just a few), it is imperative we continue to identify optimal strategies for targeted tractography for the purpose of neurosurgical navigation in individual patients [76, 77]. Although HARDI-based techniques such as the so-called high defi-

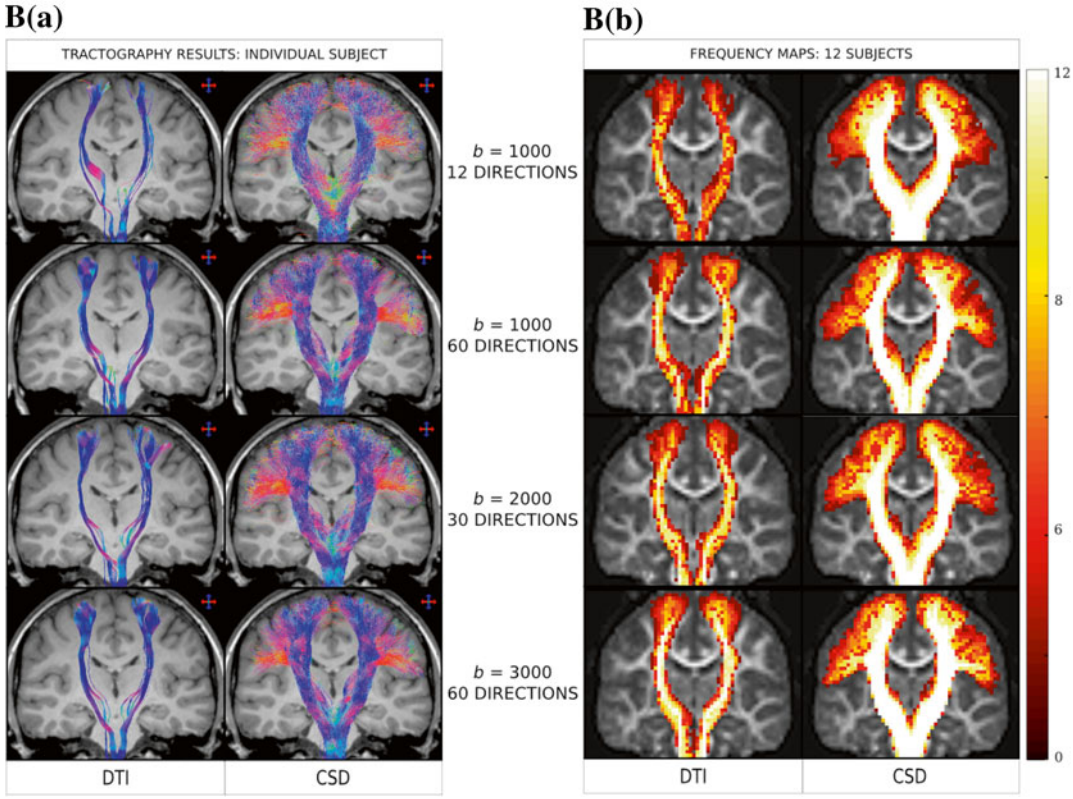

Fig. 20.12 Comparison of tractography results obtained using DTI combined with a deterministic algorithm and CSD combined with a probabilistic algorithm across a range of diffusion acquisition protocols that differed in the number of diffusion directions and *b*-value used, as indicated in the figure. Panel (**a**) shows coronal T1-weighted images overlaid with tractography results using DTI (*left column*) and CSD (*right column*) from a representative normal control subject. Panel (**b**) shows a coronal FA template image overlaid with frequency maps representing the number of subjects (out of 12 control subjects) in whom tracks were identified in any given voxel, using DTI (*left column*) and CSD (*right column*) (range 0–12). Note that CSD based tractography results in a considerable improvement in the delineation of corticospinal pathways even if using the most basic of diffusion acquisition schemes [Reprinted from Farquharson S, Tournier J-D, Calamante F, Fabinyi G, Schneider-Kolsky M, Jackson GD, et al. White matter fiber tractography: why we need to move beyond DTI: Clinical article. Journal of Neurosurgery. 2013 Jun;118(6):1367–77. With permission from AANS]

nition fiber tracking method (HDFT) (which combines diffusion spectrum imaging (DSI) [49] with generalized q-sampling imaging for estimation of fiber orientations [50]) are already being used to facilitate innovative neurosurgical applications [18], there is at present only anecdotal evidence to support the use of one HARDI-based tractography approach over another. Despite the lack of more rigorous clinically based studies into the accuracy and reproducibility of these more advanced methods, it is clear from the current body of neurosurgical evidence that the advent of HARDI-based tractography methods represents significant technical advancement that allows more biologically accurate delineation of white matter pathways than was previously achievable using DTI-based tractography techniques.

Assessment of Structural Connectivity

One of the advantages of utilizing HARDI-based methods developed specifically to attain more robust fiber orientation estimates is that it is now possible to perform more reliable tractography-based comparisons throughout the brain. One of

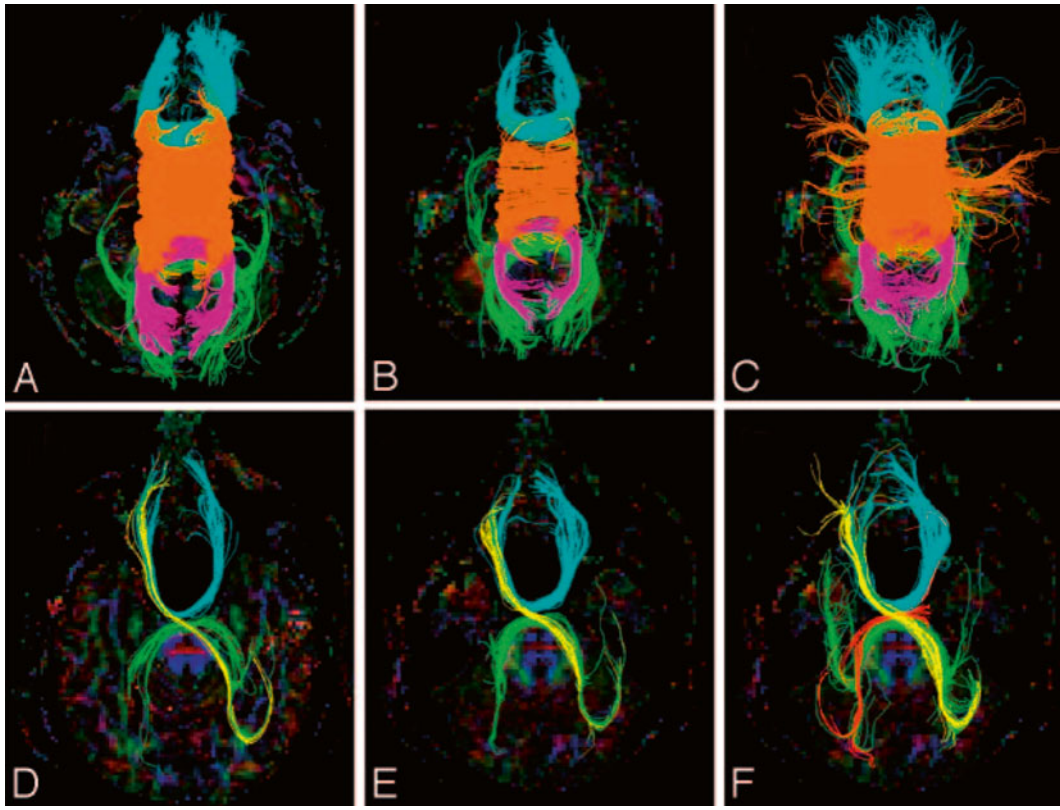

Fig. 20.13 Comparison of DTI and QBI tractography results in a control subject (*top*) and a subject with partial agenesis of the Corpus Callosum pAgCC (*bottom*) using (1) DTI tractography performed on a DTI acquisition at $b = 1000$ s/mm^2 (**a**, **d**), (2) DTI tractography on a HARDI acquisition at $b = 3000$ s/mm^2 (**b**, **e**), and (3) QBI tractography is shown for the same HARDI acquisition at $b = 3000$ s/mm^2 (**c**, **f**). Note that QBI tractography typically recovered more extensive fibers for each tract than DTI in both subjects with pAgCC and controls [Reprinted from Wahl M, Strominger Z, Jeremy RJ, Barkovich AJ, Wakahiro M, Sherr EH, et al. Variability of Homotopic and Heterotopic Callosal Connectivity in Partial Agenesis of the Corpus Callosum: A 3 T Diffusion Tensor Imaging and Q-Ball Tractography Study. AJNR Am J Neuroradiol. 2009 Feb 1;30(2):282–9. With permission from American Society of Neuroradiology]

the first applications of HARDI-based fiber tracking to assess differences in structural connectivity in a patient population was performed to investigate inter-hemispheric connections in patients with partial agenesis of the corpus callosum (pAgCC) [78]. This early study directly compared results from DTI and Q-ball imaging (QBI) reconstruction methods in six individuals with pAgCC and eight control subjects. The QBI data presented in this study revealed that individuals with pAgCC had unexpectedly highly variable callosal fiber connectivity, which included many heterotopic tracts that were not seen in the healthy subjects. The DTI technique was only able to delineate a subset of these tracts due to its in ability to tract through crossing regions (Fig. 20.13). Although the authors concede that the small cohort of subjects studied with pAgCC precluded any generalization of results to this phenotypically heterogeneous population, the variability of these aberrant structural connections in these few subjects was thought to be clinically important because individuals with agenesis of the corpus callosum often present with a broad range of behavioral and neurocognitive deficits [78].

Recent connectivity studies using HARDI-based methods have identified subtle differences in the healthy brain that may be critical to our understanding and interpretation of deviations from normal structural connectivity. One of the largest studies based on HARDI data investigated structural differences in 569 healthy twins [79]. This study utilized an orientation density function (ODF)-based tractography technique, to measure "fiber density" (i.e. the volume of streamlines successfully generated with a region) as a marker of structural connectivity [79]. While the use of volume as a measure of connectivity is not without its confounds [26], the results suggest that the proportions of fibers intersecting the left and right hemispheres vary significantly with age. In a further study by the same group, which aimed to define the normal trajectory of structural connectivity from early adolescence to early adulthood, it was also observed that increases and decreases in densities across the maturing brain are not distributed evenly [80]: the frontal cortex had a disproportionate decrease in fiber density whilst the temporal lobe showed an increase in fiber density with age in healthy participants aged of 12–30 years.

One of the limitations of current methods to assess structural connectivity using diffusion-weighted data, compared to traditional histopathology, is that the spatial resolution achievable within a clinically feasible time frame is limited. A recent technical advance that may have important future applications is the development of a post-processing technique known as Track Density Imaging (TDI) [81]. TDI is an approach that uses the spatial information from tractography streamlines to improve spatial resolution beyond that by which the data were originally acquired. The resultant super-resolution track density images reveal enhanced anatomical detail with high SNR allowing direct visualization of sub-structures in regions such as the thalamus and cerebellar peduncles [81].

The super resolution properties of TDI have recently been appreciated in a study of patients with Friedreich ataxia (FRDA) where TDI was performed to increase the resolution to 500 μm, four times the native imaging resolution [82]. The super resolution TDI tractography maps were used in conjunction with targeted tractography maps to specifically enable visualization and assessment of cerebello-cerebral connections. The findings from this interesting study go further than previous diffusion tensor-based studies, which have been successful in identifying primary sites of white matter degeneration, to identify secondary sites of degeneration that involve a network of cortical and subcortical regions. The authors suggest that these findings demonstrate that FRDA pathology extends beyond well-known primary sites of cerebellar and brainstem degeneration; and that such results provide an explanation for the non-motor symptoms seen in the disease, such as depression and cognitive difficulties (Fig. 20.14) [82].

Assessment of Structural Integrity

Recent developments in the field have emerged to allow group-wise whole-brain analysis of diffusion data, in a manner robust to crossing fibers. Apparent fiber density (AFD) is one such method, which uses the fiber orientations distributions (FOD) computed using constrained spherical deconvolution (CSD) to identify tract-specific differences in fiber density [83]. This approach was applied in a recent study investigating HARDI data collected in patients with probable or definite motor neurone disease (MND) and age matched controls [47]. The results of this study show a significant decrease in AFD, specifically within voxels and orientations corresponding to the corticospinal tract (CST) and corpus callosal (CC) fibers, in the group data of MND patients compared to healthy control subjects—pathways that are known to be affected in upper motor neuron impairment (Fig. 20.15) [47]. The advantage of using this approach is the ability to identify not only the location, but also the orientation along which differences in fiber density can be observed. Using the FOD as a measure of apparent fiber density may prove to be a more accurate and readily interpretable marker of tract "integrity" throughout the brain than DTI-derived measures of diffusion anisotropy, particularly in regions containing multiple fiber populations, since the

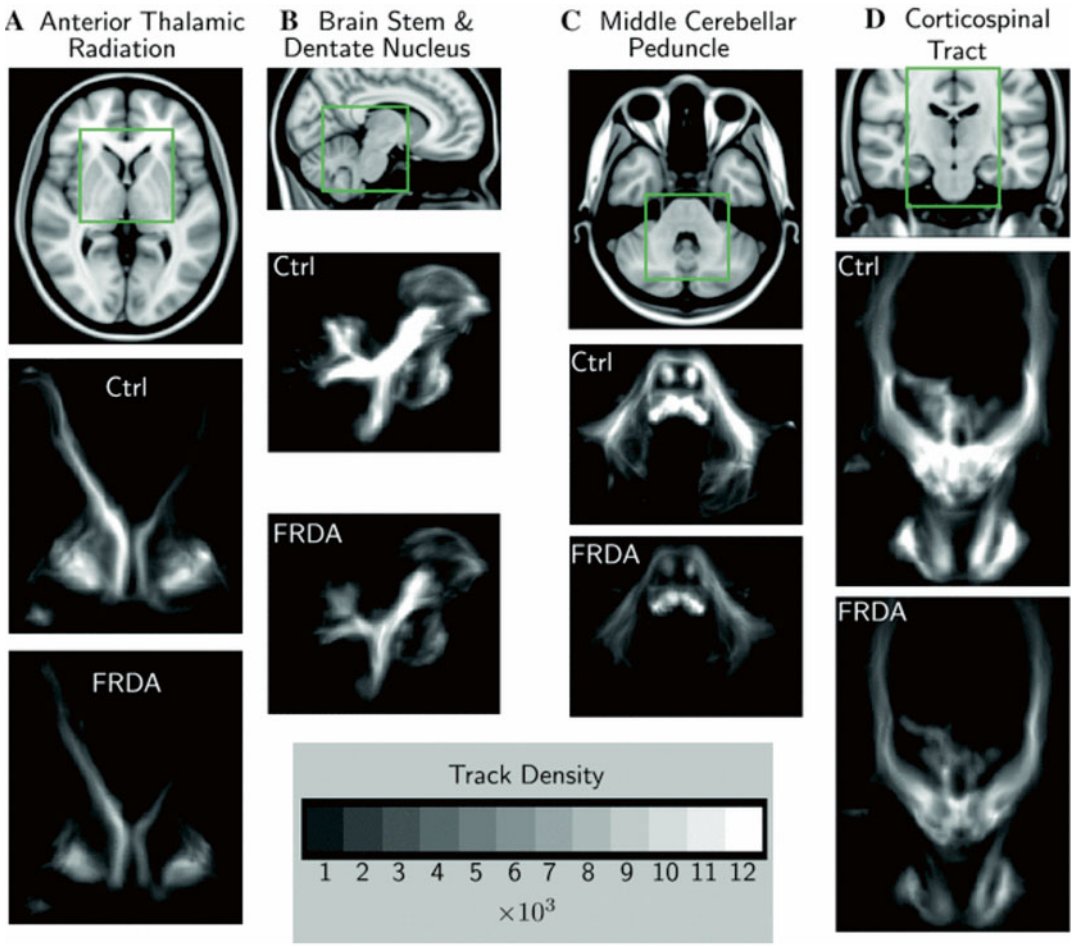

Fig. 20.14 example of group-averaged track density images (TDI) super resolved to 500 μm from HARDI data acquired at 2 mm^3 in healthy controls and patients with Friedreich ataxia (FRDA). Note the visually evident differences in structural connections from regions such as the anterior thalamic radiation (**a**), brain-stem and dentate nucleus (**b**), middle cerebellar peduncle (**c**) and cortico-spinal tract (**d**) between patients with FRDA and control subjects [Reprinted from Zalesky A, Akhlaghi H, Corben LA, Bradshaw JL, Delatycki MB, Storey E, et al. Cerebello-cerebral connectivity deficits in Friedreich ataxia. Brain Struct Funct. 2014; 219(3): 969–981. With permission from Springer-Verlag.]

fiber density estimates for one tract are no longer confounded by the presence of other tracts that might be traversing the same region.

Conclusion

The advent of HARDI-based methods specifically developed to provide more robust estimates of the fiber orientations represents an exciting development in the field of diffusion MRI. These methods are now beginning to be used for clinical and neuroscientific investigations with extremely promising results. Although further validation is necessary, it is clear that the development and application of HARDI-based methods have moved the field one important step closer to one of the great challenges for the upcoming decade—to noninvasively map the structural connectivity of the human brain.

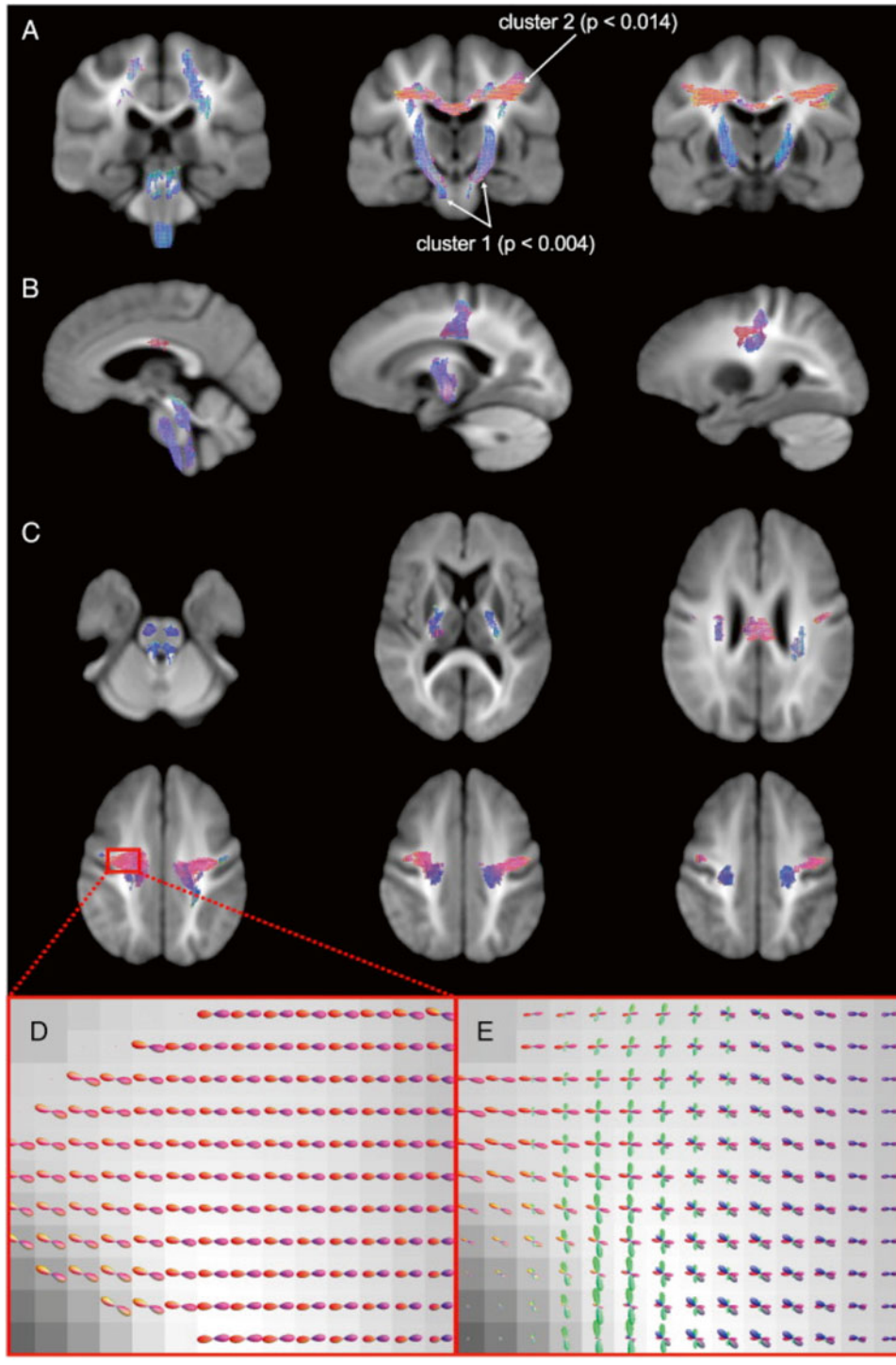

Fig. 20.15 example of Apparent Fiber Density (AFD) results of patients with motor neuron disease (MND) compared to health control subjects. Note that a significant decrease in AFD was detected in MND patients within two distinct clusters: Cluster 1 extends from the lower brain stem to the internal capsule, and cluster 2 corresponds to corpus callosal fibers connecting the left and right primary motor cortices [Reprinted from Raffelt D, Tournier J-D, Rose S, Ridgway GR, Henderson R, Crozier S, et al. Apparent Fiber Density: A novel measure for the analysis of diffusion-weighted magnetic resonance images. Neuroimage. 2012 Feb 15;59(4):3976–94. With permission from Elsevier.]

References

1. Alexander AL, Hasan KM, Lazar M, Tsuruda JS, Parker DL. Analysis of partial volume effects in diffusion-tensor MRI. Magn Reson Med. 2001;45(5):770–80.
2. Alexander DC, Barker GJ, Arridge SR. Detection and modeling of non-Gaussian apparent diffusion coefficient profiles in human brain data. Magn Reson Med. 2002;48(2):331–40.
3. Frank LR. Anisotropy in high angular resolution diffusion-weighted MRI. Magn Reson Med. 2001;45(6):935–9.
4. Tuch DS, Reese TG, Wiegell MR, Makris N, Belliveau JW, Wedeen VJ. High angular resolution diffusion imaging reveals intravoxel white matter fiber heterogeneity. Magn Reson Med. 2002;48(4):577–82.
5. Seunarine KK, Alexander DC. Multiple fibres: beyond the diffusion tensor. In: Johansen-Berg H, Behrens TEJ, editors. Diffusion MRI: from quantitative measurement to in-vivo neuroanatomy. San Diego, CA: Elsevier; 2009. p. 56–74.
6. Tournier JD. The biophysics of crossing fibres. In: Jones DK, editor. Diffusion MRI: theory, methods, and applications. New York, NY: Oxford University Press; 2010. p. 465–82.
7. Tournier J-D, Mori S, Leemans A. Diffusion tensor imaging and beyond. Magn Reson Med. 2011;65(6):1532–56.
8. Alexander DC. Multiple-fiber reconstruction algorithms for diffusion MRI. Ann N Y Acad Sci. 2005;1064(1):113–33.
9. Alexander DC, Barker GJ. Optimal imaging parameters for fiber-orientation estimation in diffusion MRI. Neuroimage. 2005;27(2):357–67.
10. Tournier J-D, Calamante F, Gadian DG, Connelly A. Direct estimation of the fiber orientation density function from diffusion-weighted MRI data using spherical deconvolution. Neuroimage. 2004;23(3):1176–85.
11. Vos SB, Jones DK, Viergever MA, Leemans A. Partial volume effect as a hidden covariate in DTI analyses. Neuroimage. 2011;55(4):1566–76.
12. Basser PJ, Pierpaoli C. Microstructural and physiological features of tissues elucidated by quantitative-diffusion-tensor MRI. J Magn Reson B. 1996;111(3):209–19.
13. Jeurissen B, Leemans A, Tournier J-D, Jones DK, Sijbers J. Investigating the prevalence of complex fiber configurations in white matter tissue with diffusion magnetic resonance imaging. Human Brain Mapping [Internet]. 2012 May 19 [cited 2012 Jun 15]; Available from: http://www.ncbi.nlm.nih.gov/pubmed/22611035
14. Behrens TEJ, Berg HJ, Jbabdi S, Rushworth MFS, Woolrich MW. Probabilistic diffusion tractography with multiple fibre orientations: what can we gain? Neuroimage. 2007;34(1):144–55.
15. Pierpaoli C, Barnett A, Pajevic S, Chen R, Penix L, Virta A, et al. Water diffusion changes in Wallerian degeneration and their dependence on white matter architecture. Neuroimage. 2001;13(6):1174–85.
16. Berman J. Diffusion MR, tractography as a tool for surgical planning. Magn Reson Imaging Clin N Am. 2009;17(2):205–14.
17. Farquharson S, Tournier J-D, Calamante F, Fabinyi G, Schneider-Kolsky M, Jackson GD, et al. White matter fiber tractography: why we need to move beyond DTI. J Neurosurg. 2013;118:1367.
18. Fernandez-Miranda JC, Pathak S, Engh J, Jarbo K, Verstynen T, Yeh F-C, et al. High-definition fiber tractography of the human brain: neuroanatomical validation and neurosurgical applications. Neurosurgery. 2012;71(2):430–53.
19. Kinoshita M, Yamada K, Hashimoto N, Kato A, Izumoto S, Baba T, et al. Fiber-tracking does not accurately estimate size of fiber bundle in pathological condition: initial neurosurgical experience using neuronavigation and subcortical white matter stimulation. Neuroimage. 2005;25(2):424–9.
20. Nimsky C, Ganslandt O, Fahlbusch R. Implementation of fiber tract navigation. Neurosurgery. 2006;58(4 Suppl 2):ONS–292–303. discussion ONS–303–304.
21. Jones DK, Cercignani M. Twenty-five pitfalls in the analysis of diffusion MRI data. NMR Biomed. 2010;23(7):803–20.
22. Vos SB, Jones DK, Jeurissen B, Viergever MA, Leemans A. The influence of complex white matter architecture on the mean diffusivity in diffusion tensor MRI of the human brain. Neuroimage. 2012;59(3):2208–16.
23. Wheeler-Kingshott CAM, Cercignani M. About "axial" and "radial" diffusivities. Magn Reson Med. 2009;61(5):1255–60.
24. Pierpaoli C, Basser PJ. Toward a quantitative assessment of diffusion anisotropy. Magn Reson Med. 1996;36(6):893–906.
25. Douaud G, Jbabdi S, Behrens TEJ, Menke RA, Gass A, Monsch AU, et al. DTI measures in crossing-fibre areas: increased diffusion anisotropy reveals early white matter alteration in MCI and mild Alzheimer's disease. Neuroimage. 2011;55(3):880–90.
26. Jones DK, Knösche TR, Turner R. White matter integrity, fiber count, and other fallacies: the do's and don'ts of diffusion MRI. Neuroimage. 2013;73:239–54.
27. Fernandez-Miranda JC. Editorial: beyond diffusion tensor imaging. J Neurosurg. 2013;118(6):1363–6.
28. Jones DK. The effect of gradient sampling schemes on measures derived from diffusion tensor MRI: a Monte Carlo study. Magn Reson Med. 2004;51(4):807–15.
29. Tournier J-D, Calamante F, Connelly A. Robust determination of the fibre orientation distribution in diffusion MRI: non-negativity constrained super-resolved spherical deconvolution. Neuroimage. 2007;35(4):1459–72.
30. Parker GJM, Alexander DC. Probabilistic Monte Carlo based mapping of cerebral connections utilising whole-brain crossing fibre information. Inf Process Med Imaging. 2003;18:684–95.

31. Hosey T, Williams G, Ansorge R. Inference of multiple fiber orientations in high angular resolution diffusion imaging. Magn Reson Med. 2005;54(6): 1480–9.
32. Hosey TP, Harding SG, Carpenter TA, Ansorge RE, Williams GB. Application of a probabilistic double-fibre structure model to diffusion-weighted MR images of the human brain. Magn Reson Imaging. 2008;26(2):236–45.
33. Assaf Y, Basser PJ. Composite hindered and restricted model of diffusion (CHARMED) MR imaging of the human brain. Neuroimage. 2005;27(1):48–58.
34. Assaf Y, Freidlin RZ, Rohde GK, Basser PJ. New modeling and experimental framework to characterize hindered and restricted water diffusion in brain white matter. Magn Reson Med. 2004;52(5):965–78.
35. Tournier J, Calamante F, Connelly A. MRtrix: diffusion tractography in crossing fiber regions. Int J Imaging Syst Technol. 2012;22(1):53–66.
36. Anderson AW. Measurement of fiber orientation distributions using high angular resolution diffusion imaging. Magn Reson Med. 2005;54(5):1194–206.
37. Dell'Acqua F, Rizzo G, Scifo P, Clarke RA, Scotti G, Fazio F. A model-based deconvolution approach to solve fiber crossing in diffusion-weighted MR imaging. IEEE Trans Biomed Eng. 2007;54(3):462–72.
38. Kaden E, Knösche TR, Anwander A. Parametric spherical deconvolution: inferring anatomical connectivity using diffusion MR imaging. Neuroimage. 2007;37(2):474–88.
39. Seunarine KK, Alexander DC. Linear Persistent Angular Structure MRI and non-linear Spherical Deconvolution for Diffusion MRI. Proceedings of the International Society for Magnetic Resonance in Medicine. Seattle, Washington, USA; 2006. p. 2767.
40. Beaulieu C, Allen PS. Determinants of anisotropic water diffusion in nerves. Magn Reson Med. 1994;31(4):394–400.
41. Beaulieu C, Allen PS. Water diffusion in the giant axon of the squid: implications for diffusion-weighted MRI of the nervous system. Magn Reson Med. 1994;32(5):579–83.
42. Beaulieu C, Does MD, Snyder RE, Allen PS. Changes in water diffusion due to Wallerian degeneration in peripheral nerve. Magn Reson Med. 1996;36(4): 627–31.
43. Song S-K, Sun S-W, Ju W-K, Lin S-J, Cross AH, Neufeld AH. Diffusion tensor imaging detects and differentiates axon and myelin degeneration in mouse optic nerve after retinal ischemia. Neuroimage. 2003;20(3):1714–22.
44. Song S-K, Sun S-W, Ramsbottom MJ, Chang C, Russell J, Cross AH. Dysmyelination revealed through MRI as increased radial (but unchanged axial) diffusion of water. Neuroimage. 2002;17(3): 1429–36.
45. Dell'acqua F, Simmons A, Williams SCR, Catani M. Can spherical deconvolution provide more information than fiber orientations? Hindrance modulated orientational anisotropy, a true-tract specific index to characterize white matter diffusion. Human Brain Mapping [Internet]. 2012 Apr 5 [cited 2012 Apr 12]; Available from: http://www.ncbi.nlm.nih.gov/pubmed/22488973
46. Jbabdi S, Behrens TEJ, Smith SM. Crossing fibres in tract-based spatial statistics. Neuroimage. 2010; 49(1):249–56.
47. Raffelt D, Tournier J-D, Rose S, Ridgway GR, Henderson R, Crozier S, et al. Apparent fibre density: a novel measure for the analysis of diffusion-weighted magnetic resonance images. Neuroimage. 2012; 59(4):3976–94.
48. Callaghan PT. NMR imaging, NMR diffraction and applications of pulsed gradient spin echoes in porous media. Magn Reson Imaging. 1996;14(7-8):701–9.
49. Wedeen VJ, Hagmann P, Tseng W-YI, Reese TG, Weisskoff RM. Mapping complex tissue architecture with diffusion spectrum magnetic resonance imaging. Magn Reson Med. 2005;54(6):1377–86.
50. Tuch DS. Q-ball imaging. Magn Reson Med. 2004; 52(6):1358–72.
51. Descoteaux M, Angelino E, Fitzgibbons S, Deriche R. Regularized, fast, and robust analytical Q-ball imaging. Magn Reson Med. 2007;58(3):497–510.
52. Hess CP, Mukherjee P, Han ET, Xu D, Vigneron DB. Q-ball reconstruction of multimodal fiber orientations using the spherical harmonic basis. Magn Reson Med. 2006;56(1):104–17.
53. Aganj I, Lenglet C, Sapiro G, Yacoub E, Ugurbil K, Harel N. Reconstruction of the orientation distribution function in single- and multiple-shell q-ball imaging within constant solid angle. Magn Reson Med. 2010;64(2):554–66.
54. Özarslan E, Shepherd TM, Vemuri BC, Blackband SJ, Mareci TH. Resolution of complex tissue microarchitecture using the diffusion orientation transform (DOT). Neuroimage. 2006;31(3):1086–103.
55. Jansons KM, Alexander DC. Persistent angular structure: new insights from diffusion magnetic resonance imaging data. Inverse Problems. 2003;19(5): 1031–46.
56. Yeh C-H, Tournier J-D, Cho K-H, Lin C-P, Calamante F, Connelly A. The effect of finite diffusion gradient pulse duration on fibre orientation estimation in diffusion MRI. Neuroimage. 2010;51(2):743–51.
57. Alexander DC, Seunarine KK. Mathematics of crossing fibers. In: Jones DK, editor. Diffusion MRI: theory, methods, and applications. New York, NY: Oxford University Press; 2010.
58. Descoteaux M, Deriche R, Knösche TR, Anwander A. Deterministic and probabilistic tractography based on complex fibre orientation distributions. IEEE Trans Med Imaging. 2009;28(2):269–86.
59. Tournier JD, Yeh C-H, Calamante F, Cho K-H, Connelly A, Lin C-P. Resolving crossing fibres using constrained spherical deconvolution: validation using diffusion-weighted imaging phantom data. Neuroimage. 2008;42(2):617–25.

60. Zhan W, Yang Y. How accurately can the diffusion profiles indicate multiple fiber orientations? A study on general fiber crossings in diffusion MRI. J Magn Reson. 2006;183(2):193–202.
61. Tournier J-D, Calamante F, Connelly A. Determination of the appropriate b value and number of gradient directions for high-angular-resolution diffusion-weighted imaging. NMR Biomed. 2013;26(12):1775–86.
62. Yamada K, Sakai K, Hoogenraad FGC, Holthuizen R, Akazawa K, Ito H, et al. Multitensor tractography enables better depiction of motor pathways: initial clinical experience using diffusion-weighted mr imaging with standard b-value. AJNR Am J Neuroradiol. 2007;28(9):1668–73.
63. Berman JI, Berger MS, Chung SW, Nagarajan SS, Henry RG. Accuracy of diffusion tensor magnetic resonance imaging tractography assessed using intraoperative subcortical stimulation mapping and magnetic source imaging. J Neurosurg. 2007;107(3):488.
64. Berman JI, Berger MS, Mukherjee P, Henry RG. Diffusion-tensor imaging-guided tracking of fibers of the pyramidal tract combined with intraoperative cortical stimulation mapping in patients with gliomas. J Neurosurg. 2004;101(1):66–72.
65. Clark CA, Barrick TR, Murphy MM, Bell BA. White matter fiber tracking in patients with space-occupying lesions of the brain: a new technique for neurosurgical planning? Neuroimage. 2003;20(3):1601–8.
66. Itoh D, Aoki S, Maruyama K, Masutani Y, Mori H, Masumoto T, et al. Corticospinal tracts by diffusion tensor tractography in patients with arteriovenous malformations. J Comput Assist Tomogr. 2006;30(4):618.
67. Mikuni N, Okada T, Enatsu R, Miki Y, Hanakawa T, Urayama S, et al. Clinical impact of integrated functional neuronavigation and subcortical electrical stimulation to preserve motor function during resection of brain tumors. J Neurosurg. 2007;106(4):593–8.
68. Okada T, Miki Y, Kikuta K, Mikuni N, Urayama S, Fushimi Y, et al. Diffusion tensor fiber tractography for arteriovenous malformations: quantitative analyses to evaluate the corticospinal tract and optic radiation. AJNR Am J Neuroradiol. 2007;28(6):1107–13.
69. Yamada K, Kizu O, Ito H, Nishimura T. Tractography for an arteriovenous malformation. Neurology. 2004;62(4):669.
70. Farquharson S, Tournier J-D, Calamante F, Fabinyi G, Schneider-Kolsky M, Jackson GD, et al. White matter fiber tractography: why we need to move beyond DTI: clinical article. J Neurosurg. 2013;118(6):1367–77.
71. Jones DK, Horsfield MA, Simmons A. Optimal strategies for measuring diffusion in anisotropic systems by magnetic resonance imaging. Magn Reson Med. 1999;42(3):515–25.
72. Tournier J-D, Calamante F, Connelly A. How many diffusion gradient directions are required for HARDI? Proceedings of the International Society for Magnetic Resonance in Medicine. Hawai'i, USA; 2009. p. 358.
73. Winston GP, Daga P, Stretton J, Modat M, Symms MR, McEvoy AW, et al. Optic radiation tractography and vision in anterior temporal lobe resection. Ann Neurol. 2012;71(3):334–41.
74. Ebeling U, Reulen H-J. Subcortical topography and proportions of the pyramidal tract. Acta Neurochir. 1992;118(3-4):164–71.
75. Nilsson D, Rydenhag B, Malmgren K, Starck G, Ljungberg M. Anatomical accuracy and feasibility of probabilistic and deterministic tractography of the optic radiation. Epilepsia [Internet]. 2010 [cited 2013 Aug 29]. p. 91. Available from: http://onlinelibrary.wiley.com.ezp.lib.unimelb.edu.au/doi/10.1111/j.1528-1167.2010.02658.x/abstract
76. Nimsky C, Ganslandt O, Merhof D, Sorensen AG, Fahlbusch R. Intraoperative visualization of the pyramidal tract by diffusion-tensor-imaging-based fiber tracking. Neuroimage. 2006;1:30(4).
77. Nimsky C, Ganslandt O, Fahlbusch R. Implementation of fiber tract navigation. Neurosurgery. 2007;61(1 Suppl):306–17. discussion 317–318.
78. Wahl M, Strominger Z, Jeremy RJ, Barkovich AJ, Wakahiro M, Sherr EH, et al. Variability of homotopic and heterotopic callosal connectivity in partial agenesis of the corpus callosum: a 3T diffusion tensor imaging and q-ball tractography study. AJNR Am J Neuroradiol. 2009;30(2):282–9.
79. Daianu M, Jahanshad N, Dennis EL, Toga AW, McMahon KL, de Zubicaray GI, et al. Left versus right hemisphere differences in brain connectivity: 4-Tesla HARDI tractography in 569 twins. 2012 9th IEEE International Symposium on Biomedical Imaging (ISBI). 2012. p. 526–9.
80. Dennis EL, Jahanshad N, McMahon KL, de Zubicaray GI, Martin NG, Hickie IB, et al. Development of brain structural connectivity between ages 12 and 30: a 4-Tesla diffusion imaging study in 439 adolescents and adults. Neuroimage. 2013;64:671–84.
81. Calamante F, Tournier J-D, Jackson GD, Connelly A. Track-density imaging (TDI): super-resolution white matter imaging using whole-brain track-density mapping. Neuroimage. 2010;53(4):1233–43.
82. Zalesky A, Akhlaghi H, Corben LA, Bradshaw JL, Delatycki MB, Storey E, et al. Cerebello-cerebral connectivity deficits in Friedreich ataxia. Brain Struct Funct. 2014;219(3):969–81.
83. Raffelt D, Tournier J-D, Crozier S, Connelly A, Salvado O, Tournier J-D. Apparent Fibre Density: a new measure for high angular resolution diffusion-weighted image analysis. International Society for Magnetic Resonance in Medicine 14th Annual Scientific Meeting and Exhibition: 2006 Proceedings. Stockholm, Sweden; 2010.

Diffusion Kurtosis Imaging

21

Jelle Veraart and Jan Sijbers

Learning Points

- DKI extends the DTI model by quantifying the degree of non-Gaussian diffusion
- DKI is clinically feasible and relevant
- DKI is a mathematical model and, as such, the biophysical interpretation might be challenging

Diffusion Concepts

As stated in Chap. 3, any type of molecule in a fluid (e.g., water) is in constant random motion agitated by thermal energy. Given a large collection of molecules in an environment without boundaries, molecules undergo a random walk consisting of independent steps with a change of direction after each collision with another molecule. This motion is named after the botanist Robert Brown, who observed the everlasting jittery motion of grains of pollen suspended in water under a microscope [1]. The Brownian motion was theoretically substantiated by Einstein [2]. He showed that the random motion of numerous molecules can mathematically be described by a displacement probability distribution function (PDF). This mathematical concept is briefly introduced with a simple example (see Box 21.1).

Free Diffusion

Einstein showed that the displacement of water molecules in an open body of water such as a glass of water can be described by a Gaussian probability distribution function [2]. In the absence of flow—so the water must be still—the Gaussian distribution will be centered around zero. The distribution has zero mean. In addition to the mean, a distribution has another important property or *statistic*: the standard deviation. The standard deviation is a measure of the width of the distribution. Its square is called the variance. If the mean displacement is zero, then the variance equals the mean squared displacement $\langle x^2 \rangle$, which is linked to the diffusion coefficient D and the diffusion time t by the Einstein equation:

$$x^2 = 2nDt, \tag{1}$$

with n the dimensionality of the diffusion. The higher the mobility of the water molecules or the

J. Veraart, PhD (✉)
iMinds-Vision Lab, Department of Physics, University of Antwerp, Universiteitsplein 1, 2610, Antwerp, Belgium

Center for Biomedical Imaging, Department of Radiology, New York University School of Medicine, New York, USA
e-mail: Jelle.Veraart@uantwerpen.be

J. Sijbers, PhD
iMinds-Vision Lab, Department of Physics, University of Antwerp, Universiteitsplein 1, 2610, Antwerp, Belgium

W. Van Hecke et al. (eds.), *Diffusion Tensor Imaging*, DOI 10.1007/978-1-4939-3118-7_21

Box 21.1 Displacement PDF

If a fair dice is thrown, then it can fall six ways. When counting the different outcomes of throwing that dice many times, one will observe that any outcome is equally probable. A visual representation might help to grasp that the probability of throwing one is equal to the probability of throwing two, three, four, five, or six. A bar plot showing the different counts divided by the total number of throws is given in Fig. 21.1. This graph shows for each possible outcome the probability of being thrown during a single experiment. The mathematical relation between the possible outcomes (discrete or continuous) and the respective probabilities is called the probability distribution function (PDF). In case of a single dice, the PDF will be uniform because all outcomes are equally probable. Let us add another dice and repeat the experiment. Now, we count the sum of the eyes of both dice. Obviously, it is more likely to throw a seven than a two. Indeed, there are six combinations that will results in a seven, whereas only one combination gives two. All combinations are equally likely to be thrown. So, one might expect to count six times more sevens than twos. Hence, the PDF will no longer be uniform. Instead, it will be a bell-shaped distribution with its peak at seven. By adding more dice to the experiment, it will eventually become a Gaussian distribution. Knowing the PDF might be important as it allows predicting the outcome of an experiment with some probability.

Similarly, rather than counting eyes on dice, one can also measure the distance traveled by a molecule given a diffusion time.

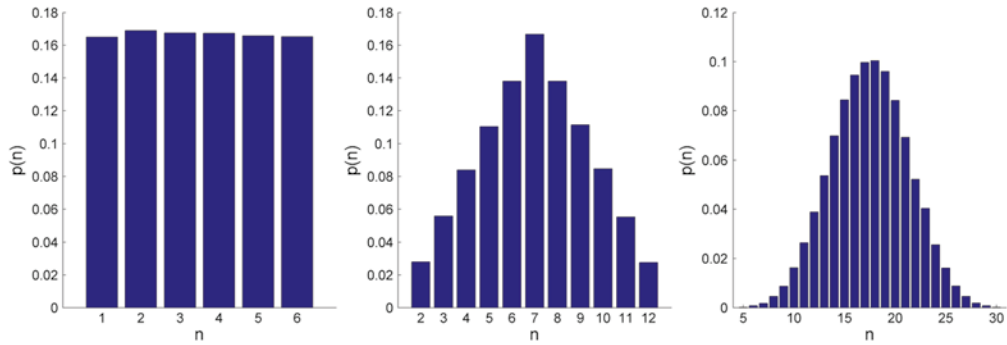

Fig. 21.1 (*Left–Middle–Right*) The probabilities of throwing n eyes with 1, 2, and 5 dice, respectively, are shown

longer the diffusion time, the wider the Gaussian distribution—or the greater the average traveled distance will be.

Hindered and Restricted Diffusion

Obviously a glass of water is a poor model to describe the diffusion in biological tissue. Given typical diffusion times in diffusion-weighted MRI—about 50–100 ms—free diffusion can only be expected in the cerebrospinal fluid in the large chambers of the ventricular system. However, biological tissues such as the brain white matter are highly heterogeneous media that consist of various individual compartments (e.g., intracellular, extracellular, neurons, glial cells, and axons) and barriers (e.g., cell membranes and myelin sheaths). Therefore, the random movement of water molecules is *hindered* and/or *restricted* by compartmental boundaries and other molecular obstacles (see Fig. 21.2). There is no doubt that molecules' mobility is reduced by their interactions with compartments and

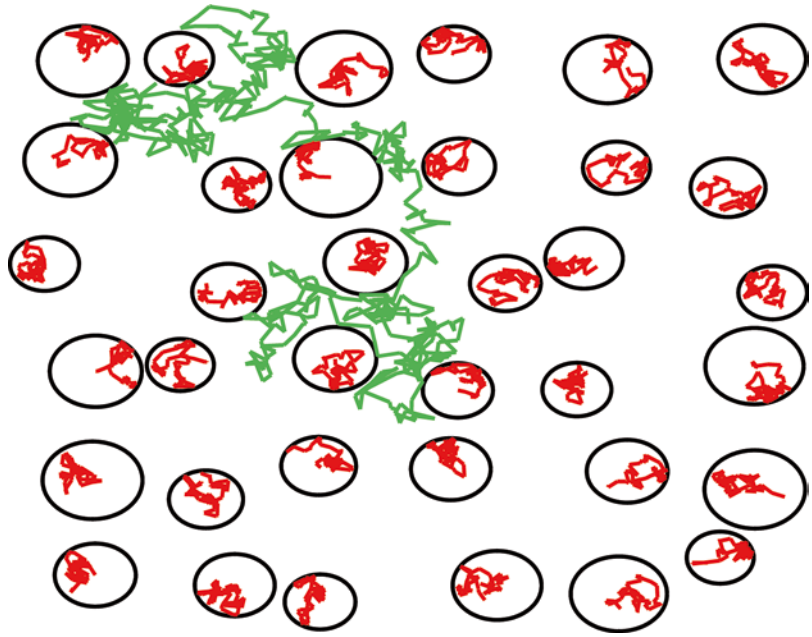

Fig. 21.2 Schematical representation of hindered (*green*) and restricted diffusion (*red*). The *black circles* represent impermeable boundaries

barriers. However, diffusion is only termed *restricted* if molecules that are confined in a bounding structure, which they are not likely to leave, collide with this structural boundary during the diffusion time. Typically, the diffusion of water molecules confined within the intra-axonal spaces is expected to be restricted. Indeed, given a diffusion time of 50 ms, a freely diffusing water molecule would displace on average 25 µm whereas the diameter of myelinated axons varies between 1 and 20 µm.

Like free diffusion, hindered diffusion can still be described by a Gaussian distribution. However, the width of the distribution will be smaller than one might expect based on properties of the tissue water itself. It is common to refer to the observed diffusion coefficient as the *apparent diffusion coefficient* (*ADC*; D_{app}) to indicate that the diffusion coefficient strongly depends on interactions of the diffusing molecules with the underlying microstructure, rather than on intrinsic diffusion properties [3]. Restricted diffusion, on the other hand, can no longer accurately be described by a Gaussian distribution [4–9]. Plotting the mean squared displacement as a function of the diffusion time

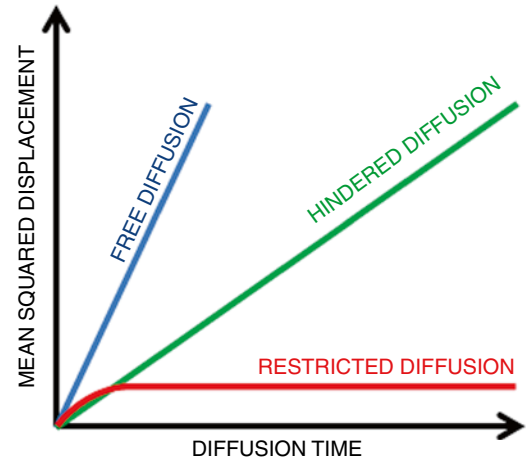

Fig. 21.3 Mean squares displacements are shown as a function of the diffusion time for free (*blue*), hindered (*green*), and restricted (*red*) diffusion

clearly indicates the difference between the different types of diffusion processes (see Fig. 21.3). In case of free and hindered diffusion, the mean squared displacement linearly increases with the diffusion time. The coefficient representing this linear relation is given by the diffusion coefficient, multiplied by $2n$, with n the dimension.

For free diffusion, the diffusion coefficient is larger than for hindered diffusion. Indeed, for the same diffusion time, hindered molecules will have displaced less than free diffusing molecules. For restricted diffusion, on the other hand, the mean squared displacement converges to an upper bound, which relates to the size of the bounding microstructure. Given the size of a typical diffusion-weighted MRI voxel (about $2\times2\times2$–$3\times3\times3$ mm^3), the biological tissue within a voxel is expected to contain a mixture of hindered and restricted compartments [10, 11]. Therefore, the primary assumption made in diffusion tensor imaging, i.e., Gaussian diffusion [12], does not hold in most voxels [13]. Hence, a more advanced diffusion model is required, that, apart from the diffusion coefficient, also describes the *deviation* from a Gaussian distribution. A distribution's deviation from a Gaussian distribution can be quantified by the excess kurtosis, hereafter shortened to kurtosis [14]. The knowledge of the kurtosis of the displacement distribution in addition to its variance improves the description of the underlying diffusion process [15]. In the next paragraph, the kurtosis of an arbitrary distribution is briefly introduced.

Kurtosis

The kurtosis K is a dimensionless statistical metric that quantifies the deviation from Gaussianity of an arbitrary distribution. In Fig. 21.4, a number of distributions that have the same mean (which is zero) and variance (which is one), but different kurtosis are shown. Indeed, the (excess) kurtosis varies from −1.2 to 3. One can observe that the kurtosis is a measure of peakedness or sharpness of an arbitrary distribution. Given that a Gaussian distribution has zero kurtosis, a positive kurtosis indicates that distribution is more peaked than a Gaussian distribution. In terms of diffusion, small displacements are more probable compared to hindered diffusion. A negative kurtosis, on the other hand, is less peaked than a Gaussian distribution. If the diffusion is described by such a distribution, small displacements are less likely compared to

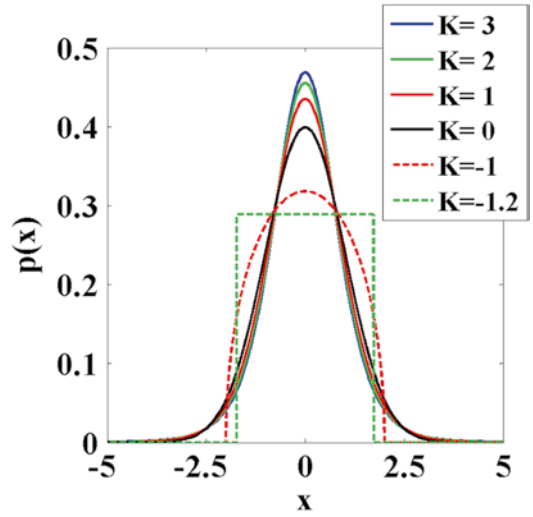

Fig. 21.4 Distributions with varying kurtosis, but with the same mean and variance are shown

Gaussian diffusion. For diffusion, a kurtosis of −3/7 is a practical minimum [15]. Such a distribution would indicate fully restricted diffusion within spherical pores with the same radius. However, fully restricted diffusion is not expected in biological tissue. As stated previously, one rather expects the imaged volume to consist of a mixture of hindered and restricted compartments [10, 11]. Therefore, it is generally assumed that the kurtosis will only take positive values in diffusion-weighted MRI [16].

It is clear that the knowledge of the kurtosis definitely contributes to a more accurate description of the underlying diffusion process. In the next section, it will be explained how kurtosis parameters can be computed from diffusion-weighted MR images.

Diffusion Kurtosis Coefficient

The natural logarithm of the diffusion weighted MR signal, S, can be approximated by an expansion in terms of the b-value [15]:

$$\log S(b) \approx \log S(0) - bD_{\text{app}} + \frac{1}{6} b^2 D_{\text{app}}^2 K_{\text{app}}, \qquad (2)$$

with $S(0)$ the nondiffusion-weighted signal, D_{app} the apparent diffusion coefficient and K_{app} the

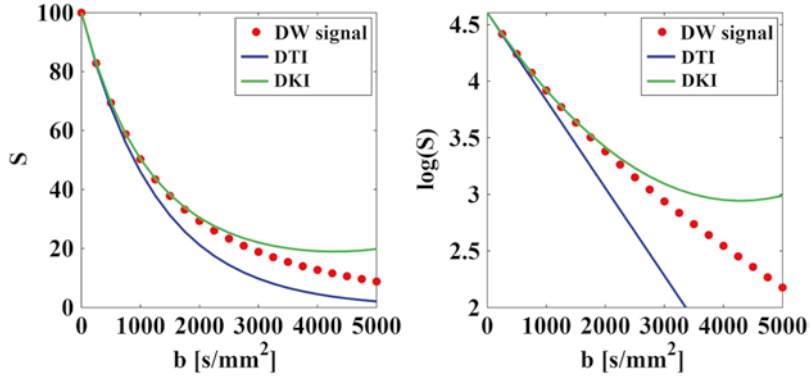

Fig. 21.5 Following diffusion-weighted signals (*left*), as well as their log-transformation (*right*) are shown as a function of the *b*-value: measured values (*red dots*), DTI model (*blue*), and DKI model (*green*). Owing to the non-Gaussian diffusion the addition of the b^2-term improves the accuracy of the fit. This is mainly noticeable at intermediate *b*-values. At high *b*-values, severe approximation errors become dominant. Therefore, DKI is a low to intermediate *b*-value technique

apparent kurtosis coefficient. Note that the term *apparent kurtosis coefficient* is used in analogy to the apparent diffusion coefficient to indicate the dependency of the measured parameter to measurement variables such as diffusion time. If diffusion is assumed to be Gaussian, or equivalently, to have zero kurtosis, then the last term nullifies and the equation reduces to the basic DTI formula [12]. Note that the additional kurtosis term depends on *b* squared. Hence, unlike Gaussian diffusion, the logtransformed diffusion-weighted signal will not decay linearly with the *b*-value (Fig. 21.5). Alternatively, one can say that the diffusion-weighted signal will decay non-monoexponentially. Just as D_{app} characterizes the diffusion coefficient in the direction parallel to the orientation of diffusion sensitizing gradients, K_{app} characterizes the diffusional kurtosis in the same direction.

Diffusion Kurtosis Tensor

In the brain white matter, molecular diffusion is more likely to be hindered and restricted perpendicular to the axonal fibers than parallel to them because of the geometry of the underlying microstructure [17, 18]. Therefore, the diffusion is anisotropic and, as such, the diffusion cannot be described adequately by a single diffusion and kurtosis coefficient. Indeed, to accurately model hindered diffusion, a three-dimensional (3D) Gaussian diffusion model that relies on a second order, symmetric diffusion tensor $\boldsymbol{D}$, instead of the scalar D_{app}, is needed [19]. This widely used diffusion tensor imaging (DTI) model has six degrees of freedom, describing the shape and orientation of a 3D ellipsoid. Like the directional dependence of D_{app} can be captured by a diffusion tensor, the directional dependence of K_{app} can be represented by a tensor as well: the *diffusion kurtosis tensor* $\boldsymbol{W}$ [15, 20]. This fourth rank 3D tensor, which is fully symmetric, has only 15 components that are independent. The generalization of Eq. (2) to 3D results in:

$$\log S(b,\mathbf{g}) \approx \log S(0) - b\sum_{i=1}^{3}\sum_{j=1}^{3} g_i g_j D_{ij} + \frac{1}{6}b^2\left(\frac{1}{3}\sum_{i=1}^{3} D_{ii}\right)\sum_{i=1}^{3}\sum_{j=1}^{3}\sum_{k=1}^{3}\sum_{l=1}^{3} g_i g_j g_k g_l W_{ijkl}, \quad (3)$$

with $\mathbf{g} = [g_x, g_y, g_z]$ the applied diffusion gradient direction. One immediately recognizes the DTI model as being the first two terms on the right-hand side of Eq. (3) [19]. Fitting this model voxelwise to a set of diffusion MR images to estimate $\boldsymbol{D}$ and $\boldsymbol{W}$, and as such, directly quantifying the direction-dependent diffusion and kurtosis information, is called Diffusion Kurtosis Imaging

[15, 21, 22]. The technique is a straightforward mathematical extension of DTI as the cumulant expansion framework overarches both models [23]. Given both diffusional tensors, the apparent diffusion and kurtosis coefficients along an arbitrary direction can be evaluated to study the diffusion properties in any direction.

Diffusion Kurtosis Parameters

In DTI, the principle axes of the ellipsoidally shaped diffusion tensor and their corresponding lengths are determined by the eigenvectors and eigenvalues of the diffusion tensor $\boldsymbol{D}$ [19]. The first eigenvalue equals the diffusivity along the main direction of diffusion, and is called *axial diffusivity*. The average of the second and third eigenvalue is called the *radial diffusivity*. The measure quantifies the average diffusivity in the equatorial plane, i.e., the plane perpendicular to the principal diffusion direction. The average of all three eigenvalues is the *mean diffusivity*. Another rotationally invariant scalar measure is the *fractional anisotropy*. It quantifies the degree of anisotropy of the apparent diffusion tensor [12]. On the one hand, DKI provides a more objective and accurate quantification of these scalar metrics in the sense that the dependence of the estimated diffusivity b-value is eliminated or at least strongly reduced [13]. On the other hand, it provides additional rotationally invariant metrics of diffusional non-Gaussianity, complementary to the diffusion metric obtained with DTI [15].

The most commonly used kurtosis metrics are mean kurtosis, radial kurtosis, and axial kurtosis. The axial kurtosis is the evaluation of the apparent kurtosis tensor along the principle diffusion direction [24]. The radial kurtosis is the average apparent kurtosis coefficient, measured in the equatorial plane [25], whereas the mean kurtosis is the overall average apparent diffusion kurtosis coefficient [20]. Furthermore, a kurtosis anisotropy metric has been proposed [25]. The complementariness of the kurtosis and diffusion measures is indicated in the scatter plots of Fig. 21.6, which show the weak correlation between directional diffusion and kurtosis metrics, observed in the white matter of the healthy human brain (cf. [15]). This implies that two voxels with equal mean diffusivity not necessarily have the same mean kurtosis. As such, kurtosis measures provide additional information regarding the underlying diffusion process. Typical values of the DKI metrics for the healthy human brain are presented by Lätt et al. [26]. The parameter maps are shown in Fig. 21.7. The diffusion kurtosis metrics are potentially more sensitive to local (microstructural) tissue properties [15]. Furthermore, it has been shown that the diffusion kurtosis metrics are less sensitive to certain confounding effects and thereby serve as a more robust biomarker. One study, for example,

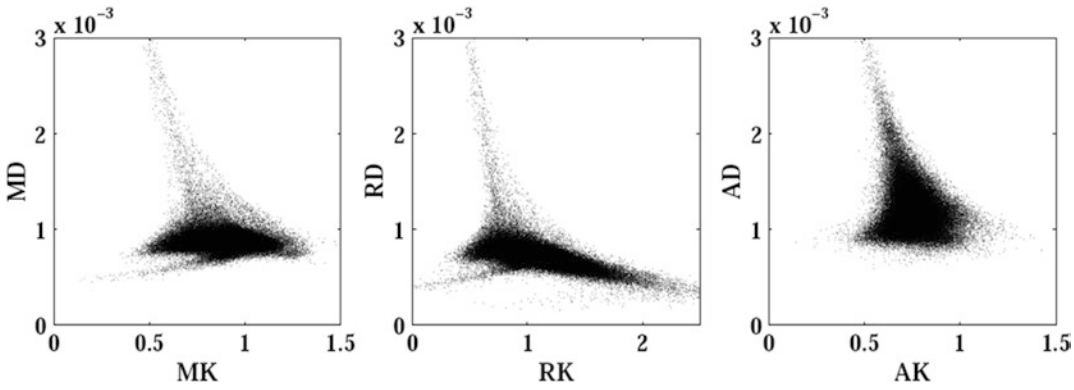

Fig. 21.6 Scatter plots show the correlation between (*left*) mean kurtosis and mean diffusivity, (*middle*) radial kurtosis and radial diffusivity, and (*right*) axial kurtosis and axial diffusivity. The corresponding metrics are only weakly correlated. The Spearman's rank correlation coefficients are –0.07, –0.65, and –0.13, respectively

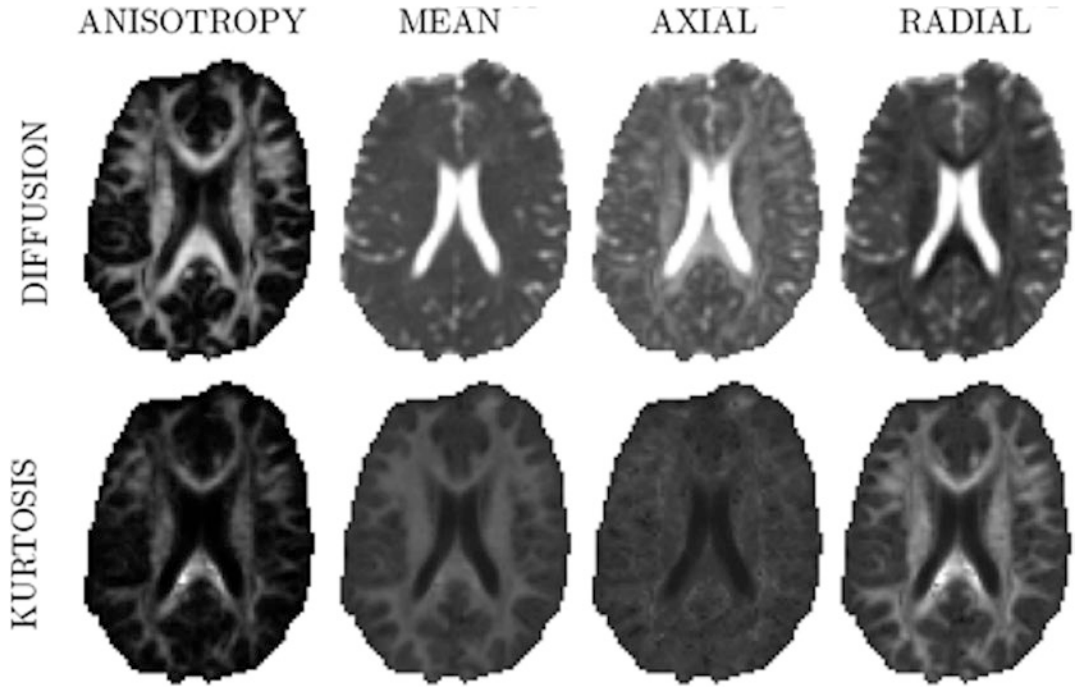

Fig. 21.7 The main diffusion and kurtosis parameter maps, obtained from the healthy human brain, are shown. The range of the mean, axial and radial diffusivity is [0, 3×10^{-3}] mm^2/s, while the range of the corresponding kurtosis metrics was [0, 1.5]. The anisotropy maps are bounded by [0, 1]

showed that the mean kurtosis in gray matter is altered substantially less by CSF contamination than either of the conventional DTI metrics [27].

Diffusion Kurtosis Imaging: Acquisition

DKI is a straightforward extension of DTI in terms of data acquisition. Indeed, the same diffusion-weighted imaging sequences can be used to record the images. However, since the apparent diffusion tensor has 6 independent elements and the kurtosis tensor has 15 independent elements, the DKI model has a total of 21 independent tensor parameters. As for DTI, the noise-free nondiffusion-weighted signal must be estimated as well. Hence, at least 22 diffusion-weighted images need to be acquired for DKI. Let us recall that for DTI only seven diffusion-weighted images were required. It can further be shown that there must be at least three distinct b-values, which only differ in the magnitude of the applied diffusion gradient. Typically, the highest b-value is somewhat higher than in DTI acquisitions. Indeed, the maximal b-value should be chosen carefully as it defines a trade-off between the accuracy and precision of diffusion parameter estimators. While for DTI diffusion-weighted images are typically acquired with rather low b-values, about 1000 s/mm^2, somewhat stronger diffusion sensitizing gradients need to be applied for DKI as the quadratic term in the b-value needs to be apparent. It has been shown that b-values of about 2000 s/mm^2 are sufficient to measure the degree of non-Gaussianity with an acceptable precision [21]. Nevertheless, several studies reported b-values up to 3000 s/mm^2 and even more (e.g., [28, 29]). The assumption that the diffusion-weighted signal is monotonically decreasing with the b-value imposes an analytical upper bound on the maximal b-value [30]:

$$b_{\max} \leq 3 / (D_{\text{app}} K_{\text{app}}). \quad (4)$$

Indeed, as can be seen in Fig. 21.5, the DKI model has a global minimum at $b = b_{\max}$. For

larger b-values the diffusion-weighted signals predicted by the DKI model start increasing again. This is in disagreement with the assumption that the diffusion-weighted signals keep decaying with increasing b-value. Therefore, the DKI model is only accurate in a limited b-value range. The upper bound of that range is difficult to determine. However, typical diffusion and kurtosis values, observed in the human brain, are $D_{\text{app}} \approx 1\ \mu\text{m}^2/\text{ms}$ and $K_{\text{app}} \approx 1$. Those values justify the use of b-values up to 3000 s/mm^2 for studies involving the human brain [21]. Given the limited maximal gradient magnitude, such b-values are often achieved by increasing the gradient duration. As the correctness of the DKI model relies on the short gradient pulse (SGP) condition, the use of high b-values will render the measured apparent kurtosis metrics more approximate [15]. Furthermore, high b-valued diffusion-weighted images suffer from low signal-to-noise ratio (SNR) due to the severe signal attenuation. Since SNR has a direct impact on the precision of the diffusion quantification, the acquisition of diffusion MR images along more diffusion directions than strictly necessary is advisable. Although in theory only 15 distinct diffusion (gradient) directions are required [15], in practice, a minimum of 30 directions for each b-value is fairly common [21]. A wide range of DKI data acquisition protocols in line with these considerations are possible. Depending on the set of diffusion parameters one is interested in, a specific acquisition protocol (i.e. b-values and gradient directions) that is optimal in terms of highest achievable precision on the measurements of interest can be computed [25]. In Table 21.1, the minimal acquisition requirements for DKI are listed and compared to DTI.

Table 21.1 Minimal acquisition requirements for DTI and DKI

	DTI	DKI
Number of diffusion-weighted images	7	22
Number of b-values	2	3
b-value range (s/mm^2)	[0–1500]	[0–3000]
Noncoplanar gradient directions	6	15

Diffusion Kurtosis Imaging: Post Processing

In general, data correction is the first step of the diffusion MR data post-processing pipeline. First, the relatively long acquisition times cause *subject motion* to become more probable, and, as such, neccessitate the alignment of all diffusion-weighted images before the model parameters are estimated [31]. Commonly, such a correction is applied by a single rigid transformation of the diffusion-weighted images to a single reference image, often a nondiffusion-weighted image. The use of a rigid transformation is motivated by the expected lack of scaling and shearing of the volumes, whereas translations and rotations are assumed to be global for brain imaging. However, note that other diffusion applications might require more complex motion correction strategies. To preserve the orientation information captured in diffusion MR data, the diffusion gradient directions need to be rotated accordingly [32]. Second, rapidly switching diffusion gradients will generate *eddy currents* in nearby conductors. These currents will perturb the spatial encoding locally and, as such, the reconstructed diffusion-weighted image will be geometrically distorted [33]. The strength of the distortions—stretch or compression of the image along the phase encoding direction—increases with the diffusion encoding amplitude. Although the effect of eddy currents can be minimized at the acquisition stage [34], residual distortions still need correction. A common strategy is to correct subject motion and eddy current distortions simultaneously by a global affine transformation. Recently, several techniques dedicated to motion/eddy current correction of high b-valued diffusion-weighted images have been presented [35, 36]. Such corrections need to be followed by signal modulation according to the volumetric change [37, 38]. The signal modulation factor will be b-value dependent as the strength of the distortions depends on the magnitude of the diffusion-encoding gradient. Not correcting such a b-value dependent signal change will bias the kurtosis parameters [13, 39]. Nonetheless, the signal modulation step is widely ignored, partly

motivated by a lack of this post-processing step in most software packages.

After data correction—and optional local smoothing to reduce the Gibbs phenomena—the DKI model parameters, i.e., the tensor elements, need to be estimated. The most popular strategies are nonlinear least squares (NLS), weighted linear least squares (WLLS), and linear least squares (LLS). Technical details on the implementation of these methods are provided in [40, 41]. It is important to grasp that not all estimation strategies show the same performance in terms of accuracy and precision [37, 38, 41]. Typically, the WLLS estimator might be preferred to the other estimators [41]. First, within the class of linearized strategies, the WLLS estimator is definitely the better choice as it accounts for the signal dependency of the variance in the log-transformed diffusion-weighted data [42]. Therefore, the WLLS estimator will show higher precision than the LLS estimator. Second, the WLLS estimator is potentially very accurate, especially compared to the NLS estimator. Indeed, if Rician distributed diffusion-weighted MR data has a minimum SNR of two, then the WLLS estimator is unbiased, that is, the estimator has no systematic estimation error [41]. Third, the WLLS estimator has a closed-form solution. Therefore, unlike the iterative NLS strategy, the WLLS estimator is computationally efficient and not prone to getting stuck in a local optimum. In practice, however, the SNR might drop below 2 because of high b-values or high spatial resolutions. In that case, the above-mentioned estimators will show a systematic overestimation of the kurtosis parameters and, as such, one might prefer using more advanced estimators that explicitly account for the actual MR data distribution [38, 39]. An overview of these estimators, their strengths, and limitations is beyond the scope of this introductory chapter.

As the diffusion of water molecules is a physical property of the tissue being measured, diffusional tensor estimates must be physically and biologically meaningful. Unfortunately, in many cases, diffusion and kurtosis values might lie outside a physically acceptable range due to the presence of noise, imaging artifacts such as Gibbs ringing, or misalignment of the diffusion-weighted images [40]. It is well known that the diffusivity should be positive along all directions. This condition holds if the apparent diffusion tensor is positive definite. In DTI, one often imposes the non-negative definiteness constraint on the diffusion tensor [43]. The same constraint can be imposed during a DKI analysis. In addition, two constraints on the apparent kurtosis coefficients might be imposed. First, while the theoretical lower bound on the kurtosis of a probability distribution is minus two, previous studies suggest that directional kurtoses should typically be positive [16, 40]. Second, an upper bound on the kurtosis that depends on the maximal b-value, cf. Eq. (4), is often imposed during the estimation of the DKI parameters.

Diffusion Kurtosis Imaging: Applications

Despite DKI being a recently developed technique, an exponential growth of publications already suggests that DKI will become a new important imaging modality in detecting microstructural changes in human living tissue that are not revealed by the Gaussian DTI model. Preliminary, yet promising results have shown that DKI measures may be able to better differentiate between high-grade and low-grade cerebral gliomas than DTI measures alone [44, 45]. Furthermore, clinical studies indicate that DKI has the potential to improve the early diagnosis of, or to gain more insight into pathologies such as Parkinson Disease [29, 46], attention-deficit hyperactivity disorder [47], temporal lobe epilepsy [48], traumatic brain [49], Alzheimer's disease [50], and cerebral infarction [51–53]. However, its potential use is not restricted to the brain. The greater relative contrast of kurtosis metrics for cancerous sextants also suggests the potential clinical advantage of incorporating DKI into liver and prostate MR imaging protocol [54, 55]. Additionally, one study has reported on the sensitivity of the DKI metrics to abnormalities in the lung, i.e., within the bronchioles and bronchi, using hyperpolarized ^{3}HE imaging [56].

Furthermore, microstructural changes associated with human development and aging have been studied with DKI [57]. This study showed different mean kurtosis patterns for different age ranges, indicating that DKI is able to detect changes in microstructural complexity in both gray and white matter. In complementary research, the practical utility of DKI for the (early) diagnosis of pathological changes has been studied using small animal imaging. For example, it has been shown that DKI improved the early detection of ischaemic lesions in a stroke model for rats, compared to DTI [28]. Moreover, DKI may help stratify heterogeneous diffusion-weighted MRI lesions for enhanced characterization of ischemic tissue injury [58]. Studies have also reported on the increased sensitivity of kurtosis metrics to changes in the white and gray matter in rodent models of Huntington Disease [59, 60], Chronicle mild stress [61], Alzheimer's disease [62], traumatic brain injury [63], and brain maturation [64]. It might be expected that many new potential applications of DKI will be revealed in the near future.

Diffusion Kurtosis Imaging: Limitations

The potential risk of DKI—just as DTI—is the over-interpretation of observed changes in diffusional measures. The kurtosis model arises simply from a mathematical expansion of the diffusion-weighted signal as a function of the *b*-value and, as such, does not involve any biophysical modeling [16, 65, 66]. From a change in kurtosis or diffusivity, one might only conclude that there is *something* in the tissue microstructure that is changing the way that molecules can diffuse. More specific inferences are not substantiated without the justification of a biophysical model that helps to interpret the biophysical meaning of DKI metric changes. Recently, the two-tensor model has been studied to elucidate the underpinnings of DKI contrast [65, 67]. In that model, it is assumed that brain white matter consists of two non-exchanging compartments: an intra-axonal space, consisting of parallel impermeable cylindrical axons and an extra-axonal space. The diffusion in both compartments is assumed to be anisotropic and Gaussian. The white matter model links the DKI metrics to microstructural properties such as the axonal water fraction and the tortuosity of the extra-axonal space. In another attempt to gain insight in the mathematical DKI model, the DKI information was matched to the information extracted from the biophysical *composite hindered and restricted model of diffusion* (*CHARMED*)model [10, 11, 16]. In that model, the white matter is again assumed to be consisting of two compartments: (a) a hindered extra-axonal space, and (b) one or more intra-axonal compartments modeled as impermeable cylinders showing restricted diffusion perpendicular to the fiber. The CHARMED model allows the description of the diffusion weighted-signals in terms of biophysical parameters such as extra- and intra-axonal volume fractions and axonal diffusivities. It was shown that those biophysical parameters correlate with the DKI parameters in areas of higher intra-voxel directional coherence, and as such, the CHARMED model might be used the get more insight into the meaning of the DKI parameters [16]. Those findings, however, only apply within the limits of the validity of both white matter models.

References

1. Brown R. A brief account of microscopical observations made in the months of June, July and August, 1827, on the particles contained in the pollen of plants; and on the general existence of active molecules in organic and inorganic bodies. Philos Mag. 1828;4:161–1763.
2. Einstein A. Über die von der molekularkinetischen Theorie der Wärme geforderte Bewegung von in ruhenden Flüssigkeiten suspendierten Teilchen. Ann Phys. 1905;322(8):549–60.
3. Le Bihan D, et al. MR imaging of intravoxel incoherent motions: application to diffusion and perfusion in neurologic disorders. Radiology. 1986;161(2):401–7.
4. Assaf Y, et al. Non-mono-exponential attenuation of water and N-Acetyl aspartate signals due to diffusion in brain tissue. J Magn Reson. 1998;131(1):69–85.

5. Beaulieu C, et al. Determinants of anisotropic water diffusion in nerves. Magn Reson Med. 1994;31(4): 394–400.
6. King MD, et al. q-space imaging of the brain. Magn Reson Med. 1994;32(6):707–13.
7. Niendorf T, et al. Biexponential diffusion attenuation in various states of brain tissue: implications for diffusion-weighted imaging. Magn Reson Med. 1996;36(6):847–57.
8. Stanisz GJ, et al. An analytical model of restricted diffusion in bovine optic nerve. Magn Reson Med. 1997;37(1):103–11.
9. Stanisz GJ, et al. Diffusional anisotropy of T2 components in bovine optic nerve. Magn Reson Med. 1998;40(3):405–10.
10. Assaf Y, et al. New modeling and experimental framework to characterize hindered and restricted water diffusion in brain white matter. Magn Reson Med. 2004;52(5):965–78.
11. Assaf Y, et al. Composite hindered and restricted model of diffusion (CHARMED) MR imaging of the human brain. Neuroimage. 2005;27(1):48–58.
12. Basser PJ. Inferring microstructural features and the physiological state of tissues from diffusion-weighted images. NMR Biomed. 1995;8(7-8):333–4.
13. Veraart J, et al. More accurate estimation of diffusion tensor parameters using diffusion Kurtosis imaging. Magn Reson Med. 2011;65(1):138–45.
14. Balanda KP, MacGillivray HL, et al. Kurtosis: a critical review. Am Stat. 1988;42(2):111–9.
15. Jensen JH, et al. Diffusional kurtosis imaging: the quantification of non-gaussian water diffusion by means of magnetic resonance imaging. Magn Reson Med. 2005;53(6):1432–40.
16. De Santis S, et al. Using the biophysical CHARMED model to elucidate the underpinnings of contrast in diffusional kurtosis analysis of diffusion-weighted MRI. MAGMA. 2012;25(4):267–76.
17. Chenevert TL, et al. Anisotropic diffusion in human white matter: demonstration with MR techniques in vivo. Radiology. 1990;177(2):401–5.
18. Moseley ME, et al. Anisotropy in diffusion-weighted MRI. Magn Reson Med. 1991;19(2):321–6.
19. Basser PJ, et al. MR diffusion tensor spectroscopy and imaging. Biophys J. 1994;66(1):259–67.
20. Lu H, et al. Three-dimensional characterization of non-gaussian water diffusion in humans using diffusion kurtosis imaging. NMR Biomed. 2006;19(2): 236–47.
21. Jensen JH, et al. MRI quantification of non-Gaussian water diffusion by kurtosis analysis. NMR Biomed. 2010;23(7):698–710.
22. Wu EX, et al. MR diffusion kurtosis imaging for neural tissue characterization. NMR Biomed. 2010;23(7): 838–48.
23. Kiselev VG. The cumulant expansion: an overarching framework for understanding diffusion MRI. In: Jones DK, editor. Diffusion MRI: theory, methods and applications. Oxford: Oxford University Press; 2010. p. 152–68.
24. Hui ES, et al. Towards better MR characterization of neural tissues using directional diffusion kurtosis analysis. Neuroimage. 2008;42(1):122–34.
25. Poot DHJ, et al. Optimal experimental design for diffusion kurtosis imaging. IEEE Trans Med Imaging. 2010;29(3):819–29.
26. Lätt J, et al. Regional values of diffusional kurtosis estimates in the healthy brain. J Magn Reson Imaging. 2013;37(3):610–8.
27. Yang AW, et al. Effect of cerebral spinal fluid suppression for diffusional kurtosis imaging. J Magn Reson Imaging. 2013;37(2):365–71.
28. Grinberg F, et al. Diffusion kurtosis imaging and log-normal distribution function imaging enhance the visualisation of lesions in animal stroke models. NMR Biomed. 2012;25(11):1295–304.
29. Wang J-J, et al. Parkinson disease: diagnostic utility of diffusion kurtosis imaging. Radiology. 2011;261(1): 210–7.
30. Lazar M, et al. Estimation of the orientation distribution function from diffusional kurtosis imaging. Magn Reson Med. 2008;60(4):774–81.
31. Jenkinson M, et al. A global optimisation method for robust affine registration of brain images. Med Image Anal. 2001;5(2):143–56.
32. Leemans A, et al. The B-matrix must be rotated when correcting for subject motion in DTI data. Magn Reson Med. 2009;61(6):1336–49.
33. Horsfield M. Mapping eddy current induced fields for the correction of diffusion-weighted echo planar images. Magn Reson Imaging. 1999;17(9):1335–45.
34. Reese TG, et al. Reduction of eddy-current-induced distortion in diffusion MRI using a twice-refocused spin echo. Magn Reson Med. 2003;49(1):177–82.
35. Andersson J et al. 2012. A comprehensive Gaussian process framework for correcting distortions and movements in diffusion images. In Proceedings of the international society for Magnetic Resonance in Medicine, p. 2426
36. Ben-Amitay S, et al. Motion correction and registration of high b-value diffusion weighted images. Magn Reson Med. 2012;67(6):1694–702.
37. Jones DK, et al. Twenty-five pitfalls in the analysis of diffusion MRI data. NMR Biomed. 2010;23(7): 803–20.
38. Veraart J, et al. Comprehensive framework for accurate diffusion MRI parameter estimation. Magn Reson Med. 2013;81(4):972–84.
39. Veraart J, et al. Constrained maximum likelihood estimation of the diffusion kurtosis tensor using a Rician noise model. Magn Reson Med. 2011;66(3):678–86.
40. Tabesh A, et al. Estimation of tensors and tensor-derived measures in diffusional kurtosis imaging. Magn Reson Med. 2011;65(3):823–36.
41. Veraart J, et al. Weighted linear least squares estimation of diffusion MRI parameters: strengths, limitations, and pitfalls. Neuroimage. 2013;81:335–46.
42. Salvador R, et al. Formal characterization and extension of the linearized diffusion tensor model. Hum Brain Mapp. 2005;24(2):144–55.

43. Koay CG, et al. A unifying theoretical and algorithmic framework for least squares methods of estimation in diffusion tensor imaging. J Magn Reson. 2006;182(1):115–25.
44. Van Cauter S, et al. Gliomas: diffusion kurtosis MR imaging in grading. Radiology. 2012;263(2):492–501.
45. Raab P, et al. Cerebral gliomas: diffusional kurtosis imaging analysis of microstructural differences. Radiology. 2010;254(3):876–81.
46. Giannelli M, et al. Diffusion kurtosis and diffusion-tensor MR imaging in Parkinson disease. Radiology. 2012;265(2):645–6. author reply 646–7.
47. Helpern J, et al. Preliminary evidence of altered gray and white matter microstructural development in the frontal lobe of adolescents with attention-deficit hyperactivity disorder: a diffusional kurtosis imaging study. J Magn Reson Imaging. 2011;33(1):17–23.
48. Gao Y, et al. Diffusion abnormalities in temporal lobes of children with temporal lobe epilepsy: a preliminary diffusional kurtosis imaging study and comparison with diffusion tensor imaging. NMR Biomed. 2012;25(12):1369–77.
49. Grossman EJ, et al. Thalamus and cognitive impairment in mild traumatic brain injury: a diffusional kurtosis imaging study. J Neurotrauma. 2012;29(13):2318–27.
50. Gong N-J, et al. Correlations between microstructural alterations and severity of cognitive deficiency in Alzheimer's disease and mild cognitive impairment: a diffusional kurtosis imaging study. Magn Reson Imaging. 2013;31(5):688–94.
51. Jensen JH, et al. Preliminary observations of increased diffusional kurtosis in human brain following recent cerebral infarction. NMR Biomed. 2011;24(5): 452–7.
52. Hori M, et al. A new diffusion metric, diffusion kurtosis imaging, used in the serial examination of a patient with stroke. Acta Radiol Short Rep. 2012;1(12):1–3.
53. Hui ES, et al. Stroke assessment with diffusional kurtosis imaging. Stroke. 2012;43(11):2968–73.
54. Rosenkrantz AB, et al. Assessment of hepatocellular carcinoma using apparent diffusion coefficient and diffusion kurtosis indices: preliminary experience in fresh liver explants. Magn Reson Imaging. 2012; 30(10):1534–40.
55. Rosenkrantz AB, et al. Prostate cancer: feasibility and preliminary experience of a diffusional kurtosis model for detection and assessment of aggressiveness of peripheral zone cancer. Radiology. 2012;264(1): 126–35.
56. Trampel R, et al. Diffusional kurtosis imaging in the lung using hyperpolarized 3He. Magn Reson Med. 2006;56(4):733–7.
57. Falangola MF, et al. Age-related non-gaussian diffusion patterns in the prefrontal brain. J Magn Reson Imaging. 2008;28(6):1345–50.
58. Cheung JS, et al. Stratification of heterogeneous diffusion MRI ischemic lesion with kurtosis imaging: evaluation of mean diffusion and kurtosis MRI mismatch in an animal model of transient focal ischemia. Stroke. 2012;43(8):2252–4.
59. Blockx I, et al. Identification and characterization of Huntington related pathology: an in vivo DKI imaging study. Neuroimage. 2012;63(2):653–62.
60. Blockx I, et al. Microstructural changes observed with DKI in a transgenic Huntington rat model: evidence for abnormal neurodevelopment. Neuroimage. 2012;59(2):957–67.
61. Delgado y Palacios R, et al. Magnetic resonance imaging and spectroscopy reveal differential hippocampal changes in anhedonic and resilient subtypes of the chronic mild stress rat model. Biol Psychiatry. 2011;70(5):449–57.
62. Zhang L, et al. Current neuroimaging techniques in Alzheimer's disease and applications in animal models. Am J Nucl Med Mol Imaging. 2012;2(3): 386–404.
63. Zhuo J, et al. Diffusion kurtosis as an in vivo imaging marker for reactive astrogliosis in traumatic brain injury. Neuroimage. 2012;59(1):467–77.
64. Cheung MM, et al. Does diffusion kurtosis imaging lead to better neural tissue characterization? A rodent brain maturation study. Neuroimage. 2009;45(2): 386–92.
65. Fieremans E, et al. White matter characterization with diffusional kurtosis imaging. Neuroimage. 2011;58(1): 177–88.
66. Nilsson M, et al. The role of tissue microstructure and water exchange in biophysical modelling of diffusion in white matter. MAGMA. 2013;26(4):345–70.
67. Fieremans E, et al. Monte Carlo study of a two-compartment exchange model of diffusion. NMR Biomed. 2010;23(7):711–24.

Acknowledgements

The editors would like to extend their gratitude to the following authors for providing additional glossary contributions to this chapter: (in alphabetical order) Mattan Caan, Thijs Dhollander, Eric Peterson, Matthew Rowe, Jacques-Donald Tournier, Jelle Veraart, and Sjoerd B Vos.

W. Van Hecke et al. (eds.), *Diffusion Tensor Imaging*, DOI 10.1007/978-1-4939-3118-7

Glossary

Louise Emsell and Wim Van Hecke

The language of DTI is complex and sometimes ill-defined. The following glossary has been assembled by the editors based on a selection of key terms provided by the contributing authors to this book as a guide to understanding some key terms related to DTI. Please note that in the absence of standard terminology, some words or phrases may be defined differently in other sources.

Angular resolution The power to unambiguously resolve closely aligned directions, much like spatial resolution relates to the ability to resolve closely spaced points. May also be used to refer to the density of DW sampling over the sphere in a HARDI acquisition.

Anisotropic diffusion Diffusion of atoms or molecules, which is dependent on orientation—i.e., the rate of diffusion is different for different directions.

Apparent diffusion coefficient The measured diffusion coefficient for water in a medium in which diffusion is not free as it is impeded by boundaries such as cellular structures. The water behaves more like a viscous fluid with a lower diffusion coefficient.

Apparent fiber density A framework for the analysis of diffusion MRI data, which relies on estimates of the fiber ODF as obtained from spherical deconvolution methods and interprets the amplitude of the fiber ODF as approximately proportional to the density of the fibers aligned with the corresponding direction.

Association fibers White matter connections between gyri within one hemisphere.

Atlas A reference image constructed by coregistering and averaging multiple scans in order to create a representation of the image characteristics of a given study population. Atlases are used for image normalization. Standard atlases can be used to label regions-of- interest and to report research findings in a common reference space.

Automated tractography Tractography driven by atlases based on anatomical information, and requiring no user annotation.

Axial diffusivity (or longitudinal diffusivity) Equals the largest eigenvalue, and thus represents the ADC value along the main direction of diffusion. This is hypothesized to relate to the orientation of an axonal bundle in the tensor model.

Axial Kurtosis (AK, abbreviated form of *axial apparent kurtosis coefficient***)** The apparent kurtosis coefficient, measured along the principal direction of diffusion.

B0 (or B = 0) A term used to informally refer to a non diffusion weighted image, acquired as part of a full diffusion weighted imaging dataset.

***b*-value** A measure of the strength of the applied diffusion-weighting, and a function of the sequence timings and DW gradient amplitude. This is a generalization of the *q*-value, valid under the assumption of free diffusion.

Cardiac-gating Gating, or triggering the scanner to acquire data only during specific phases in the cardiac cycle in which pulsation (and thus pulsation artifacts) is at a minimum

Cartesian A common method of sampling *k*-space using a rectilinear or raster trajectory.

W. Van Hecke et al. (eds.), *Diffusion Tensor Imaging*, DOI 10.1007/978-1-4939-3118-7

Chemical shift artifact Different chemical species have different resonance frequencies. These differences lead to mismatches in the frequency (*k*-space) and spatial domain (image). For example, differences between water and fat molecules in the same physical location, manifest as image artifacts characterized by bright or dark rims shifted relative to this location.

Combined Hindered and Restricted Model of Diffusion A model for white matter as consisting of hindered axonal compartments and a hindered extra-axonal compartment. Can be used to extract information from DWI data given multi-shell HARDI data.

Commissural fibers White matter connections between both hemispheres.

Constant solid angle Q-ball imaging A method to estimate the diffusion ODF based on the theory of *q*-space, which provides a more meaningful diffusion ODF than the original QBI method.

Crossing fibers The situation whereby multiple white matter bundles cross, fan, bend, or kiss within a single voxel. Crossing fibers present considerable challenges to DTI because it can only model a single principle direction of diffusion.

Deterministic tractography Tractography based on the estimated average principal diffusion orientation (or eigenvector), resulting in one streamline per seed point.

Diffusion orientation density function A function on the sphere providing an estimate of the proportion of spins (e.g., water molecules) diffusing along any given orientation.

Diffusion orientation transform A method to estimate a diffusion ODF-like measure, based on the theory of *q*-space. The dODF differs in that it represents the proportion of spins (e.g., water molecules) that have diffused by a given absolute distance along any given orientation (rather than by any distance as it is typically defined).

Diffusion spectrum imaging A method to estimate the per-voxel average spin propagator, based on the theory of *q*-space. This is typically used to estimate the diffusion ODF by radial projection of the spin propagator.

Diffusion tensor (model) A 3×3 symmetric tensor (six unique parameters) representing the diffusion process in each voxel of a DTI image. The diffusion tensor "evaluated" along any direction to obtain ADC values as represented by that tensor.

Directionally encoded color (DEC) maps Maps that use RGB (red, green, blue) encoding to map directions. In DTI, red is typically associated with left-right, green with back-front and blue with bottom-top.

Displacement probability distribution function The mathematical function that expresses the probability that a molecule has displaced from point *a* to point *b* within a given period, i.e., the diffusion time.

Dual spin echo (DSE) See twice-refocused spin echo

Echo planar imaging (EPI) Rapid method of signal readout that acquires multiple lines of *k*-space after a single excitation without any refocusing RF pulses during the readout.

Eddy current-induced distortions Image distortions due to the presence of eddy currents. The image in usually warped in nonlinear fashion leading to skewing and shearing distortions that manifest as a bright rim around reconstructed images.

Eddy currents Electrical currents in the conducting materials in the scanner, induced by the changing magnetic field, and especially the large and fast-switching diffusion-weighting gradients.

Eigendecomposition The process of obtaining eigenvectors and eigenvalues of a tensor. Computer science provides reliable algorithms for this task.

Eigenvalues The ADC values of the tensor along the directions of the eigenvectors. They provide the complete information on the shape and size of a tensor, independently of its orientation.

Eigenvectors A new set of customized axes for a tensor, aligned along its specific orientation. They provide the complete information on the orientation of a tensor, independently of its size and shape.

Fast Spin Echo (FSE) An image acquisition sequence consisting of a single 90° excitation RF pulse followed by a train of 180° refocusing RF pulses, often called a *Carr-Purcell-Meiboom-Gill* (CPMG) pulse train. A less

widely used alternative to EPI, for DTI. FSE is slower but more robust to off-resonance distortions.

Fat suppression Nulling the signal from hydrogen atoms in fat to prevent chemical shift artifacts.

Fiber orientation density function A function on the sphere providing an estimate of the amount of fibers aligned along any given orientation.

Field map A map quantifying the deviation of the magnetic field from the desired B0-field (off-resonance). Can be used for unwarping.

Fractional anisotropy (FA) The standard deviation of the eigenvalues, divided by their root mean square. A measure of how much the eigenvalues differ, but carefully normalized so it becomes independent of their absolute magnitude. It quantifies how much the tensor deviates from representing isotropic diffusion. It has a range between zero and one—from perfect isotropy to perfect anisotropy.

Free diffusion Diffusion unimpeded by boundaries or obstacles, such as in the center of a glass of water.

Generalized fractional anisotropy A metric to characterize a diffusion or fiber ODF, given as the standard deviation of the ODF over its RMS value.

Geometric distortions Distortions in the image, causing a mismatch between the image and the geometry or anatomy of the object being scanned.

Gibbs ringing Steep intensity transitions in the image cannot be represented correctly in the *k*-space domain, resulting in artifactual ringing in the image around this transition

Global tractography A simultaneously global and local estimation of a pathway, driven by the data. Less affected by error propagation than classical deterministic or probabilistic approaches.

Grey matter One of the major tissue classes in the brain, consisting of the neuronal bodies (soma) and dendritic projections, as well as neuroglia.

HARDI High angular resolution diffusion imaging—a general type of diffusion-weighted MRI acquisition, whereby a relatively large number of diffusion-sensitizing gradients are applied along a set of uniformly distributed directions.

Hardware phantoms Physical phantoms that can be used to test the performance of diffusion MRI acquisition as well as processing.

Hindered diffusion Diffusion that is impeded by non-enclosing boundaries or obstacles, such that the rate of diffusion is reduced, but there is no limit on the maximum possible displacement of an atom or molecule.

Histogram analysis (DTI) A histogram is a frequency distribution that displays the number of voxels with a specific value of the diffusion measure (e.g., FA) obtained within an ROI (e.g., brain mask). From this histogram, the mean, median, peak height, and peak location can be extracted and compared statistically between groups.

In-plane motion Subject motion in the plane parallel to the slice-orientation

Interleaved acquisition Scan in which the slices are acquired in an interleaved fashion, e.g., first all the odd slices are acquired and then all the even slices (1, 3, 5, … 2, 4, 6, …).

Inter-slice instabilities A difference between the odd and even slices as a result of for example subject motion, during scanning of a single volume in an interleaved acquisition

Isotropic diffusion Diffusion of atoms or molecules that is orientationally invariant—i.e., the rate of diffusion is the same in every direction.

***k*-space** The spatial frequency spectrum of the MR image as acquired directly from the MRI scanner. A Fourier transform can be used to convert *k*-space to an image.

Kurtosis The kurtosis is a dimensionless statistical metric that quantifies the deviation from Gaussianity of an arbitrary distribution.

Linear least squares (LLS) A fitting method that is fast but not very accurate. It is perfectly suited to generate maps for qualitative use though.

Mean diffusivity (MD) The average of the three eigenvalues. Represents a rotationally invariant average ADC value for each voxel.

Mean Kurtosis (MK) The average apparent kurtosis coefficient

Multi-shell Referring to a diffusion MRI acquisition with more than one non-zero *b*-value.

Multi-shell HARDI An extension of the HARDI acquisition consisting of multiple HARDI acquisitions (shells) each its distinct *b*-value.

Multi-shot Refers to the acquisition of MRI data whereby segments of *k*-space are acquired with different excitations. In DTI, specialist multi-shot EPI techniques may reduce image artifacts at the expense of increased scan time and relatively complex post-processing.

Multi-tensor fitting A method for estimating the fiber orientations and partial volume fractions, based on a model of white matter whereby each fiber population is modeled by its own diffusion tensor.

Narrow pulse approximation The main assumption for the theory of *q*-space to be valid, whereby the duration of the DW gradient pulses is sufficiently short that motion of the spins during that time can be neglected.

Nonlinear least squares (NLS) A fitting method that solves the correctly formulated fitting problem in DTI. It requires a lot of computation time and resources though, and can still get stuck in local optima. The nonlinear search allows the incorporation of extra constraints, such as not allowing for tensors with negative eigenvalues.

Normalization (Image) The process of bringing images into a common reference space. See also, Registration.

Nyquist ghosting A copy of the image (the 'ghost') that is shifted by half a field-of-view in the phase-encoding direction, due to a miscalibration in the acquisition of EPI images.

Parallel Imaging A method of speeding up image acquisition and reducing off-resonance distortions in EPI by acquiring a reduced amount of *k*-space. Common approaches include GRAPPA and SENSE.

Partial Fourier A method of speeding up image acquisition by exploiting the symmetry of *k*-space. In partial-fourier techniques, only the lower frequencies and half the higher frequencies in *k*-space are sampled.

Persistent Angular Structure MRI A method for the estimation of the diffusion ODF, based on the theory of *q*-space. Relies on the approximation that all spins diffuse by the same fixed distance, coupled with a maximum entropy constraint.

Phase Fundamental property of the MRI signal, which is used in image generation. Unwanted/incorrect phase is the most common source of artifacts in EPI.

Physically implausible signals Signals that could not exist physically, i.e., signals in the diffusion-weighted scans that are higher than in the corresponding voxels of image without, or with a lower, diffusion-weighting.

Principal eigenvector The eigenvector associated to the largest eigenvalue. In voxels containing a single coherent bundle of axons, the principal eigenvector indicates the local orientation of the axon bundle.

Probabilistic tractography Tractography based on random sampling of the distribution of the diffusion orientation in each voxel, resulting in a tract probability map.

Projection fibers White matter connections between the cortex and lower brain areas, as well as the spinal cord.

Propagation of uncertainty Increased localization error in a computed tract based on the error in the orientation estimation of each individual voxel.

Pulsation Pulsation of the veins and ventricles as a result of cardiac pulsation. A source of physiological image artifacts that may be ameliorated using cardiac-gating during data acquisition.

Q-ball imaging A method to estimate the diffusion ODF, based on the theory of *q*-space. Relies on large *q*-values (cf. *b*-values) and the Funk-Radon transform to obtain an estimate of the radial projection of the average spin propagator from HARDI data.

***q*-space** A theory relating the DW signal measured over a range of different *q*-values to the Fourier transform of the average spin propagator. Forms the basis of all methods that estimate the diffusion ODF, and valid under the narrow pulse approximation.

Quality assurance Procedure to ensure and check data quality, including scanner performance, inspection of the DWIs, tensor fits, and any subsequent processing.

q-value, q-vector A measure of the strength of the applied diffusion-weighting, given as the product of the DW gradient pulse amplitude and its duration. The q-vector refers to the q-value combined with the direction along which the corresponding DW gradient is applied.

Radial diffusivity (or transverse diffusivity) Equals the average of the smallest two eigenvalues, and thus represents an average ADC for the directions perpendicular to the orientation of an axonal bundle.

Radial Kurtosis The average apparent kurtosis coefficient, measured in the plane perpendicular to the principal direction of diffusion.

Random walk A path constructed of a series of steps of random deviation, i.e., each step is random and independent of previous steps; the location of the path at any time step cannot be definitively predicted but only statistically described.

Real-time prospective motion correction The real-time adjustment of the scan parameters, including slice location and orientation, gradients, and readout to correct for subject motion.

Region-of-interest (ROI) An a priori selected area for investigation, which may be defined manually or using an automated approach (e.g., based on atlas-labels or tractography).

Registration (Image) The process whereby two images are brought into voxel level alignment. The target image is warped into the same "space" as the source or reference image based on different types of information in either or both images.

Residual The difference between the measured data and the values evaluated from a model fit to the data. A good fit would result in the residuals containing all the measurement noise as well as outliers caused by various artifacts.

Restricted diffusion Diffusion that is constrained by impermeable boundaries, such that the maximum possible displacement for a diffusing molecule has a strict limit in any direction, which impinges on the boundary.

Reverse polarity gradient method (RPGM) Acquires EPI images with opposite phase-encoding direction in order to perform image unwarping.

Robust estimation of tensors by outlier rejection (RESTORE) A nonlinear fitting method that can handle outliers (by detecting and rejecting them). It requires, on average, triple the computation time as compared to NLS. Data redundancy is also a requirement in order for a robust outlier detection, whilst ensuring enough data to work with after the outlier rejection.

ROI (see Region-of-Interest)

Rotationally invariant tensor based scalar measures or properties that are independent of tensor orientation, and thus describe aspects of its size or shape. Rotationally invariant tensor measures are typically calculated based on the eigenvalues.

Rotationally variant Dependent or influenced by the orientation of the tensor/microstructure relative to the diffusion-weighting gradient.

Seed point Single initiation point of tractography in one voxel. Practically, many seed points may be generated, e.g., in a cross-sectional slice.

Self-diffusion coefficient A measure of the freedom of movement of any single molecule of a certain substance, within the substance itself. The self-diffusion coefficient of water is about 2.2×10^{-3} mm^2/s at room temperature.

Shimming Adapting the magnetic field within the scanner to improve the field homogeneity

Signal dropout Artifacts where the signal is artificially low.

Signal-to-noise ratio (SNR) The ratio between the measured signal and the background noise

Single-Shot Refers to the acquisition of a whole 2D image in a single excitation. Single-shot EPI allows a full DTI dataset to be acquired in a very short amount of time compared to other approaches.

Slice dropout Artifacts where the signal in the entire slice is artificially low.

Smoothing (in VBA) The application of a (usually) Gaussian kernel to the image, which results in alteration of the voxel-wise metric values according to the full-width half maximum of the kernel (typically 3–8 mm). Used to increase signal-to-noise and reduce intra-subject variability.

Spherical deconvolution A method to estimate the fiber ODF, based on the assumption of a canonical fiber population with fixed diffusion properties.

Spin propagator A function giving the probability that a spin (e.g., a water molecule) initially at position x_0 will have move to x_1 during the diffusion time τ, i.e., $P(x_1|x_0,\tau)$. Also referred to as the displacement probability density function. In diffusion MRI, the quantity measured is typically the *average* spin propagator, the average probability that a spin chosen at random from within the voxel will have moved by a distance $\underline{r}$, i.e., $P(\underline{r}|\tau)$.

Streamline Virtual reconstruction of a single pathway through the diffusion field.

Subject motion Bulk motion of the imaged participant during scanning.

Susceptibility The degree of magnetization in response to a magnetic field. Susceptibility artifacts arise near the interfaces of matter with different magnetic susceptibility, e.g., air and tissue.

Susceptibility-induced distortions Image distortions due to field inhomogeneities that are especially present in EPI acquisitions

T2 shine-through A term referring to the fact that a DWI (not normalized) represents partially decayed T2 weighted signal. A high intensity in a DWI can thus also be caused by an originally high T2 intensity. To rule out this effect, DWIs should be normalized by a B0, or ADC maps should be used instead.

TBSS (see Tract-based spatial statistics)

Template A reference image constructed by coregistering and averaging multiple scans in order to create a representation of the image characteristics of a given study population. Templates are used for image normalization. Standard templates are often used to report research findings.

Tensor residuals The 'residual' of the diffusion-weighted signals after tensor estimation, i.e., the absolute average difference between signal and fit (see also, Residual).

Through-plane motion Subject motion in the direction perpendicular to the slice-orientation

Trace A measure of average diffusivity in a voxel, calculated by summing the three eigenvalues or the sum of the diagonal elements of the diffusion tensor.

Track Density Imaging A method for the reconstruction of high-resolution images based on the results of whole-brain fiber-tracking.

(Fiber) Tract Reconstructed pathway on millimeter scale in DWMRI data using a computer algorithm. Often confused with anatomical term "white matter fiber bundle."

Tract-based spatial statistics A popular type of voxel-based analysis that evaluates changes in a skeleton comprising a limited amount of white matter, in order to increase sensitivity by reducing registration error and partial volume effects.

Twice-refocused spin echo (TRSE) Diffusion preparation with two 180° refocusing pulses, designed to cancel eddy-currents

Unwarping Image processing methods to correct or reduce susceptibility-induced distortions.

VBA (see Voxel-based analysis)

Voxel-based analysis (DTI) An exploratory approach often used in group analysis to investigate voxel-wise alterations in DTI parameters in brain white matter. A VBA pipeline typically consists of an image normalization step, a smoothing step and statistics that control family-wise error. See also *TBSS*.

Weighted linear least squares (WLLS) A fitting method that is still fast yet more accurate than LLS. It accounts for the logarithmic transformation of the data (and the noise) up to some extent, but is confronted with a chicken-and-egg problem to tackle this issue.

Westin measures A set of metrics that characterize the geometric properties of the diffusion tensor, including linear (C_l), planar (C_p) and spherical (C_s) components.

White matter One of the major tissue classes in the brain, consisting of tightly packed, predominantly myelinated neuronal axons and associated neuroglia that link functional areas of the central nervous system.

White matter bundle Anatomical structure comprising ten thousands (and in some bundles, millions) of axons connecting distant mainly grey matter brain regions. Although this term includes anatomical structures with

"tract" in their anatomical name, e.g., corticospinal tract; it is not synonymous with virtually reconstructed "fiber tracts" or tracks.

Whole-brain tractography A tractography approach whereby streamlines are initiated locally in all voxels of the brain mask in order to reconstruct the entire image tractogram. May be confused with *Global tractography*, which is a different and unrelated technique.

Index

W. Van Hecke et al. (eds.), *Diffusion Tensor Imaging*, DOI 10.1007/978-1-4939-3118-7